

Tuning π -Conjugated Polymers with Heteroatoms: Synthesis of Polytellurophenes
and Soluble Polyacetylenes

by

Bruno T. Luppi

A thesis submitted in partial fulfillment of the requirements for the degree of

Doctor of Philosophy

Department of Chemistry
University of Alberta

© Bruno T. Luppi, 2021

Abstract

This Thesis describes the synthesis and investigation of π -conjugated oligomers and polymers with optoelectronic properties affected by the presence of a heteroatom. Two major classes of polymers are discussed: 1) polytellurophenes, where the backbone is formed by 5-membered heterocycles containing tellurium (Te), and 2) heteroatom (B, N, P)-appended polyacetylenes, where the polymer backbone consists of $-(HC=CH)-$ repeat units.

To begin, pinacolboronate (BPin)-functionalized tellurophenes with fused cycloalkane side group (5- or 6-membered rings) are transformed into new diiodinated tellurophene monomers to allow for homopolymerization through Yamamoto coupling. The size of the side group is found to drastically alter the HOMO-LUMO energy gap (E_g) of the resulting oligomers due to changes in backbone planarity. Density functional theory computations show that the effect is carried into copolymers with 3-alkylthiophenes, pointing at the tellurophene fused with the 5-membered ring as the best choice for planar backbones with extended π -conjugation.

Additionally, a 3-borylated tellurophene was used in a Suzuki-Miyaura cross-coupling protocol to synthesize a new tellurophene monomer containing a cumenyl ($-C_6H_4^iPr$) side chain. The corresponding poly(3-aryltellurophene) later obtained through Grignard metathesis (GRIM) polymerization shows a reduced HOMO-LUMO energy gap (E_g) when compared to the analogous polythiophene. The presence of aryl

(cumenyl) side chains further reduces E_g below the values reported for its poly(3-alkyltellurophene) counterparts.

Finally, a modified ring-opening metathesis polymerization (ROMP) protocol is used to prepare soluble functionalized polyacetylenes (PA) bearing: 1) electron-deficient boryl ($-BR_2$) and phosphoryl ($-P(O)R_2$) side chains, 2) electron-donating amino ($-NR_2$) groups, and 3) ring-fused 1,2,3-triazolium units via strain-promoted Click chemistry. Not only are most of these new functional polyacetylenes soluble in conventional organic solvents, allowing film formation via ubiquitous spin coating methods, they retain similar intense light absorption across much of the visible spectral region as parent polyacetylene. Some of the resulting polyacetylenes also show greatly enhanced stability in air when compared to parent polyacetylene. Furthermore, placement of redox-active boryl and amino groups directly onto a polyacetylene backbone leads to switchable near-IR optical responses in the telecommunications range (ca. 1500 nm) upon chemical reduction or oxidation. A general route to cross-linked networks is also presented, and is based on the reduction of the polyacetylenes in solution.

Preface

Portions of the work discussed in this Thesis were complete in collaboration with researchers from the Rivard group, as well as with others in the Department of Chemistry (University of Alberta) and researchers outside of the University of Alberta.

All X-ray crystallographic studies described in this Thesis were performed by Dr. M. J. Ferguson or Dr. R. McDonald, including the mounting of crystals, diffractometer operation, data collection, structure refinement, and the preparation of crystallographic data tables. Elemental analyses, thermal analyses and Fourier-transform infrared spectroscopy were performed by the Analytical Instrument Laboratory at the Department of Chemistry, University of Alberta. Mass spectrometry analyses were performed at the Mass Spectrometry Laboratory at the Department of Chemistry, University of Alberta.

The computational studies in this Thesis were made possible by the facilities of the Shared Hierarchical Academic Computing Network (SHARCNET: www.sharcnet.ca), WestGrid (www.westgrid.ca), and Compute Canada (www.computecanada.ca). The work in this Thesis was supported by the Natural Sciences and Engineering Research Council of Canada, the Canada Foundation for Innovation, and the Faculty of Science at the University of Alberta.

In Chapter 2, cyclic voltammetry studies were guided by Prof. L. Sang (University of Alberta). Valuable input and assistance were also provided by Prof. W. Torres Delgado (a previous Ph.D. student in the Rivard group) with initial synthesis of

tellurophene precursors, Dr E. Hupf (a previous postdoctoral fellow in the Rivard group) with discussions on computations, J. Zheng (University of Alberta) with MALDI-MS measurements, and W. Moffat and J. Jones (University of Alberta) with analytical measurements.

In Chapter 3, the synthesis and characterization of phosphine monomers and polymers were performed in close collaboration with A. V. Muralidharan (a Ph.D. student in the Rivard Group). A. V. Muralidharan also assisted in the synthesis and characterization of triazolium ring-fused polyacetylenes. Cyclic voltammetry and spectroelectrochemical measurements were performed by N. Ostermann and guided by Prof. I. Siewert (both from the University of Göttingen). Optical profilometry measurements and assistance in dynamic light-scattering were provided by I T. Cheong (University of Alberta). Valuable input and assistance were also provided by Dr E. Hupf with discussions on computations, and W. Moffat and J. Jones with analytical measurements.

In Chapter 4, the preliminary near-IR photodetectors mentioned were fabricated in collaboration with Dr. S. K. Saxena (substrate preparation, contact deposition, measurements) and Prof. R. L. McCreery, both from the University of Alberta.

According to the policy within our research group, each Chapter of this Thesis is essentially self-contained and prepared in the form of a paper that is intended for publication in peer-reviewed journals. A portion of this Thesis has been published previously elsewhere, and this publication is listed below:

Chapter 2: B. T. Luppi, R. McDonald, M. J. Ferguson, L. Sang and E. Rivard, *Chem. Commun.*, **2019**, 55, 14218–14221.

In addition to the work described in this Thesis, contributions were also made to the following peer-reviewed publications:

B. T. Luppi, D. Majak, M. Gupta, E. Rivard and K. Shankar, *J. Mater. Chem. A*, **2019**, 7, 2445–2463.

I T. Cheong, W. Morrish, W. Sheard, H. Yu, B. T. Luppi, L. Milburn, A. Meldrum and J. G. C. Veinot, *ACS Appl. Mater. Interfaces*, **2021**, 13, 27149–27158.

Dedicated to my family and mentors

“You realize that when you know how to think, it empowers you far beyond those who know only what to think” — Neil DeGrasse Tyson

Acknowledgements

First and foremost, I would like to thank Prof. Eric Rivard for all his mentorship, support, and encouragement throughout these years. He believed in my potential from the start, was always excited to discuss Chemistry, remained open to providing advice about research and career options, and helped me achieve numerous accomplishments. I would also like to thank my supervisory committee members, Prof. Arthur Mar and Prof. Michael Serpe, for their support and valuable input with regards to research and career options. I must also thank Dr. Jason Cooke who, not only provided guidance with regards to TA responsibilities, but was also always available to chat about the academic life.

My sincerest thank you to the present and past Rivard group members, who quickly made me part of the family. Specially, thank you to William Torres Delgado, Olena Shynkaruk, Emanuel Hupf, Sarah Parke, Matthew Roy, Eike Dornsiepen, Jocelyn Sinclair, Ian Watson, Alvaro Omaña, Samuel Baird, Brandon Frenette, William Medroa and Abhishek Muralidharan. Special thanks also to my “bestie” and previous fume hood neighbour Chrissy Braun (also, please remember that Edward Snowden is not a character in Game of Thrones)! Additionally, I had a great time working alongside several undergraduate and visiting students in the Rivard group, as well as meeting people around the department for research discussions and for fun outside of the lab – thank you all!

The University of Alberta also has amazing technical and support staff, full of people that were great to chat with and learn from. Special thanks to Anita Weiler, Wayne Moffat, Jennifer Jones, Mark Miskolzie, Jason Dibbs, Michael Ferguson, Jing Zheng, Dirk Kelm, Paul Crothers, Ryan Lewis, Michael Barteski and all the rest of the wonderful staff in Chemistry stores.

Next, I must thank my parents, Anderson and Deise, for always supporting me even when we are 10,700 km away, and my sister Carla, with whom I still grow closer despite the distance. Thank you also to the rest of my family and all my friends from Brazil, some of whom are now spread across the world but stay in touch. Finally, thank you to my amazing girlfriend Lynn for the support and for enduring my grumpy moments throughout these years, encouraging me to see the bright side and achieve my goals.

Table of Contents

Chapter 1: Introduction	1
1.1 Conjugated Polymers	1
1.2 Polyacetylenes	2
1.2.1 Classic Synthesis of Polyacetylene	3
1.2.2 Electronic Structure of Polyacetylene	6
1.2.3 Chemical Doping and Onset of Metallic Behavior	9
1.2.4 Challenges for Current Applications	11
1.2.5 Modern Synthesis of Polyacetylene	13
1.2.5.1 Soluble Polyacetylenes from the ROMP of Cyclooctatetraene (COT)	15
1.2.5.2 Polyacetylenes from Polymeric Precursors	31
1.3 Polytellurophenes	40
1.3.1 Replacement of S by Se and Te	41
1.3.2 Synthesis of Polytellurophenes	46
1.3.2.1 Electropolymerization and the First Polytellurophenes	47
1.3.2.2 Palladium-Catalyzed Cross-Coupling	50
1.3.2.3 Catalyst-Transfer Polymerization	57
1.3.2.4 Other Synthetic Methods	62
1.3.3 Recent Applications of Polytellurophenes	65
1.3.3.1 Organic Photovoltaics (OPV)	65
1.3.3.2 Organic Field-Effect Transistors (OFET)	69

1.3.3.3 Photothermal/Photodynamic Therapy	71
1.3.3.4 Photodetection	72
1.4 Scope of this Thesis	73
1.5 References	74
Chapter 2: Rapid Access to (Cycloalkyl)tellurophene Oligomer Mixtures and the First Poly(3-aryltellurophene)	95
2.1 Introduction	95
2.2 Results and Discussions	97
2.2.1 Synthesis of (Cyclo)tellurophene Oligomers	97
2.2.2 Influence of Cyclic Side Groups on Optoelectronic Properties	101
2.2.3 Synthesis of a Poly(3-aryl)tellurophene	106
2.2.4 Attempts to Improve End-Group Control	109
2.2.5 Optoelectronic Properties of Poly(3-aryl)tellurophene	113
2.3 Conclusions	118
2.4 Experimental Section	119
2.4.1 General Information, Materials and Instrumentation	119
2.4.2 Synthetic Procedures	122
2.4.2.1 Polymerization Trials using Ni(dppe)Cl ₂ as a Pre-catalyst	132
2.4.3 NMR Data	135
2.4.4 GPC Data	153
2.4.5 Thermal Analysis Data	154
2.4.6 Additional UV-Vis Data	157

2.4.7 Additional MALDI-MS Data	158
2.4.8 Crystallographic Data	159
2.5 DFT Computations and Methodology	161
2.5.1 Additional Computed Excited State Data	163
2.6 References	165
Chapter 3: Soluble Electronically Modified Polyacetylenes	171
3.1 Introduction	171
3.2 Results and Discussion	173
3.2.1 Monomer Synthesis	173
3.2.2 Polymer Synthesis	177
3.2.2.1 Boryl-Functionalized Polyacetylene	177
3.2.2.2 Amino-Functionalized Polyacetylenes	181
3.2.2.3 Phosphorus-Functionalized Polyacetylenes	182
3.2.2.4 Triazolium Ring-Fused Polyacetylene	185
3.2.3 Reactivity and Properties of pCOT-BMes₂	188
3.2.4 Optoelectronic Data of the Functional Polyacetylenes	193
3.2.5 Redox Activity of the Functionalized Polyacetylenes	200
3.2.6 Conductivity Measurements	212
3.2.7 Improved Air Stability of Films	213
3.2.8 Polyacetylene Cross-Linking Reactions with Benzoquinone	216
3.3 Conclusions	219
3.4 Experimental Section	219

3.4.1 General Information, Materials and Instrumentation	219
3.4.2 Synthetic Procedures	224
3.4.3 X-Ray Crystallographic Data	243
3.4.4 Additional NMR Data	246
3.4.5 Determination of Backbiting Percentage and Side Chain Density for Polyacetylenes	295
3.4.6 GPC Data	300
3.4.7 Calculation of Estimated M_n by Dynamic Light-Scattering (DLS)	303
3.4.8 Thermal Gravimetric Analysis (TGA) Data	304
3.4.9 Additional UV-Vis Data	308
3.4.10 Photoluminescence Data	311
3.4.11 Additional CV and NIR-SEC Data	313
3.4.12 Additional Optical Profilometry Data	324
3.5 DFT Computations and Methodology	326
3.5.1 Additional DFT and TD-DFT Data	327
3.6 References	341
Chapter 4: Summary and Future Directions	348
4.1 Synthesis of New Polytellurophenes	348
4.2 Soluble Polyacetylenes in Organic Electronics	351
4.3 Exploring Side Chain Functionality of Polyacetylenes	353
4.4 Synthesis of Soluble Triazolium Ring-Fused Polyacetylenes	360
4.5 Concluding Remarks	362

4.6 References	363
Complete Bibliography	365

List of Figures

Figure 1.1. Structure of common π -conjugated organic polymers.....	2
Figure 1.2. Structural isomers of polyacetylene.....	3
Figure 1.3. Molecular orbital diagram showing the frontier orbitals of a polyene chain of increasing length, leading to bands in polyacetylene.....	7
Figure 1.4. HOMO and LUMO in <i>trans</i> -polyacetylene compared to degenerate orbitals in a hypothetical, fully delocalized, polyacetylene.....	9
Figure 1.5. Boat-shaped molecular structure of cyclooctatetraene (COT).....	15
Figure 1.6. Tungsten catalysts initially used in the ROMP of COT.....	16
Figure 1.7. Alkyl-, aryl- and alkoxy-substituted <i>trans</i> -polyacetylenes and their absorption maxima in THF.....	23
Figure 1.8. Ruthenium-based olefin metathesis catalysts (G1-G3) developed by Grubbs and coworkers.....	29
Figure 1.9. Chalcogenophenes formed by sulfur, selenium and tellurium.....	41
Figure 1.10. Molecular structures of P3HT (P62), P3HSe (P63) and P3HTe (P64)....	43
Figure 1.11. a) Representation of Te---Te interactions in polytellurophenes; b) Simplified MO diagram showing the orbitals involved in the σ -hole interaction.....	44
Figure 1.12. A simplified Jablonski diagram showing formation of triplet excited states.....	45
Figure 1.13. Tellurium-containing polymers studied in OPV and OFET applications.....	66

Figure 1.14. Alkyl-substituted polytellurophenes studied in the context of OFETs....	71
Figure 1.15. Polymer mixture forming nanoparticles for cancer treatment.....	72
Figure 1.16. Structure of random tellurophene copolymers used in photodetectors....	73
Figure 2.1. Molecular structure of 1,3-diiodo-4,5,6,7-tetrahydro-benzo[<i>c</i>]tellurophene (I-Te-6-I , left) and 1,3-diiodo-4,5,6,7-tetrahydro-cyclopenta[<i>c</i>]tellurophene (I-Te-5-I , right).....	98
Figure 2.2. MALDI-MS of Oligo-Te6	100
Figure 2.3. MALDI-MS of Oligo-Te5	101
Figure 2.4. UV-Vis spectra and images of Oligo-Te5 and Oligo-Te6 in CHCl ₃	102
Figure 2.5. Structure optimization of heptamers of Oligo-Te6 and Oligo-Te5	103
Figure 2.6. Energy change of oligomers upon change in torsion angle.....	104
Figure 2.7. TD-DFT computed UV-Vis absorptivity for trimers of Oligo-Te5 (I-[Te5]₃-I) and Oligo-Te6 (I-[Te6]₃-I) and the three main oscillator strengths (bars below the curves) associated with the absorptions.....	105
Figure 2.8. DFT computed orbitals for trimeric models of Oligo-Te6 and Oligo-Te5	105
Figure 2.9. Molecular structure of 3-(4-isopropylphenyl)-tellurophene (Te-cumenyl).....	107
Figure 2.10. MALDI-MS of PolyTe-cumenyl	108
Figure 2.11. MALDI-MS of PolyS-cumenyl	109
Figure 2.12. a) ¹ H NMR study of the GRIM activation step for I-S-cumenyl-I ; b) ¹ H NMR study of the GRIM activation step for I-Te-cumenyl-I	110

Figure 2.13. MALDI-MS of PolyS-cumenyl and PolyTe-cumenyl prepared with Ni(dppe)Cl ₂ as a pre-catalyst.....	112
Figure 2.14. ¹ H NMR spectra in CDCl ₃ of the isopropyl region of the low regioregularity polymers obtained during polymerization trials with Ni(dppe)Cl ₂ (1 mol. %) as pre-catalyst.....	113
Figure 2.15. UV-Vis spectra and photos of PolyS-cumenyl (top) and PolyTe-cumenyl (bottom) normalized at the most red-shifted absorption maxima.....	114
Figure 2.16. Determination of the onset of absorption for a film of PolyTe-cumenyl	115
Figure 2.17. Cyclic voltammogram (scan rate = 100 mV/s) of PolyTe-cumenyl and PolyS-cumenyl annealed films on ITO.....	117
Figure 2.18. Cyclic voltammogram of PolyTe-cumenyl (scan rate = 100 mV/s) over different cycles.....	118
Figure 2.19. ¹ H NMR spectrum (500 MHz) of 1,3-diiodo-4,5,6,7-tetrahydrobenzo[<i>c</i>]tellurophene (I-Te-6-I) in CDCl ₃	135
Figure 2.20. ¹³ C{ ¹ H} NMR spectrum (126 MHz) of 1,3-diiodo-4,5,6,7-tetrahydrobenzo[<i>c</i>]tellurophene (I-Te-6-I) in CDCl ₃	136
Figure 2.21. ¹ H NMR spectrum (500 MHz) of 1,3-diiodo-4,5,6,7-tetrahydrocyclopenta[<i>c</i>]tellurophene (I-Te-5-I) in CDCl ₃	137
Figure 2.22. ¹³ C{ ¹ H} NMR spectrum (126 MHz) of 1,3-diiodo-4,5,6,7-tetrahydrocyclopenta[<i>c</i>]tellurophene (I-Te-5-I) in CDCl ₃	138
Figure 2.23. ¹ H NMR spectrum (500 MHz) of Oligo-Te5 in CDCl ₃	139

Figure 2.24. ^1H NMR spectrum (400 MHz) of Oligo-Te6 in CDCl_3	140
Figure 2.25. ^1H NMR spectrum (400 MHz) of 3-(4-isopropylphenyl)-tellurophene (Te cumenyl) in CDCl_3	141
Figure 2.26. $^{13}\text{C}\{^1\text{H}\}$ NMR (126 MHz) of 3-(4-isopropylphenyl)-tellurophene (Te cumenyl) in CDCl_3	142
Figure 2.27. ^1H NMR spectrum (700 MHz) of crude 2-iodo-3-(4-isopropylphenyl)-tellurophene (H-Te-cumenyl-I) in CDCl_3	143
Figure 2.28. $^{13}\text{C}\{^1\text{H}\}$ NMR spectrum (176 MHz) of crude 2-iodo-3-(4-isopropylphenyl)-tellurophene (H-Te-cumenyl-I) in CDCl_3	144
Figure 2.29. ^1H NMR spectrum (500 MHz) of 2,5-diiodo-3-(4-isopropylphenyl)-tellurophene (I-Te-cumenyl-I) in CDCl_3	145
Figure 2.30. $^{13}\text{C}\{^1\text{H}\}$ NMR spectrum (126 MHz) of 2,5-diiodo-3-(4-isopropylphenyl)-tellurophene (I-Te-cumenyl-I) in CDCl_3	146
Figure 2.31. ^1H NMR spectrum (500 MHz) of 3-(4-isopropylphenyl)-thiophene (S cumenyl) in CDCl_3	147
Figure 2.32. $^{13}\text{C}\{^1\text{H}\}$ NMR spectrum (126 MHz) of 3-(4-isopropylphenyl)-thiophene (S-cumenyl) in CDCl_3	148
Figure 2.33. ^1H NMR spectrum (400 MHz) of 2,5-diiodo-3-(4-isopropylphenyl)-thiophene (I-S-cumenyl-I) in CDCl_3	149
Figure 2.34. $^{13}\text{C}\{^1\text{H}\}$ NMR spectrum (101 MHz) of 2,5-diiodo-3-(4-isopropylphenyl)-thiophene (I-S-cumenyl-I) in CDCl_3	150

Figure 2.35. ¹ H NMR spectrum (400 MHz) of poly(3-(4-isopropylphenyl)-thiophene) (PolyS-cumenyl) in CDCl ₃	151
Figure 2.36. ¹ H NMR spectrum (500 MHz) of poly(3-(4-isopropylphenyl)-tellurophene) (PolyTe-cumenyl) in CDCl ₃	152
Figure 2.37. GPC elution profile for PolyS-cumenyl	153
Figure 2.38. GPC elution profile for PolyTe-cumenyl	154
Figure 2.39. TGA plots of I-Te-6-I (left) and I-Te-5-I (right) obtained at a heating rate of 10 °C/min under N ₂	154
Figure 2.40. TGA plots of Oligo-Te6 (left) and Oligo-Te5 (right) obtained at a heating rate of 10 °C/min under N ₂	155
Figure 2.41. TGA plots of I-S-cumenyl-I (left) and I-Te-cumenyl-I (right) obtained at a heating rate of 10 °C/min under N ₂	155
Figure 2.42. TGA plots of PolyS-cumenyl (left) and PolyTe-cumenyl (right) obtained at a heating rate of 10 °C/min under N ₂	156
Figure 2.43. DSC trace of PolyS-cumenyl (left) and PolyTe-cumenyl (right) obtained at a heating rate of 20 °C/min under N ₂	156
Figure 2.44. UV-Vis spectra of I-Te-5-I/I-Te-6-I in THF and Oligo-Te5/Oligo-Te6 in CHCl ₃ (left); UV-Vis spectra of Oligo-Te6/Oligo-Te5 films before and after annealing at 70 °C (right).....	157
Figure 2.45. UV-Vis spectra of I-S-cumenyl-I and I-Te-cumenyl-I in THF.....	157
Figure 2.46. a) UV-Vis spectra of PolyS-cumenyl in THF; b) UV-Vis spectra of PolyTe-cumenyl in THF.....	158

Figure 2.47. MALDI-MS of a self-oligomerized sample of I-Te-6-I after one month.....	158
Figure 2.48. MALDI-MS of a self-oligomerized sample of I-Te-5-I after one week.....	159
Figure 2.49. Powder XRD of PolyTe-cumenyl and PolyS-cumenyl before and after solvent vapor annealing.....	161
Figure 3.1. Functionalized polyacetylenes discussed in this Chapter.....	173
Figure 3.2. Crystal structures of: a) COT-BMes₂ ; b) COT-P(O)ⁱPr₂ (H ₂ O solvate omitted); c) COT-NPh₂ ; d) [COT-N₃-Mes]OTf (OTf anion omitted) with thermal ellipsoids at a 30 % probability level.....	176
Figure 3.3. a) ROMP leading to polymer formation and backbiting side-product; b) Polymerization progress as a function of time for monosubstituted monomers; c) Alkyl region of ¹ H NMR spectra (in C ₆ D ₆ /THF) during the polymerization of COT-BMes₂	180
Figure 3.4. ³¹ P{ ¹ H} NMR spectrum of pCOT-P(O)ⁱPr₂ in C ₆ D ₆	183
Figure 3.5. Size distribution by volume for pCOT-BMes₂ , pCOT-P(O)ⁱPr₂ and pCOT-PiPr₂ as determined by dynamic light-scattering (DLS) in THF.....	183
Figure 3.6. ³¹ P{ ¹ H} NMR spectrum of pCOT-PⁱPr₂ in C ₆ D ₆	185
Figure 3.7. Absorption spectrum of p{[COT-N₃(Me)-Mes]OTf} as a suspension in THF (<i>ca.</i> 1 mg/mL).....	186
Figure 3.8. Solid state FT-IR spectra of [COT-N₃(Me)-Mes]OTf and its polymer p{[COT-N₃(Me)-Mes]OTf}	187

Figure 3.9. Crude ^{11}B NMR spectrum after fluoride binding to COT-BMes₂ (C_6D_6 , top) and pCOT-BMes₂ (THF + CDCl_3 , bottom).....	190
Figure 3.10. Molecular structure of $[\text{nBu}_4\text{N}][\text{COT-BMes}_2(\text{F})]$ with thermal ellipsoids plotted at a 30 % probability level.....	191
Figure 3.11. $^{11}\text{B}\{^1\text{H}\}$ NMR spectrum of the reaction mixture from pCOT-BMes₂ and $\text{Li}[\text{HBEt}_3]$ in THF.....	192
Figure 3.12. A film of pCOT-BMes₂ obtained after slow evaporation of THF.....	194
Figure 3.13. Picture of polymers in THF (top) and UV-Vis spectra of soluble polyacetylenes in THF (bottom).....	195
Figure 3.14. UV-Vis spectra of polymers as drop-cast films.....	196
Figure 3.15. Computed frontier molecular orbitals (B3LYP/cc-pVDZ) for models of pCOT-SiMe₃ , pCOT-BMes₂ and pCOT-N(C₆H₄^tBu)₂	198
Figure 3.16. Computed UV-Vis spectra (B3LYP/cc-pVDZ) and comparison with parent polyacetylene (PA).....	200
Figure 3.17. CV of pCOT-SiMe₃ , pCOT-BMes₂ and pCOT-N(C₆H₄^tBu)₂ in THF (0.1 M $[\text{nBu}_4\text{N}]\text{BAr}^{\text{F}_4}$, scan rate = 100 mV/s).....	201
Figure 3.18. Scan rate-dependent CV data of COT-BMes₂ (1 mM) in THF (0.10 M $[\text{nBu}_4\text{N}]\text{BAr}^{\text{F}_4}$ electrolyte).....	202
Figure 3.19. Scan rate-dependent CV data of COT-N(C₆H₄^tBu)₂ (1 mM) in THF (0.10 M $[\text{nBu}_4\text{N}]\text{BAr}^{\text{F}_4}$ electrolyte).....	203
Figure 3.20. NIR-SEC (top: oxidative, bottom: reductive) scans of pCOT-BMes₂ and pCOT-N(C₆H₄^tBu)₂ in THF (0.10 M $[\text{nBu}_4\text{N}]\text{BAr}^{\text{F}_4}$ electrolyte).....	204

Figure 3.21. NIR-SEC (top: oxidative, bottom: reductive) of pCOT-SiMe₃ in THF (0.10 M [ⁿ Bu ₄ N]BAR ^F ₄ electrolyte).....	205
Figure 3.22. UV-Vis-NIR spectra of pCOT-BMes₂ (left) and pCOT-N(C₆H₄^tBu)₂ (right) in THF (0.3×10^{-5} M) after chemical oxidation with [Fc]OTf and reduction with Na[COPh ₂].....	206
Figure 3.23. Computed SOMOs (B3LYP/cc-pVDZ) of pCOT-BMes₂ and pCOT-N(C₆H₄^tBu)₂ after oxidation and reduction.....	207
Figure 3.24. Energy of frontier molecular orbitals for oxidized and reduced polymer chain fragments obtained by DFT (B3LYP/cc-pVDZ).....	208
Figure 3.25. Optical images of polymer films with their thicknesses determined by profilometry and pictures of the films deposited onto quartz substrates with gold bottom contacts.....	210
Figure 3.26. UV-Vis-NIR spectra of polymers as spin-coated films after doping with I ₂ vapor.....	211
Figure 3.27. UV-Vis-NIR spectra of films of pCOT-BMes₂ and pCOT-SiMe₃ oxidized with [Fc]OTf.....	212
Figure 3.28. Air stability of neat films as tracked by UV-Vis spectroscopy.....	214
Figure 3.29. Air stability of THF solutions of pCOT-SiMe₃ , pCOT-BMes₂ and pCOT-N(C₆H₄^tBu)₂ tracked by UV-Vis spectroscopy.....	214
Figure 3.30. Change in light absorption intensity at λ_{\max} for a film of pCOT-PⁱPr₂ exposed to air over time.....	215

Figure 3.31. Solid state FT-IR spectra of cross-linked pCOT-BMes₂ , pCOT-SiMe₃ and pCOT-N(C₆H₄^tBu)₂ , and the spectrum of pCOT-BMes₂ for comparison.....	217
Figure 3.32. UV-Vis spectra of pCOT-N(C₆H₄^tBu)₂ in THF after reduction with Na[COPh ₂] followed by re-oxidation by air exposure (solid line), and as a suspension in THF after cross-linking with 1,4-benzoquinone (dashed line).....	218
Figure 3.33. ¹ H NMR spectrum (400 MHz) of NBE-C₆H₄-BMes₂ in CDCl ₃	246
Figure 3.34. ¹³ C { ¹ H} NMR spectrum (101 MHz) of NBE-C₆H₄-BMes₂ in CDCl ₃	247
Figure 3.35. ¹¹ B NMR spectrum (101 MHz) of NBE-C₆H₄-BMes₂ in CDCl ₃	248
Figure 3.36. ¹ H NMR spectrum (400 MHz) of pNBE-C₆H₄-BMes₂ in CDCl ₃	249
Figure 3.37. ¹ H NMR spectrum (500 MHz) of COT-BMes₂ in CDCl ₃	250
Figure 3.38. ¹³ C { ¹ H} NMR spectrum (126 MHz) of COT-BMes₂ in CDCl ₃	251
Figure 3.39. ¹¹ B NMR spectrum (126 MHz) of COT-BMes₂ in CDCl ₃	252
Figure 3.40. ¹ H NMR spectrum (700 MHz) of [ⁿ Bu ₄ N][COT-BMes₂(F)] in CDCl ₃	253
Figure 3.41. ¹³ C { ¹ H} NMR spectrum (176 MHz) of [ⁿ Bu ₄ N][COT-BMes₂(F)] in CDCl ₃	254
Figure 3.42. ¹ H gHSQCAD NMR spectrum (700 MHz) of [ⁿ Bu ₄ N][COT-BMes₂(F)] in CDCl ₃	255
Figure 3.43. ¹¹ B NMR spectrum (128 MHz) of [ⁿ Bu ₄ N][COT-BMes₂(F)] in CDCl ₃	256

Figure 3.44. ^{19}F NMR spectrum (376 MHz) of $[\text{Bu}_4\text{N}][\text{COT-BMes}_2(\text{F})]$ in C_6D_6	257
Figure 3.45. ^1H NMR spectrum (400 MHz) of COT-NPh₂ in C_6D_6	258
Figure 3.46. $^{13}\text{C}\{^1\text{H}\}$ NMR spectrum (101 MHz) of COT-NPh₂ in C_6D_6	259
Figure 3.47. ^1H NMR spectrum (500 MHz) of COT-N(C₆H₄^tBu)₂ in C_6D_6	260
Figure 3.48. $^{13}\text{C}\{^1\text{H}\}$ NMR spectrum (126 MHz) of COT-N(C₆H₄^tBu)₂ in C_6D_6 ...	261
Figure 3.49. ^1H NMR spectrum (500 MHz) of COT-PⁱPr₂ in CDCl_3	262
Figure 3.50. $^1\text{H}\{^{31}\text{P}\}$ NMR spectrum (500 MHz) of COT-PⁱPr₂ in CDCl_3	263
Figure 3.51. $^{13}\text{C}\{^1\text{H}\}$ NMR spectrum (126 MHz) of COT-PⁱPr₂ in CDCl_3	264
Figure 3.52. $^{13}\text{C}\{^1\text{H}\}$ DEPTq NMR spectrum (126 MHz) of COT-PⁱPr₂ in CDCl_3	265
Figure 3.53. $^{31}\text{P}\{^1\text{H}\}$ NMR spectrum (202 MHz) of COT-PⁱPr₂ in CDCl_3	266
Figure 3.54. ^1H NMR spectrum (500 MHz) of COT-P(O)ⁱPr₂ in CDCl_3	267
Figure 3.55. $^1\text{H}\{^{31}\text{P}\}$ NMR spectrum (500 MHz) of COT-P(O)ⁱPr₂ in CDCl_3	268
Figure 3.56. $^{13}\text{C}\{^1\text{H}\}$ NMR spectrum (176 MHz) of COT-P(O)ⁱPr₂ in CDCl_3	269
Figure 3.57. $^{13}\text{C}\{^1\text{H}\}$ DEPTq NMR spectrum (176 MHz) of COT-P(O)ⁱPr₂ in CDCl_3	270
Figure 3.58. $^{31}\text{P}\{^1\text{H}\}$ NMR spectrum (202 MHz) of COT-P(O)ⁱPr₂ in CDCl_3	271

Figure 3.59. ^1H NMR spectrum (500 MHz) of COT-N₃-Mes in CDCl_3	272
Figure 3.60. $^{13}\text{C}\{^1\text{H}\}$ NMR spectrum (126 MHz) of COT-N₃-Mes in CDCl_3	273
Figure 3.61. ^1H gHSQCAD NMR spectrum (500 MHz) of COT-N₃-Mes in CDCl_3	274
Figure 3.62. ^1H NMR spectrum (400 MHz) of [COT-N₃(Me)-Mes]OTf in CDCl_3	275
Figure 3.63. $^{13}\text{C}\{^1\text{H}\}$ NMR spectrum (101 MHz) of [COT-N₃(Me)-Mes]OTf in CDCl_3	276
Figure 3.64. ^1H gHSQCAD NMR spectrum (500 MHz) of [COT-N₃(Me)-Mes]OTf in CDCl_3	277
Figure 3.65. $^{19}\text{F}\{^1\text{H}\}$ NMR spectrum (500 MHz) of [COT-N₃(Me)-Mes]OTf in CDCl_3	278
Figure 3.66. ^1H NMR spectrum (400 MHz) of pCOT-SiMe₃ in C_6D_6	279
Figure 3.67. ^1H NMR spectrum (400 MHz) of pCOT-BMes₂ in C_6D_6	280
Figure 3.68. ^1H NMR spectrum (500 MHz) of pCOT-NPh₂ in CDCl_3	281
Figure 3.69. ^1H NMR spectrum (400 MHz) of pCOT-N(C₆H₄^tBu)₂ in CDCl_3	282
Figure 3.70. ^1H NMR spectrum (400 MHz) of p[COT-N(C₆H₄^tBu)₂-<i>r</i>-COT-BMes₂] in CDCl_3	283
Figure 3.71. ^1H NMR spectrum (500 MHz) of pCOT-P(O)ⁱPr₂ in C_6D_6	284

Figure 3.72. ^1H NMR spectrum (500 MHz) of pCOT-PⁱPr₂ in C_6D_6	285
Figure 3.73. ^1H NMR monitoring (500 MHz) of the polymerization of COT-BMes₂ in a 1:1 THF: C_6D_6 mixture.....	286
Figure 3.74. ^1H NMR monitoring (500 MHz) of the polymerization of COT-NPh₂ in a 1:1 THF: C_6D_6 mixture.....	287
Figure 3.75. ^1H NMR monitoring (500 MHz) of the polymerization of COT-N(C₆H₄^tBu)₂ in a 1:1 THF: C_6D_6 mixture.....	288
Figure 3.76. ^1H NMR monitoring (400 MHz) of the polymerization of COT-SiMe₃ in a 1:1 THF: C_6D_6 mixture.....	289
Figure 3.77. ^1H NMR monitoring (500 MHz) of the polymerization of COT-P(O)ⁱPr₂ in a 1:1 THF: C_6D_6 mixture.....	290
Figure 3.78. ^{31}P NMR monitoring (202 MHz) of the polymerization of COT-P(O)ⁱPr₂ in a 1:1 THF: C_6D_6 mixture.....	291
Figure 3.79. ^1H NMR monitoring (500 MHz) of the polymerization of [COT-N₃(Me)-Mes] OTf in THF- d_8	292
Figure 3.80. Conversion of monomers during polymerization as measured by NMR in a 1:1 THF: C_6D_6 mixture (0.080 M, 1 mol. % of 3 rd gen. Grubbs catalyst).....	293
Figure 3.81. ^{19}F NMR spectrum (376 MHz) after fluoride binding to COT-BMes₂ (C_6D_6 , top) and pCOT-BMes₂ (THF + CDCl_3 , bottom).....	294

Figure 3.82. Example of the calculation of parameters used to obtain %CE and the average number of carbons between each side chain for polyacetylenes.....	297
Figure 3.83. GPC elution profile for pNBE-C₆H₄-BMes₂ in THF.....	300
Figure 3.84. GPC elution profile for pCOT-SiMe₃ in THF.....	300
Figure 3.85. GPC elution profile for pCOT-BMes₂ in THF.....	301
Figure 3.86. GPC elution profile for pCOT-NPh₂ in THF.....	301
Figure 3.87. GPC elution profile for pCOT-N(C₆H₄^tBu)₂ in THF.....	302
Figure 3.88. GPC elution profile for p[COT-N(C₆H₄^tBu)₂-<i>r</i>-COT-BMes₂] in THF.....	302
Figure 3.89. TGA of NBE-C₆H₄-BMes₂ (left) and pNBE-C₆H₄-BMes₂ (right) at 10 °C/min under N ₂	304
Figure 3.90. TGA of COT-BMes₂ (left) and pCOT-BMes₂ (right) at 10 °C/min under N ₂	304
Figure 3.91. TGA of COT-NPh₂ (left) and pCOT-NPh₂ (right) at 10 °C/min under N ₂	305
Figure 3.92. TGA of COT-N(C₆H₄^tBu)₂ (left) and pCOT-N(C₆H₄^tBu)₂ (right) at 10 °C/min under N ₂	305
Figure 3.93. TGA of COT-PⁱPr₂ (left) and p[COT-N(C₆H₄^tBu)₂-<i>r</i>-COT-BMes₂] (right) at 10 °C/min under N ₂	306

Figure 3.94. TGA of COT-P(O)ⁱPr₂ (left) and pCOT-P(O)ⁱPr₂ (right) at 10 °C/min under N ₂	306
Figure 3.95. TGA of COT-N₃-Mes (left) and [COT-N₃(Me)-Mes]OTf (right) at 10 °C/min under N ₂	307
Figure 3.96. UV-Vis spectra of NBE-C₆H₄-BMes₂ and pNBE-C₆H₄-BMes₂ (left) and COT-based monomers (right) in THF.....	308
Figure 3.97. Molar absorptivity spectra (per repeat unit) of polymers in THF.....	308
Figure 3.98. Isomerization of pCOT-BMes₂ in THF at different total times of exposure to a mercury lamp (125 W high pressure, left) and absorption of a film of pCOT-BMes₂ freshly drop-casted and degraded after 2 weeks of exposure to air and light (right).....	309
Figure 3.99. Normalized UV-Vis spectra of pCOT-BMes₂ before and after addition of 1 eq. of tetrabutylammonium fluoride ([ⁿ Bu ₄ N]F).....	310
Figure 3.100. Emission and excitation spectra comparing the monomer NBE-C₆H₄-BMes₂ and polymer pNBE-C₆H₄-BMes₂ in THF solutions (left) and comparing the THF solution and powder of the polymer pNBE-C₆H₄-BMes₂ (right).....	311
Figure 3.101. Scan rate dependent CV data of pCOT-SiMe₃ (0.5 mg/mL) in THF (0.10 M [ⁿ Bu ₄ N]BAR ^F ₄ electrolyte).....	314
Figure 3.102. Scan rate dependent CV data of pCOT-BMes₂ (0.5 mg/mL) in THF (0.10 M [ⁿ Bu ₄ N]BAR ^F ₄ electrolyte).....	314

Figure 3.103. Scan rate dependent CV data of pCOT-N(C₆H₄^tBu)₂ (0.5 mg/mL) in THF (0.10 M [ⁿ Bu ₄ N]BAr ^F ₄ electrolyte).....	315
Figure 3.104. CV data of polymer films in MeCN (0.035 M [ⁿ Bu ₄ N]BAr ^F ₄ electrolyte, scan rate = 100 mV/s).....	316
Figure 3.105. UV-Vis-NIR-SEC data of pCOT-N(C₆H₄^tBu)₂ (left, 0.5 mg/mL) and pCOT-BMes₂ (right, 0.5 mg/mL) in THF (0.10 M [ⁿ Bu ₄ N]BAr ^F ₄ electrolyte).....	317
Figure 3.106. NIR-SEC data of pCOT-SiMe₃ (0.5 mg/mL) in THF (0.10 M [ⁿ Bu ₄ N]BAr ^F ₄ electrolyte). Left: oxidation (1.4 V vs. Ag/AgNO ₃), right: re-reduction (-1.0 V vs. Ag/AgNO ₃).....	318
Figure 3.107. NIR-SEC data of pCOT-SiMe₃ (0.5 mg/mL) in THF (0.10 M [ⁿ Bu ₄ N]BAr ^F ₄ electrolyte). Left: reduction (-2.5 V vs. Ag/AgNO ₃), right: re-oxidation (0.5 V vs. Ag/AgNO ₃).....	319
Figure 3.108. NIR-SEC data of pCOT-N(C₆H₄^tBu)₂ (0.5 mg/mL) in THF (0.10 M [ⁿ Bu ₄ N]BAr ^F ₄ electrolyte). Left: oxidation (1.0 V vs. Ag/AgNO ₃), right: re-reduction (-1.2 V vs. Ag/AgNO ₃).....	320
Figure 3.109. NIR-SEC of pCOT-N(C₆H₄^tBu)₂ (0.5 mg/mL) in THF (0.10 M [ⁿ Bu ₄ N]BAr ^F ₄ electrolyte). Left: reduction (-2.0 V vs. Ag/AgNO ₃), right: re-oxidation (-0.4 V vs. Ag/AgNO ₃).....	321

Figure 3.110. NIR-SEC data of pCOT-BMes₂ (0.5 mg/mL) in THF (0.10 M [ⁿ Bu ₄ N]BAR ^F ₄ electrolyte). Left: oxidation (1.3 V vs. Ag/AgNO ₃), right: re-reduction (-1.2 V vs. Ag/AgNO ₃).....	322
Figure 3.111. NIR-SEC data of pCOT-BMes₂ (0.5 mg/mL) in THF (0.10 M [ⁿ Bu ₄ N]BAR ^F ₄ electrolyte). Left: reduction (-2.0 V vs. Ag/AgNO ₃), right: re-oxidation (-0.1 V vs. Ag/AgNO ₃).....	323
Figure 3.112. Representative height profiles of polymer films obtained by optical profilometry.....	324
Figure 3.113. Optical microscope image of a spin-coated film of pCOT-BMes₂ doped with [Fc]OTf (top) and representative height profile of the film obtained by optical profilometry (bottom).....	325
Figure 3.114. Frontier molecular orbitals for chain fragments of pCOT-P(O)ⁱPr₂ (left) and pCOT-PⁱPr₂ (right) computed at the B3LYP/cc-pVDZ level of theory.....	327
Figure 3.115. Frontier molecular orbitals for models of p[COT-N(C₆H₄^tBu)₂-r-COT-BMes₂] (left) and p[COT-N₃(Me)-Mes]⁺ (right) computed at the B3LYP/cc-pVDZ level of theory.....	328
Figure 3.116. Computed UV-Vis spectra and corresponding oscillator strengths for all COT-based polymers with pendant side chains and one without (PA) for comparison.....	330

Figure 3.117. Frontier molecular orbitals for models of p[COT-SiMe₃⁺] (left) and p[COT-SiMe₃⁻] (right) computed at the B3LYP/cc-pVDZ level of theory.....	335
Figure 3.118. Frontier molecular orbitals for models of p[COT-BMes₂⁺] (left) and p[COT-BMes₂⁻] (right) computed at the B3LYP/cc-pVDZ level of theory.....	336
Figure 3.119. Frontier molecular orbitals for chain fragments of p[COT-N(C₆H₄^tBu)₂⁺] (left) and p[COT-N(C₆H₄^tBu)₂⁻] (right) computed at the B3LYP/cc-pVDZ of theory.....	337
Figure 3.120. UV-Vis-NIR spectra computed for p[COT-SiMe₃⁺] and p[COT-SiMe₃⁻] by TD-DFT at different levels of theory.....	338
Figure 3.121. UV-Vis-NIR spectra computed for p[COT-BMes₂⁺] and p[COT-BMes₂⁻] by TD-DFT at different levels of theory.....	339
Figure 3.122. UV-Vis-NIR spectra computed for p[COT-N(C₆H₄^tBu)₂⁺] and p[COT-N(C₆H₄^tBu)₂⁻] by TD-DFT at different levels of theory.....	340
Figure 4.1. Photodetectors during fabrication with undoped films of functional polyacetylenes spin coated onto quartz substrates with contacts.....	352
Figure 4.2. Nitrogen-appended polyacetylenes for spintronics.....	353
Figure 4.3. DFT computation of average bond length alternation (BLA, difference between the length of C–C and C=C bonds) in the polyacetylene fragment in between side chains.....	357

List of Schemes

Scheme 1.1. a) Synthesis of polyacetylene powder by Natta's method; b) Synthesis of polyacetylene films by Shirakawa's procedure.....	5
Scheme 1.2. Iodine doping of polyacetylene leading to the formation of radicals.....	11
Scheme 1.3. Degradation of polyacetylene by exposure to air leading to cleavage of the polymeric chain.....	12
Scheme 1.4. Formation of polyacetylene with large side chain density from substituted acetylenes.....	14
Scheme 1.5. Polymers with a polyacetylene backbone formed by cyclopolymerization of α,ω -diynes.....	14
Scheme 1.6. a) Synthesis of polyacetylene through the ROMP of COT using a well-defined tungsten catalyst; b) Steps involved in the polymerization.....	17
Scheme 1.7. a) ROMP of COT ($R = H$) and its derivatives ($R \neq H$) leading to formation of polyacetylenes and benzene or substituted benzenes; b) Mechanism of backbiting.....	18
Scheme 1.8. Synthesis of a Me_3Si -substituted polyacetylene through the ROMP of COT- SiMe_3	19
Scheme 1.9. Comparison of polyacetylene chains obtained from different Si-substituted precursors.....	20
Scheme 1.10. Reaction of COT with two equivalents of an organolithium species followed by reoxidation with I_2	21

Scheme 1.11. Synthesis of polyacetylenes with chiral side chains.....	26
Scheme 1.12. Synthesis of polyacetylenes with ionic side chains.....	27
Scheme 1.13. Synthesis of end-functionalized COT oligomers by ROMP.....	30
Scheme 1.14. ROMP of COT in the presence of alkene-terminated polymers.....	30
Scheme 1.15. Synthesis of block copolymers with COT.....	31
Scheme 1.16. Initial routes used for the synthesis of polyacetylene from polymeric precursors.....	33
Scheme 1.17. Isomerization of cyclobutene into 1,3-butadiene.....	33
Scheme 1.18. Mechanochemical unzipping of poly ladderenes to form polyacetylene block copolymers.....	35
Scheme 1.19. Synthesis of a partly fluorinated polyacetylene by mechanochemical unzipping of a poly ladderene.....	36
Scheme 1.20. a) Synthesis of <i>trans</i> -PA from the spontaneous isomerization of a cyclobutene-containing polymer, P54 ; b) Synthesis of a triblock copolymer (P55) through a similar route.....	38
Scheme 1.21. a) Synthesis of substituted polyacetylenes from disubstituted cyclobutenes; b) Molecular structure of C4	39
Scheme 1.22. Synthesis of carboxylic acid-substituted polyacetylenes from the base-induced hydrolysis of ester side chains.....	40
Scheme 1.23. Resonance structures of polychalcogenophenes.....	42
Scheme 1.24. Synthesis of parent polytellurophene through electropolymerization methods.....	48

Scheme 1.25. Synthesis of poly(3,4-bis(methoxy)tellurophene), P66	48
Scheme 1.26. Synthesis of soluble copolymers with tellurophene through oxidative polymerization.....	49
Scheme 1.27. Formation of a tellurophene copolymer (P69) by Wittig polycondensation.....	50
Scheme 1.28. a) Synthesis of a diiodinated bitellurophene and its copolymerization through Pd-mediated cross-coupling; b) Oxidation of Te centers by addition of Br ₂	51
Scheme 1.29. a) Synthesis of a homopolymer through Suzuki-Miyaura cross-coupling; b) Visualization of a head-to-tail regioregularity.....	52
Scheme 1.30. a) Synthesis of tellurophene monomers mediated by formation of a zirconacycle; b) Synthesis of copolymers from a BPin-functionalized tellurophene.....	53
Scheme 1.31. <i>Ipso</i> -arylation copolymerization of tellurophene.....	54
Scheme 1.32. Examples of copolymers synthesized through Stille coupling.....	55
Scheme 1.33. Synthesis of a vinylene-spaced polytellurophene through Stille cross-coupling.....	56
Scheme 1.34. Direct heteroarylation polymerization of bitellurophene.....	57
Scheme 1.35. a) Synthesis of poly(3-alkyltellurophene)s through CTP; b) Structure of Ni catalysts used.....	58
Scheme 1.36. Mechanism of CTP with “Ni(dppe)” as the active catalyst.....	60
Scheme 1.37. Activation step of 3-alkyltellurophene monomers for CTP.....	61
Scheme 1.38. Synthesis of a polytellurophene from an unsymmetrically halogenated monomer.....	62

Scheme 1.39. Synthesis of a tellurophene-Pt acetylide copolymer (P92).....	63
Scheme 1.40. a) Synthesis of a tellurophene copolymer from a titanacycle-containing polymer; b) Model tellurophene compound before and after reaction with Br ₂	64
Scheme 1.41. Diagram showing singlet fission.....	69
Scheme 2.1. Tellurophene project overview. Center: BPin-functionalized (cycloalkyl)tellurophenes B-Te-5-B and B-Te6-B , and the monoborylated tellurophene (BTe). Left: A copolymer derived from B-Te-6-B (top) and an example of a protodeboration side-product derived from B-Te-6-B (bottom). Right: New tellurophene oligomers and polymers synthesized in this Chapter.....	96
Scheme 2.2. Synthesis and oligomerization of I-Te-5-I and I-Te-6-I	98
Scheme 2.3. Synthesis of the poly(3-aryltellurophene) PolyTe-cumenyl	106
Scheme 3.1. Synthesis of the strained COT monomers.....	174
Scheme 3.2. Polymer synthesis.....	178
Scheme 3.3. Copolymerization of COT-BMes₂ and COT-N(C₆H₄^tBu)₂	181
Scheme 3.4. Reduction of pCOT-P(O)ⁱPr₂ into pCOT-PⁱPr₂	184
Scheme 3.5. Reaction of pCOT-BMes₂ with [ⁿ Bu ₄ N]F.....	189
Scheme 3.6. Synthetic route to a polynorbornadiene (pNBE-C₆H₄-BMes₂) with BMes ₂ groups.....	193
Scheme 3.7. Possible reaction of reduced polyacetylenes with 1,4-benzoquinone leading to cross-linking.....	217

Scheme 4.1. a) Use of the pinacolborane-functionalized tellurophene B-Te-6-B to form copolymers of large E_g values (right) and its protodeboronation under basic conditions (left); b) Possible uses of I-Te-5-I to form copolymers with planar backbones.....	349
Scheme 4.2. Possible improved synthesis of an aryl-substituted polytellurophene...	350
Scheme 4.3. a) Possible synthesis of an insulating/semiconductor block copolymer with a $-BMe_2$ unit; b) Micelle formation upon F^- binding by the polyacetylene block.....	355
Scheme 4.4. Synthesis of ionic polyacetylene copolymers with B and N from the polymerization of neutral monomers followed by post-polymerization reactions (top) or directly from ionic monomers (bottom).....	356
Scheme 4.5. Formation of a cross-linked polyacetylene <i>via</i> FLP interactions.....	358
Scheme 4.6. a) Direct ROMP of COT- P^iPr_2 , shown to not proceed in Chapter 3; b) Synthetic pathway to a Me_2P -functionalized COT; c) Possible reversible cross-linking of polyacetylenes containing $-B(C_6F_5)_2$ and $-PMe_2$ units <i>via</i> FLP interactions.....	360
Scheme 4.7. Synthesis of new triazolium-fused polyacetylenes through the route developed in Chapter 3.....	361

List of Tables

Table 1.1. Summary of reported properties for P2-P17	24
Table 1.2. Atomic properties of sulfur, selenium and tellurium.....	42
Table 1.3. Conditions and results for the synthesis of polytellurophenes through CTP.....	59
Table 1.4. Results of solar cells fabricated with polytellurophenes.....	68
Table 1.5. Results for OFETs fabricated with polytellurophenes.....	70
Table 2.1. Crystallographic data for I-Te-6-I , T-Te-5-I and Te-cumenyl	160
Table 2.2. Computed excited states of trimers of Oligo-Te5 (I-[Te5]3-I) by TD-DFT.....	163
Table 2.3. Computed excited states of trimers of Oligo-Te6 (I-[Te6]3-I) by TD-DFT.....	164
Table 3.1. Summary of polymerization trials.....	188
Table 3.2. Summary of experimental UV-Vis-NIR data for polyacetylenes.....	197
Table 3.3. Crystallographic data for COT-BMes₂ , [ⁿBu₄N][COT-BMes₂(F)] and COT-NPh₂	244
Table 3.4. Crystallographic data for COT-P(O)ⁱPr₂ and [COT-N₃(Me)-Mes]OTf	245
Table 3.5. Summary of calculated cycloextrusion percentage (%CE) and average number of carbon atoms in the backbone between each side chain (#C) compared to yield and number average molecular weight (M _n) of polymers.....	299

Table 3.6. Summary of luminescence data and absolute quantum yields for NBE-C₆H₄-BMes₂ and pNBE-C₆H₄-BMes₂	312
Table 3.7. Peak potentials of the oxidation and reduction events of the monomers (scan rate = 100 mV/s).....	313
Table 3.8. Peak potentials of the oxidation and reduction events of the polymers (scan rate = 100 mV/s).....	313
Table 3.9. Computed frontier orbital energies (eV) for polymer models in the gas phase (B3LYP/cc-pVDZ level).....	329
Table 3.10. TD-DFT computed excited states for pCOT-BMes₂ (B3LYP/cc-pVDZ level).....	331
Table 3.11. TD-DFT computed excited states for pCOT-N(C₆H₄^tBu)₂ (B3LYP/cc-pVDZ level).....	332
Table 3.12. TD-DFT computed excited states for pCOT-P(O)ⁱPr₂ (B3LYP/cc-pVDZ level).....	333
Table 3.13. TD-DFT computed excited states for pCOT-PⁱPr₂ (B3LYP/cc-pVDZ level).....	334

List of Symbols, Nomenclature and Abbreviations

{ ⁿ X}	Decoupled to ⁿ X nucleus
A	Ampere
Å	Angstrom
OAc	Acetate (H ₃ CCO ⁻)
AFM	Atomic force microscopy
Ar	Aryl
Ar ^F	3,5-(F ₃ C) ₂ C ₆ H ₂
BHJ	Bulk heterojunction
BHT	Butylated hydroxytoluene
bipy	2,2'-Bipyridine
BLA	Bond length alternation
BPin	Pinacolboronate
br	Broad
°C	Degrees Celsius
C ₆ D ₆	Benzene-d ₆
<i>ca.</i>	<i>Circa</i> ; approximately
CDCl ₃	Chloroform-d
CE	Cycloextrusion
<i>c.f.</i>	<i>Confer</i> ; compare
cm ⁻¹	Wavenumber

COD	Cyclooctadiene
COT	Cyclooctatetraene
CPE	Controlled potential electrolysis
CTP	Catalyst-transfer polymerization
CV	Cyclic voltammetry
Cy	Cyclohexyl (C ₆ H ₁₁)
d	Doublet
dba	Dibenzylideneacetone
DCTB	<i>trans</i> -2-[3-(4- <i>tert</i> -butylphenyl)-2-methyl-2-propenylidene]malononitrile
dd	Doublet of doublets
DEAD	Diethyl azodicarboxylate
DEPTq	Distortions enhancement by polarization transfer with quaternary C
DFT	Density functional theory
DLS	Dynamic light-scattering
DMAP	4-Dimethylaminopyridine
DMF	<i>N,N'</i> -Dimethylformamide
DMSO	Dimethylsulfoxide
dppe	Bis(diphenylphosphino)ethane
DPP	Diketopyrrolopyrrole
dppp	Bis(diphenylphosphino)propane
DSC	Differential-scanning calorimetry

dt	Doublet of triplets
E	Variable main group element
EA	Elemental analysis
E _g	HOMO-LUMO energy gap
<i>e.g.</i>	<i>Exempli gratia</i> ; for example
EI	Electron ionization
eq	Molar equivalents
EQCM	Electrochemical quartz crystal microbalance
EQE	External quantum efficiency
Et	Ethyl (C ₂ H ₅)
eV	Electron volt
<i>f</i>	Oscillator strength
FF	Fill factor
Fc	Ferrocene (or ferrocenyl)
FLP	Frustrated Lewis pair
FTIR	Fourier-transform infrared spectroscopy
g	Gram
G1	Grubbs 1 st generation catalyst
G2	Grubbs 2 nd generation catalyst
G3	Grubbs 3 rd generation catalyst
GIWAX	Grazing-incidence wide angle X-ray scattering
GPC	Gel permeation chromatography

GRIM	Grignard metathesis
HOMO	Highest occupied molecular orbital
HSQC	Heteronuclear single quantum coherence
ⁱ Pr	<i>iso</i> -Propyl (Me ₂ CH)
ITO	Indium tin oxide
<i>J</i>	NMR coupling constant
J _{sc}	Short-circuit current
kcal	Kilocalorie
kDa	Kilodalton (1,000 g/mol)
kJ	Kilojoule
LALS	Low-angle light-scattering
lp	Lone pair
LUMO	Lowest unoccupied molecular orbital
m	Multiplet
M	Molar (mol/L)
m/z	Mass-to-charge ratio
MALDI	Matrix assisted laser desorption/ionization
mbar	Millibar
Me	Methyl (CH ₃)
Me-THF	2-Methyltetrahydrofuran
MeCN	Acetonitrile
Mes	Mesityl (2,4,6-Me ₃ C ₆ H ₂)

mg	Milligram
MHz	Megahertz
mL	Milliliter
mmol	Millimole
M_n	Number average molecular weight
MO	Molecular orbital
mol	Mole
mol. %	Mole percent
Mp	Melting point
MS	Mass spectrometry
M_w	Weight average molecular weight
NBE	Norbornene
NBS	<i>N</i> -Bromosuccinimide
ⁿ Bu	<i>n</i> -Butyl (C ₄ H ₉)
NIR	Near-infrared
NIS	<i>N</i> -Iodosuccinimide
nm	Nanometer
NMR	Nuclear magnetic resonance
ns	Nanosecond
OA	Oxidative addition
OFET	Organic field-effect transistor
OLED	Organic light-emitting diode

OPV	Organic photovoltaics
OTf	Triflate (F_3CSO_3^-)
<i>o</i> -tolyl	<i>ortho</i> - MeC_6H_4
P3HSe	Poly(3-hexylselenophene)
P3HT	Poly(3-hexylthiophene)
P3HTe	Poly(3-hexytellurophene)
PA	Polyacetylene
PANI	Polyaniline
PC ₆₁ BM	[6,6]-phenyl-C ₆₁ -butyric acid methyl ester
PCE	Power conversion efficiency
PDI	Polydispersity index
PEG	Poly(ethylene glycol)
Ph	Phenyl (C_6H_5)
PMMA	Poly(methyl methacrylate)
ppm	Parts per million
PPV	Polyphenylenevinylene
PPy	Polypyrrole
PS	Polystyrene
PSS	Poly(styrene sulfonate)
PT	Polythiophene
R	Variable functional group
RALS	Right-angle light-scattering

RE	Reductive elimination
R _h	Hydrodynamic radius
RI	Refractive index
ROMP	Ring-opening metathesis polymerization
rpm	Rotations per minute
r.t.	Room temperature
RW	Ring-walking
s	Singlet
S	Siemens (ohm ⁻¹)
S-cumenyl	3-Cumenylthiophene
SEC	Spectroelectrochemistry
sept	Septet
S _n	nth singlet state
SOMO	Singly occupied molecular orbital
t	Triplet
TBS	<i>tert</i> -Butyldimethylsilyl
^t Bu	<i>tert</i> -Butyl (C(CH ₃) ₃)
TD-DFT	Time-dependent density functional theory
Te5	Tetrahydro-cyclopenta[<i>c</i>]-tellurophene
Te6	Tetrahydro-benzo[<i>c</i>]-tellurophene
Te-cumenyl	3-Cumenyltellurophene
T _g	Polymer glass transition temperature

TGA	Thermogravimetric analysis
THF	Tetrahydrofuran
T_m	Polymer melt transition temperature
TM	Transmetallation
TMEDA	Tetramethylethylenediamine
T_n	nth triplet state
TT	Triplet-triplet pair
UV	Ultraviolet
UV-Vis	Ultraviolet/visible spectroscopy
V	Volt
ν	Stretching vibration
V_{oc}	Open-circuit voltage
V_{th}	Threshold voltage
W	Watt
wt%	Percent by weight
XPhos	2-Dicyclohexylphosphino-2',4',6'-triisopropylbiphenyl
XRD	X-ray diffraction
δ	Chemical shift in ppm
ϵ	Molar absorptivity
σ	Conductivity
ϕ	Quantum yield
μ_{hole}	Hole mobility

μs	Microsecond
μw	Microwave
λ	Wavelength
λ_{em}	Wavelength of maximum emission
λ_{max}	Wavelength of maximum absorbance

Chapter 1: Introduction

1.1 Conjugated Polymers

Organic polymers with alternating single and double bonds between carbon atoms in the backbone (C-C and C=C bonds), or π -conjugated polymers, have become increasingly important since the discovery of their semiconducting behavior in the 1960s.¹ The resulting π -electron delocalization reduces the HOMO-LUMO energy gap to give properties similar to traditional inorganic semiconductors.² Additionally, due to the extensively developed synthesis of organic molecules, monomers and polymers can be chemically designed to tune properties such as light absorption, conductivity, crystallinity, and thermal or air stability, offering vast possibilities currently inaccessible to inorganic materials.

Another crucial difference between π -conjugated polymers and inorganic semiconductors is the possibility of preparing soluble polymers that facilitate the synthesis, handling and fabrication of devices. Unlike conjugated small molecules, which can also exhibit semiconducting properties as well as be soluble in common solvents, the higher viscosity of polymeric solutions offers processing advantages such as the possibility to use spin coating and roll-to-roll printing to produce films with reduced costs and on a large scale.³⁻⁵ These properties have led to great interest in conjugated polymers in the field of organic electronics, finding applications in organic photovoltaics (OPV),⁶⁻¹⁰ organic light-emitting diodes (OLED),^{11,12} organic field-

effect transistors (OFET)^{12,13} and photodetectors.^{14,15} Films of π -conjugated polymers can also show flexibility with retention of optoelectronic properties, leading to further applications such as the fabrication of wearable devices.^{16,17} Additionally, π -conjugated polymers may change their properties depending on their surrounding environment or in response of chemical analytes to produce sensors.¹⁸

Typical π -conjugated polymers include: polyaniline (PANI),^{19,20} polypyrrole (PPy),^{21,22} polyphenylenevinylene (PPV),¹² and polythiophene (PT)^{6,12,14} (Figure 1.1). To achieve desirable performances in current applications, these polymers and their derivatives require careful optimization of molecular structure and side chains, leading to more complex structures. On the other hand, a major pillar on which the development of conjugated polymers was built upon was the synthesis and characterization of linear polyacetylene, $[-HC=CH-]_n$, a novel material that will be described in detail below.

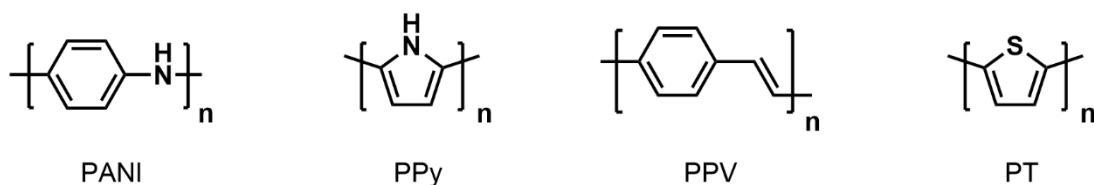


Figure 1.1. Structure of common π -conjugated organic polymers.

1.2 Polyacetylenes

Parent polyacetylene (PA) is the simplest hydrocarbon polymer, consisting of a linear chain of carbon atoms with an alternating π -system. As such, it can be considered a model to understand the properties of many other conjugated polymers.

Its controlled synthesis and doping (addition or removal of electrons from the unsaturated backbone) to further reduce the HOMO-LUMO energy gap and reach metallic conductivity led to the 2000 Nobel Prize in Chemistry being awarded to Alan J. Heeger, Alan G. MacDiarmid and Hideki Shirakawa.^{23–25}

Polyacetylene (PA) can exist as three different isomers: a *trans-transoid*, *cis-transoid* or *trans-cisoid* chain (Figure 1.2).²⁶ However, the main forms observed after synthesis are the *trans-transoid* and *cis-transoid* forms,^{27,28} which will be referred here as *trans*- and *cis*-PA, respectively, for simplicity. The *trans-cisoid* form can occur during the *cis-trans* isomerization of transoid polymer structures.^{29,30}

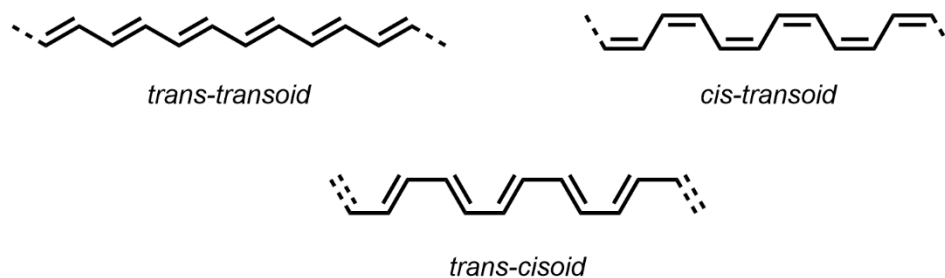
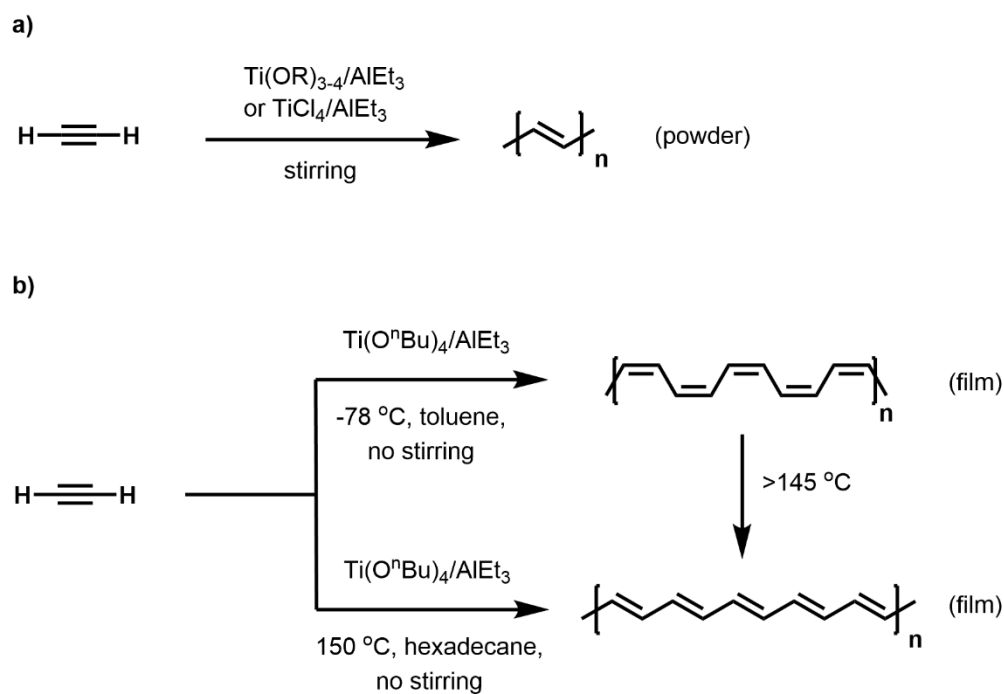


Figure 1.2. Structural isomers of polyacetylene.

1.2.1 Classic Synthesis of Polyacetylene

The synthesis of linear polyacetylene was first reported by Giulio Natta in the mid-late 1950s using mixtures of titanium alkoxydes ((TiOR)₃₋₄) and triethylaluminum (AlEt₃) as a catalyst to polymerize acetylene gas.^{1,31} Similar procedures were then used to synthesize polyacetylene by different groups, also employing the use of catalyst

systems composed of mixtures of TiCl_4 and AlEt_3 .^{32,33} Typically, acetylene gas was bubbled through a solution or suspension of the catalysts to form an insoluble black powder that was difficult to structurally characterize (Scheme 1.1a). Central to the discussion was the amount of *cis* and *trans*-double bonds in the backbone, since a polymer with a mixture of both forms was normally achieved.¹ Hideki Shirakawa later optimized the reaction conditions such that a large excess of catalyst and lack of stirring led to formation of polyacetylene films with a silver luster at the solution/gas interface or on the walls of the flask (Scheme 1.1b).^{25,26,34} The catalyst system used, $\text{Ti}(\text{O}^n\text{Bu})_4/\text{AlEt}_3$, was chosen for its good solubility in solvents such as hexanes or toluene, since concentrations above 3 mM was necessary for the formation of polyacetylene films.³⁴



Scheme 1.1. a) Synthesis of polyacetylene powder by Natta's method; b) Synthesis of polyacetylene films by Shirakawa's procedure.

The Shirakawa method allowed for better characterization^{26,35} and for improved control over the final structure, as lower reaction temperatures (-78 °C in toluene) led to the formation of *cis*-PA with a copper-like color, while higher temperatures (150 °C in hexadecane) afforded silver-colored *trans*-PA.²⁶ It was also discovered that heating *cis*-polyacetylene above 145 °C, led to isomerization into the thermodynamically more stable *trans*-PA,³⁶ consistent with the direct synthesis of *trans*-PA at elevated temperatures. Conductivity measurements of the films revealed that the polymer was semiconducting in either the *cis* ($\sigma \sim 10^{-5}$ S/cm) or *trans* form ($\sigma \sim 10^{-8}$ S/cm),³⁷

indicating the presence of an energy gap between the HOMO and the LUMO in polyacetylene.

1.2.2 Electronic Structure of Polyacetylene

The electronic structure of polyacetylene can be derived from increasing the linear polyene chain length, starting from ethylene (Figure 1.3).^{2,38} The HOMO of ethylene is formed by the bonding interaction of the p_z atomic orbitals in each carbon (π molecular orbital) while the LUMO is a result of the antibonding interaction of the p_z atomic orbitals (π^* molecular orbital). In this case, there is a relatively large energy difference between the HOMO and the LUMO (7.0 eV).³⁹ When a second ethylene unit is added to the chain, forming the dimer butadiene, another filled bonding orbital is created as well as its empty antibonding counterpart. When the bonding frontier orbitals in butadiene are examined, it is possible to note that one is purely bonding and has an energy lower than the starting HOMO of ethylene, since more bonding interactions are possible between the p_z orbitals. However, the second bonding orbital (the HOMO of the dimer) has one antibonding interaction between the p_z orbitals located in the central carbons, and therefore it has an increased energy. An analogous situation happens with the antibonding orbitals, with one of them (the LUMO of the dimer) having a decreased energy relative to the LUMO of ethylene due to one bonding interaction. This situation effectively leads to the decrease of the HOMO-LUMO gap relative to ethylene.

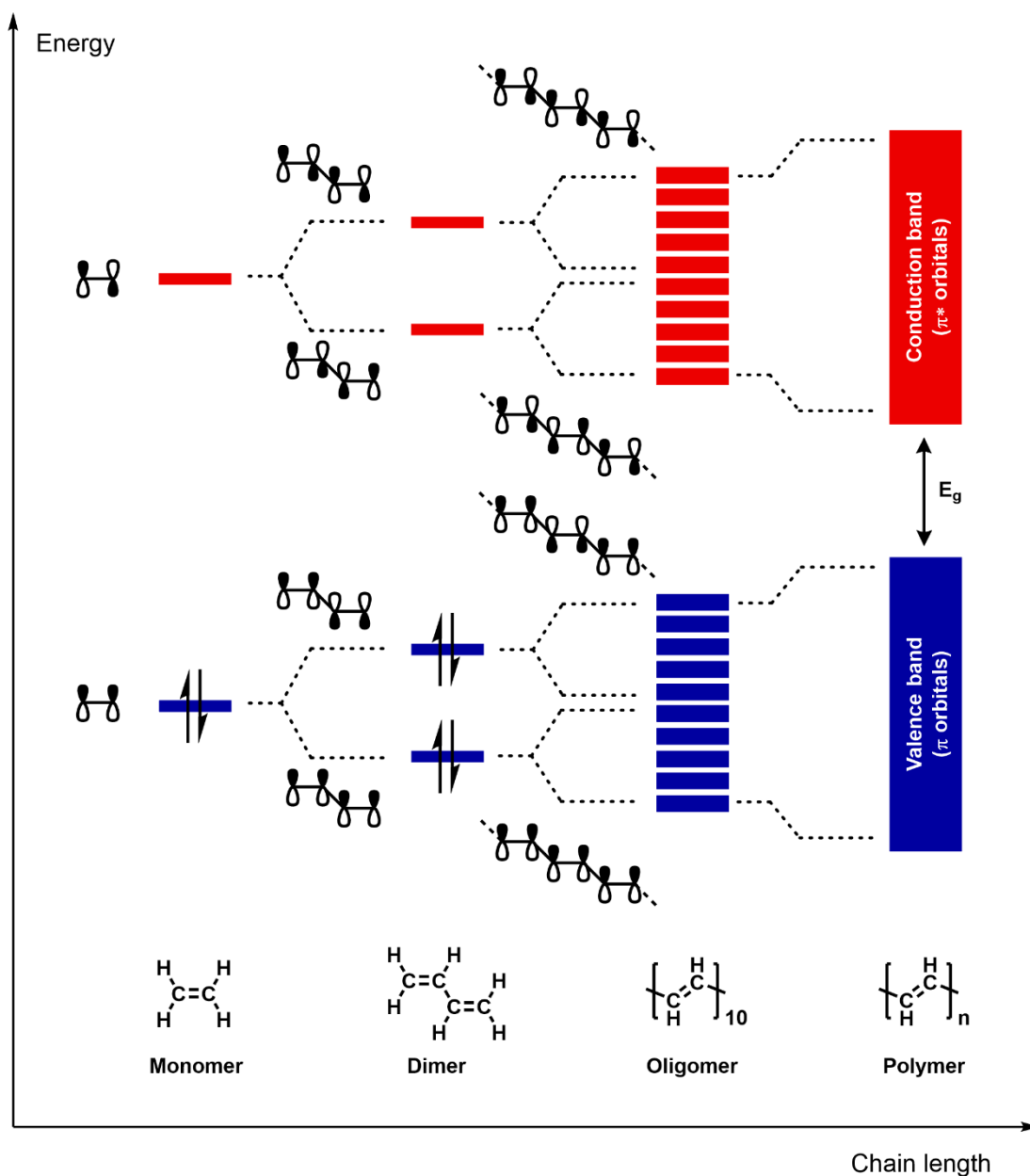


Figure 1.3. Molecular orbital diagram showing the frontier orbitals of a polyene chain of increasing length, leading to bands in polyacetylene. E_g indicates the energy of the HOMO-LUMO (or band) gap.

As more ethylene units are added, and more bonding and antibonding orbitals are created, an overall decrease in energy difference occurs among orbitals of the same group (bonding and antibonding) as well as a further decrease in HOMO-LUMO energy gap. If chain growth is carried out until an infinite chain is attained, the energy difference between orbitals of the same group becomes so small that they effectively function as a single band. The filled band formed by orbitals of bonding character is called the valence band, while the empty antibonding band is called the conduction band, borrowing terminology that is applied to inorganic semiconductors. In this case, the energy difference between the two bands is now deemed the band gap (E_g), which for *trans*-polyacetylene is considerably smaller than ethylene (1.4 vs. 7.0 eV, respectively).^{39,40}

It is important to notice that molecular orbitals at the edge of each band (top of valence and bottom of conduction band) are very similar, but not identical. In fact, if the bond lengths between the carbon atoms in polyacetylene were the same (*i.e.* with a length in between that of double, C=C, and single bonds, C-C), then these two orbitals would be indistinguishable in an infinite chain and should, therefore, have the same energy and be degenerate (Figure 1.4). In this case, both of these orbitals would have an overall non-bonding character and only two electrons, which would be divided among the two orbitals. One can see how breaking degeneracy (going back to *trans*-PA) is favorable in this case, as even though one of the orbitals gains antibonding character, the two electrons are located entirely in the orbital that gains bonding character, decreasing the overall energy of the system. This break in symmetry is called

Peierls Distortion⁴¹ and happens with half-filled bands, as it leads to an overall stabilization of the system.^{38,42}

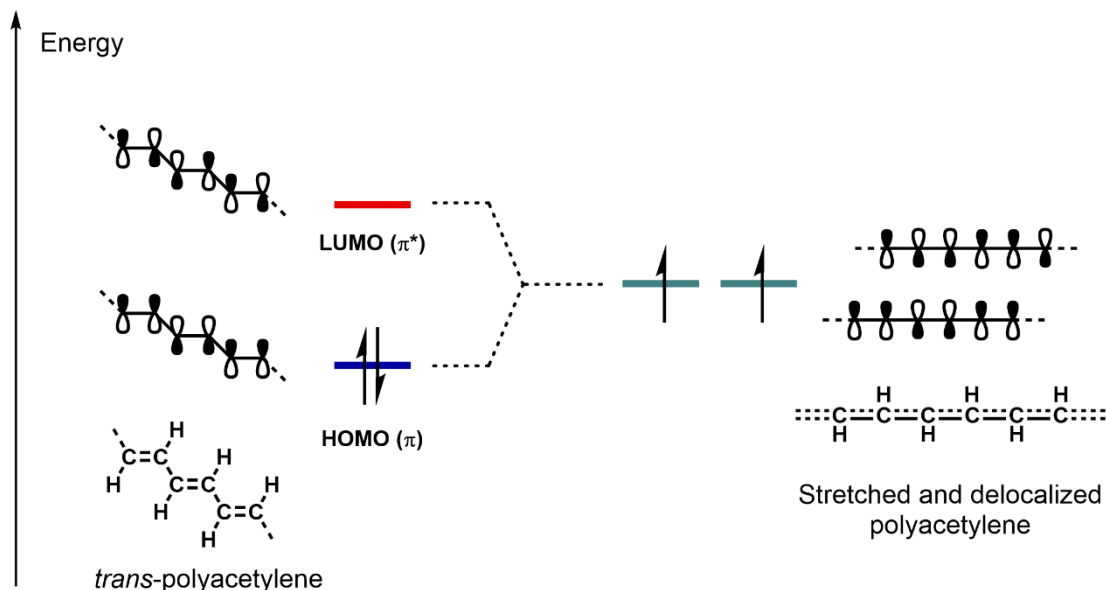


Figure 1.4. HOMO and LUMO in *trans*-polyacetylene compared to degenerate orbitals in a hypothetical, fully delocalized, polyacetylene.

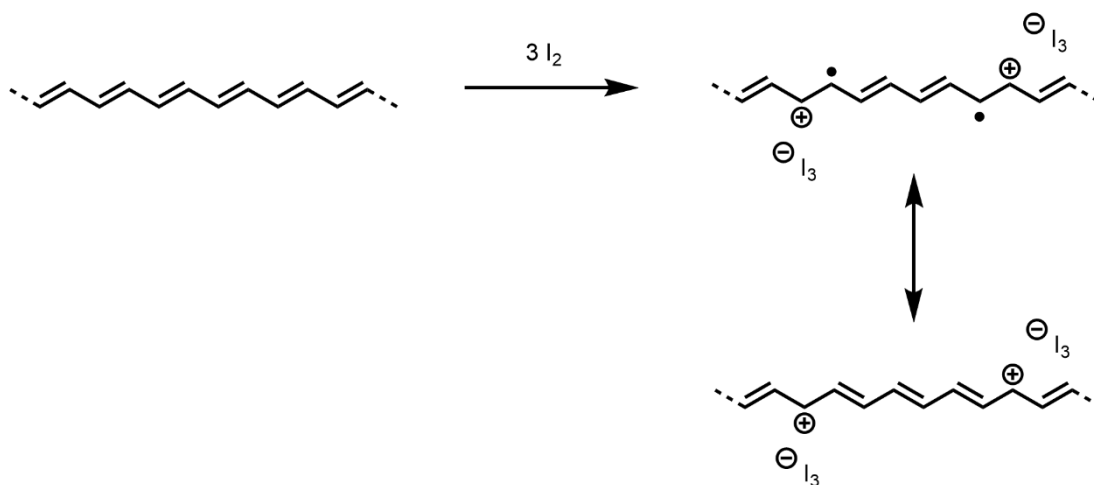
Effectively, this translates into a bond length alternation in pure polyacetylene, where the C=C bond length is 1.36 Å and the C-C bond length is 1.44 Å (measured by nutation NMR spectroscopy),^{43,44} and a band gap between the valence and conduction bands, even for an infinite chain, rendering polyacetylene a semiconductor.

1.2.3 Chemical Doping and Onset of Metallic Behavior

Despite the presence of a band gap, polyacetylene can become conducting when doped by molecules that can either oxidize or reduce it. Exposure of as-prepared *trans*-

polyacetylene films to Cl_2 , Br_2 , I_2 or AsF_5 vapor can oxidatively dope it (p-doping) to increase conductivity up to 10^2 S/cm.^{45,46} Likewise, polyacetylene can be reductively doped (n-doping) with metals such as Li, Na or K, although the resulting films have lower conductivities (*ca.* 10 S/cm) than their p-doped counterparts and are extremely sensitive to air and moisture.⁴⁷⁻⁴⁹ If the polyacetylene chains, which form a fibrillar network, are stretch-aligned prior to doping,⁵⁰ the conductivity can be further increased to 10^4 - 10^5 S/cm by doping with I_2 .^{51,52} These values of conductivity bring doped polyacetylene very close to the conductivity of common metals (10^6 - 10^7 S/cm), which caused polyacetylene to be included in the class of materials called “synthetic metals”.⁵³

Chemically, doping leads to the formation of radicals on the backbone of the polymer and incorporation of the dopant as a counterion.⁴² In the case of oxidative doping with I_2 , incorporation of I_3^- anions (and a minor contribution from I_5^-) is observed (Scheme 1.2),^{54,55} which also leads to swelling of the polymeric fibers.⁵⁶ Physically, the radical is seen as a perturbation of the conjugated structure of polyacetylene, which can be modeled as a wave, or a soliton.^{23,42} This perturbation leads to the formation of energy states in between the valence and conduction bands, a midgap state, locally suppressing Peierls Distortion and removing the band gap to afford the metallic behavior.^{23,42} Additionally, it was later discovered that doping can lead to *cis-to-trans* isomerization, even at low levels of doping.^{57,58}



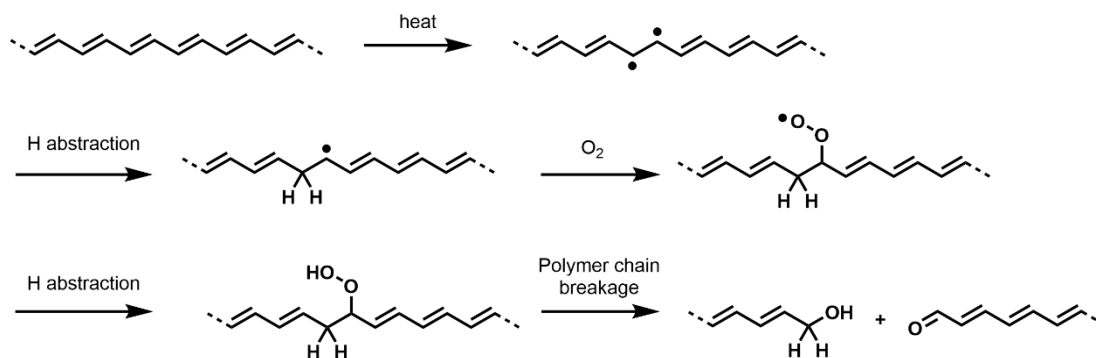
Scheme 1.2. Iodine doping of polyacetylene leading to the formation of radicals.

1.2.4 Challenges for Current Applications

Despite the unprecedented conductivity of doped polyacetylene and the theoretical knowledge that its study afforded, it is difficult to find the use of polyacetylene in modern applications. This is due to challenges in both the processability and air stability of parent polyacetylene.

As mentioned in Section 1.1, one major selling point of conjugated polymers in modern applications is their ease of processing. This is usually tied with the polymer being soluble so that solution-processing techniques such as spin coating, roll-to-roll printing or ink-jet printing can be performed,³⁻⁵ since the deposition of polymers onto substrates by thermal or vacuum assisted evaporation, techniques commonly used for small molecules,⁵⁹⁻⁶¹ is normally not possible. Unfortunately, parent polyacetylene (in either the *cis* or *trans* forms) is completely insoluble and therefore cannot be easily processed after either the powder or films are made.²⁵

Another common processing method for polymers that is extensively used in industry is melt-processing. This process is normally compatible with non-conjugated polymers with relatively low melt transition temperatures (T_m) such as polyolefins, but can be used for π -conjugated polymers in a few cases.⁶²⁻⁶⁴ However, polyacetylene is also infusible (with hydrogen migration and cross-linking occurring at 325 °C, followed by decomposition at 420 °C),³⁶ leaving no option but the use of free-standing films formed directly by polymerization through Shirakawa's procedure.³⁴



Scheme 1.3. Degradation of polyacetylene by exposure to air leading to cleavage of the polymeric chain.

Additionally, most π -conjugated polymers employed in modern applications, such as polythiophenes, are air stable, while polyacetylene slowly degrades upon air exposure. Initial exposure of polyacetylene to air leads to a reversible oxidative doping and a slight increase in conductivity,^{65,66} but over time peroxide radicals are formed that ultimately lead to the breakdown of the polymeric chain and a decrease in molecular weight (Scheme 1.3).⁶⁷ Oxidative doping of polyacetylene can increase its

air stability, but samples still degrade after a week,^{68,69} which means that encapsulation (protection by a gas-diffusion barrier) would be required for devices based on polyacetylene to be operated under ambient conditions.^{70,71}

1.2.5 Modern Synthesis of Polyacetylene

Modern research in the synthesis of polyacetylene has been aimed at solving the drawbacks of insolubility and air-instability of polyacetylene. A large body of work can be found on the polymerization of mono or disubstituted acetylenes (*e.g.* $\text{RC}\equiv\text{CH}$ and $\text{RC}\equiv\text{CR}$) to afford polyacetylenes with high density of solubilizing side chains (Scheme 1.4).⁷²⁻⁷⁵ These polymers are indeed soluble in common organic solvents and are also air stable. However, these features come at the cost of loss of properties from that of parent polyacetylene, since the high density of side chains leads to steric repulsions that cause severe twisting of the backbone, leading to helical structures.⁷⁶⁻⁷⁸ Twisting significantly reduces π -conjugation, which increases E_g (>2.0 eV) and reduces the reactivity of the backbone towards O_2 . Rich chemistry has also been developed *via* the cyclopolymerization of α,ω -diynes to afford polyacetylene backbones fused with cycloalkenes (Scheme 1.5).⁷⁹⁻⁸⁴ The resulting polymers often have a larger band gap due to both the steric bulk of side chains and the presence of *cis* C=C bonds along the polymer backbone.

Common strategies to obtain polyacetylene derivatives that more closely resemble the properties of the parent polymer are the synthesis of soluble polymer precursors which can later be converted into PA, or through the ring-opening metathesis polymerization (ROMP) of cyclooctatetraene (COT) derivatives.

1.2.5.1. Soluble Polyacetylenes from the ROMP of Cyclooctatetraene (COT)

Soluble polyacetylene derivatives that maintain extended π -conjugation were synthesized by the teams of Höcker and Grubbs. Work in this area started with the synthesis of parent polyacetylene through the ring-opening metathesis polymerization (ROMP) of cyclooctatetraene (COT).^{85,86} COT, a liquid at room temperature, is an unsaturated ring formed by 8 carbons and 8 π -electrons and adopts a boat-shaped geometry in the ground state with localized C=C double bonds (Figure 1.5),⁸⁷ in part to avoid the antiaromaticity associated with a planar structure.⁸⁸⁻⁹⁰ With intra-ring bond angles of 126-127°, ⁸⁷ the ROMP of the COT ring is thermodynamically favored as this process releases ring strain (*ca.* 2.5 kcal/mol).⁹¹⁻⁹³



Figure 1.5. Boat-shaped molecular structure of cyclooctatetraene (COT).

Taking advantage of the ring strain inherent to COT, Höcker and coworkers synthesized polyacetylene in routes similar to the classic procedures. By introducing

cyclooctatetraene into a mixture of $WCl_6/AlEt_2Cl$ in toluene, an insoluble black powder was formed in 6 % yield. Additionally, vapor deposition of COT into a flask containing a slurry of the same catalyst system led to the formation of a polyacetylene film (40 % yield).⁸⁵ Grubbs and coworkers later used a similar approach to synthesize polyacetylene using well-defined, soluble tungsten-based olefin metathesis catalysts (Figure 1.6, Scheme 1.6).⁸⁶ In addition to polymerizing COT in dilute solutions or by vacuum deposition over the solid catalyst, addition of catalyst **C2** to neat COT afforded a freestanding film of polyacetylene. Oxidative doping of the films with I_2 led to conductivities of 10^2 S/cm, similar to initial studies with Shirakawa's polyacetylene.^{45,46} This strategy also allowed for the polymerization of bromocyclooctatetraene (COT-Br) and the formation of copolymers with cyclooctadiene (COD) and norbornene (NBE).

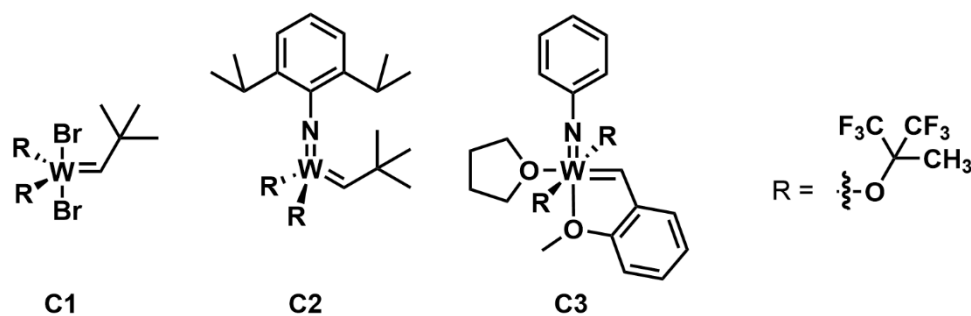
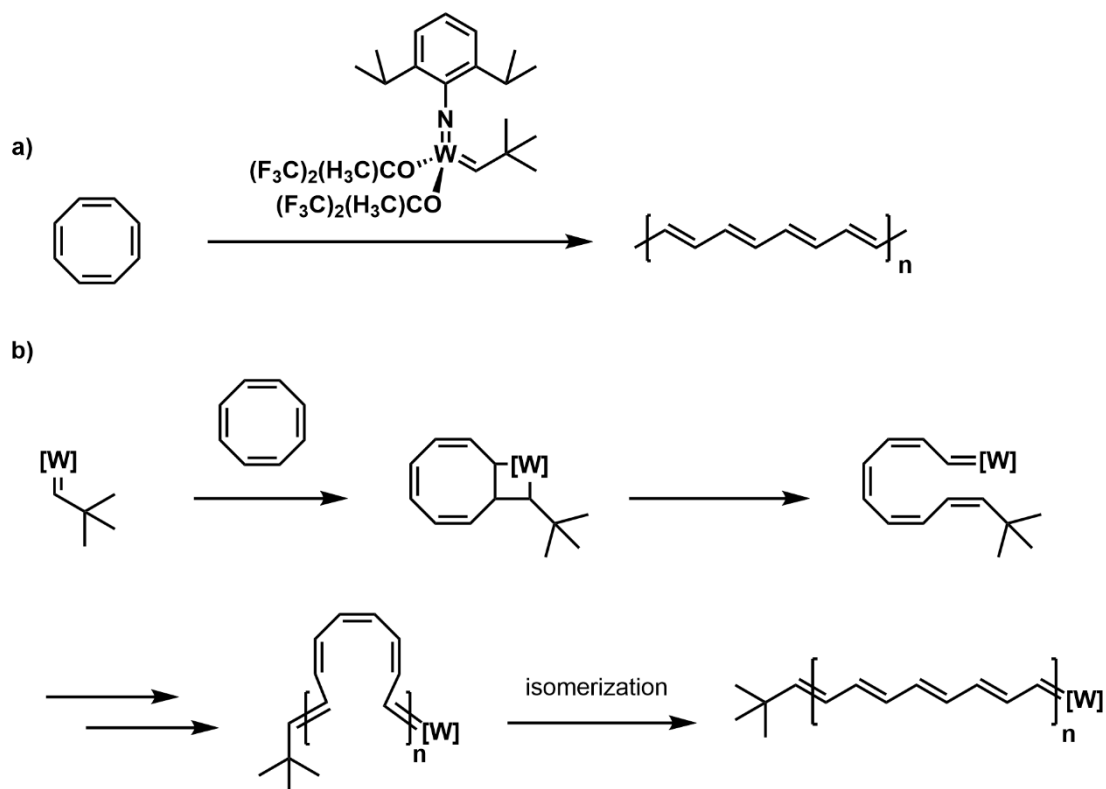
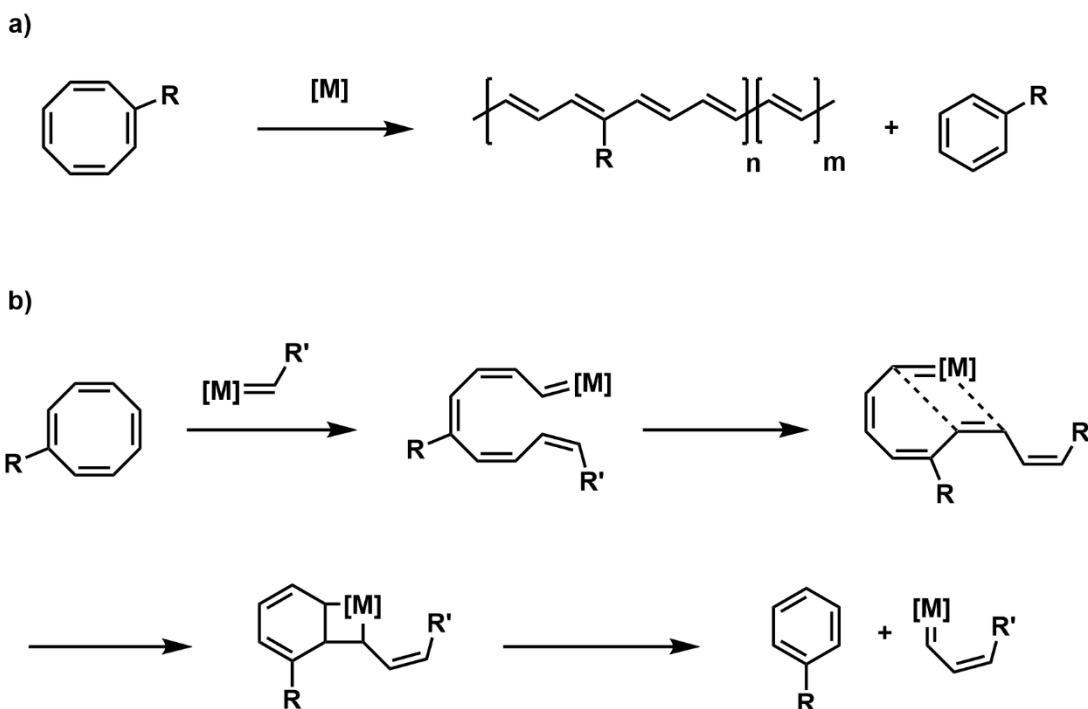


Figure 1.6. Tungsten catalysts initially used in the ROMP of COT.



Scheme 1.6. a) Synthesis of polyacetylene through the ROMP of COT using a well-defined tungsten catalyst; b) Steps involved in the polymerization.

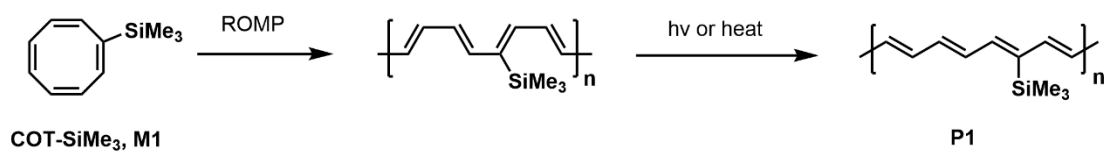
However, it was observed that the ROMP of COT in dilute toluene solutions led to formation of benzene as a side product in 75 % yield. This was explained by a backbiting reaction (Scheme 1.7; for COT, R = H), where the catalyst attached at one end of the polymer during chain growth folds over and performs olefin metathesis with the backbone itself, instead of with a new molecule of COT. This side reaction is heavily favored in dilute conditions as it leads to the formation of benzene, an aromatic molecule, and increases the overall entropy of the system. After backbiting, the catalyst remains attached to the growing chain and can continue reacting with new monomers.



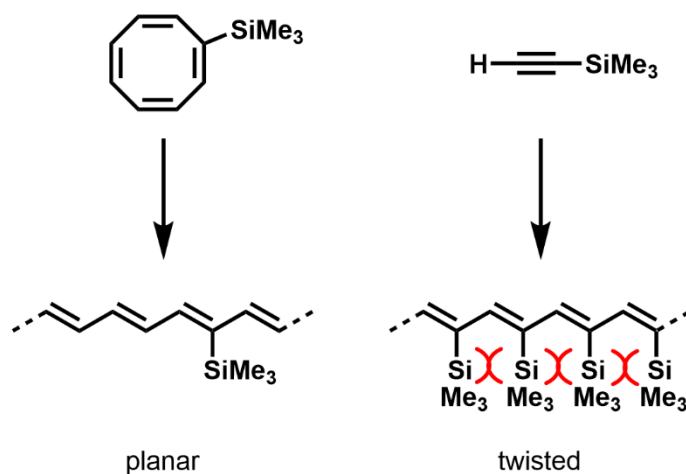
Scheme 1.7. a) ROMP of COT ($R = H$) and its derivatives ($R \neq H$) leading to formation of polyacetylenes and benzene or substituted benzenes; b) Mechanism of backbiting.

Despite the drawback of backbiting, this route allowed for the synthesis of soluble polyacetylenes through the ROMP of monosubstituted COT derivatives. The first example was the ROMP of **COT-SiMe₃ (M1)** using the tungsten catalyst **C2** (Scheme 1.8).⁹⁴ Addition of the catalyst to a mixture of COT-SiMe₃ and THF, afforded a polymer (number average molecular weight, $M_n = 137$ kDa relative to polystyrene) that is soluble in toluene, benzene and THF. UV-Vis absorption spectra of the polymer in CCl₄ showed an absorption maximum at around 380 nm, which is converted into absorption at 512 nm upon exposure to UV light (using a high-pressure mercury lamp).

This change in absorption was due to isomerization from the *cis*-isomer formed immediately after reaction with the catalyst (Scheme 1.6) into *trans*-polyacetylene, as confirmed by the absence of an exothermic event at 145 °C during differential-scanning calorimetry (DSC) after photoisomerization.³⁶ The resulting polymer could also be doped by I₂ to increase the conductivity from 10⁻⁵ S/cm (neat) to 0.2 S/cm. In comparison, the conductivity of poly(trimethylsilylacetylene),⁹⁵ a Me₃Si-substituted polyacetylene with side chains on alternating carbons (Scheme 1.9), after doping with iodine only reaches a maximum of 10⁻⁴ S/cm, due to steric repulsions between side chains that cause twisting and reduce π-conjugation along the backbone. Finally, using the soluble, π-conjugated polyacetylene **P1** after I₂ doping, it was possible to build solar cells with efficiencies of 1-5%.⁹⁶



Scheme 1.8. Synthesis of a Me₃Si-substituted polyacetylene through the ROMP of COT-SiMe₃.

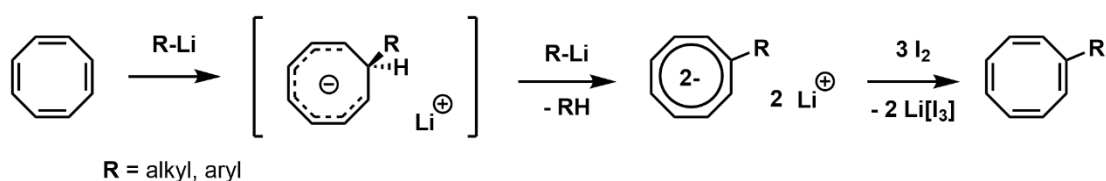


Scheme 1.9. Comparison of polyacetylene chains obtained from different Si-substituted precursors.

It is important to note that **COT-SiMe₃** is also prone to backbiting reactions during polymerization. For substituted COTs, backbiting not only reduces the yield of polymer but also effectively adds -HC=CH- units to the backbone (compare the starting $[\text{M}]=\text{C-R}'$ and the final $[\text{M}]=\text{C-C}=\text{C-R}'$ in Scheme 1.7b). The -HC=CH- units left in the backbone after backbiting are unimportant in the polymerization of unsubstituted COT, since they do not change the final repeat unit of the polymer, but are important for substituted COT, as they act as spacers between side chains and change the final polymer composition. For simplicity, the structure of polymers discussed in this section will be based on the ideal situation when no backbiting happens.

Following the synthesis of a soluble polyacetylene from **COT-SiMe₃**, different side chains were investigated. Alkyl and aryl side chains were installed through the

reaction of COT with the corresponding alkyl and aryl lithium species.^{97,98} This route involves reaction of COT with two equivalents of lithiated alkyl or aryl chains to form a COT dianion (Scheme 1.10),⁹⁹ an aromatic species,¹⁰⁰ which is later oxidized with I_2 . The ROMP of COT monomers bearing alkoxide substituents was also reported,⁹⁸ although the synthetic procedure used to access those monomers was not described.



Scheme 1.10. Reaction of COT with two equivalents of an organolithium species followed by re-oxidation with I_2 . For the different substituents used (R), see Figure 1.7.

The corresponding functionalized polyacetylenes were then obtained through ROMP (Figure 1.7, Table 1.1) using catalysts **C2** and **C3**.^{97,98} When using **C2**, the catalyst is initially mixed with THF to slow down polymerization through THF coordination, an unnecessary step for **C3**. The resulting polymers showed varying chain lengths depending on the nature of the side chain ($M_n = 3\text{-}250$ kDa) but little control over molecular weight, even though the extent of backbiting was reduced by performing the polymerization with neat monomer. Of the polyacetylenes obtained, the ones containing side chains without steric bulk at the α -carbon (**P2-7**, **P13-17**) were only fully soluble in their *cis* form and showed insolubility or partial solubility after isomerization to their *trans* isomer; secondary (**P8**, **P9**, **P11**) and tertiary (**P10**) alkyl

chains afforded solubility for both the *cis* and *trans* isomers. The polyacetylene containing a smaller cyclopropyl side chain (**P12**) was also insoluble in its *trans* form. These results indicate that steric bulk at the α -position is important for imparting polymer solubility. Additionally, molecular dynamics calculations (MM2 force field) indicated that the secondary and tertiary alkyl side chains improve solubility by increasing the torsional flexibility of the backbone.

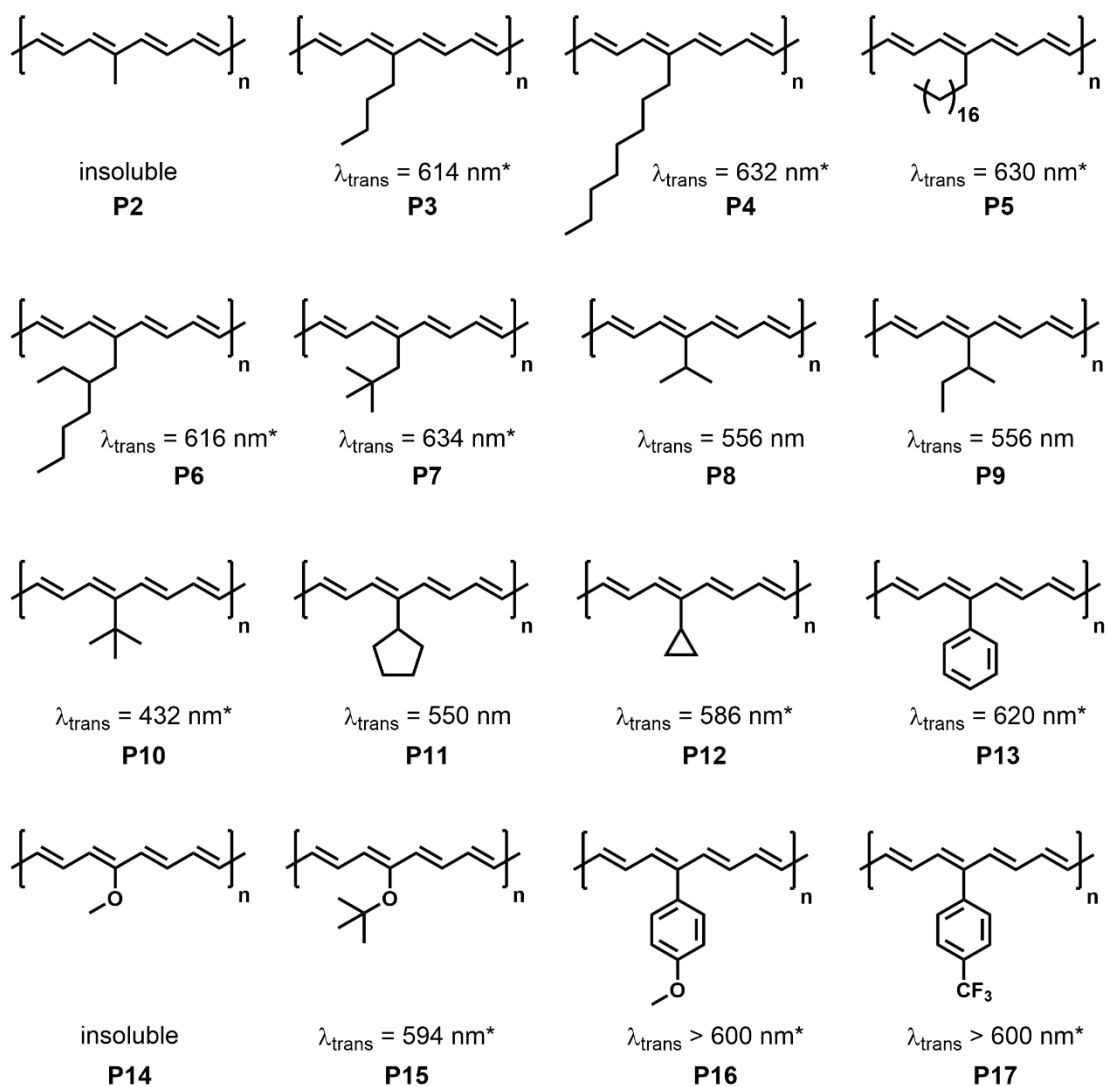


Figure 1.7. Alkyl-, aryl- and alkoxy-substituted *trans*-polyacetylenes and their absorption maxima in THF. * These values were obtained from suspensions in THF.

Absorption maxima for these polymers were reported (Figure 1.7), however these have to be interpreted with caution because the red-shifted absorption maxima for the poorly soluble polymers could be due to their insolubility, since conjugated polymers tend to have a red-shifted absorption in the solid state (where twisting of the

backbone is minimized and conjugation length is maximized). Finally, the polymer bearing the largest steric bulk at the α -carbon, *i.e.* a *tert*-butyl group, also affords the most blue-shifted absorption ($\lambda_{\text{trans}} = 432 \text{ nm}$) in the series, presumably due to increased backbone twisting in solution.

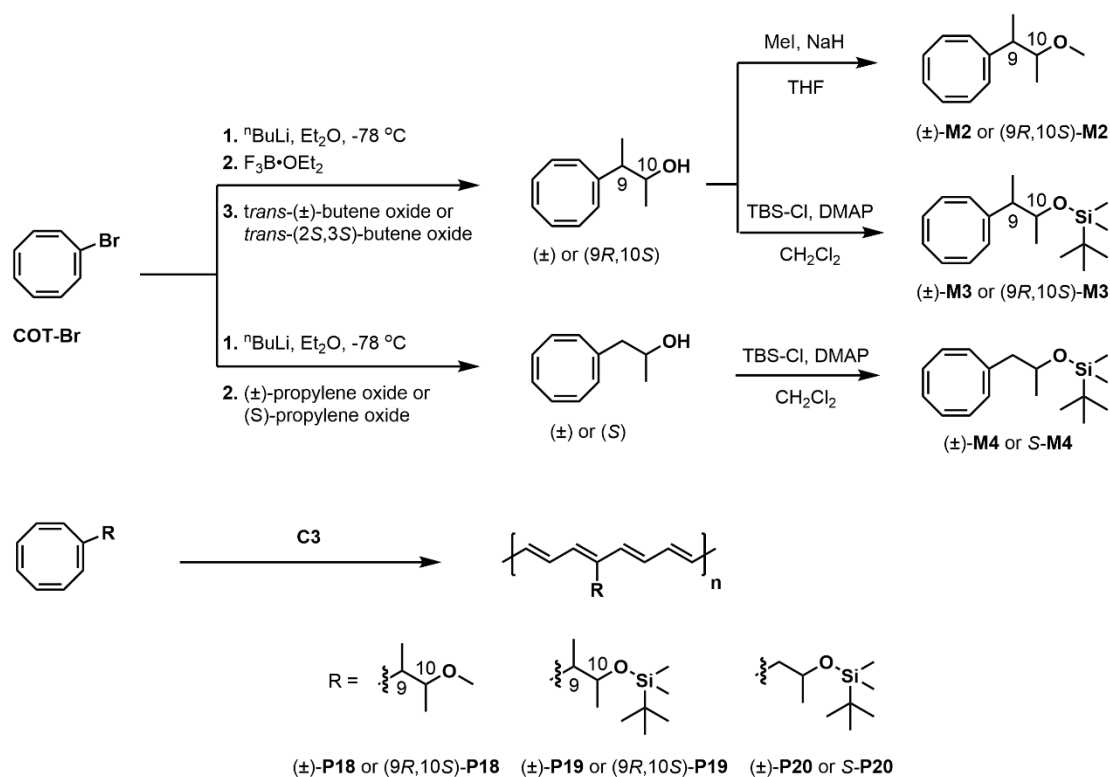
Table 1.1. Summary of reported properties for **P2-P17**.^a Reported relative to polystyrene.^b Maximum conductivity reported after I₂ doping.

Polymer	M _n (kDa) ^a	PDI	Conductivity (S/cm) ^b
P1	137	-	0.2
P2	-	-	-
P3	2.9	4.7	0.7
P4	47	2.5	50
P5	14	3.2	3.65
P6	238	1.5	-
P7	93	1.4	21
P8	10.0	5.7	-
P9	24.8	2.0	2×10^{-4}
P10	25	1.7	$< 10^{-8}$
P11	16.0	7.6	-
P12	20.4	2.6	-
P13	233	1.5	0.6
P14	-	-	-
P15	252	1.4	$\sim 10^{-7}$
P16	-	-	-
P17	-	-	-

Grubbs and coworkers later studied the electrochemical doping of some of the polymers found in Figure 1.7.¹⁰¹ Through Coulometric measurements, it was possible to determine that films of the soluble trimethylsilyl- (**P1**) and *sec*-butyl- (**P9**) substituted polyacetylenes could accept/donate one electron per 14-15 C=C units along the backbone (while parent PA can accept/donate one electron per 5 C-C units). Films of **P1** and **P9** also showed matching near-IR (NIR) absorption by spectroelectrochemical measurements after oxidation or reduction (**P1** $\lambda_{\text{max}}^{\text{ox/red}} = 1200\text{-}1300$ nm; **P9** $\lambda_{\text{max}}^{\text{ox/red}} = 1400\text{-}1550$), similar to parent polyacetylene, but at a lower wavelength (PA $\lambda_{\text{max}}^{\text{ox/red}} = 1650\text{-}1900$). Through cyclic voltammetry (CV), the authors also suggested that an inductive effect was possible, since the alkoxy-substituted **P15** was more easily oxidized than its alkyl counterparts. Finally, CV showed that a *cis-trans* isomerization of films was possible through doping, consistent with chemical doping-induced isomerization of parent PA.^{57,58}

In a separate study, the effect of chiral side chains was assessed.¹⁰² Reaction of COT-Li (obtained from COT-Br and ⁿBuLi) with alkene oxides mediated by F₃B•OEt₂,¹⁰³ afforded COT with chiral alcohol side chains.¹⁰² Since tungsten catalysts are sensitive to alcohols,¹⁰⁴ these groups were further transformed into ether or siloxy moieties. The resulting monomers (Scheme 1.11) were polymerized by adding catalyst **C3** in pentane, followed by transferring the reaction mixture onto a glass slide to afford polymer films. The polymers ($M_n = 150\text{-}1,240$ kDa vs polystyrene, PDI = 1.3-1.5) could then be isomerized to their *trans* forms either by UV light irradiation or spontaneously in solution over several hours. Polymers **P18** and **P19** were soluble as

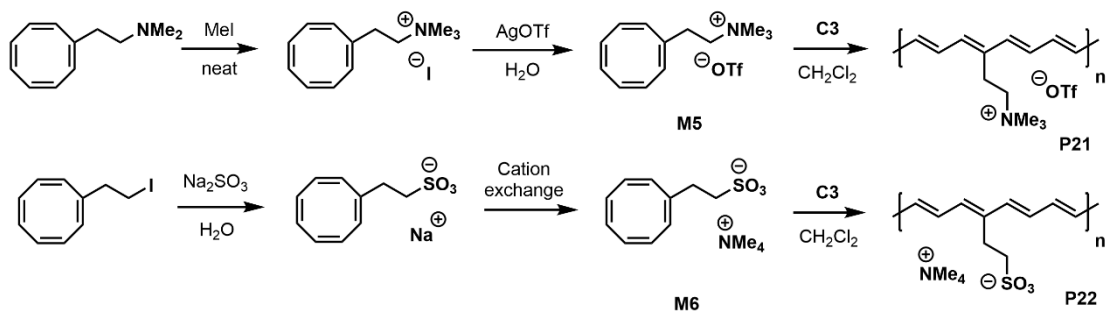
both the *cis* and *trans* isomers, regardless of absolute configuration, while **P20** was only soluble before isomerization to the *trans* form, consistent with the need of steric bulk for solubility.⁹⁸



Scheme 1.11. Synthesis of polyacetylenes with chiral side chains.

Due to the chirality of the side chains in **P18-P20**, the HOMO-LUMO transitions (π - π^*) of the chiral polymers exhibited circular dichroism, indicating that the chains can preferentially twist the backbone in one direction. This effect is similar to what is displayed by some highly substituted polyacetylenes,^{72,105} but only in the former cases is extended π -conjugation (estimated to be over 20 C-C units) maintained.

Expanding the scope of polymerization with catalyst **C3**, Lonergan and coworkers later explored the formation of polymers with ionic side chains (Scheme 1.12).^{106–108} The syntheses of monomers **M5** and **M6** were based on the copolymerization of acetylene gas and substituted acetylenes.¹⁰⁹ For **M5**, acetylene was copolymerized with *N,N*-dimethyl-3-butynylamine,¹⁰⁹ followed by methylation with methyl iodide (MeI) and anion exchange using silver triflate (AgOTf; OTf = F₃CSO₃⁻). For **M6**, COT-CH₂CH₂-I was reacted with sodium sulfite (Na₂SO₃), followed by cation exchange using an exchange resin. The synthetic procedure used to make COT-CH₂CH₂-I is unclear, but it was possibly achieved by reaction of COT-CH₂CH₂-OH, obtained either by copolymerization of acetylene and 3-butynol¹⁰⁹ or by reaction of COT-Li and ethylene oxide,¹¹⁰ with PI₃ in the presence of pyridine.¹⁰⁹



Scheme 1.12. Synthesis of polyacetylenes with ionic side chains.

Polymerization of **M5** and **M6** with **C3** in CH₂Cl₂, leads to formation of **P21** (M_n not determined) and **P22** (M_n = 35 kDa relative to tetramethylamino poly(styrene

sulfonate), PDI = 2.9) as dark blue, DMSO-soluble polymers.¹⁰⁶ **P22** also showed solubility in DMF, methanol and could become water-soluble after cation exchange with Na⁺. Contrary to alkyl-substituted polyacetylenes, these results suggest that ionic side chains can impart solubility even in the absence of steric bulk at the α -carbon.^{97,98} Additionally, their relatively red-shifted absorption (**P21** λ_{max} = 614 nm; **P22** λ_{max} = 624 nm) is comparable to the poorly soluble polymers synthesized by Grubbs (**P3-7**, **P13**, Figure 1.7), indicating minimal twisting of the conjugated backbone. This afforded conductivities of 0.01-1 S/cm (**P21**) and 0.4-0.7 S/cm (**P22**) after I₂ doping, which are larger than the conductivities of doped alkyl-substituted polymers (Figure 1.7).

A detailed electrochemical study of **P21** and **P22** showed the formation of internally compensated states at low levels of doping.¹⁰⁸ As determined by electrochemical quartz crystal microbalance (EQCM) measurements, oxidation (p-doping) of **P22** leads to loss of the counter cations and reduction (n-doping) of **P21** leads to loss of counter anions. However, the maximum doping achieved (1 e⁻ per 12-16 C-C units) was still similar to the polymers synthesized by Grubbs, yet slightly below that of parent PA.¹⁰¹ Additionally, by using an electrolyte with bulky anion (tetrabutylamino poly(styrene sulfonate), [nBu₄N]PSS) the authors were able to suppress oxidation of **P21** films, since it cannot internally compensate the extra positive charge and the bulky anionic PSS⁻ polymers cannot be incorporated into the film.

Kinetics studies of the ROMP of monomer **M5** with **C3** in CHCl₃ were also performed, showing that the polymerization of **M5** could be inhibited by addition of

[ⁿBu₄N]OTf, either due weak coordination of OTf⁻ to the catalyst or by ion-pairing effects.^{107,111} Slow initiation relative to propagation was also observed. However, Grubbs and coworkers were concomitantly working on Ru catalysts (Figure 1.8) that would later improve polymerization control.^{104,112}

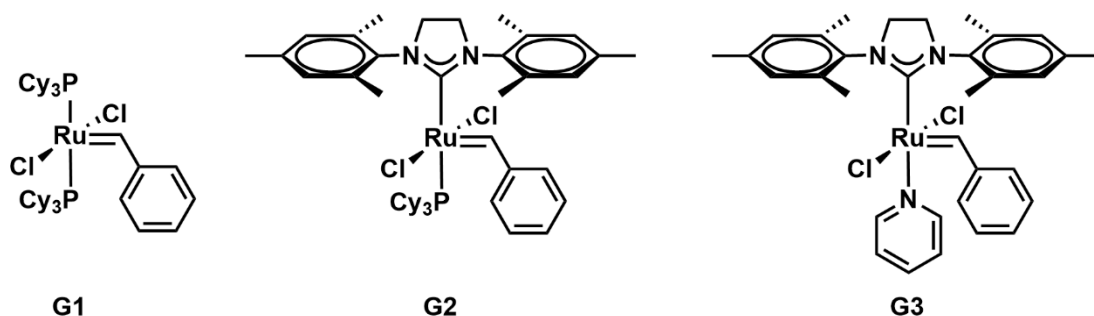
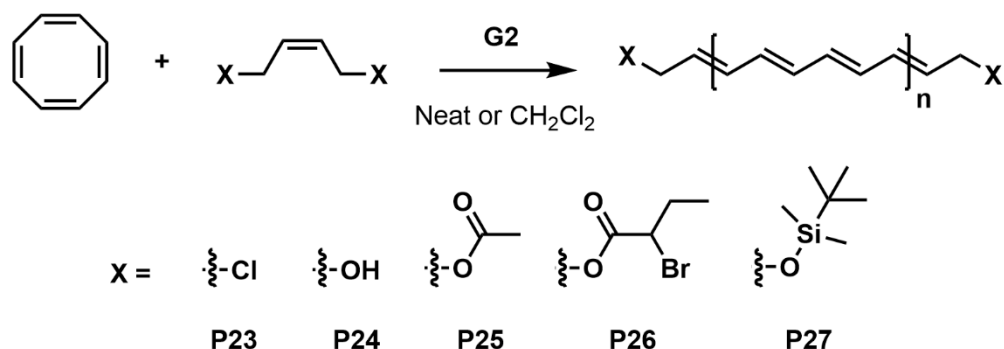


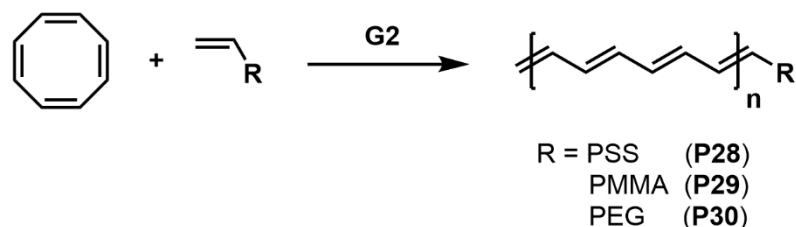
Figure 1.8. Ruthenium-based olefin metathesis catalysts (**G1-G3**) developed by Grubbs and coworkers.

COT is unreactive in the presence of **G1** (known as Grubbs' first generation catalyst) due to its low ring strain of 2.5 kcal/mol.^{93,113} However, polymerization of neat COT with catalyst **G2** (Grubbs' second generation catalyst) was able to produce films that were nearly identical to the ones previously obtained with **C2**.^{86,114} Additionally, the increased functional group tolerance of **G2** allowed for the formation of different end-functionalized soluble COT oligomers (up to 20 double bonds in the backbone) through the ROMP of COT in the presence of disubstituted *cis*-alkenes (Scheme 1.13). The same strategy also allowed for the synthesis of block copolymers with polystyrene (PS), poly(methyl methacrylate) (PMMA), and poly(ethylene glycol)

(PEG) when performing ROMP of COT in the presence of the alkene-terminated polymers (Scheme 1.14).



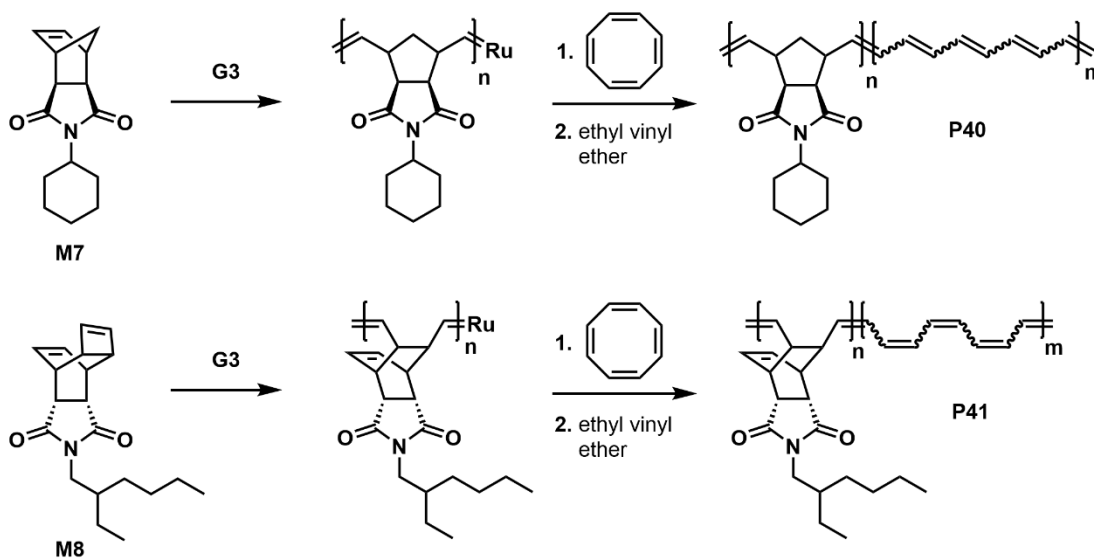
Scheme 1.13. Synthesis of end-functionalized COT oligomers by ROMP.



Scheme 1.14. ROMP of COT in the presence of alkene-terminated polymers

More recently, Choi and coworkers also explored the ROMP of a norbornene (NBE, **M7**) derivative with **G3** followed by addition of COT to give block copolymers (Scheme 1.15).¹¹⁵ The incorporation of 28 COT units was estimated (112 PA repeat units) with minimal back-biting side product (<10 % relative to COT incorporated) when using high concentrations of COT (700 mM). However, the presence of both *cis* and *trans*-PA was inferred from the UV-Vis spectral data. The different affinities

between the π -conjugated (PA) and the non π -conjugated blocks afforded spontaneous self-assembly in solution to give core-shell-like structures with overall morphologies resembling caterpillars. Interestingly, the protective shell formed by **M7** in **P40** afforded air stability to the PA core. Similar results were later achieved by addition of **G3** to a mixture of both monomers,¹¹⁶ suggesting that the larger ring strain of norbornene (27 kcal/mol)^{93,117} leads to preferential polymerization before the COT molecules. Additionally, by swapping **M7** for **M8**, the supramolecular assembly could be altered to yield three-dimensional aggregates (**P41**).¹¹⁸



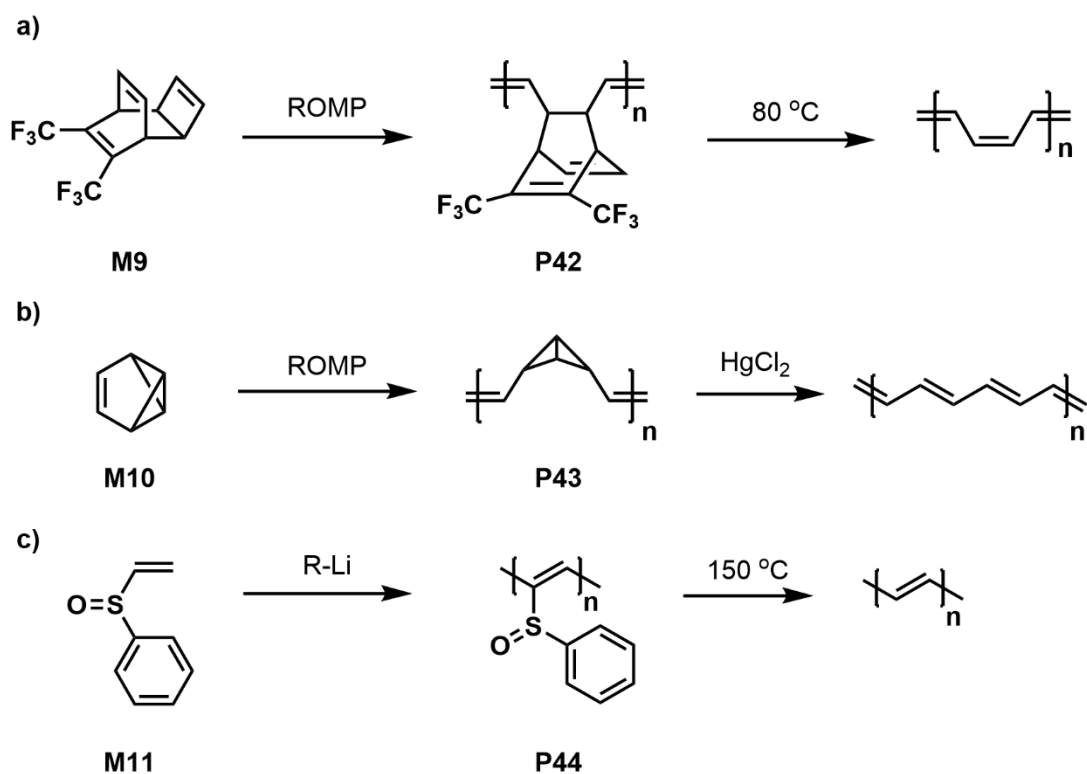
Scheme 1.15. Synthesis of block copolymers with COT.

1.2.5.2. Polyacetylenes from Polymeric Precursors

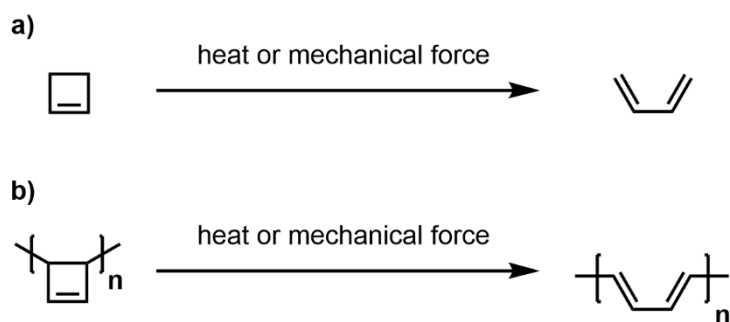
Since polyacetylene is insoluble, different research groups focused on producing soluble polymeric precursors that could be thoroughly characterized and

later converted into PA. “Durham polyacetylene”, synthesized by Feast and coworkers, allowed formation of films of **P42** before heating at 80 °C to eliminate hexafluoroorthoxylene (Scheme 1.16a).^{119–121} This provided a path to devices based on parent polyacetylene (PA).^{122,123} Additionally, Grubbs and coworkers showed that ROMP of benzvalene (**M10**) afforded a polymer with strained (and potentially explosive) bicyclobutane moieties (**P43**) that could be converted into polyacetylene by reaction with HgCl₂ (Scheme 1.16b).^{124,125} The resulting polyacetylene showed lower conductivities of 0.1 S/cm after doping with I₂, presumably due to the presence of sp³-carbons as a result of added olefin cross-linking during reaction with HgCl₂. Finally, Leung and coworkers have shown that loss of benzenesulfenic acid from poly(phenylvinyl sulfoxide) (**P44**) in THF at 150 °C led to the formation of PA (Scheme 1.16c).^{126–128}

Polymeric precursors based on cyclobutenes have been explored by different groups and enabled the subsequent formation of both parent and side chain-substituted PA. Cyclobutene itself is an unsaturated ring with high degree of ring strain (30.6 kcal/mol)⁹³ and is known to undergo a ring-opening isomerization, upon heating or by use of mechanical force, to form 1,3-butadiene (Scheme 1.17a).^{129–134} Therefore, a polymer based on cyclobutene could, in principle, be transformed into polyacetylene (Scheme 1.17b). Depending on its substituents, however, thermal isomerization can be facilitated, which can render cyclobutenes unstable at room temperature,¹²⁹ and provides a challenge for this route.



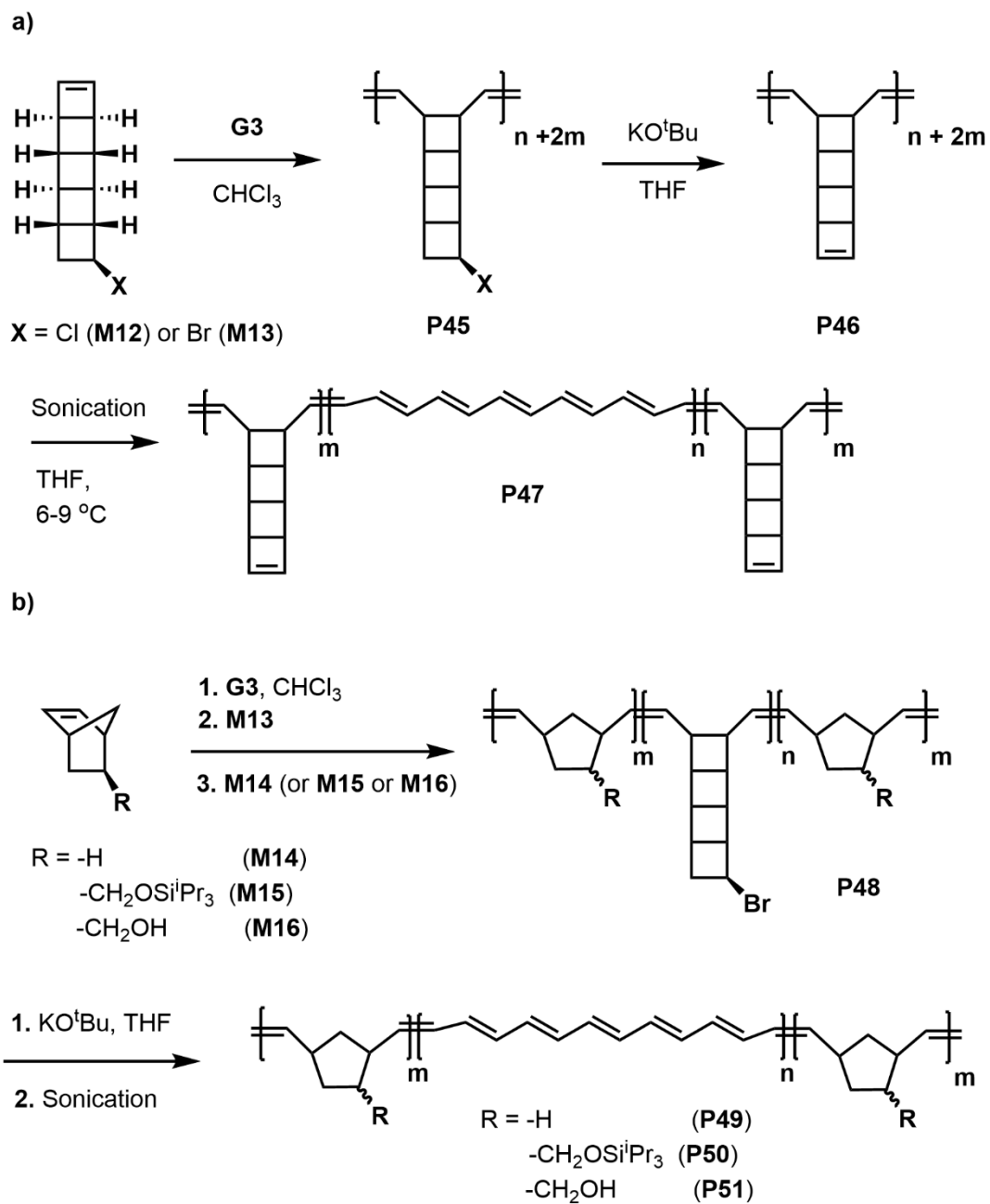
Scheme 1.16. Initial routes used for the synthesis of polyacetylene from polymeric precursors.



Scheme 1.17. Isomerization of cyclobutene into 1,3-butadiene.

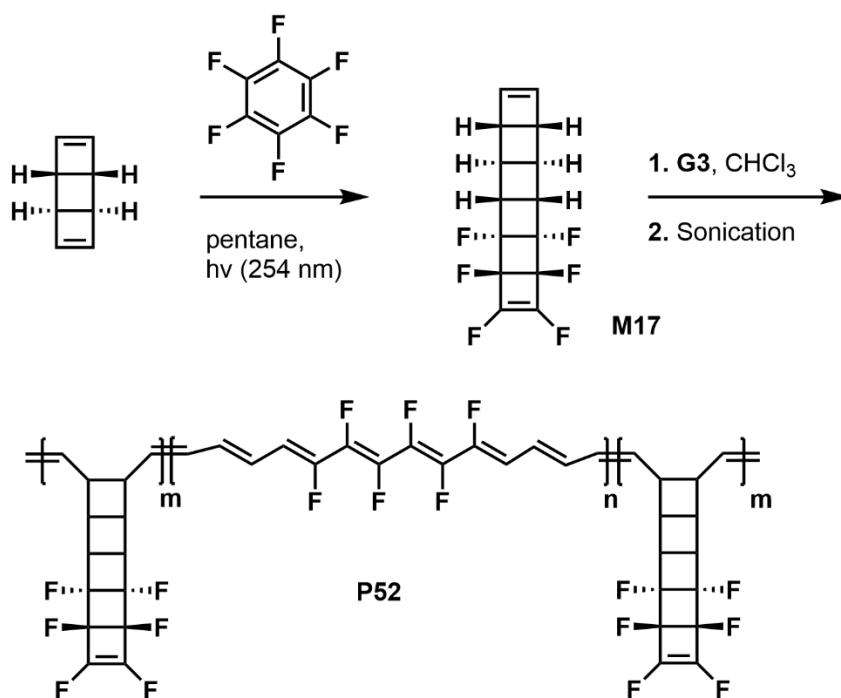
The instability of substituted cyclobutenes was recently overcome by Xia, Burns and coworkers, who synthesized PA from polymers based on ladderenes.¹³⁵

Initially, a polymer is formed by ROMP of a chloroladderene (**M12**). The resulting poly ladderane (**P45**) then undergoes an elimination reaction to form a poly ladderene (**P46**) where cyclobutene spacers are located between the fused cyclobutene moiety and the unsaturated C=C units along the backbone, affording stability. A cascade mechanochemical conversion of **P46** into polyacetylene copolymers is then performed through sonication, leading to an unzipping of the ladderane unit from the backbone towards the cyclobutene unit.^{135,136} As the ladderenes are converted into polyacetylene fragments, block copolymers form and afford, which assemble into micelles. FTIR, Raman and UV-Vis ($\lambda_{\text{max}} = 605\text{-}636\text{ nm}$) characterization indicate formation of *trans*-PA with over 100 C=C conjugated bonds (determined by the frequency of C=C vibration in Raman).¹³⁷ The same mechanochemical conversion could also be applied to the preparation of norbornene-ladderane block copolymers (**P49-51**).¹³⁸



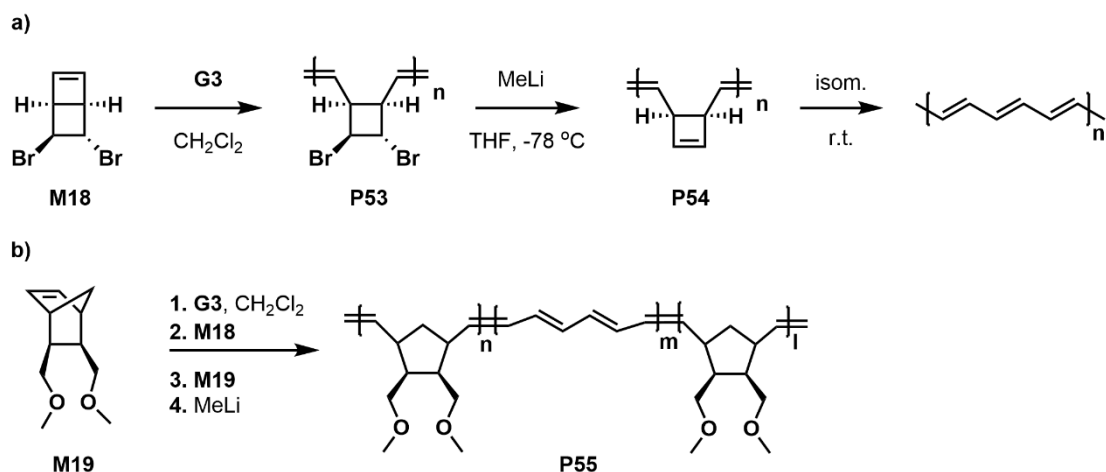
Scheme 1.18. Mechanochemical unzipping of polyadderenes to form polyacetylene block copolymers.

Additionally, a partially fluorinated polyacetylene was synthesized from the chemoselective ROMP of a fluorinated ladderane (**M17**), followed by sonication to give **P52** (Scheme 1.19).¹³⁹ Fluorinated polyacetylene has long been proposed to have increased air stability due to the stability of C-F bonds and reduced HOMO energy, as well as being expected to be a better option for n-doping due to its increased electron affinity.^{140–142} Polymer **P52** provided some confirmation of this theory by retaining 70 % of its initial UV-Vis absorption ($\lambda_{\text{max}} = 591 \text{ nm}$) after 2 days, while the analogous unfluorinated polymer had only retained 10 % of the initial absorption after this time frame. Unfortunately, no doping studies have been reported thus far.



Scheme 1.19. Synthesis of a partly fluorinated polyacetylene by mechanochemical unzipping of a poly(ladderene).

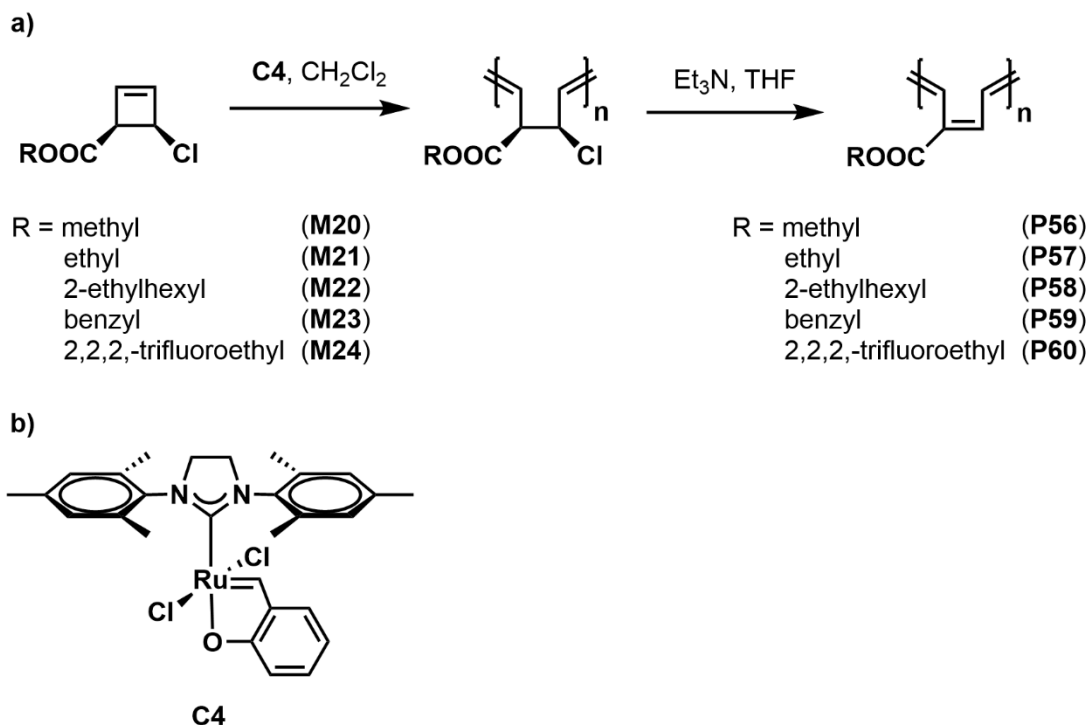
A similar strategy was used by Bielawski and coworkers to synthesize polyacetylenes starting from *trans*-5,6-dibromobicyclo[2.2.0]hex-1-ene (**M18**),¹⁴³ a derivative of Dewar benzene.¹⁴⁴ Polymerization of **M18** proceeds through a controlled chain-growth mechanism, leading to a polymer with narrow molecular weight distribution (**P53**, $M_n = 16.4$ kDa, polydispersity index (PDI) = 1.14). **P53** can be converted into *trans*-PA by addition of containing cyclobutene units (**P54**), which isomerizes to PA at room temperature. Interestingly, FTIR, Raman and solid state ¹³C NMR spectroscopy indicated formation of only the *trans* isomer, suggesting a pathway where **P54** isomerizes to PA through a radical mechanism. The resulting polyacetylene showed conductivity of 30 S/cm when doped with iodine vapor.¹⁴³ Finally, due to the controlled polymerization of **M18**, a triblock copolymer could also be synthesized and converted into the corresponding polyacetylene-containing polymer (**P55**) while maintaining solubility.



Scheme 1.20. a) Synthesis of *trans*-PA from the spontaneous isomerization of a cyclobutene-containing polymer, **P54**; b) Synthesis of a triblock copolymer (**P55**) through a similar route.

Bielawski also recently developed a route to synthesize side chain-substituted soluble polyacetylenes through direct ROMP of substituted cyclobutenes.¹⁴⁵ ROMP of monomers **M20-24** affords intermediate polymers (Scheme 1.21a), which react with Et_3N in elimination reactions to yield side chain-functionalized polyacetylenes (**P56-60**, $M_n = 7.3\text{--}24.9$ kDa, PDI = 1.2–1.6). Interestingly, **G3** failed to catalyze the polymerization of **M20-24**, presumably due to deactivation by side chain coordination through the oxygen atom, therefore catalyst **C4** (Hoveyda-Grubbs 2nd generation catalyst, Scheme 1.21b) was used. The resulting polyacetylenes contain one side chain for every 4 carbon atoms along the polymer backbone, however, UV-Vis data ($\lambda_{\text{max}} = 322\text{--}414$ nm) indicates that the polyacetylenes have a reduced conjugation length, likely due to backbone twisting caused by the side groups. The absorption maxima are

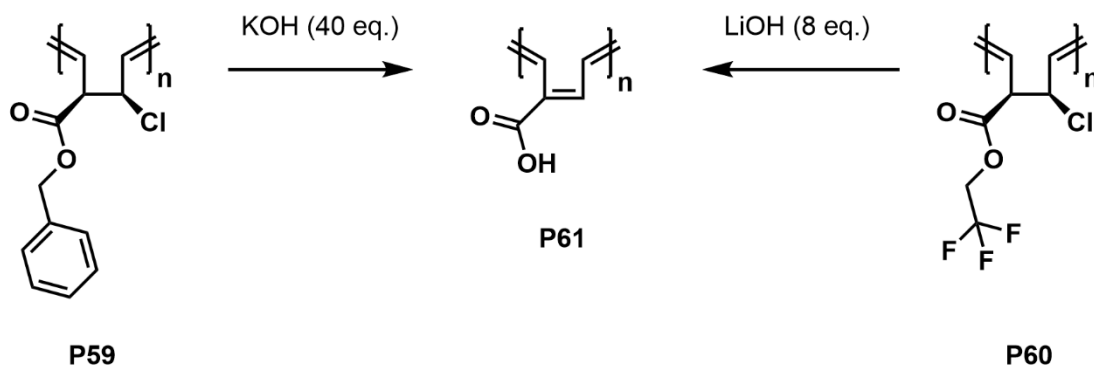
red-shifted compared to highly twisted polyacetylenes with substituents at every other carbon ($\lambda_{\text{max}} \sim 325$ nm for ester substituents)¹⁴⁶ but blue-shifted when compared to polymers obtained through the ROMP of COT ($\lambda_{\text{max}} > 500$ nm, see Section 1.2.5.1).



Scheme 1.21. a) Synthesis of substituted polyacetylenes from disubstituted cyclobutenes; b) Molecular structure of C4.

Finally, water soluble polyacetylenes could also be formed by performing the elimination reactions for **P59** and **P60** with an excess of nucleophilic bases KOH and LiOH leading to hydrolysis of the ester side chains (Scheme 1.22).¹⁴⁵ The resulting products (**P61**) were insoluble in aqueous acid solutions or in distilled water, but

soluble in aqueous solutions of bases, presumably due to deprotonation of the carboxylic acid moieties in **P61**.



Scheme 1.22. Synthesis of carboxylic acid-substituted polyacetylenes from the base-induced hydrolysis of ester side chains.

1.3 Polytellurophenes

While the use of polyacetylenes in modern applications still faces challenges, polythiophenes found great success in organic photovoltaics (OPVs) and as field-effect transistors (OFETs).^{6,12,14} In contrast to polyacetylene, polythiophene is stable to ambient conditions in its neutral state and has improved stability when oxidatively doped.^{147–150} Additionally, soluble, processable polythiophenes have been synthesized through rich chemistry, including catalyst-transfer polymerization (CTP) and Pd-catalyzed cross-coupling reactions, such as Suzuki-Miyaura cross-coupling and Stille cross-coupling.

Looking to improve upon the properties of polythiophene, researchers have also developed ways to access heavier analogues of polythiophenes with Se

(polyselenophenes) and Te (polytellurophenes). Although the synthesis of these polymers can be more challenging, especially for polytellurophenes, the final materials show several advantages, even in areas where polythiophenes are extensively used.

1.3.1 Replacement of S by Se and Te

Thiophene, selenophene and tellurophene, also known as chalcogenophenes, are five-membered rings containing four carbons and one group 16 heteroatom (Figure 1.9). Due to the different atomic properties of S, Se and Te, (Table 1.2), the properties of the resulting heterocycles also vary as the heteroatom becomes heavier. Especially, the presence of tellurium is accompanied by the most drastic changes, as expected from a relatively large difference in properties between Se and Te (Table 1.2).

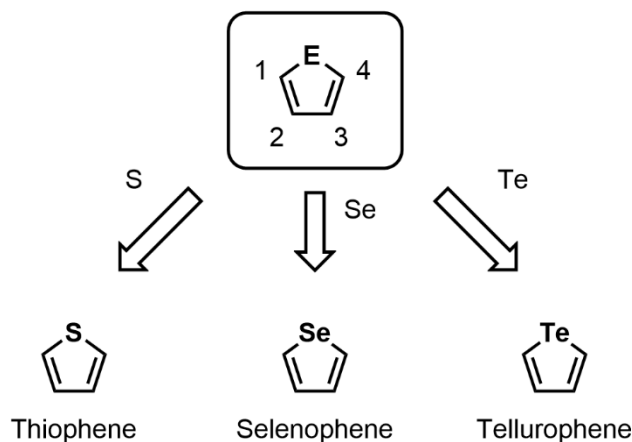
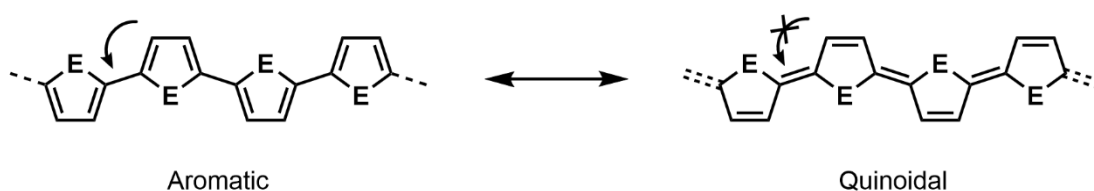


Figure 1.9. Chalcogenophenes formed by sulfur, selenium and tellurium. The usual numbering of carbon atoms is shown in the generic structure.

Table 1.2. Atomic properties of sulfur, selenium and tellurium.

	S	Se	Te
Pauling electronegativity ¹⁵¹	2.6	2.6	2.1
Covalent radius (Å) ¹⁵¹	1.03	1.17	1.35
van der Waals radius (Å) ¹⁵²	1.80	1.90	2.06
Polarizability ($\times 10^{-24} \text{ cm}^3$) ¹⁵³	2.90	3.77	5.5
Spin orbit coupling constant ($\times 10^3 \text{ cm}^{-1}$) ¹⁵⁴	0.29	1.67	4.48

As chalcogens have lone pairs available to interact with π -systems, chalcogenophenes follow Hückel's rule ($4n + 2$, where $n = 1$) and have aromatic character.¹⁵⁵ However, the aromaticity decreases down the Periodic Table from S to Se and Te,^{156,157} due to reduced orbital overlap between the chalcogen atoms and the adjacent π -system. This tendency is also reflected in the weaker nature of C=Se and C=Te bonds (vs. C=S) observed in other compounds.¹⁵⁸ In polymers, the reduced aromaticity leads to an increased quinoidal character (Scheme 1.23), and consequently enhanced delocalization of electrons throughout the C=C backbone, which reduces the HOMO-LUMO energy gap (E_g) following: $S > Se > Te$.¹⁵⁹

**Scheme 1.23.** Resonance structures of polychalcogenophenes. Arrows indicate the possibility of bond rotations between chalcogenophene units.

The expected decrease in E_g as S is replaced by Se or Te has been observed for various analogous polymers with the different heteroatoms.^{160–164} For example, while films of the well-studied regioregular poly(3-hexylthiophene) (P3HT, **P62**) show an E_g of 1.9 eV,¹⁶⁰ poly(3-hexylselenophene) (P3HSe, **P63**) and poly(3-hexyltellurophene) (P3HTe, **P64**) have reduced HOMO-LUMO gaps of 1.6 and 1.4 eV, respectively (see Figure 1.10 for their structures).^{160,161} Cyclic voltammetry measurements have shown that while the HOMO energy level of these polymers remains almost constant at around 0 eV (*vs.* $\text{Fc}^{+/0}$), the reduced band gap is a result of the stabilization of the LUMO, (reduction potential *vs.* $\text{Fc}^{+/0}$: $V_{\text{P3HT}} = -1.95$ eV, $V_{\text{P3HSe}} = -1.80$ eV, $V_{\text{P3HTe}} = -1.35$ eV).^{160,161}

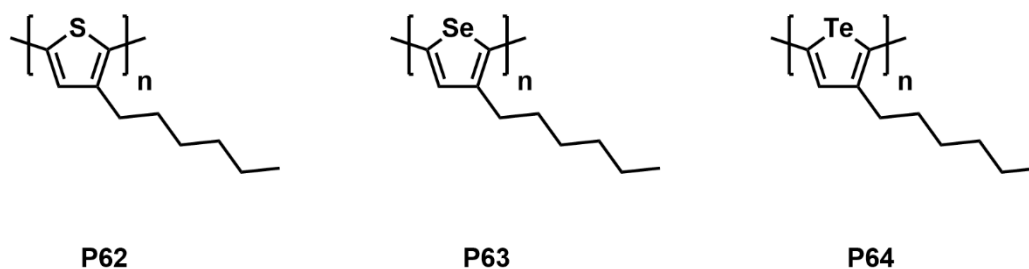


Figure 1.10. Molecular structures of P3HT (**P62**), P3HSe (**P63**) and P3HTe (**P64**).

Another effect of the increased quinoidal character when using Se and Te is the increase in backbone planarity, due to the double bond character between each chalcogenophene unit, and a corresponding increase in energy barrier for rotation of the chalcogenophene units (Scheme 1.23).¹⁶⁵ This characteristic has been shown to afford better charge transport in organic field-effect transistors,^{165,166} and could also

lead to better diffusion of photo-excited states.^{167,168} However, the rigidity of the backbone in polytellurophenes can also reduce solubility, providing a synthetic challenge.

The presence of Te also brings additional characteristics to the polymers, such as interchain Te---Te interactions mediated by σ -holes (also described as chalcogen bonding).^{169,170} This intermolecular bonding mode involves the donation of electron density from a lone pair located in one Te atom into the Te-C σ^* orbital(s) in a separate tellurophene unit, leading to an overall decrease in the energy of the system (Figure 1.11). Crucial to this interaction is the increased polarizability of Te ($5.5 \times 10^{-24} \text{ cm}^3$, Table 1.2) and its lower electronegativity (2.1, Table 1.2) to facilitate lone pair donation, which makes these interactions more prevalent in tellurophenes than in selenophenes or thiophenes.^{171–173}

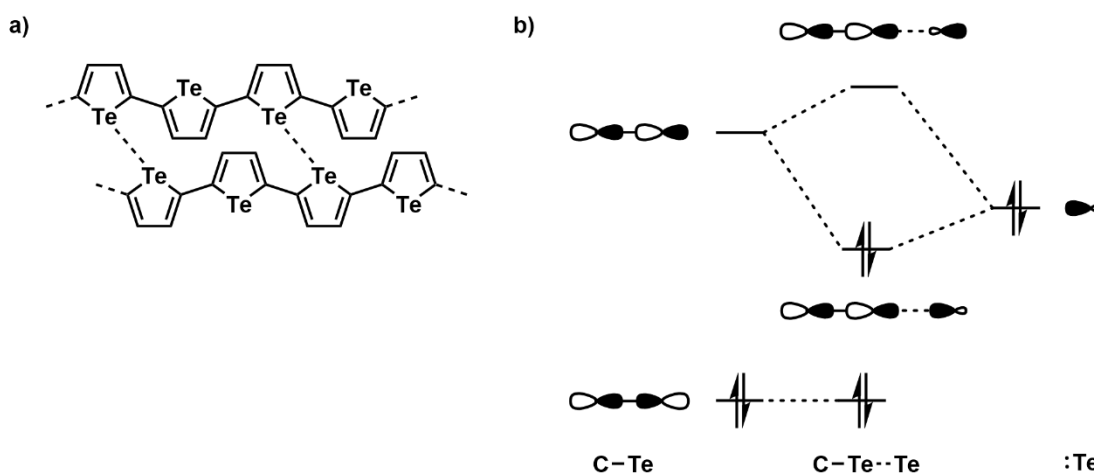


Figure 1.11. a) Representation of Te---Te interactions in polytellurophenes; b) Simplified MO diagram showing the orbitals involved in the σ -hole interaction.

Additionally, the presence of Te can lead to the formation of triplet excited states upon light absorption. This effect is more pronounced in tellurophenes due to the larger spin orbit coupling constant of Te (Table 1.2), which increases the rate of intersystem crossing to convert formally singlet excited states into triplet excited states (Figure 1.12). This feature of Te has been confirmed in small molecules that show phosphorescence (luminescent relaxation of triplet states).¹⁷⁴⁻¹⁷⁸

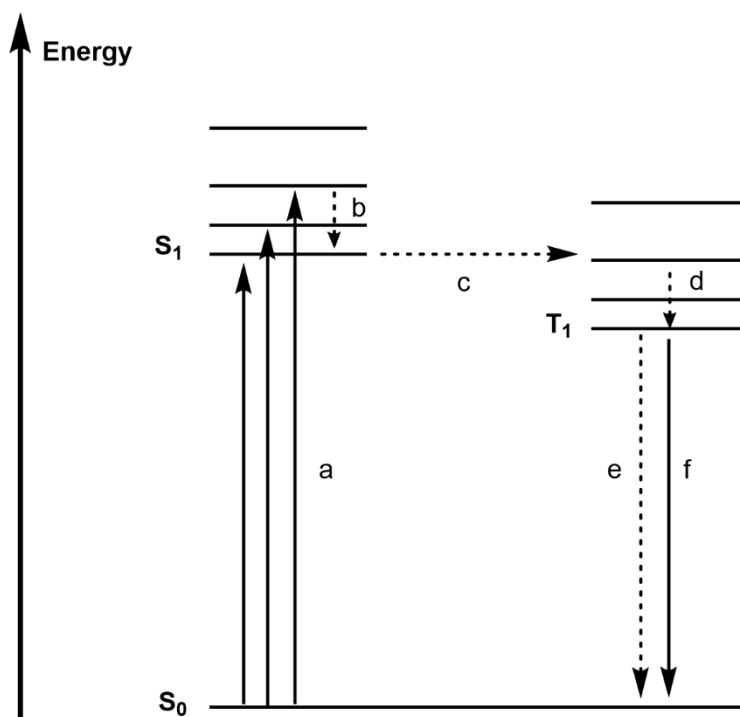


Figure 1.12. A simplified Jablonski diagram showing formation of triplet excited states. S_0 = singlet ground state, S_1 = first excited singlet state, T_1 = first excited triplet state, a = photoexcitation, b or d = vibrational relaxation, c = intersystem crossing, e = non-radiative decay, f = phosphorescence.

In polymeric films these photoexcited states are viewed as quasiparticles (formed by an electron-hole pair) called excitons, and are of special importance in organic solar cells. For current to be generated in solar cells, excitons must be dissociated before they eventually undergo electron-hole recombination.¹⁷⁹ While singlet excitons are short-lived and must be dissociated within a nanosecond time-scale, triplet excitons are longer lived (typically in the μs scale) and therefore have the potential to travel longer distances before being dissociated,¹⁸⁰⁻¹⁸² which could facilitate current generation in solar cells.¹⁶⁷ Encouragingly, there is evidence of triplet exciton formation in polyselenophenes and, especially, in polytellurophenes.¹⁸³⁻¹⁸⁷

Finally, replacement of S by Se and Te can facilitate doping, leading to larger electrical conductivities at smaller doping levels, which can be beneficial for thermoelectric applications.¹⁸⁸⁻¹⁹⁰ Doping also leads to polaronic absorption bands in the NIR region that shift bathochromically as the heteroatom becomes heavier.¹⁸⁸

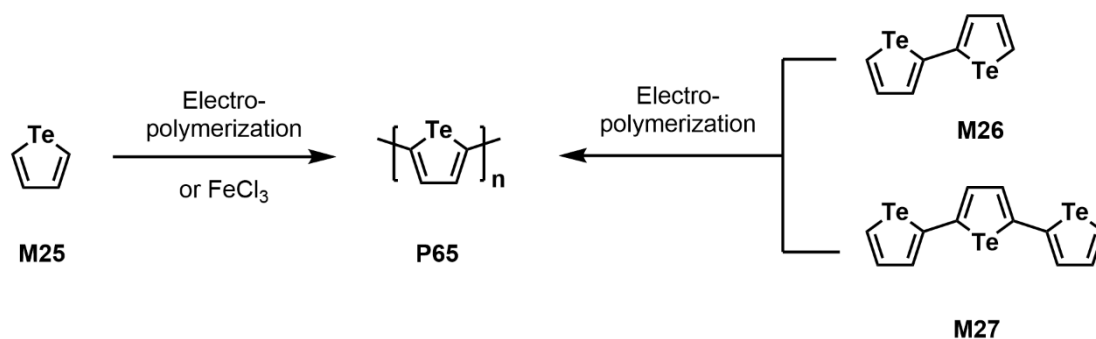
1.3.2 Synthesis of Polytellurophenes

Despite the several advantages of polytellurophenes in the context of organic electronics, their application lags behind that of polythiophenes, mainly due to more challenging syntheses. For example, while thiophenes can be extracted from oil reserves, tellurophenes are typically made from the reaction of diacetylene (1,3-butadiyne) gas and sodium telluride (Na_2Te).^{191,192} Additionally, due to enhanced planarity, polytellurophenes are usually less soluble than their thiophene analogues, which can lead to precipitation during polymerization in solution and make device

fabrication more challenging. However, considerable progress has been made in the last decade and polytellurophenes can now be obtained by several different methods.

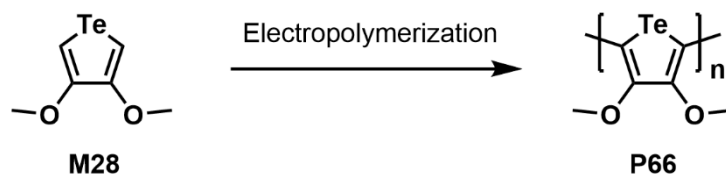
1.3.2.1. Electropolymerization and the First Polytellurophenes

The first polytellurophene was synthesized by Tsukagoshi and coworkers by the oxidative polymerization of an unsubstituted tellurophene (Scheme 1.24).¹⁹³ Similarly to the classic synthesis of polyacetylene (Section 1.2.1), the catalyst FeCl_3 was deposited on a glass plate followed by the vapor deposition of tellurophene to produce an insoluble powder (**P65**). This material showed low conductivities even when doped with I_2 (10^{-6} S/cm, compared to 10^{-12} S/cm when undoped). Through electrochemical polymerization, Ogura and coworkers later discovered that black films of polytellurophenes could be prepared from a tellurophene dimer or a trimer (**M26** and **M27**, Scheme 1.24) to reach neat (undoped) conductivities of 7.6×10^{-6} and 1.3×10^{-5} S/cm, respectively.^{194,195} The formation of films was thought to be dependent on the potential used for polymerization. As more tellurophene units are linked together, the potential required to oxidize the chain is reduced, which allows the dimer and trimer to be used in galvanostatic polymerizations at a reduced current (50 μA), when compared to the parent tellurophene (1 mA).



Scheme 1.24. Synthesis of parent polytellurophene through electropolymerization methods.

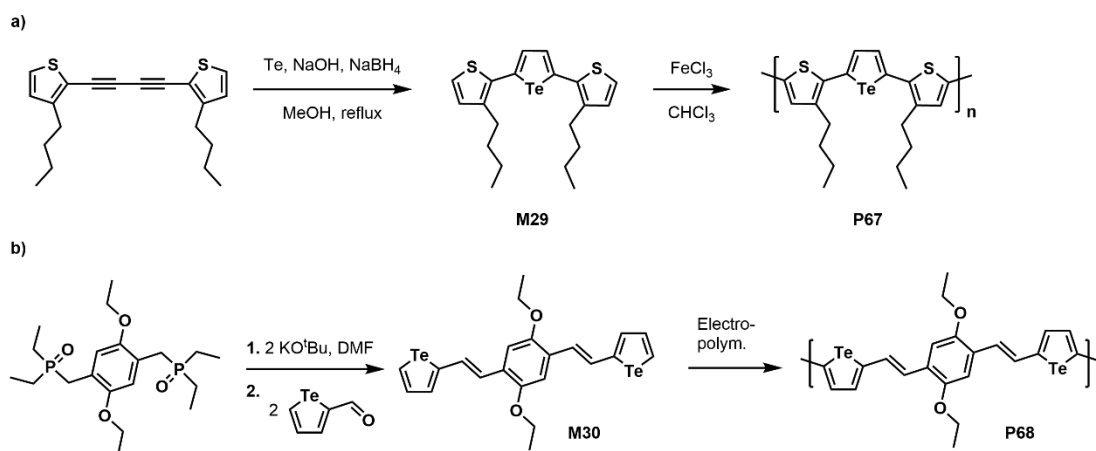
A methoxy-substituted tellurophene (**M28**) was later synthesized by Bendikov.¹⁹⁶ However, electropolymerization still led to insoluble, poorly defined films of low stability (**P66**). Conversely, polymerization of the analogous selenophene monomer led to the formation of a stable film, exemplifying how the synthesis of polytellurophenes can be more challenging.



Scheme 1.25. Synthesis of poly(3,4-bis(methoxy)tellurophene), **P66**.

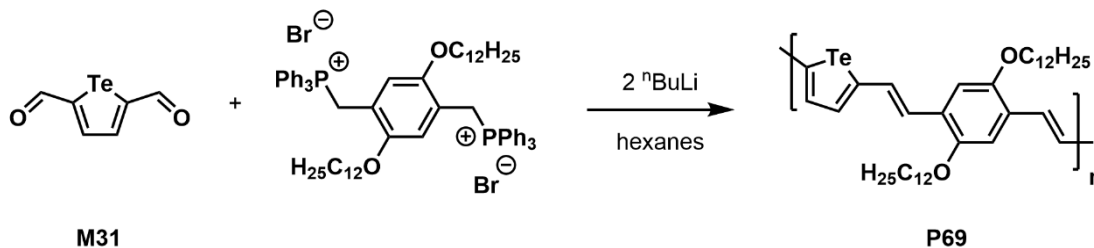
A soluble copolymer was synthesized by the Chan group by installing a tellurophene ring in between 3-butylthiophenes (**M29**) prior to electropolymerization with FeCl₃ (Scheme 1.26a).¹⁹⁷ The tellurophene unit was formed by reaction of a

thiophene-capped diyne with *in situ*-generated Na_2Te .¹⁹² The final polymer (**P67**, $M_n = 2.9$ kDa, PDI = 1.2) had a regioregular arrangement with tail-to-tail coupling between thiophenes in adjacent repeat units, leading to an optical band gap of 1.71 eV, which is smaller than that of P3HT (1.9 eV). Additionally, a high conductivity of 0.42 S/cm was achieved after I_2 doping. A soluble copolymer was also later reported by Data and coworkers (**P68**, Scheme 1.26b).¹⁹⁸ The authors were able to grow films of **P68** on ITO (indium tin oxide) and, although **P68** showed a larger E_g than **P65** (1.67 vs 1.52 eV, respectively), the luminescence of **M30** was retained in **P68** (quantum yield was not reported).



Scheme 1.26. Synthesis of soluble copolymers with tellurophene through oxidative polymerization.

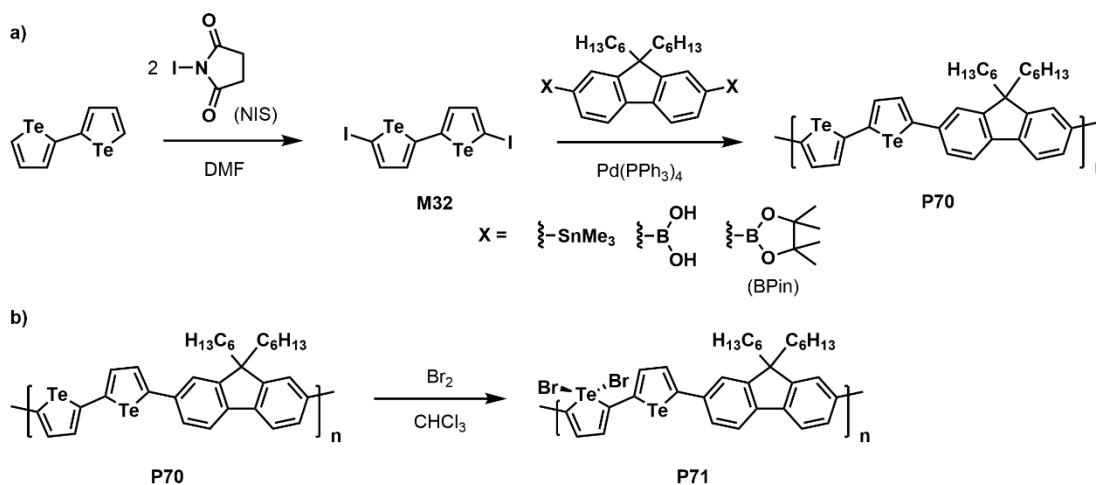
1.3.2.2. Palladium-Catalyzed Cross-Coupling



Scheme 1.27. Formation of a tellurophene copolymer (**P69**) by Wittig polycondensation.

The first non-oxidative polymerization of a tellurophene was reported by Kubo and coworkers in 1995 through Wittig polycondensation of tellurophenedialdehyde and a phenyl phosphonium salt (Scheme 1.27) to form soluble copolymers (**P67**, $M_n = 7$ kDa vs. polystyrene).¹⁹⁹ However, another non-oxidative procedure to polytellurophenes was only reported in 2010, by Seferos and coworkers through versatile Pd-catalyzed cross-coupling reactions.²⁰⁰ Seferos' route was based on the halogenation of bitellurophenes, followed by copolymerization with a fluorene monomer. Initial attempts to halogenate bitellurophene with *N*-bromosuccinimide (NBS) and I₂/HIO₃ were unsuccessful, but reaction with *N*-iodosuccinimide (NIS) afforded the desired monomer (**M32**, Scheme 1.28a). Stille-type copolymerization with a trimethylstannyl-functionalized fluorene comonomer gave very little polymer, indicating that iodinated tellurophenes react poorly under these conditions. However, optimized conditions under a Suzuki-Miyaura cross-coupling protocol with fluorene

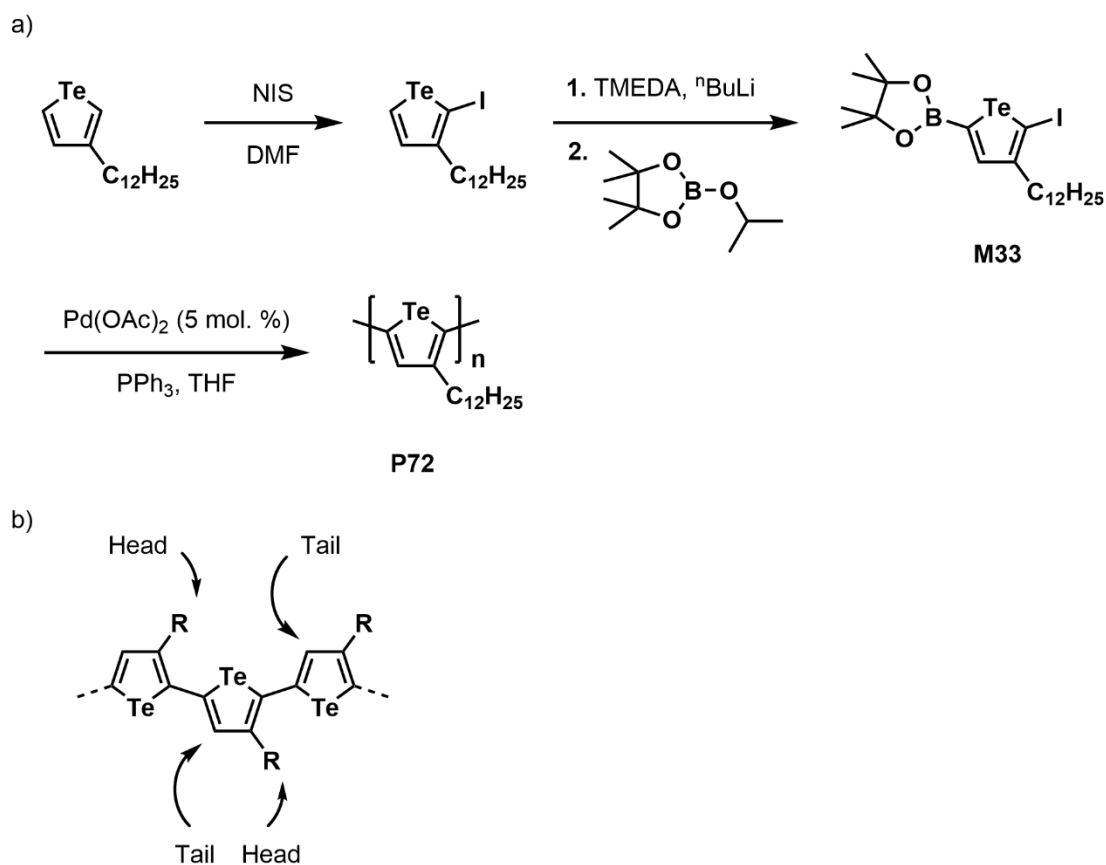
functionalized with pinacolborane (BPin) moieties afforded the desired polymer (**P70**, 32 % yield, $M_n = 3.1$ kDa vs. polystyrene, PDI = 1.2).²⁰⁰ Interestingly, the polymer's optoelectronic properties could be tuned by Br_2 oxidative addition at the Te centers (Scheme 1.28b), leading to a red-shift in absorption (λ_{onset} before = 624 nm; λ_{onset} after = 727 nm) and a reduction in HOMO and LUMO levels (-5.28 to -5.40 eV and -3.50 to -3.78 eV, respectively).^{200,201} This oxidation of the Te centers was reversible as Br_2 could be eliminated by heating at 150 °C or, as reported later, photoeliminated.^{202,203}



Scheme 1.28. a) Synthesis of a diiodinated bitellurophene and its copolymerization through Pd-mediated cross-coupling; b) Oxidation of Te centers by addition of Br_2 .

Suzuki-Miyaura cross-coupling was used by Kang to form a homopolymer of an alkyl-substituted tellurophene (Scheme 1.29a).²⁰⁴ This procedure required the unsymmetric iodination of a tellurophene, followed by reaction with $^n\text{BuLi}$ in the presence of tetramethylethylenediamine (TMEDA), to install a BPin unit.

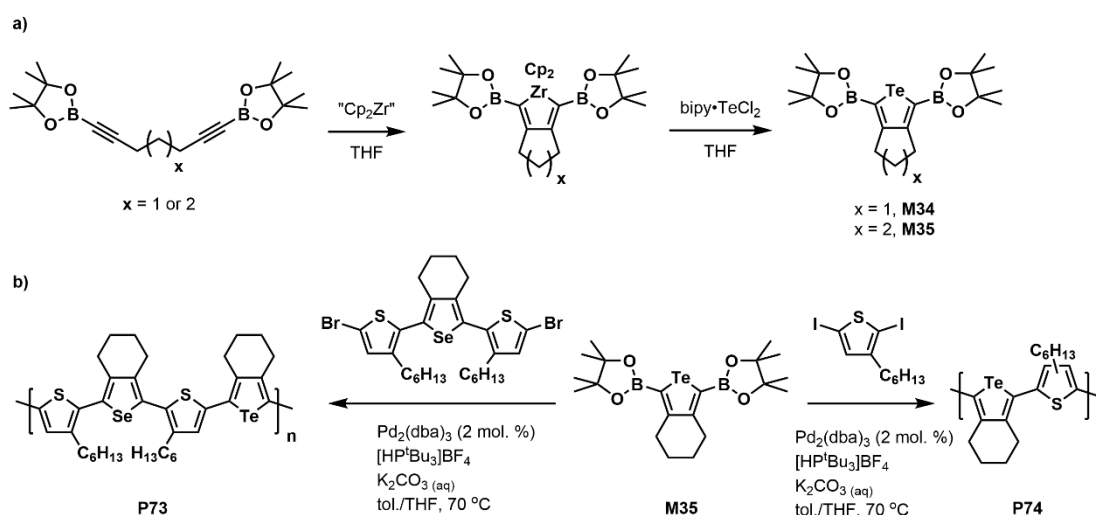
Polymerization of **M33** affords the homopolymer **P72** (60 % yield, $M_n = 20$ kDa vs. polystyrene, PDI = 2.4) that features a regioregular structure (87 % head-to-tail coupling, Scheme 1.29b). Regioregularity for unsymmetrically-substituted polychalcogenophenes is crucial to reduce the band gap and improve crystallinity.²⁰⁵



Scheme 1.29. a) Synthesis of a homopolymer through Suzuki-Miyaura cross-coupling; b) Visualization of a head-to-tail regioregularity.

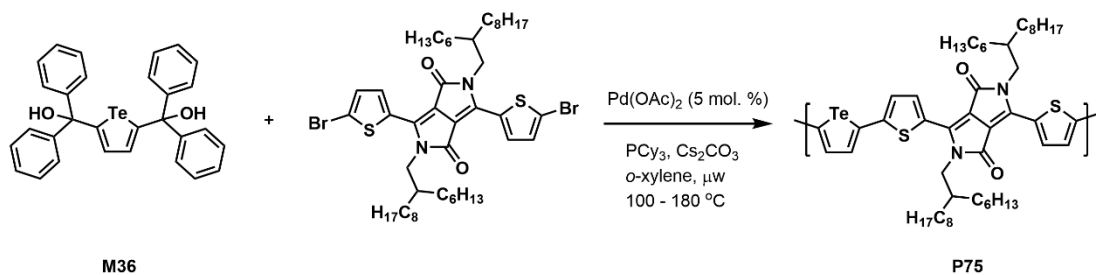
Rivard and coworkers also explored Suzuki-Miyaura coupling after developing a new synthetic protocol for BPin-functionalized tellurophene building blocks.¹⁶² This

protocol involved the formation of zirconacycles, followed by metallacycle transfer with halides of main group elements, to synthesize thiophenes, selenophenes and tellurophenes. This general method allowed for the use of the more stable $\text{bipy}\cdot\text{TeCl}_2$ ($\text{bipy} = 2,2'$ -bipyridine) as a source of tellurium,²⁰⁶ to form tellurophenes fused with 5- or 6-membered cycloalkyl rings (**M34** and **M35**). The 6-membered ring building block was then copolymerized with 2,5-diiodo-3-hexylthiophene (**P74**, 35 % yield, $M_n = 5.3$ kDa *vs.* polystyrene, PDI = 1.97) or with a comonomer containing both thiophene and selenophene rings (**P73**, 69 % yield, $M_n = 4.3$ kDa *vs.* polystyrene, PDI = 1.62). While **P74** was a regiorandom polymer, **P73** maintained regioregularity. It is noteworthy that the band gap of **P73** (*ca.* 2.5 eV) was wider than the E_g of P3HT (1.9 eV). Additionally, annealing studies showed that increased temperatures increased π - π stacking but reduced the conjugation length for **P73**, likely due to chain twisting.²⁰⁷



Scheme 1.30. a) Synthesis of tellurophene monomers mediated by formation of a zirconacycle; b) Synthesis of copolymers from a BPin-functionalized tellurophene.

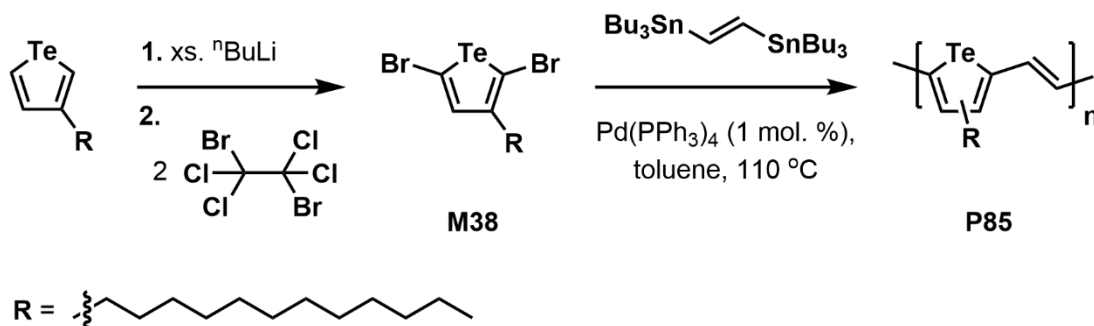
Grubbs explored a different route based on Pd-catalyzed *ipso*-arylation polymerization under microwave radiation.²⁰⁸ In this case, the monomer (**M36**) was formed by reaction of lithiated tellurophene with benzophenone and could then be copolymerized with a diketopyrrolopyrrole (DPP) derivative, a common building block for polymers used in OPVs and OFETs, to give **P75** (25 %, $M_n = 23.2$ kDa, PDI = 3.7). This method gave similar results to Stille and Suzuki-Miyaura cross-coupling, with the advantages of avoiding toxic organotin compounds and having an easy purification protocol for the monomer.



Scheme 1.31. *Ipso*-arylation copolymerization of tellurophene.

While the above studies uncovered the possibility of several types of polymerization, the reliability offered by Stille coupling polymerization made it the usual route for the synthesis of polytellurophenes copolymers. Several groups found success when using stannylated tellurophenes with brominated comonomers (Scheme 1.32).^{209–214} By comparing analogous copolymers with S and Se, it was repeatedly found that Te affords the smallest HOMO-LUMO energy gaps. Polymers **P80** and **P81**

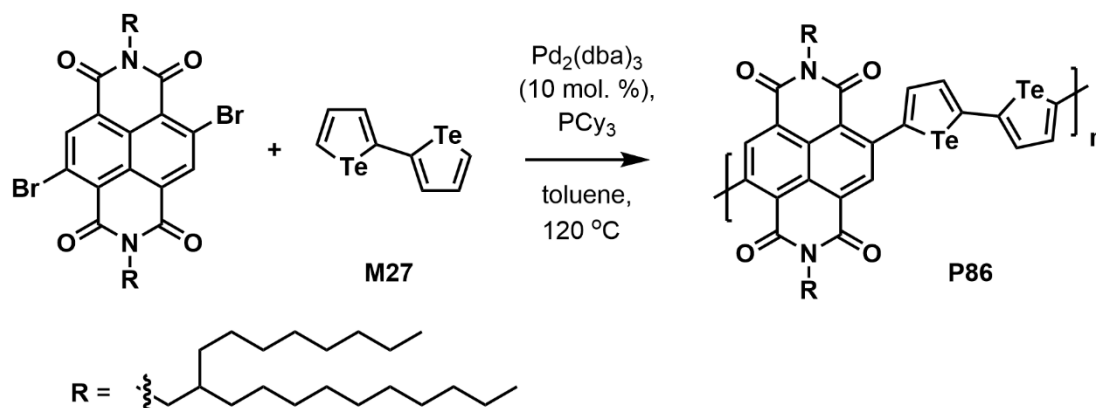
prepared by dilithiation followed by addition of 1,2-dibromotetrachloroethane, and coupled with (*E*)-1,2-bis(tributylstannyl)ethylene (Scheme 1.33). The resulting polymer (**P85**, 57 % yield, $M_n = 10$ kDa vs. polystyrene, PDI = 2.4) was likely regiorandom, but the vinylene spacers help avoid backbone twisting. Comparison with the S and Se analogues showed that **P85** had reduced solubility, only being soluble in chlorobenzene or chloroform upon prolonged heating.



Scheme 1.33. Synthesis of a vinylene-spaced polytellurophene through Stille cross-coupling.

Due to toxicity of the organotin compounds used (and formed as a byproduct) in Stille coupling, Huang and coworkers decided to explore direct heteroarylation polymerization as a route to polytellurophenes.²¹⁶ This method also improves atom economy compared to Suzuki-Miyaura or other traditional cross-coupling reactions.²¹⁷ After optimizing the reaction conditions, coupling of **M27** with a dibrominated naphthalene diimide afforded **P86** in good yield (45 % yield, $M_n = 7.9$ kDa vs.

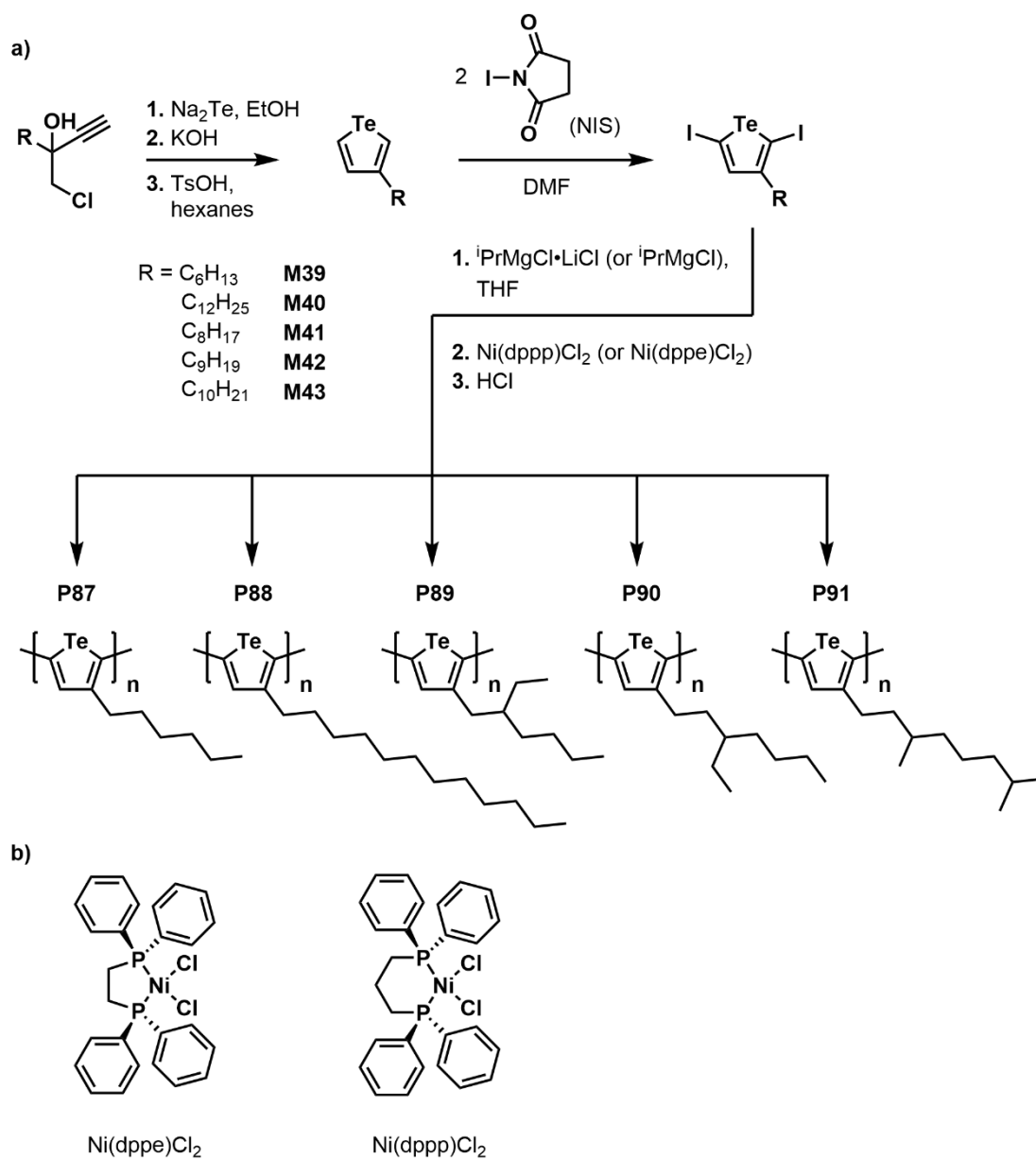
polystyrene, PDI = 1.68). Polymer **P86** shows a broad absorption and has a narrow HOMO-LUMO energy gap of 1.38 eV in CHCl_3 .



Scheme 1.34. Direct heteroarylation polymerization of bitellurophene.

1.3.2.3. Catalyst-Transfer Polymerization

As briefly mentioned before, regioregularity has been found to be a crucial characteristic for poly(3-alkylthiophene)s, such as P3HT, to reduce the HOMO-LUMO gap, increase crystallinity, and improve characteristics such as conductivity and charge carrier mobility.^{218–220} The most common way to synthesize these polymers with high regioregularity is through catalyst-transfer polymerization (CTP), also known as Grignard metathesis (GRIM) polymerization, since the chain-growth is determined by the position of the alkyl side chain.^{221–224} Seferos and coworkers were the first to apply this type of polymerization to synthesize poly(3-alkyltellurophene)s (**P87–91**, Scheme 1.35a, Table 1.3) and have since studied this process in depth.^{161,184,225,226}

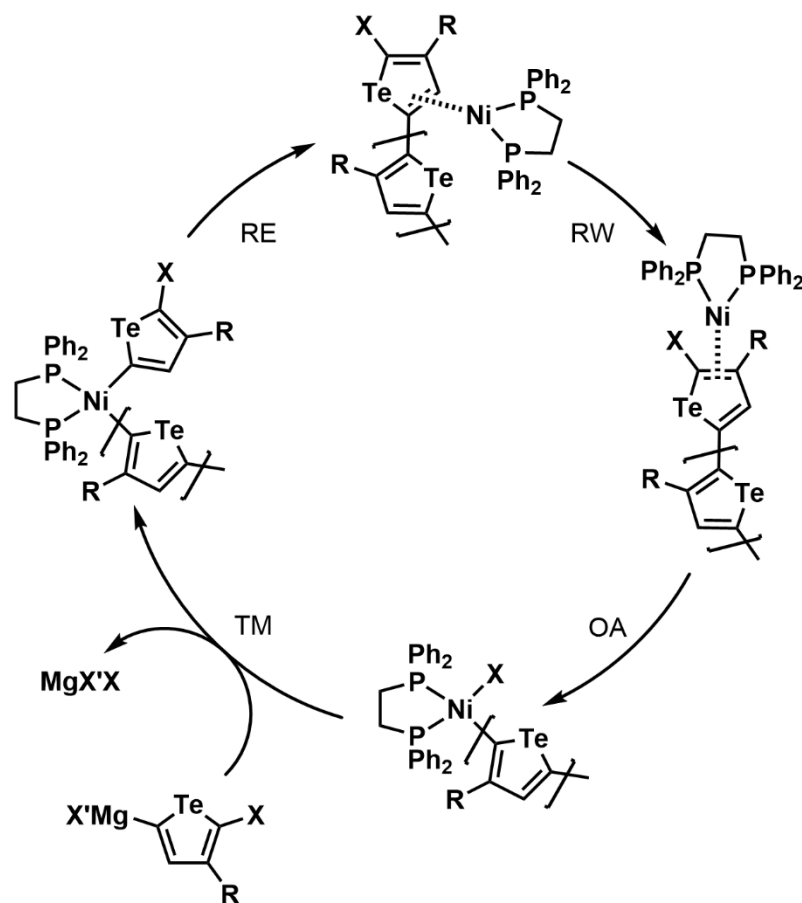


Scheme 1.35. a) Synthesis of poly(3-alkyltellurophene)s through CTP; b) Structure of Ni catalysts used.

Table 1.3. Conditions and results for the synthesis of polytellurophenes through CTP. HOMO-LUMO gaps (E_g) are given for films; M_n is reported vs. polystyrene.

Polymer	Grignard reagent	Catalyst	Yield	M_n (kDa)	PDI	E_g (eV)
P87	$i\text{PrMgCl}\cdot\text{LiCl}$	$\text{Ni}(\text{dppp})\text{Cl}_2$	33 %	9.9	2.2	1.44
P88	$i\text{PrMgCl}\cdot\text{LiCl}$	$\text{Ni}(\text{dppp})\text{Cl}_2$	62 %	11.3	2.0	1.44
P89	$i\text{PrMgCl}\cdot\text{LiCl}$	$\text{Ni}(\text{dppp})\text{Cl}_2$	35 %	5.4	1.9	1.57
P90	$i\text{PrMgCl}$	$\text{Ni}(\text{dppe})\text{Cl}_2$	65 %	14	1.1	-
P91	$i\text{PrMgCl}$	$\text{Ni}(\text{dppe})\text{Cl}_2$	55 %	36.6	1.2	1.45

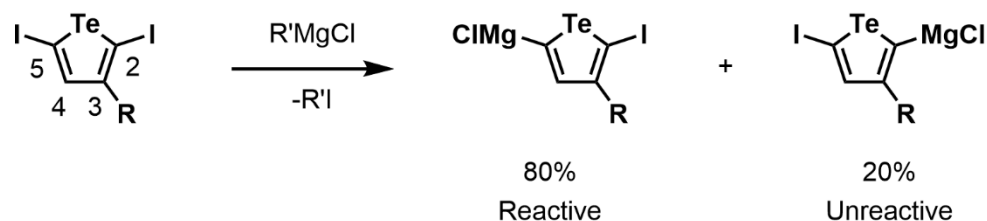
The route used by Seferos and coworkers starts with halogenated tellurophenes, obtained by reaction with NIS, followed by reaction with one equivalent of a Grignard reagent for monomer activation. Typically, isopropylmagnesium chloride ($i\text{PrMgCl}$) or its more reactive version with lithium chloride ($i\text{PrMgCl}\cdot\text{LiCl}$)²²⁷ are used for activation. The activated monomer is then added to a catalytic amount of $\text{Ni}(\text{dppp})\text{Cl}_2$ (dppp = bis(diphenylphosphino)propane) or $\text{Ni}(\text{dppe})\text{Cl}_2$ (dppe = bis(diphenylphosphino)ethane) to promote polymerization (see Scheme 1.35b for structures, and Scheme 1.36 for mechanism). The choice of catalyst depends on the nature of the side chains and temperature used, since the size of the phosphine ligand can alter the rate-determining step of the polymerization.^{228,229} Initial studies by Seferos relied upon the use of $\text{Ni}(\text{dppp})\text{Cl}_2$ and an increased temperature (80 °C) for the synthesis of **P87-89** to maintain solubility of the growing chains.¹⁶¹ This was especially important for **P87**, which showed solubility limitations; for comparison, the thiophene analogue, P3HT is highly soluble.



Scheme 1.36. Mechanism of CTP with “Ni(dppe)” as the active catalyst. The mechanism involves transmetalation (TM), reductive elimination (RE), ring-walking (RW) and oxidative addition (OA).

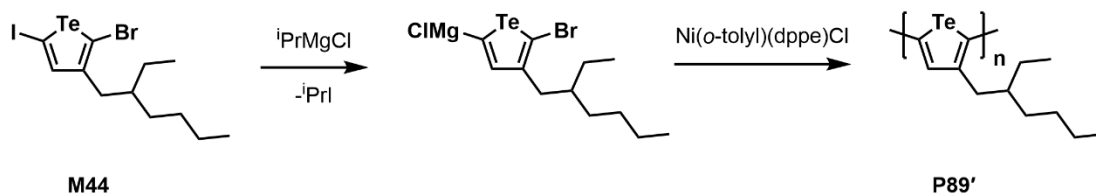
In a later study,²²⁵ the CTP polymerization of tellurophenes was studied in depth and it was determined that a branched side chain was important to maintain solubility, and to allow the polymerization to proceed at room temperature, leading to narrow polydispersities. Activation of the monomers was analyzed by NMR spectroscopy, showing that 80 % of the monomers are activated in the 5-position

(desirable for CTP), while 20 % are activated in the 2-position (unreactive in CTP, Scheme 1.37). Additionally, it was determined that Ni(dppe)Cl₂ gave faster polymerization for bulkier side chains, and that branching farther away from the tellurophene ring (**M42** or **M43** vs. **M41**) improved both the polymerization rate and control over molecular weight. Optimization of the conditions also allowed for the formation of block copolymers with P3HT due to the *quasi*-living character of the polymerization.



Scheme 1.37. Activation step of 3-alkyltellurophene monomers for CTP.

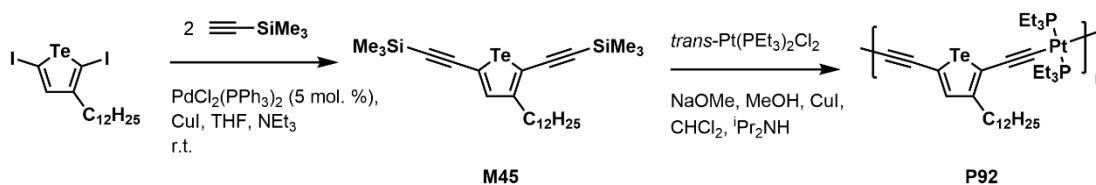
The polymerization kinetics could be further improved by using an unsymmetrically halogenated monomer (**M44**, Scheme 1.38).²²⁶ The presence of Br in the 2-position ensures quantitative activation in the 5-position (reaction of RMgX with I) and increases the speed of the polymerization, so that even a monomer with a bulky 2-ethylhexyl chain could be polymerized efficiently (**P89'**, 85 % yield, $M_n \sim 8.7$ kDa, PDI = 1.2)



Scheme 1.38. Synthesis of a polytellurophene from an unsymmetrically halogenated monomer.

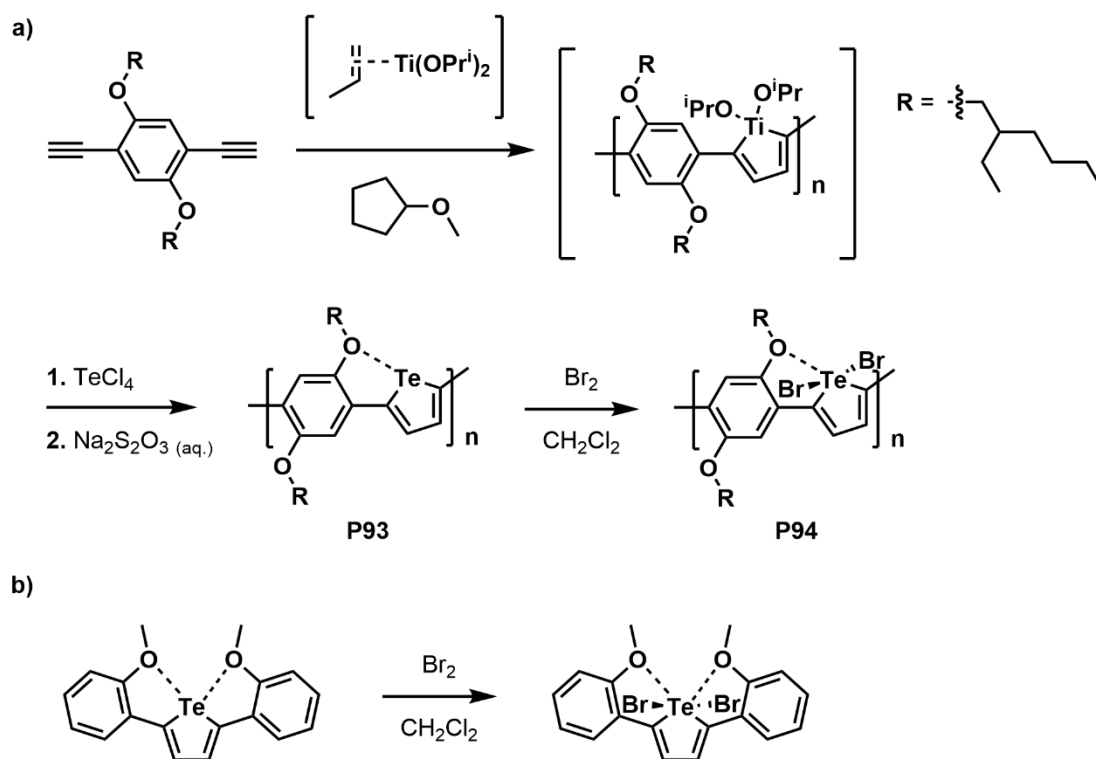
1.3.2.4. Other Synthetic Methods

Seferos also compared the influence of S, Se and Te in copolymers with platinum acetylide,²³⁰ an interesting class of polymers due to the potential of excited state intersystem crossing induced by Pt.^{231,232} A new tellurophene monomer with trimethylsilylethynyl functionalization (**M45**) was synthesized through Sonogashira cross-coupling, and could be polymerized by reaction with *trans*-bis(triethylphosphine)platinum(II) dichloride (*trans*-Pt(PEt₃)₂Cl₂) to afford **P92** (47 % yield, $M_n = 13.9$ kDa vs. polystyrene, PDI = 3.7). As expected, **P92** had a red-shifted absorption compared to its S and Se counterparts.²³⁰ This trend also applied to the photoluminescence spectra of the polymers, with phosphorescence at 671 nm noted for the Te congener ($\lambda_{em} = 617$ and 641 nm for the corresponding S and Se analogues, respectively). However, heavy-atom substitution negatively affected the intensity of phosphorescence, since replacement of S by Se or Te (**P92**) led to a 50 % and 80 % reduction in intensity, respectively (phosphorescence quantum yields not determined).



Scheme 1.39. Synthesis of a tellurophene-Pt acetylide copolymer (**P92**).

Tomita and coworkers were able to synthesize copolymers with tellurophene by a metallacycle transfer from polymers containing titanacycles (Scheme 1.40a).²³³ This route is analogous to the reported by Rivard with zirconacycles (see Section 1.3.2.2),¹⁶² with the difference that the formation of titanacycles yields a polymer directly, which can then be modified into a tellurophene copolymer. Another difference between the Tomita and Rivard routes is that a source of Te(IV), TeCl₄, is used in the former, and, therefore the tellurium center had to be reduced with sodium thiosulfate (Na₂S₂O₃) to afford the final polymer (**P93**, 68 % yield, M_n = 5.1 kDa vs. polystyrene, PDI = 2.4). A possible challenge with this route is that the titanacycles in the polymer are sensitive to moisture, leading to potential defects in the chain upon partial hydrolysis.²³⁴



Scheme 1.40. a) Synthesis of a tellurophene copolymer from a titanacycle-containing polymer; b) Model tellurophene compound before and after reaction with Br_2 .

Interestingly, the alkoxy groups on the aryl units in **P93** (Scheme 1.40) were able to interact with Te through intramolecular chalcogen bonding to improve ring subunit planarity,¹⁷⁰ as confirmed in a model monomeric compound (Scheme 1.40b, dihedral angles of $2.6(14)^\circ$ and $-0.9(14)^\circ$). Similarly to work by Seferos,²⁰⁰ **P93** (and the model compound) could be brominated to reduce the HOMO-LUMO gap (from 2.1 eV in **P93** to 1.8 eV in **P94**), while maintaining Te---O interactions. Once again, comparison with S and Se analogues showed a reduction in E_g when using Te.²³⁵

1.3.3 Recent Applications of Polytellurophenes

Polytellurophenes have been explored in photovoltaics, in field-effect transistors, photodetectors, and even in cancer treatment. The following sections outline these studies and further highlights the effect of the heavy element, tellurium.

1.3.3.1. Organic Photovoltaics (OPV)

With a reduced HOMO-LUMO gap, polytellurophenes show enhanced sunlight absorption across the visible spectral region, a property that is desirable for solar cells.²³⁶ Additionally, the possibility of forming triplet excited states could ultimately simplify device architecture from the currently used bulk heterojunctions (where there is a nanoscale mixing of donor and acceptor materials in the active layer),²³⁷ to planar heterojunctions.¹⁶⁷ Therefore, different groups have explored the use of polytellurophenes as donor materials in organic photovoltaic devices (Figure 1.13). The best results achieved in each case are summarized in Table 1.4.

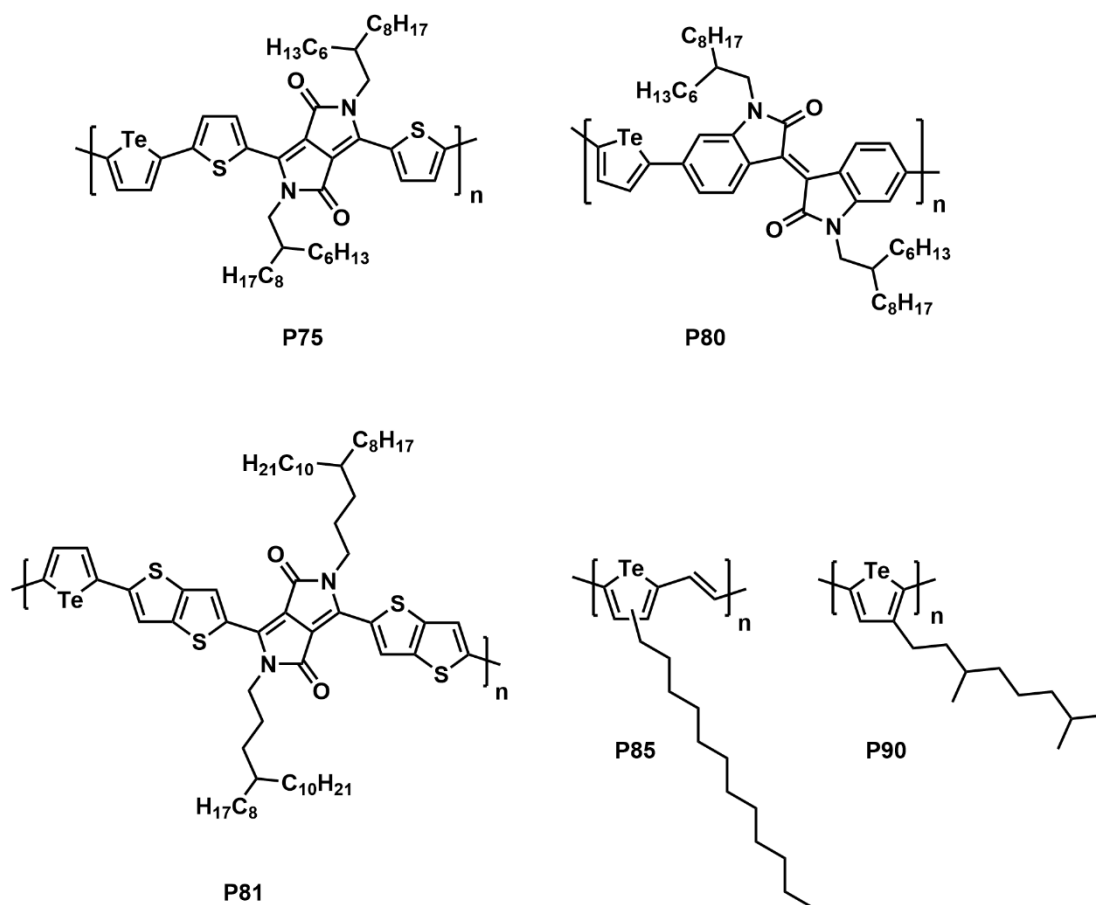


Figure 1.13. Tellurium-containing polymers studied in OPV and OFET applications.

The use of polymer **P75** (Figure 1.13) in bulk heterojunctions (BHJ) afforded a power conversion efficiency (PCE) of 4.4 %. A comparison of different molecular weights for **P75** showed that reduced molecular weights ($M_n = 8$ kDa instead of 23.2 kDa) also led to a reduced PCE (2.44 %), highlighting the importance of polymer molecular weights on device performance. Additionally, **P75** showed photocurrent generation with an onset at *ca.* 970 nm, matching the light absorption of a film of **P75**. For comparison, the S analogue of **P75** shows photoresponse up to 900 nm, but a

similar overall PCE of 4.7 %.²³⁸ **P80** (Figure 1.13) afforded a reduced PCE of 1.16 % compared to its S analogue (3.98 %).²¹⁰ The reduced PCE in this case can be attributed to aggregation of **P80** in the blend with PC₆₁BM (phenyl-C₆₁-butyric acid methyl ester, a fullerene derivative), as observed by TEM (transmission electron microscopy). This aggregation results in a reduced short circuit current (J_{SC}) of 2.51 mA/cm², compared to 7.71 mA/cm² for the S analogue.

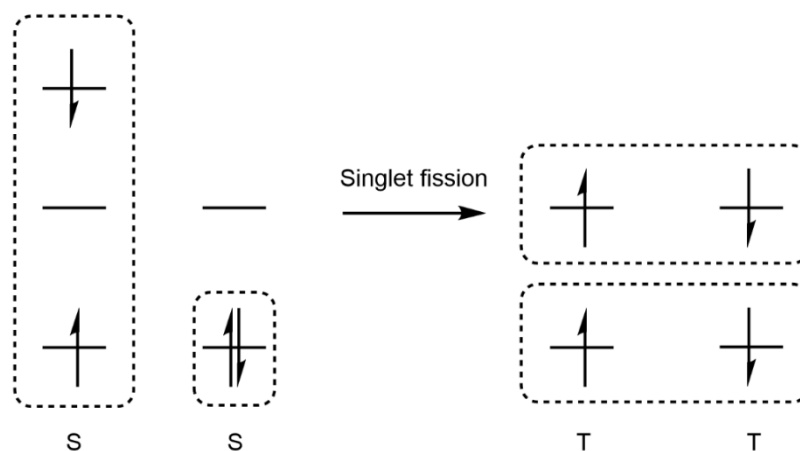
Similarly to the above studies, **P81** showed a photoresponse beyond 900 nm, with an external quantum efficiency (EQE) of 35 % at 900 nm,²¹¹ meaning that 35 % of the incident photons at 900 nm are converted into charge carriers (electrons and holes) when using **P81**. However, formation of a more coarse film morphology was observed once again by AFM (atomic force microscopy).²¹¹ These results underscore the need for device optimization since the solid state properties of tellurophenes differ from that of thiophenes.

Seferos studied the performance of **P90** in devices where the PC₆₁BM blend was formed by either fast- or slow-drying.¹⁸⁴ Fast-dried devices of **P90** showed reduced PCE (0.64 %), reduced π - π stacking and a smaller contribution from the polytellurophene to light absorption when compared to the slow-dried devices, indicating the need for an increased film formation time, or solvent vapor annealing, to achieve optimal morphology. Interestingly, **P90** contributed less to photocurrent at its absorption maximum (even for slow-dried devices) compared to S and Se analogues. The authors attributed this effect to the generation of excited triplet states, which could lead to recombination losses.¹⁸²

Table 1.4. Results of solar cells fabricated with polytellurophenes. Abbreviations: BHJ = bulk heterojunction; V_{OC} = open circuit voltage; J_{SC} = short circuit current; FF = fill factor; PCE = power conversion efficiency.

Polymer	Architecture	Acceptor	V_{OC} (V)	J_{SC} (mA/cm ²)	FF	PCE (%)
P75 ²⁰⁸	BHJ	PC ₇₁ BM	0.61	12.9	0.56	4.4
P80 ²¹⁰	BHJ	PC ₆₁ BM	0.92	2.51	0.50	1.16
P81 ²¹¹	BHJ	PC ₇₁ BM	0.52	21.7	0.63	7.1
P90 ¹⁸⁴	BHJ	PC ₇₁ BM	0.59	3.69	0.47	1.02

The effect of spin orbit coupling introduced by tellurophenes was also studied in the context of singlet fission, a spin-allowed process that can transform a high energy singlet excited state into two lower energy triplet excited states (Scheme 1.41).^{239–241} Singlet fission potentially allows for increased efficiencies in solar cells due to the possibility of harvesting photons with energies larger than the optical band gap. Heeney and coworkers observed that the photophysics of **P85** (Figure 1.13) were initially the same as its S and Se analogues, with the splitting of high energy singlet states into a triplet-triplet pair (TT). These states are susceptible to fast recombination, but introduction of Se and Te reduced recombination by facilitating the separation of the TT state into independent triplet states,²⁴⁰ an effect of increased spin orbit coupling.



Scheme 1.41. Diagram showing singlet fission. Note: the overall spin of the system does not change (indicated by electrons of opposite spin in the dashed boxes), making this an allowed process.

1.3.3.2. Organic Field-Effect Transistors (OFET)

Due to the improved backbone planarity and Te---Te interactions, it is expected that polytellurophenes would have a higher charge carrier mobility in field-effect transistors. Accordingly, polytellurophenes have also been used in the fabrication of such devices (Figure 1.13, Table 1.5).

Choi and coworkers observed that the hole mobility for **P75** increased upon annealing due to an increased size of crystalline domains (accompanied by an increased surface roughness, as determined by AFM).²⁴² The larger hole mobility of **P75** ($1.47 \text{ cm}^2 \text{ V}^{-1} \text{ s}^{-1}$) compared to its S analogue ($0.62 \text{ cm}^2 \text{ V}^{-1} \text{ s}^{-1}$) was attributed to increased perpendicular orientation of the polytellurophene chains relative to the substrate (edge-on) compared to the polythiophene.²⁴³ McCulloch also observed an increased edge-on

conformation for **P81**, but noted that **P81** and its Se analogue had a larger off current than their S counterpart (attributed to oxygen sensitivity).²¹¹ Heeney fabricated OFET devices of **P85** with either a top- or bottom-gate configuration, but achieved low mobilities due to the poor solubility, and the resulting poor film formation characteristics of **P85**.²¹⁵

Table 1.5. Results for OFETs fabricated with polytellurophenes. Abbreviations: μ_{hole} = hole mobility, V_{th} = threshold voltage, $J_{\text{on}}/J_{\text{off}}$ = ratio between the on and off currents.

Polymer	Architecture	μ_{hole} ($\text{cm}^2 \text{V}^{-1} \text{s}^{-1}$)	V_{th} (V)	$J_{\text{on}}/J_{\text{off}}$
P75	Bottom-gate, top-contact	1.47	2.2	$\sim 10^5$
P81	Top-gate, bottom contact	1.6	-8	$\sim 10^3$
P85	Bottom-gate, bottom-contact	1×10^{-3}	-	-
P87	Bottom-gate, bottom-contact	1.6×10^{-3}	-2	4.9×10^3
P88	Bottom-gate, bottom-contact	1.6×10^{-3}	-30	1.1×10^3
P89	Bottom-gate, bottom-contact	7.8×10^{-5}	-11	1×10^2
P91	Bottom-gate, top-contact	2.5×10^{-2}	-17	1.1×10^4

Seferos and coworkers conducted studies on the aggregation and charge transport of tellurophene homopolymers with alkyl side chains (**P87-89** and **P91**, Figure 1.14).^{165,244} The branched 2-ethylhexyl side chain in **P89** was found to be detrimental to charge transport,²⁴⁴ likely due to twisting of the polymeric backbone, but by placement of the branching point further from the tellurophene ring (**P91**), better results were achieved.¹⁶⁵ Compared to its S ($\mu_{\text{hole}} = 6.2 \times 10^{-5}$) and Se ($\mu_{\text{hole}} = 8.0 \times 10^{-4}$) analogues, **P91** showed a much improved hole mobility. Additionally, grazing-

incidence wide angle X-ray scattering (GIWAX) showed that the use of **P91** leads to edge-on alignment, consistent with the previous reports. However, **P91** had the lowest crystallinity among the other polychalcogenophene, despite more aggregation being visible by AFM. The increased hole mobility was then explained by the increased backbone rigidity of the polytellurophene, as determined by DFT computations.¹⁶⁵

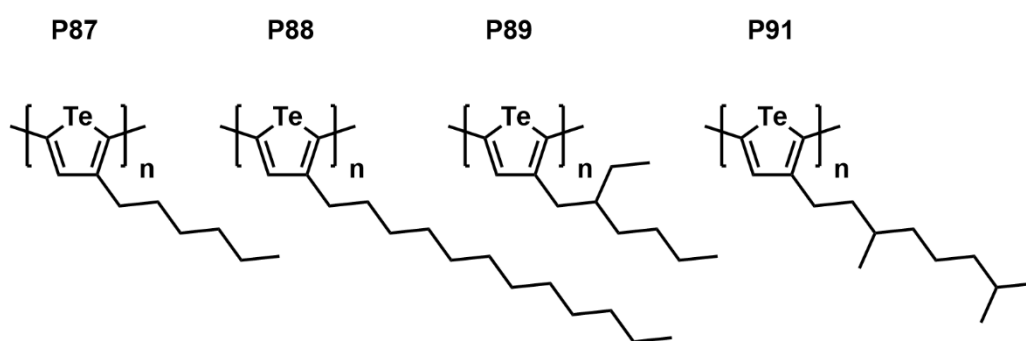
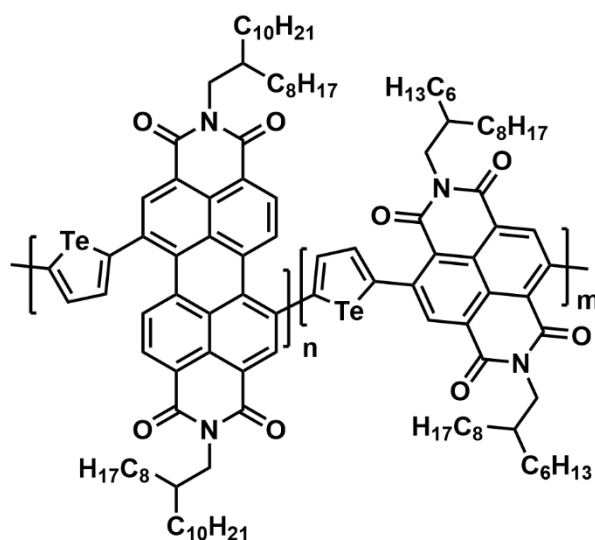


Figure 1.14. Alkyl-substituted polytellurophenes studied in the context of OFETs.

1.3.3.3. Photothermal/Photodynamic Therapy

Huang decided to investigate the use of polymeric nanoparticles containing **P86** as photothermal and photodynamic agents for cancer treatment.²¹⁶ Nanoparticles of **P86** (Figure 1.15) were prepared by mixing **P86** with a non-conjugated polymer in THF, followed by water addition under sonication to afford uniform spheres ($d = 110 \pm 3$ nm). Irradiation of the nanoparticles at 808 nm led to the formation of reactive oxygen species ($\bullet\text{OH}$ and $\text{O}_2^{\bullet-}$) by a photodynamic process at high efficiency (38.7 %). This process was accompanied by a rapid increase in temperature (up to 48.3 °C in 10 min when the concentration used was 100 $\mu\text{g/mL}$) by a photothermal effect.

output per optical input) could be tuned. Optimal performance was achieved for a n/m ratio of 7/3, affording smoother films and leading to low dark current (4.17×10^{-6} A/cm²) and high responsivity (19.11 A/W) at 600 nm. The authors note that the responsivity is among the highest values for organic photodetectors and comparable to devices based on inorganic materials.^{245,246}



P84

Figure 1.16. Structure of random tellurophene copolymers used in photodetectors.

1.4 Scope of this Thesis

As illustrated by the previous sections, the synthesis of new polymers is crucial to bridge the gap between design and applications for both polyacetylenes and polytellurophenes. On one hand, synthesis of soluble, air-stable polyacetylenes that retain interesting optoelectronic properties is necessary to bring these polymers into

modern applications. On the other hand, the field of polytellurophenes is still emerging and new routes to polymers are needed to further improve polymer properties and provide a variety of options for device fabrication.

In this context, this Thesis describes the synthesis of tellurophene oligomers and studies the effect of fused cycloalkyl side chains on backbone planarity, with the hypothesis that a smaller cycloalkyl ring could lead to improved backbone planarity. Additionally, the synthesis of a new poly(3-aryltellurophene) is described, wherein the aryl side chains are expected to further reduce the polymer's HOMO-LUMO energy gap in the solid state.

Lastly, the synthesis of soluble polyacetylenes with heteroatom-containing side chains is described. The presence of side chains attached to the polyacetylene backbone are expected to provide solubility to the final polymer, while heteroatoms can tune optoelectronic properties through orbital interactions with the backbone to reduce E_g by an intrinsic doping effect.

1.5 References

1. S. C. Rasmussen, *ChemPlusChem*, **2020**, 85, 1412–1429.
2. G. Li, W.-H. Chang and Y. Yang, *Nat. Rev. Mater.*, **2017**, 2, 17043.
3. F. C. Krebs, *Sol. Energy Mater. Sol. Cells*, **2009**, 93, 394–412.
4. R. R. Søndergaard, M. Hösel and F. C. Krebs, *J. Polym. Sci. Part B Polym. Phys.*, **2013**, 51, 16–34.

5. K. Norrman, A. Ghanbari-Siahkali and N. B. Larsen, *Annu. Rep. Prog. Chem., Sect. C: Phys. Chem.*, **2005**, *101*, 174–201.
6. G. Li, R. Zhu and Y. Yang, *Nat. Photonics*, **2012**, *6*, 153–161.
7. N. Liang, W. Jiang, J. Hou and Z. Wang, *Mater. Chem. Front.*, **2017**, *1*, 1291–1303.
8. J. Hou, O. Inganäs, R. H. Friend and F. Gao, *Nat. Mater.*, **2018**, *17*, 119–128.
9. L. Zhu, M. Zhang, G. Zhou, T. Hao, J. Xu, J. Wang, C. Qiu, N. Prine, J. Ali, W. Feng, X. Gu, Z. Ma, Z. Tang, H. Zhu, L. Ying, Y. Zhang and F. Liu, *Adv. Energy Mater.*, **2020**, *10*, 1904234.
10. L. Meng, Y. Zhang, X. Wan, C. Li, X. Zhang, Y. Wang, X. Ke, Z. Xiao, L. Ding, R. Xia, H. L. Yip, Y. Cao and Y. Chen, *Science*, **2018**, *361*, 1094–1098.
11. Y. Zhu, Y. Zhang, B. Yao, Y. Wang, Z. Zhang, H. Zhan, B. Zhang, Z. Xie, Y. Wang and Y. Cheng, *Macromolecules*, **2016**, *49*, 4373–4377.
12. X. Zhao and X. Zhan, *Chem. Soc. Rev.*, **2011**, *40*, 3728–3743.
13. H. Sirringhaus, *Adv. Mater.*, **2014**, *26*, 1319–1335.
14. L. Dou, Y. Liu, Z. Hong, G. Li and Y. Yang, *Chem. Rev.*, **2015**, *115*, 12633–12665.
15. J. Qi, W. Qiao and Z. Y. Wang, *Chem. Rec.*, **2016**, *16*, 1531–1548.
16. M. Wang, P. Baek, A. Akbarinejad, D. Barker and J. Travas-Sejdic, *J. Mater. Chem. C*, **2019**, *7*, 5534–5552.
17. Z. Zhang, M. Liao, H. Lou, Y. Hu, X. Sun and H. Peng, *Adv. Mater.*, **2018**, *30*, 1704261.

18. D. T. McQuade, A. E. Pullen and T. M. Swager, *Chem. Rev.*, **2000**, *100*, 2537–2574.
19. T. H. Qazi, R. Rai and A. R. Boccaccini, *Biomaterials*, **2014**, *35*, 9068–9086.
20. T. Sen, S. Mishra and N. G. Shimpi, *RSC Adv.*, **2016**, *6*, 42196–42222.
21. H. N. M. E. Mahmud, A. K. O. Huq and R. B. Yahya, *RSC Adv.*, **2016**, *6*, 14778–14791.
22. R. Jain, N. Jadon and A. Pawaiya, *Trends Anal. Chem.*, **2017**, *97*, 363–373.
23. A. J. Heeger, *Angew. Chem. Int. Ed.*, **2001**, *40*, 2591–2611.
24. A. G. MacDiarmid, *Angew. Chem. Int. Ed.*, **2001**, *40*, 2581–2590.
25. H. Shirakawa, *Angew. Chem. Int. Ed.*, **2001**, *40*, 2574–2580.
26. H. Shirakawa and S. Ikeda, *Polym. J.*, **1971**, *2*, 231–244.
27. G. Perego, G. Lugli, U. Pedretti and M. Cesari, *Makromol. Chem.*, **1988**, *189*, 2657–2669.
28. C. Q. Wu, J. Miao, J.-Z. Yu and Y. Kawazoe, *Phys. Rev. B*, **1998**, *57*, 6–9.
29. K. Tanaka, K. Yoshizawa, K. Ohzeki and T. Yamabe, *Solid State Commun.*, **1983**, *45*, 391–393.
30. K. Tanaka, T. Koike, K. Yoshizawa, K. Ohzeki and T. Yamabe, *Solid State Commun.*, **1984**, *49*, 165–167.
31. G. Natta, F. Danusso and G. Moraglio, *Angew. Chem.*, **1957**, *69*, 686–687.
32. M. Hatano, S. Kambara and S. Okamoto, *J. Polym. Sci.*, **1961**, *51*, S26–S29.
33. S. Ikeda and A. Tamaki, *J. Polym. Sci. Part B*, **1966**, *4*, 605–607.

34. T. Ito, H. Shirakawa and S. Ikeda, *J. Polym. Sci. Polym. Chem. Ed.*, **1974**, *12*, 11–20.
35. H. Shirakawa, T. Ito and S. Ikeda, *Polym. J.*, **1973**, *4*, 460–462.
36. T. Ito, H. Shirakawa and S. Ikeda, *J. Polym. Sci. Polym. Chem. Ed.*, **1975**, *13*, 1943–1950.
37. H. Shirakawa, T. Ito and S. Ikeda, *Makromol. Chem.*, **1978**, *179*, 1565–1573.
38. R. Hoffmann, *Angew. Chem. Int. Ed. Engl.*, **1987**, *26*, 846–878.
39. P. G. Wilkinson and H. L. Johnston, *J. Chem. Phys.*, **1950**, *18*, 190–193.
40. N. Suzuki, M. Ozaki, S. Etemad, A. J. Heeger and A. G. MacDiarmid, *Phys. Rev. Lett.*, **1980**, *45*, 1209–1213.
41. R. E. Peierls, *Quantum Theory of Solids*, Oxford University Press, 1974, 108–112.
42. S. Roth and H. Bleier, *Adv. Phys.*, **1987**, *36*, 385–462.
43. C. S. Yannoni and T. C. Clarke, *Phys. Rev. Lett.*, **1983**, *51*, 1191–1193.
44. C. H. Choi, M. Kertesz and A. Karpfen, *J. Chem. Phys.*, **1997**, *107*, 6712–6721.
45. H. Shirakawa, E. J. Louis, A. G. MacDiarmid, C. K. Chiang and A. J. Heeger, *J. Chem. Soc., Chem. Commun.*, **1977**, 578–580.
46. C. K. Chiang, Y. W. Park, A. J. Heeger, H. Shirakawa, E. J. Louis and A. G. MacDiarmid, *J. Chem. Phys.*, **1978**, *69*, 5098–5104.
47. C. K. Chiang, M. A. Druy, S. C. Gau, A. J. Heeger, E. J. Louis, A. G. MacDiarmid, Y. W. Park and H. Shirakawa, *J. Am. Chem. Soc.*, **1978**, *100*, 1013–1015.

48. R. H. Baughman, N. S. Murthy and G. G. Miller, *J. Chem. Phys.*, **1983**, *79*, 515–520.
49. A. G. MacDiarmid and A. J. Heeger, *Synth. Met.*, **1979**, *1*, 101–118.
50. H. Shirakawa and S. Ikeda, *Synth. Met.*, **1979**, *1*, 175–184.
51. N. Basescu, Z. X. Liu, D. Moses, A. J. Heeger, H. Naarmann and N. Theophilou, *Nature*, **1987**, *327*, 403–405.
52. J. Tsukamoto, A. Takahashi and K. Kawasaki, *Jpn. J. Appl. Phys.*, **1990**, *29*, 125–130.
53. S. C. Rasmussen, *Mater. Today*, **2016**, *19*, 244–245.
54. S. Lefrant, L. S. Lichtmann and H. Temkin, *Solid State Commun.*, **1979**, *29*, 191–196.
55. G. Kaindl, G. Wortmann, S. Roth and K. Menke, *Solid State Commun.*, **1982**, *41*, 75–78.
56. B. François, N. Mermilliod and L. Zuppiroli, *Synth. Met.*, **1981**, *4*, 131–138.
57. J. C. W. Chien, F. E. Karasz and K. Shimamura, *Macromolecules*, **1982**, *15*, 1012–1017.
58. B. Francois, M. Bernard and J. J. Andre, *J. Chem. Phys.*, **1981**, *75*, 4142–4152.
59. C. D. Dimitrakopoulos and D. J. Mascaró, *IBM J. Res. Dev.*, **2001**, *45*, 11–27.
60. A. C. Jones and M. L. Hitchman, Overview of Chemical Vapour Deposition, in *Chemical Vapour Deposition: Precursors, Processes and Applications*, Royal Society of Chemistry, 2009.
61. P. Sundberg and M. Karppinen, *Beilstein J. Nanotechnol.*, **2014**, *5*, 1104–1136.

62. C. Müller, C. P. Radano, P. Smith and N. Stingelin-Stutzmann, *Polymer*, **2008**, *49*, 3973–3978.
63. Y. Zhao, X. Zhao, M. Roders, A. Gumyusenge, A. L. Ayzner and J. Mei, *Adv. Mater.*, **2017**, *29*, 1605056.
64. Y. Zhao, A. Gumyusenge, J. He, G. Qu, W. W. McNutt, Y. Long, H. Zhang, L. Huang, Y. Diao and J. Mei, *Adv. Funct. Mater.*, **2018**, *28*, 1705584.
65. J. M. Pochan, D. F. Pochan, H. Rommelmann and H. W. Gibson, *Macromolecules*, **1981**, *14*, 110–114.
66. D. J. Berets and D. S. Smith, *Trans. Faraday Soc.*, **1968**, *64*, 823–828.
67. T. Masuda, B. Z. Tang, T. Higashimura and H. Yamaoka, *Macromolecules*, **1985**, *18*, 2369–2373.
68. M. Aldissi, *Synth. Met.*, **1984**, *9*, 131–141.
69. R. Huq and G. C. Farrington, *J. Electrochem. Soc.*, **1984**, *131*, 819–823.
70. D. Yu, Y. Q. Yang, Z. Chen, Y. Tao and Y. F. Liu, *Opt. Commun.*, **2016**, *362*, 43–49.
71. J. Ahmad, K. Bazaka, L. J. Anderson, R. D. White and M. V. Jacob, *Renew. Sustain. Energy Rev.*, **2013**, *27*, 104–117.
72. J. W. Y. Lam and B. Z. Tang, *Acc. Chem. Res.*, **2005**, *38*, 745–754.
73. T. Masuda, *J. Polym. Sci. Part A Polym. Chem.*, **2007**, *45*, 165–180.
74. J. Z. Sun, A. Qin and B. Z. Tang, *Polym. Chem.*, **2013**, *4*, 211–223.
75. H. Murata, D. Miyajima, R. Tkada and H. Nishide, *Polym. J.*, **2005**, *37*, 818–825.

76. K. Akagi, *Chem. Rev.*, **2009**, *109*, 5354–5401.
77. H. Murata, D. Miyajima and H. Nishide, *Macromolecules*, **2006**, *39*, 6331–6335.
78. K. Shimomura, T. Ikai, S. Kanoh, E. Yashima and K. Maeda, *Nat. Chem.*, **2014**, *6*, 429–434.
79. S. Naumann, J. Unold, W. Frey and M. R. Buchmeiser, *Macromolecules*, **2011**, *44*, 8380–8387.
80. J. Kim, E.-H. Kang and T.-L. Choi, *ACS Macro Lett.*, **2012**, *1*, 1090–1093.
81. J.-A. Song and T.-L. Choi, *Macromolecules*, **2017**, *50*, 2724–2735.
82. K. Jung, K. Kim, J. C. Sung, T. S. Ahmed, S. H. Hong, R. H. Grubbs and T.-L. Choi, *Macromolecules*, **2018**, *51*, 4564–4571.
83. C. Kang, K. Jung, S. Ahn and T.-L. Choi, *J. Am. Chem. Soc.*, **2020**, *142*, 17140–17146.
84. G. I. Peterson, S. Yang and T.-L. Choi, *Acc. Chem. Res.*, **2019**, *52*, 994–1005.
85. Y. Korshak, V. Korshak, G. Kanischka and H. Höcker, *Makromol. Chem., Rapid Commun.*, **1985**, *6*, 685–692.
86. F. L. Klavetter and R. H. Grubbs, *J. Am. Chem. Soc.*, **1988**, *110*, 7807–7813.
87. K. H. Claus and C. Krüger, *Acta Cryst.*, **1988**, *44*, 1632–1634.
88. F. G. Klärner, *Angew. Chem. Int. Ed.*, **2001**, *40*, 3977–3981.
89. T. Nishinaga, T. Ohmae, K. Aita, M. Takase, M. Iyoda, T. Arai and Y. Kunugi, *Chem. Commun.*, **2013**, *49*, 5354–5356.

90. T. Hensel, D. Trpceviski, C. Lind, R. Grosjean, P. Hammershøj, C. B. Nielsen, T. Brock-Nannestad, B. E. Nielsen, M. Schau-Magnussen, B. Minaev, G. V. Baryshnikov and M. Pittelkow, *Chem.-Eur. J.*, **2013**, *19*, 17097–17102.
91. D. H. Lo and M. A. Whitehead, *J. Am. Chem. Soc.*, **1969**, *91*, 238–242.
92. A. R. Hlil, J. Balogh, S. Moncho, H. L. Su, R. Tuba, E. N. Brothers, M. Al-Hashimi and H. S. Bazzi, *J. Polym. Sci. Part A Polym. Chem.*, **2017**, *55*, 3137–3145.
93. P. v. R. Schleyer, J. E. Williams and K. R. Blanchard, *J. Am. Chem. Soc.*, **1970**, *92*, 2377–2386.
94. E. J. Ginsburg, C. B. Gorman, S. R. Marder and R. H. Grubbs, *J. Am. Chem. Soc.*, **1989**, *111*, 7621–7622.
95. T. Masuda and T. Higashimura, *Polyacetylenes with Substituents: Their Synthesis and Properties*, in *Advances in Polymer Science*, Vol. 81, Springer-Verlag Berlin GmbH, 2013, 122-165.
96. M. J. Sailor, E. J. Ginsburg, C. B. Gorman, A. Kumar, R. H. Grubbs and N. S. Lewis, *Science*, **1990**, *249*, 1146–1149.
97. C. B. Gorman, E. J. Ginsburg, S. R. Marder and R. H. Grubbs, *Angew. Chem. Adv. Mater.*, **1989**, *101*, 1603–1606.
98. C. B. Gorman, E. J. Ginsburg and R. H. Grubbs, *J. Am. Chem. Soc.*, **1993**, *115*, 1397–1409.
99. J. T. Miller, C. W. DeKock and M. A. Brault, *J. Org. Chem.*, **1979**, *44*, 3508–3510.

100. A. Y. Sokolov, D. B. Magers, J. I. Wu, W. D. Allen, P. v. R. Schleyer and H. F. Schaefer, *J. Chem. Theory Comput.*, **2013**, *9*, 4436–4443.
101. T. H. Jozefiak, E. J. Ginsburg, C. B. Gorman, R. H. Grubbs and N. S. Lewis, *J. Am. Chem. Soc.*, **1993**, *115*, 4705–4713.
102. J. S. Moore, C. B. Gorman and R. H. Grubbs, *J. Am. Chem. Soc.*, **1991**, *113*, 1704–1712.
103. M. J. Eis, J. E. Wrobel and B. Ganem, *J. Am. Chem. Soc.*, **1984**, *106*, 3693–3694.
104. T. M. Trnka and R. H. Grubbs, *Acc. Chem. Res.*, **2001**, *34*, 18–29.
105. F. Ciardelli, S. Lanzillo and O. Pieroni, *Macromolecules*, **1974**, *7*, 174–179.
106. B. L. Langsdorf, X. Zhou, D. H. Adler and M. C. Lonergan, *Macromolecules*, **1999**, *32*, 2796–2798.
107. B. L. Langsdorf, X. Zhou and M. C. Lonergan, *Macromolecules*, **2001**, *34*, 2450–2458.
108. M. C. Lonergan, C. H. Cheng, B. L. Langsdorf and X. Zhou, *J. Am. Chem. Soc.*, **2002**, *124*, 690–701.
109. A. C. Cope and D. F. Rugen, *J. Am. Chem. Soc.*, **1953**, *75*, 3215–3219.
110. L. A. Paquette and K. A. Henzel, *J. Am. Chem. Soc.*, **1975**, *97*, 4649–4658.
111. D. N. Bhattacharyya, C. L. Lee, J. Smid and M. Szwarc, *J. Phys. Chem.*, **1965**, *69*, 612–623.
112. C. W. Bielawski and R. H. Grubbs, *Prog. Polym. Sci.*, **2007**, *32*, 1–29.

113. O. A. Scherman, I. M. Rutenberg and R. H. Grubbs, *J. Am. Chem. Soc.*, **2003**, *125*, 8515–8522.
114. O. A. Scherman and R. H. Grubbs, *Synth. Met.*, **2001**, *124*, 431–434.
115. K.-Y. Yoon, I.-H. Lee, K. O. Kim, J. Jang, E. Lee and T.-L. Choi, *J. Am. Chem. Soc.*, **2012**, *134*, 14291–14294.
116. S. Shin, K.-Y. Yoon and T.-L. Choi, *Macromolecules*, **2015**, *48*, 1390–1397.
117. L. R. Gilliom and R. H. Grubbs, *J. Am. Chem. Soc.*, **1986**, *108*, 733–742.
118. K.-Y. Yoon, S. Shin, Y.-J. Kim, I. Kim, E. Lee and T.-L. Choi, *Macromol. Rapid Commun.*, **2015**, *36*, 1069–1074.
119. J. H. Edwards and W. J. Feast, *Polymer*, **1980**, *21*, 595–596.
120. K. Knoll and R. R. Schrock, *J. Am. Chem. Soc.*, **1989**, *111*, 7989–8004.
121. P. Dounis, W. J. Feast and G. Widawski, *J. Mol. Catal. A*, **1997**, *115*, 51–60.
122. J. H. Burroughes, C. A. Jones and R. H. Friend, *Nature*, **1988**, *335*, 137–141.
123. J. H. Burroughes, R. H. Friend and P. C. Allen, *J. Phys. D Appl. Phys.*, **1989**, *22*, 956–958.
124. T. M. Swager, D. A. Dougherty and R. H. Grubbs, *J. Am. Chem. Soc.*, **1988**, *110*, 2973–2974.
125. T. M. Swager and R. H. Grubbs, *Synth. Met.*, **1989**, *28*, D57–D62.
126. L. M. Leung and K. H. Tan, *Macromolecules*, **1993**, *26*, 4426–4436.
127. L. M. Leung and K. H. Tan, *Polymer*, **1994**, *35*, 1556–1560.
128. C. Wu, A. Niu, L. M. Leung and T. S. Lam, *J. Am. Chem. Soc.*, **1999**, *121*, 1954–1955.

129. J. I. Brauman and W. C. Archie Jr., *Tetrahedron*, **1971**, *27*, 1275–1280.
130. W. R. Dolbier Jr. and H. Koroniak, *J. Am. Chem. Soc.*, **1984**, *106*, 1871–1872.
131. S. F. Martin, M. S. Dappen, B. Dupre and C. J. Murphy, *J. Org. Chem.*, **1987**, *52*, 3708–3710.
132. M. Murakami, Y. Miyamoto and Y. Ito, *Angew. Chem. Int. Ed.*, **2001**, *40*, 189–190.
133. Q. Z. Yang, Z. Huang, T. J. Kucharski, D. Khvostichenko, J. Chen and R. Boulatov, *Nat. Nanotechnol.*, **2009**, *4*, 302–306.
134. M. T. Ong, J. Leiding, H. Tao, A. M. Virshup and T. J. Martínez, *J. Am. Chem. Soc.*, **2009**, *131*, 6377–6379.
135. Z. Chen, J. A. M. Mercer, X. Zhu, J. A. H. Romaniuk, R. Pfattner, L. Cegelski, T. J. Martinez, N. Z. Burns and Y. Xia, *Science*, **2017**, *357*, 475–479.
136. Z. Chen, X. Zhu, J. Yang, J. A. M. Mercer, N. Z. Burns, T. J. Martinez and Y. Xia, *Nat. Chem.*, **2020**, *12*, 302–309.
137. F. B. Schügerl and H. Kuzmany, *J. Chem. Phys.*, **1981**, *74*, 953–958.
138. J. K. Su, J. D. Feist, J. Yang, J. A. M. Mercer, J. A. H. Romaniuk, Z. Chen, L. Cegelski, N. Z. Burns and Y. Xia, *J. Am. Chem. Soc.*, **2018**, *140*, 12388–12391.
139. B. R. Boswell, C. M. F. Mansson, J. M. Cox, Z. Jin, J. A. H. Romaniuk, K. P. Lindquist, L. Cegelski, Y. Xia, S. A. Lopez and N. Z. Burns, *Nat. Chem.*, **2021**, *13*, 41–46.
140. T. Yamabe, K. Tanaka, H. Terema-E, K. Fukui, H. Shirakawa and S. Ikeda, *Synth. Met.*, **1979**, *1*, 321–327.

141. M. Springborg, *J. Am. Chem. Soc.*, **1999**, *121*, 11211–11216.
142. L. M. Abreu, T. L. Fonseca and M. A. Castro, *J. Chem. Phys.*, **2012**, *136*, 234311.
143. J. Seo, S. Y. Lee and C. W. Bielawski, *Macromolecules*, **2019**, *52*, 2923–2931.
144. E. E. van Tamelen and D. Carty, *J. Am. Chem. Soc.*, **1971**, *93*, 6102–6110.
145. J. Seo, S. Y. Lee and C. W. Bielawski, *Polym. Chem.*, **2019**, *10*, 6401–6412.
146. H. Nakako, Y. Mayahara, R. Nomura, M. Tabata and T. Masuda, *Macromolecules*, **2000**, *33*, 3978–3982.
147. G. Tourillon and F. Garnier, *J. Electrochem. Soc.*, **1983**, *130*, 2042–2044.
148. Y. Cao, P. Wang and R. Qian, *Makromol. Chem.*, **1985**, *186*, 1093–1100.
149. N. C. Billingham, P. D. Calvert, P. J. S. Foot and F. Mohammad, *Polym. Degrad. Stab.*, **1987**, *19*, 323–341.
150. F. Mohammad, P. D. Calvert and N. C. Billingham, *Bull. Mater. Sci.*, **1995**, *18*, 255–261.
151. C. E. Housecroft and A. G. Sharpe, *Inorganic Chemistry*, 4th Ed., Pearson, 2012, 546–590.
152. A. Bondi, *J. Phys. Chem.*, **1964**, *68*, 441–451.
153. *CRC Handbook of Chemistry and Physics*, 97th Ed., CRC Press, 2017, 10–190.
154. W. C. Martin, *J. Res. Natl. Bur. Stand., Sect. A*, **1971**, *75A*, 109–111.
155. E. Hückel, *Z. Phys.*, **1931**, *70*, 204–286.
156. C. W. Bird, *Tetrahedron*, **1985**, *41*, 1409–1414.
157. C. W. Bird, *Tetrahedron*, **1992**, *48*, 335–340.

158. J. E. McDonough, A. Mendiratta, J. J. Curley, G. C. Fortman, S. Fantasia, C. C. Cummins, E. V Rybak-Akimova, S. P. Nolan and C. D. Hoff, *Inorg. Chem.*, **2008**, *47*, 2133–2141.
159. U. Salzner, J. B. Lagowski, P. G. Pickup and R. A. Poirier, *Synth. Met.*, **1998**, *96*, 177–189.
160. M. Heeney, W. Zhang, D. J. Crouch, M. L. Chabinye, S. Gordeyev, R. Hamilton, S. J. Higgins, I. McCulloch, P. J. Skabara, D. Sparrowe and S. Tierney, *Chem. Commun.*, **2007**, 5061–5063.
161. A. A. Jahnke, B. Djukic, T. M. McCormick, E. Buchaca Domingo, C. Hellmann, Y. Lee and D. S. Seferos, *J. Am. Chem. Soc.*, **2013**, *135*, 951–954.
162. G. He, L. Kang, W. Torres Delgado, O. Shynkaruk, M. J. Ferguson, R. McDonald and E. Rivard, *J. Am. Chem. Soc.*, **2013**, *135*, 5360–5363.
163. B. T. Luppi, R. McDonald, M. J. Ferguson, L. Sang and E. Rivard, *Chem. Commun.*, **2019**, *55*, 14218–14221.
164. A. Patra and M. Bendikov, *J. Mater. Chem.*, **2010**, *20*, 422–433.
165. S. Ye, L. Janasz, W. Zajaczkowski, J. G. Manion, A. Mondal, T. Marszalek, D. Andrienko, K. Mülllen, W. Pisula and D. S. Seferos, *Macromol. Rapid Commun.*, **2018**, *40*, 1800596.
166. D. Venkateshvaran, M. Nikolka, A. Sadhanala, V. Lemaur, M. Zelazny, M. Kepa, M. Hurhangee, A. J. Kronemeijer, V. Pecunia, I. Nasrallah, I. Romanov, K. Broch, I. McCulloch, D. Emin, Y. Olivier, J. Cornil, D. Beljonne and H. Sirringhaus, *Nature*, **2014**, *515*, 384–388.

167. B. T. Luppi, D. Majak, M. Gupta, E. Rivard and K. Shankar, *J. Mater. Chem. A*, **2019**, *7*, 2445–2463.
168. M. Samiullah, D. Moghe, U. Scherf and S. Guha, *Phys. Rev. B*, **2010**, *82*, 205211.
169. K. T. Mahmudov, M. N. Kopylovich, M. F. C. Guedes da Silva and A. J. L. Pombeiro, *Dalton Trans.*, **2017**, *46*, 10121–10138.
170. D. J. Pascoe, K. B. Ling and S. L. Cockroft, *J. Am. Chem. Soc.*, **2017**, *139*, 15160–15167.
171. A. Bauzá and A. Frontera, *Angew. Chem. Int. Ed.*, **2015**, *54*, 7340–7343.
172. A. F. Cozzolino, P. J. W. Elder and I. Vargas-Baca, *Coord. Chem. Rev.*, **2011**, *255*, 1426–1438.
173. T. Chivers and R. S. Laitinen, *Chem. Soc. Rev.*, **2015**, *44*, 1725–1739.
174. G. He, W. Torres Delgado, D. J. Schatz, C. Merten, A. Mohammadpour, L. Mayr, M. J. Ferguson, R. McDonald, A. Brown, K. Shankar and E. Rivard, *Angew. Chem. Int. Ed.*, **2014**, *53*, 4587–4591.
175. E. Rivard, *Chem. Lett.*, **2015**, *44*, 730–736.
176. W. Torres Delgado, C. A. Braun, M. P. Boone, O. Shynkaruk, Y. Qi, R. McDonald, M. J. Ferguson, P. Data, S. K. C. Almeida, I. De Aguiar, G. L. C. De Souza, A. Brown, G. He and E. Rivard, *ACS Appl. Mater. Interfaces*, **2018**, *10*, 12124–12134.
177. C. A. Braun, E. Rivard, N. Martinek, Y. Zhou and M. J. Ferguson, *Dalton Trans.*, **2019**, *48*, 10210–10219.

178. C. A. Braun, M. J. Ferguson and E. Rivard, *Inorg. Chem.*, **2021**, *60*, 2672–2679.
179. B. A. Gregg, *MRS Bull.*, **2005**, *30*, 20–22.
180. D. R. Kozub, K. Vakhshouri, S. V. Kesava, C. Wang, A. Hexemer and E. D. Gomez, *Chem. Commun.*, **2012**, *48*, 5859–5861.
181. S. R. Yost, E. Hontz, S. Yeganeh and T. Van Voorhis, *J. Phys. Chem. C*, **2012**, *116*, 17369–17377.
182. A. Köhler and H. Bässler, *Mater. Sci. Eng. R Rep.*, **2009**, *66*, 71–109.
183. R. D. Pensack, Y. Song, T. M. McCormick, A. A. Jahnke, J. Hollinger, D. S. Seferos and G. D. Scholes, *J. Phys. Chem. B*, **2014**, *118*, 2589–2597.
184. J. G. Manion, S. Ye, A. H. Proppe, A. W. Laramée, G. R. McKeown, E. L. Kynaston, S. O. Kelley, E. H. Sargent and D. S. Seferos, *ACS Appl. Energy Mater.*, **2018**, *1*, 5033–5042.
185. F. Zheng, Y. Komatsuzaki, N. Shida, H. Nishiyama, S. Inagi and I. Tomita, *Macromol. Rapid Commun.*, **2019**, *40*, 1900171.
186. A. J. Musser, M. Al-Hashimi, M. Heeney and J. Clark, *J. Chem. Phys.*, **2019**, *151*, 044902.
187. K. Wen, L. Wu, X. Wu, Y. Lu, T. Duan, H. Ma, A. Peng, Q. Shi and H. Huang, *Angew. Chem. Int. Ed.*, **2020**, *59*, 12756–12761.
188. S. A. Gregory, A. K. Menon, S. Ye, D. S. Seferos, J. R. Reynolds and S. K. Yee, *Adv. Energy Mater.*, **2018**, *8*, 1802419.
189. J. R. Panchuk, A. W. Laramée, J. G. Manion, S. Ye and D. S. Seferos, *Synth. Met.*, **2019**, *253*, 57–61.

190. M. P. Gordon, S. A. Gregory, J. P. Wooding, S. Ye, G. M. Su, D. S. Seferos, M. D. Losego, J. J. Urban, S. K. Yee and A. K. Menon, *Appl. Phys. Lett.*, **2021**, *118*, 233301.
191. W. Mack, *Angew. Chem. Int. Ed. Engl.*, **1966**, *5*, 896.
192. D. P. Sweat and C. E. Stephens, *J. Organomet. Chem.*, **2008**, *693*, 2463–2464.
193. R. Sugimoto, K. Yoshino, S. Inoue and K. Tsukagoshi, *Jpn. J. Appl. Phys.*, **1985**, *24*, L425–L427.
194. S. Inoue, T. Jigami, H. Nozoe, T. Otsubo and F. Ogura, *Tetrahedron Lett.*, **1994**, *35*, 8009–8012.
195. T. Otsubo, S. Inoue, H. Nozoe, T. Jigami and F. Ogura, *Synth. Met.*, **1995**, *69*, 537–538.
196. A. Patra, Y. H. Wijsboom, G. Leitus and M. Bendikov, *Org. Lett.*, **2009**, *11*, 1487–1490.
197. S. C. Ng, H. Ding and H. S. O. Chan, *Chem. Lett.*, **1999**, *28*, 1325–1326.
198. M. Lapkowski, R. Motyka, J. Suwiński and P. Data, *Macromol. Chem. Phys.*, **2012**, *213*, 29–35.
199. H. Saito, S. Ukai, S. Iwatsuki, T. Itoh and M. Kubo, *Macromolecules*, **1995**, *28*, 8363–8367.
200. A. A. Jahnke, G. W. Howe and D. S. Seferos, *Angew. Chem. Int. Ed.*, **2010**, *49*, 10140–10144.
201. T. M. McCormick, A. A. Jahnke, A. J. Lough and D. S. Seferos, *J. Am. Chem. Soc.*, **2012**, *134*, 3542–3548.

202. E. I. Carrera and D. S. Seferos, *Dalton Trans.*, **2015**, 44, 2092–2096.
203. E. I. Carrera, A. E. Lanterna, A. J. Lough, J. C. Scaiano and D. S. Seferos, *J. Am. Chem. Soc.*, **2016**, 138, 2678–2689.
204. W.-H. Lee, S. K. Lee, W. S. Shin, S.-J. Moon and I.-N. Kang, *J. Polym. Sci., Part A Polym. Chem.*, **2013**, 51, 2753–2758.
205. X. M. Jiang, R. Österbacka, O. Korovyanko, C. P. An, B. Horovitz, R. A. J. Janssen and Z. V. Vardeny, *Adv. Funct. Mater.*, **2002**, 12, 587–597.
206. J. L. Dutton, G. J. Farrar, M. J. Sgro, T. L. Battista and P. J. Ragogna, *Chem.-Eur. J.*, **2009**, 15, 10263–10271.
207. D. M. González, K. N. Raftopoulos, G. He, C. M. Papadakis, A. Brown, E. Rivard and P. Müller-Buschbaum, *Macromol. Rapid Commun.*, **2017**, 38, 1700065.
208. Y. S. Park, Q. Wu, C.-Y. Nam and R. B. Grubbs, *Angew. Chem. Int. Ed.*, **2014**, 53, 10691–10695.
209. M. Planells, B. C. Schroeder and I. McCulloch, *Macromolecules*, **2014**, 47, 5889–5894.
210. E. H. Jung, S. Bae, T. W. Yoo and W. H. Jo, *Polym. Chem.*, **2014**, 5, 6545–6550.
211. R. S. Ashraf, I. Meager, M. Nikolka, M. Kirkus, M. Planells, B. C. Schroeder, S. Holliday, M. Hurhangee, C. B. Nielsen, H. Sirringhaus and I. McCulloch, *J. Am. Chem. Soc.*, **2015**, 137, 1314–1321.

212. M. Kaur, D. H. Lee, D. S. Yang, H. A. Um, M. J. Cho, J. S. Kang and D. H. Choi, *Dyes Pigm.*, **2015**, *123*, 317–322.
213. L. Lv, X. Wang, X. Wang, L. Yang, T. Dong, Z. Yang and H. Huang, *ACS Appl. Mater. Interfaces*, **2016**, *8*, 34620–34629.
214. K. Zhang, L. Lv, X. Wang, Y. Mi, R. Chai, X. Liu, G. Shen, A. Peng and H. Huang, *ACS Appl. Mater. Interfaces*, **2018**, *10*, 1917–1924.
215. M. Al-Hashimi, Y. Han, J. Smith, H. S. Bazzi, S. Y. A. Alqaradawi, S. E. Watkins, T. D. Anthopoulos and M. Heeney, *Chem. Sci.*, **2016**, *7*, 1093–1099.
216. K. Wen, X. Xu, J. Chen, L. Lv, L. Wu, Y. Hu, X. Wu, G. Liu, A. Peng and H. Huang, *ACS Appl. Mater. Interfaces*, **2019**, *11*, 17884–17893.
217. B. M. Trost, *Science*, **1991**, *254*, 1471–1477.
218. R. D. McCullough, S. P. Williams, S. Tristram-Nagle, M. Jayaraman, P. C. Ewbank and L. Miller, *Synth. Met.*, **1995**, *69*, 279–282.
219. Z. Bao, A. Dodabalapur and A. J. Lovinger, *Appl. Phys. Lett.*, **1996**, *69*, 4108–4110.
220. H. Sirringhaus, P. J. Brown, R. H. Friend, M. M. Nielsen, K. Bechgaard, B. M. W. Langeveld-Voss, A. J. H. Spiering, R. A. J. Janssen, E. W. Meijer, P. Herwig and D. M. de Leeuw, *Phys. Rev. B*, **2000**, *62*, 685–688.
221. R. S. Loewe, P. C. Ewbank, J. Liu, L. Zhai and R. D. McCullough, *Macromolecules*, **2001**, *34*, 4324–4333.
222. R. Tkachov, V. Senkovskyy, H. Komber and A. Kiriy, *Macromolecules*, **2011**, *44*, 2006–2015.

223. A. Kiriy, V. Senkovskyy and M. Sommer, *Macromol. Rapid Commun.*, **2011**, *32*, 1503–1517.
224. Z. J. Bryan and A. J. McNeil, *Macromolecules*, **2013**, *46*, 8395–8405.
225. S. Ye, M. Steube, E. I. Carrera and D. S. Seferos, *Macromolecules*, **2016**, *49*, 1704–1711.
226. S. Ye, S. M. Foster, A. A. Pollit, S. Cheng and D. S. Seferos, *Chem. Sci.*, **2019**, *10*, 2075–2080.
227. R. L.-Y. Bao, R. Zhao and L. Shi, *Chem. Commun.*, **2015**, *51*, 6884–6900.
228. E. L. Lanni and A. J. McNeil, *J. Am. Chem. Soc.*, **2009**, *131*, 16573–16579.
229. E. L. Lanni and A. J. McNeil, *Macromolecules*, **2010**, *43*, 8039–8044.
230. A. K. Mahrok, E. I. Carrera, A. J. Tilley, S. Ye and D. S. Seferos, *Chem. Commun.*, **2015**, *51*, 5475–5478.
231. U. Belluco, R. Bertani, R. A. Michelin and M. Mozzon, *J. Organomet. Chem.*, **2000**, *600*, 37–55.
232. F. Guo, Y. G. Kim, J. R. Reynolds and K. S. Schanze, *Chem. Commun.*, **2006**, 1887–1889.
233. H. Nishiyama, F. Zheng, S. Inagi, H. Fueno, K. Tanaka and I. Tomita, *Polym. Chem.*, **2020**, *11*, 4693–4698.
234. T. Hamada, D. Suzuki, H. Urabe and F. Sato, *J. Am. Chem. Soc.*, **1999**, *121*, 7342–7344.
235. H. Nishiyama, T. Kino and I. Tomita, *Macromol. Rapid Commun.*, **2012**, *33*, 545–549.

236. S. Rühle, *Sol. Energy*, **2016**, *130*, 139–147.
237. S. Rafique, S. M. Abdullah, K. Sulaiman and M. Iwamoto, *Renew. Sustain. Energy Rev.*, **2018**, *84*, 43–53.
238. J. C. Bijleveld, A. P. Zoombelt, S. G. J. Mathijssen, M. M. Wienk, M. Turbiez, D. M. de Leeuw and R. A. J. Janssen, *J. Am. Chem. Soc.*, **2009**, *131*, 16616–16617.
239. M. B. Smith and J. Michl, *Chem. Rev.*, **2010**, *110*, 6891–6936.
240. M. J. Y. Tayebjee, S. N. Sanders, E. Kumarasamy, L. M. Campos, M. Y. Sfeir and D. R. McCamey, *Nat. Phys.*, **2017**, *13*, 182–189.
241. B. S. Basel, J. Zirzmeier, C. Hetzer, B. T. Phelan, M. D. Krzyaniak, S. R. Reddy, P. B. Coto, N. E. Horwitz, R. M. Young, F. J. White, F. Hampel, T. Clark, M. Thoss, R. R. Tykwinski, M. R. Wasielewski and D. M. Guldi, *Nat. Commun.*, **2017**, *8*, 1–8.
242. M. Kaur, D. S. Yang, J. Shin, T. W. Lee, K. Choi, M. J. Cho and D. H. Choi, *Chem. Commun.*, **2013**, *49*, 5495–5497.
243. I. Osaka and K. Takimiya, *Polymer*, **2015**, *59*, A1–A15.
244. A. A. Jahnke, L. Yu, N. Coombs, A. D. Scaccabarozzi, A. J. Tilley, P. M. Dicarmine, A. Amassian, N. Stingelin and D. S. Seferos, *J. Mater. Chem. C*, **2015**, *3*, 3767–3773.
245. J. Miao, F. Zhang, Y. Lin, W. Wang, M. Gao, L. Li, J. Zhang and X. Zhan, *Adv. Opt. Mater.*, **2016**, *4*, 1711–1717.

246. Y. Jin, J. Wang, B. Sun, J. C. Blakesley and N. C. Greenham, *Nano Lett.*, **2008**, 8, 1649–1653.

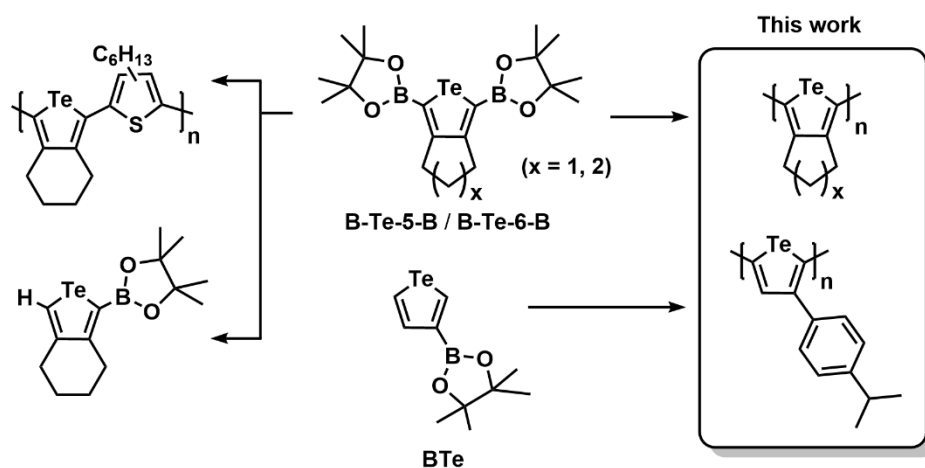
Chapter 2: Rapid Access to (Cycloalkyl)tellurophene Oligomer Mixtures and the First Poly(3-aryltellurophene)

2.1 Introduction

Polytellurophenes, the heavier element (Te) containing analogues of polythiophenes, have been gaining momentum as promising optoelectronic materials.^{1,2} Replacement of S by Te within a heterocyclic building block can lead to increased quinoidal character of the resulting polyheteroles (and a reduced HOMO–LUMO gap, E_g), along with an increase in hole mobility. Accordingly, polytellurophenes are being explored for next generation organic solar cells and field effect transistors.^{3,4} The presence of the heavy element tellurium can also increase spin orbit coupling, enabling efficient phosphorescence to transpire, both in the solid state and in the presence of the known quencher O_2 .^{5,6} Access to photoexcited triplet states can also yield longer exciton (electron–hole pair) diffusion lengths, which can increase solar cell efficiency and simplify working device architectures.⁷⁻⁹

A key challenge in the development of new polytellurophenes is efficient access to monomers. For example, Seferos and coworkers have used Na_2Te -mediated ring formation to selectively place alkyl-substituents onto monomeric tellurophenes,^{3a,10} while our group has used zirconium-instigated alkyne coupling, followed by Zr/Te metallacycle transfer, to yield tellurophenes with reactive pinacolboronate (BPin) groups at the 2- and 5-positions.^{3b,5,6,11,12} The latter procedure has been used to synthesize (cycloalkyl)tellurophenes such as **B-Te-6-B** (Scheme 2.1) that undergo

Suzuki–Miyaura coupling to yield phosphorescent molecules^{6b,11} or copolymers.^{3b} Thus far, all copolymers synthesized from **B-Te-6-B** have wide optical band gaps (>2.3 eV),^{3b} suggesting substantial twisting of the tellurophene units away from coplanarity. In addition, low polymer molecular weights (3–7 kDa)^{3b} are often observed due to competitive protodeboronation and the accompanying termination of polymerization.



Scheme 2.1 Tellurophene project overview. Center: BPin-functionalized (cycloalkyl)tellurophenes **B-Te-5-B** and **B-Te-6-B**, and the monoborylated tellurophene (**BTe**). Left: A copolymer derived from **B-Te-6-B** (top) and an example of a protodeboronation side-product derived from **B-Te-6-B** (bottom). Right: New tellurophene oligomers and polymers synthesized in this Chapter.

In this Chapter, the reactivity of ring-bound BPin groups is used to advance tellurophene chemistry in two distinct ways: first, the efficient syntheses of the 2,5-iodonated tellurophene building blocks **I-Te-5-I** and **I-Te-6-I** (Scheme 2.2) now

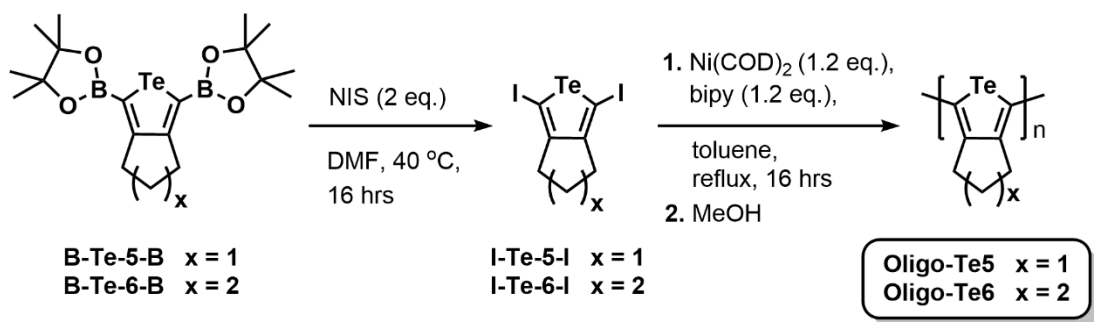
enables their direct homopolymerization by Yamamoto coupling to form mixture of oligomers that show different optical band gaps (E_g) depending on the size of the cyclic side group. Second, the first poly(3-aryltellurophene) is reported,¹³ which features cumenyl (4-ⁱPrC₆H₄) side groups and a low E_g of *ca.* 1.3 eV.

2.2 Results and Discussions

2.2.1 Synthesis of (Cyclo)tellurophene Oligomers

Initial attempts to form cycloalkyl-functionalized tellurophene homopolymers involved subjecting the known 2,5-dibrominated tellurophene **Br-Te-6-Br**^{11a} to widely used Grignard metathesis (GRIM)¹⁴ and Yamamoto¹⁵ polymerization protocols. For GRIM, **Br-Te-6-Br** was reacted with ⁱPrMgCl in THF for followed by addition of 1 mol. % of Ni(dppe)Cl₂ (dppe = Ph₂P(CH₂)₂PPh₂). On the other hand, for Yamamoto polymerization, **Br-Te-6-Br** was reacted with stoichiometric Ni(COD)₂/bipy (COD = 1,5-cyclooctadiene; bipy = 2,2'-bipyridine) in toluene under reflux. Unfortunately, both routes only resulted in low isolated yields (*ca.* 5–10 %) of oligomers. In order to improve the efficiency of polymerization,^{14b} the 2,5-diiodinated tellurophenes **I-Te-5-I** and **I-Te-6-I** were prepared by reacting N-iodosuccinimide (NIS) with **B-Te-5-B** and **B-Te-6-B** in DMF at 40 °C (25 and 31 % yields, respectively; Scheme 2.2). The X-ray structure of both iodinated tellurophenes is shown below (Figure 2.1). To my knowledge, these are the first examples of direct –BR₂ to –I conversion on a tellurophene, however, related chemistry involving boronic acid-functionalized thiophenes is known.^{16,17} **I-Te-5-I** and **I-Te-6-I** are air stable yellow needle-like

crystals but were stored at -30 °C in the dark to prevent their self-oligomerization (see Section 2.4.7).¹⁸



Scheme 2.2 Synthesis and oligomerization of **I-Te-5-I** and **I-Te-6-I**. NIS = N-iodosuccinimide, COD=1,5-cyclooctadiene, bipy = 2,2'-bipyridine.

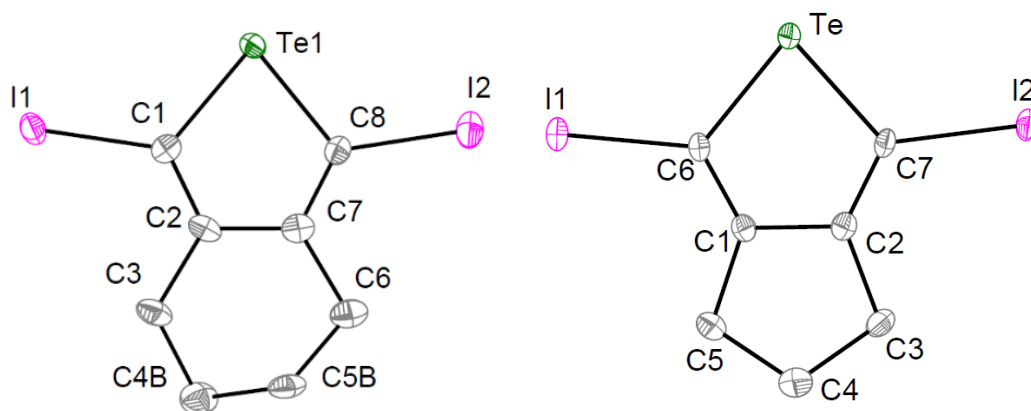


Figure 2.1. Molecular structure of 1,3-diiodo-4,5,6,7-tetrahydro-benzo[*c*]tellurophene (**I-Te-6-I**, left) and 1,3-diiodo-4,5,6,7-tetrahydro-cyclopenta[*c*]tellurophene (**I-Te-5-I**, right). Thermal ellipsoids plotted at a 30 % probability level with hydrogen atoms omitted for clarity. Selected bond lengths (Å) and angle (°): **I-Te-6-I**: Te1-C1 2.080(3), Te1-C8 2.090(3), I1-C1 2.079(2), I2-C8 2.083(3); C1-Te1-C8 80.92(11). **I-Te-5-I**: Te1-C6 2.076(9), Te-C7 2.080(10), I1-C6 2.062(9), I2-C7 2.081(10); C6-Te-C7 79.2(4).

The Yamamoto polymerization of **I-Te-5-I** and **I-Te-6-I** in the presence of stoichiometric Ni(COD)₂/bipy (Scheme 2.2) afforded the corresponding oligomer mixtures **Oligo-Te5** and **Oligo-Te6** as red and orange solids in 49 and 52 % purified yields, respectively. These products were characterized by NMR spectroscopy (Section 2.4.3) and were stable up to *ca.* 200 °C as determined by TGA (Section 2.4.5)

MALDI-MS (Figures 2.2 and 2.3) indicates that high molecular weight polymers were not formed, probably due to a lack of solubility. However, as explained below, these oligomers provide insight into the influence of the cycloalkyl side groups on optoelectronic properties. The formation of longer (more soluble) chains of **Oligo-Te6** ($n \leq 12$ in Scheme 2.2) versus **Oligo-Te5** ($n \leq 5$) is likely due to enhanced backbone ring twisting in **Oligo-Te6**, leading to reduced interchain polymer interactions; this point will be discussed in the next section.

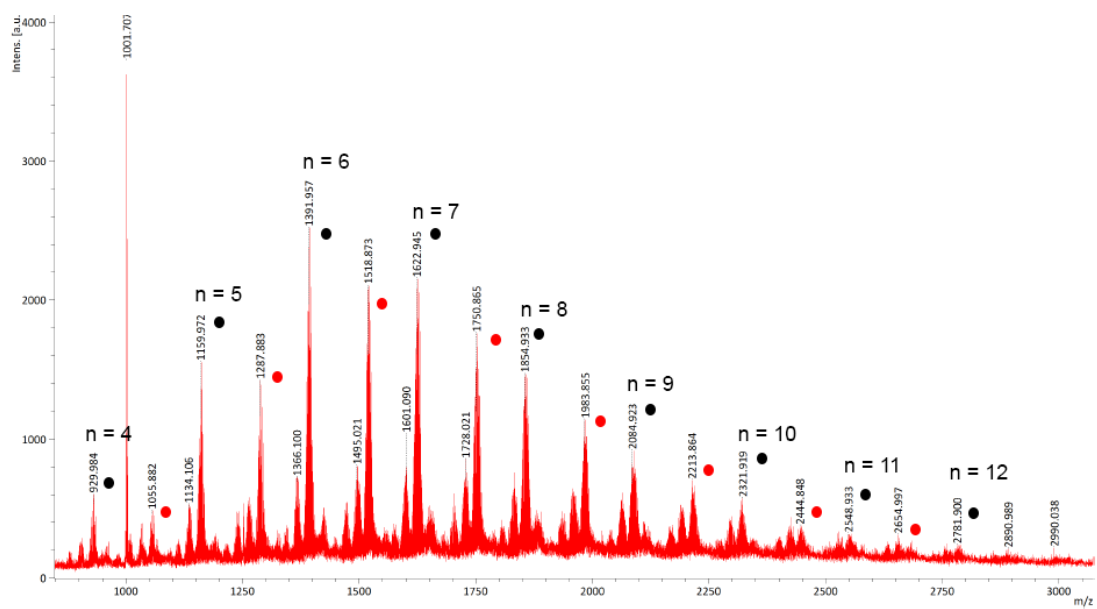


Figure 2.2. MALDI-MS of **Oligo-Te6**. Black dots represent H/H termination, red dots represent H/I termination.

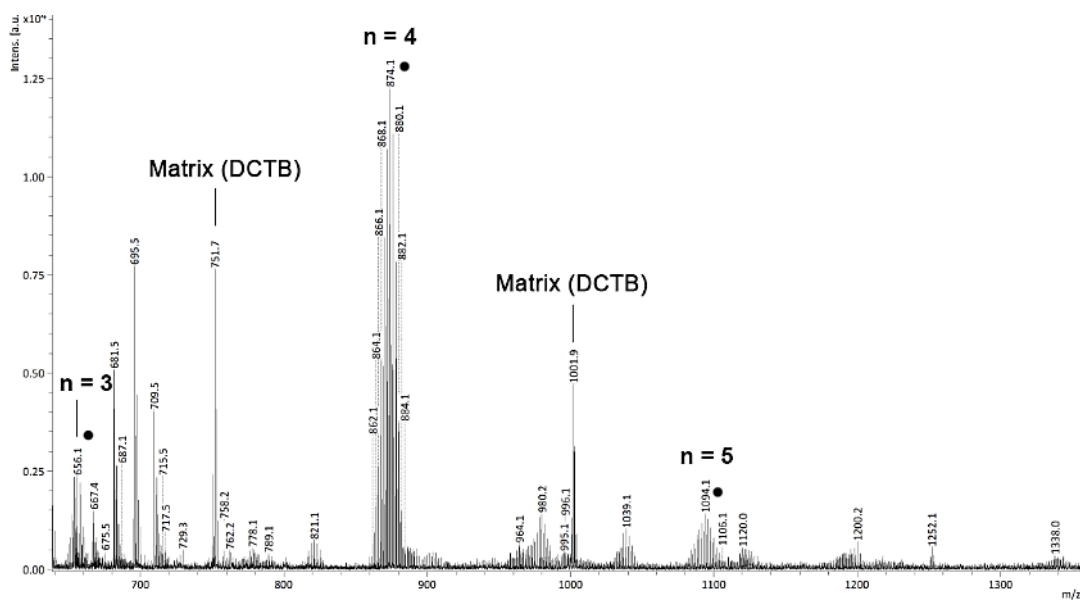


Figure 2.3. MALDI-MS of **Oligo-Te5**. The marked peaks (black dot) correspond to oligomers showing mass matching H/H termination. DCTB = *trans*-2-[3-(4-*tert*-butylphenyl)-2-methyl-2-propenylidene]malononitrile.

2.2.2 Influence of Cyclic Side Groups on Optoelectronic Properties

UV-Vis spectroscopy in CHCl_3 shows a λ_{max} at 295 nm for **Oligo-Te6**, while a substantially red-shifted λ_{max} at 471 nm is seen for **Oligo-Te5** (Figure 2.4). Thus, removing one $-\text{CH}_2-$ group from the cyclic side chain leads to a decrease in optical HOMO-LUMO gap (E_g) to a value of 1.97 eV for **Oligo-Te5** in solution (estimated from the onset of absorption) that is significantly red-shifted in comparison to **Oligo-Te6** (2.72 eV) and other known tellurophene copolymers with **Te6** subunits (e.g., Scheme 2.1).^{3b} As expected, the E_g is further reduced to 2.22 and 1.82 eV for films of **Oligo-Te6** and **Oligo-Te5** (Section 2.4.6).

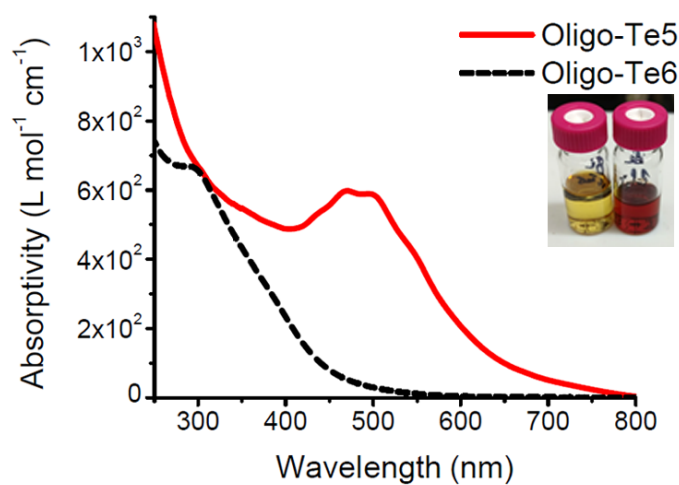


Figure 2.4. UV-Vis spectra and images of **Oligo-Te5** and **Oligo-Te6** in CHCl_3 .

To understand this significant difference in absorption for these oligotellurophenes, density functional theory (DFT) computations [B3LYP/6-31G(d,p) (with LANL2DZ for Te and I)] were performed on the oligomeric models **I-[Te5]7-I** and **I-[Te6]7-I** (Figure 2.5). The presence of **Te6** units in **I-[Te6]7-I** yields nearly perpendicular tellurophene rings (89° twist angle), while the less hindered **Te5** units in **I-[Te5]7-I** enable a preferential coplanar arrangement of the tellurophene subunits (1° twist angle). As expected, the computed E_g value for planar **I-[Te5]7-I** (2.17 eV) is much smaller than in **I-[Te6]7-I** (4.18 eV).¹⁹ An energetic penalty of 90 kJ/mol was also computed for twisting the tellurophene rings into a planar arrangement within a tetrameric model for **Oligo-Te6** (**I-[Te6]4-I**, Figure 2.6), while for **Oligo-Te5** (**I-[Te5]4-I**) an energy change of -20 kJ/mol is observed upon twisting the rings from being mutually perpendicular to coplanar. Both behaviors are reproduced when the

tellurophene units are spaced by 3-methyl thiophene units. Closer inspection of the optimized structures indicates that unfavorable Te–H₂C (side group) interactions in this model for **Oligo-Te6** are responsible for ring twisting. Thus, copolymers bearing the less hindered **Te5** subunit are now being investigated, as the cyclopentane side chain functionality leads to a preference for planar structures in the resulting oligo- and polychalcogenophenes.

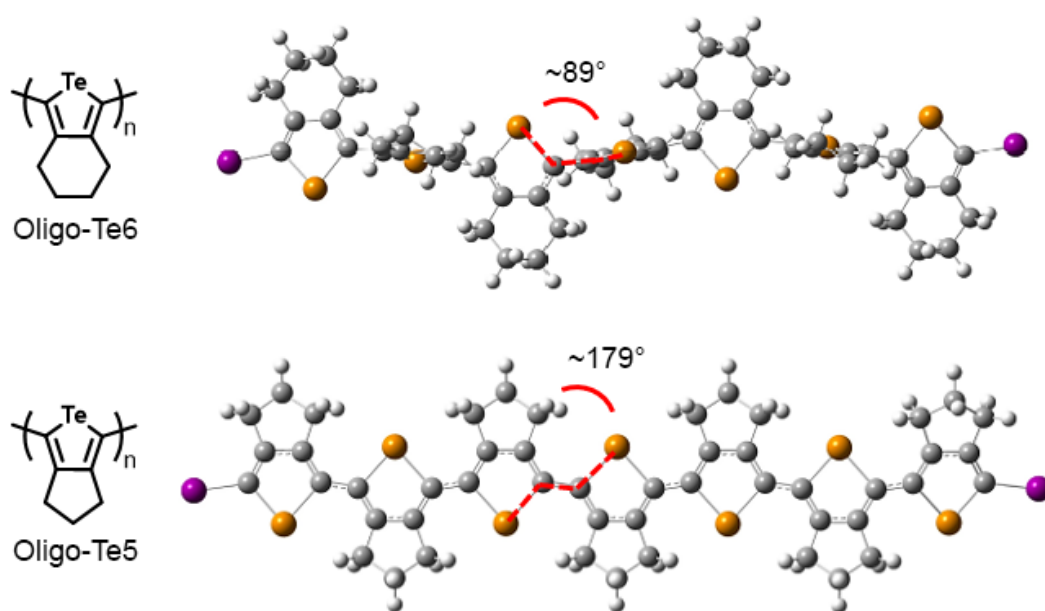


Figure 2.5. Structure optimization of heptamers of **Oligo-Te6** and **Oligo-Te5**. The average torsional angle for the oligomers is highlighted in the Figure. Level of theory: B3LYP/6-31G(d,p) (with LANL2DZ for Te and I).

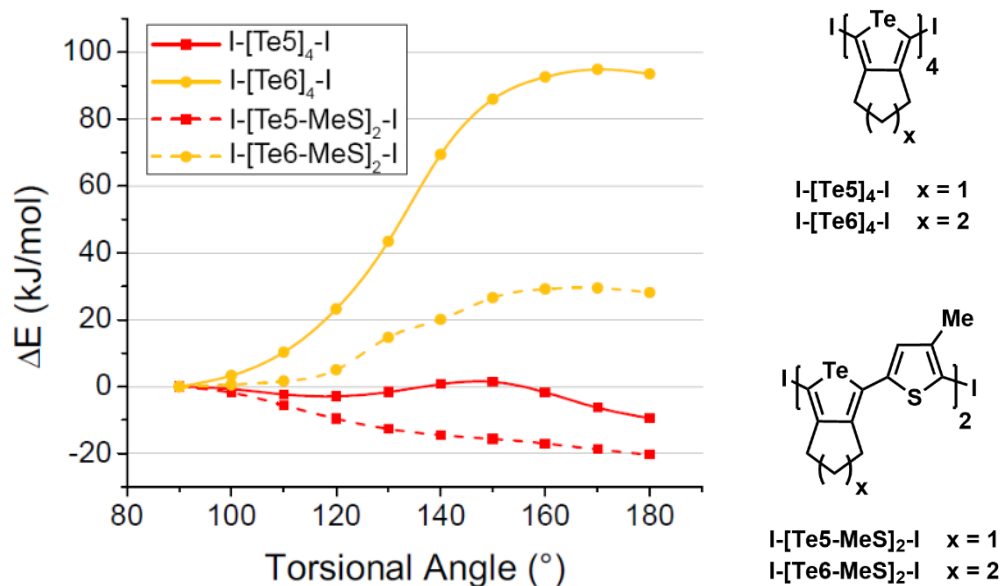


Figure 2.6. Energy change of oligomers upon change in torsion angle. The energy is calculated relative to the 90° position for tetrameric models of oligomers terminated by iodine consisting of four units of each tellurophene (**I-[Te6]₄-I** and **I-[Te5]₄-I**) or a copolymer of same length with 3-methylthiophene subunits (**I-[Te6-MeS]₂-I** and **I-[Te5-MeS]₂-I**). Level of theory: B3LYP/6-31G(d,p) (with LANL2DZ for Te and I).

The computed UV-Vis spectra (by TD-DFT) for trimeric models of **Oligo-Te5** and **Oligo-Te6** reproduced the overall spectral features found by experiment (Figure 2.7). In each case, the HOMO–LUMO transition has C–C π character in the HOMO (with a small iodine(lp) admixture; lp = lone pair) and quinoidal C–C π and Te(lp) contributions to the LUMO (Figure 2.8).

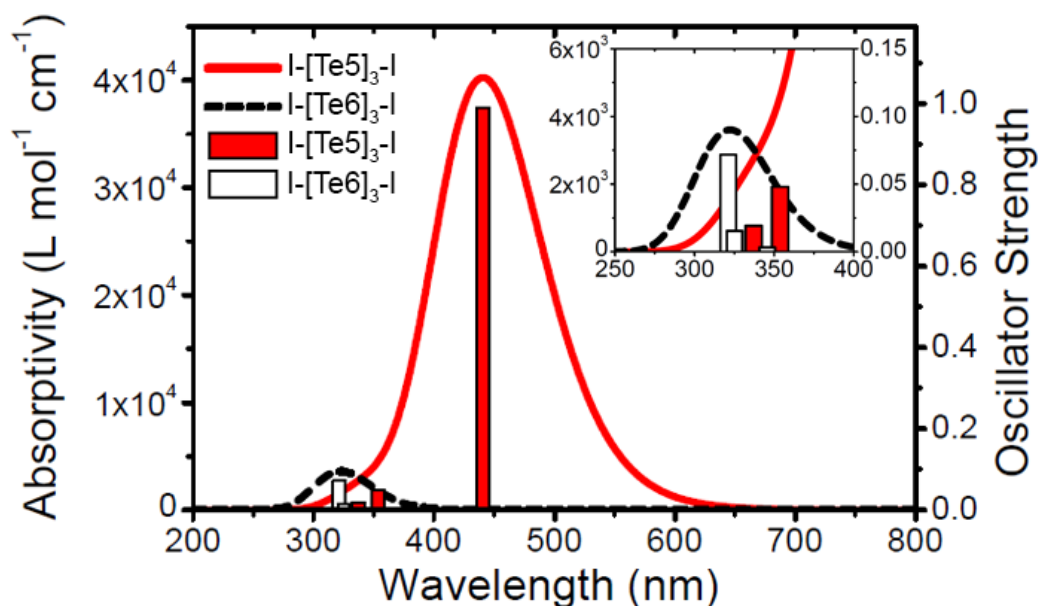


Figure 2.7. TD-DFT computed UV-Vis absorptivity for trimers of **Oligo-Te5** (**I-[Te5]₃-I**) and **Oligo-Te6** (**I-[Te6]₃-I**) and the three main oscillator strengths (bars below the curves) associated with the absorptions. The inset shows an expansion of the short wavelength region.

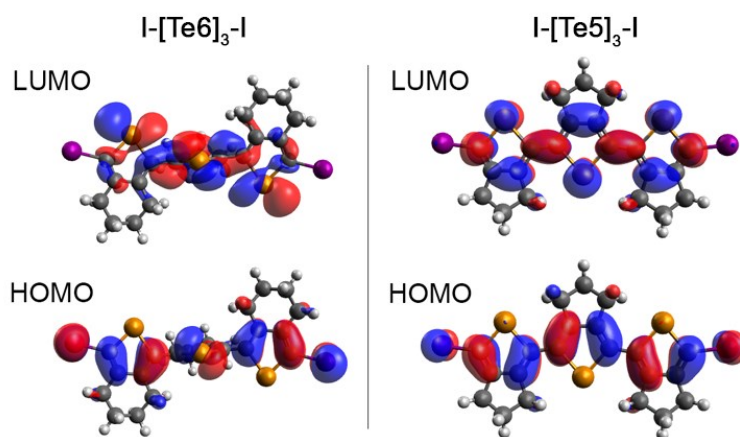
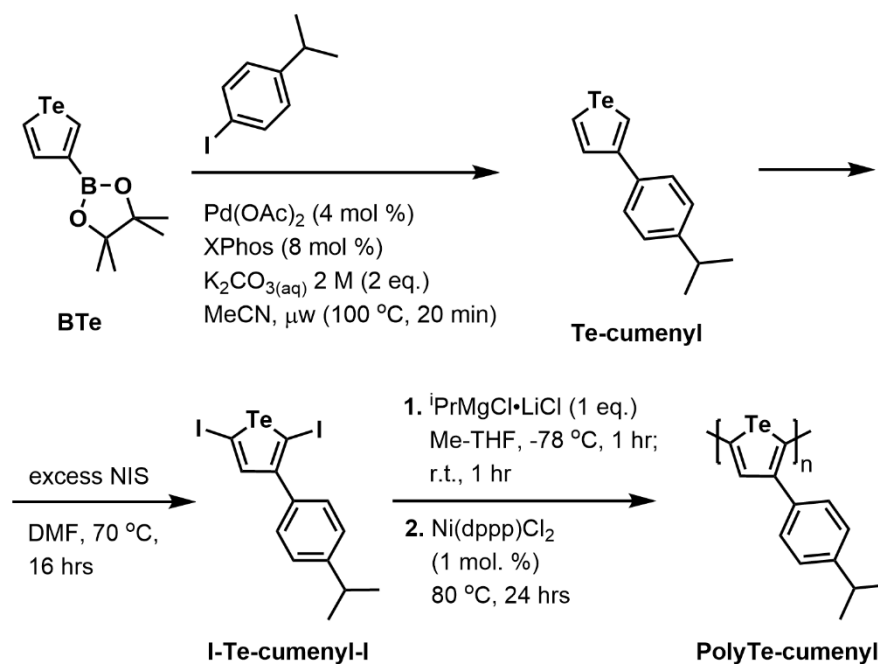


Figure 2.8. DFT computed orbitals for trimeric models of **Oligo-Te6** and **Oligo-Te5**.

2.2.3 Synthesis of a Poly(3-aryl)tellurophene

Soluble polytellurophenes with long alkyl side chains have been developed by Seferos and coworkers.^{3a,10} The corresponding poly(3-aryltellurophenes) are unknown and could yield enhanced crystallinity/charge mobility in the solid state, due to added π - π stacking interactions. Towards this goal, the known 3-borylated tellurophene **BTe** (Scheme 2.3)^{11a} was coupled with 4-iodocumene to yield the new 3-arylated tellurophene **Te-cumenyl** (see Figure 2.9 for its X-ray structure); in principle, this procedure could be used to graft a wide range of different aryl groups onto a tellurophene. Iodination of **Te-cumenyl** with NIS in DMF at 70 °C affords the requisite polymer precursor **I-Te-cumenyl-I** as an air-stable orange oil (57 %) after purification (Scheme 2.3).



Scheme 2.3 Synthesis of the poly(3-aryltellurophene) **PolyTe-cumenyl**.

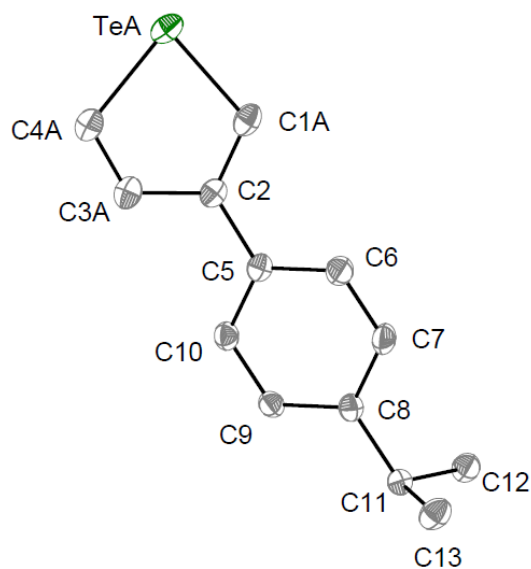
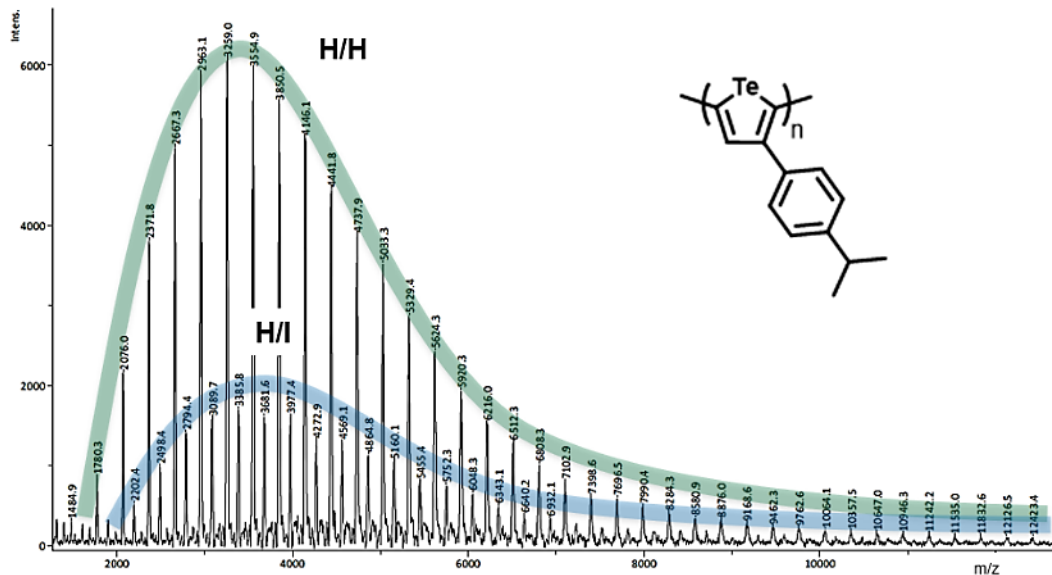


Figure 2.9. Molecular structure of 3-(4-isopropylphenyl)-tellurophene (**Te-cumenyl**). Thermal ellipsoids plotted at a 30 % probability level with hydrogen atoms omitted for clarity. Selected bond lengths (Å), angle and dihedral angle (°): Te-C1 2.053(9), Te-C4 2.088(5), C2-C5 1.486(3); C4-Te-C1 80.4(3); C1-C2-C5-C6 24.9(13).

I-Te-cumenyl-I was then polymerized via the GRIM (Grignard metathesis) method using stoichiometric ${}^i\text{PrMgCl}\cdot\text{LiCl}$ for monomer activation ($-78\text{ }^\circ\text{C}$ to room temperature), followed by addition of $\text{Ni}(\text{dppp})\text{Cl}_2$ as a pre-catalyst ($\text{dppp} = \text{Ph}_2\text{P}(\text{CH}_2)_3\text{PPh}_2$) and heating to $80\text{ }^\circ\text{C}$. The resulting polymer **PolyTe-cumenyl** ($M_w = 8\text{ kDa}$, $\text{PDI} = 1.1$) was obtained as an air- and moisture-stable deep blue-purple solid. Integration of the major and minor isopropyl signals in the ${}^1\text{H}$ NMR spectrum of **PolyTe-cumenyl** indicates 94 % head– tail regioregularity, which matches values found within known poly(3-alkyltellurophenes).^{3a,10} For comparison, the analogous

polythiophene was synthesized and the same route as described above afforded **PolyS-cumenyl** ($M_w = 12$ kDa, PDI = 1.1) as a dark purple solid. Both polymers are stable up to 200 °C as solids under N_2 , as determined by TGA (Section 2.4.5).

End group analysis by MALDI-MS shows two major sets of peaks for **PolyTe-cumenyl** (Figure 2.10) and **PolyS-cumenyl** (Figure 2.11) assigned to chains with either H/I or H/H end groups. For controlled GRIM (also known as catalyst-transfer polymerization)^{14, 20} of a mono-activated monomer (e.g., **RMg-Te-cumenyl-I**) one would expect only H/I end groups after work-up. Thus, the presence of H/H end groups suggests that some double activation/metallation of the tellurophene monomer is occurring.



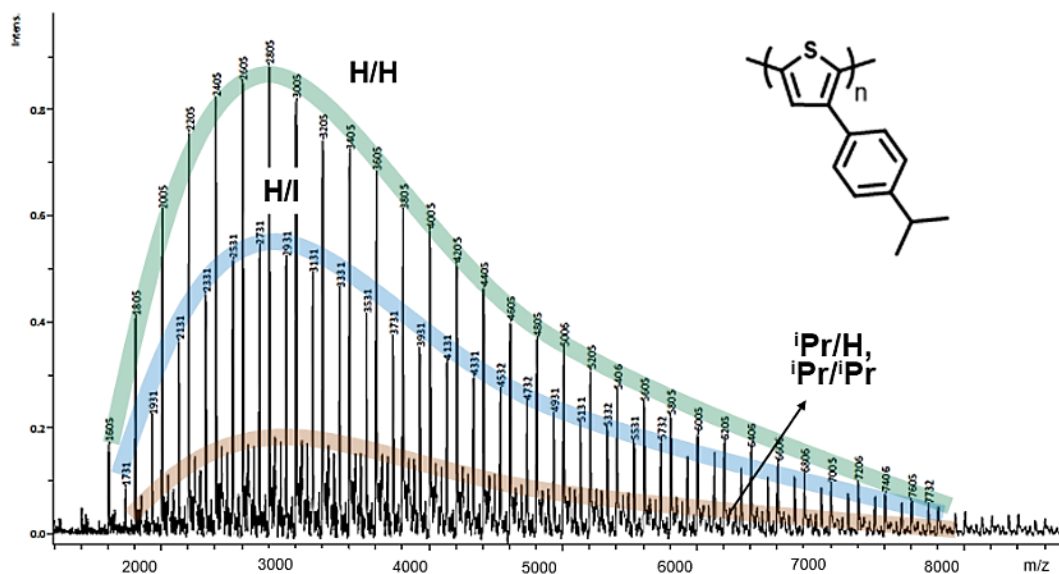


Figure 2.11. MALDI-MS of PolyS-cumenyl. Green curve highlights H/H termination, while the blue highlights H/I termination and brown $i\text{Pr}/i\text{Pr}$ and $i\text{Pr}/\text{H}$.

2.2.4 Attempts to Improve End-Group Control

Double activation was confirmed in model/stoichiometric activation studies of the iodinated monomers. The regioselectivity of the initial C–I metallation step was verified for both **I-S-cumenyl-I** and **I-Te-cumenyl-I** by adding $i\text{PrMgCl}\cdot\text{LiCl}$, followed by quenching with HCl, and analysis of the product(s) by ^1H NMR spectroscopy (Figure 2.12).

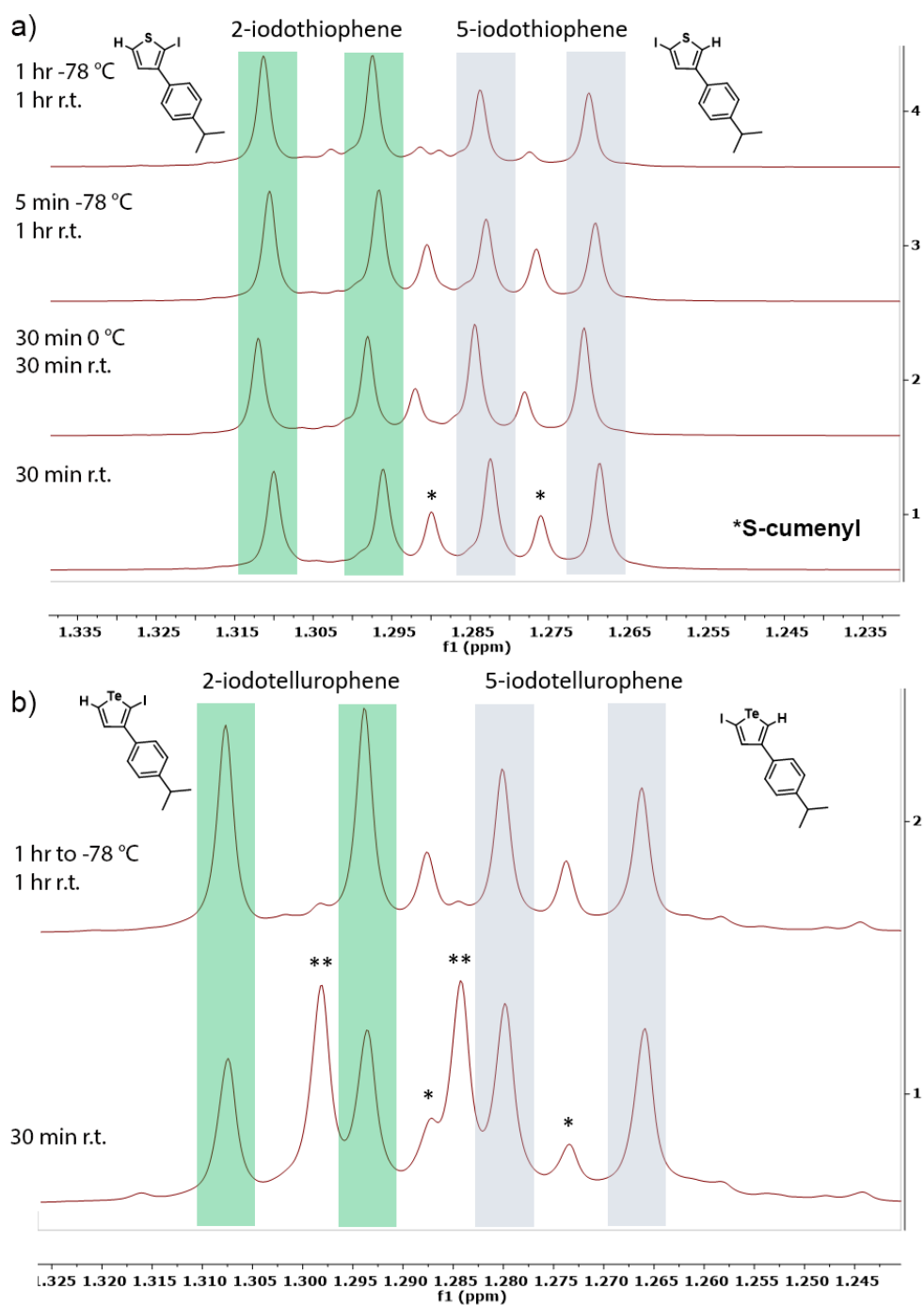


Figure 2.12. a) ^1H NMR study of the GRIM activation step for **I-S-cumenyl-I**; b) ^1H NMR study of the GRIM activation step for **I-Te-cumenyl-I**. Spectra were collected after reaction with $^i\text{PrMgCl}\cdot\text{LiCl}$ at different temperatures and quenching with $\text{HCl}_{(\text{aq})}$.

After 30 minutes at room temperature, formation of 5-iodochalcogenophenes (from metallation close to the cumenyl group) and 2-iodochalcogenophenes (from metallation away from the cumenyl group) is observed, as well as unsubstituted chalcogenophenes (from double metallation) and unreacted **I-Te-cumenyl-I** for the tellurophene. It is also notable that the intensity of peaks corresponding to 5-iodochalcogenophenes is larger, indicating an undesirable majority of activation close to the cumenyl group at room temperature.¹⁴ When the activation temperature is lowered, metallation away from the cumenyl group can be favored, but in both cases double-metallation of the monomer is still observed even at -78 °C.

In attempts to improve end group control, polymerization trials with the more active pre-catalyst Ni(dppe)Cl₂ (dppe = Ph₂P(CH₂)₂PPh₂) were performed. With higher catalytic activity, one would be able to carry out the polymerization at a lower temperature for improved control. However, the products recovered under these alternate polymerization conditions did not show improvement by MALDI-MS (Figure 2.13) and significantly reduced regioregularity was noted by ¹H NMR spectroscopy (Figure 2.14). In these trials, **PolyS-cumenyl** (M_w = 13 kDa, PDI = 1.1; 65 % regioregularity) was synthesized at 80 °C, while **PolyTe-cumenyl** (M_w = 4.1 kDa, PDI = 1.5; 73 % regioregularity) was synthesized at a reduced 40 °C, both with 1 mol. % of catalyst in 2-methyltetrahydrofuran (Me-THF).

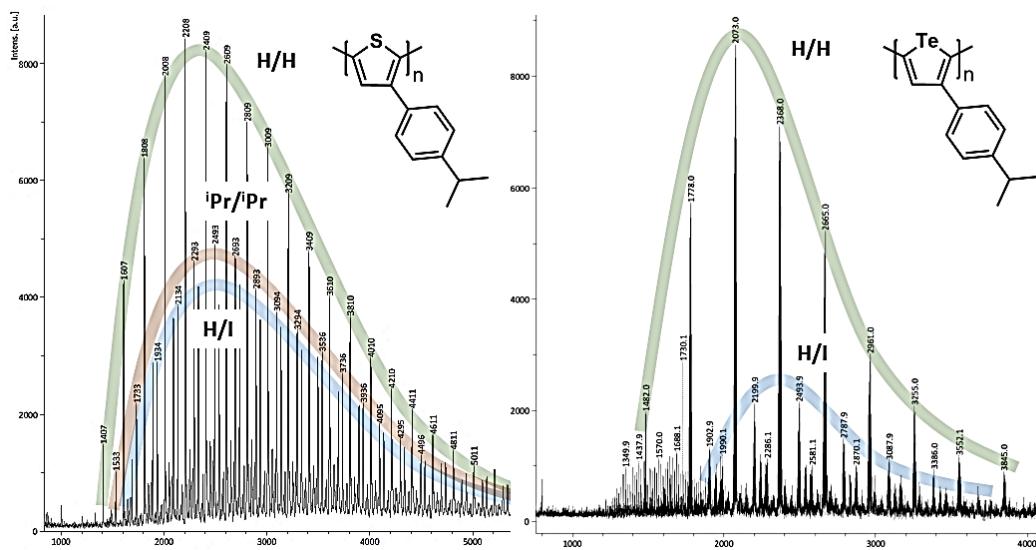


Figure 2.13. MALDI-MS of PolyS-cumenyl and PolyTe-cumenyl prepared with Ni(dppe)Cl₂ as a pre-catalyst. Green curve highlights H/H termination, while the blue traces highlight H/I termination and brown curves ⁱPr/ⁱPr termination.

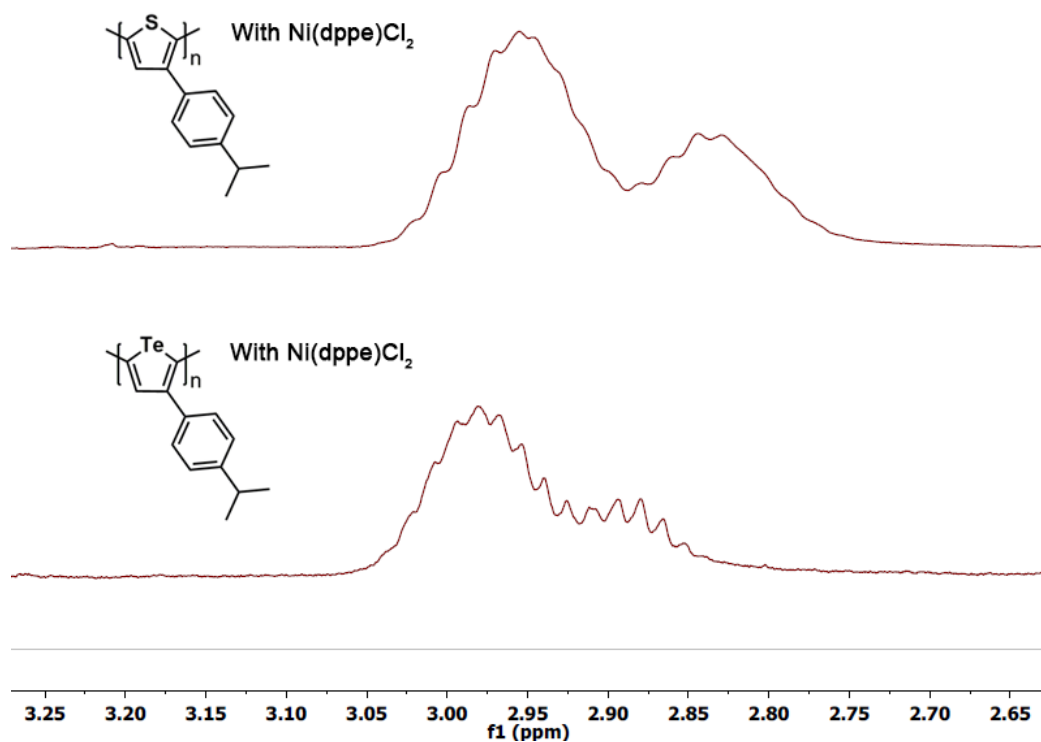


Figure 2.14. ^1H NMR spectra in CDCl_3 of the isopropyl region of the low regioregularity polymers obtained during polymerization trials with $\text{Ni}(\text{dppe})\text{Cl}_2$ (1 mol. %) as pre-catalyst.

2.2.5 Optoelectronic Properties of Poly(3-aryl)tellurophene

The UV-Vis spectra for **PolyS-cumenyl** and **PolyTe-cumenyl** synthesized with $\text{Ni}(\text{dppp})\text{Cl}_2$ reveal important differences. For **PolyS-cumenyl** (Figure 2.15, top), there is an expected red-shift in absorption maximum from 455 nm in THF to 467 nm as a film, and finally to 542 nm ($E_g = 1.77$ eV) after vapor annealing with CHCl_3 at 35 °C. This observation points to improved polymer backbone ring coplanarity in the film versus in solution. For **PolyTe-cumenyl** (Figure 2.15, bottom), the λ_{max} shifts from 606

nm in THF to 631 nm as a film, but CHCl_3 vapor annealing did not have a pronounced effect. However, one sees a substantial tailing of the absorption profile of **PolyTe-cumenyl** in the solid state with an estimated E_g of 1.30 eV, compared to an E_g of 1.72 eV in solution.

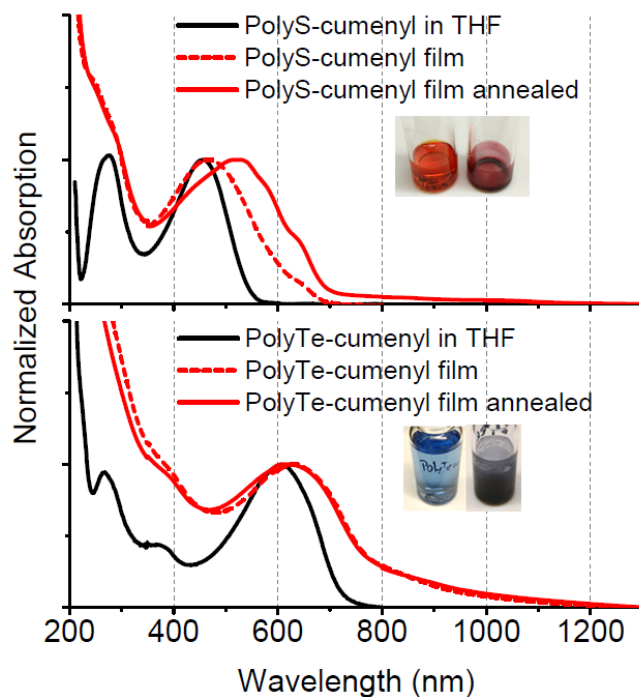


Figure 2.15. UV-Vis spectra and photos of **PolyS-cumenyl** (top) and **PolyTe-cumenyl** (bottom) normalized at the most red-shifted absorption maxima. Films were drop-cast from CHCl_3 and solvent vapor annealed with CHCl_3 (at 35 °C).

As the absorption onset for **PolyTe-cumenyl** can be difficult to visualize, the fitting protocol involved is outlined below in Figure 2.16. The intersection of linear fits (red dashed lines) at the initial absorption increase (<1000 nm) and at long wavelengths (>1100 nm) was used to determine the optical HOMO-LUMO gap (956 nm; $E_g = 1.30$

eV). To account for the possibility of light-scattering effects at long wavelengths, a much more conservative onset was also determined by fitting a Gaussian function to the main peak and determining the intersection of a linear fit (black dashed line) with the wavelength axis (826 nm; $E_g = 1.50$ eV).

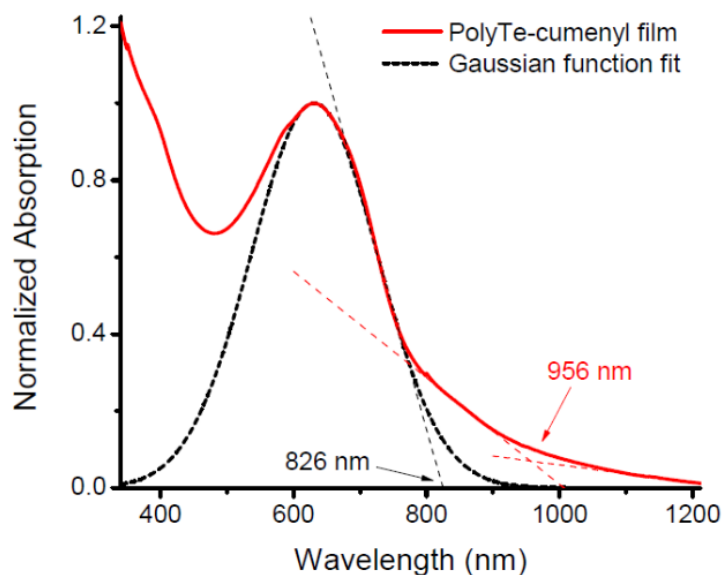


Figure 2.16. Determination of the onset of absorption for a film of **PolyTe-cumenyl**. The Gaussian function is centered at 631 nm and has root mean square width of 95 nm.

Considering the E_g of 1.3 eV, **PolyTe-cumenyl** has a film HOMO-LUMO gap that is smaller than poly(3-hexyltellurophene) ($E_g = 1.4$ eV).^{3a} This observation is consistent with **PolyS-cumenyl** which has an E_g of 1.77 eV, smaller than poly(3-hexylthiophene) (1.9 eV), showing that the presence of an aryl side group can help induce planarity in the solid state, presumably via enhanced π - π stacking. Attempts to

verify crystallinity by powder XRD were hindered by low signal intensity (Section 2.4.8)

Cyclic voltammograms (CV) of films of **PolyTe-cumenyl** and **PolyS-cumenyl** are shown in Figure 2.17. **PolyTe-cumenyl** shows two redox pairs at 0.3 and 2.0 V (*vs.* Fc/Fc⁺). From their onset of oxidation and reduction, (-0.05 and -1.60 V, respectively), an E_g value of 1.55 eV was obtained;²¹ this value is lower than the corresponding E_g derived for **PolyS-cumenyl** through CV (1.94 eV). Additionally, the redox onsets of **PolyTe-cumenyl** indicate a HOMO that is 0.20 eV higher and a LUMO that is 0.19 eV lower in comparison to **PolyS-cumenyl**.^{3a,21a} The larger value of E_g obtained by CV compared to UV-Vis is a common observation for polychalcogenophenes.^{21b} As a final point, polymer degradation was noted upon repeated redox cycling (Figure 2.18), likely due to the formation of reactive radicals.^{3a}

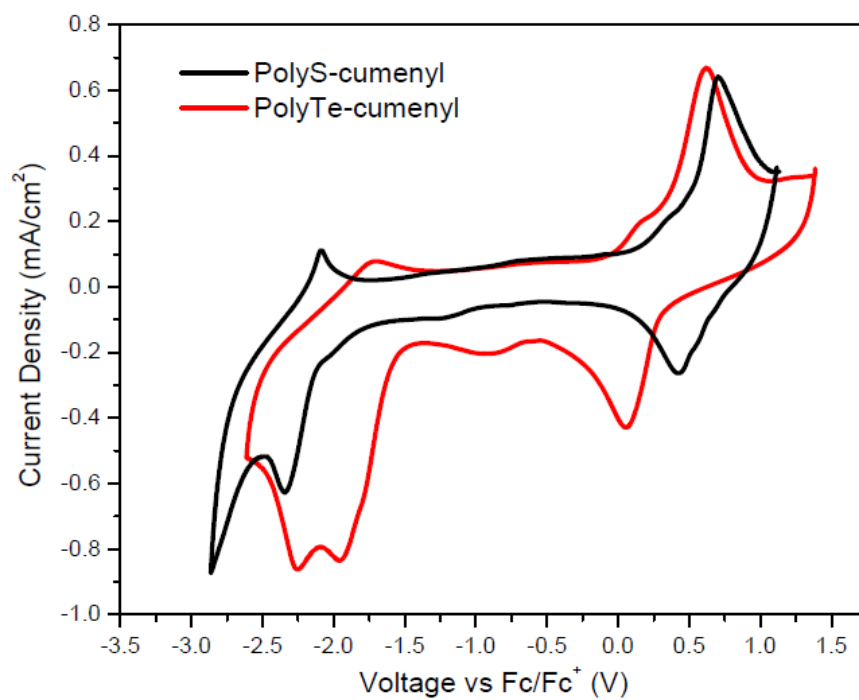


Figure 2.17. Cyclic voltammogram (scan rate = 100 mV/s) of **PolyTe-cumenyl** and **PolyS-cumenyl** annealed films on ITO. Onset of oxidation at positive potentials: **PolyTe-cumenyl**: -0.05 V; **PolyS-cumenyl**: 0.15 V. Onset of reduction at negative potentials: **PolyTe-cumenyl**: -1.60 V; **PolyS-cumenyl**: -1.79 V.

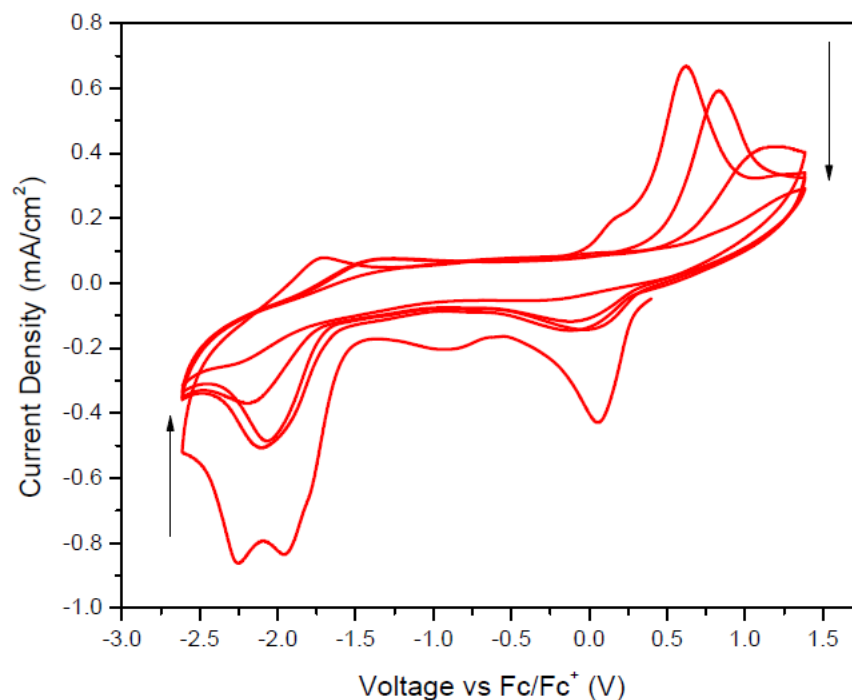


Figure 2.18. Cyclic voltammogram of **PolyTe-cumenyl** (scan rate = 100 mV/s) over different cycles. Arrows show the direction of current intensity change.

2.3 Conclusions

In conclusion, readily available pinacolboronate (BPin)-substituted tellurophenes were used for the synthesis of new tellurophene oligomers and polymers. The effect of the cycloalkyl substituents in **Oligo-Te5** and **Oligo-Te6** was examined by computations and experiment, revealing that the less hindered 5-membered side groups in **Oligo-Te5** yields a substantially more planar backbone and a large reduction in E_g . The first poly(3-aryltellurophene) **PolyTe-cumenyl** was also synthesized, showing a high degree of regioregularity (94%) and a small E_g (1.30 eV) corresponding to an onset of absorption at *ca.* 1000 nm. The related 3-arylated polythiophene

PolyS-cumenyl also yields a smaller E_g when compared to the ubiquitous poly(3-alkylthiophene), thus chalcogenophene-bound aryl groups can yield advantageous optoelectronic properties in the solid state. The polymer design concepts introduced herein should be of great value to those seeking new optoelectronic materials with thermal stability and narrow optical band gaps,²² and could ultimately lead to materials with increased exciton diffusion length and hole mobilities.

2.4 Experimental Section

2.4.1 General Information, Materials and Instrumentation

Unless specified, all reactions were performed under inert atmosphere of N_2 by using Schlenk techniques or a glovebox (MBraun) with dry and degassed solvents from a Grubbs-type solvent system (manufactured by Innovative Technology Inc.) Microwave reactions were performed on a Biotage Initiator reactor. DMF was dried over 4 Å molecular sieves and degassed via three freeze-pump-thaw cycles. The compounds 4-isopropylphenylboronic acid,²³ $\text{PinBC}\equiv\text{C}(\text{CH}_2)_4\text{C}\equiv\text{CBPin}$,²⁴ $\text{PinBC}\equiv\text{C}(\text{CH}_2)_3\text{C}\equiv\text{CBPin}$,²⁴ $\text{PinBC}\equiv\text{CBPin}$,²⁵ $\text{bipy}\cdot\text{TeCl}_2$,²⁶ and the tellurophenes **B-Te-5-B**,⁵ **B-Te-6-B**,^{11a} **4BTe**^{11a} and **BTe**^{11a} (see Schemes 2.2 and 2.3 for the molecular structures) were synthesized according to literature procedures. N-Iodosuccinimide (NIS) and $\text{Pd}(\text{OAc})_2$ (Oakwood Chemical), $\text{Ni}(\text{dppp})\text{Cl}_2$, $\text{Ni}(\text{dppe})\text{Cl}_2$, and $\text{Pd}(\text{PPh}_3)_4$ (Strem Chemicals), 2,2'-bipyridine (GFS Organic Chemicals), and 1-bromo-4-isopropylbenzene (Matrix Scientific) were used as received. All other chemicals were purchased from Sigma-Aldrich and used as

received. Solutions of $^i\text{PrMgCl}\cdot\text{LiCl}$ used for GRIM polymerization had their concentration determined beforehand by ^1H NMR spectrometry using 1,5-cyclooctadiene (COD) as an internal standard or via titration with a solution of I_2 .^{27,28}

^1H and $^{13}\text{C}\{^1\text{H}\}$ NMR spectra were collected on Varian Inova 400, 500 or 700 MHz spectrometers and referenced externally to SiMe_4 . Melting points were measured using a MelTemp apparatus and are reported without correction. Thermogravimetric analysis (TGA) and differential scanning calorimetry (DSC) were performed under N_2 atmosphere on a PerkinElmer Pyris 1 instrument. UV-Vis spectra were collected on a Varian Cary 300 Scan spectrometer. Gel permeation chromatography (GPC) was performed with THF (flow rate = 0.5 mL/min) using either absolute calibration with right- and low-angle light-scattering detectors plus a refractive index detector (GPC 270 Max dual detector + Viscotek VE 3580) with a 99 kDa polystyrene standard (Malvern), or conventional calibration relative to Agilent “EasiVial” polystyrene standards (using a Viscotek VE 3580 refractive index detector), both with three Viscotek I-MBMMW-3078 columns and a Viscotek VE 2001 autosampler. The GPC analysis was accomplished via the OmniSEC 4.6 software package. Single crystal X-ray crystallography, elemental analyses and mass spectrometry (MALDI and EI-MS) were performed by the X-Ray Crystallography Laboratory, Analytical and Instrumentation Laboratory and by the Mass Spectrometry Facility, respectively, at the University of Alberta. For MALDI-MS, *trans*-2-[3-(4-*tert*-butylphenyl)-2-methyl-2-propenyldene]malononitrile (DCTB) was used as a matrix.

Cyclic voltammetry (CV) was performed on a CHI 660E electrochemical workstation (CH Instruments, TX, USA). The three-electrode system was assembled and tested in an Ar-filled glovebox. ITO coated glass (20 nm thick ITO, 8-10 Ω /sq, Aldrich) was used as the working electrode. Ag wire (99.9 %, Aldrich) and Pt wire (99.9 %, BASi) were used as the pseudoreference and counter electrode, respectively. The electrolyte consisted of a 1.0 M solution of tetrabutylammonium hexafluorophosphate (n Bu₄NPF₆, >99.0 %) in degassed acetonitrile, and was dried over 3 Å molecular sieves prior to use. Ferrocene (98 %) was used as internal standard. The electrochemical cell consisted of a Teflon tube pressed onto an ITO substrate, which was coated with the polymer of interest. A Viton o-ring was used to provide the hermetic seal between the Teflon cell body and the working electrode. The voltage of the working electrode was scanned at 100 mV/s. Films of **PolyTe-cumenyl** and **PolyS-cumenyl** for CV measurements were drop-cast from 5 mg/mL CHCl₃ solutions followed by one hour of exposure to CHCl₃ vapor (at 35 °C) for annealing, and subsequently dried under ambient conditions overnight. The same annealing procedure was applied before UV-Vis and powder XRD analysis of these samples.

Optical HOMO-LUMO gaps (E_g) were extracted from UV-Vis spectra by calculating the energy associated with the onset of absorption. The onset of absorption for solutions of oligomer mixtures and their films are presented in Figure 2.44. For the cumenyl-substituted polymers in solution, the onset values are presented in Figure 2.46 while values for films (Figure 2.15) are: **PolyS-cumenyl**: 688 nm (as cast) and 698 nm (annealed); **PolyTe-cumenyl**: 956 nm (as cast or annealed – Figure 2.16). To extract

E_g values from cyclic voltammetry, the difference between the onset of oxidation in more positive potentials and the onset of reduction in more negative potentials was calculated. The CV onset values are shown in Figure 2.17.

2.4.2 Synthetic Procedures

Synthesis of 1,3-diiodo-4,5,6,7-tetrahydro-benzo[c]tellurophene (I-Te-6-I): In the absence of light, **B-Te-6-B** (0.4128 g, 0.8250 mmol) and N-iodosuccinimide (0.459 g, 2.04 mmol) were placed in a Schlenk flask and 6 mL of DMF was added. The flask was then wrapped in aluminum foil and the slurry heated to 40 °C for 16 hrs. After cooling to room temperature, 5 mL of distilled water was then added to the mixture, creating a light-yellow slurry that was then added to 60 mL of saturated $\text{Na}_2\text{S}_2\text{O}_3$ (aq). The product was extracted with two 100 mL portions of Et_2O and the combined organic fraction was washed twice with 100 mL of distilled water, once with 100 mL of brine, dried over MgSO_4 , and filtered. Removal of the volatiles from the filtrate *in vacuo* gave the crude **I-Te-6-I** as a brown solid. The product was then washed with three 10 mL portions of MeOH and column chromatography (silica gel, hexanes) yielded yellow, needle-like crystals (0.126 g, 31 %). Single crystals for X-ray crystallography were grown by preparing a saturated solution in hexanes and cooling it down to -30 °C. ^1H NMR (500 MHz, CDCl_3): δ 2.45-2.50 (m, 4H, I-C=CCH₂CH₂), 1.60-1.67 (m, 4H, I-C=CCH₂CH₂). $^{13}\text{C}\{^1\text{H}\}$ NMR (126 MHz, CDCl_3): δ 151.3 (I-C=C), 71.1 (I-C), 34.9 (C=CCH₂CH₂), 23.4 (C=CCH₂CH₂). HR-MS (EI) ($\text{C}_8\text{H}_8\text{I}_2\text{Te}$): m/z calcd. for $\text{C}_8\text{H}_8\text{I}_2^{130}\text{Te}$ 487.77767; found 487.77777 ($\Delta\text{ppm} = 0.2$). Anal. Calcd. for $\text{C}_8\text{H}_8\text{I}_2\text{Te}$: C

19.79, H 1.66; Found C 19.77, H 1.76. Mp: 107-108 °C. UV-Vis (in THF): $\lambda_{\text{max}} = 295$ nm, $\epsilon = 7.39 \times 10^3 \text{ L mol}^{-1} \text{ cm}^{-1}$.

Synthesis of 1,3-diiodo-4,5,6,7-tetrahydro-cyclopenta[c]-tellurophene (I-Te-5-I):

In the absence of light, **B-Te-5-B** (0.3909 g, 0.8288 mmol) and NIS (0.532 g, 2.37 mmol) were loaded into a Schlenk flask and 10 mL of DMF was added. The flask was then wrapped in aluminum foil and the slurry heated to 40 °C for 16 hrs. After cooling to room temperature, 10 mL of distilled water was then added, creating a light-yellow slurry that was then added to 100 mL of saturated $\text{Na}_2\text{S}_2\text{O}_3$ (aq). The product was extracted with two 100 mL portions of CH_2Cl_2 and the combined organic fraction was washed twice with 200 mL portions of distilled water, once with 200 mL of brine, dried over MgSO_4 , and filtered. The volatiles were removed from the filtrate *in vacuo* to afford the crude product as a brown solid. Further purification with column chromatography (silica gel, 80:1 hexanes/ CH_2Cl_2) affords **I-Te-5-I** as yellow, needle-like crystals (99 mg, 25 %). Single crystals for X-ray crystallography were grown by preparing a saturated solution in hexanes and cooling it down to -30 °C. ^1H NMR (500 MHz, CDCl_3): δ 2.60 (t, $^3J_{\text{HH}} = 7.0$ Hz, 4H, I-C=CCH₂CH₂), 2.44 (pentet, $^3J_{\text{HH}} = 7.0$ Hz, 2H, I-C=CCH₂CH₂). $^{13}\text{C}\{^1\text{H}\}$ NMR (126 MHz, CDCl_3): δ 163.5 (I-C=C), 58.9 (I-C), 35.4 (C=CCH₂CH₂), 29.0 (C=CCH₂CH₂). HR-MS (EI) ($\text{C}_7\text{H}_6\text{I}_2\text{Te}$): m/z calcd. for $\text{C}_7\text{H}_6\text{I}_2^{130}\text{Te}$ 473.76288; found 473.76215 ($\Delta\text{ppm} = 1.5$). Anal. Calcd. for $\text{C}_7\text{H}_6\text{I}_2\text{Te}$: C 17.83, H 1.28; Found C 17.87, H 1.35. Mp: 130-131 °C. UV-Vis (in THF): $\lambda_{\text{max}} = 293$ nm, $\epsilon = 7.83 \times 10^3 \text{ L mol}^{-1} \text{ cm}^{-1}$.

Synthesis of Oligo-Te6: Ni(COD)₂ (0.1212 g, 0.4404 mmol) was dissolved in 3 mL of toluene to give a yellow solution. 2,2'-Bipyridine (71.3 mg, 0.457 mmol) in 3 mL of toluene was then added to form a deep purple solution. After 2 min of stirring, a solution of **I-Te-6-I** (0.1689 g, 0.3478 mmol) in 9 mL of toluene was added to give a dark brown mixture, which was heated to reflux for 16 hrs. After cooling to room temperature, the mixture was added dropwise to 300 mL of stirring MeOH under ambient conditions to precipitate **Oligo-Te6**, which was collected by suction filtration onto a cellulose thimble; this solid was purified by Soxhlet with MeOH and hexanes washes, followed by Soxhlet extraction with CHCl₃. After drying the CHCl₃ fraction over MgSO₄, the fraction was filtered and the volatiles were removed from the filtrate *in vacuo* to yield **Oligo-Te6** as an orange solid (42 mg, 52 %). ¹H NMR (400 MHz, CDCl₃): δ 2.41-2.67 (br, 4H, C=CCH₂CH₂), 1.64 (br, 4H, C=CCH₂CH₂). UV-Vis (in CHCl₃): λ_{max} = 294 nm, ε (per repeating unit) = 6.66 × 10² L mol⁻¹ cm⁻¹.

Synthesis of Oligo-Te5: Ni(COD)₂ (81.9 mg, 0.289 mmol) was dissolved in 1 mL of toluene to form a yellow solution. A solution of 2,2'-bipyridine (47.9 mg, 0.307 mmol) in 1 mL of toluene was then added to give a deep purple solution. After stirring for 2 min, a solution of **I-Te-5-I** (113.0 mg, 0.2398 mmol) in 3 mL of toluene was added and the resulting dark brown mixture was heated to reflux for 16 hrs. After cooling to room temperature, the mixture was added to 300 mL of stirring MeOH under ambient conditions to precipitate **Oligo-Te5**, which was collected by suction filtration onto a

cellulose thimble; the recovered solid was purified by Soxhlet with MeOH and hexanes washes, followed by Soxhlet extraction with CHCl₃. After drying the CHCl₃ fraction over MgSO₄, the fraction was filtered and the volatiles were removed from the filtrate *in vacuo* to yield **Oligo-Te5** as a dark red solid (28 mg, 49 %). ¹H NMR (500 MHz, CDCl₃): δ 2.04 (br, 4H, C=CCH₂CH₂), 1.68 (br, 2H, C=CCH₂CH₂). UV-Vis (in CHCl₃): λ_{max} = 471 nm, ε (per repeating unit) = 5.98 × 10² L mol⁻¹ cm⁻¹.

Synthesis of 1-iodo-4-isopropylbenzene: This procedure has been adapted from the literature.²⁹ To a solution of 1-bromo-4-isopropylbenzene (6.0 mL, 39 mmol) in 100 mL of THF at -78 °C was added ⁿBuLi (19 mL, 2.5 M solution in hexanes, 48 mmol) dropwise, and the reaction mixture was stirred at -78 °C for 1 hr. A solution of I₂ (11.804 g, 46.507 mmol) in 50 mL of THF was then added dropwise via an addition funnel to form a dark red reaction mixture, which was then stirred for 16 hrs at room temperature. The reaction mixture was quenched by addition of 100 mL of a saturated Na₂S₂O_{3(aq)}. The product was then extracted with 3 × 100 mL of Et₂O, followed by washing of the combined organic layers with 3 × 100 mL of water, and drying of the combined organic fractions over MgSO₄. The mixture was then filtered and the volatiles were removed *in vacuo* to give a yellow oil. Further purification of the product by distillation under vacuum (*ca.* 0.2 mbar, 65 °C) afforded 1-iodo-4-isopropylbenzene as a colorless liquid (8.192 g, 86 %) with NMR data that matched literature values.²⁹

Synthesis of 3-(4-cumenyl)-tellurophene (Te-cumenyl): In a glovebox, Pd(OAc)₂ (2.5 mg, 4.2 mol. %) and XPhos (10.1 mg, 8.0 mol. %) were added to a microwave tube along with 1.5 mL of acetonitrile. The resulting suspension was stirred at room temperature until the color changed from yellow to red, at which point a solution of **BTe** (80.7 mg, 0.264 mmol) and 1-iodo-4-isopropylbenzene (75.5 mg, 0.307 mmol) in 1.5 mL of acetonitrile was added. The vial was then sealed and brought out of the glovebox for the addition of a freeze-pump-thaw degassed solution of 2.0 M K₂CO₃ (aq) (0.26 mL) via syringe through the cap. Heating under microwave irradiation at 100 °C for 20 min, followed by cooling of the mixture to room temperature, filtration of the reaction mixture through a short (*ca.* 1 cm) plug of diatomaceous earth, and solvent removal from the filtrate *in vacuo* afforded the crude product. Purification by column chromatography (silica gel, 25:1 hexanes/CH₂Cl₂; R_f = 0.45) yields **Te-cumenyl** as a light yellow solid (56 mg, 71 %). Single crystals for X-ray crystallography were grown by slow diffusion of a hexanes layer on top of a saturated CH₂Cl₂ solution of the product. Unreacted **BTe** (28.0 mg) could then be recovered by flushing the residual sample in the column with CH₂Cl₂ or CHCl₃. **Data for Te-cumenyl:** ¹H NMR (400 MHz, CDCl₃): δ 8.94 (dd, ³J_{HH} = 6.6 Hz, ⁴J_{HH} 1.9 Hz, 1H, TeCH=CH), 8.91 (t, ⁴J_{HH} = 1.8 Hz, 1H, Te-CH=C), 8.27 (dd, ³J_{HH} = 6.6 Hz, ⁴J_{HH} = 1.6 Hz, 1H, Te-CH=CH), 7.54 (d, ³J_{HH} = 8.4 Hz, 2H, *o*-ArH), 7.28 (d, ³J_{HH} = 8.0 Hz, 2H, *m*-ArH), 2.95 (sept, ³J_{HH} = 6.9 Hz, 1H, CH(CH₃)₂), 1.30 (d, ³J_{HH} = 6.9 Hz, 6H, CH(CH₃)₂). ¹³C {¹H} NMR (126 MHz, CDCl₃): δ 152.3 (ArC), 147.9 (ArC), 138.6 (ArC), 137.5 (ArC), 127.1 (ArC), 126.8 (ArC), 125.1 (ArC), 120.0 (ArC), 34.0 (CH(CH₃)₂), 24.1 (CH(CH₃)₂).

HR-MS (EI) ($C_{13}H_{14}Te$): m/z calcd. for $C_{13}H_{14}^{130}Te$ 300.01578; found 300.01637 ($\Delta ppm = 2.0$). Anal. Calcd. for $C_{13}H_{14}Te$: C 52.42, H 4.74; Found C 52.94, H 4.96. Mp: 60-62 °C.

Synthesis of 2,5-diiodo-3-(4-cumenyl)-tellurophene (I-Te-cumenyl-I): In the absence of light, **Te-cumenyl** (0.260 g, 0.873 mmol) and N-iodosuccinimide (0.8227 g, 3.657 mmol) were combined in a Schlenk flask and 27 mL of DMF was added. The flask was then wrapped in aluminum foil and the mixture stirred at 70 °C for 16 hrs. The reaction mixture was then quenched by the addition of 100 mL of saturated $Na_2S_2O_3$ (aq), to give a light-yellow slurry. The product was extracted with two 100 mL portions of CH_2Cl_2 , and the volume of the combined extracts was reduced to 75 mL *in vacuo*. The resulting solution was washed four times with 100 mL portions of distilled water and once again with 100 mL of brine. After drying the combined organic phases over $MgSO_4$, the mixture was filtered and the volatiles were removed from the filtrate *in vacuo* to give crude **I-Te-cumenyl-I** (0.424 g, 88 %) as an oil. Although mono-iodinated tellurophene impurities elute very close to the product, purification by repeating three column chromatographic separations in a row (silica gel, hexanes) to remove trace quantities (*ca.* 4-8 %) of the mono-iodinated product (**H-Te-cumenyl-I**) from the crude product to give analytically pure **I-Te-cumenyl-I** as an orange oil (0.274 g, 57 %). 1H NMR (400 MHz, $CDCl_3$): δ 7.93 (s, 1H, Te-C(I)=CH), 7.25-7.33 (m, 4H, ArH), 2.96 (sept, $^3J_{HH} = 7.0$ Hz, 1H, CH(CH₃)₂), 1.30 (d, $^3J_{HH} = 6.9$ Hz, 6H, CH(CH₃)₂). $^{13}C\{^1H\}$ NMR (101 MHz, $CDCl_3$): δ 157.8 (ArC), 149.8 (ArC), 148.7 (ArC), 136.3

(ArC), 129.0 (ArC), 126.4 (ArC), 70.7 (C-I), 70.0 (C-I), 34.1 (CH(CH₃)₂), 24.1 (CH(CH₃)₂). HR-MS (EI) (C₁₃H₁₂I₂Te): m/z calcd. for C₁₃H₁₂¹³⁰TeI₂ 551.80908; found 551.80898 (Δ ppm = 0.2). Anal. Calcd. for C₁₃H₁₂I₂Te: C 28.41, H 2.20; Found C 28.56, H 2.26. UV-Vis (in THF): λ_{max} = 242 nm, ϵ = 2.35×10^4 L mol⁻¹ cm⁻¹; λ_{max} = 299 nm, ϵ = 2.01×10^4 L mol⁻¹ cm⁻¹.

Synthesis of 2-iodo-3-(4-cumenyl)-tellurophene (H-Te-cumenyl-I): In the absence of light, **Te-cumenyl** (0.0551 g, 0.1850 mmol) and N-iodosuccinimide (0.0874 g, 0.3885 mmol) were combined in a Schlenk flask and 4 mL of DMF was added. The flask was then wrapped in aluminum foil and the mixture stirred at 40 °C for 14 hrs. The reaction mixture was then allowed to cool to room temperature and quenched by the addition of 80 mL of saturated Na₂S₂O₃ (aq), to give a light-yellow slurry. The product was extracted with two 100 mL portions of CH₂Cl₂ and the combined organic fractions were washed twice with 130 mL portions of brine. After drying the combined organic phases over MgSO₄, the mixture was filtered and the volatiles were removed from the filtrate *in vacuo* to give crude **H-Te-cumenyl-I** as a yellow oil (0.080 g, 87 % of **H-Tecumenyl-I** and 13% of **I-Te-cumenyl-I**, as determined by ¹H NMR spectroscopy). **Data for H-Te-cumenyl-I:** ¹H NMR (700 MHz, CDCl₃): δ 9.02 (d, ³J_{HH} = 7.1 Hz, 1H, Te-CH=CH), 7.63 (d, ³J_{HH} = 7.7 Hz, 1H, TeCH=CH), 7.28-7.64 (m, 4H, ArH), 2.96 (sept, ³J_{HH} = 6.3 Hz, 1H, CH(CH₃)₂), 1.29 (d, ³J_{HH} = 7.0 Hz, 6H, CH(CH₃)₂). ¹³C {¹H} NMR (176 MHz, CDCl₃): δ 156.6 (ArC), 148.3 (ArC), 140.2 (ArC), 137.8 (ArC), 130.2 (ArC), 129.0 (ArC), 126.4 (ArC), 66.3 (C-I), 34.1 (CH(CH₃)₂), 24.1

(CH(CH₃)₂). HR-MS (EI) (C₁₃H₁₃I¹³⁰Te): m/z calcd. for C₁₃H₁₃I¹³⁰Te 425.91245; found 425.91290 (Δ ppm = 1.1).

Synthesis of 3-(4-cumenyl)-thiophene (S-cumenyl): This procedure was adapted from the literature.³⁰ Pd(PPh₃)₄ (0.3522 g, 0.3048 mmol) was loaded into a Schlenk flask and 20 mL of N₂-sparged 1,2-dimethoxyethane was added, followed by 3-bromothiophene (1.00 mL, 10.7 mmol) and freeze-pump-thaw degassed 2.0 M K₂CO₃ (aq) (13 mL). The mixture was stirred at room temperature for 10 min and then a solution of 4-isopropylphenylboronic acid (2.137 g, 13.03 mmol) in 20 mL of N₂-sparged anhydrous EtOH was added. The mixture was heated to reflux for 1 hr and then allowed to cool to room temperature with additional stirring for 16 hrs. The mixture was filtered through a *ca.* 1 cm plug of diatomaceous earth, followed by solvent removal from the filtrate under vacuum. Column chromatography (silica gel, hexanes) afforded **S-cumenyl** as a white solid (2.074 g, 97 %). ¹H NMR (500 MHz, CDCl₃) δ 7.53 (d, ³J_{HH} = 8.3 Hz, 2H, *o*-ArH), 7.35-7.45 (m, 3H, ArH thienyl), 7.21-7.30 (d, ³J_{HH} = 8.0 Hz, 2H, *m*-ArH), 2.94 (sept, ³J_{HH} = 6.9 Hz, 1H, CH(CH₃)₂), 1.28 (d, ³J_{HH} = 6.9 Hz, 6H, CH(CH₃)₂). ¹³C{¹H} NMR (126 MHz, CDCl₃): δ 148.0 (ArC), 142.5 (ArC), 133.7 (ArC), 127.0 (ArC), 126.6 (ArC), 126.5 (ArC), 126.1 (ArC), 119.9 (ArC), 34.0 (CH(CH₃)₂), 24.1 (CH(CH₃)₂). HR-MS (EI) (C₁₃H₁₄S): m/z calcd. 202.08162; found 202.08187 (Δ ppm = 1.2). Anal. Calcd. for C₁₃H₁₄S: C 77.18, H 6.98, S 15.85; found C 78.14, H 7.08, S 14.39. Mp: 62-63 °C.

Synthesis of 2,5-diiodo-3-(4-cumenyl)-thiophene (I-S-cumenyl-I): Procedure adapted from the literature.³¹ In the absence of light, N-iodosuccinimide (0.523 g, 2.32 mmol) and **S-cumenyl** (0.196 g, 0.969 mmol) were loaded into a Schlenk flask that was wrapped in aluminum foil. An N₂-sparged mixture of CHCl₃ (5 mL) and AcOH (5 mL) was added and the mixture stirred at room temperature for 16 hrs. Saturated Na₂S₂O_{3(aq)} was added until the mixture turned yellow. The resulting mixture was added to water (20 mL) and extracted with two portions of CH₂Cl₂ (20 mL). The combined organic fractions were washed with distilled water (20 mL) and brine (20 mL), and the dried over MgSO₄. Filtration of the mixture followed by removal of the solvent from the filtrate gave a crude product that was further purified by column chromatography (silica gel, hexanes) to afford **I-S-cumenyl-I** as a light yellow oil (0.360 g, 82 %). ¹H NMR (400 MHz, CDCl₃): δ 7.40 (d, ³J_{HH} = 8.2 Hz, 2H, *o*-ArH), 7.30 (d, ³J_{HH} = 8.2 Hz, 2H, *m*-ArH), 7.10 (s, 1H, S-C(I)=CH), 2.98 (sept, ³J_{HH} = 6.9 Hz, 1H, CH(CH₃)₂), 1.32 (d, ³J_{HH} = 7.0 Hz, 6H, CH(CH₃)₂). ¹³C{¹H} NMR (101 MHz, CDCl₃): δ 148.9 (ArC), 148.9 (ArC), 138.8 (ArC), 132.8 (ArC), 128.7 (ArC), 126.6 (ArC), 77.0 (C-I), 75.9 (C-I), 34.0 (CH(CH₃)₂), 24.1 (CH(CH₃)₂). HR-MS (EI) (C₁₃H₁₂SI₂): m/z calcd. 453.87494; found 453.87516 (Δppm = 0.5). Anal. Calcd. for C₁₃H₁₂SI₂: C 34.38, H 2.66, S 7.06; found C 35.22, H 2.68, S 7.14. UV-Vis (in THF): λ_{max} = 245 nm, ε = 2.97 × 10⁴ L mol⁻¹ cm⁻¹; λ_{max} = 270 nm, ε = 1.34 × 10⁴ L mol⁻¹ cm⁻¹.

Synthesis of poly(3-(4-cumenyl)-thiophene) (PolyS-cumenyl): To a mixture of **I-S-cumenyl-I** (0.3500 g, 0.7707 mmol) and Me-THF (6 mL) cooled to -78 °C was

added dropwise a solution of $i\text{PrMgCl}\cdot\text{LiCl}$ (0.77 mmol; 1.3 M solution in THF). The mixture was stirred at $-78\text{ }^{\circ}\text{C}$ for 1 hr followed by stirring at room temperature for 1 hr. The mixture was then transferred to a Teflon-capped Schlenk flask containing $\text{Ni}(\text{dppp})\text{Cl}_2$ (0.0042 g, 1.0 mol. %) and stirred at $80\text{ }^{\circ}\text{C}$ for 24 hrs. The reaction mixture was quenched by addition of 2.0 mL of 1.2 M $\text{HCl}_{(\text{aq})}$; the resulting mixture was then added dropwise to 300 mL of stirring acetone (cooled to $-30\text{ }^{\circ}\text{C}$) to precipitate the polymer, followed by polymer isolation by suction filtration onto a cellulose thimble. The isolated polymer was then purified by subsequent Soxhlet washings with MeOH and hexanes and recovered by Soxhlet extraction with CHCl_3 ; removal of the solvent from the CHCl_3 extract afforded **PolyS-cumenyl** as a dark purple solid (58.8 mg, 39 %). $^1\text{H NMR}$ (500 MHz, CDCl_3): δ 7.02-7.49 (br, 4H, ArH), 6.67-6.99 (br, 1H, S-C=CH), 2.94 (br sept, $^3J_{\text{HH}} = 7.0\text{ Hz}$, 1H, $\text{CH}(\text{CH}_3)_2$), 1.28 (br d, $^3J_{\text{HH}} = 6.6\text{ Hz}$, 6H, $\text{CH}(\text{CH}_3)_2$). $M_w = 12\text{ kDa}$ (absolute) or 8.5 kDa (relative to polystyrene standards), $\text{PDI} = 1.1$. $T_g = 176\text{ }^{\circ}\text{C}$ (by DSC). UV-Vis (in THF): $\lambda_{\text{max}} = 275\text{ nm}$, ϵ (per repeating unit) = $3.09 \times 10^3\text{ L mol}^{-1}\text{ cm}^{-1}$; $\lambda_{\text{max}} = 455\text{ nm}$, ϵ (per repeating unit) = $3.00 \times 10^3\text{ L mol}^{-1}\text{ cm}^{-1}$.

Synthesis of poly(3-(4-cumenyl)-tellurophene) (PolyTe-cumenyl): To a solution of **I-Tecumenyl-I** (0.1943 g, 0.3535 mmol) in 2.7 mL of Me-THF at $-78\text{ }^{\circ}\text{C}$ was added a solution of $i\text{PrMgCl}\cdot\text{LiCl}$ (0.35 mmol; 1.4 M solution in THF) dropwise. The mixture was stirred at $-78\text{ }^{\circ}\text{C}$ for 1 hr followed by stirring at room temperature for another 1 hr. The mixture was then transferred to a Teflon-capped Schlenk flask containing

Ni(dppp)Cl₂ (0.0019 g, 1.0 mol. %) and the mixture stirred at 80 °C for 24 hrs. The reaction mixture was quenched by addition of 1.0 mL of 1.2 M HCl (aq); the resulting mixture was then added dropwise to 300 mL of stirring acetone (cooled to -30 °C) to precipitate the polymer, followed by polymer isolation by suction filtration onto a cellulose thimble. The collected polymer was then purified by subsequent Soxhlet washings with MeOH and hexanes and recovered by Soxhlet extraction with CHCl₃; removal of the solvent from the CHCl₃ extract afforded **PolyTe-cumenyl** as a dark blue-purple solid (24.0 mg, 23 %). ¹H NMR (500 MHz, CDCl₃) δ 6.81-7.52 (br m, 5H, ArH and Te-C=CH), 2.80-3.07 (br m, 1H, CH(CH₃)₂), 1.28 (br, 6H, CH(CH₃)₂). M_w = 5.8 kDa (relative to polystyrene standards), PDI = 1.1. **PolyTe-cumenyl** absorbs strongly at the wavelength used for light-scattering detection (670 nm), thus molecular weights were determined only with refractive index detectors. If it is assumed that **PolyTe-cumenyl** behaves similarly to **PolyS-cumenyl** in the GPC column, one can multiply its M_w relative to polystyrene by 1.41 (ratio of M_w absolute/M_w relative for **PolyS-cumenyl**) to obtain an estimated absolute M_w of 8.2 kDa. UV-Vis (in THF): λ_{max} = 267 nm, ε (per repeating unit) = 4.53 × 10³ L mol⁻¹ cm⁻¹; λ_{shoulder} = 372 nm; λ_{max} = 607 nm, ε (per repeating unit) = 4.66 × 10³ L mol⁻¹ cm⁻¹.

2.4.2.1. Polymerization Trials using Ni(dppe)Cl₂ as a Pre-catalyst

Synthesis of poly(3-(4-cumenyl)-thiophene) (PolyS-cumenyl) with Ni(dppe)Cl₂ at 80 °C: To a mixture of **I-S-cumenyl-I** (0.1502 g, 0.3307 mmol) and Me-THF (2.6 mL) cooled to -78 °C was added dropwise a solution of ⁱPrMgCl•LiCl (0.33 mmol; 0.56 M

solution in THF). The mixture was stirred at -78 °C for 1 hr followed by stirring at room temperature for 1 hr. The mixture was then transferred to a Teflon-capped Schlenk flask containing Ni(dppe)Cl₂ (0.0018 g, 1.0 mol. %) and stirred at 80 °C for 24 hrs. The reaction mixture was quenched by addition of 1.0 mL of 1.2 M HCl (aq); the resulting mixture was then added dropwise to 300 mL of stirring MeOH (cooled to -30 °C) to precipitate the polymer, followed by isolation by suction filtration onto a cellulose thimble. The isolated polymer was then purified by subsequent Soxhlet washings with MeOH and hexanes and recovered by Soxhlet extraction with CHCl₃; removal of the solvent from the CHCl₃ extract afforded **PolyS-cumenyl** as a dark purple solid (7.2 mg, 11 %). Regioregularity = 88 %, M_w = 6.1 kDa (absolute), PDI = 1.1. Additionally, a large amount of crude orange solid was recovered in the hexanes fraction (40 mg, 60 %, M_w = 13 kDa (absolute), PDI = 1.1) corresponding to polythiophene of lower regioregularity (65 %, as determined by ¹H NMR spectroscopy).

Synthesis of poly(3-(4-cumenyl)-tellurophene) (PolyTe-cumenyl) with Ni(dppe)Cl₂ at 80 °C: To a solution of **I-Te-cumenyl-I** (0.1733 g, 0.3153 mmol) in 2.4 mL of Me-THF at -78 °C was added a solution of ⁱPrMgCl•LiCl (0.35 mmol; 0.56 M solution in THF) dropwise. The mixture was stirred at -78 °C for 1 hr followed by stirring at room temperature for 1 hr. The mixture was then transferred to a Teflon-capped Schlenk flask containing Ni(dppe)Cl₂ (0.0017 g, 1.0 mol. %) and the mixture stirred at 80 °C for 24 hrs. The reaction mixture was quenched by addition of 1.0 mL

of 1.2 M HCl_(aq); the resulting mixture was then added dropwise to 300 mL of stirring MeOH (cooled to -30 °C) to precipitate the polymer, followed by isolation by suction filtration onto a cellulose thimble. The collected polymer was then purified by subsequent Soxhlet washings with MeOH and hexanes and recovered by Soxhlet extraction with CHCl₃; removal of the solvent from the CHCl₃ extract afforded minimal **PolyTe-cumenyl** as a dark purple solid (< 1 mg, 1 %) that could not be characterized by NMR spectroscopy or GPC. Most of the product was recovered in the hexanes fraction (from Soxhlet) as a crude red-purple solid (24 mg, 26 %, M_w = 2.5 kDa (absolute), PDI = 1.5) and red-shifted absorption of $\lambda_{\text{max}} = 495$ nm in THF.

Synthesis of poly(3-(4-cumenyl)-tellurophene) (PolyTe-cumenyl) with Ni(dppe)Cl₂ at 40 °C: To a solution of **I-Te-cumenyl-I** (0.0558 g, 0.1015 mmol) in 0.77 mL of Me-THF at -78 °C was added a solution of ⁱPrMgCl•LiCl (0.10 mmol; 0.56 M solution in THF) dropwise. The mixture was stirred at -78 °C for 1 hr followed by stirring at room temperature for 1 hr. The mixture was then transferred to a Teflon-capped Schlenk flask containing Ni(dppe)Cl₂ (0.0006 g, 1.1 mol. %) and the mixture stirred at 40 °C for 1 day. The reaction mixture was quenched by addition of 1.0 mL of 1.2 M HCl_(aq); the resulting mixture was then added dropwise to 300 mL of stirring MeOH (cooled to -30 °C) to precipitate the polymer, followed by isolation by suction filtration onto a cellulose thimble. The collected polymer was then purified by subsequent Soxhlet washings with MeOH and hexanes and recovered by Soxhlet extraction with CHCl₃; removal of the solvent from the CHCl₃ extract afforded

PolyTe-cumenyl as a dark blue-purple solid (4.0 mg, 13 %). Regioregularity = 73 % (determined by ^1H NMR spectroscopy), $M_w = 2.9$ kDa (relative to polystyrene standards), $M_w = 4.1$ kDa (estimated absolute), PDI = 1.5.

2.4.3 NMR Data

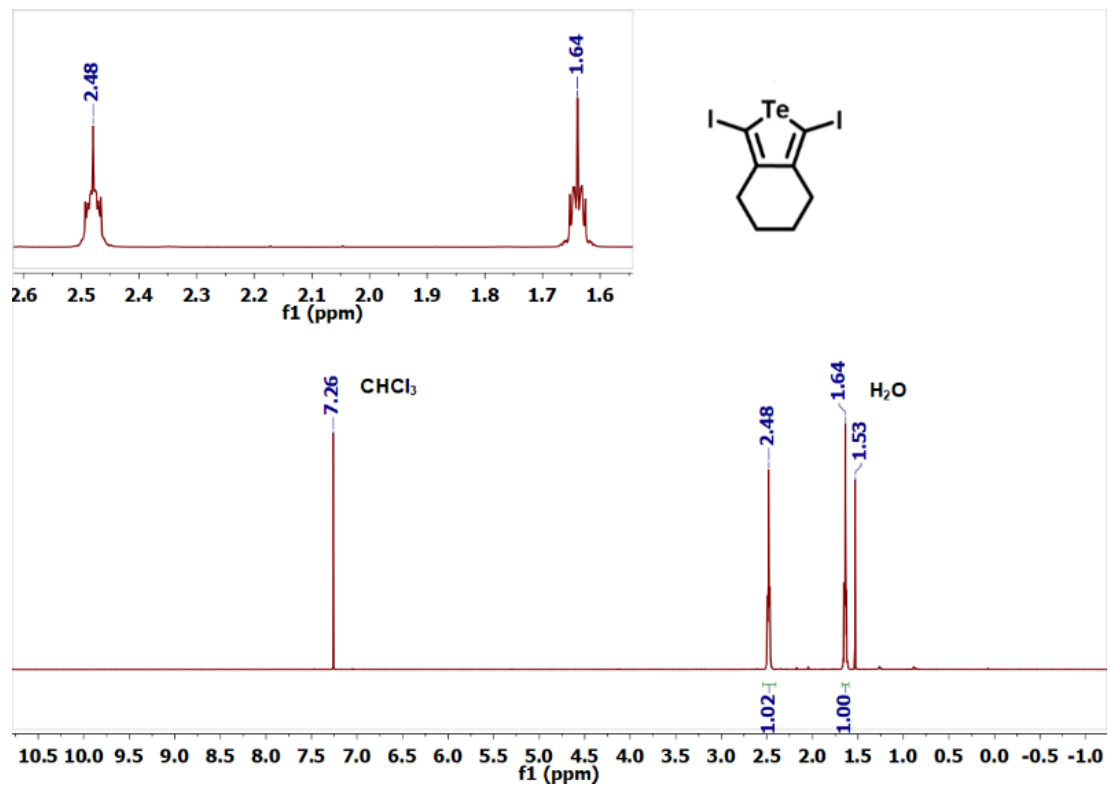


Figure 2.19. ^1H NMR spectrum (500 MHz) of 1,3-diiodo-4,5,6,7-tetrahydrobenzo[*c*]tellurophene (I-Te-6-I) in CDCl_3 .

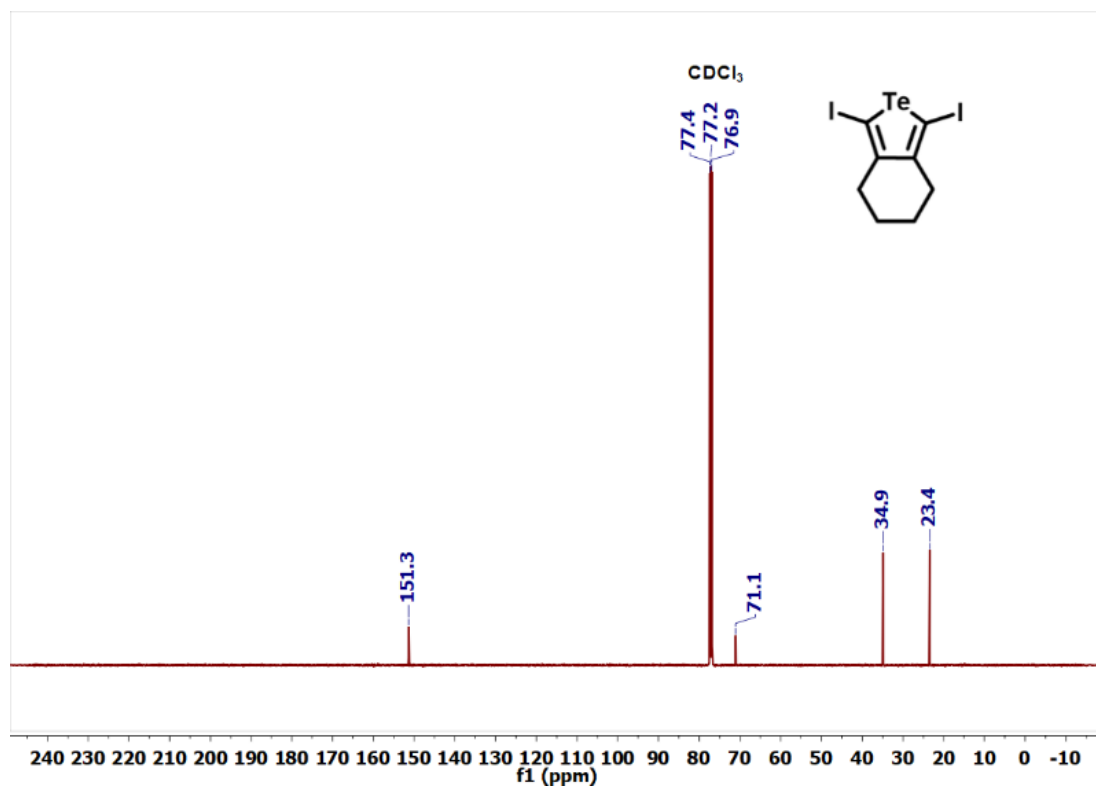


Figure 2.20. $^{13}\text{C}\{^1\text{H}\}$ NMR spectrum (126 MHz) of 1,3-diiodo-4,5,6,7-tetrahydrobenzo[*c*]tellurophene (**I-Te-6-I**) in CDCl_3 .

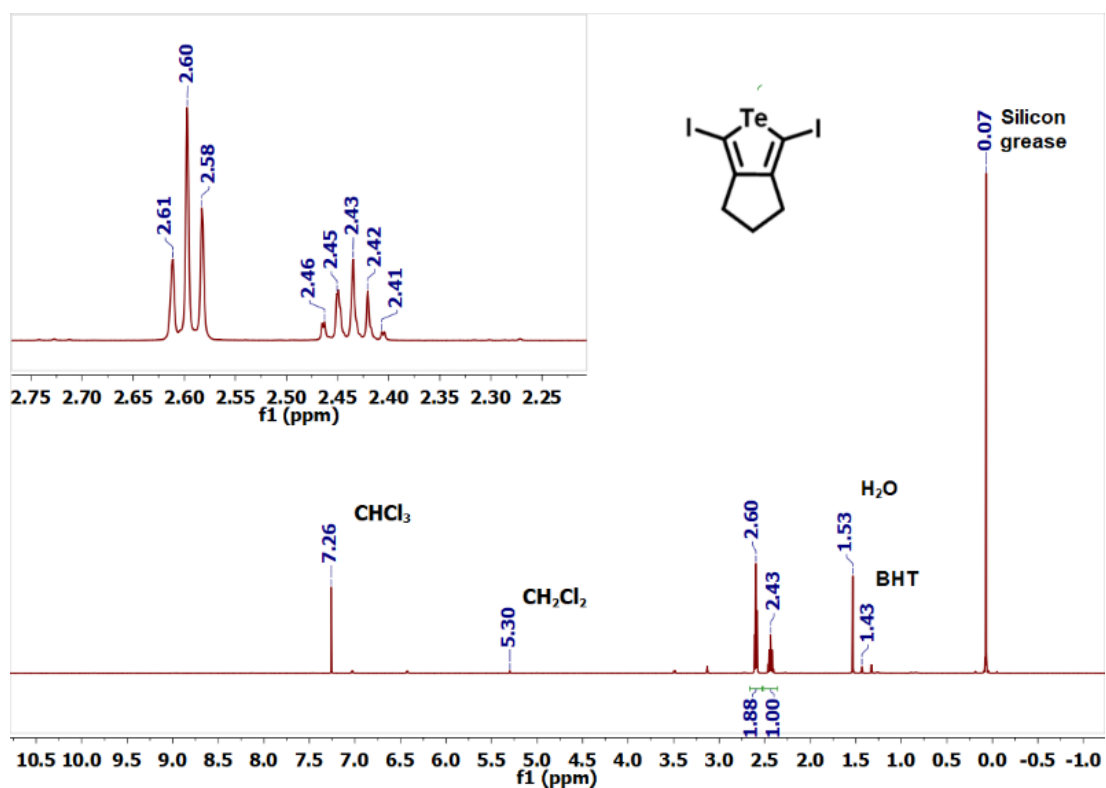


Figure 2.21. ¹H NMR spectrum (500 MHz) of 1,3-diiodo-4,5,6,7-tetrahydro-cyclopenta[*c*]-tellurophene (**I-Te-5-I**) in CDCl₃; BHT = trace butylated hydroxytoluene.

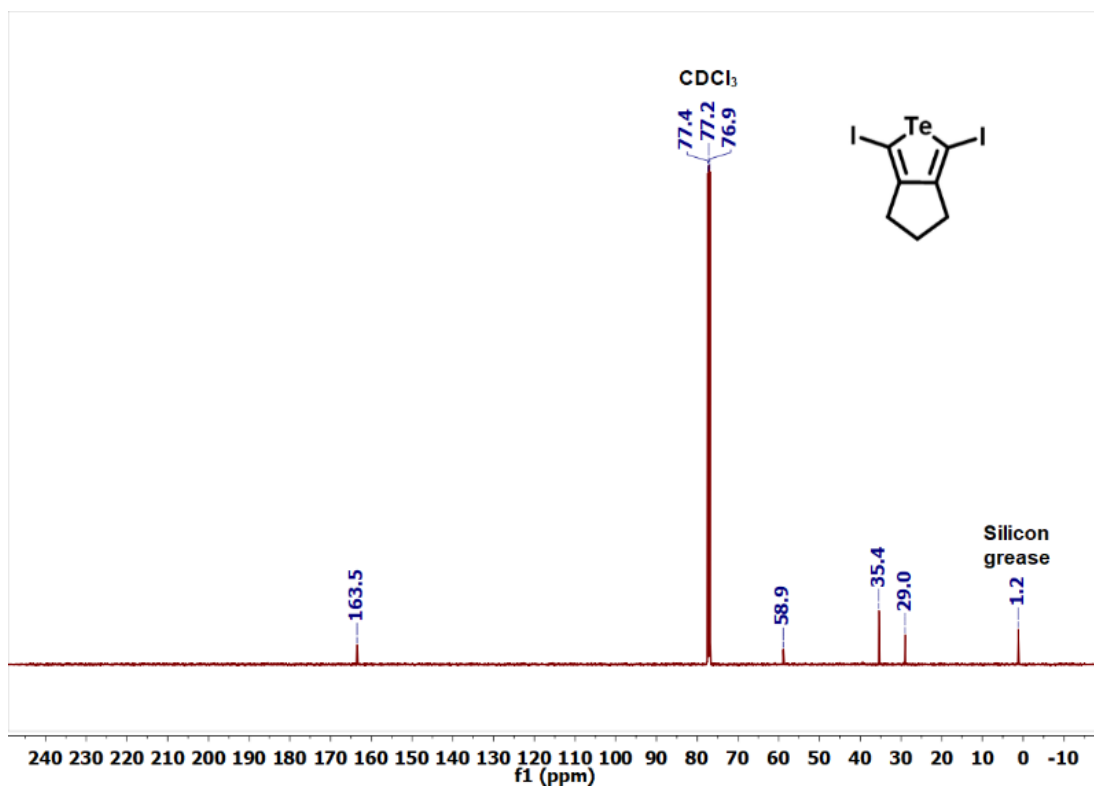


Figure 2.22. $^{13}\text{C}\{^1\text{H}\}$ NMR spectrum (126 MHz) of 1,3-diiodo-4,5,6,7-tetrahydro-cyclopenta[*c*]-tellurophene (**I-Te-5-I**) in CDCl_3 .

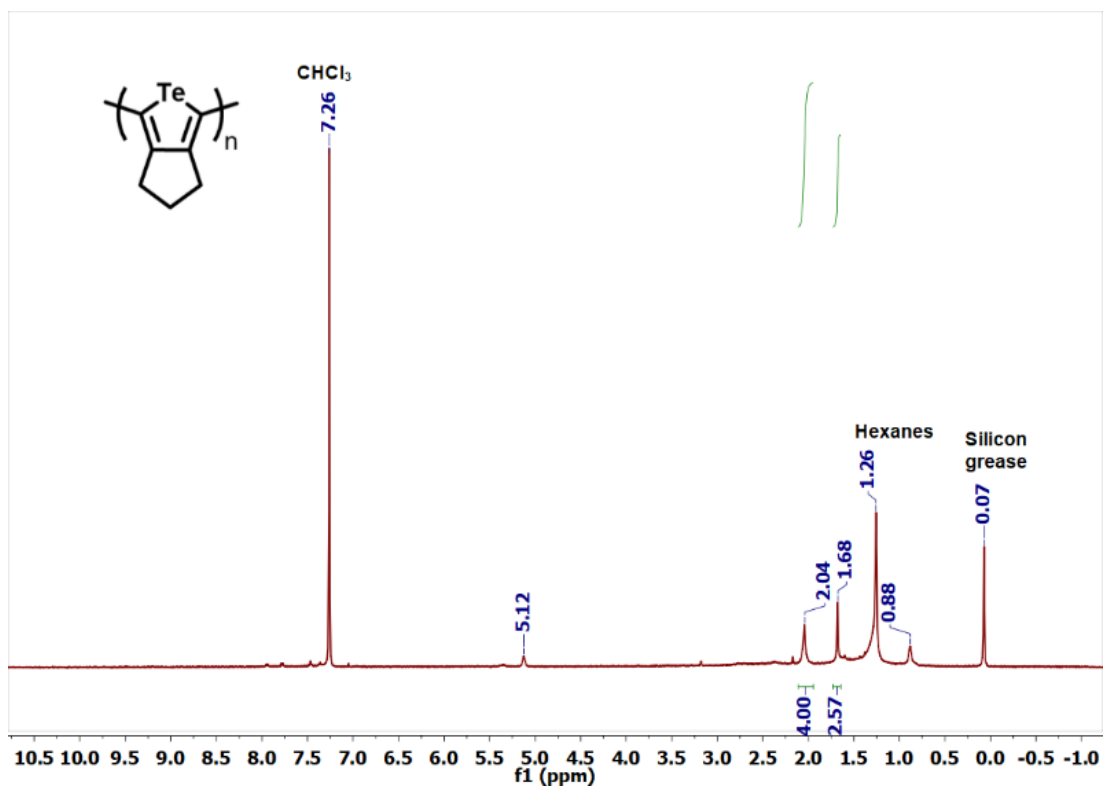


Figure 2.23. ^1H NMR spectrum (500 MHz) of Oligo-Te5 in CDCl_3 .

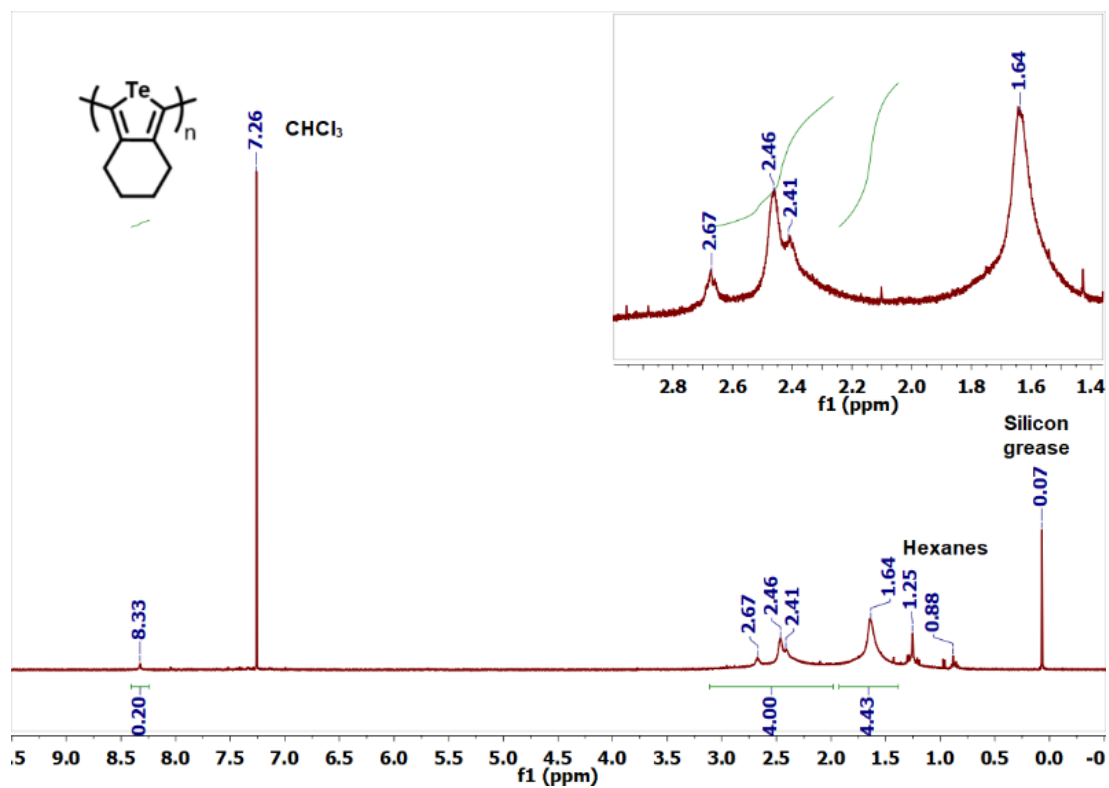


Figure 2.24. ^1H NMR spectrum (400 MHz) of Oligo-Te6 in CDCl_3 .

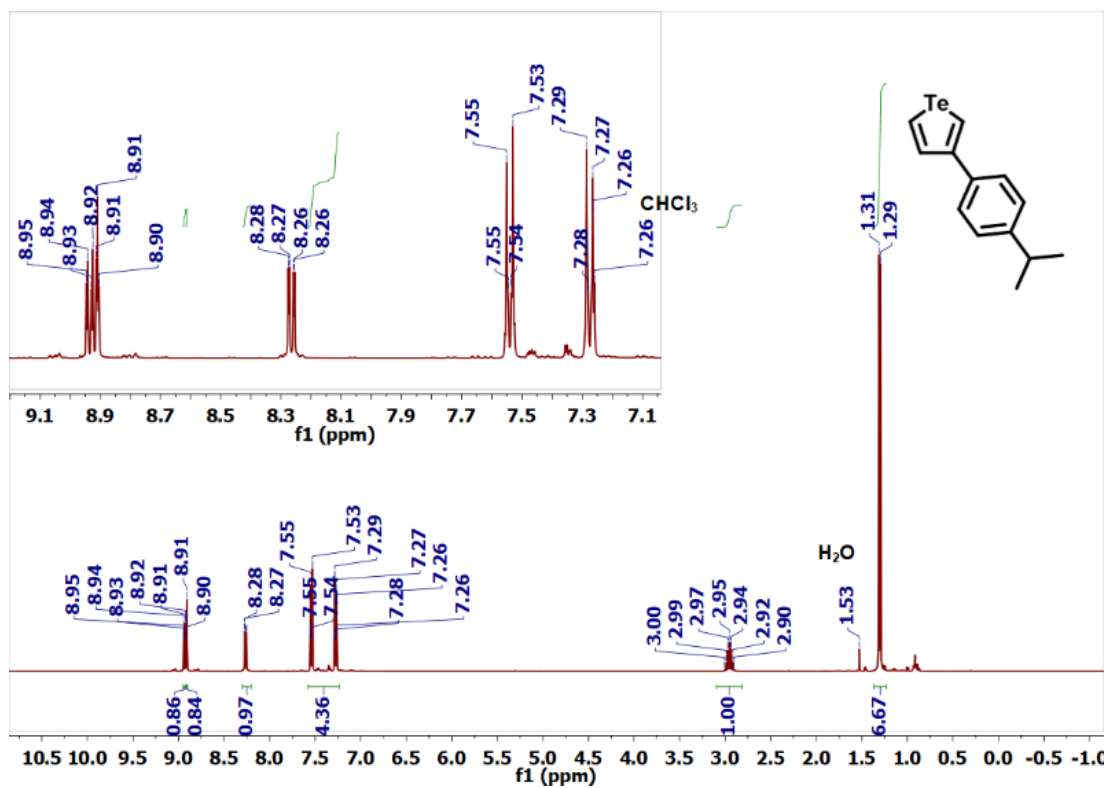


Figure 2.25. ^1H NMR spectrum (400 MHz) of 3-(4-isopropylphenyl)-tellurophene (Te-cumenyl) in CDCl_3 .

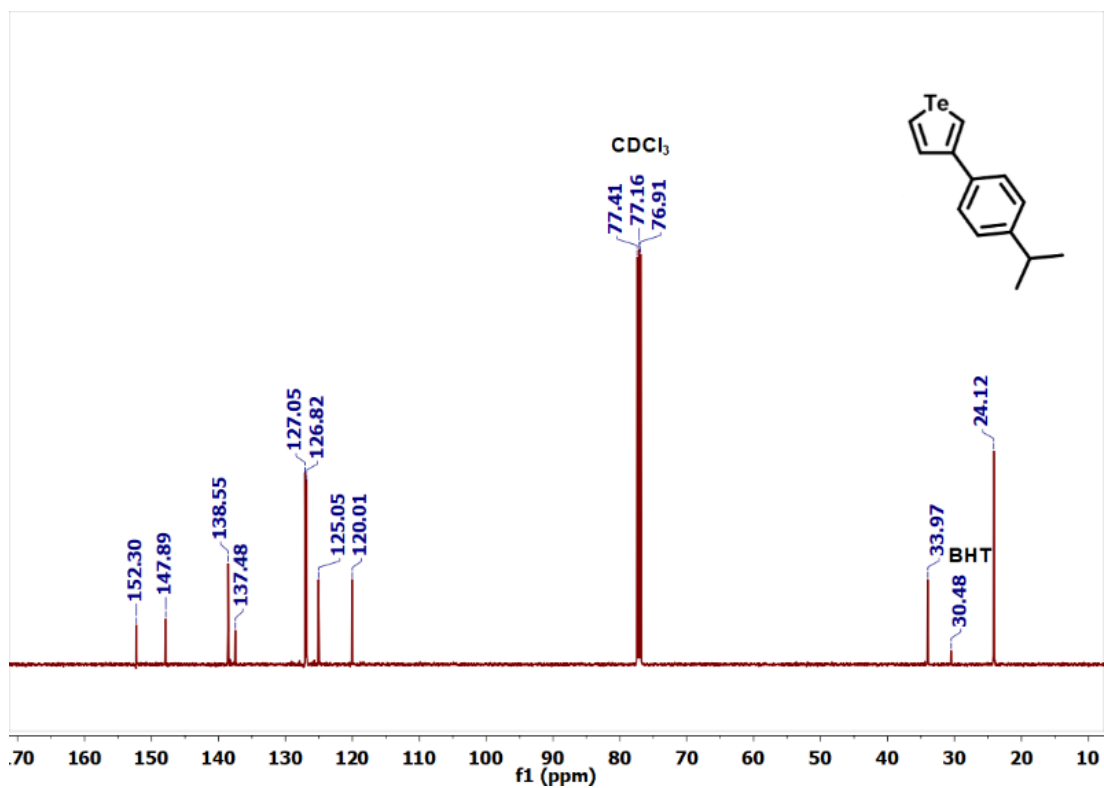


Figure 2.26. $^{13}\text{C}\{^1\text{H}\}$ NMR (126 MHz) of 3-(4-isopropylphenyl)-tellurophene (Te-cumenyl) in CDCl_3 . BHT = butylated hydroxytoluene.

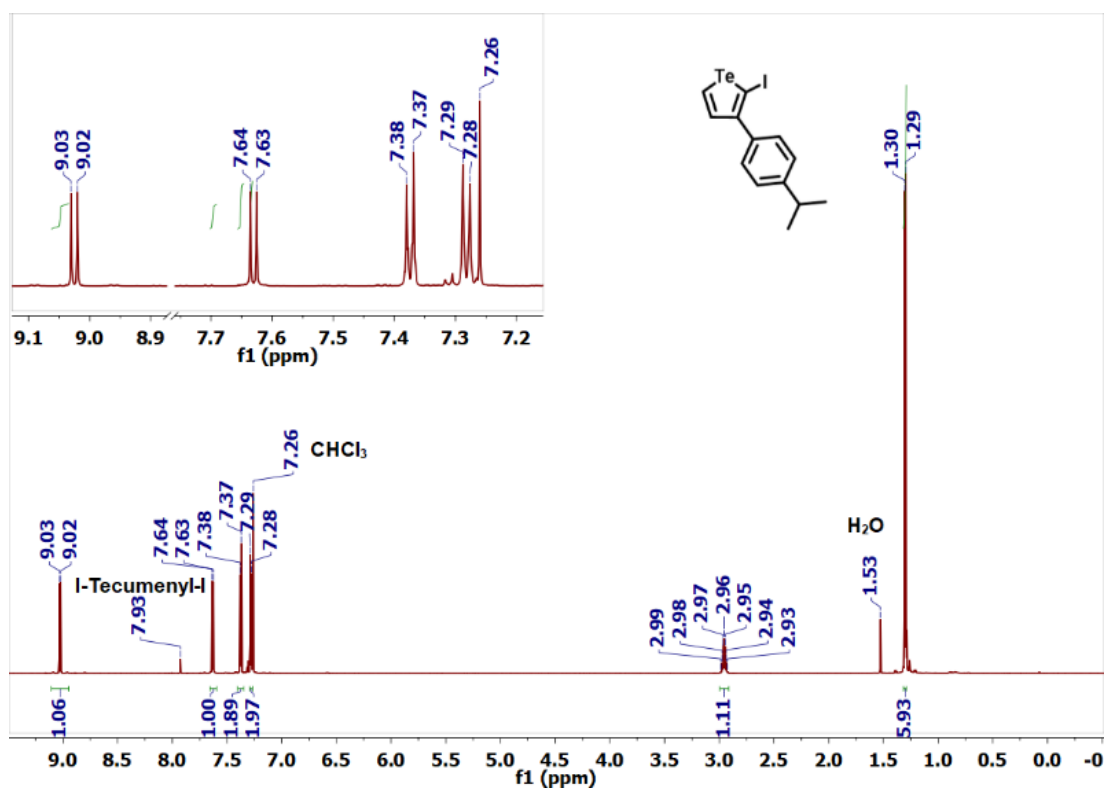


Figure 2.27. ¹H NMR spectrum (700 MHz) of crude 2-iodo-3-(4-isopropylphenyl)-tellurophene (**H-Te-cumenyl-I**) in CDCl₃.

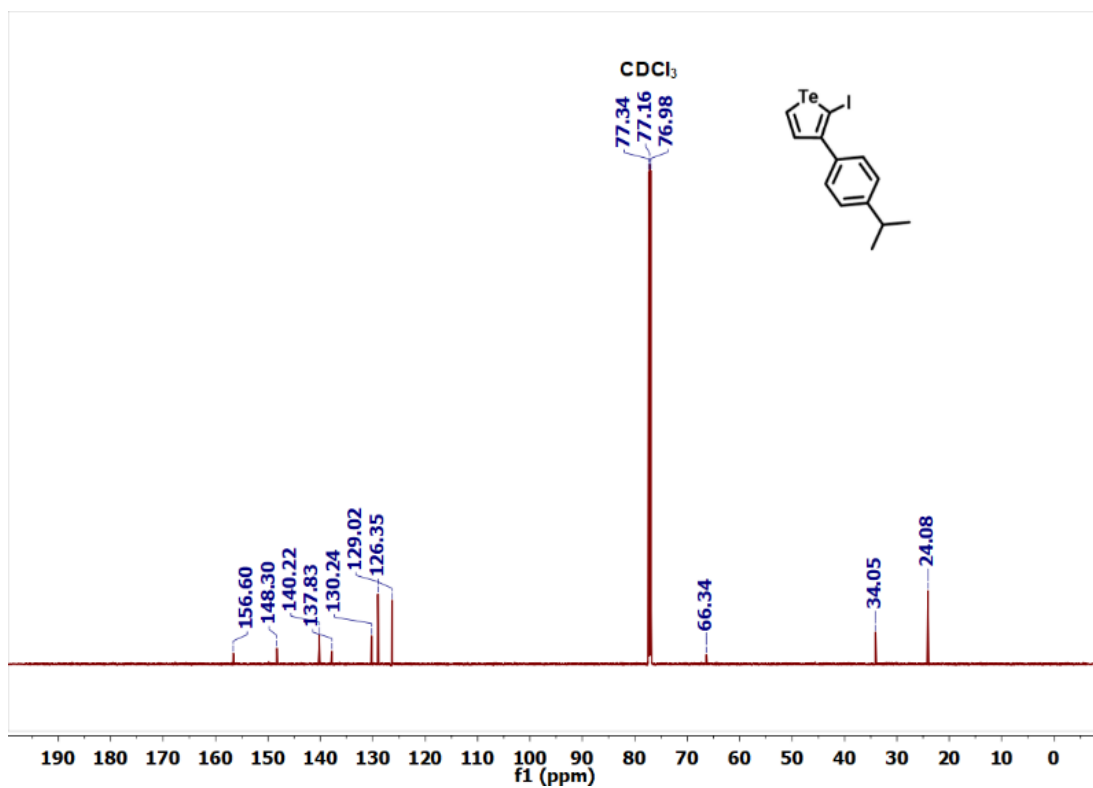


Figure 2.28. $^{13}\text{C}\{^1\text{H}\}$ NMR spectrum (176 MHz) of crude 2-iodo-3-(4-isopropylphenyl)-tellurophene (**H-Te-cumenyl-I**) in CDCl_3 .

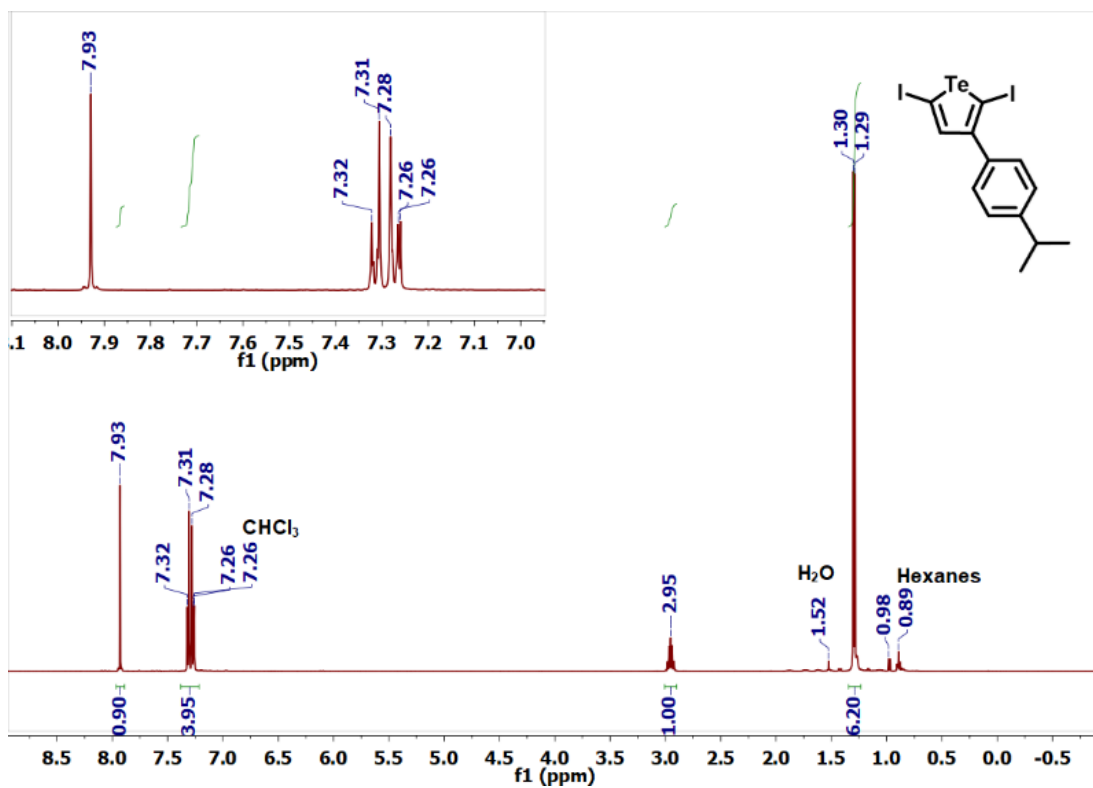


Figure 2.29. ¹H NMR spectrum (500 MHz) of 2,5-diiodo-3-(4-isopropylphenyl)-tellurophene (**I-Te-cumenyl-I**) in CDCl₃.

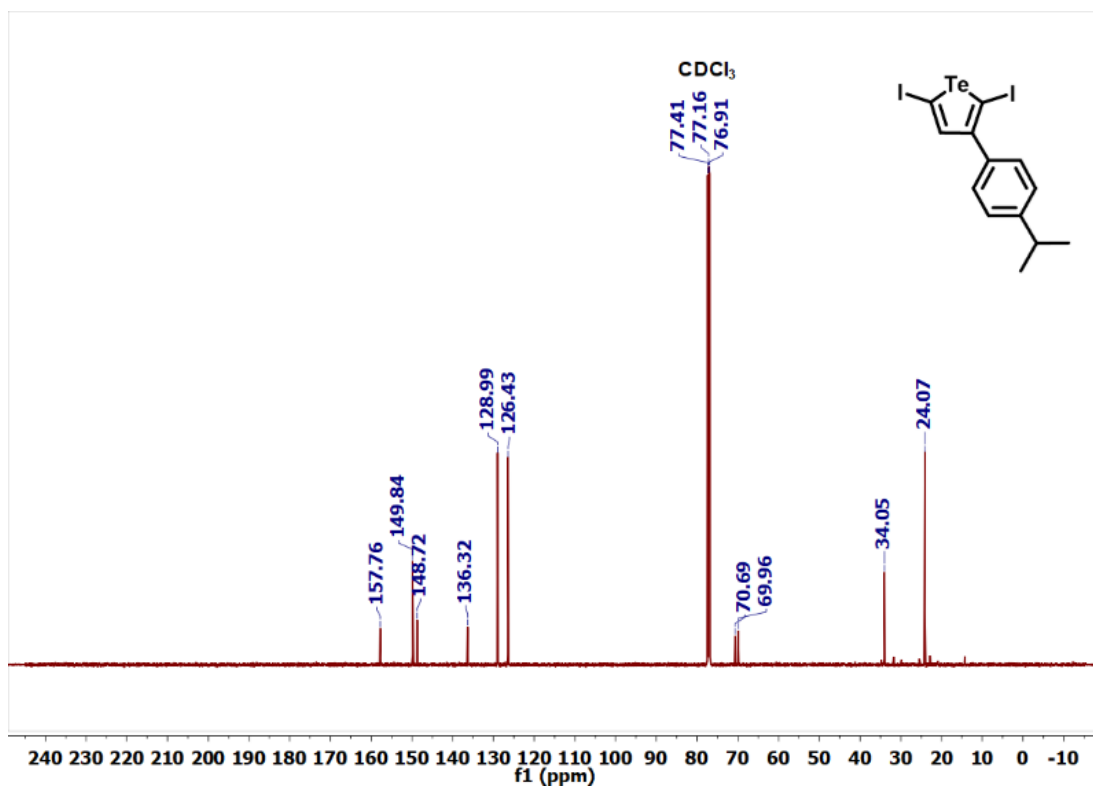


Figure 2.30. $^{13}\text{C}\{^1\text{H}\}$ NMR spectrum (126 MHz) of 2,5-diiodo-3-(4-isopropylphenyl)-tellurophene (**I-Te-cumenyl-I**) in CDCl_3 .

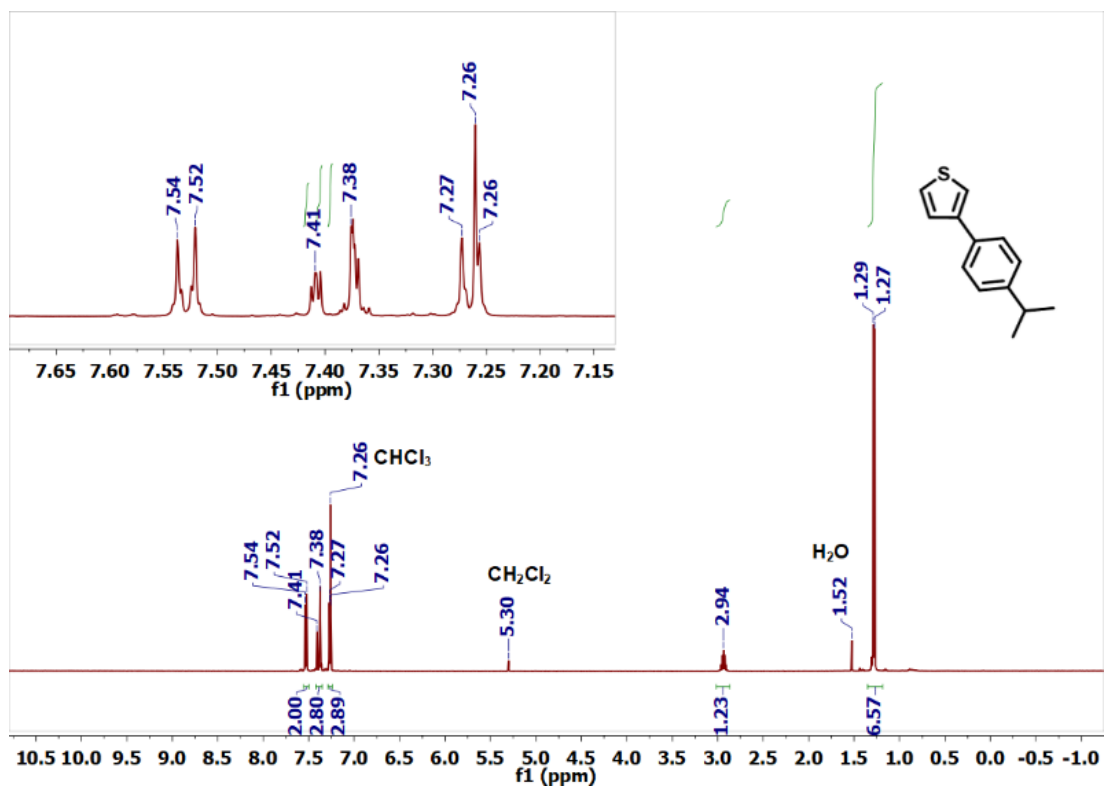


Figure 2.31. ^1H NMR spectrum (500 MHz) of 3-(4-isopropylphenyl)-thiophene (S-cumenyl) in CDCl_3 .

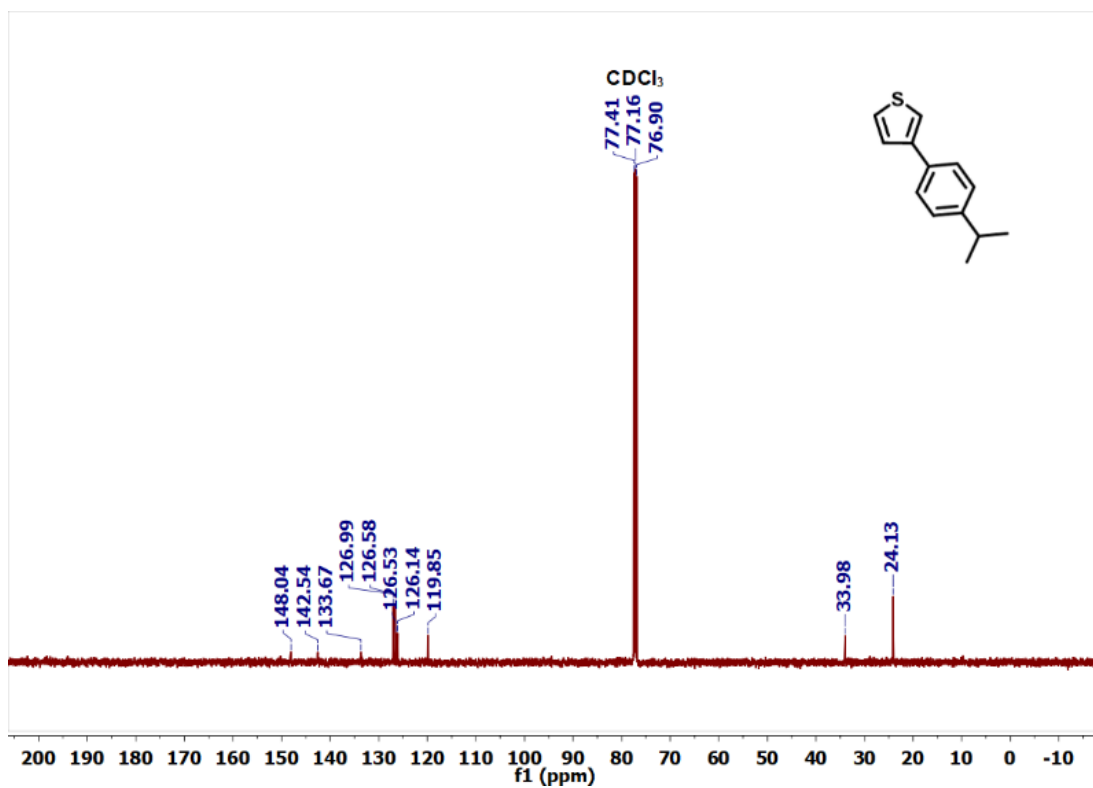


Figure 2.32. $^{13}\text{C}\{^1\text{H}\}$ NMR spectrum (126 MHz) of 3-(4-isopropylphenyl)-thiophene (S-cumenyl) in CDCl_3 .

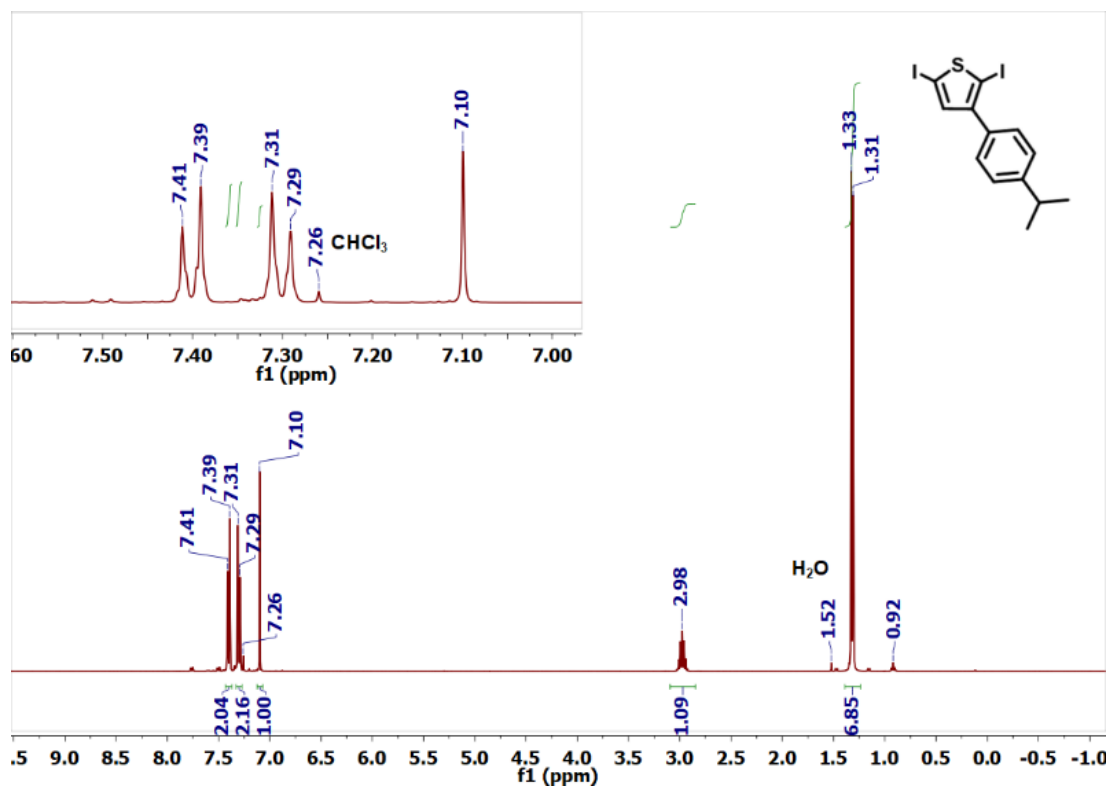


Figure 2.33. ¹H NMR spectrum (400 MHz) of 2,5-diiodo-3-(4-isopropylphenyl)-thiophene (**I-S-cumenyl-I**) in CDCl₃.

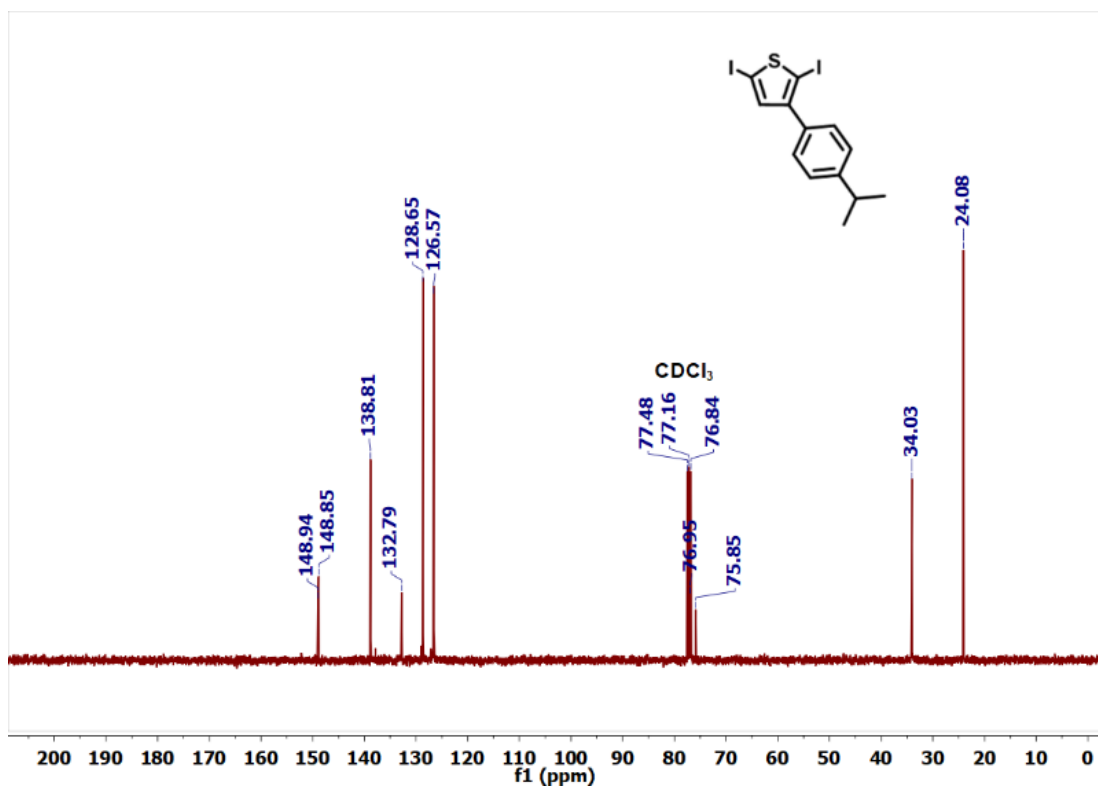


Figure 2.34. $^{13}\text{C}\{^1\text{H}\}$ NMR spectrum (101 MHz) of 2,5-diiodo-3-(4-isopropylphenyl)-thiophene (**I-S-cumenyl-I**) in CDCl_3 .

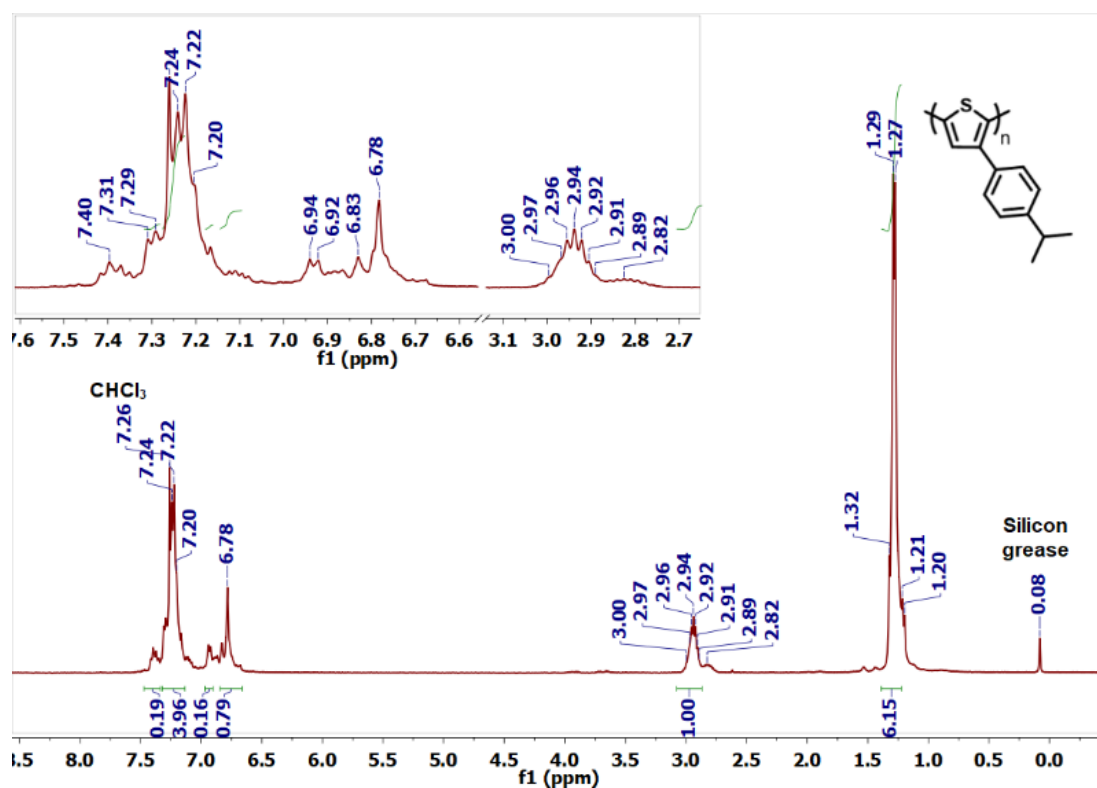


Figure 2.35. ^1H NMR spectrum (400 MHz) of poly(3-(4-isopropylphenyl)-thiophene) (PolyS-cumenyl) in CDCl_3 .

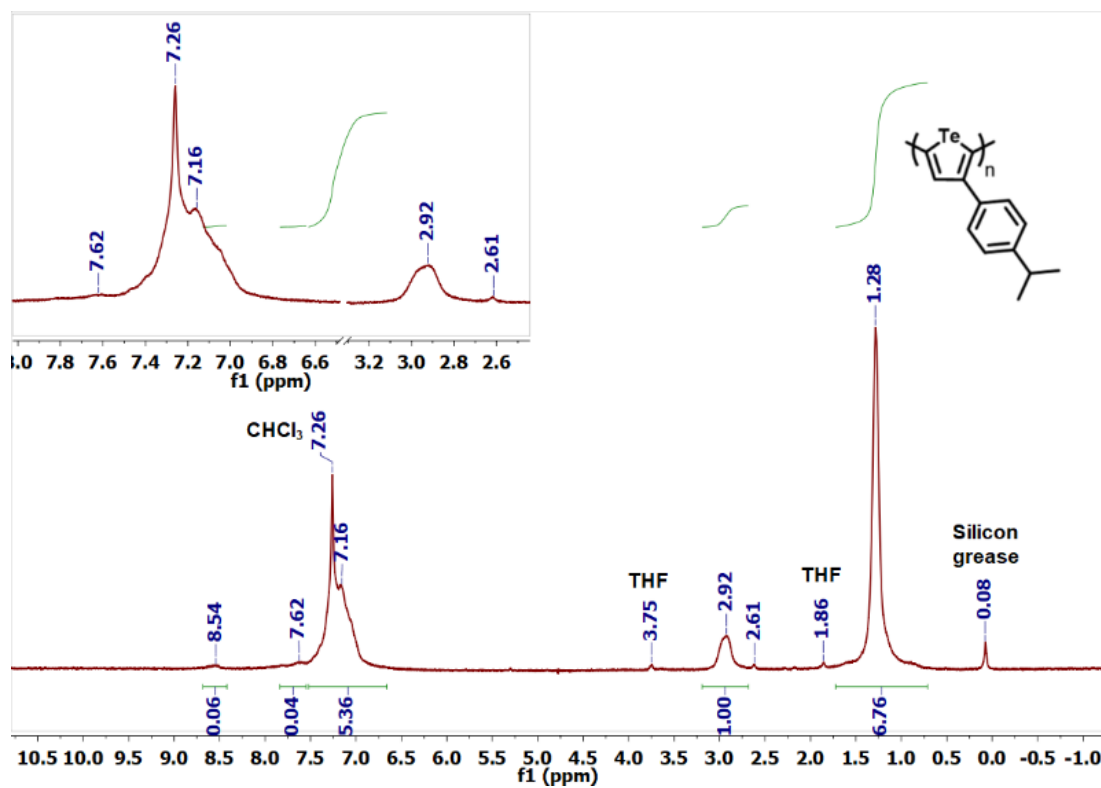


Figure 2.36. ^1H NMR spectrum (500 MHz) of poly(3-(4-isopropylphenyl)-tellurophene) (**PolyTe-cumenyl**) in CDCl_3 .

2.4.4 GPC Data

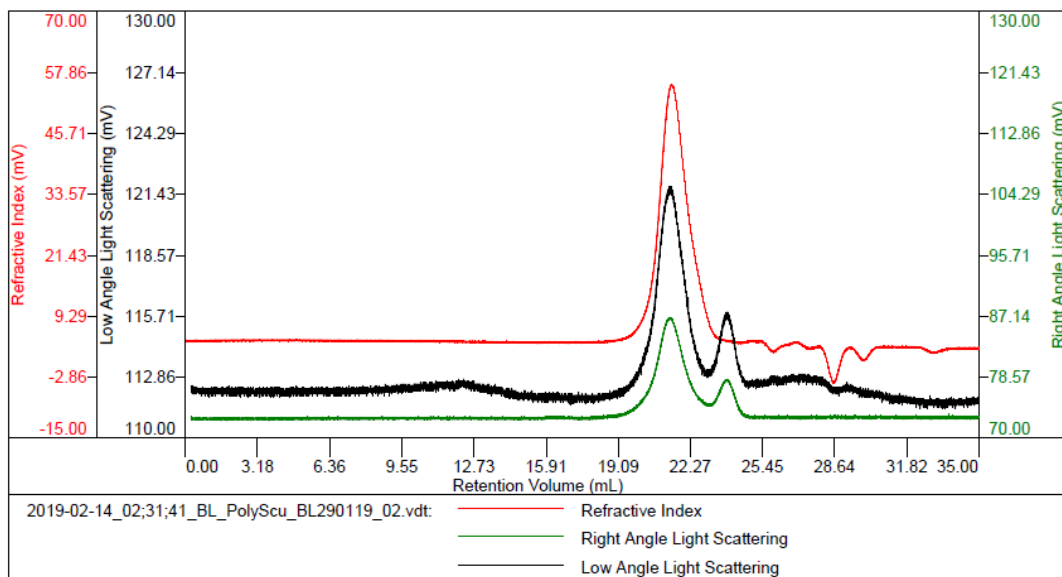


Figure 2.37. GPC elution profile for **PolyS-cumenyl**. The negative peaks in the refractive index detector are artifacts of injection.

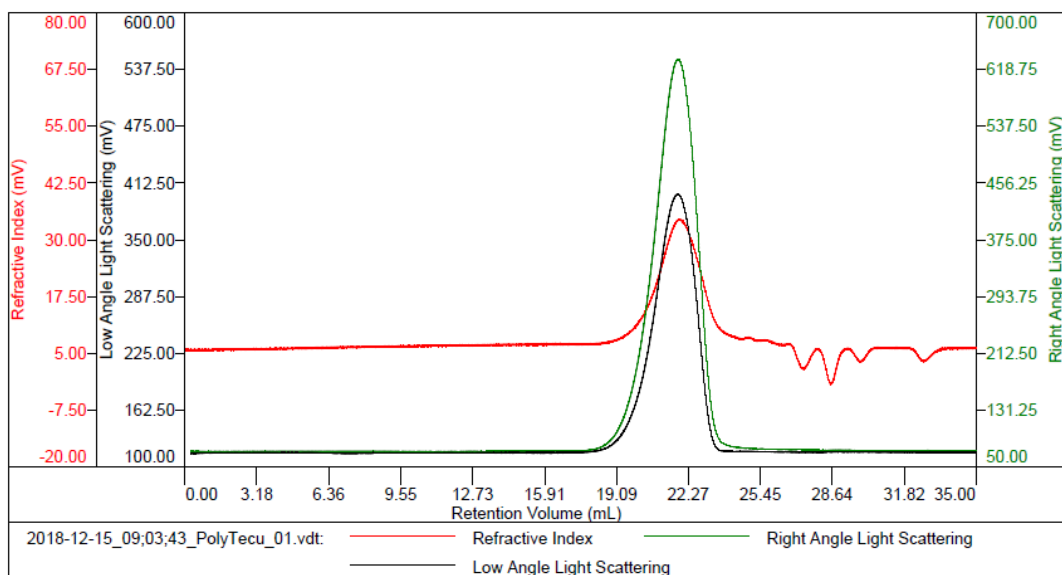


Figure 2.38. GPC elution profile for **PolyTe-cumenyl**. The negative peaks in the refractive index detector are artifacts of injection.

2.4.5 Thermal Analysis Data

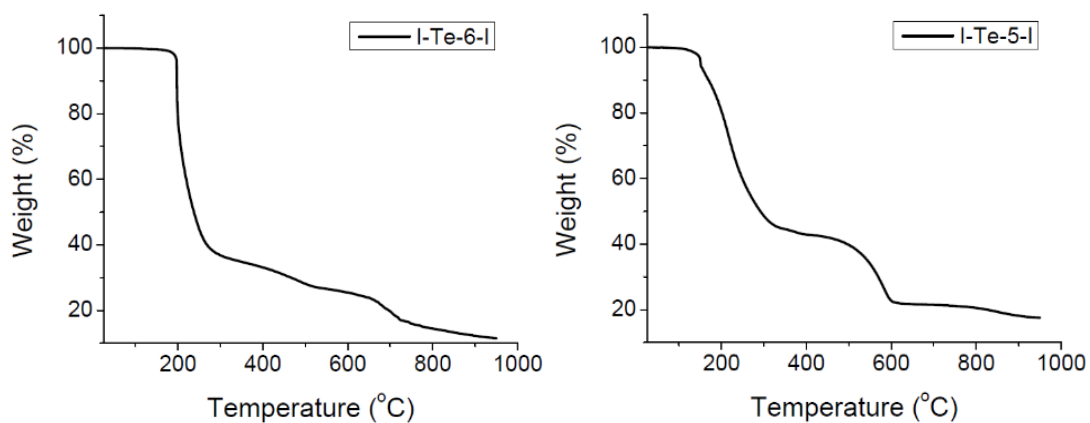


Figure 2.39. TGA plots of **I-Te-6-I** (left) and **I-Te-5-I** (right) obtained at a heating rate of 10 °C/min under N₂.

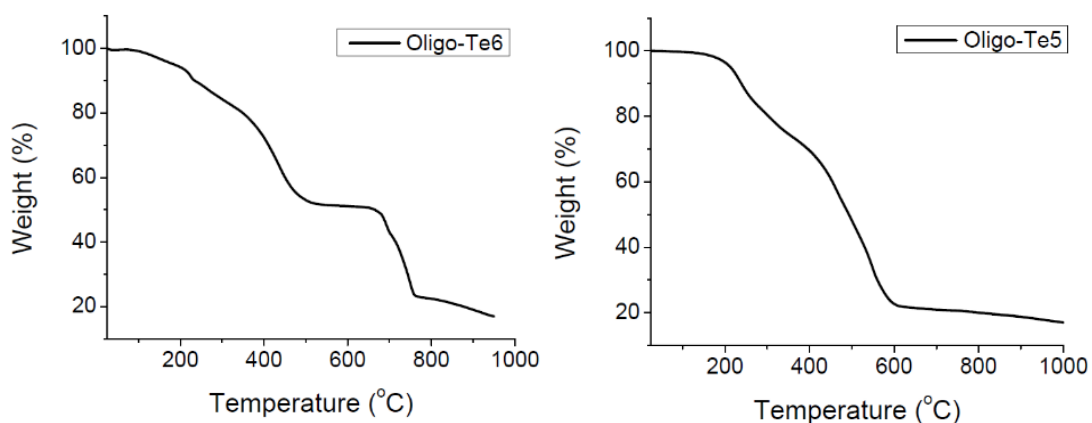


Figure 2.40. TGA plots of **Oligo-Te6** (left) and **Oligo-Te5** (right) obtained at a heating rate of 10 °C/min under N₂.

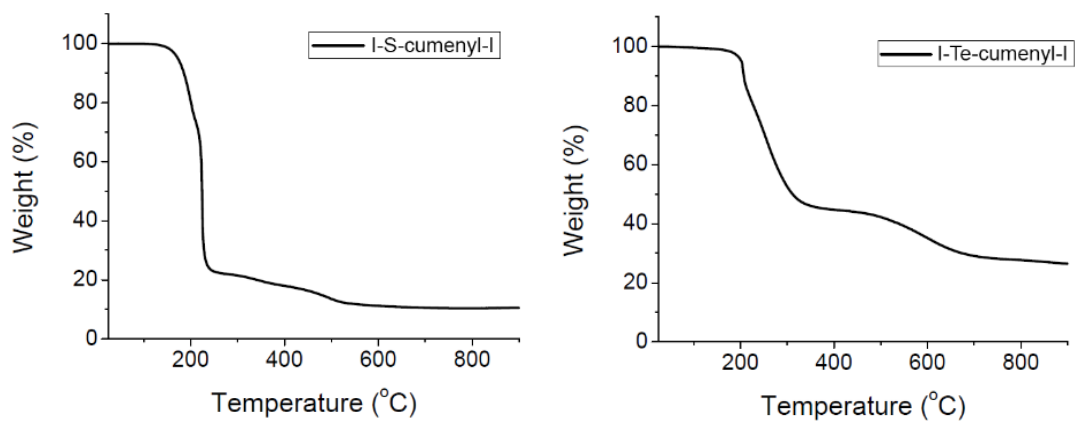


Figure 2.41. TGA plots of **I-S-cumenyl-I** (left) and **I-Te-cumenyl-I** (right) obtained at a heating rate of 10 °C/min under N₂.

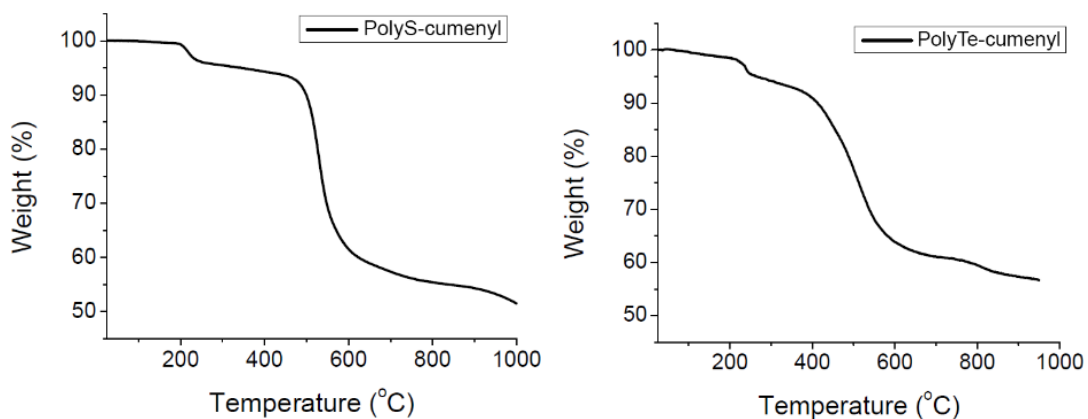


Figure 2.42. TGA plots of **PolyS-cumenyl** (left) and **PolyTe-cumenyl** (right) obtained at a heating rate of 10 °C/min under N₂.

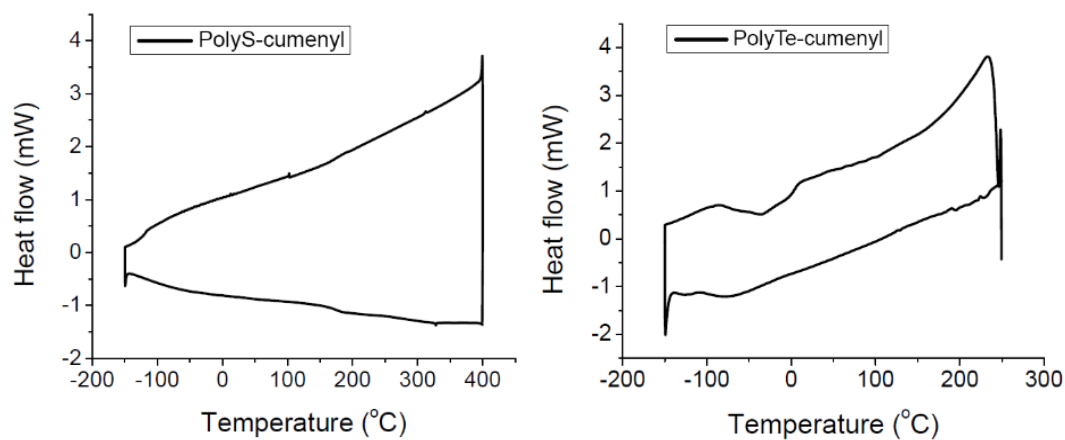


Figure 2.43. DSC trace of **PolyS-cumenyl** (left) and **PolyTe-cumenyl** (right) obtained at a heating rate of 20 °C/min under N₂.

2.4.6 Additional UV-Vis Data

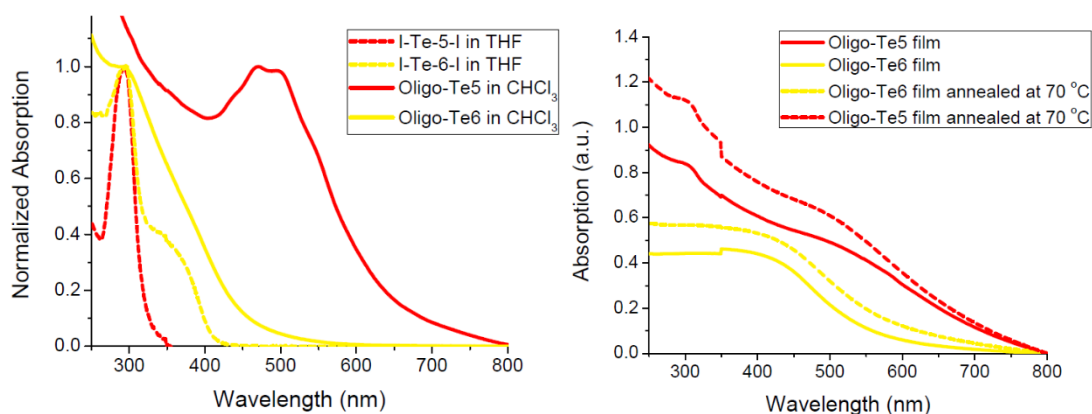


Figure 2.44. UV-Vis spectra of **I-Te-5-I/I-Te-6-I** in THF and **Oligo-Te5/Oligo-Te6** in CHCl₃ (left); UV-Vis spectra of **Oligo-Te6/Oligo-Te5** films before and after annealing at 70 °C (right). Onset of absorption for oligomers: **Oligo-Te6**: 456 nm (THF), 558 nm (film); **Oligo-Te5**: 629 nm (THF), 683 nm (film).

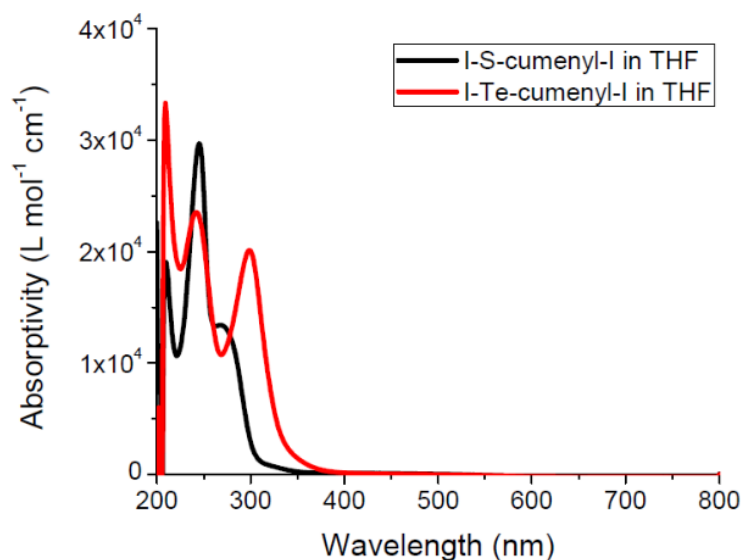


Figure 2.45. UV-Vis spectra of **I-S-cumenyl-I** and **I-Te-cumenyl-I** in THF.

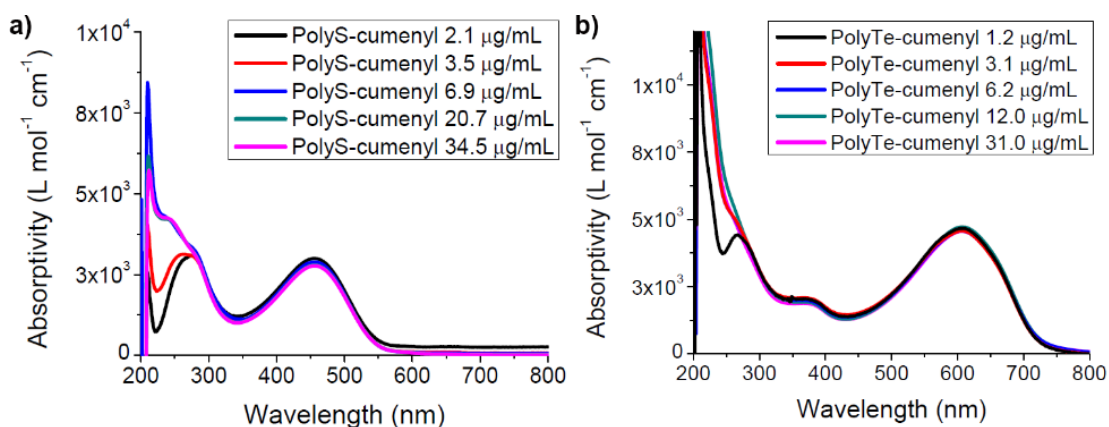


Figure 2.46. a) UV-Vis spectra of **PolyS-cumenyl** in THF; b) UV-Vis spectra of **PolyTe-cumenyl** in THF. A shoulder appears at ~ 250 nm as the concentration increases, indicating some degree of intermolecular interaction. Onset of absorption: **PolyS-cumenyl**: 544 nm; **PolyTe-cumenyl**: 721 nm.

2.4.7 Additional MALDI-MS Data

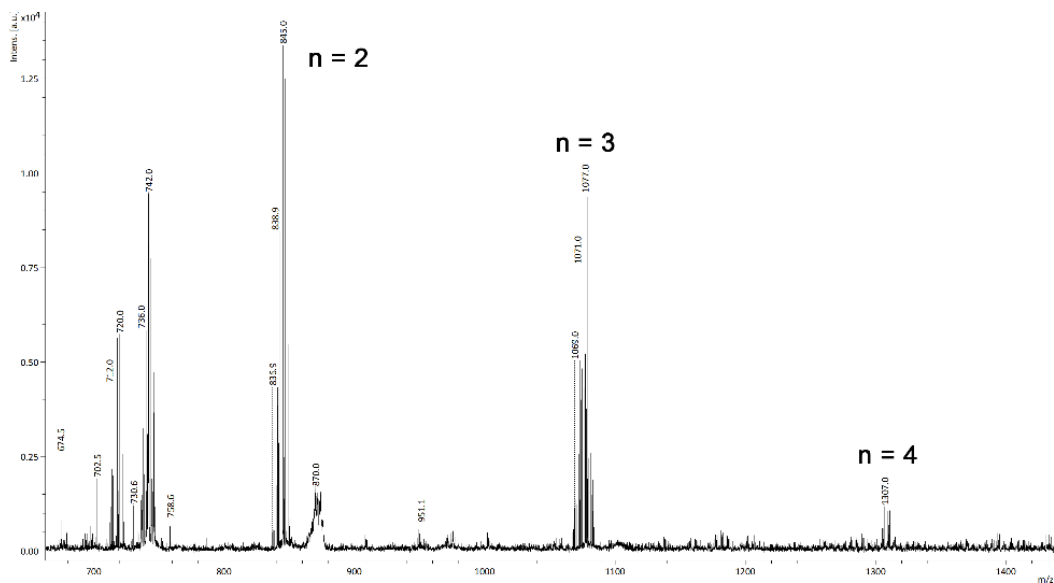


Figure 2.47. MALDI-MS of a self-oligomerized sample of **I-Te-6-I** after one month. Isotope pattern matching points to the presence as three iodine atoms as end groups.

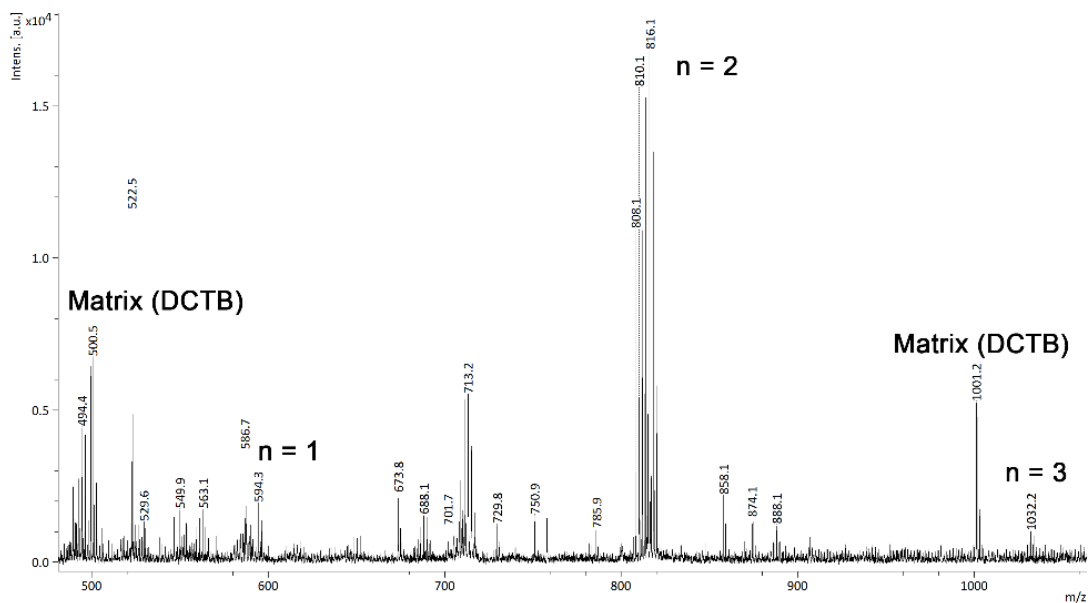


Figure 2.48. MALDI-MS of a self-oligomerized sample of **I-Te-5-I** after one week. Isotope pattern matching points to the presence as three iodine atoms as end groups.

2.4.8 Crystallographic Data

All single crystal XRD data was collected using a Bruker D8 diffractometer with APEX II CCD detector. Graphite-monochromated Mo K α radiation was used and the data was corrected for absorption with Gaussian integration (face-indexed). Crystal structures were solved using SHELXT-2014 and DIRDIF-2008,^{32,33} while refinements were completed with SHELXT-2014. Powder X-ray diffraction was performed on a Rigaku Ultima IV Diffractometer by the Earth and Atmospheric Sciences' X-Ray Diffraction Laboratory at the University of Alberta.

Table 2.1. Crystallographic data for **I-Te-6-I**, **T-Te-5-I** and **Te-cumenyl**.

Compound	I-Te-6-I	I-Te-5-I	Te-cumenyl
Formula	C ₈ H ₈ I ₂ Te	C ₇ H ₆ I ₂ Te	C ₁₃ H ₁₄ Te
Formula weight	485.54	471.52	297.84
Cryst. dimens. (mm)	0.58 × 0.06 × 0.06	0.42 × 0.16 × 0.05	0.41 × 0.18 × 0.04
Crystal system	monoclinic	monoclinic	orthorhombic
Space group	<i>P</i> 2 ₁ / <i>n</i> (No. 14)	<i>P</i> 2 ₁ / <i>n</i> (No. 14)	<i>Pbca</i> (No. 61)
<i>a</i> (Å)	22.122 (5)	12.4859 (6)	9.1429 (5)
<i>b</i> (Å)	4.6531 (12)	4.5525 (2)	8.1178 (5)
<i>c</i> (Å)	22.137 (5)	17.4405 (8)	31.1553 (18)
β (deg)	108.971 (3)	100.5674 (5)	---
<i>V</i> (Å ³)	2154.9 (9)	974.54 (8)	2312.4 (2)
<i>Z</i>	8	4	8
ρ_{calcd} (g cm ⁻³)	2.993	3.214	1.711
μ (mm ⁻¹)	8.433	9.319	2.532
T (°C)	-100	-100	-100
2 θ_{max} (deg)	53.46	56.73	55.05
Total data	14132	8738	19073
Unique data (<i>R</i> _{int})	4556 (0.0361)	2413 (0.0143)	2658 (0.0381)
Obs data [<i>I</i> ≥ 2 σ (<i>I</i>)]	3959	2278	2173
Parameters	236	91	149
<i>R</i> ₁ [<i>I</i> ≥ 2 σ (<i>I</i>)] ^a	0.038	0.0184	0.0319
<i>wR</i> ₂ [all data] ^a	0.0922	0.0428	0.084
Max/min $\Delta\rho$ (e ⁻ Å ⁻³)	3.394/-0.697	0.512/-0.836	0.573/-0.466

$$^a R_1 = \sum |F_o| - |F_c| / \sum |F_o|; wR_2 = [\sum w(F_o^2 - F_c^2)^2 / \sum w(F_o^4)]^{1/2}.$$

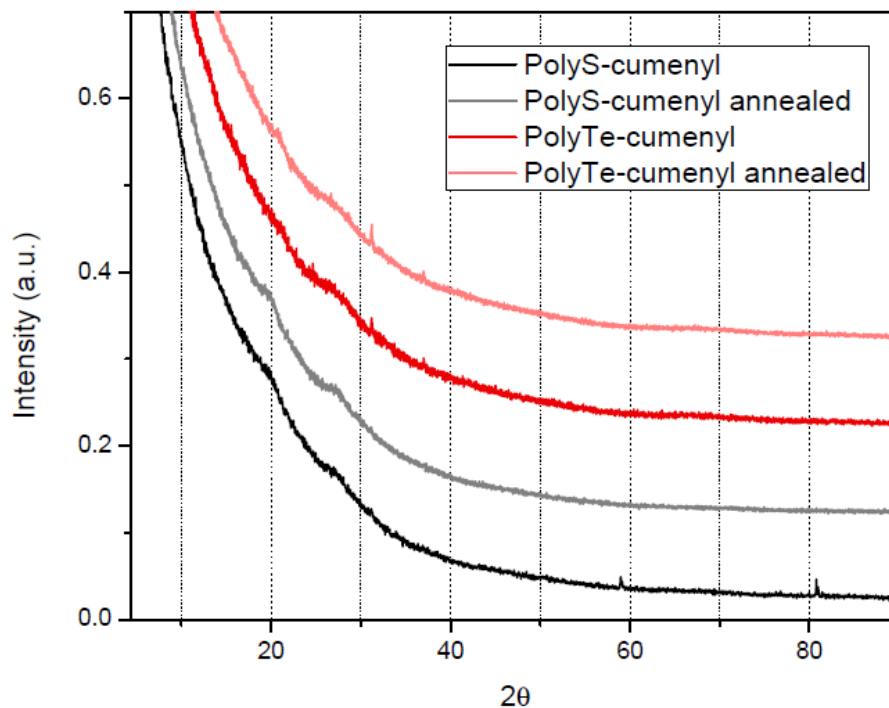


Figure 2.49. Powder XRD of **PolyTe-cumenyl** and **PolyS-cumenyl** before and after solvent vapor annealing. The polymers were drop cast from 5 mg/mL CHCl₃ solutions and annealed by exposure to CHCl₃ vapor at 35 °C for one hour.

2.5 DFT Computations and Methodology

Gas-phase structure optimization was performed using density functional theory (DFT) with the B3LYP functional^{34,35} and the basis sets 6-31G(d,p), for C, H and S,^{36,37} and LANL2DZ, for Te and I.³⁸ Computations were performed with Gaussian09 or Gaussian16 software and frequency analysis confirmed all structures to be in local minima on the potential energy surface.^{39,40} The structures and orbitals are shown as visualized in Avogadro.⁴¹ As a starting point for the computation of oligomers, the chains were built by linking monomer structures determined by single

crystal XRD, which were then optimized. The average dihedral (torsional) angle between tellurophene units of **Oligo-Te6** and **Oligo-Te5** remained the same for optimizations with 3-, 5- or 7-units in the oligomeric chain. For the calculation of energy change with torsion angle (Figure 2.6), the respective structures were optimized with a fixed dihedral angle.

For time-dependent DFT calculations (TD-DFT), trimers were used for simplicity using the same level of theory as stated above. The three strongest oscillators at their respective wavenumbers were used to calculate absorptivity and to build the computational UV-Vis spectra. Using all calculated oscillators leads to a very similar absorption profile and the same conclusion of a red-shifted absorption for **Oligo-Te5**, as supported by experiment.

2.5.1 Additional Computed Excited State Data

Table 2.2. Computed excited states of trimers of **Oligo-Te5 (I-[Te5]₃-I)** by TD-DFT.

The three strongest oscillators are shown in bold, and the main orbitals involved in singlet state transitions are shown.

I-[Te5] ₃ -I			
Excited state	Energy (eV)	Oscillator strength	Main orbitals involved
T ₁	1.5346	0.0000	
T ₂	2.5209	0.0000	
S ₁	2.8119	0.9915	HOMO/LUMO
T ₃	2.8138	0.0000	
T ₄	2.8920	0.0000	
S ₂	2.9745	0.0003	HOMO/LUMO+1
T ₅	2.9780	0.0000	
T ₆	2.9899	0.0000	
T ₇	3.0015	0.0000	
S ₃	3.0894	0.0001	HOMO/LUMO+2 HOMO/LUMO+3
T ₈	3.1421	0.0000	
S ₄	3.1665	0.0004	HOMO/LUMO+2 HOMO/LUMO+3
T ₉	3.1688	0.0000	
S ₅	3.2455	0.0001	HOMO/LUMO+4
T ₁₀	3.3096	0.0000	
S ₆	3.5047	0.0479	HOMO-1/LUMO
S ₇	3.6234	0.0005	HOMO/LUMO+6
S ₈	3.6413	0.0030	HOMO-2/LUMO
S ₉	3.6581	0.0002	HOMO/LUMO+5
S ₁₀	3.6764	0.0191	HOMO-3/LUMO

Table 2.3. Computed excited states of trimers of **Oligo-Te6 (I-[Te6]₃-I)** by TD-DFT.

The three strongest oscillators are shown in bold, and the main orbitals involved in singlet state transitions are shown.

I-[Te6] ₃ -I			
Excited state	Energy (eV)	Oscillator strength	Main orbitals involved
T ₁	2.5546	0.0000	
T ₂	2.6745	0.0000	
T ₃	2.6803	0.0000	
T ₄	3.1543	0.0000	
T ₅	3.1628	0.0000	
T ₆	3.1863	0.0000	
T ₇	3.1936	0.0000	
T ₈	3.2390	0.0000	
T ₉	3.2909	0.0000	
T ₁₀	3.4031	0.0000	
S ₁	3.4634	0.0007	HOMO/LUMO
S ₂	3.5199	0.0003	HOMO/LUMO+2
S ₃	3.5862	0.0032	HOMO-2/LUMO
S ₄	3.6065	0.0008	HOMO-4/LUMO
S ₅	3.6264	0.0022	HOMO-1/LUMO+3
S ₆	3.6280	0.0004	HOMO/LUMO+2
S ₇	3.6770	0.0001	HOMO-2/LUMO+3
S ₈	3.7612	0.0001	HOMO-3/LUMO
S ₉	3.8135	0.0154	HOMO-2/LUMO
S ₁₀	3.8601	0.0717	HOMO-1/LUMO

2.6 References

1. E. I. Carrera and D. S. Seferos, *Macromolecules*, **2015**, *48*, 297–308.
2. (a) S. M. Parke, M. P. Boone and E. Rivard, *Chem. Commun.*, **2016**, *52*, 9485–9505, and references therein; (b) G. C. Hoover and D. S. Seferos, *Chem. Sci.*, **2019**, *10*, 9182–9188.
3. (a) A. A. Jahnke, B. Djukic, T. M. McCormick, E. Buchaca Domingo, C. Hellmann, Y. Lee and D. S. Seferos, *J. Am. Chem. Soc.*, **2013**, *135*, 951–954; (b) G. He, L. Kang, W. Torres Delgado, O. Shynkaruk, M. J. Ferguson, R. McDonald and E. Rivard, *J. Am. Chem. Soc.*, **2013**, *135*, 5360–5363; (c) L. Lv, X. Wang, X. Wang, L. Yang, T. Dong, Z. Yang and H. Huang, *ACS Appl. Mater. Interfaces*, **2016**, *8*, 34620–34629; (d) M. Al-Hashimi, Y. Han, J. Smith, H. S. Bazzi, S. Y. A. Alqaradawi, S. E. Watkins, T. D. Anthopoulos and M. Heeney, *Chem. Sci.*, **2016**, *7*, 1093–1099.
4. (a) S. Ye, L. Janasz, W. Zajaczkowski, J. G. Manion, A. Mondal, T. Marszalek, D. Andrienko, K. Mülllen, W. Pisula and D. S. Seferos, *Macromol. Rapid Commun.*, **2019**, *40*, 1800596; (b) W. Xing, P. Ye, J. Lu, X. Wu, Y. Chen, T. Zhu, A. Peng and H. Huang, *J. Power Sources*, **2018**, *401*, 13–19.
5. G. He, W. Torres Delgado, D. J. Schatz, C. Merten, A. Mohammadpour, L. Mayr, M. J. Ferguson, R. McDonald, A. Brown, K. Shankar and E. Rivard, *Angew. Chem., Int. Ed.*, **2014**, *53*, 4587–4591.
6. (a) G. He, B. D. Wiltshire, P. Choi, A. Savin, S. Sun, A. Mohammadpour, M. J. Ferguson, R. McDonald, S. Farsinezhad, A. Brown, K. Shankar and E.

- Rivard, *Chem. Commun.*, **2015**, *51*, 5444–5447; (b) W. Torres Delgado, C. A. Braun, M. P. Boone, O. Shynkaruk, Y. Qi, R. McDonald, M. J. Ferguson, P. Data, S. K. C. Almeida, I. de Aguiar, G. L. C. de Souza, A. Brown, G. He and E. Rivard, *ACS Appl. Mater. Interfaces*, **2018**, *10*, 12124–12134; (c) E. Hupf, Y. Tsuchiya, W. Moffat, L. Xu, M. Hirai, Y. Zhou, M. J. Ferguson, R. McDonald, T. Murai, G. He and E. Rivard, *Inorg. Chem.*, **2019**, *58*, 13323–13336.
7. R. D. Pensack, Y. Song, T. M. McCormick, A. A. Jahnke, J. Hollinger, D. S. Seferos and G. D. Scholes, *J. Phys. Chem. B*, **2014**, *118*, 2589–2597.
 8. L. Yang, W. Gu, L. Lv, Y. Chen, Y. Yang, P. Ye, J. Wu, L. Hong, A. Peng and H. Huang, *Angew. Chem., Int. Ed.*, **2018**, *57*, 1096–1102.
 9. B. T. Luppi, D. Majak, M. Gupta, E. Rivard and K. Shankar, *J. Mater. Chem. A*, **2019**, *7*, 2445–2463.
 10. S. Ye, M. Steube, E. I. Carrera and D. S. Seferos, *Macromolecules*, **2016**, *49*, 1704–1711.
 11. (a) W. Torres Delgado, F. Shahin, M. J. Ferguson, R. McDonald, G. He and E. Rivard, *Organometallics*, **2016**, *35*, 2140–2148; (b) C. A. Braun, N. Martinek, Y. Zhou, M. J. Ferguson and E. Rivard, *Dalton Trans.*, **2019**, *48*, 10210–10219.
 12. For related studies, see: (a) B. Jiang and T. D. Tilley, *J. Am. Chem. Soc.*, **1999**, *121*, 9744–9745; (b) S. M. Parke, E. Hupf, G. K. Matharu, I. de Aguiar, L. Xu, H. Yu, M. P. Boone, G. L. C. de Souza, R. McDonald, M. J. Ferguson, G. He,

- A. Brown and E. Rivard, *Angew. Chem., Int. Ed.*, **2018**, *57*, 14841–14846; (c) S. Das and S. S. Zade, *Chem. Commun.*, **2010**, *46*, 1168–1170.
13. (a) K. Ohshimizu, A. Takahashi, Y. Rho, T. Higashihara, M. Ree and M. Ueda, *Macromolecules*, **2011**, *44*, 719–727; (b) For examples of monomeric (unpolymerized) 3-aryltellurophenes, see: V. Krishna Karapala, H.-P. Shih and C.-C. Han, *Org. Lett.*, **2018**, *20*, 1550–1554.
14. (a) I. Osaka and R. D. McCullough, *Acc. Chem. Res.*, **2008**, *41*, 1202–1214; (b) M. A. Baker, C.-H. Tsai and K. J. T. Noonan, *Chem. -Eur. J.*, **2018**, *50*, 13078–13088.
15. T. Yamamoto, A. Morita, Y. Miyazaki, T. Maruyama, H. Wakayama, Z. H. Zhou, Y. Nakamura, T. Kanbara, S. Sasaki and K. Kubota, *Macromolecules*, **1992**, *25*, 1214–1223.
16. C. Thiebes, G. K. Surya Prakash, N. A. Petasis and G. A. Olah, *Synlett*, **1998**, 141–142.
17. M. Kitano, T. Tanaka and A. Osuka, *Organometallics*, **2017**, *36*, 2559–2564.
18. Both **I-Te-5-I** and **I-Te-6-I** yield oligomers ($n \leq 4$) over time. This process takes months for **I-Te-6-I** but only days for **I-Te-5-I**. 2,5-Dibromoselenophenes are known to undergo the same process in the solid state: A. Patra, Y. H. Wijsboom, S. S. Zade, M. Li, Y. Sheynin, G. Leitius and M. Bendikov, *J. Am. Chem. Soc.*, **2008**, *130*, 6734–6736.
19. S. S. Zade and M. Bendikov, *Chem. -Eur. J.*, **2007**, *13*, 3688–3700.

20. For additional leading reviews on this topic, see: (a) K. Okamoto and C. K. Luscombe, *Polym. Chem.*, **2011**, *2*, 2424–2434; (b) J. P. Lutz, M. D. Hannigan and A. J. McNeil, *Coord. Chem. Rev.*, **2018**, *376*, 225–247.
21. (a) A. Patra, Y. H. Wijsboom, G. Leitus and M. Bendikov, *Org. Lett.*, **2009**, *11*, 1487–1490; (b) T. Johansson, W. Mammo, M. Svensson, M. R. Andersson and O. Inganäs, *J. Mater. Chem.*, **2003**, *13*, 1316–1323; (c) Y. Li, Y. Cao, J. Gao, D. Wang, G. Yu and A. J. Heeger, *Synth. Met.*, **1999**, *99*, 243–248.
22. S. Rühle, *Sol. Energy*, **2016**, *130*, 139–147.
23. D. Barnes-Seeman, M. Jain, L. Bell, S. Ferreira, S. Cohen, X.-H. Chen, J. Amin, B. Snodgrass and P. Hatsis, *ACS Med. Chem. Lett.*, **2013**, *4*, 514–516.
24. V. Gandon, D. Leca, T. Aechtner, K. P. C. Vollhardt, M. Malacria and C. Aubert, *Org. Lett.*, **2004**, *6*, 3405–3407.
25. J. Lozada, Z. Liu and D. M. Perrin, *J. Org. Chem.*, **2014**, *79*, 5365–5368.
26. J. L. Dutton, G. J. Farrar, M. J. Sgro, T. L. Battista and P. J. Ragona, *Chem. - Eur. J.*, **2009**, *15*, 10263–10271.
27. T. R. Hoye, B. M. Eklov and M. Voloshin, *Org. Lett.*, **2004**, *6*, 2567–2570.
28. A. Krasovskiy and P. Knochel, *Synthesis*, **2006**, *5*, 890–891.
29. E. L. Tyson, M. S. Ament and T. P. Yoon, *J. Org. Chem.*, **2013**, *78*, 2046–2050.
30. J. K. Yano, T. T. Denton, M. A. Cerny, X. Zhang, E. F. Johnson and J. R. Cashman, *J. Med. Chem.*, **2006**, *49*, 6987–7001.
31. M. A. Truong, S. Fukuta, T. Koganezawa, Y. Shoji, M. Ueda and T. Higashihara, *J. Polym. Sci. Part A Polym. Chem.*, **2015**, *53*, 875–887.

32. G. M. Sheldrick, *Acta Cryst. A* **2015**, *71*, 3–8.
33. P. T. Beurskens, G. Beurskens, R. de Gelder, J. M. M. Smits, S. Garcia-Granda and R. O. Gould, The DIRDIF-2008 program system, Crystallography Laboratory, Radboud University Nijmegen, The Netherlands.
34. A. D. Becke, *J. Chem. Phys.*, **1993**, *98*, 5648–5652.
35. C. Lee, W. Yang and R. G. Parr, *Phys. Rev. B*, **1988**, *37*, 785–789.
36. A. Bennett, W. A. Shirley, M. A. Al-Laham, T. G. Tensfeldt, G. A. Petersson and J. Mantzaris, *J. Chem. Phys.*, **2002**, *89*, 2193–2218.
37. G. A. Petersson and M. A. Al-Laham, *J. Chem. Phys.*, **1991**, *94*, 6081–6090.
38. W. R. Wadt and P. J. Hay, *J. Chem. Phys.*, **1985**, *82*, 284–298.
39. M. J. Frisch, G. W. Trucks, H. B. Schlegel, G. E. Scuseria, M. A. Robb, J. R. Cheeseman, G. Scalmani, V. Barone, G. A. Petersson, H. Nakatsuji, M. C. X. Li, A. Marenich, J. Bloino, B. G. Janesko, R. Gomperts, B. Mennucci, H. P. Hratchian, J. V. Ortiz, A. F. Izmaylov, J. L. Sonnenberg, D. Williams-Young, F. Ding, F. Lipparini, F. Egidi, J. Goings, B. Peng, A. Petrone, T. Henderson, D. Ranasinghe, V. G. Zakrzewski, J. Gao, N. Rega, G. Zheng, W. Liang, M. Hada, M. Ehara, K. Toyota, R. Fukuda, J. Hasegawa, M. Ishida, T. Nakajima, Y. Honda, O. Kitao, H. Nakai, T. Vreven, K. Throssell, J. A. J. Montgomery, J. E. Peralta, F. Ogliaro, M. Bearpark, J. J. Heyd, E. Brothers, K. N. Kudin, V. N. Staroverov, T. Keith, R. Kobayashi, J. Normand, K. Raghavachari, A. Rendell, J. C. Burant, S. S. Iyengar, J. Tomasi, M. Cossi, J. M. Millam, M. Klene, C. Adamo, R. Cammi, J. W. Ochterski, R. L. Martin, K. Morokuma, O. Farkas, J.

- B. Foresman and D. J. Fox, Gaussian 09, Revision A.02, *Gaussian, Inc., Wallingford CT*.
40. M. J. Frisch, G. W. Trucks, H. B. Schlegel, G. E. Scuseria, M. A. Robb, J. R. Cheeseman, G. Scalmani, V. Barone, G. A. Petersson, H. Nakatsuji, X. Li, M. Caricato, A. V. Marenich, J. Bloino, B. G. Janesko, R. Gomperts, B. Mennucci, H. P. Hratchian, J. V. Ortiz, A. F. Izmaylov, J. L. Sonnenberg, D. Williams-Young, F. Ding, F. Lipparini, F. Egidi, J. Goings, B. Peng, A. Petrone, T. Henderson, D. Ranasinghe, V. G. Zakrzewski, J. Gao, N. Rega, G. Zheng, W. Liang, M. Hada, M. Ehara, K. Toyota, R. Fukuda, J. Hasegawa, M. Ishida, T. Nakajima, Y. Honda, O. Kitao, H. Nakai, T. Vreven, K. Throssell, J. A. J. Montgomery, J. E. Peralta, F. Ogliaro, M. J. Bearpark, J. J. Heyd, E. N. Brothers, K. N. Kudin, V. N. Staroverov, T. A. Keith, R. Kobayashi, J. Normand, K. Raghavachari, A. P. Rendell, J. C. Burant, S. S. Iyengar, J. Tomasi, M. Cossi, J. M. Millam, M. Klene, C. Adamo, R. Cammi, J. W. Ochterski, R. L. Martin, K. Morokuma, O. Farkas, J. B. Foresman and D. J. Fox, Gaussian 16, Revision B.01, *Gaussian, Inc., Wallingford CT*.
41. M. D. Hanwell, D. E. Curtis, D. C. Lonie, T. Vandermeersch, E. Zurek and G. R. Hutchison, *J. Cheminf.*, **2012**, *4*, 17.

Chapter 3: Soluble Electronically Modified Polyacetylenes

3.1 Introduction

Polyacetylene ($-\text{HC}=\text{CH}-$)_n (PA) is of great historical importance to materials science due to the discovery of its metal-like conductivity when doped.¹⁻³ The resulting increase in π -electron delocalization along the unsaturated backbone in doped PA leads to absorption in the telecommunications region, around 1500 nm.³ Thus, polyacetylene and its derivatives are of interest as near-IR optical switches⁴ and as photodetectors that could operate beyond the optical limit of common silicon-based systems (> 1100 nm).⁵ Despite these desirable optoelectronic properties, the use of polyacetylene in applications has lagged, as it is air-sensitive,⁶ completely insoluble in any solvent, and methods to prepare soluble variants that retain small HOMO-LUMO gaps (E_g) remain scarce.^{7,13} As a result, researchers have often shied away from PAs and have instead focused on the incorporation of heavy elements⁸ or the design of complex "donor-acceptor" architectures⁹ to obtain soluble (processable) π -conjugated polymers for optoelectronics. However, recent reports of novel cyclopolyacetylenes¹⁰ and linear poly(fluoroacetylenes)¹¹ with enhanced solubility and air stability show that polyacetylene chemistry is making a well-deserved comeback.

Polyalkynes of the general formula $(\text{RC}=\text{CH})_n$ or $(\text{RC}=\text{CR})_n$ have been studied extensively, yet these densely-functionalized polymers possess highly twisted polyolefin backbones (and larger HOMO-LUMO energy gaps) due to steric interactions between the closely spaced side chains.¹² On the other hand, soluble PAs

with organic (R) side groups placed (ideally) at every 8 carbon atoms can be obtained through the ring-opening metathesis polymerization (ROMP) of monosubstituted cyclooctatetraenes (R-COT).^{7,13} The increased spacing between side chains in these cases affords untwisted polyacetylene backbones and enhanced conductivity in the solid state upon doping.^{7c,14} Recently, this route has been used to synthesize processable polyacetylene block copolymers,¹⁵ but the scope of side chain functionality remains limited. In this Chapter, a modified ROMP strategy is presented and used to yield conjugated polyacetylenes with electronically active amino, boryl (-BR₂) and phosphoryl (-P(O)R₂) groups (Figure 3.1). In addition, Click chemistry between a strained COT-derived alkyne and an azide¹⁶ provides access to a new class of π -conjugated triazolium-based polymer, wherein a triazolium ring is directly fused onto a polyacetylene without disruption of backbone unsaturation (Figure 3.1). Overall, the synthetic methods introduced in this work greatly expands the scope and structural variety of new π -conjugated polyacetylenes that can be obtained in the future. Of added note, the incorporation of redox active functional groups onto a polyacetylene unlocks novel near-IR optical switching behavior and enhanced polymer stability in air. Finally, a general route to cross-linked networks of functionalized polyacetylenes is presented.

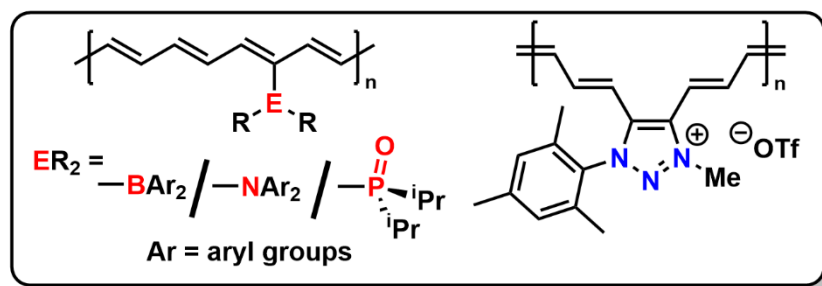
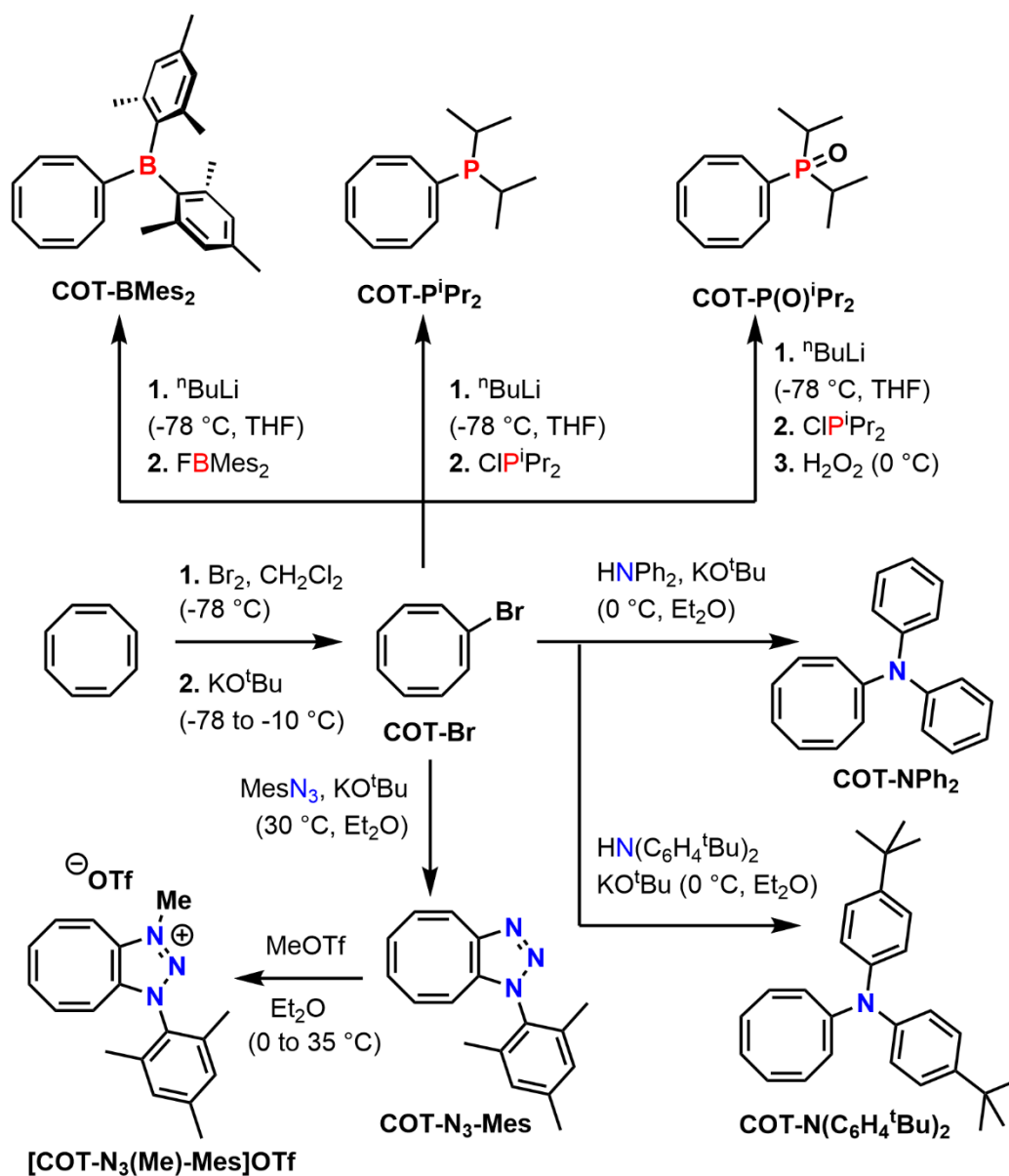


Figure 3.1. Functionalized polyacetylenes discussed in this Chapter.

3.2 Results and Discussion

3.2.1 Monomer Synthesis

In this study, the ring-opening metathesis polymerization (ROMP) of cyclic cyclooctatetraene analogues was used to access electronically modified polyacetylenes. Focus was given to Grubbs' 3rd generation ruthenium-based catalyst¹⁷ for ROMP, as prior work in the Rivard group on luminescent poly(norbornadienes) revealed that this catalyst tolerated monomers bearing electron-deficient boryl and phosphoryl substituents.¹⁸ Fortunately, all of the monomers required for this work were synthesized from the readily available starting material, bromocyclooctatetraene (COT-Br, Scheme 3.1).



Scheme 3.1. Synthesis of the strained COT monomers.

The borylated monomer **COT-BMes₂** was accessed as an air-stable yellow crystalline solid (55 % yield) via lithiation of COT-Br with ⁿBuLi in THF, followed by addition of FBMe₂ (Mes = 2,4,6-Me₃C₆H₂). **COT-BMes₂** can be purified by column

chromatography in air and the single crystal X-ray structure of this monomer is shown in Figure 3.2a. A similar route involving the reaction of *in-situ* formed COT-Li with ClPⁱPr₂ either affords **COT-PⁱPr₂** as a mildly air-sensitive orange oil (72 % yield) or the air-stable phosphine-oxide **COT-P(O)ⁱPr₂** as a yellow solid (51 % yield), when the phosphine **COT-PⁱPr₂** is oxidized with H₂O₂ (Scheme 3.1). Structural characterization of **COT-P(O)ⁱPr₂** was also possible by single crystal X-ray crystallography (Figure 3.2b). For later comparisons (*vide infra*), Grubbs' silylated monomer **COT-SiMe₃**⁷ was also synthesized.

For the preparation of the amine-substituted monomers **COT-NPh₂** and **COT-N(C₆H₄^tBu)₂**, COT-Br is premixed with a 20-30 mol.% excess of the respective diarylamine in Et₂O and cooled to 0 °C before addition of KO^tBu (Scheme 3.1). This route was used in the past to prepare dialkylamino-COT derivatives,¹⁹ and likely involves the generation of the transient strained alkyne, 1,3,5-cyclooctatriene-7-yne, from COT-Br and KO^tBu.²⁰ Column chromatography in air was used to yield pure **COT-NPh₂** and **COT-N(C₆H₄^tBu)₂** as orange solids (37 and 20 % isolated yields, respectively); the single crystal X-ray structure of **COT-NPh₂** is found in Figure 3.2c and shows a similar saddle-shaped COT unit as in **COT-BMes₂** and **COT-P(O)ⁱPr₂**.

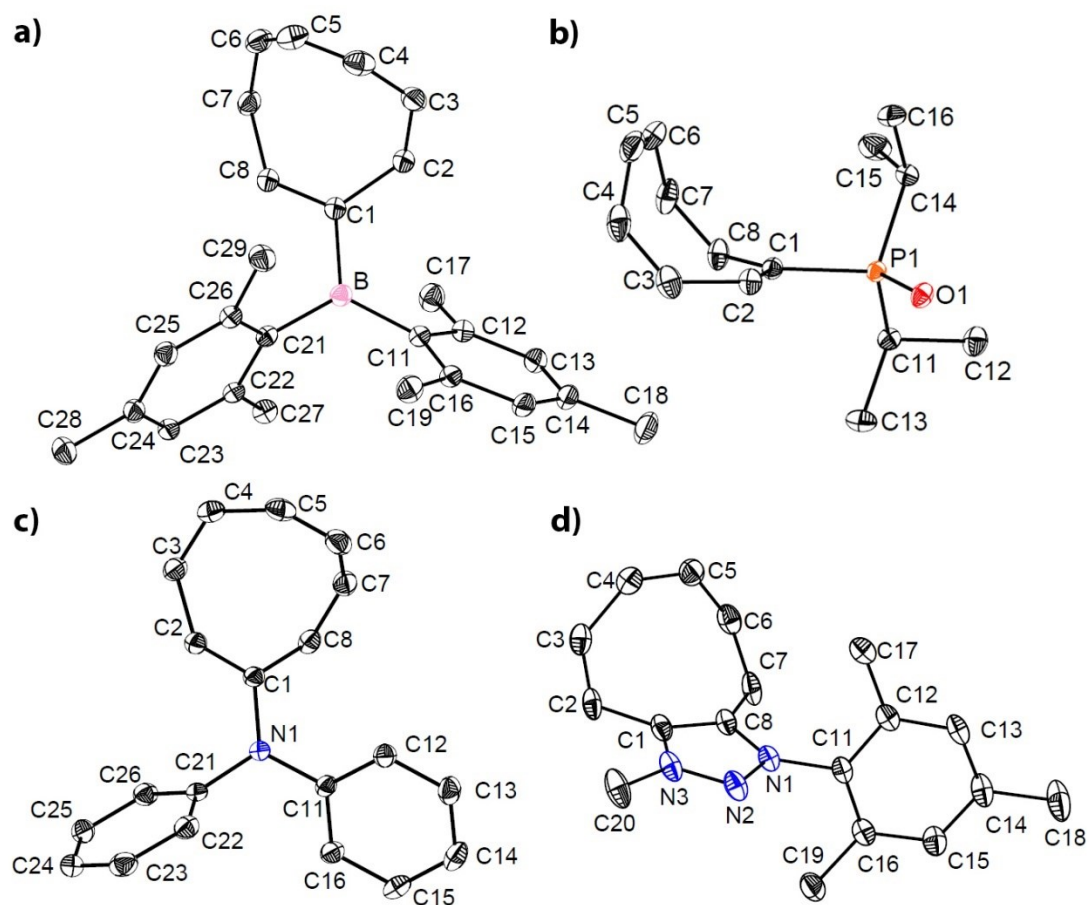


Figure 3.2. Crystal structures of: a) **COT-BMes₂**; b) **COT-P(O)ⁱPr₂** (H_2O solvate omitted); c) **COT-NPh₂**; d) **[COT-N₃-Mes]OTf** (OTf anion omitted) with thermal ellipsoids at a 30 % probability level; all hydrogen atoms omitted for clarity.

The COT-Br/ KO^tBu -derived alkyne, 1,3,5-cyclooctatriene-7-yne,^{20a,21} was also used to yield the ring-fused triazole-cyclooctatetraene precursor **COT-N₃-Mes** (Scheme 3.1) via strain-promoted Click chemistry. Specifically, addition of KO^tBu to a 1.3:1 mixture of COT-Br and mesityl azide (MesN_3) at 30 °C, followed by product purification by column chromatography, affords **COT-N₃-Mes** as a light-yellow solid

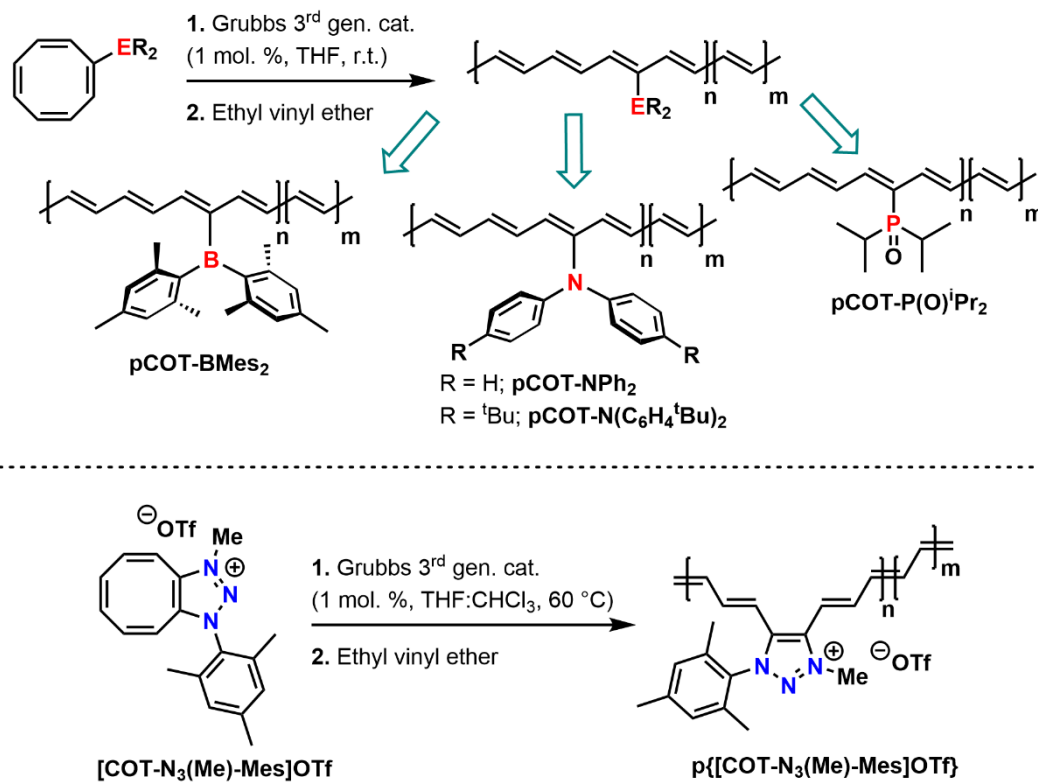
in 81 % yield. The required monomer for the ring-opening polymerization chemistry mentioned later, **[COT-N₃(Me)-Mes]OTf**, was obtained as a white solid in a 93 % yield via the addition methyl triflate to **COT-N₃-Mes** in Et₂O (Scheme 3.1). The single crystal X-ray structure of **[COT-N₃(Me)-Mes]OTf** shows retention of the eight-membered COT unit that is fused to a planar triazolium heterocycle. The intraring N-N distances in this salt range from 1.3183(19) to 1.3274(17) Å and are consistent with the retention of π -bonding character within the triazole scaffold (Figure 3.2d). Given that the formal alkyne/azide "Click" cycloaddition reaction used to form **COT-N₃-Mes** transpired under mild conditions, and in the absence of a Cu-catalyst, it is expected that a very wide range of new COT-based monomers for polymerization could be obtained *via* this simple protocol.

3.2.2 Polymer Synthesis

3.2.2.1. Boryl-Functionalized Polyacetylene

The initial polymerization trials focused on the borylated monomer **COT-BMes₂**. It was hoped that incorporation of an electron-deficient -BMes₂ group onto an unsaturated polyacetylene backbone would lead to redox behavior not found in previously known soluble alkyl- and trimethylsilyl-substituted variants.^{7,13c,14b} Added motivation for this work stems from the known use of -BR₂ groups to tune the optoelectronic (and often luminescent) properties of conjugated polymers through π -B(p) interactions and the corresponding use of this property for F⁻ and CN⁻ ion

sensing.²² Furthermore, the presence of Lewis acidic boryl sites might enable future structural manipulation, as demonstrated by self-healing frustrated Lewis pair (FLP)-containing polymers.²³



Scheme 3.2. Polymer synthesis.

When **COT-BMes₂** was mixed with 1 mol. % of Grubbs' 3rd generation (**G3**) catalyst in THF, the reaction mixture went from yellow to deep purple within 3 hrs. Work-up of the reaction mixture (including quenching of the mixture with EtO-CH=CH₂) and subsequent polymer purification yielded the functionalized polyacetylene **pCOT-BMes₂** as a deep blue solid in a 39 % yield (Scheme 3.2). As

expected, broadened ^1H NMR resonances for **pCOT-BMes₂** were found in C_6D_6 , and gel permeation chromatography (GPC) confirmed the formation of a polymer with a weight-average molecular weight (M_w) of 65 kDa. The accompanying polydispersity index (PDI) of the polymer was 3.1 (Table 3.1), suggesting that competing backbiting chemistry was transpiring, leading to a large distribution in chain length. This postulate was confirmed when the polymerization of **COT-BMes₂** was tracked by ^1H NMR spectroscopy in a 1:1 THF: C_6D_6 mixture (Figure 3.3). During the ROMP of **COT-BMes₂**, the backbiting/cycloextrusion product PhBMes₂ could be detected overtime (Figure 3.3c, see also Figure 3.73 in Section 3.4.4).²⁴ While this side reaction does lead to a loss of side group regioregularity, it does bring an added benefit: this process leads to an overall increase in the average number of carbon atoms between -BMes₂ side chains from an expected value of 8 to approximately 11 (as determined by ^1H NMR analysis) which further decreases side chain density and facilitates the retention of extended π -conjugation along the polymer backbone.

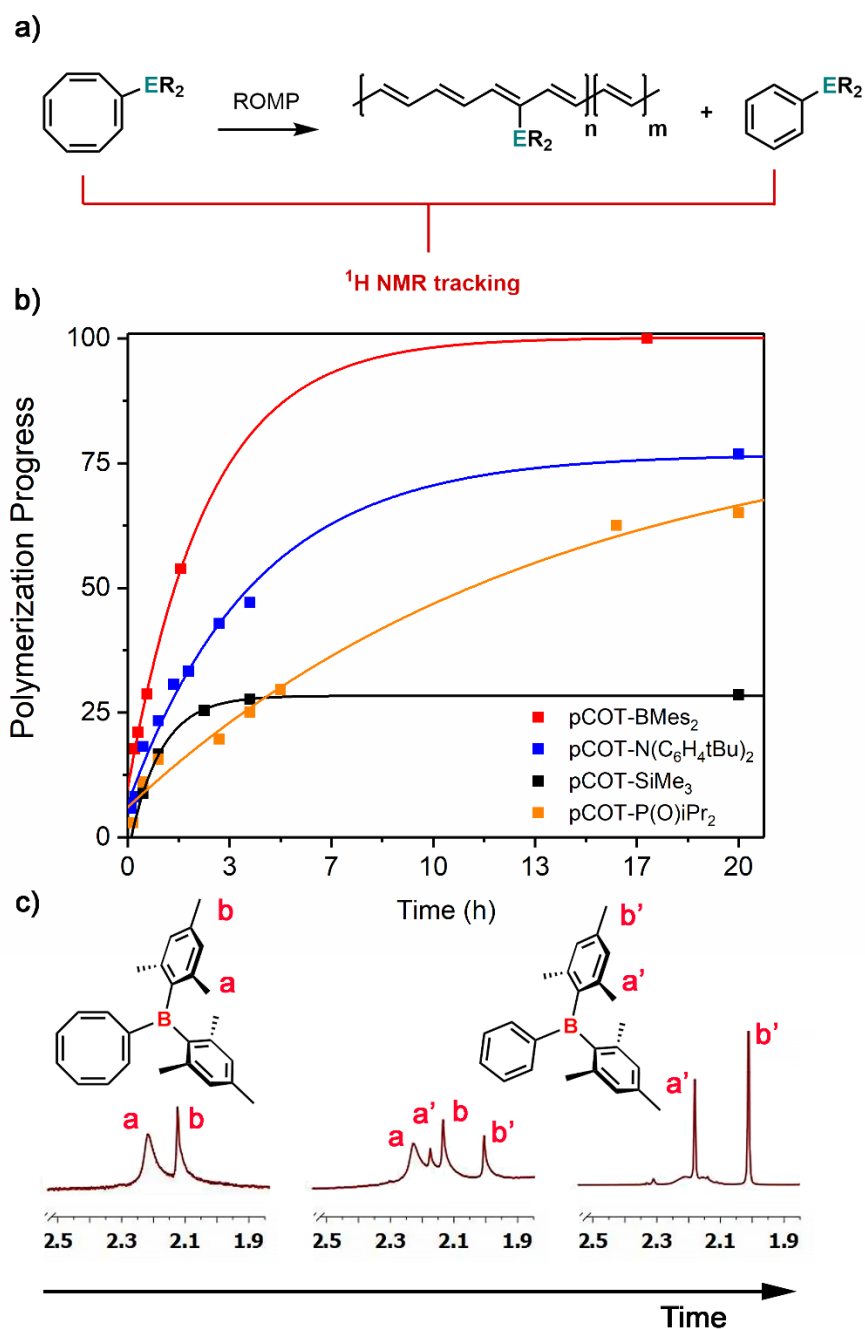
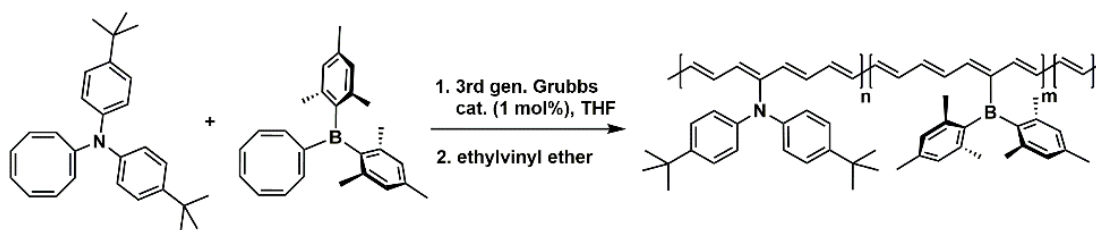


Figure 3.3. a) ROMP leading to polymer formation and backbiting side-product; b) Polymerization progress as a function of time for monosubstituted monomers; c) Alkyl region of ¹H NMR spectra (in C₆D₆/THF) during the polymerization of COT-BMes₂.

3.2.2.2. Amino-Functionalized Polyacetylenes

Due to the successful ROMP of **COT-BMes₂**, a series of polymers bearing potentially electron-donating (n-doping) diarylamino groups were then prepared. Since triaryl amines, Ar₃N, have shown redox activity (*e.g.*, via formation of stable Ar₃N^{•+} radicals),²⁵ one could hope that this property would open up new avenues of study for diarylamino-functionalized polyacetylenes, including in spintronics.²⁶ As shown in Figure 3.3, the polymerization of **COT-N(C₆H₄^tBu)₂** is considerably slower than for **COT-BMes₂** with 50 % monomer conversion after 3 hrs, possibly due to weak/reversible coordination of the -NAr₂ sites to the Ru center in Grubbs' **G3** catalyst. The resulting purified polymer **pCOT-N(C₆H₄^tBu)₂** was obtained as a blue solid with a modest M_w value of 32 kDa (PDA = 4.1), as determined by GPC analysis. Similar results were noted for the polymerization of **COT-NPh₂**, although the resulting dark polymer, **pCOT-NPh₂**, was less soluble and GPC afforded a lower M_w value of 13 kDa. Additionally, it is possible to copolymerize **COT-BMes₂** and **COT-N(C₆H₄^tBu)₂** to obtain the random copolymer **p[COT-N(C₆H₄^tBu)₂-*r*-COT-BMes₂]** (Scheme 3.3) with a monomodal molecular weight distribution determined by GPC (Figure 3.88 in Section 3.4.6).



Scheme 3.3. Copolymerization of **COT-BMes₂** and **COT-N(C₆H₄^tBu)₂**.

3.2.2.3. Phosphorus-Functionalized Polyacetylenes

Phosphorus-containing polymers have attracted interest from the scientific community due to their ability to coordinate metals (*e.g.*, in Au recovery), and their often luminescent and even their flame-resistant properties.²⁷ Despite the vast knowledge related to the synthesis of phosphorus-based molecules and polymers, a P-functionalized polyacetylene was absent from the literature. Combining **COT-PⁱPr₂** with up to 5 mol. % of Grubbs' 3rd generation catalyst (**G3**) showed no sign of polymer formation, even after heating in THF to 60 °C; it is likely that **COT-PⁱPr₂** coordinates to the active site of the catalyst, thus obviating ROMP. When the phosphine-oxide monomer **COT-P(O)ⁱPr₂** was mixed with 1 mol. % of **G3** catalyst in THF, a polymeric red solid **pCOT-P(O)ⁱPr₂** was obtained in a 38 % yield after work-up. This polymer displayed the expected broadened ¹H NMR resonances in C₆D₆ (Figure 3.71 in Section 3.4.4), and evidence for the regiorandom placement of the **-P(O)ⁱPr₂** groups along the polymer chain arose via the observation of a cluster of three ³¹P resonances at 46.9, 49.2, and 51.4 ppm (Figure 3.4). Unfortunately, it was not possible to obtain reliable GPC data for **pCOT-P(O)ⁱPr₂** due to absorption of this polymer onto the column, even in the presence of a salt (0.1 w/w % of [ⁿBu₄N]Br); however dynamic light-scattering (DLS) was consistent with polymer formation (Figure 3.5).

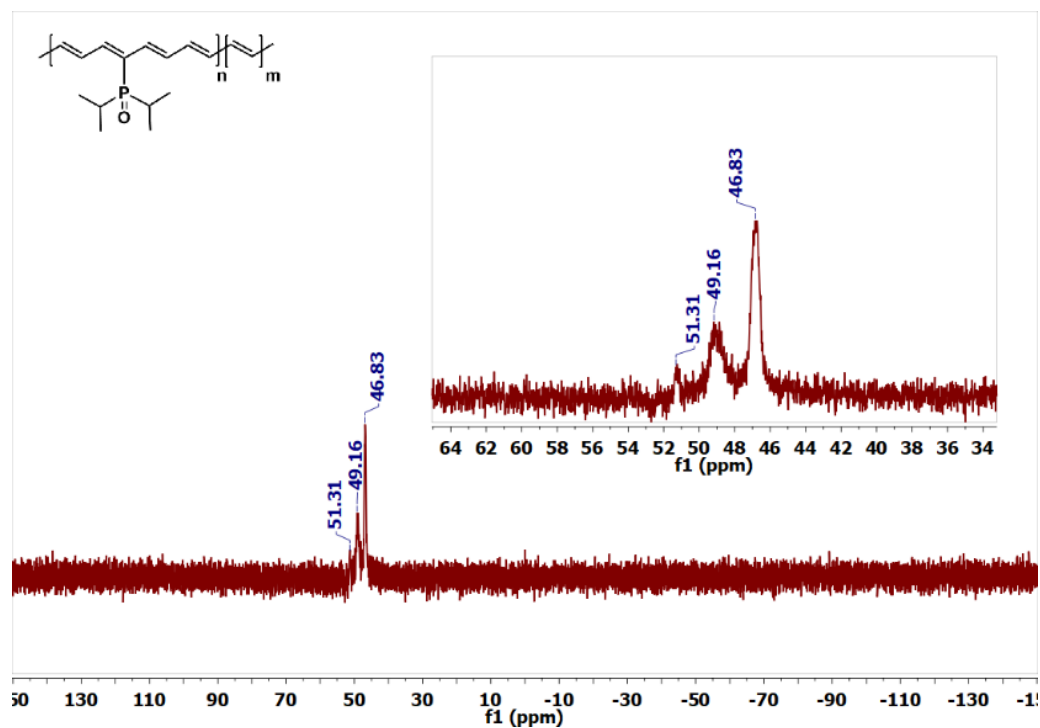


Figure 3.4. $^{31}\text{P}\{^1\text{H}\}$ NMR spectrum of $\text{pCOT-P(O)}^i\text{Pr}_2$ in C_6D_6 .

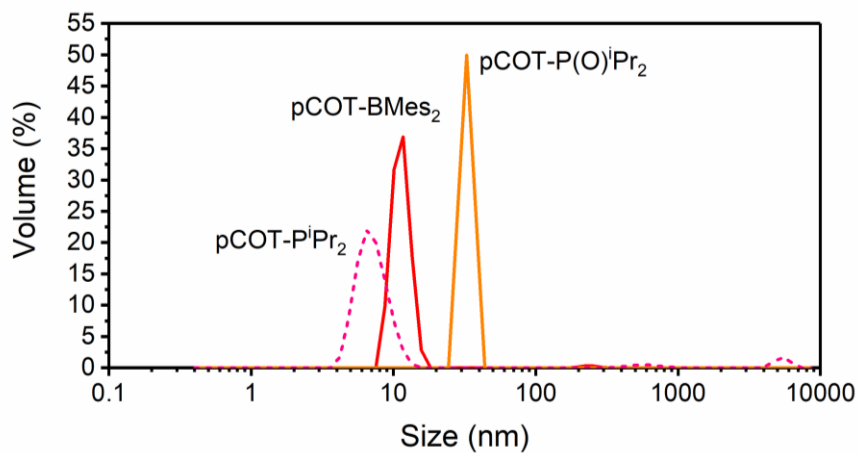
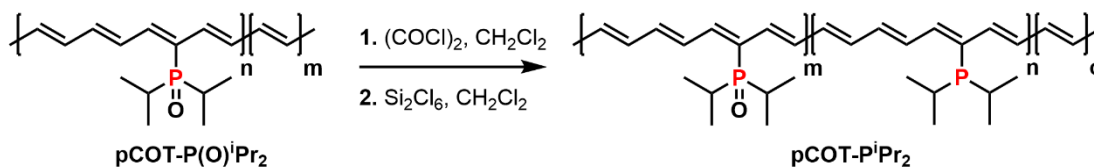


Figure 3.5. Size distribution by volume for pCOT-BMes_2 , $\text{pCOT-P(O)}^i\text{Pr}_2$ and pCOT-Pr_2 as determined by dynamic light-scattering (DLS) in THF. Based on size relative to pCOT-BMes_2 (M_n determined by GPC = 20.7 kDa), M_n values were estimated to be: $\text{pCOT-P(O)}^i\text{Pr}_2$ M_n = 41 kDa, pCOT-Pr_2 , M_n = 8 kDa.

To obtain a polymer with potentially coordinating/ligating $-P^iPr_2$ groups, a post-polymerization protocol involving reduction of the $-P(O)^iPr_2$ groups in **pCOT- $P(O)^iPr_2$** was attempted (Scheme 3.4). Specifically, combining **pCOT- $P(O)^iPr_2$** with $(COCl)_2$ followed by addition of Si_2Cl_6 and purification afforded a pink-colored product, **pCOT- P^iPr_2** , in 12 % yield. The UV-Vis spectral shift for **pCOT- P^iPr_2** ($\lambda_{max} = 503$ nm) compared to **pCOT- $P(O)^iPr_2$** ($\lambda_{max} = 460$ nm) along with the emergence of a new set of three broad peaks in the ^{31}P NMR spectrum of **pCOT- P^iPr_2** assigned to $-P^iPr_2$ (24.1, 4.2, and -3.1 ppm, Figure 3.6) provide evidence for the successful transformation. However, it must be noted that the ^{31}P NMR spectrum of **pCOT- P^iPr_2** also shows the presence of leftover $-P(O)^iPr_2$ moieties (Figure 3.6), indicating that the conversion into $-P^iPr_2$ was not quantitative. DLS measurements of **pCOT- P^iPr_2** in THF indicate retention of a hydrodynamic radius ($R_h = 6$ nm) that is similar to **pCOT-BMes₂** ($R_h = 10$ nm, Figure 3.5).



Scheme 3.4. Reduction of **pCOT- $P(O)^iPr_2$** into **pCOT- P^iPr_2** .

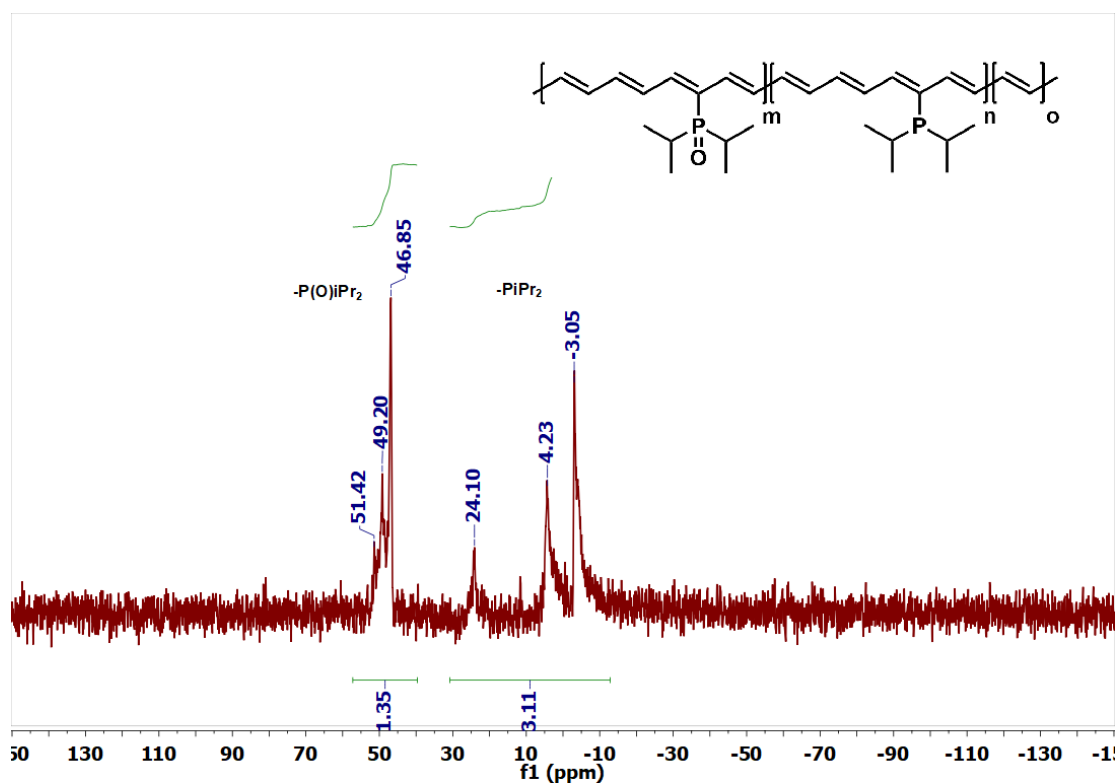


Figure 3.6. $^{31}\text{P}\{^1\text{H}\}$ NMR spectrum of pCOT- P^iPr_2 in C_6D_6 .

3.2.2.4. Triazolium Ring-Fused Polyacetylene

To further increase the possible side group diversity in polyacetylenes, the formation of triazolium ring-fused polyacetylenes was studied. Initial attempts to ring-open polymerize **COT-N₃-Mes** with Grubbs' **G3** catalyst led to no reaction; which parallels the lack of ROMP activity found for arene-fused cyclooctatetraenes.²⁸ However, the monomer containing a cationic triazolium unit, [**COT-N₃(Me)-Mes**]**OTf**, possessed sufficient internal ring strain to enable ROMP to occur, either in THF or CHCl_3 :THF 1:1 mixtures, as indicated by a color change of the mixture from

light yellow to deep orange upon addition of 1 mol. % of **G3** (Figure 3.7). As with the previously described COT-R monomers, the ROMP of **[COT-N₃(Me)-Mes]OTf** generated some backbiting side product, which could be identified in solution by ¹H NMR spectroscopy (Figure 3.79).

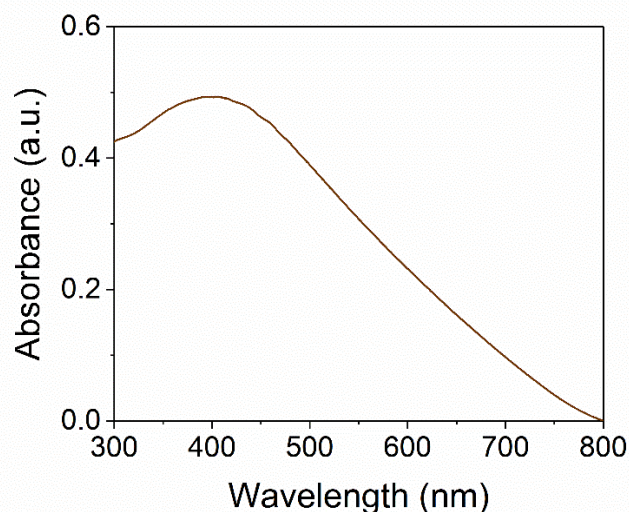


Figure 3.7. Absorption spectrum of **p{[COT-N₃(Me)-Mes]OTf}** as a suspension in THF (*ca.* 1 mg/mL). The mixture was sonicated for one minute prior to recording the data.

Unfortunately, the resulting dark-brown polymer **p{[COT-N₃(Me)-Mes]OTf}** is insoluble in standard solvents. Analysis of the polymer by solid state IR revealed retention of the expected triazolium $\nu(\text{N-N})$, OTf $\nu(\text{C-F})$ and $\nu(\text{SO}_3)$ stretches, while the characteristic C-H out of plane deformation for *trans*-polyacetylene was noted at 1007 cm^{-1} (Figure 3.8).¹⁰ Despite the low solubility of this first generation triazolium

ring-fused polyacetylene, the overall synthetic protocol introduced is likely applicable to the extensive library of known azides in order to synthesize countless new polyelectrolytes of interest for batteries and other electronic devices;²⁹ work towards this goal is ongoing.

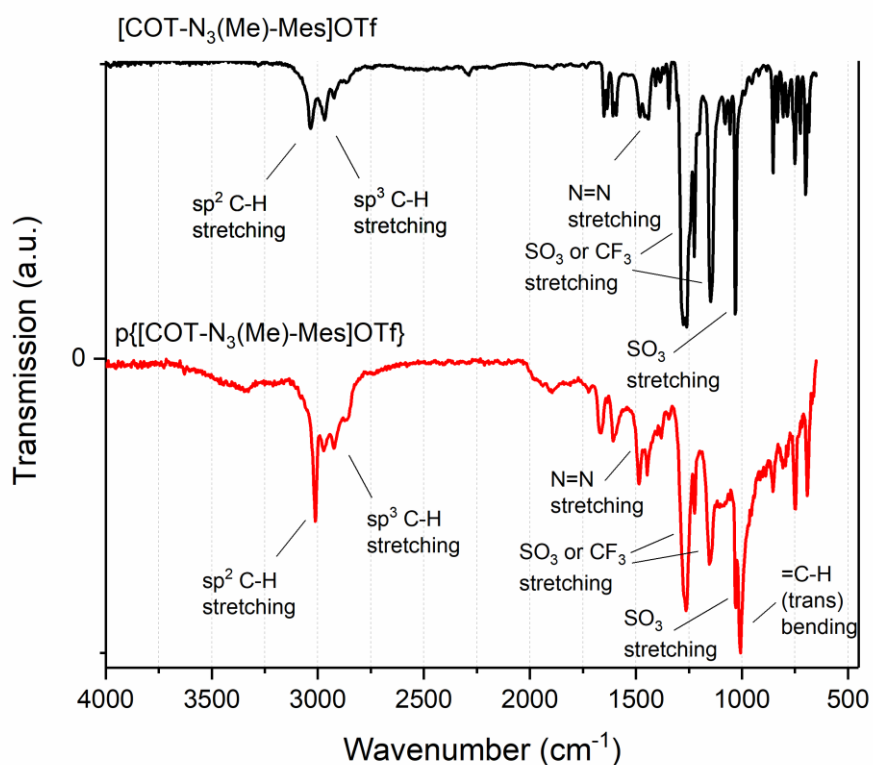


Figure 3.8. Solid state FT-IR spectra of $[\text{COT-N}_3(\text{Me})\text{-Mes}]\text{OTf}$ and its polymer $\text{p}\{[\text{COT-N}_3(\text{Me})\text{-Mes}]\text{OTf}\}$.

The soluble functionalized polyacetylenes listed in Table 3.1 can be dissolved in THF, CH_2Cl_2 or toluene, and are stable as solids (under N_2) up to *ca.* 180-200 °C, as

determined by thermal gravimetric analysis (TGA, Section 3.4.8). As a result of the regiorandom structure of the polymers (due to backbiting), it was not possible to obtain informative differential-scanning calorimetry (DSC) data for the determination of glass transition temperatures (T_g). The impressive impact of introducing inorganic functional groups onto a polyacetylene backbone on air stability will be mentioned later in this Chapter.

Table 3.1. Summary of polymerization trials.

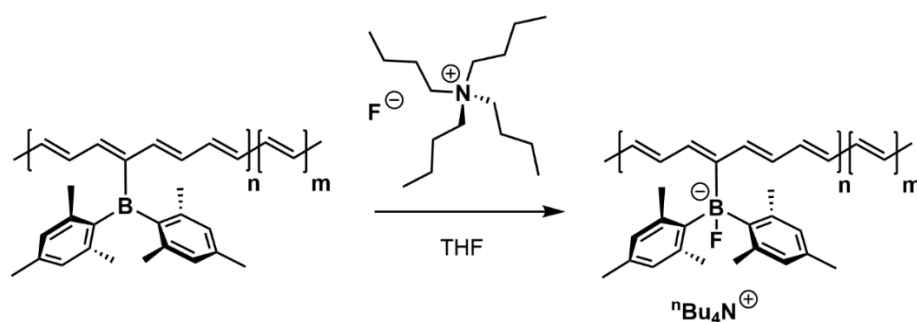
Polymer	Yield	M_w	PDI	#C *	Soluble?
pCOT-SiMe ₃	7 %	41 kDa	4.2	11	Yes
pCOT-BMes ₂	39 %	65 kDa	3.1	11	Yes
pCOT-NPh ₂	36 %	13 kDa	3.2	11	Yes
pCOT-N(C ₆ H ₄ ^t Bu) ₂	13 %	32 kDa	4.1	10	Yes
pCOT-P(O) ⁱ Pr ₂	38 %	--	--	11	Yes
p{[COT-N ₃ (Me)-Mes]OTf}	20 %	--	--	--	No

* - Average number of carbons per side chain

3.2.3 Reactivity and Properties of pCOT-BMes₂

Due to the availability of the empty p-orbital on boron, the reactivity of pCOT-BMes₂ towards electron-rich species was studied. As an initial test for the Lewis acidity of the -BMes₂ sites in pCOT-BMes₂, this polymer was combined with [ⁿBu₄N]F in THF/CDCl₃ (Scheme 3.5) to give a new species with a broad ¹¹B NMR resonance at 2.5 ppm (Figure 3.9). Repeating the same reaction between F⁻ and monomeric COT-BMes₂ gave a well-defined fluoroborate salt [ⁿBu₄N][COT-BMes₂(F)], which was

structurally characterized by single crystal X-ray crystallography (Figure 3.10) and a similar ^{11}B resonance (4.7 ppm in CDCl_3) was found as in $[\text{pCOT-BMes}_2(\text{F})]^-$; furthermore, both the fluorinated monomer and polymer gave ^{19}F resonances in the -167 to -172 ppm spectral region (Figure 3.81 in Section 3.4.4). Thus, pCOT-BMes_2 is sufficiently Lewis acidic to bind fluoride.



Scheme 3.5. Reaction of pCOT-BMes_2 with $[\text{nBu}_4\text{N}]\text{F}$.

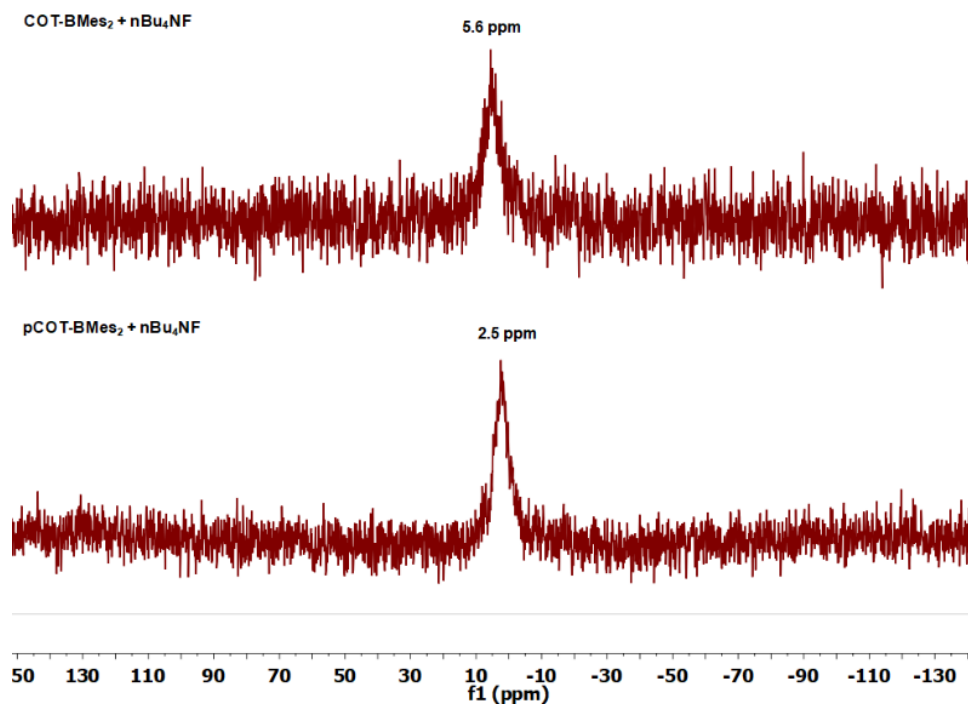


Figure 3.9. Crude ^{11}B NMR spectrum after fluoride binding to **COT-BMes₂** (C_6D_6 , top) and **pCOT-BMes₂** (THF + CDCl_3 , bottom).

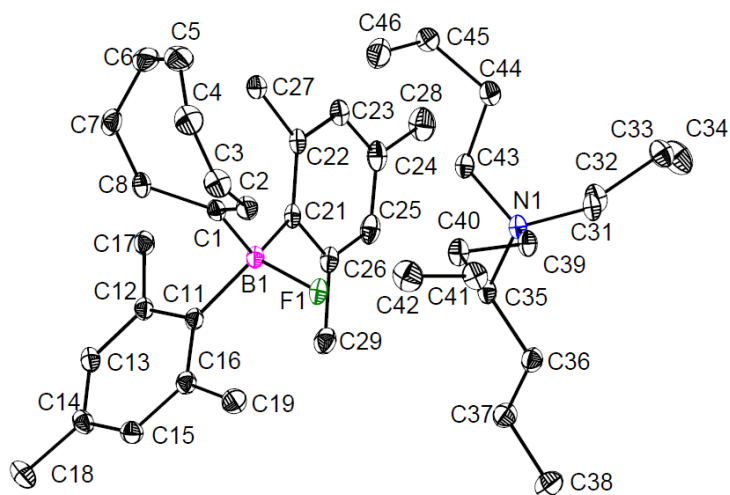


Figure 3.10. Molecular structure of $[n\text{Bu}_4\text{N}][\text{COT-BMes}_2(\text{F})]$ with thermal ellipsoids plotted at a 30 % probability level; all hydrogen atoms omitted for clarity.

The ability of $p\text{COT-BMes}_2$ to bind a hydride (H^-) was evaluated through the addition of the soluble hydride source $\text{Li}[\text{HBEt}_3]$. ^{11}B NMR spectroscopic analysis of the resulting crude product indicated the presence of multiple species (Figure 3.11), but, interestingly, there is a detectable amount of a compound containing a boron atom linked to two hydrogen atoms at -22.6 ppm ($^1J_{\text{BH}} = 63$ Hz). Additional analysis through ^1H NMR spectroscopy shows the presence of sharp peaks related to mesityl groups (Mes), which suggests formation of $[\text{H}_2\text{BMes}_2]^-$ from cleavage of the $-\text{BMes}_2$ moieties from polymeric backbone. As a result of this deboronation process, further reactivity with hydrides was not explored.

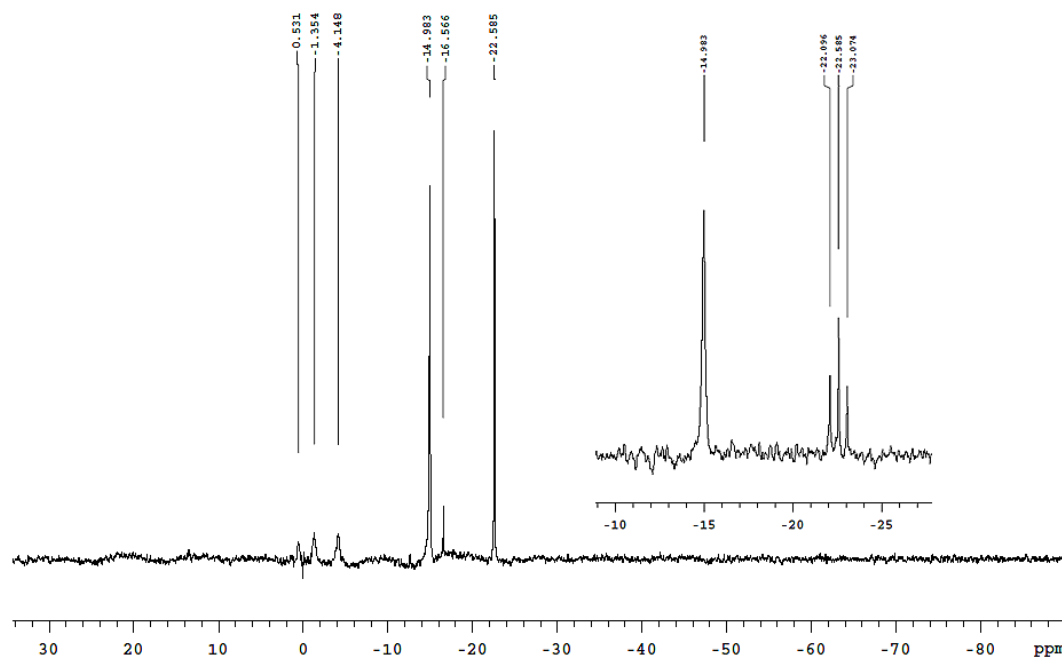
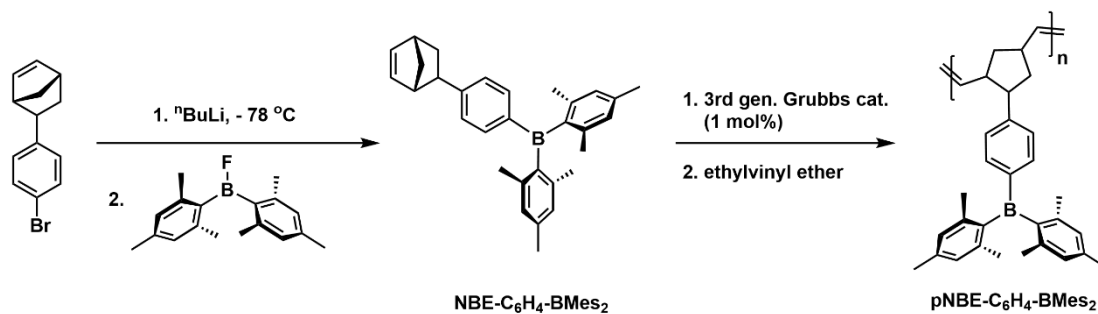


Figure 3.11. $^{11}\text{B}\{^1\text{H}\}$ NMR spectrum of the reaction mixture from **pCOT-BMes₂** and $\text{Li}[\text{HBET}_3]$ in THF. The inset shows the splitting of the signal at -23 ppm into a triplet in the H-coupled ^{11}B NMR spectrum (128 MHz).

The possible luminescence of **pCOT-BMes₂** was also investigated, however, no emission was noted upon excitation at 350 nm. One postulate for this observation is that communication between the -BMes₂ groups and the polyacetylene chain occurs in the excited state (*vide infra*), providing a pathway for non-radiative decay. A polynorbornadiene with -BMes₂ side groups was also prepared, **pNBE-C₆H₄-BMes₂** (Scheme 3.6), and showed blue fluorescence (Section 3.4.10), as expected for a R-BMes₂ species;³⁰ this provides added support for the postulate that the polyacetylene backbone is facilitating emission quenching in **pCOT-BMes₂**.



Scheme 3.6. Synthetic route to a polynorbornadiene (**pNBE-C₆H₄-BMes₂**) with -BMes₂ groups.

3.2.4 Optoelectronic Data of the Functional Polyacetylenes

The polymer with largest M_w , **pCOT-BMes₂**, forms a lustrous golden film upon slow evaporation of the solvent (THF) (Figure 3.12); of note, formation of metal-colored films is a hallmark of parent polyacetylene,^{1-3,13d} similarly to a partially fluorinated polyacetylene recently reported that shows a golden color in the film state.¹¹ UV-Vis spectra of the functionalized polyacetylenes in THF (Figure 3.13) show red-shifting of the absorption maxima (λ_{max}) in THF from 552 nm (**pCOT-SiMe₃**) to 569 nm (**pCOT-BMes₂** and **pCOT-NPh₂**) and 603 nm (**pCOT-N(C₆H₄^tBu)₂**); the phosphoryl-substituted polymer **pCOT-P(O)ⁱPr₂** exhibits the most blue-shifted absorption profile of the series, with a λ_{max} of 460 nm. At this stage it is unclear why the absorption profile of **pCOT-P(O)ⁱPr₂** is blue-shifted, but the onset of light absorption for this species, 651 nm ($E_g = 1.90$ eV), is similar to that of **pCOT-SiMe₃**, which also shows minimal participation of the side group in the HOMO-LUMO

transition. It should be stated that all of these polymers show intense light absorption in THF with estimated molar extinction coefficients $> 10^4$ L/mol•cm per monomer unit.



Figure 3.12. A film of pCOT-BMes₂ obtained after slow evaporation of THF.

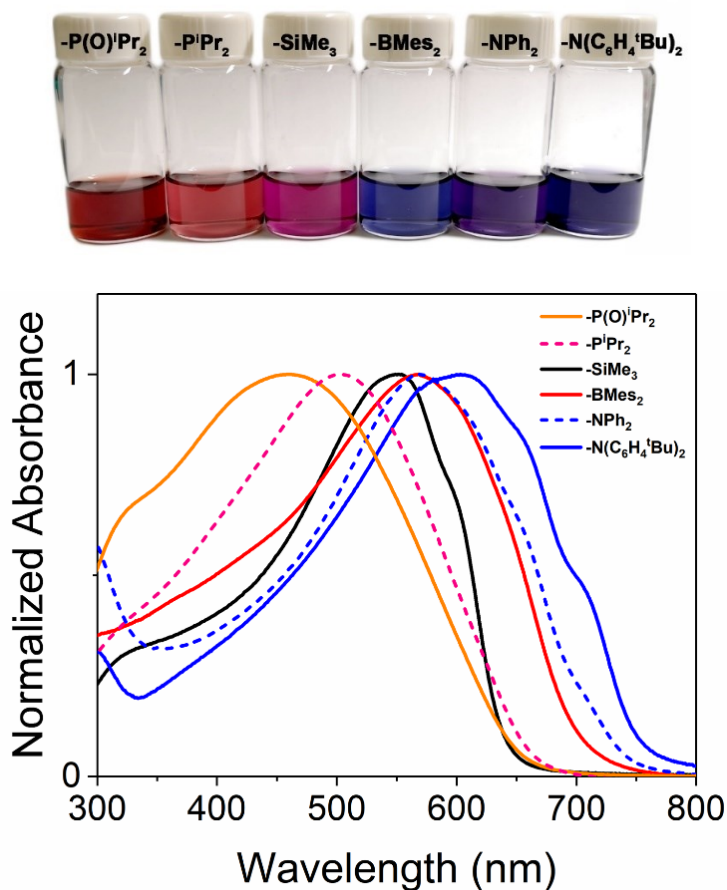


Figure 3.13. Picture of polymers in THF (top) and UV-Vis spectra of soluble polyacetylenes in THF (bottom).

The trend in UV-Vis absorption for the polyacetylenes is maintained in the solid state (Figure 3.14) with red-shifted λ_{max} compared to in solution, and noticeable light absorption tailing up to 700-800 nm in most cases. Fitting the solid state absorption data results in extracted optical HOMO-LUMO gaps (E_g) that rank (highest to lowest) from: **pCOT-SiMe₃** (1.75 eV) > **pCOT-P(O)ⁱPr₂** (1.71 eV) > **pCOT-BMes₂** (1.63 eV) > **pCOT-N(C₆H₄^tBu)₂** (1.58 eV) > **pCOT-NPh₂** (1.55 eV). These results indicate

retention of a non-twisted backbone, even in the solid state, and HOMO-LUMO gaps that are close to that found in parent polyacetylene (*ca.* 1.4 eV).³ The effect of heteroatoms on the ground state optoelectronic properties are summarized in Table 3.2.

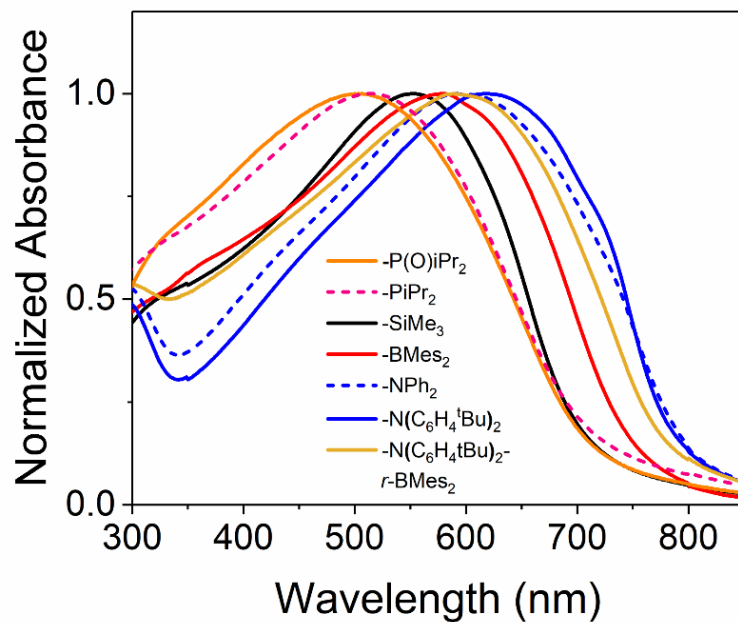


Figure 3.14. UV-Vis spectra of polymers as drop-cast films.

Table 3.2. Summary of experimental UV-Vis-NIR data for polyacetylenes.

	Solution (THF)			Drop-Cast Film			I ₂ Doped Film (spin coated)		
	λ_{\max} (nm)	λ_{onset} (nm)	E_g (eV)	λ_{\max} (nm)	λ_{onset} (nm)	E_g (eV)	NIR λ_{\max} (nm)	λ_{onset} (nm)	E_g (eV)
pCOT-SiMe₃	552	641	1.93	552	708	1.75	1953	>3000 ^a	<0.4 ^a
pCOT-P(O)ⁱPr₂	460	651	1.90	504	716	1.73	1039	1686	0.74
pCOT-PⁱPr₂	503	661	1.88	512	727	1.71	1012	1579	0.79
pCOT-BMes₂	569	703	1.76	579	757	1.63	1364	>3000 ^a	<0.4 ^a
pCOT-NPh₂	569	745	1.66	592	801	1.55	1030 ^b	1479	0.84
pCOT-N(C₆H₄^tBu)₂	603	755	1.64	617	787	1.58	1020 ^b	1553	0.80
p[COT-N(C₆H₄^tBu)₂-<i>r</i>-COT-BMes₂]	596	715	1.73	588	795	1.56	1130	>3000 ^a	<0.4 ^a

^a The identification of the absorption onset was not possible in the available spectrometer. ^b The absorption band in the NIR appears as a shoulder

Density functional theory computations (B3LYP/cc-pVDZ level) on polymer models revealed the non-innocent nature of the side groups. Specifically, a significant contribution of the p-orbital on B to the LUMO of **pCOT-BMes₂** and of the p-orbital on N to the HOMO of **pCOT-N(C₆H₄^tBu)₂** is present (Figure 3.15). In contrast, the SiMe₃ unit in **pCOT-SiMe₃** has no direct orbital influence, as the HOMO and LUMO are localized entirely on the olefinic backbone.

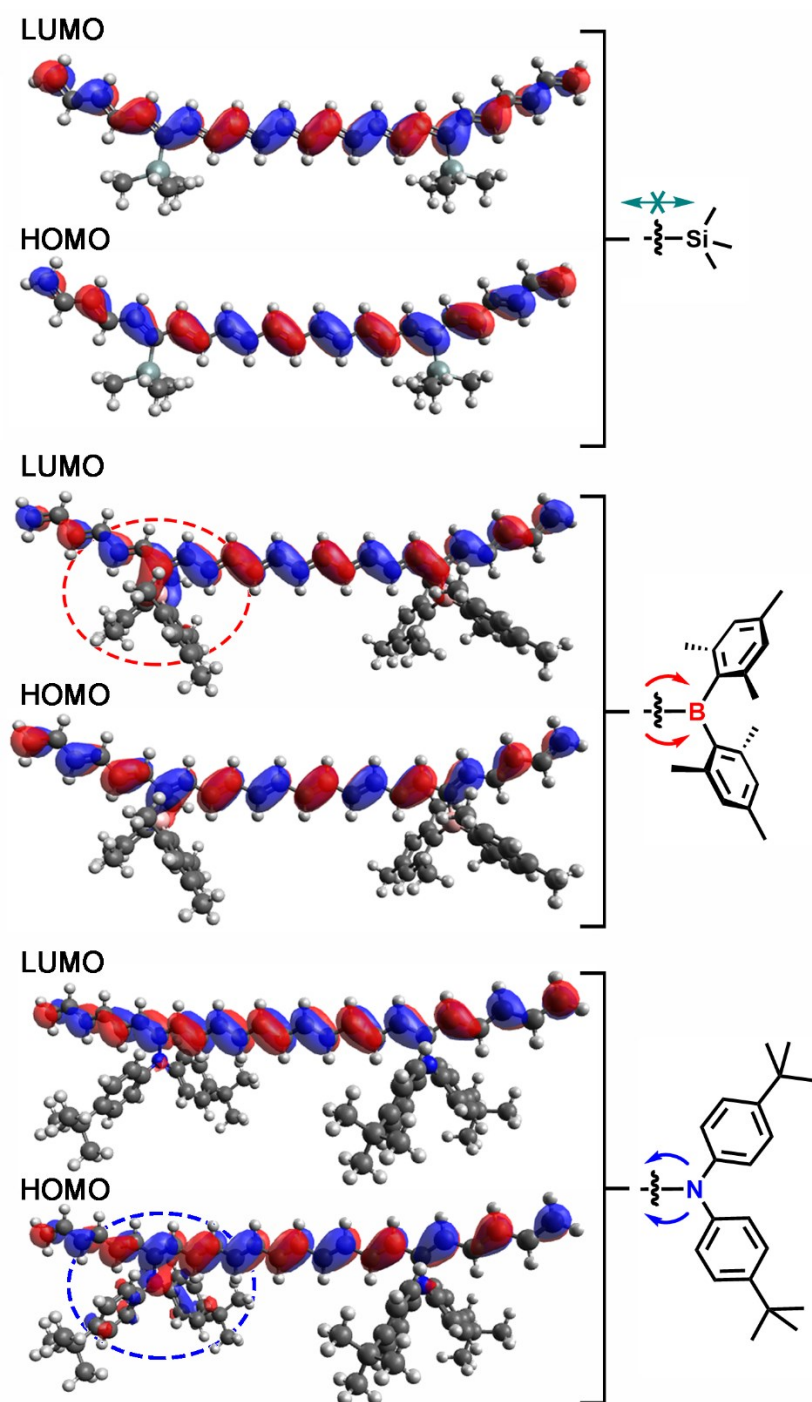


Figure 3.15. Computed frontier molecular orbitals (B3LYP/cc-pVDZ) for models of pCOT-SiMe₃, pCOT-BMes₂ and pCOT-N(C₆H₄^tBu)₂.

Side group influence was further confirmed by time-dependent DFT (Figure 3.16) where the computed energy of the HOMO-LUMO transitions decrease from the model of **pCOT-SiMe₃** (2.04 eV) to **pCOT-BMe₂** (1.93 eV) and **pCOT-N(C₆H₄^tBu)₂** (1.86 eV), matching the overall trend observed experimentally. To compare these results with parent polyacetylene (PA), a chain with no substituents was modeled (Figure 3.16). As expected, the unsubstituted chain shows a HOMO-LUMO transition closer to **pCOT-SiMe₃** at 2.09 eV, further confirming the ability of B and N to tune the E_g by side chain/polymer backbone interactions, while maintaining backbone planarity. The DFT computations also reveal that for structural models of **pCOT-P(O)ⁱPr₂** and **pCOT-PⁱPr₂**, the phosphorus-based side groups have no orbital participation to the HOMO or LUMO (Figure 3.114 in Section 3.5.1), which explains the matching E_g with **pCOT-SiMe₃** in both solution and films (Table 3.2).

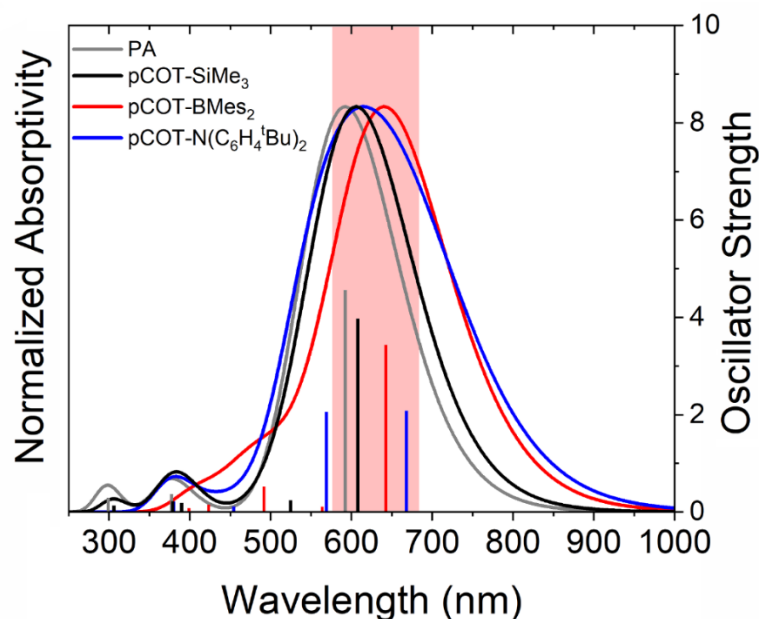


Figure 3.16. Computed UV-Vis spectra (B3LYP/cc-pVDZ) and comparison with parent polyacetylene (PA). The highlighted section shows transitions with predominantly HOMO to LUMO character.

3.2.5 Redox Activity of the Functionalized Polyacetylenes

An initial postulate associated with this work is that one can influence the redox properties of polyacetylenes via placement of redox-active groups directly onto the unsaturated polyolefin chain. To gain added insight into the influence of the potentially redox-active boryl and amino groups, cyclic voltammetry (CV) studies were performed on **pCOT-BMes₂** and **pCOT-N(C₆H₄^tBu)₂**. For reference, parallel CV measurements on **pCOT-SiMe₃**^{7,14b} were conducted, as DFT indicated a lack of participation of the -SiMe₃ groups in the frontier molecular orbitals, thus representing an example of an

electronically unperturbed polyacetylene. Scanning polymer solutions in THF with 0.10 M [ⁿBu₄N]BAr^F₄ (Ar^F = 3,5-(F₃C)₂C₆H₃) at a scan rate of 100 mV/s (Figure 3.17) reveals oxidation at more negative potentials for **pCOT-N(C₆H₄^tBu)₂** (-0.26 V compared to -0.01 V for **pCOT-SiMe₃**; relative to Fc⁺/Fc⁰), and reduction at more positive potentials for **pCOT-BMes₂** (-1.49 V compared to -1.60 V for **pCOT-SiMe₃**).

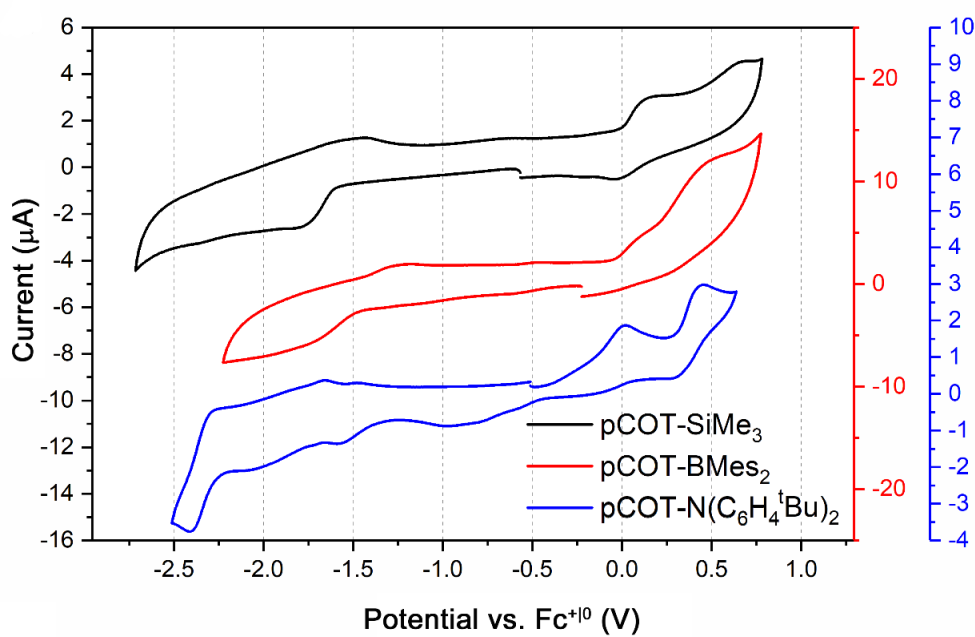


Figure 3.17. CV of **pCOT-SiMe₃**, **pCOT-BMes₂** and **pCOT-N(C₆H₄^tBu)₂** in THF (0.1 M [ⁿBu₄N]BAr^F₄, scan rate = 100 mV/s); Ar^F = 3,5-(F₃C)₂C₆H₃.

Both the oxidation for **pCOT-N(C₆H₄^tBu)₂** and reduction for **pCOT-BMes₂** are shifted towards 0 V relative to the monomers in solution, indicating that these events are not originating from the side chain alone (Figure 3.18 and Figure 3.19).

These results support the effective role of the side groups as intrinsic dopants that can either remove (-BMes₂, p-type doping) or donate electron density (-N(C₆H₄^tBu)₂, n-type doping) to shift the redox potentials, and the E_g levels of the polyacetylene units.

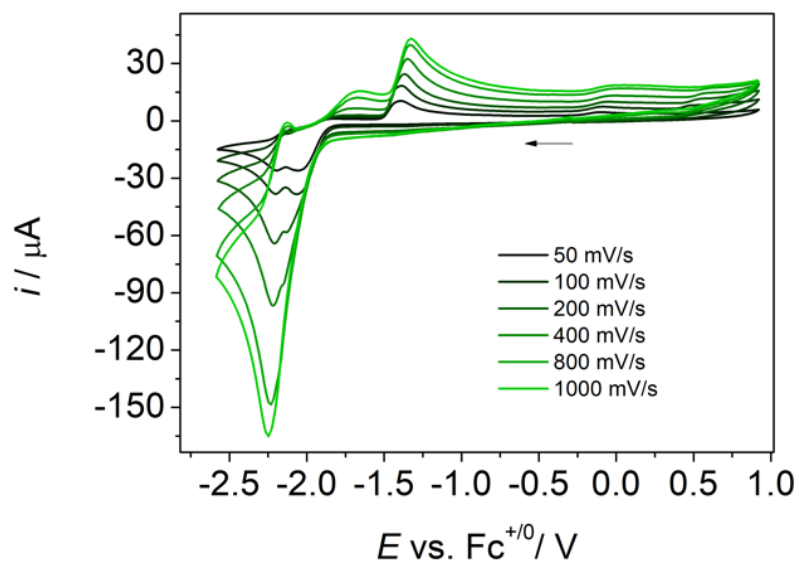


Figure 3.18. Scan rate-dependent CV data of **COT-BMes₂** (1 mM) in THF (0.10 M [ⁿBu₄N]BAr^F₄ electrolyte).

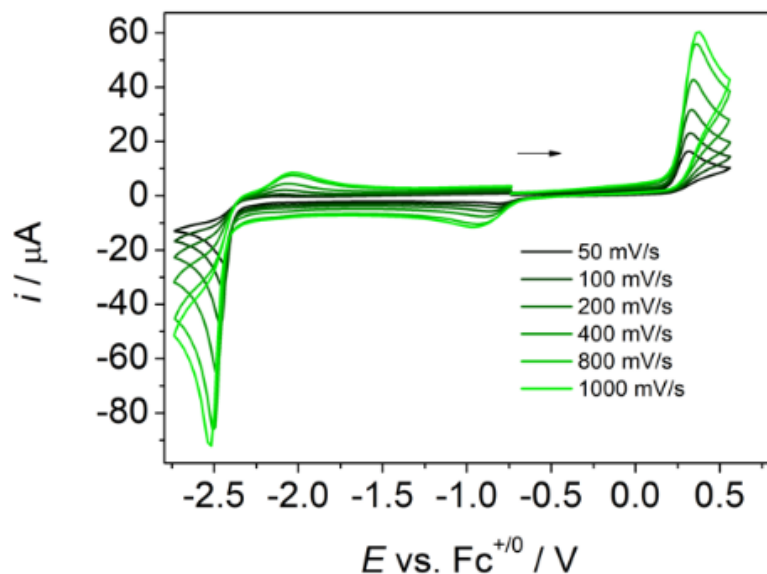


Figure 3.19. Scan rate-dependent CV data of **COT-N(C₆H₄^tBu)₂** (1 mM) in THF (0.10 M [ⁿBu₄N]BARF₄ electrolyte).

A dramatic effect is found in the near-IR spectral profiles of the functionalized polyacetylenes after oxidation/reduction, as shown by NIR spectroelectrochemistry (NIR-SEC). Solutions of **pCOT-BMes₂** and **pCOT-N(C₆H₄^tBu)₂** in THF (Figure 3.20) show opposing trends in absorption maxima when oxidized at 0.50 or 0.25 V ($\lambda_{\max}^{\text{BMes}_2} = 1396 \text{ nm}$; $\lambda_{\text{shoulder}}^{\text{NAr}_2} = \text{ca. } 900 \text{ nm}$) or reduced at -1.50 V vs. Fc⁺⁰ ($\lambda_{\max}^{\text{BMes}_2} = \text{ca. } 900 \text{ nm}$; $\lambda_{\max}^{\text{NAr}_2} = 1633 \text{ nm}$). In other words, oxidation of **pCOT-BMes₂** leads to an optical switch from the polymer being largely transparent in the telecommunications region (1500 nm) to being strongly absorbing/opaque. Conversely, **pCOT-N(C₆H₄^tBu)₂** is transparent at 1500 nm when neutral or oxidized, but reduction leads to the onset of substantial optical absorption at 1500 nm. However,

in the case of **pCOT-SiMe₃** (Figure 3.21), a similar and less pronounced absorption at 1500 nm is noted upon both oxidation and reduction: oxidation $\lambda_{\max}^{\text{SiMe}_3} = 1299$ nm; reduction $\lambda_{\max}^{\text{SiMe}_3} = 1244$ nm. Some reversibility of the reduction of **pCOT-SiMe₃** and oxidation of **pCOT-BMes₂** was noted after 3 cycles (see Section 3.4.11, Figure 3.107).

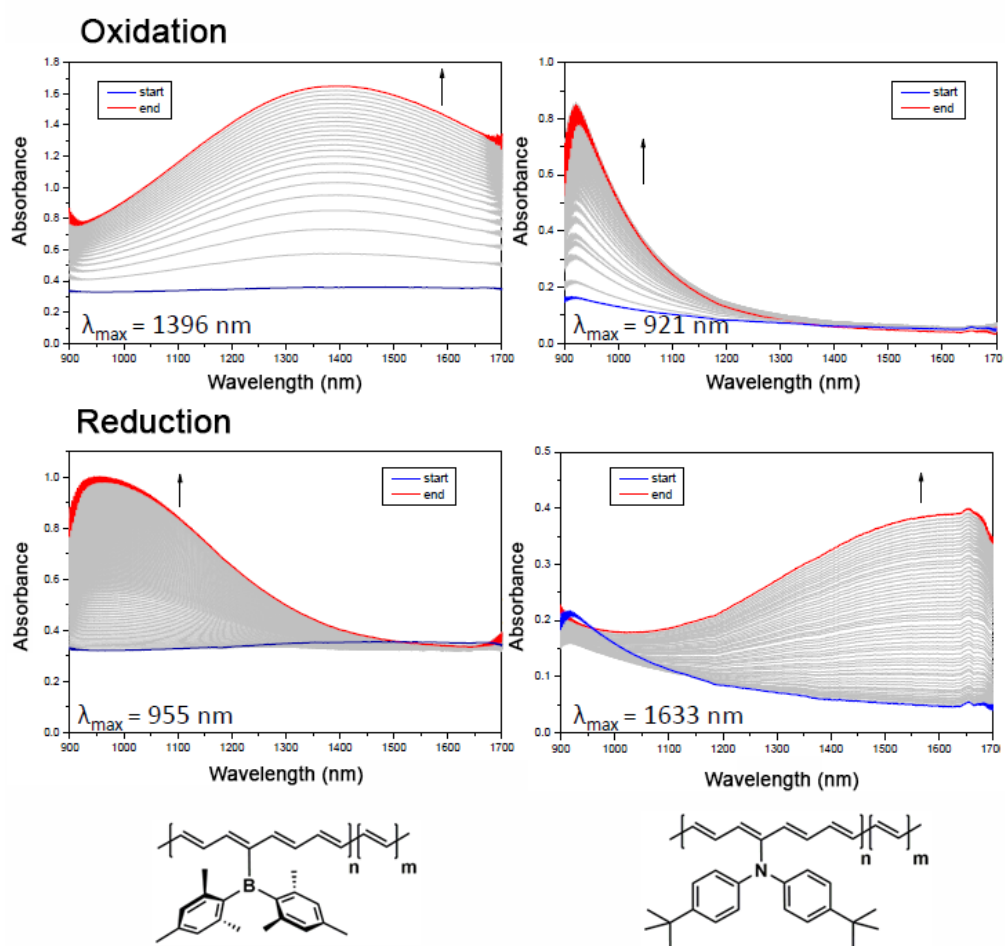


Figure 3.20. NIR-SEC (top: oxidative, bottom: reductive) scans of **pCOT-BMes₂** and **pCOT-N(C₆H₄^tBu)₂** in THF (0.10 M [ⁿBu₄N]BAR^F₄ electrolyte). Absorption profiles were measured every 12 seconds.

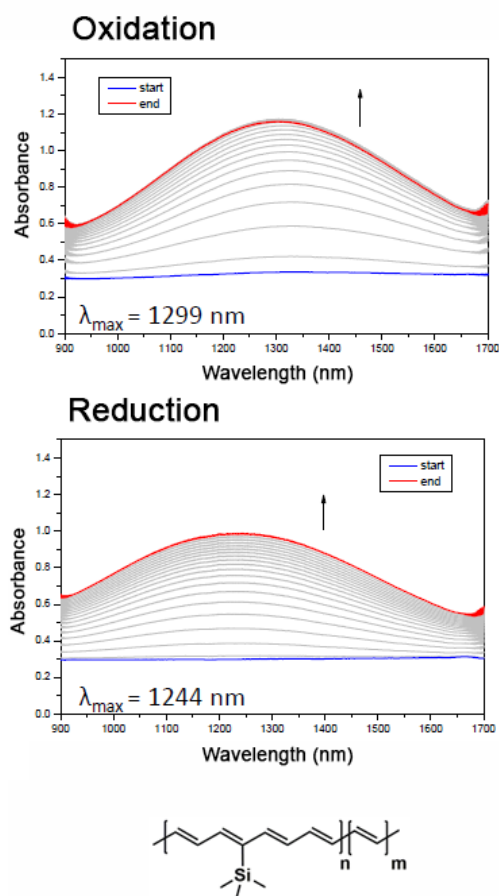


Figure 3.21. NIR-SEC (top: oxidative, bottom: reductive) of **pCOT-SiMe₃** in THF (0.10 M [ⁿBu₄N]BAR^F₄ electrolyte). Absorption profiles were measured every 12 seconds.

The opposing redox-triggered near-IR optical behavior of **pCOT-BMes₂** and **pCOT-N(C₆H₄^tBu)₂** has been seen before in some small molecule systems,³¹ but is new to polyacetylenes.^{14b} The spectral changes found in these NIR-SEC studies are also reproduced chemically, using Na[COPh₂] for reduction and [Fc]OTf for oxidation

(Figure 3.22), leading to doping in solution and intense NIR absorption profiles (*ca.* $1-3 \times 10^4$ L mol⁻¹cm⁻¹/monomer unit) that mirror those found by NIR-SEC.

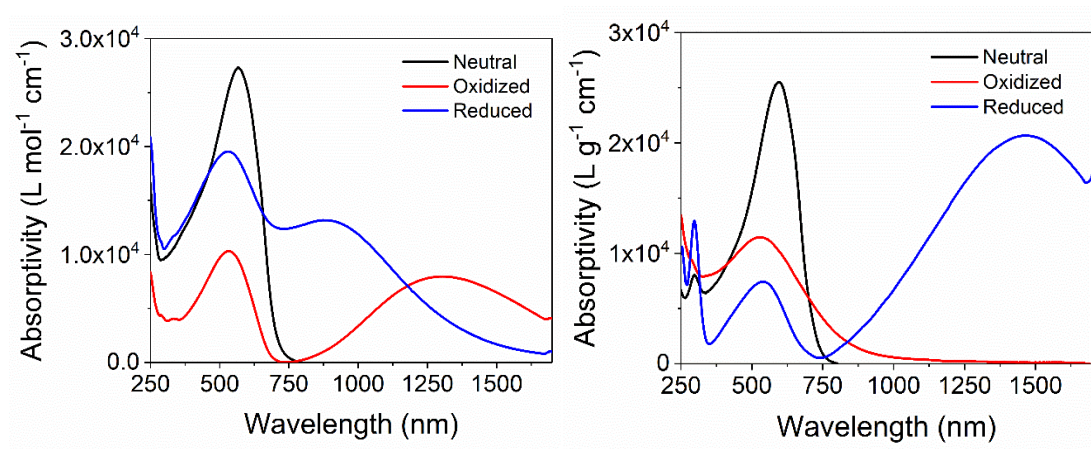


Figure 3.22. UV-Vis-NIR spectra of **pCOT-BMes₂** (left) and **pCOT-N(C₆H₄Bu)₂** (right) in THF (0.3×10^{-5} M) after chemical oxidation with [Fc]OTf and reduction with Na[COPh₂].

DFT computations on polymer models suggest involvement of boron in the SOMO of reduced **p[COT-BMes₂•]** and the nitrogen atom in the SOMO of the oxidized polymer **p[COT-N(C₆H₄Bu)₂•⁺]** (Figure 3.23), leading to the hypsochromic near-IR shift and the largely silent absorption behavior at 1500 nm. Unfortunately, TD-DFT computations with different basis sets and functionals could not reproduce the experimental results, with the oxidation and reduction maxima matching for the B, N and Si polyacetylenes (Section 3.5.1). However, by analysing the computed orbital energies for the three polymers, it appears that heteroatom involvement in the SOMO

leads to a higher energy SOMO to LUMO transition for $\text{p}[\text{COT-BMes}_2^{\bullet-}]$ and $\text{p}[\text{COT-N}(\text{C}_6\text{H}_4^t\text{Bu})_2^{\bullet+}]$, instead of a lower energy HOMO to SOMO transition that is seen for pCOT-SiMe_3 after either oxidation or reduction (Figure 3.24, see also Section 3.5.1).

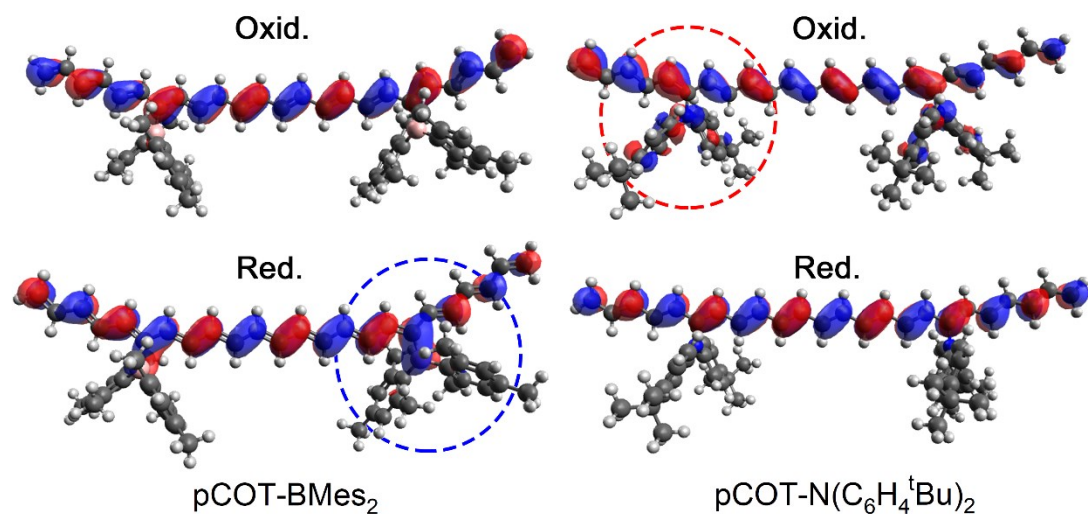


Figure 3.23. Computed SOMOs (B3LYP/cc-pVDZ) of pCOT-BMes_2 and $\text{pCOT-N}(\text{C}_6\text{H}_4^t\text{Bu})_2$ after oxidation and reduction. Dashed circles highlight orbital participation from the side group.

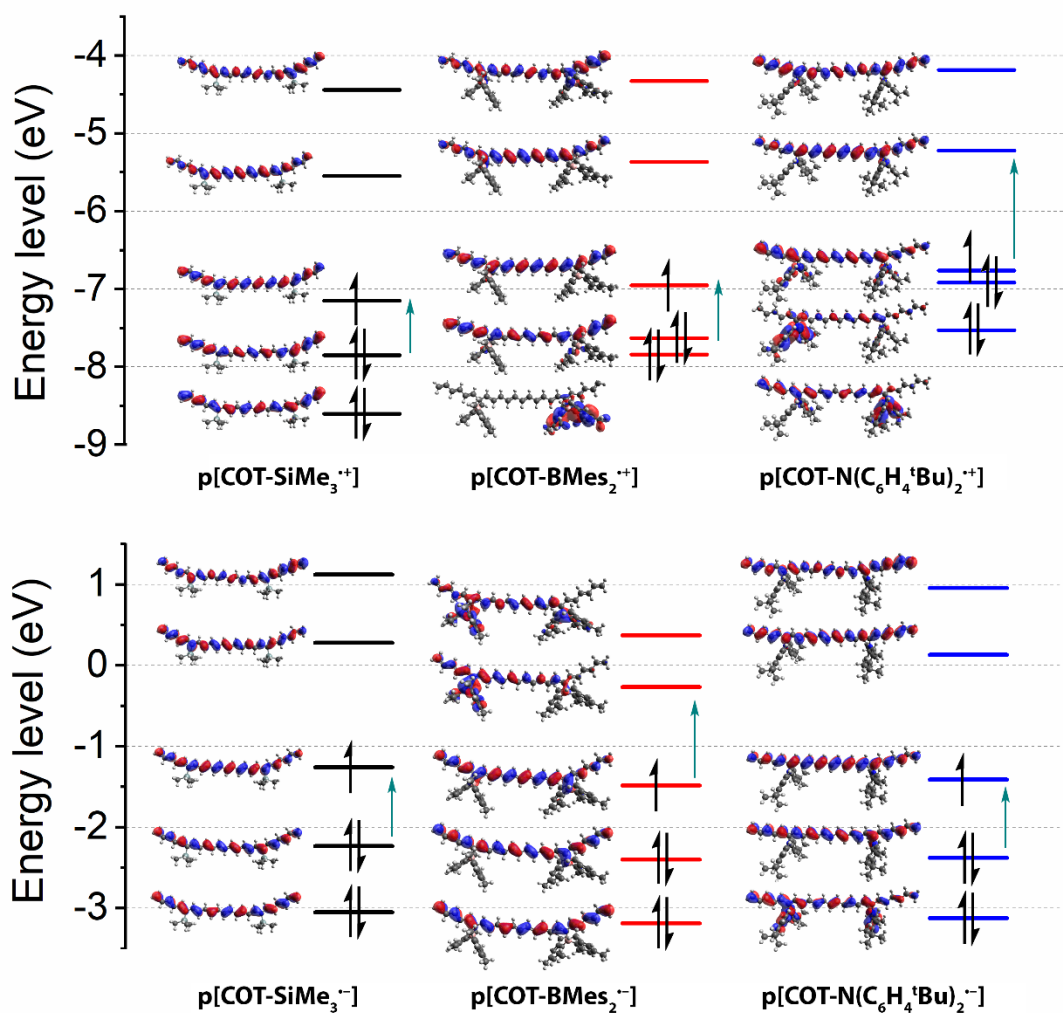


Figure 3.24. Energy of frontier molecular orbitals for oxidized and reduced polymer chain fragments obtained by DFT (B3LYP/cc-pVDZ). Green arrow indicates probable transition observed experimentally in the NIR region.

Based on the abovementioned results and the ongoing interest in near-IR absorbers for electronic devices,^{4,5,32} it was decided to further investigate the redox/optoelectronic properties of the functional polyacetylenes as films. Upon spin

coating 10 mg/mL THF solutions of **pCOT-SiMe₃**, **pCOT-BMes₂** and **pCOT-N(C₆H₄^tBu)₂**, uniform ~50 nm thick films are formed (Figure 3.25, Figure 3.112). These films can be oxidatively doped by exposure to I₂ vapor, leading to differently positioned NIR bands depending on the nature of the side groups (Figure 3.26). While the oxidation of **pCOT-BMes₂** and **pCOT-N(C₆H₄^tBu)₂** with I₂ in the film state give NIR spectral profiles that match those obtained from electrochemical oxidation (or by treatment with [Fc]OTf), the NIR profile of I₂-doped **pCOT-SiMe₃** is much more red-shifted than what is seen via NIR-SEC (Figure 3.21), with a λ_{max} of *ca.* 2000 nm. This might indicate undesired reactivity of **pCOT-SiMe₃** when exposed to iodine, with possible cleavage of C–Si bonds promoted by I₂.³³

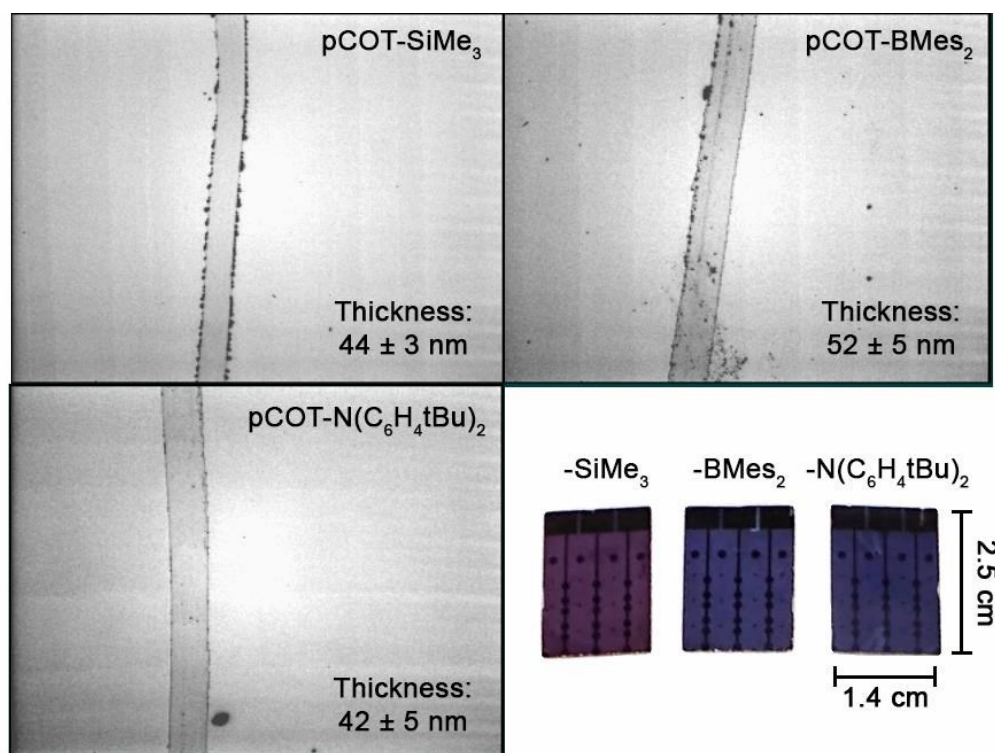


Figure 3.25. Optical images of polymer films with their thicknesses determined by profilometry and pictures of the films deposited onto quartz substrates with gold bottom contacts. Trenches were made with steel needles prior to Au-coating.

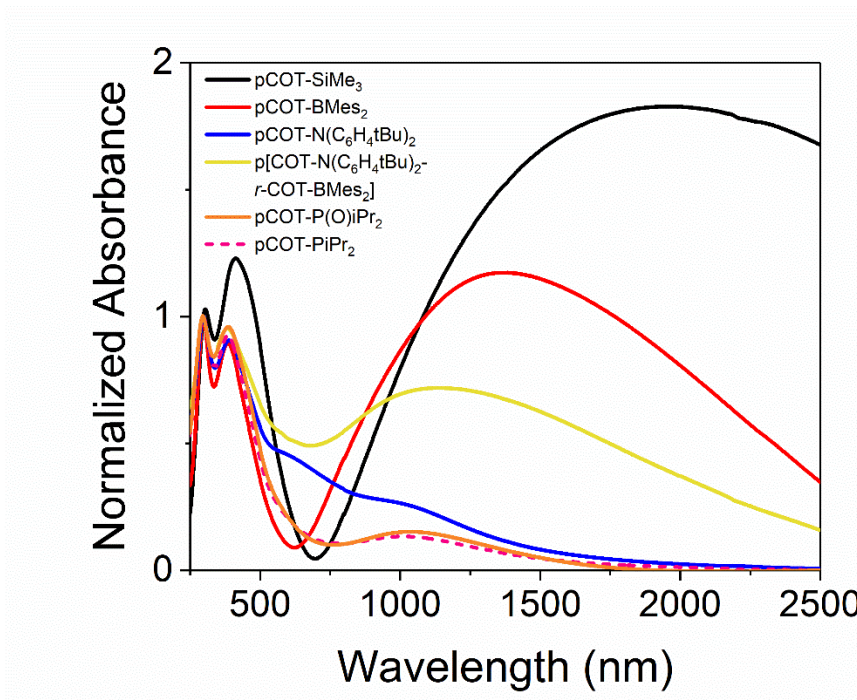


Figure 3.26. UV-Vis-NIR spectra of polymers as spin-coated films after doping with I_2 vapor.

Due to the soluble nature of **pCOT-BMes₂** and **pCOT-SiMe₃**, replacing I_2 vapor by the oxidant [Fc]OTf, yields soluble, near-IR absorbing polymers (**p{[COT-BMes₂]OTf}** and **p{[COT-SiMe₃]OTf}**, Figure 3.27) that are amenable to controllable film formation. The film of **p{[COT-BMes₂]OTf}**, formed by spin coating a 10 mg/mL THF solution, is as uniform as the deposited films of undoped **pCOT-BMes₂**, but of greater thickness (*ca.* 150 nm, Figure 3.113). Additionally, the NIR absorption profile of **p{[COT-SiMe₃]OTf}** ($\lambda_{\max} = 1300$ nm) matches the spectral profile observed by NIR-SEC ($\lambda_{\max} = 1299$ nm, Figure 3.21). The possibility of processing doped polymers in solution opens the door for the controlled deposition of conductive polyacetylene

films. In comparison, it is much harder to control the film forming properties of I₂-doped polyacetylene due to its insolubility.

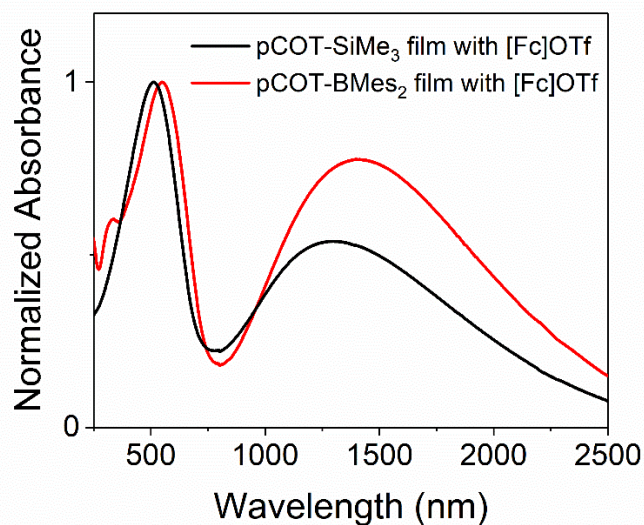


Figure 3.27. UV-Vis-NIR spectra of films of **pCOT-BMes₂** and **pCOT-SiMe₃** oxidized with [Fc]OTf. For doping, solutions of the polymers in THF (10 mg/mL) were mixed with a solution of [Fc]OTf (1.4×10^{-3} M in THF, 1 eq. per side chain) for one minute, then concentrated under vacuum until the initial polymer concentration was reached, filtered through a 0.45 μ m Nylon filter, and spin coated at 2200 rpm.

3.2.6 Conductivity Measurements

Based on the high conductivities achieved with doped polyacetylenes, the conductivity of spin-coated and doped **pCOT-BMes₂** and **pCOT-N(C₆H₄^tBu)₂** was measured and compared to the known **pCOT-SiMe₃** by using a four-point probe under

N₂. Unfortunately, doping with I₂ only afforded high conductivity for **pCOT-SiMe₃** ($\sigma = 8.7$ S/cm), similar to the value previously reported,⁷ while **pCOT-BMes₂** and **pCOT-N(C₆H₄^tBu)₂** retained their semiconducting properties ($\sigma \sim 10^{-6}$ S/cm) after exposure to I₂. The conductivity of **pCOT-BMes₂** could be improved significantly by oxidative doping with Fc[OTf] followed by spin coating ($\sigma = 2.1 \times 10^{-4}$ S/cm), but the value remains below what is often found in p-doped polyacetylenes. These results may be improved in the future with careful film morphology optimization and by changing the oxidant used.

3.2.7 Improved Air Stability of Films

The presence of -NAr₂ and -P(O)ⁱPr₂ groups were found to significantly increase the air stability of the polyacetylene films (Figure 3.28). For example, **pCOT-N(C₆H₄^tBu)₂** retains 70 % of its initial absorption at λ_{max} after two days in air, while **pCOT-P(O)ⁱPr₂** retains more than 90 % (Figure 3.28). For comparison, degradation of these polymers in THF solutions in air is more rapid, with almost complete degradation after two days (Figure 3.29). Based on the differences in stability as films, it appears that the increased stability of the N- and P-containing polymers may be related to a solid state (packing) effects. A film of **pCOT-PⁱPr₂** also shows retention of *ca.* 90 % of its initial light absorption after two days (Figure 3.30), but care must be taken when analyzing this data due to the presence of leftover -P(O)ⁱPr₂ groups.

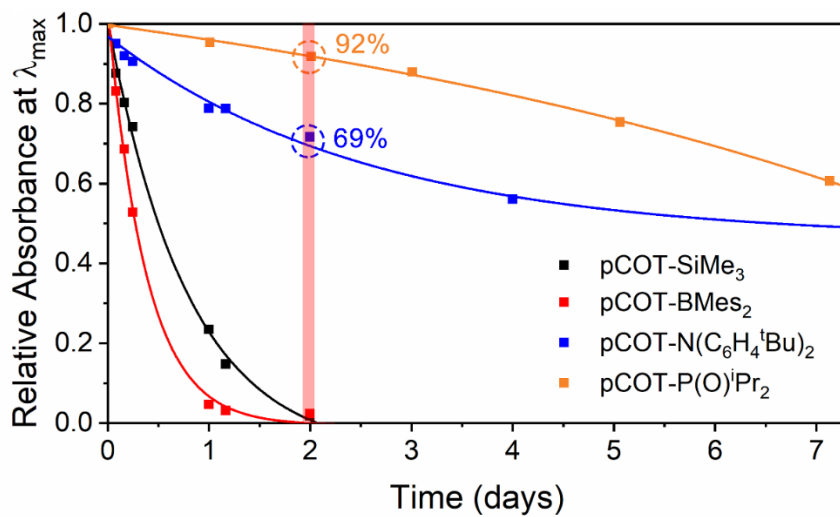


Figure 3.28. Air stability of neat films as tracked by UV-Vis spectroscopy; the deviation from exponential decay for **pCOT-P(O)ⁱPr₂** is due to a blue-shift in λ_{\max} .

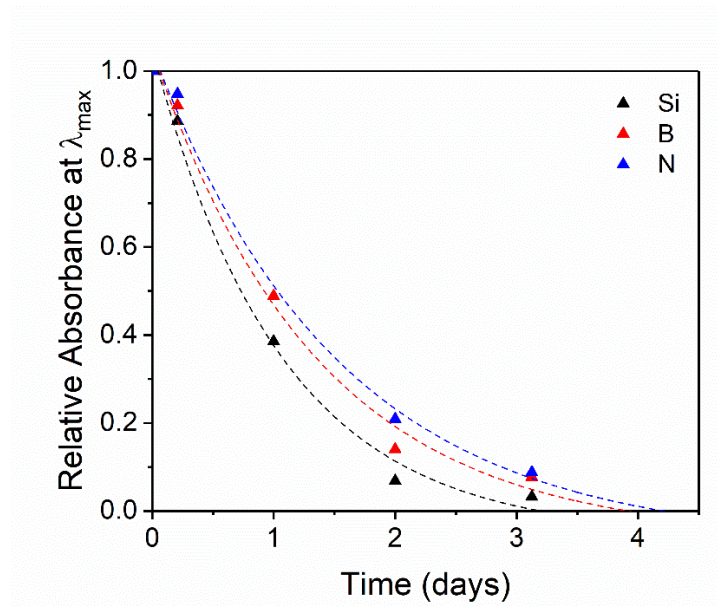


Figure 3.29. Air stability of THF solutions of **pCOT-SiMe₃**, **pCOT-BMe₂** and **pCOT-N(C₆H₄^tBu)₂** tracked by UV-Vis spectroscopy

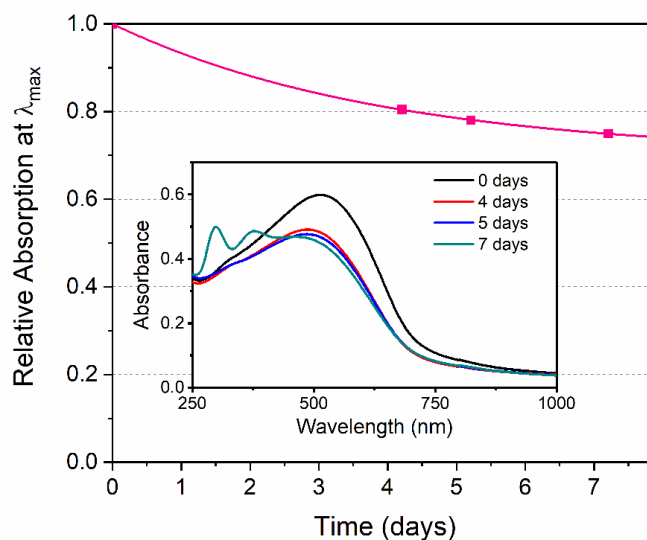


Figure 3.30. Change in light absorption intensity at λ_{\max} for a film of **pCOT-PiPr₂** exposed to air over time. Inset: UV-Vis spectra of the corresponding film over time.

The high stability of these soluble polyacetylenes in the solid state can be compared to an insoluble partly fluorinated polyacetylene recently reported to retain 70 % of absorption after the same time period (2 days).¹¹ Given the very high levels of structural tunability that are inherent to the synthetic methods introduced in this work, it is likely that further side group manipulations will lead to even further increases in air stability (from days to weeks, or longer), while retaining the desirable optoelectronic properties of polyacetylenes.

3.2.8 Polyacetylene Cross-Linking Reactions with Benzoquinone

Since it was possible to chemically reduce the polymers in solution, investigations were carried out with the goal of using the radicals formed to promote cross-linking. To start, the reduced polymer **p[COT-BMes₂•]** was combined with 1,4-benzoquinone with the expectation of forming B-O-C₆H₄-O-B cross-links, as seen with other small molecules containing three-coordinate boron.³⁴ As expected, this reaction in THF gave an insoluble black solid; in line with the formation of a cross-linked network. However, the same reaction with **p[COT-SiMe₃•]** and **p[COT-N(C₆H₄^tBu)₂•]** also afforded insoluble black and deep blue solids, respectively.

Analysis of the solids by FT-IR spectroscopy (Figure 3.31) indicates the presence of polyacetylene backbones with the characteristic C-H out of plane deformation of *trans*-PA at *ca.* 1000 cm⁻¹. The FT-IR spectra also show the presence of O-H stretching vibrations at 3300-3600 cm⁻¹, suggesting that the reaction with 1,4-benzoquinone also leads to the formation of -OH groups. Based on these results and the formation of insoluble material independent of the nature of the side chain, it is believed that cross-linking can also transpire by the attack of radicals located in the polyacetylene backbone onto a β-carbon in 1,4-benzoquinone followed by H migration, a known reaction pathway,³⁵ ultimately leading to a structure such as the depicted in Scheme 3.7.

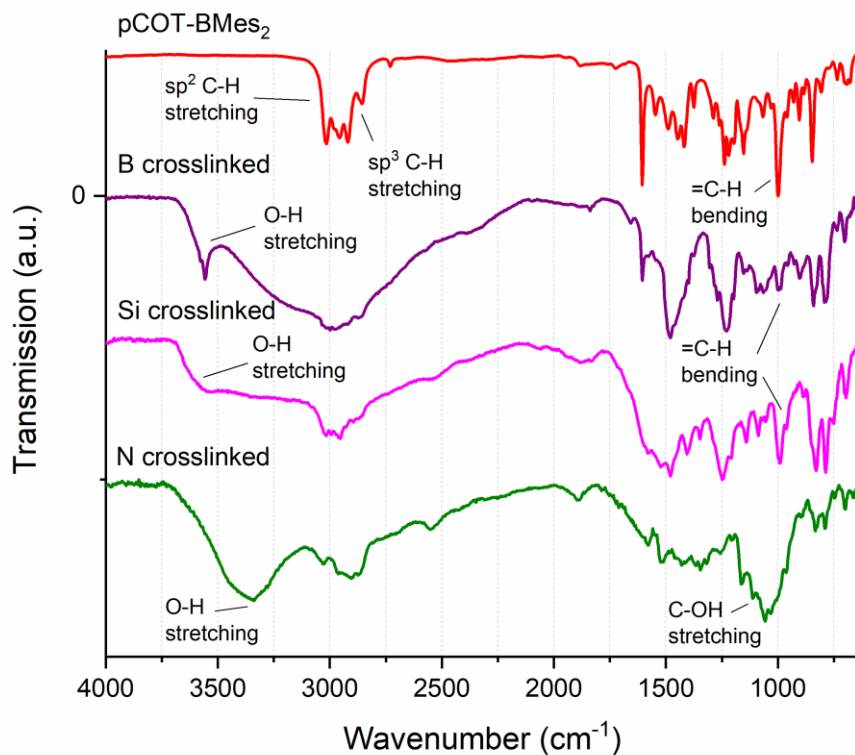
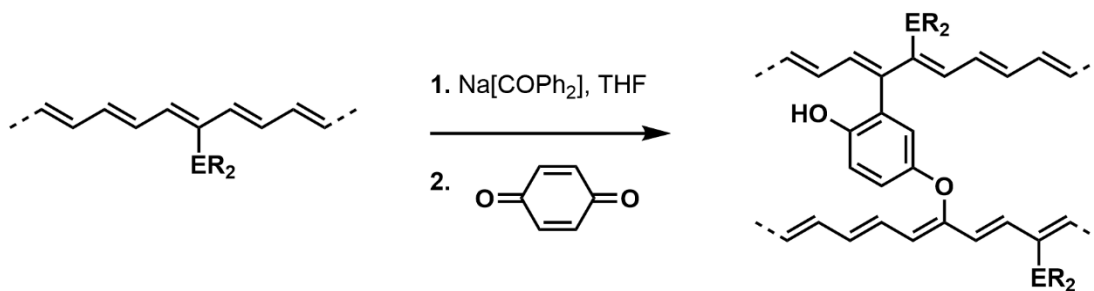


Figure 3.31. Solid state FT-IR spectra of cross-linked **pCOT-BMes₂**, **pCOT-SiMe₃** and **pCOT-N(C₆H₄^tBu)₂**, and the spectrum of **pCOT-BMes₂** for comparison.



Scheme 3.7. Possible reaction of reduced polyacetylenes with 1,4-benzoquinone leading to cross-linking.

Additional studies are being carried out to determine the structure and composition of the insoluble material. However, more evidence for the formation of cross-linked networks was obtained by UV-Vis spectroscopy. While the cross-linked products from **pCOT-BMe₂** and **pCOT-SiMe₃** could not be well-dispersed in THF, sonication of cross-linked **pCOT-N(C₆H₄^tBu)₂** in THF leads to the formation of a blue suspension. Analysis of the UV-Vis spectrum of the suspension reveals a profile that matches that of reduced **pCOT-N(C₆H₄^tBu)₂** after re-oxidation by exposure to air (Figure 3.32).

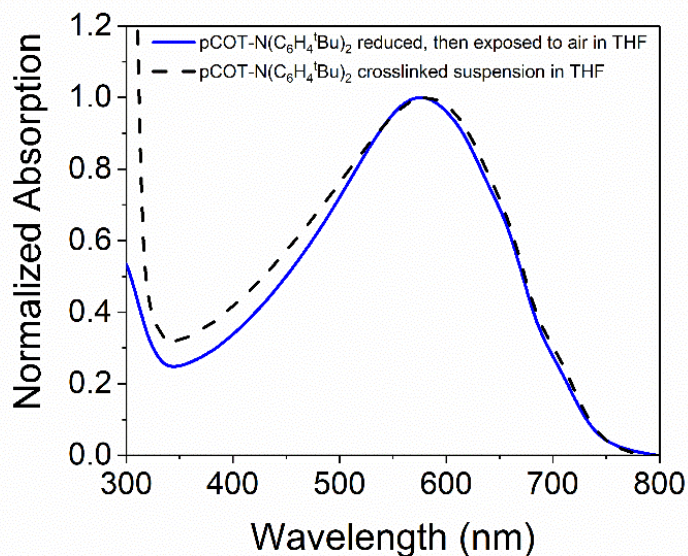


Figure 3.32. UV-Vis spectra of **pCOT-N(C₆H₄^tBu)₂** in THF after reduction with Na[COPh₂] followed by re-oxidation by air exposure (solid line), and as a suspension in THF after cross-linking with 1,4-benzoquinone (dashed line).

3.3 Conclusions

This Chapter described the synthesis and properties of soluble, heteroatom-appended polyacetylenes and a triazolium ring-fused polyacetylene. Heteroatoms were found to drastically improve air stability in the solid state and led to tuning of the optoelectronic properties, while maintaining solubility. Placement of redox-active boryl and amino groups directly onto a polyacetylene backbone led to switchable near-IR optical responses in the telecommunications range (*ca.* 1500 nm) upon chemical reduction or oxidation. Additionally, the solubility of these functionalized polyacetylenes allowed for formation of cross-linked networks from solution. Through the synthetic routes presented herein, it should be possible to synthesize uncountable new polymers of interest for organic electronics and sensing; bringing added interest back to the field of polyacetylene-based conjugated materials.

3.4 Experimental Section

3.4.1 General Information, Materials and Instrumentation

Synthesis: Unless specified, all reactions were performed under an inert atmosphere of N₂ with Schlenk techniques or a glovebox (MBraun), with dry and degassed solvents from a Grubbs-type solvent system manufactured by Innovative Technology, Inc. For the polymer reduction experiments, THF was dried further by stirring over Na/K overnight. For polymer preparation and purification, stabilizer-free THF was used. *p*-Norbornenephenylenebromide (NBE-C₆H₄-Br),³⁶ bromocyclooctatetraene (COT-

Br),^{37,38} trimethylsilylcyclooctatetraene (COT-SiMe₃),³⁹ dimesitylfluoroborane (Mes₂BF, Mes = 2,4,6-Me₃C₆H₂),⁴⁰ mesityl azide (Mes-N₃),⁴¹ NaBARF,⁴² and [ⁿBu₄N]BARF₄⁴³ were synthesized according to literature procedures. Solutions of ⁿBuLi in hexanes (Sigma-Aldrich) were titrated before use.⁴⁴ 1,4-Benzophenone (Sigma-Aldrich) was purified by sublimation at 110 °C before use. KO^tBu, F₃B•OEt₂ and HN(4-C₆H₄^tBu)₂ (TCI), MgSO₄ (Caledon), Mes-Br and I₂ (Alfa-Aesar), ⁱPr₂PCl, (COCl)₂ and MeOTf (Oakwood) PdCl₂(PPh₃)₂ (Strem), Si₂Cl₆ (Gelest), 88 % formic acid, HNPh₂ (Fischer), and [ⁿBu₄N]Br (Eastman) were used without further purification. All other chemicals were purchased from Sigma-Aldrich and used as received. Cyclooctatetraene (Matrix Scientific) was shipped with 0.1% hydroquinone, however, no purification was performed before use. For the column chromatography of amine-containing products, the silica gel was packed and treated with 100 % Et₃N before use. For photoisomerization experiments, UV irradiation was accomplished using a Philips HPK 125 W high pressure mercury lamp (main emission peaks at 590, 560, 450 and 410 nm) or a Hanovia 400 W medium pressure mercury lamp (main emission peaks at 435, 405, 365, 315 and 300 nm).

Spectroscopy: NMR spectra were collected on Varian Inova 400, 500 or 700 MHz spectrometers (¹H and ¹³C{¹H}) and 400 or 500 MHz spectrometers (¹¹B and ¹⁹F) referenced externally to SiMe₄ (¹H and ¹³C{¹H}), F₃B•OEt₂ (¹¹B) and CFCl₃ (¹⁹F). UV-Vis spectra were collected on a Varian Cary 300 Scan spectrometer, with optical HOMO-LUMO gaps (E_g) extracted from UV-Vis spectra by calculating the energy

associated with the onset of absorption. Photoluminescence data was obtained using a Horiba PTI QuantaMaster 8075 fluorescence spectrophotometer equipped with a 75 W xenon lamp. For absolute quantum yield measurements, an integrating sphere as well as long pass and short pass cut-off filters of 400 and 320 nm, respectively, were used.

Thermal analysis: Melting points were measured using a MelTemp apparatus and are reported without correction. Thermogravimetric analysis (TGA) was performed under a N₂ atmosphere on a PerkinElmer Pyris 1 instrument.

Gel permeation chromatography (GPC): GPC was performed in THF (flow rate = 0.5 mL/min) with a Viscotek T6000M column and a Viscotek VE 2001 autosampler. For **pNBE-C₆H₄-BMes₂**, absolute molecular weight determination was performed using right- and low-angle light-scattering detectors plus a refractive index detector (GPC 270 Max dual detector + Viscotek VE 3580) calibrated with a narrow dispersity 99 kDa polystyrene standard (Malvern). For all other polymers, light absorption at the wavelength of the light-scattering detectors (670 nm) hinders absolute molecular weight determination. Thus, for all COT-based polymers, conventional calibration relative to Agilent “EasiVial” polystyrene standards (using Viscotek VE 3580) was performed. For **pCOT-P(O)ⁱPr₂**, GPC was performed with the conditions above except the THF eluent contained 0.1 w/w % of [ⁿBu₄N]Br to reduce polymer interaction with the column. Analysis of all GPC data was accomplished with the OmniSEC 4.6 software package.

Polymer films and their characterization: For spin coating, 10 mg/mL solutions of polymer in toluene (**pCOT-SiMe₃** and **pCOT-BMes₂**) or THF (**pCOT-N(C₆H₄^tBu)₂**) were prepared and filtered through a 0.45 μm Nylon syringe filter. Then, 55 μL of each solution was spread onto quartz substrates that were taped onto a home-made spin coater. The mixtures were spun at 2200 rpm (as measured by a Strobotac type 1531-A stroboscope by General Radio Company) for 2 min and allowed to dry overnight at room temperature inside a dry box. To measure film thickness, spin-coated films were scratched using steel needles and then sputtered with a 16 nm layer of gold for reflectivity. The sputtering was performed using Denton Desk II Sputter Coater under a pressure at 100 mT of N₂ flow during 120 s (deposition rate of *ca.* 8 nm/min). Film thickness was then measured in air using a Zygo Optical Profilometer.

I₂ doping of polymer films: When doping films with iodine vapor, the films were transferred into a glass Schlenk vessel connected through an L-shaped connection to an empty round bottom flask, and placed under an atmosphere of N₂. The empty round bottom flask was then quickly swapped, under strong N₂ flow, by a round bottom flask containing 0.7 g of ground iodine and the whole setup was placed under vacuum. Static vacuum was held for 4 hrs to allow the I₂ vapor to dope the films, followed by removal of excess iodine and at least 2 hrs of dynamic vacuum. UV-Vis spectra of the polymers were recorded with brief air exposure (< 5 min).

Cyclic voltammetry (CV): Measurements of the monomers (1.0 mM) and the polymers (0.5 mg/mL) were recorded with a Gamry Instruments Reference 600+ in dry THF under N₂ atmosphere. A common three electrode setup was used with a glassy carbon working electrode (GC: CH Instruments, ALS Japan; A = 7.1 mm²) for the monomer solutions, a platinum working electrode (GC: CH Instruments, ALS Japan; A = 2.0 mm²) for the polymer solutions, a platinum wire as a counter electrode and a silver wire in silver nitrate solution (0.010 M in MeCN) in a sample holder with a Vycor frit as pseudo reference electrode. [nBu₄N]BAR^F₄ (Ar^F = 3,5-(F₃C)₂C₆H₃) was dried at 50 °C *in vacuo* for 3 days. All data were referenced internally vs. the Fc⁺¹⁰ redox couple (Fc = Cp₂Fe). iR compensation was performed by the positive feedback method, which is implemented in the PHE200 software from Gamry.

Spectroelectrochemistry (SEC): All data were collected in a nitrogen filled glovebox. The polymer solution (0.5 mg/mL) in THF (0.10 M [nBu₄N]BAR^F₄) was added into a thin-layer quartz cuvette (0.1 cm path length). The cuvette was equipped with a Pt-gauze working electrode, a Pt counter electrode, and a silver wire in silver nitrate solution (0.010 M in MeCN) in a sample holder with a Vycor frit as pseudo reference electrode. At first, a cyclic voltammogram was recorded in order to determine the potentials of the redox processes. Subsequently, the solution was replaced by a fresh polymer solution. In controlled potential electrolysis (CPE) experiments, the constant potential was applied until the current dropped to approximately 5 % of the initial current. A UV-Vis-NIR spectrum was recorded every 12 s.

Conductivity measurements: Sheet resistance was measured using a Lucus Pro4 4000 probe equipped with a Keithley 2601A potentiostat. Measurements were performed under N₂ using a glove bag and converted into bulk conductivity based on the film thickness measured by optical profilometry.

Other details: Single crystal X-ray crystallography (XRD), elemental analysis (EA), Fourier-transform infrared spectroscopy (FT-IR), and mass spectrometry (EI-MS) were performed by different laboratories at the University of Alberta: XRD - X-Ray Crystallography Laboratory; EA, FT-IR - Analytical and Instrumentation Laboratory; EI-MS - Mass Spectrometry Facility.

3.4.2 Synthetic Procedures

Synthesis of dimesityl-*p*-norbornenephenyleneborane (NBE-C₆H₄-BMes₂): A solution of NBE-C₆H₄-Br (0.1027 g, 0.4122 mmol) in 3 mL of THF was cooled to -78 °C and ⁿBuLi (0.42 mmol, 2.5 M solution in hexanes) was added dropwise. The reaction mixture was kept at -78 °C and stirred for 1 hr, followed by the dropwise addition of a solution of Mes₂BF (0.1885 g, 0.7029 mmol) in 1.5 mL of THF at -78 °C. The mixture was then stirred at room temperature for 2 hrs. For purification, the mixture was added to 5 mL of CH₂Cl₂, washed with 2 × 10 mL of brine, and the organic fraction dried over MgSO₄. The organic fraction was then filtered, and the volatiles were removed from the filtrate under vacuum. Column chromatography (silica gel, hexanes) followed by solvent removal *in vacuo* afforded NBE-C₆H₄-BMes₂ as a

colorless film that could be scraped off from the containing flask as a white solid (0.159 g, 92 %). ^1H NMR (400 MHz, CDCl_3): δ 1.40-1.46 (m, 1H, NBE alkyl CH), 1.55-1.68 (m, 2H, NBE alkyl CH_2), 1.71-1.79 (m, 1H, NBE alkyl CH), 2.01 (s, 12H, mesityl o - CH_3), 2.31 (s, 6H, mesityl p - CH_3), 2.74 (dd, $^3J_{\text{HH}} = 8.8$ Hz, $^3J_{\text{HH}} = 8.4$ Hz, 1H, NBE CH), 2.95 (br d, $^3J_{\text{HH}} = 15.5$ Hz, 2H, NBE CH_2), 6.14-6.19 (m, 1H, NBE olefinic CH), 6.23-6.28 (m, 1H, NBE olefinic CH), 6.81 (s, 4H, mesityl aryl CH), 7.21-7.25 (m, 2H, C_6H_4), 7.40-7.46 (m, 2H, C_6H_4). $^{13}\text{C}\{^1\text{H}\}$ NMR (126 MHz, CDCl_3): δ 21.4 (mesityl p - CH_3), 23.6 (mesityl o - CH_3), 33.9 (NBE alkyl C), 42.5 (NBE alkyl C), 44.3 (NBE alkyl C), 46.1 (NBE alkyl C), 48.4 (NBE alkyl C), 127.3 (C_6H_4), 128.2 (C_6H_4 or mesityl ArC), 137.0 (mesityl ArC), 137.5 (NBE olefinic C), 137.6 (NBE olefinic C), 138.5 (mesityl ArC), 140.9 (mesityl ArC), 151.0 (C_6H_4). ^{11}B NMR (128 MHz, CDCl_3): δ 74.6. HR-MS (EI): m/z calcd. for $\text{C}_{31}\text{H}_{35}^{11}\text{B}$ 418.28317; found: 418.28315 ($\Delta\text{ppm} = 0.1$). Anal. Calcd. for $\text{C}_{31}\text{H}_{35}\text{B}$: C 88.99, H 8.43; found: C 89.13, H 8.47. Mp: 62-65 $^\circ\text{C}$. UV-Vis (in THF): $\lambda_{\text{max}} = 313$ nm, $\epsilon = 1.15 \times 10^4$ L mol $^{-1}$ cm $^{-1}$; $\lambda_{\text{max}} = 270$ nm, $\epsilon = 9.01 \times 10^3$ L mol $^{-1}$ cm $^{-1}$.

Synthesis of poly[dimesityl-*p*-norbornenephenyleneborane] (pNBE- C_6H_4 -BMes $_2$**):** To a stirring solution of NBE- C_6H_4 -**BMes $_2$** (88.0 mg, 0.143 mmol) in 2.7 mL of THF, 83 μL of a solution of Grubbs' 3rd generation catalyst in THF (0.025 M) was added in one portion. After 10 min, the reaction mixture was quenched with *ca.* 1 mL of ethylvinyl ether and stirred for an extra 1 min. The yellow solution was then concentrated under vacuum to a volume of *ca.* 1.5 mL, and then added dropwise to 200

mL of vigorously stirred methanol under air to precipitate the polymeric product. The resulting solid was collected by vacuum filtration and washed with methanol (3×3 mL), followed by drying under vacuum for *ca.* 30 min to afford **pNBE-C₆H₄-BMes₂** as a white powder (76 mg, 86 %). ¹H NMR (400 MHz, C₆D₆): δ 1.62-3.30 (br m, 7H, alkyl -CH₂ and -CH), 1.75-2.05 (br m, 12H, mesityl *o*-CH₃), 2.26 (br s, 6H, mesityl *p*-CH₃), 4.75-5.60 (br m, 2H, olefinic CH), 6.60-6.83 (br m, 4H, mesityl ArH), 6.87-7.20 (br m, 2H, C₆H₄), 7.28-7.50 (br m, 2H, C₆H₄). M_w = 64.9 kDa (absolute molecular weight), PDI = 1.13. T_g = -70 °C (by DSC). UV-Vis (in THF): λ_{max} = 271 nm, ϵ (per repeat unit) = 1.46×10^4 L mol⁻¹ cm⁻¹; λ_{max} = 312 nm, ϵ (per repeat unit) = 1.98×10^4 L mol⁻¹ cm⁻¹.

Synthesis of dimesitylborylcyclooctatetraene (COT-BMes₂): A solution of **COT-Br** (1.0030 g, 5.477 mmol) in 30 mL of THF was cooled to -78 °C and ⁿBuLi (5.5 mmol, 2.5 M solution in hexanes) was added dropwise under vigorous stirring. The mixture was kept at -78 °C for 1 hr and then a pre-cooled solution of Mes₂BF (1.6112 g, 6.007 mmol) in 15 mL of THF (at -78 °C) was added dropwise. The final mixture was allowed to warm to room temperature and was stirred for 16 hrs. The mixture was then added to 100 mL of brine and extracted with 50 mL of CH₂Cl₂ under ambient conditions. The organic phase was washed once more with 100 mL of brine, dried over MgSO₄ and filtered. The filtrate was then concentrated under vacuum to a volume of *ca.* 3 mL and added in three portions to three separate flasks with rapidly stirring MeOH (500 mL in each flask) and each was filtered once more. The volatiles in the combined

filtrates were removed under vacuum and the product was extracted into 60 mL of hexanes, filtered, and the solvent was removed from the filtrate to give crude **COT-BMes₂**. Added purification of the product by column chromatography (silica gel, hexanes), followed by recrystallization (by cooling a saturated solution in warm, *ca.* 50 °C, hexanes to -30 °C) yielded **COT-BMes₂** as yellow crystals of suitable quality for single crystal X-ray crystallography (1.0340 g, 54 %). ¹H NMR (500 MHz, CDCl₃): δ 2.21 (s, 12H, mesityl *o*-CH₃), 2.28 (s, 6H, mesityl *p*-CH₃), 5.66-5.92 (m, 5H, COT), 6.02-6.34 (m, 2H, COT), 6.79 (s, 4H, mesityl ArH). ¹³C{¹H} NMR (126 MHz, CDCl₃): δ 21.3 (mesityl *o*-CH₃), 23.3 (mesityl *p*-CH₃), 128.2 (mesityl ArC), 130.1 (COT), 132.1 (mesityl ArC), 132.8 (COT), 133.2 (COT), 133.5 (COT), 135.8 (COT), 138.6 (mesityl ArC), 140.6 (mesityl ArC), 141.3 (COT), 147.0 (COT). ¹¹B NMR (128 MHz, CDCl₃): δ 71.3. HR-MS (EI): *m/z* calcd. for C₂₆H₂₉¹¹B 352.23624; found: 352.23613 (Δppm = 0.3). Anal. Calcd. for C₂₆H₂₉B: C 88.64, H 8.30; found: C 88.47, H 8.46. Mp: 135-138 °C. UV-Vis (in THF): λ_{shoulder} = 255 nm; λ_{max} = 309 nm, ε = 7.79 × 10³ L mol⁻¹ cm⁻¹.

Synthesis of [ⁿBu₄N][COT-BMes₂(F)]: To a solution of **COT-BMes₂** (42.7 mg, 0.121 mmol) in benzene (4.1 mL) was added 0.14 mL of a 1.0M solution of [ⁿBu₄N]F in THF dropwise. The mixture was swirled briefly (*ca.* 5 s) and left standing for 16 hrs, which led to the formation of yellow crystals of suitable quality for single crystal X-ray diffraction. The crystals were purified further by washing with benzene (2 × 1 mL), cold THF (-30 °C, 1 × 1 mL) and hexanes (1 × 1 mL). Drying under vacuum affords

[ⁿBu₄N][COT-BMes₂(F)] as a yellow crystalline solid (40.3 mg, 54 %). ¹H NMR (700 MHz, CDCl₃): δ 0.99 (t, ³J_{HH} = 7.7 Hz, 12H, CH₃ in [ⁿBu₄N]⁺), 1.42 (sext, ³J_{HH} = 7.7 Hz, 8H, CH₂-CH₃ in [ⁿBu₄N]⁺), 1.55-1.64 (m, 8H, CH₂-CH₂-CH₃ in [ⁿBu₄N]⁺), 2.11-2.25 (m, 12H, mesityl *o*-CH₃), 2.26 (s, 6H, mesityl *p*-CH₃), 2.99-3.07 (m, 8H, N-CH₂ in [ⁿBu₄N]⁺), 5.38-6.35 (m, 6H, COT), 6.54 (s, 1H, COT), 6.77 (s, 4H, mesityl ArH). ¹³C{¹H} NMR (176 MHz, CDCl₃): δ 13.9 (CH₃ in [ⁿBu₄N]⁺), 19.9 (CH₂-CH₃ in [ⁿBu₄N]⁺), 21.3 (mesityl *o*-CH₃), 23.3 (mesityl *p*-CH₃), 24.3 (CH₂-CH₂-CH₃ in [ⁿBu₄N]⁺), 58.9 (N-CH₂ in [ⁿBu₄N]⁺), 128.0 (COT), 128.2 (mesityl ArC), 132.1 (COT), 138.6 (mesityl ArC), 140.6 (mesityl ArC); not all the expected ¹³C{¹H} resonances could be located due to the broad nature of the peaks. ¹¹B NMR (128 MHz, CDCl₃): δ 4.7 (s). ¹⁹F NMR (376 MHz, C₆D₆): δ -169.3, -167.6; two peaks were observed likely due to the formation of different conformers. HR-MS (ESI): m/z calcd. for [C₂₆H₂₉¹¹BF]⁻ 371.2348; found: 371.2346 (Δppm = 0.4). Anal. Calcd. for C₄₂H₆₅BFN: C 82.19, H 10.67, N 2.28; found: C 82.23, H 10.57, N 2.36. Mp: 152-153 °C (decomp.).

Synthesis of diphenylaminocyclooctatetraene (COT-NPh₂): A solution of **COT-Br** (0.2000 g, 1.093 mmol) and diphenylamine (0.2219 g, 1.311 mmol) in 3.3 mL of Et₂O was prepared in a Schlenk flask and cooled to 0 °C. Under a strong counterflow of N₂, KO^tBu (0.1207 g, 1.076 mmol) was added as a solid in four portions over 1 hr. The mixture was then stirred at 0 °C for 3 hrs and then stirred at room temperature for an additional 16 hrs. Addition of 3 mL of Et₂O to the turbid mixture under air followed by filtration and removal of the volatiles from the filtrate under reduced pressure

afforded the crude product as a brown oil. Column chromatography (silica gel, 9:1 hexanes:Et₃N) then gave **COT-NPh₂** as a yellow solid (0.109 g, 37 %). Crystals of suitable quality for single crystal X-ray diffraction were grown by layering MeOH on top of a saturated solution of **COT-NPh₂** in CHCl₃ at room temperature. ¹H NMR (400 MHz, C₆D₆): δ 5.45-5.85 (m, 7H, COT), 6.84 (t, ³J_{HH} = 7.6 Hz, 2H, *p*-PhH), 7.08 (t, ³J_{HH} = 8.4 Hz, 4H, *m*-PhH), 7.15-7.21 (m, 4H, *o*-PhH). ¹³C{¹H} NMR (101 MHz, C₆D₆): δ 123.0 (Ph), 124.8 (Ph), 129.3 (Ph), 131.6 (COT), 131.0-132.4 (br, COT), 145.5 (COT or Ph), 147.5 (COT or Ph); not all the expected ¹³C{¹H} resonances could be located due to the broad nature of the peaks. HR-MS (EI): *m/z* calcd. for C₂₀H₁₇N 271.13611; found: 271.13553 (Δppm = 2.1). Anal. Calcd. for C₂₀H₁₇N: C 88.52, H 6.31, N 5.16; found: C 88.19, H 6.38, N 5.06. Mp: 107-110 °C. UV-Vis (in THF): λ_{max} = 267 nm, ε = 8.03 × 10³ L mol⁻¹ cm⁻¹; λ_{max} = 300 nm, ε = 1.24 × 10⁴ L mol⁻¹ cm⁻¹; λ_{shoulder} = 350 nm.

Synthesis of bis(4-*tert*-butylphenyl)aminocyclooctatetraene (COT-N(C₆H₄^{*t*}Bu)₂):

A solution of **COT-Br** (0.4022 g, 2.197 mmol) and bis(4-*tert*-butylphenyl)amine (0.8217 g, 2.920 mmol) in 6.6 mL of Et₂O was prepared in a Schlenk flask and cooled down to 0 °C. Under a strong counterflow of N₂, KO^{*t*}Bu (0.2455 g, 2.189 mmol) was added as a solid in four portions over 1 hr. The mixture was then stirred at 0 °C for 3 hrs and allowed to reach room temperature for an additional 16 hrs. Under air, the mixture was then washed with 20 mL of distilled H₂O. The aqueous fraction was extracted with 2 × 10 mL of Et₂O, and the combined organic fractions were washed

with 10 mL of distilled H₂O and 10 mL of brine. The resulting organic fraction was then dried over MgSO₄, filtered and the volatiles were removed from the filtrate under reduced pressure. Column chromatography (silica gel, 18:1 hexanes:Et₃N) followed by recrystallization by cooling a saturated solution of product in hexanes to -30 °C yielded **COT-N(C₆H₄^tBu)₂** as a crystalline yellow solid (0.238 g, 20 %). ¹H NMR (500 MHz, C₆D₆): δ 1.21 (s, 18H, -C(CH₃)₃), 5.35-5.90 (m, 7H, COT), 7.19-7.28 (m, 8H, C₆H₄). ¹³C {¹H} NMR (126 MHz, C₆D₆): δ 31.6 (-C(CH₃)₃), 34.3 (-C(CH₃)₃), 120.2 (br, COT), 124.7 (C₆H₄), 126.2 (C₆H₄), 131.1 (br, COT), 131.9 (br, COT), 133.8 (COT), 145.3 (COT or C₆H₄), 145.6 (COT or C₆H₄) 145.9 (COT or C₆H₄); not all of the expected ¹³C {¹H} resonances could be located due to the broad nature of the peaks. HR-MS (EI): m/z calcd. for C₂₈H₃₃N 383.26129; found: 383.26153 (Δppm = 0.6). Anal. Calcd. for C₂₈H₃₃N: C 87.68, H 8.67, N 3.65; found: C 87.75, H 8.91, N 3.69. Mp: 117-120 °C. UV-Vis (in THF): λ_{shoulder} = 271 nm; λ_{max} = 300 nm, ε = 1.54 × 10⁴ L mol⁻¹ cm⁻¹; λ_{max} = 353 nm, ε = 3.07 × 10³ L mol⁻¹ cm⁻¹.

Synthesis of diisopropylphosphinocyclooctatetraene (COT-PⁱPr₂): A solution of **COT-Br** (1.0050 g, 5.487 mmol) in 30 mL of THF was cooled to -78 °C and ⁿBuLi (5.49 mmol, 2.45 M solution in hexanes) was added dropwise under stirring. The mixture was kept at -78 °C for 1 hr, followed by the dropwise addition of ClPⁱPr₂ (0.88 mL, 5.5 mmol). The reaction mixture was allowed to reach room temperature and stirred for 16 hrs, followed by removal of volatiles under vacuum. While still under inert atmosphere, the product was extracted into 10 mL of hexanes, followed by

filtration and removal of the volatiles from the filtrate. The crude product was then dissolved in 20 mL of a 1:4 THF:hexanes mixture and silica gel (*ca.* 1.6 g) was added; the mixture was then stirred for 2 hrs. Filtration of the mixture followed by removal of the volatiles under vacuum afforded **COT-PⁱPr₂** as an orange oil (0.870 g, 72 %). ¹H NMR (700 MHz, C₆D₆): δ 0.78-1.40 (br m, 12H, CH(CH₃)₂), 1.73 (sept of d, ³J_{HH} = 7.0 Hz, ²J_{HP} = 4.0 Hz, 2H, CH(CH₃)₂), 5.59-5.74 (m, 5H, COT), 5.86 (d, ³J_{HH} = 11.5 Hz, 1H, COT), 6.45 (dd, ³J_{HP} = 15.5 Hz, ⁴J_{HH} = 3.5 Hz, 1H, COT CH=C-P). ¹³C{¹H} NMR (126 MHz, C₆D₆): δ 20.3 (d, ²J_{CP} = 11.6 Hz, CH(CH₃)₂), 23.9 (br d, ¹J_{CP} = 130 Hz, CH(CH₃)₂), 130.4 (COT), 132.1 (COT), 132.4 (COT), 132.8 (d, ²J_{CP} = 16.3 Hz, COT HC=C-P), 133.9 (COT), 143.0 (d, ¹J_{CP} = 23 Hz, COT C-P), 144.1 (d, ²J_{CP} = 48 Hz, COT HC=C-P). ³¹P{¹H} NMR (202 MHz, C₆D₆): δ 22.2 (s). HR-MS (EI): m/z calcd. for C₁₄H₂₁P: 220.13809; found: 220.13810 (Δppm = 0.01). Anal. Calcd. for C₁₄H₂₁P: C 76.33, H 9.61; found: C 75.48, H 9.62. UV-Vis (in THF): λ_{shoulder} = 285 nm.

Synthesis of diisopropylloxophosphoraneocyclooctatetraene (COT-P(O)ⁱPr₂): A solution of **COT-Br** (0.9989 g, 5.457 mmol) in 30 mL of THF was cooled to -78 °C and ⁿBuLi (5.46 mmol, 2.45 M solution in hexanes) was added dropwise under stirring. The mixture was kept at -78 °C for 1 hr, followed by the dropwise addition of ClPⁱPr₂ (0.87 mL, 5.5 mmol). The mixture was allowed to reach room temperature and was stirred for 16 hrs. Finally, the reaction mixture was cooled to 0 °C, opened to air and H₂O₂ (5 mL, 30 w/w % in water) was added. The mixture was then stirred for 2 hrs and

100 mL of brine was added. The product was then extracted with 50 mL of CH₂Cl₂ under ambient conditions and the resulting organic phase was washed once more with 100 mL of brine, dried over MgSO₄, and filtered. The volatiles were removed from filtrate under vacuum and the product was purified by column chromatography (silica gel, 19:1 CH₂Cl₂:MeOH mixture). Lastly, the product was washed twice with *ca.* 1 mL portions of hexanes and dried under vacuum to yield **COT-P(O)ⁱPr₂** as a pure yellow solid (0.6354 g, 51 %). Single crystals of suitable quality for single crystal X-ray diffraction were grown by cooling a saturated solution in hexanes to -30 °C. ¹H NMR (500 MHz, CDCl₃): δ 1.14 (br d, ³J_{HH} = 57.5 Hz, 12H, CH(CH₃)₂), 1.98 (br, 2H, CH(CH₃)₂), 5.65-5.98 (m, 6H, COT), 6.69 (d, ³J_{HP} = 16.5 Hz, 1H, COT -CH=C-P). ¹³C {¹H} NMR (176 MHz, CDCl₃): δ 15.8 (br d, ²J_{CP} = 188 Hz, CH(CH₃)₂), 24.9 (br d, ¹J_{CP} = 296 Hz, CH(CH₃)₂), 130.3 (d, J_{CP} = 11 Hz, COT), 131.5 (COT), 131.5 (d, J_{CP} = 13.6 Hz, COT), 132.9 (d, J_{CP} = 2.6 Hz, COT), 133.0 (d, J_{CP} = 2.1 Hz, COT), 134.1 (d, J_{CP} = 9.9 Hz, COT), 135.4 (d, ¹J_{CP} = 76.7 Hz, COT C-P), 146.6 (d, J_{CP} = 4.8 Hz, COT). ³¹P {¹H} NMR (202 MHz, C₆D₆): δ 49.3 (s). HR-MS (EI): m/z calcd. for C₁₄H₂₁OP 236.13301; found: 236.13273 (Δppm = 1.2). Anal. Calcd. for C₁₄H₂₁OP: C 71.16, H 8.96; found: C 70.35, H 8.93. Mp: 83-85 °C. UV-Vis (in THF): λ_{shoulder} = 295 nm.

Synthesis of 1-mesityl-1H-cyclooctatriazole (COT-N₃-Mes): *CAUTION! Azides should never be handled with metals due to the risk of explosion.* A solution of **COT-Br** (0.2196 g, 1.200 mmol) in 9.5 mL of Et₂O was prepared in a Schlenk flask wrapped in aluminum foil. Mes-N₃ (0.1410 g, 0.8746 mmol) was then added with a glass pipette

under a strong counterflow of N₂ and the mixture was warmed to 30 °C. A similarly strong counterflow of N₂ was used to add KO^tBu (0.1998 g, 1.781 mmol) in one portion. The reaction mixture was then stirred at 30 °C for 3 days. The crude mixture was then added to 10 mL of Et₂O and the mixture washed twice with 20 mL of H₂O. The combined H₂O fractions were extracted twice with 20 mL portions of Et₂O, the combined Et₂O layers were dried over MgSO₄, and filtered. Removal of volatiles from the filtrate under vacuum afforded a yellow/orange solid, which was purified further by column chromatography (silica gel, 1:9 Et₃N:hexanes mixture) to yield a yellow oil. Trituration of the oil with *ca.* 1 mL of hexanes at 0 °C yields pure **COT-N₃-Mes** as a light-yellow solid (0.1855 g, 81 %). ¹H NMR (500 MHz, CDCl₃): δ 1.98 (s, 6H, mesityl *o*-CH₃), 2.33 (s, 3H, mesityl *p*-CH₃), 5.52 (d, ³J_{HH} = 11.5 Hz, 1H, COT), 5.63 (dd, ³J_{HH} = 12.0 Hz, ⁴J_{HH} = 4.0 Hz, 1H, COT), 5.73 (dd, ³J_{HH} = 12.0 Hz, ⁴J_{HH} = 4.5 Hz, 1H, COT), 6.00 (dd, ³J_{HH} = 11.5 Hz, ⁴J_{HH} = 4.5 Hz, 1H, COT), 6.06 (dd, ³J_{HH} = 12.0 Hz, ⁴J_{HH} = 4.5 Hz, 1H, COT), 6.40 (d, ³J_{HH} = 11.5 Hz, 1H, COT), 6.96 (s, 2H, mesityl ArH). ¹³C{¹H} NMR (126 MHz, CDCl₃): δ 17.3 (mesityl *o*-CH₃), 21.2 (mesityl *p*-CH₃), 118.8 (COT), 124.9 (COT), 129.2 (mesityl ArC), 130.7 (COT), 131.6 (COT or mesityl ArC), 133.4 (COT), 134.1 (COT), 134.6 (COT or mesityl ArC), 135.8 (COT or mesityl ArC), 137.7 (COT), 140.3 (COT or mesityl ArC), 143.9 (COT or mesityl ArC). HR-MS (EI): m/z calcd. for C₂₈H₃₃N 263.14224; found: 263.14205 (Δppm = 0.7). Anal. Calcd. for C₁₇H₁₇N₃: C 77.54, H 6.51, N 15.96; found: C 77.56, H 6.58, N 15.70. Mp: 92-93 °C. UV-Vis (in THF): λ_{shoulder} = 260 nm.

Synthesis of 1-mesityl-3-methyl-1*H*-cyclooctatriazolium triflate ([COT-N₃(Me)-Mes]OTf): To a stirring cold solution (*ca.* 0 °C) of COT-N₃-Mes (0.8263 g, 3.277 mmol) in 8.5 mL of Et₂O, was added MeOTf (555 mL, 4.92 mmol) dropwise, leading to the immediate formation of a white precipitate. The exothermic nature of the reaction causes some of the solvent to boil during addition. The reaction mixture was stirred for another 1 hr and the white precipitate was allowed to settle. The mother liquor was decanted away and the remaining solid was washed with three 5 mL portions of Et₂O and once with 5 mL of hexanes. After drying the remaining solid under vacuum, [COT-N₃(Me)-Mes]OTf was obtained as a pure white solid (1.2990 g, 92 %). Single crystals of suitable quality for X-ray diffraction were obtained by layering hexanes onto a concentrated solution of [COT-N₃(Me)-Mes]OTf in CH₂Cl₂ at room temperature. ¹H NMR (400 MHz, CDCl₃): δ 2.02 (s, 6H, mesityl *o*-CH₃), 2.33 (s, 3H, mesityl *p*-CH₃), 4.29 (s, 3H, N-CH₃), 5.56 (d, ³J_{HH} = 11.6 Hz, 1H, COT), 5.84 (dd, ³J_{HH} = 12.4 Hz, ⁴J_{HH} = 4.0 Hz, 1H, COT), 5.94 (dd, ³J_{HH} = 12.4 Hz, ⁴J_{HH} = 4.0 Hz, 1H, COT), 6.36 (dd, ³J_{HH} = 11.6 Hz, ⁴J_{HH} = 4.4 Hz, 1H, COT), 6.44-6.58 (m, 2H, COT), 7.01 (s, 2H, mesityl ArH). ¹³C{¹H} NMR (100 MHz, C₆D₆): δ 17.2 (mesityl *o*-CH₃), 21.2 (mesityl *p*-CH₃), 37.7 (N-CH₃), 115.2 (COT), 116.2 (COT), 122.4 (OTf), 128.8 (COT or mesityl ArC), 129.9 (mesityl ArC), 130.9 (COT), 132.9 (COT), 135.1 (COT or mesityl ArC), 139.8 (COT or mesityl ArC), 140.1 (COT or mesityl ArC), 142.6 (COT), 142.8 (COT), 142.9 (COT). HR-MS (ESI): *m/z* calcd. for C₁₈H₂₀N⁺ 278.1652; found: 278.1659 (Δppm = 0.5). Anal. Calcd. for (C₁₉H₂₀F₃N₃O₃S): C 53.39, H 4.72, N 9.83, S 7.50; found: C

53.34, H 4.66, N 9.63, S 7.31. Mp: 137-138 °C. UV-Vis (in THF): $\lambda_{\max} = 269$ nm, $\epsilon = 3.94 \times 10^3$ L mol⁻¹ cm⁻¹.

Synthesis of poly[(trimethylsilyl)cyclooctatetraene] (pCOT-SiMe₃): To a stirring solution of COT-SiMe₃ (180.5 mg, 1.024 mmol) in 13.0 mL of THF was added 360 μ L of a solution of Grubbs' 3rd generation catalyst in THF (0.027 M) in one portion. The mixture then gradually changed color from yellow to deep red-purple. After 3 hrs, the reaction mixture was quenched with *ca.* 1 mL of ethylvinyl ether and stirred for an extra 16 hrs. At this point, the mixture was concentrated under vacuum to a final volume of *ca.* 3 mL and added dropwise to 50 mL of stirring hexanes, resulting in precipitation of the polymeric product. The mixture was then filtered through Celite and the retained solid on the Celite-packed frit (containing the polymer) was washed with 4 \times 20 mL hexanes to remove any unreacted monomer and side products. The remaining polymer was then extracted by passing THF (*ca.* 3 \times 20 mL) through the Celite. Removal of the solvent from the filtrate/washings gave pCOT-SiMe₃ as a dark pink solid (14.4 mg, 8 %). ¹H NMR (400 MHz, C₆D₆): δ 0.05-0.43 (br m, 9H, -Si(CH₃)₃), 5.88-7.32 (br m, >7H, olefinic CH). M_w = 41 kDa (relative to polystyrene standards), PDI = 4.2. UV-Vis (in THF): $\lambda_{\text{shoulder}} = 324$ nm; $\lambda_{\max} = 552$ nm, ϵ (per repeat unit) = 3.06×10^4 L mol⁻¹ cm⁻¹; $\lambda_{\text{shoulder}} = 598$ nm.

Synthesis of poly[(dimesitylboryl)cyclooctatetraene] (pCOT-BMes₂): To a stirring solution of COT-BMes₂ (70.0 mg, 0.199 mmol) in 0.6 mL of THF was added 70 μ L

of a solution of Grubbs' 3rd generation catalyst in THF (0.027 M) in one portion. The mixture then gradually changed color from yellow to deep purple. After 3 hrs, the reaction mixture was quenched with *ca.* 1 mL of ethylvinyl ether and stirred for an extra 16 hrs. At this point, the mixture was concentrated to a volume of *ca.* 1 mL under vacuum and added dropwise to 100 mL of stirring hexanes to precipitate the polymeric product. The mixture was then filtered through a Celite-packed frit and the retained solid (containing polymer) was washed with 4 × 20 mL hexanes to remove any unreacted monomer and side products. The remaining polymer was then extracted by passing THF (*ca.* 3 × 20 mL) through the Celite. Removal of the solvent from the filtrate/washings gave **pCOT-BMes₂** as a deep blue solid (27.5 mg, 39 %). ¹H NMR (400 MHz, C₆D₆): δ 2.18 (br s, 6H, mesityl *p*-CH₃), 2.34 (br s, 12H, mesityl *o*-CH₃), 5.52-7.62 (br m, >11H, olefinic CH). M_w = 65 kDa (relative to polystyrene standards), PDI = 3.1. UV-Vis (in THF): λ_{shoulder} = 357 nm; λ_{max} = 569 nm, ε (per repeat unit) = 2.73 × 10⁴ L mol⁻¹ cm⁻¹.

Synthesis of poly(diphenylaminocyclooctatetraene) (pCOT-NPh₂): To a stirring solution of **COT-NPh₂** (312.2 mg, 1.153 mmol) in 14.8 mL of THF was added 410 μL of a solution of Grubbs' 3rd generation catalyst in THF (0.027 M) in one portion. The mixture then gradually changed color from yellow to deep purple. After 4 hrs, the reaction mixture was quenched with *ca.* 3 mL of ethylvinyl ether and stirred for an extra 16 hrs. At this point, the mixture was concentrated under vacuum to a volume of *ca.* 3 mL and added dropwise to 60 mL of stirring hexanes to precipitate the polymeric

product. The mixture was then filtered through Celite and the retained solid (containing polymer) was washed with 4×20 mL hexanes to remove any unreacted monomer and side products. The remaining polymer was then extracted by passing THF (*ca.* 3×20 mL) through the Celite. Removal of the solvent from the filtrate/washings afforded **pCOT-NPh₂** as a deep blue solid (31.0 mg, 10 %). ¹H NMR (500 MHz, CDCl₃): δ 5.70-6.65 (br m, >7H, olefinic CH), 6.75-7.32 (br m, 10H, Ph). $M_w = 13$ kDa (relative to polystyrene standards), PDI = 3.2. UV-Vis (in THF): $\lambda_{\max} = 569$ nm, ϵ (per repeat unit) = 2.84×10^4 L mol⁻¹ cm⁻¹; $\lambda_{\text{shoulder}} = 655$ nm, $\lambda_{\text{shoulder}} = 708$ nm.

Synthesis of poly[bis(4-*tert*-butylphenyl)aminocyclooctatetraene] (pCOT-N(C₆H₄^tBu)₂): To a stirring solution of COT-N(C₆H₄^tBu)₂ (214.3 mg, 0.5590 mmol) in 7.1 mL of THF was added 192 μ L of a solution of Grubbs' 3rd generation catalyst in THF (0.027 M) in one portion. The mixture then gradually changed color from yellow to deep purple. After 4 hrs, the reaction mixture was quenched with *ca.* 1 mL of ethylvinyl ether and stirred for an extra 16 hrs. At this point, the mixture was concentrated under vacuum to a volume of *ca.* 2 mL and added dropwise to 60 mL of stirring hexanes to precipitate the polymeric product. The mixture was then filtered through Celite and the retained solid (containing polymer) was washed with 4×20 mL hexanes to remove any unreacted monomer and side products. The remaining polymer was then extracted by passing THF (*ca.* 3×20 mL) through the Celite. Removal of the solvent from the filtrate/washings afforded **pCOT-N(C₆H₄^tBu)₂** as a deep blue solid (20.4 mg, 10 %). ¹H NMR (400 MHz, CDCl₃): δ 1.28 (br s, 18H, -C(CH₃)₃), 5.00-6.70

(br m, >7H, olefinic CH), 6.70-7.50 (br m, 8H, ArH). $M_w = 32$ kDa (relative to polystyrene standards), PDI = 4.1. UV-Vis (in THF): $\lambda_{\max} = 603$ nm, ϵ (per repeat unit) = 2.82×10^4 L mol⁻¹ cm⁻¹; $\lambda_{\text{shoulder}} = 655$ nm, $\lambda_{\text{shoulder}} = 703$ nm.

Synthesis of poly[bis(4-*tert*-butylphenyl)aminocyclooctatetraene-*random*-(dimesitylboryl)cyclooctatetraene] (p[COT-N(C₆H₄^{*t*}Bu)₂-*r*-COT-BMes₂]): To a stirring solution of COT-N(C₆H₄^{*t*}Bu)₂ (108.6 mg, 0.2835 mmol) and COT-BMes₂ (100.4 mg, 0.2840 mmol) in 7.2 mL of THF was added 200 μ L of a solution of Grubbs' 3rd generation catalyst in THF (0.027 M) in one portion. The mixture then gradually changed color from yellow to deep purple. After 3 hrs, the reaction mixture was quenched with *ca.* 2 mL of ethylvinyl ether and stirred for an extra 16 hrs. At this point, the mixture was concentrated under vacuum to a volume of *ca.* 1 mL and added dropwise to 60 mL of stirring hexanes to precipitate the polymeric product. The mixture was then filtered through a Celite-packed frit and the retained solid (containing the polymer) was washed with 4 \times 20 mL hexanes to remove any unreacted monomer and side products. The remaining polymer was then extracted by passing THF (*ca.* 3 \times 20 mL) through the Celite. Removal of the solvent from the filtrate/washings gave p[COT-N(C₆H₄^{*t*}Bu)₂-*r*-COT-BMes₂] as a deep blue solid (13.3 mg, 19 %, 1:1.8 ratio of -N(C₆H₄^{*t*}Bu)₂ to -BMes₂ incorporation determined by ¹H NMR). ¹H NMR (400 MHz, CDCl₃): δ 1.28 (br s, 18H, -C(CH₃)₃), 2.09 (br s, 12H \times 1.8, mesityl *o*-CH₃), 2.27 (br s, 6H \times 1.8, mesityl *p*-CH₃), 5.00-7.50 (br m, >14H, olefinic CH; 4H \times 1.8, ArH in BMes₂; 8H, ArH in N(C₆H₄^{*t*}Bu)₂). $M_w = 61$ kDa (relative to polystyrene standards),

PDI = 4.2. UV-Vis (in THF): $\lambda_{\text{max}} = 298 \text{ nm}$, ϵ (per repeat unit) = $8.0 \times 10^3 \text{ L mol}^{-1}$; $\lambda_{\text{max}} = 596 \text{ nm}$, ϵ (per repeat unit) = $2.55 \times 10^4 \text{ L mol}^{-1} \text{ cm}^{-1}$.

Synthesis of poly[diisopropylloxophosphoranocyclooctatetraene] (pCOT-P(O)ⁱPr₂): To a stirring solution of COT-P(O)ⁱPr₂ (384.8 mg, 1.629 mmol) in 20.6 mL of THF was added 0.57 mL of a solution of Grubbs' 3rd generation catalyst in THF (0.027 M) in one portion. The mixture then gradually changed color from yellow to deep red. After 4 hrs, the reaction mixture was quenched with *ca.* 1 mL of ethylvinyl ether and stirred for an extra 16 hrs. At this point, the mixture was concentrated under vacuum to a volume of *ca.* 3 mL and added dropwise to 250 mL of stirring hexanes to precipitate the polymeric product. The mixture was then filtered through a Celite-packed frit and the retained solid (containing polymer) was washed with 4 × 50 mL hexanes to remove any unreacted monomer and side products. The remaining polymer was then extracted by passing THF (*ca.* 3 × 20 mL) through the Celite. Removal of the solvent from the filtrate/washings gave pCOT-P(O)ⁱPr₂ as a deep red solid (145.1 mg, 38 %). ¹H NMR (500 MHz, C₆D₆): δ 1.14 (br d, ³J_{HH} = 84 Hz, 12H, CH(CH₃)₂), 1.86 (br, 2H, CH(CH₃)₂), 5.45-8.82 (br, >7H, olefinic CH). ³¹P{¹H} NMR (202 MHz, C₆D₆): δ 46.8, 49.1, 51.3. M_w = 41 kDa (approximated by DLS; R_h = 33 nm). UV-Vis (in THF): $\lambda_{\text{shoulder}} = 327 \text{ nm}$; $\lambda_{\text{max}} = 460 \text{ nm}$, ϵ (per repeat unit) = $1.22 \times 10^4 \text{ L mol}^{-1} \text{ cm}^{-1}$.

Synthesis of poly[diisopropylphosphinocyclooctatetraene] (pCOT-PⁱPr₂): Based on a literature procedure for the reduction of molecular phosphine oxides,⁴⁵ pCOT-P(O)ⁱPr₂ (96.8 mg, 0.336 mmol considering an average of 1 side chain every 12 C in backbone) was dissolved in 15 mL of CH₂Cl₂, followed by the dropwise addition of 0.49 mL of a stock solution of (COCl)₂ in CH₂Cl₂ (1.16 M) at room temperature; some evolution of gas was observed. The homogeneous mixture was stirred for 1 hr followed by removal of the volatiles under vacuum. The remaining solid was then redissolved in 15 mL of CH₂Cl₂ followed by the dropwise addition of 0.11 mL of a stock solution of Si₂Cl₆ in CH₂Cl₂ (0.58 M) and stirring for 30 min, which resulted in the formation of a deep purple-black precipitate. The volatiles were removed under vacuum and the crude product was dissolved in 4 mL of toluene and added to 60 mL of rapidly stirring hexanes. For purification, the precipitate formed was allowed to settle and the solvents were decanted off. Another 60 mL of hexanes is then added to wash the precipitate followed by decantation; this process was repeated for a total of four times. Finally, the product was extracted from the precipitate with toluene (*ca.* 60 mL) followed by filtration to remove undissolved material. Removal of volatiles from the toluene fraction affords pCOT-PⁱPr₂ as a deep pink solid (10.7 mg, 12 %). NMR spectroscopy indicates that this polymer has leftover -P(O)ⁱPr₂ moieties (see Figure 3.6 in Section 3.2.2.3). ¹H NMR (500 MHz, C₆D₆): δ 1.10 (br d, 12H, CH(CH₃)₂), 1.95 (br, 2H, CH(CH₃)₂), 5.43-7.90 (br, >7H, olefinic CH). ³¹P {¹H} NMR (202 MHz, C₆D₆): δ -3.1, 4.2, 24.1 (-PⁱPr₂), and 46.9, 49.2, 51.4 (-P(O)ⁱPr₂). M_w = 8 kDa (approximated by DLS,

$R_h = 6$ nm). UV-Vis (in THF): $\lambda_{\text{shoulder}} = 330$ nm; $\lambda_{\text{shoulder}} = 270$ nm; $\lambda_{\text{max}} = 503$ nm, ϵ (per repeat unit) = 1.58×10^4 L mol⁻¹ cm⁻¹.

Synthesis of poly[1-mesityl-3-methyl-1*H*-cyclooctatriazolium triflate] (p{[COT-N₃(Me)-Mes]OTf}): To a stirring solution of [COT-N₃(Me)-Mes]OTf (54.1 mg, 0.126 mmol) in 1.8 mL of CHCl₃, was added 1.8 mL of a solution of Grubbs' 3rd generation catalyst in THF (7.7×10^{-4} M) in one portion. The reaction mixture was then heated at 60 °C for 20 hrs, leading to a color change from pale yellow to orange and the eventual formation of a dark brown precipitate. After 20 hrs, the reaction mixture was cooled to room temperature and quenched with *ca.* 1 mL of ethylvinyl ether, followed by stirring for an extra one hour. The mixture was transferred to a glass centrifugation tube, THF was added to a total volume of *ca.* 7 mL, and the tube was sealed and centrifuged at 3150 rpm for 15 minutes. The supernatant was removed from the tube and the process was repeated until colorless THF was observed (*ca.* 4-6 times). Drying the resulting insoluble solid under vacuum affords a dark brown powder (12.0 mg, 21 %). FT-IR (wavenumber, cm⁻¹): 2805-3045 (C-H sp³ and sp² C-H stretching) 1606 (C=C stretching), 1400-1503 (N=N stretching), 1270 (SO₃ or CF₃ stretching), 1146 (SO₃ or CF₃ stretching), 920-1071 (SO₃ stretching and *trans* =C-H bending), 851 (*cis* =C-H bending). UV-Vis (suspension in THF): $\lambda_{\text{max}} = 404$ nm.

Reaction of reduced polymers and 1,4-benzoquinone: To a stirring solution of polymer (see below) in dry THF (10 mg/mL), was added dropwise a freshly prepared

solution of sodium benzophenone in THF (5.6×10^{-2} M, 1.0 eq.). After stirring for *ca.* 1 min, a solution of 1,4-benzoquinone in dry THF (25 mg/mL) was then added dropwise. The mixture was stirred at room temperature for 16 hrs to yield a deep blue/purple mixture (in all cases) with dark precipitate. The mixture was transferred to a glass centrifugation tube, THF was added to a total volume of *ca.* 7 mL, and the tube was sealed and centrifuged at 3150 rpm for 15 minutes. The supernatant was removed from the tube and the process was repeated until colorless THF was observed (*ca.* 4-6 times). The precipitate was washed a final time with 7 mL of hexanes and dried under vacuum.

- For **pCOT-BMes₂**: used 9.93 mg of polymer (0.025 mmol of repeat units) in 1.0 mL THF, 440 mL of sodium benzophenone in THF (5.6×10^{-2} M, 1.0 eq.), 2.5 mg of 1,4-benzoquinone in 100 mL of THF (0.023 mmol, 0.9 eq.). Final product is a black solid (0.3 mg, 3 %). FT-IR (wavenumber, cm^{-1}): 3556 (O-H stretching), 2805-3050 (C-H sp^3 and sp^2 C-H stretching), 999 (*trans* =C-H bending).
- For **pCOT-SiMe₃**: used 5.08 mg of polymer (0.022 mmol of repeat units) in 0.5 mL THF, 391 mL of sodium benzophenone in THF (5.6×10^{-2} M, 1.0 eq.), 2.4 mg of 1,4-benzoquinone in 50 mL of THF (0.022 mmol, 1.0 eq.). Final product is a black solid (0.7 mg, 14 %). FT-IR (wavenumber, cm^{-1}): 3552 (O-H stretching), 2835-3090 (C-H sp^3 and sp^2 C-H stretching), 991 (*trans* =C-H bending).

- For **pCOT-N(C₆H₄Bu)₂**: used 5.34 mg of polymer (0.012 mmol of repeat units) in 0.5 mL THF, 219 mL of sodium benzophenone in THF (5.6×10^{-2} M, 1.0 eq.), 1.3 mg of 1,4-benzoquinone in 30 mL of THF (0.012 mmol, 1.0 eq.). Final product is a black/deep blue solid (3.4 mg, 63 %). FT-IR (wavenumber, cm⁻¹): 3100-3600 (O-H stretching), 2825-3070 (C-H sp³ and sp² C-H stretching), 962 (*trans* =C-H bending).

3.4.3 X-Ray Crystallographic Data

All single crystal XRD data was collected using a Bruker D8 diffractometer with APEX II CCD detector. Graphite-monochromated Mo K α radiation was used and the data was corrected for absorption with Gaussian integration (face-indexed). Crystal structures were solved using SHELXT-2014 and DIRDIF-2008,^{46,47} while refinements were completed with SHELXT-2014.

Table 3.3. Crystallographic data for **COT-BMes₂**, **[ⁿBu₄N][COT-BMes₂(F)]** and **COT-NPh₂**.

Compound	COT-BMes ₂	[ⁿ Bu ₄ N] [COT-BMes ₂ (F)]	COT-NPh ₂
Formula	C ₂₆ H ₂₉ B	C ₄₂ H ₆₅ BFN	C ₂₀ H ₁₇ N
Formula weight	352.3	613.76	271.35
Cryst. dimens. (mm)	0.28 × 0.24 × 0.21	0.21 × 0.16 × 0.08	0.38 × 0.06 × 0.03
Crystal system	triclinic	monoclinic	monoclinic
Space group	<i>P</i> 1 (No. 2)	<i>P</i> 2 ₁ / <i>c</i> (No. 14)	<i>P</i> 2 ₁ / <i>c</i> (No. 14)
<i>a</i> (Å)	8.0695(17)	10.3877(4)	5.9034(3)
<i>b</i> (Å)	11.405(3)	20.5429(7)	16.2465(9)
<i>c</i> (Å)	12.166(3)	17.5200(7)	15.6405(9)
<i>α</i> (deg)	79.918(4)	-	-
<i>β</i> (deg)	82.561(4)	90.325(3)	99.918(4)
<i>γ</i> (deg)	69.374(4)	-	-
<i>V</i> (Å ³)	1028.9(4)	3738.6(2)	1477.65(14)
<i>Z</i>	2	4	4
<i>ρ</i> _{calcd} (g cm ⁻³)	1.137	1.09	1.22
<i>μ</i> (mm ⁻¹)	0.063	0.485	0.537
T (°C)	-80	-100	-100
2 <i>θ</i> _{max} (deg)	61.11	144.88	144.65
Total data	24316	144301	10111
Unique data (<i>R</i> _{int})	6288 (0.0477)	7380 (0.0596)	2894 (0.0560)
Obs data [<i>I</i> ≥ 2σ(<i>I</i>)]	4148	6521	2374
Parameters	249	412	190
<i>R</i> ₁ [<i>I</i> ≥ 2σ(<i>I</i>)] ^a	0.0634	0.0432	0.056
<i>wR</i> ₂ [all data] ^a	0.1886	0.1235	0.1647
Max/min Δ <i>ρ</i> (e ⁻ Å ⁻³)	0.315/-0.307	0.305/-0.246	0.445/-0.310

^a*R*₁ = Σ||*F*_o| - |*F*_c|/Σ|*F*_o|; *wR*₂ = [Σ*w*(*F*_o² - *F*_c²)²/Σ*w*(*F*_o⁴)]^{1/2}.

Table 3.4. Crystallographic data for COT-P(O)ⁱPr₂ and [COT-N₃(Me)-Mes]OTf.

Compound	COT-P(O) ⁱ Pr ₂	[COT-N ₃ (Me)-Mes]OTf
Formula	C ₁₄ H ₂₃ O ₂ P	C ₁₉ H ₂₀ F ₃ N ₃ O ₃ S
Formula weight	254.29	427.44
Cryst. dimens. (mm)	0.31 × 0.25 × 0.07	0.23 × 0.20 × 0.04
Crystal system	monoclinic	monoclinic
Space group	<i>P</i> 21/ <i>n</i> (an alt. set. of <i>P</i> 21/ <i>c</i> [No. 14])	<i>P</i> 21/ <i>c</i> (No. 14)
<i>a</i> (Å)	6.6287(2)	8.1843(2)
<i>b</i> (Å)	15.2257(4)	8.3594(2)
<i>c</i> (Å)	14.8419(4)	29.3138(6)
β (deg)	99.9203(9)	93.6753(10)
<i>V</i> (Å ³)	1475.55(7)	2001.40(8)
<i>Z</i>	4	4
ρ_{calcd} (g cm ⁻³)	1.145	1.419
μ (mm ⁻¹)	1.562	1.922
T (°C)	-100	-100
$2\theta_{\text{max}}$ (deg)	144.87	148.02
Total data	59661	33729
Unique data (<i>R</i> _{int})	2922 (0.0269)	4024 (0.0285)
Obs data [<i>I</i> ≥ 2σ(<i>I</i>)]	2881	3682
Parameters	162	382
<i>R</i> ₁ [<i>I</i> ≥ 2σ(<i>I</i>)] ^a	0.0323	0.0415
<i>wR</i> ₂ [all data] ^a	0.0905	0.1147
Max/min Δρ (e ⁻ Å ⁻³)	0.293/-0.414	0.273/-0.252

$$^a R_1 = \frac{\sum ||F_o| - |F_c||}{\sum |F_o|}; wR_2 = \left[\frac{\sum w(F_o^2 - F_c^2)^2}{\sum w(F_o^4)} \right]^{1/2}.$$

3.4.4 Additional NMR Data

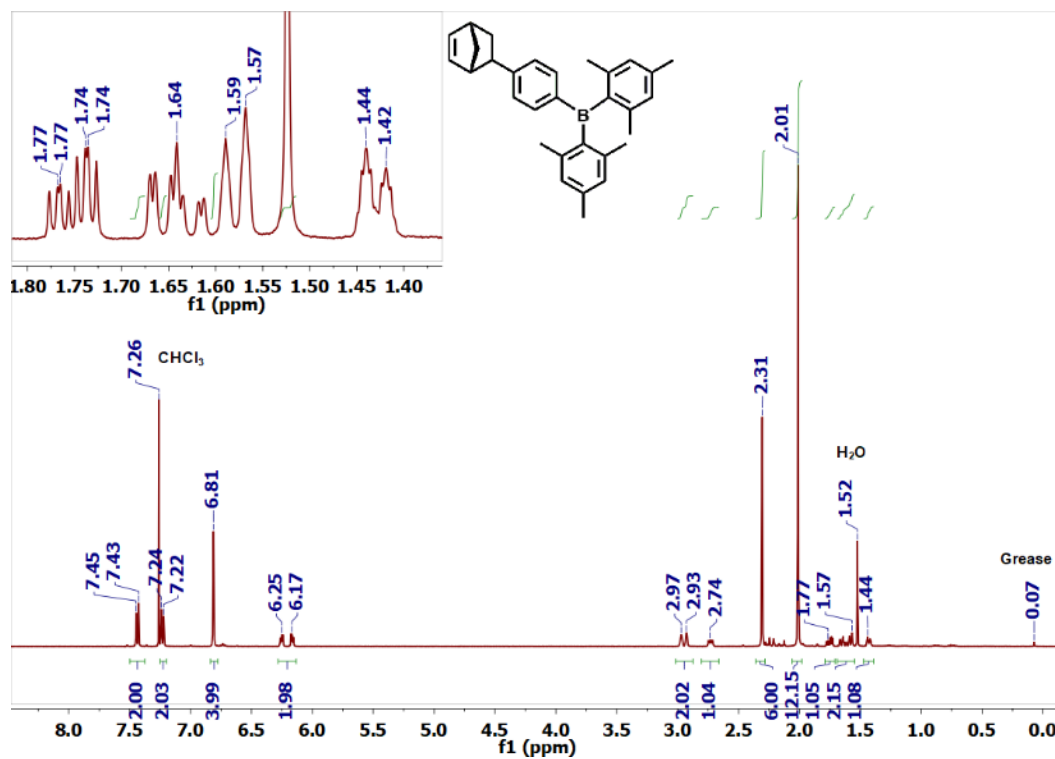


Figure 3.33. ^1H NMR spectrum (400 MHz) of NBE- C_6H_4 -BMes $_2$ in CDCl_3 .

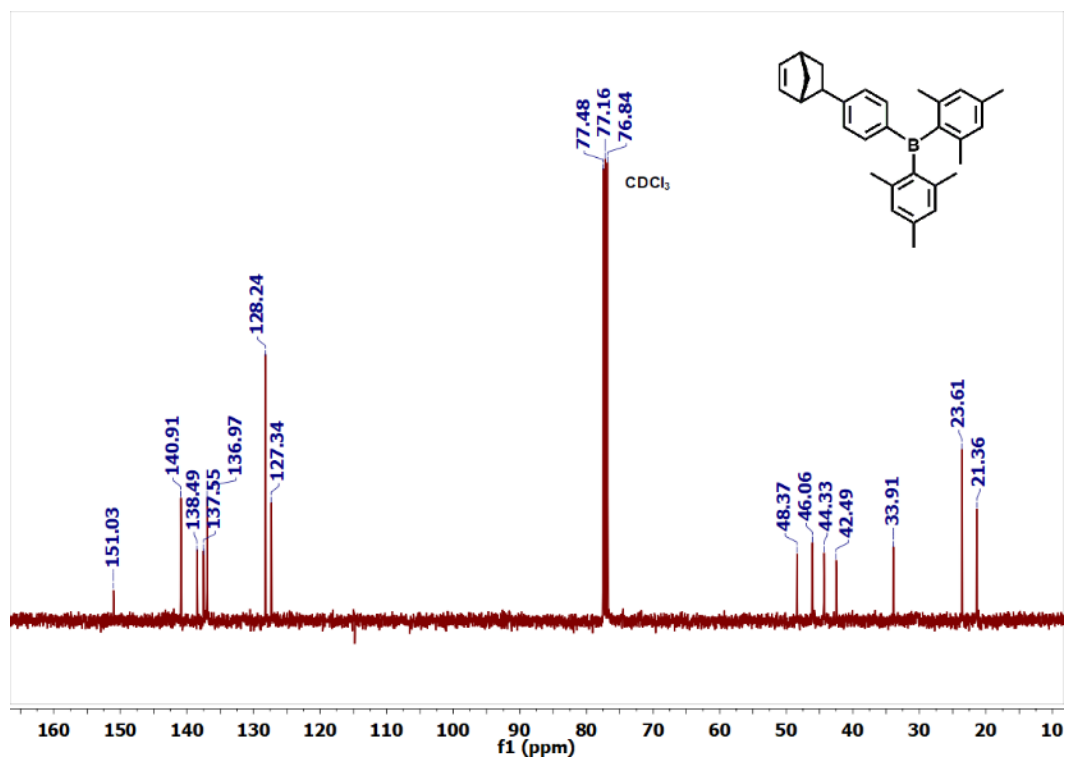


Figure 3.34. $^{13}\text{C}\{^1\text{H}\}$ NMR spectrum (101 MHz) of NBE- C_6H_4 -BMes $_2$ in CDCl_3 .

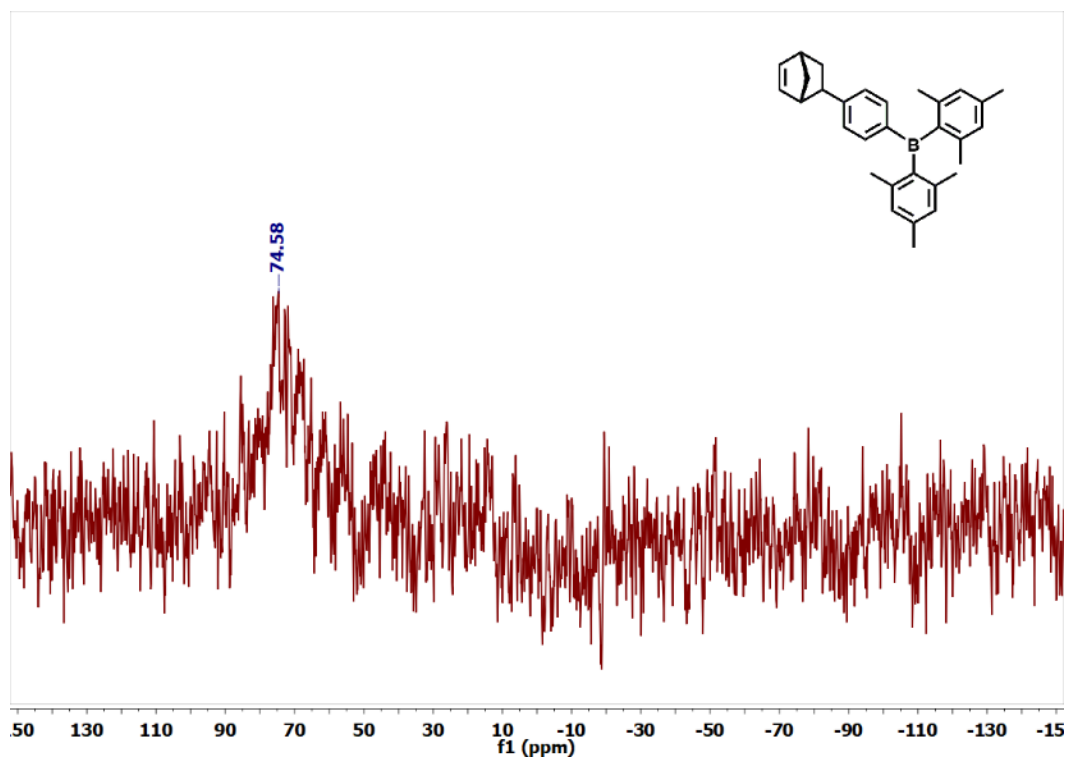


Figure 3.35. ^{11}B NMR spectrum (101 MHz) of $\text{NBE-C}_6\text{H}_4\text{-BMes}_2$ in CDCl_3 .

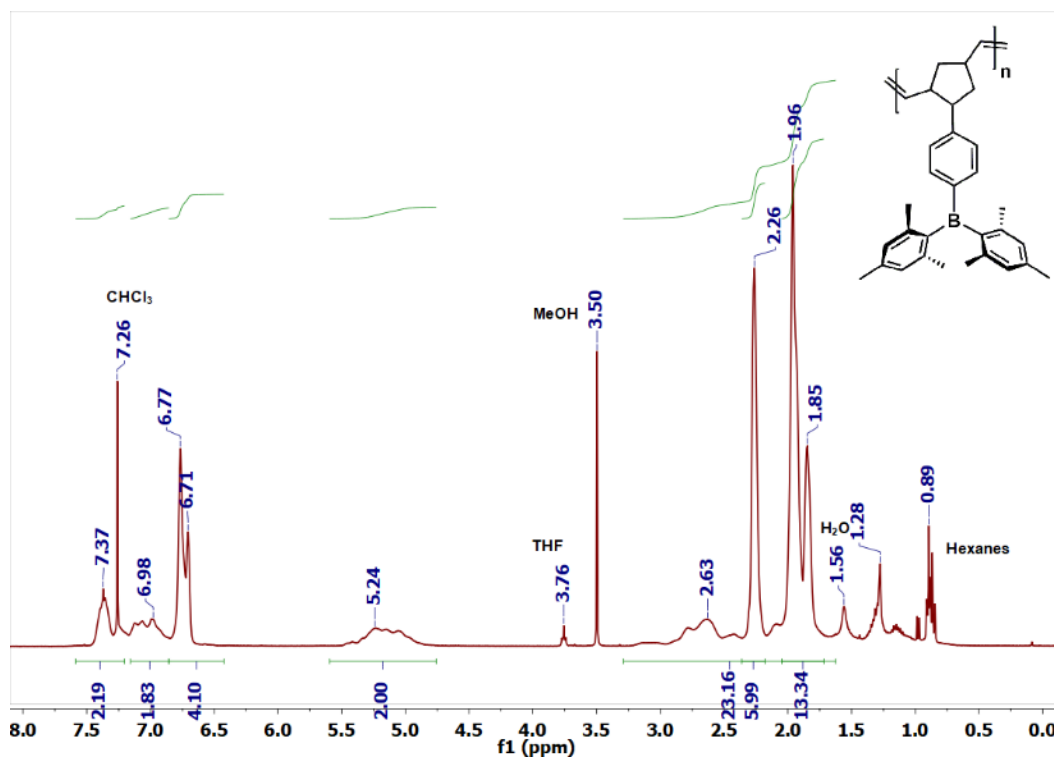


Figure 3.36. ^1H NMR spectrum (400 MHz) of $\text{pNBE-C}_6\text{H}_4\text{-BMes}_2$ in CDCl_3 .

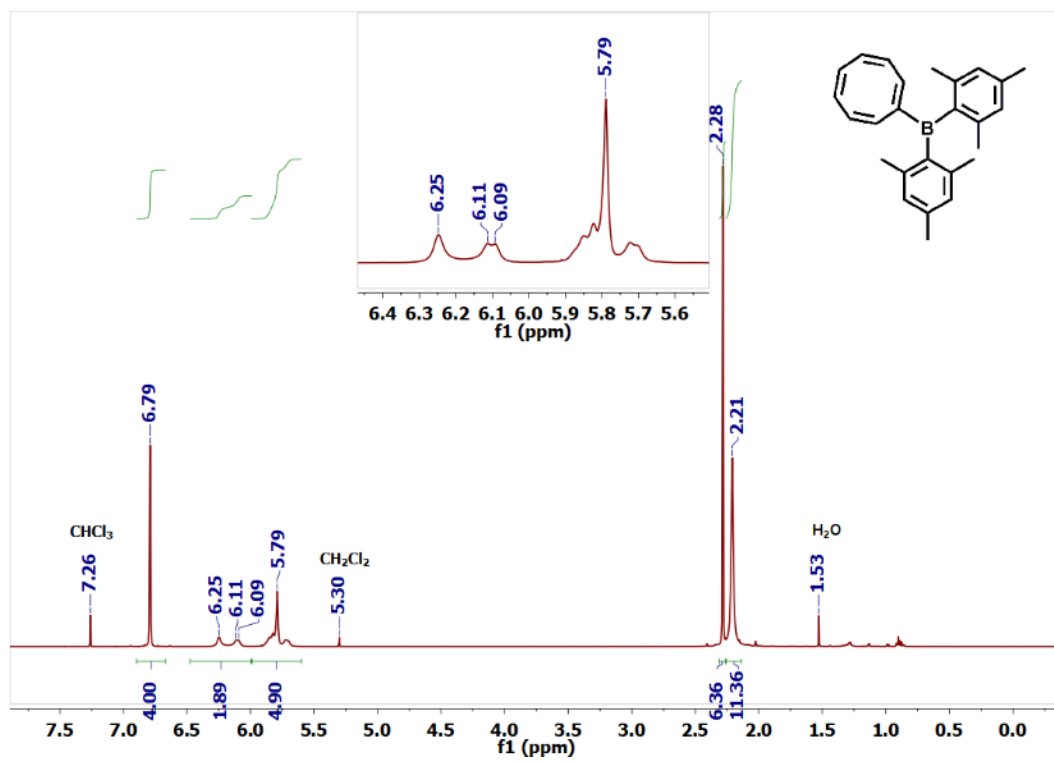


Figure 3.37. ^1H NMR spectrum (500 MHz) of COT-BMes₂ in CDCl₃.

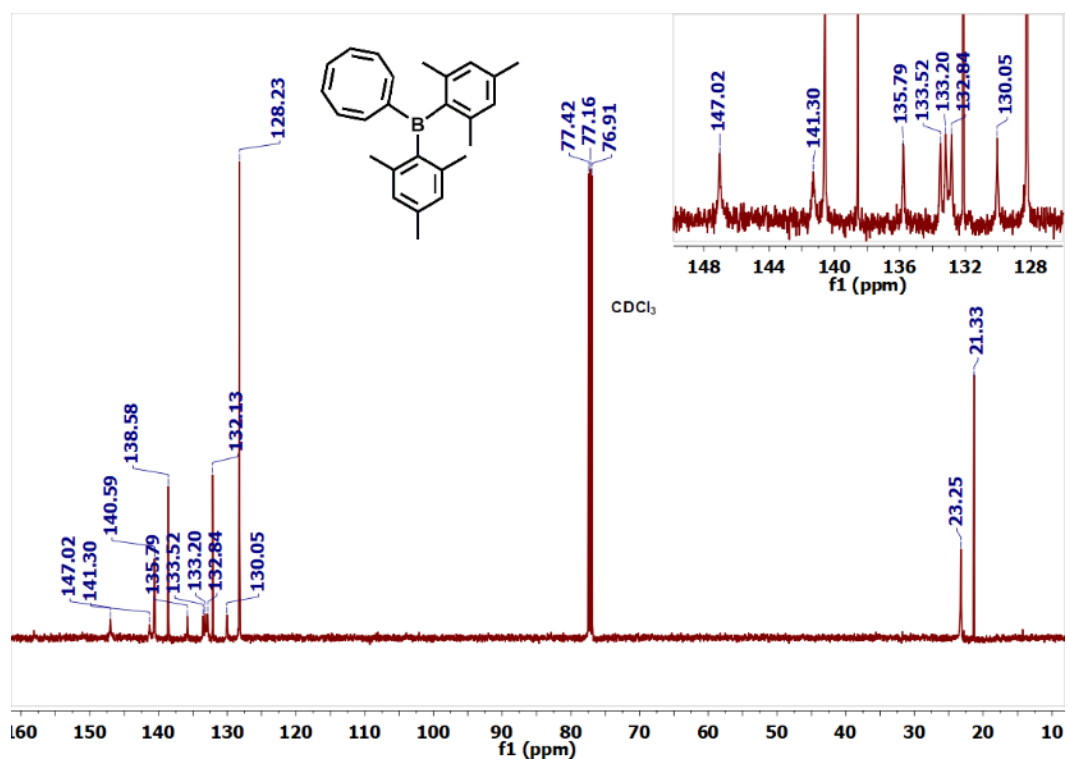


Figure 3.38. $^{13}\text{C}\{^1\text{H}\}$ NMR spectrum (126 MHz) of COT-BMes₂ in CDCl₃.

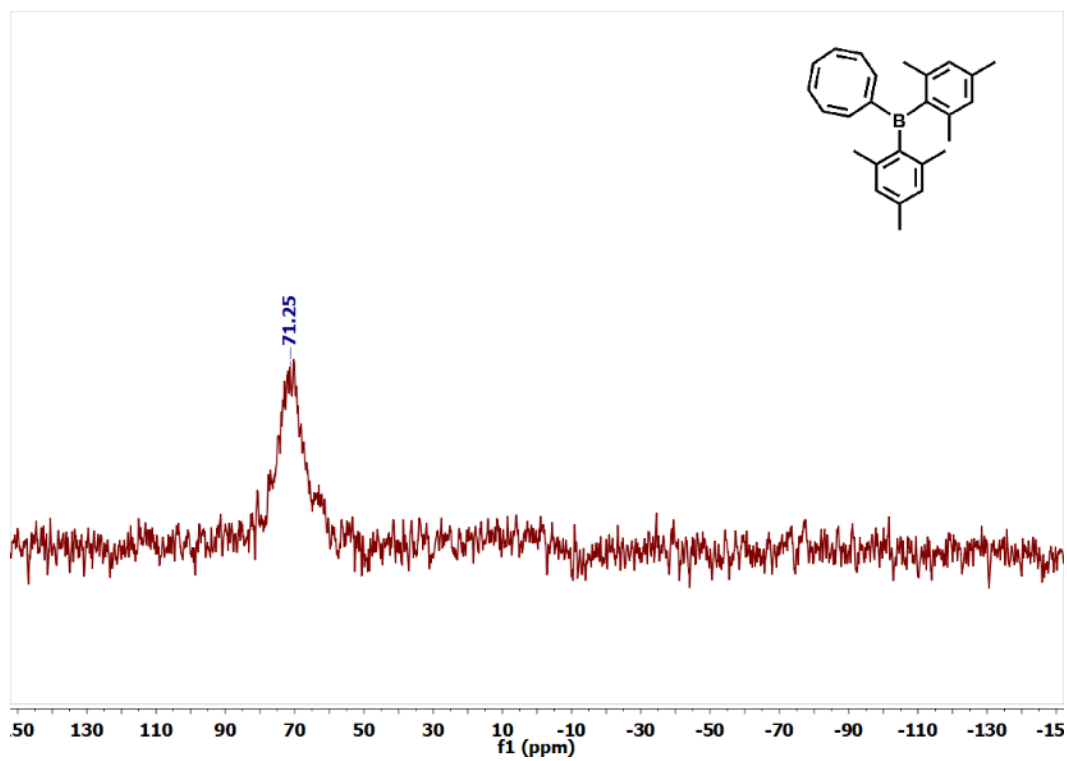


Figure 3.39. ^{11}B NMR spectrum (126 MHz) of COT-BMes₂ in CDCl₃.

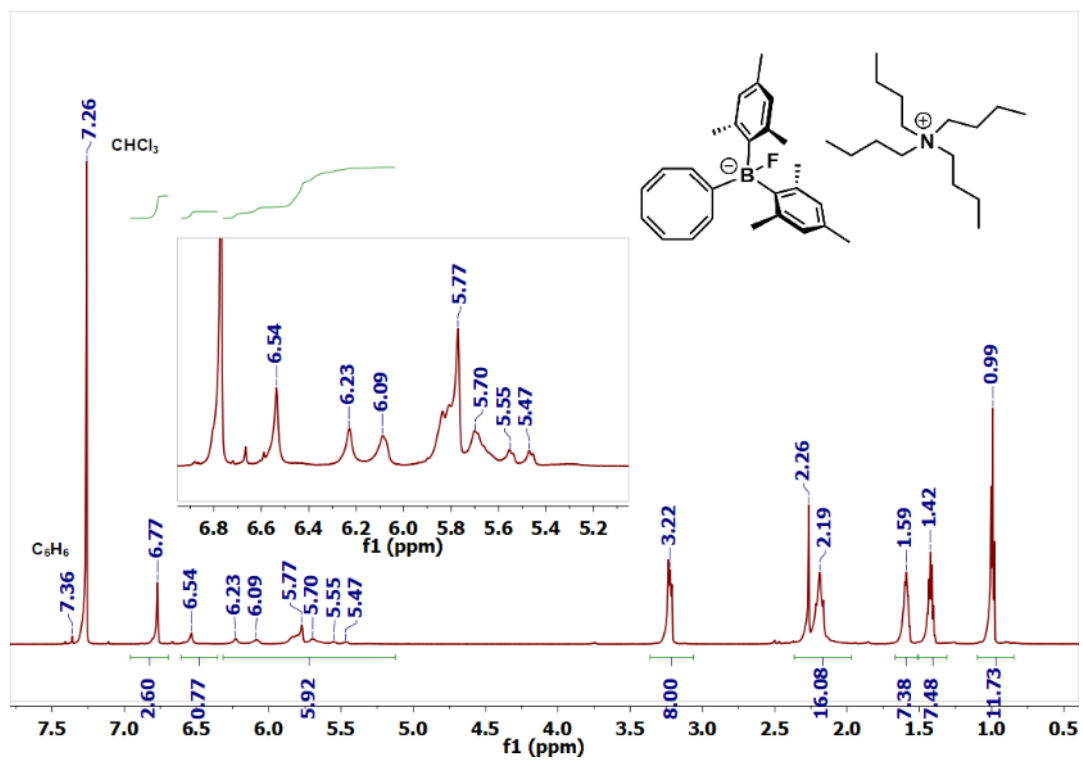


Figure 3.40. ^1H NMR spectrum (700 MHz) of $[\text{nBu}_4\text{N}][\text{COT-BMes}_2(\text{F})]$ in CDCl_3 .

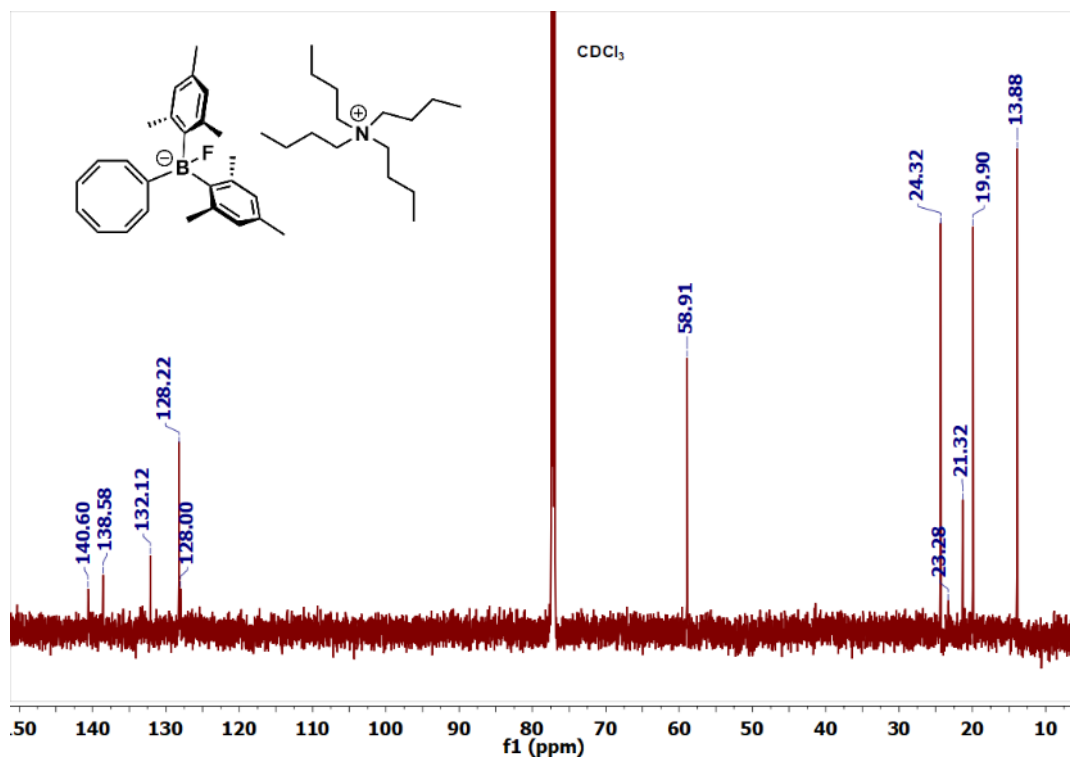


Figure 3.41. $^{13}\text{C}\{^1\text{H}\}$ NMR spectrum (176 MHz) of $[\text{nBu}_4\text{N}][\text{COT-BMes}_2(\text{F})]$ in CDCl_3 .

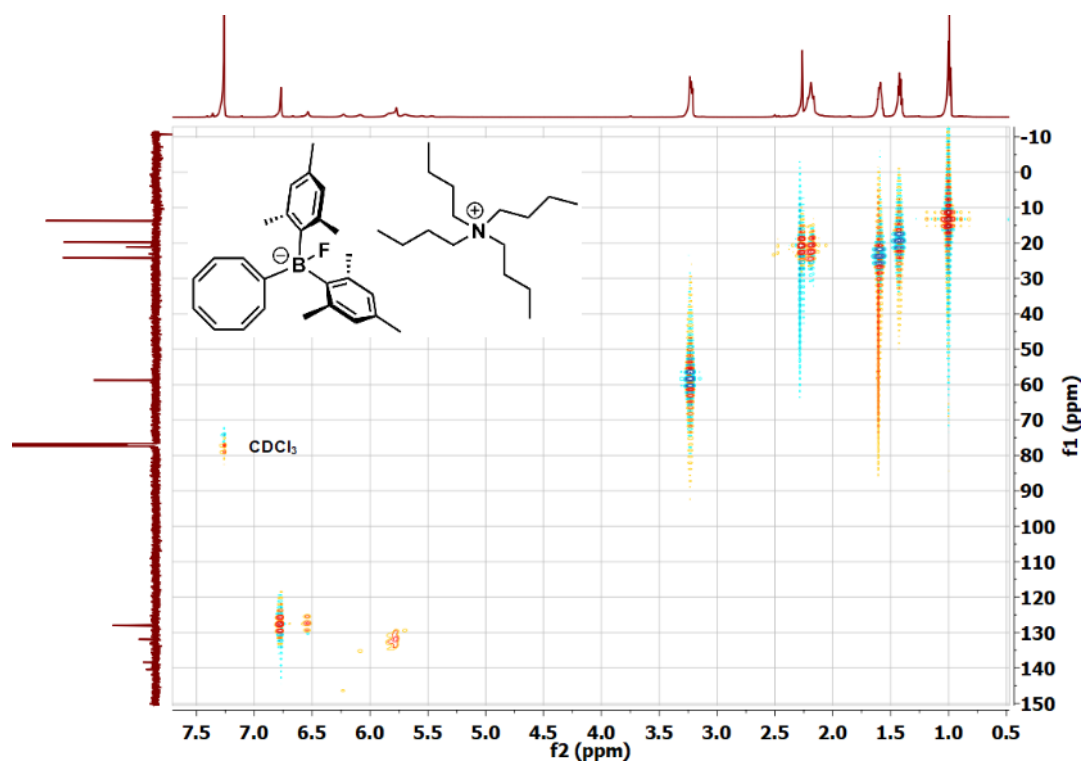


Figure 3.42. ^1H gHSQCAD NMR spectrum (700 MHz) of $[\text{nBu}_4\text{N}][\text{COT-BMes}_2(\text{F})]$ in CDCl_3 .

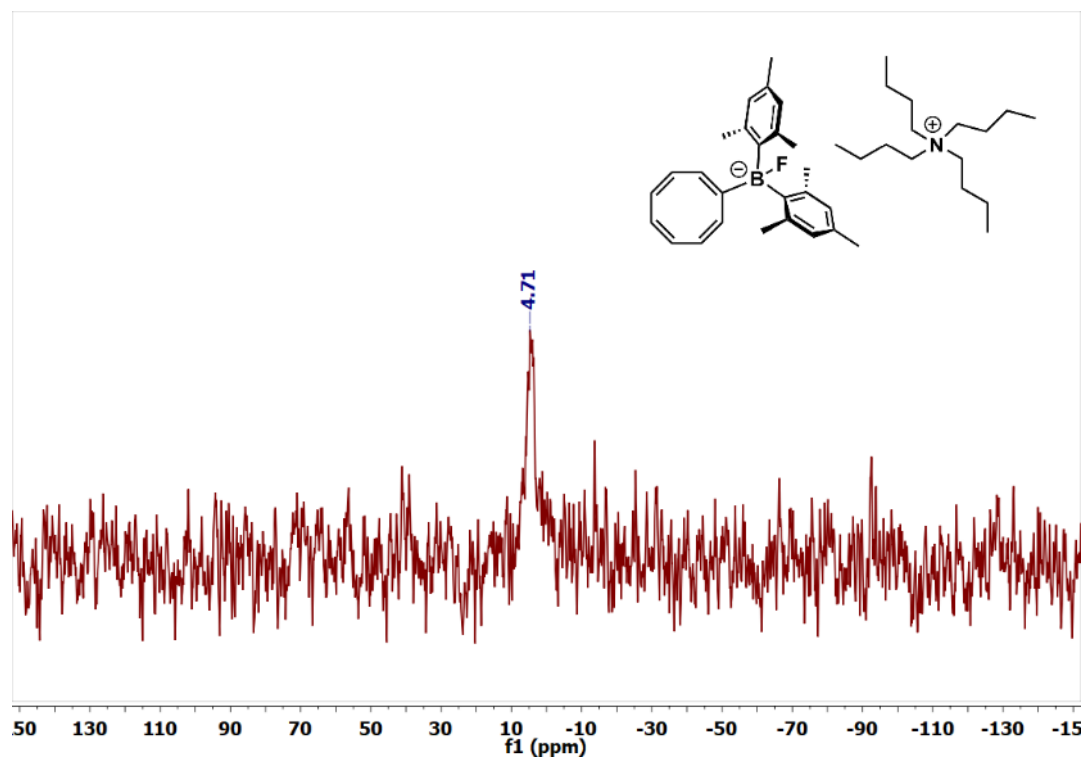


Figure 3.43. ^{11}B NMR spectrum (128 MHz) of $[\text{nBu}_4\text{N}][\text{COT-BMes}_2(\text{F})]$ in CDCl_3 .

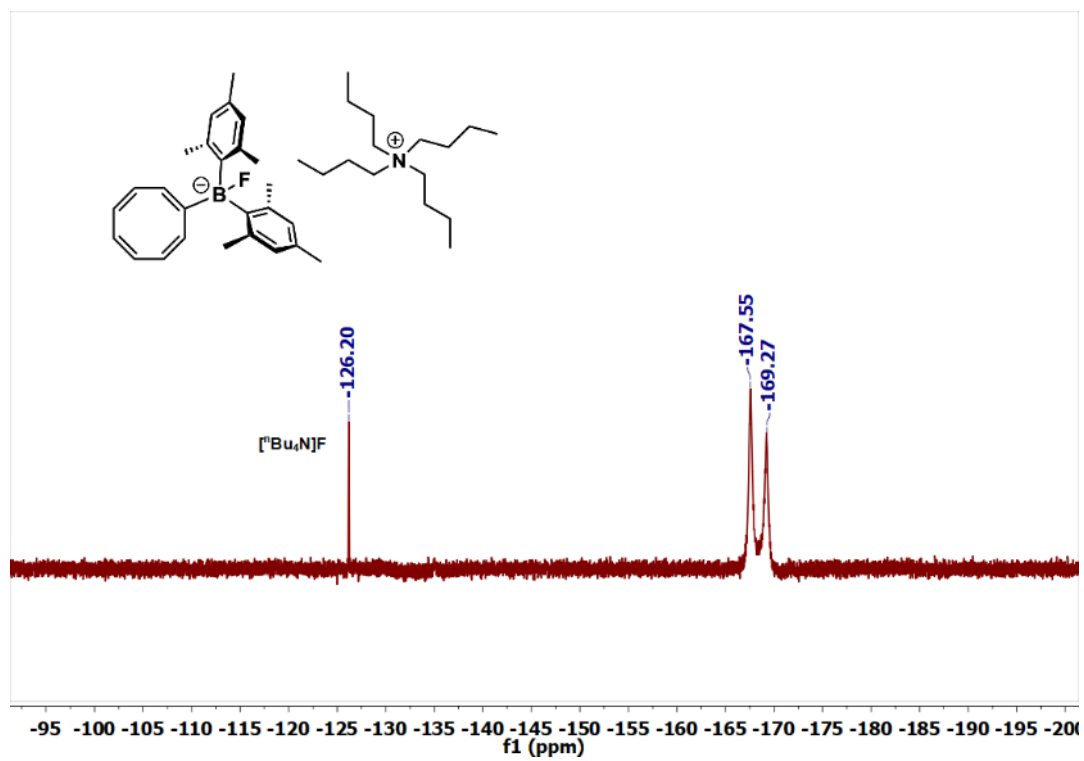


Figure 3.44. ^{19}F NMR spectrum (376 MHz) of $[\text{nBu}_4\text{N}][\text{COT-BMes}_2(\text{F})]$ in C_6D_6 .

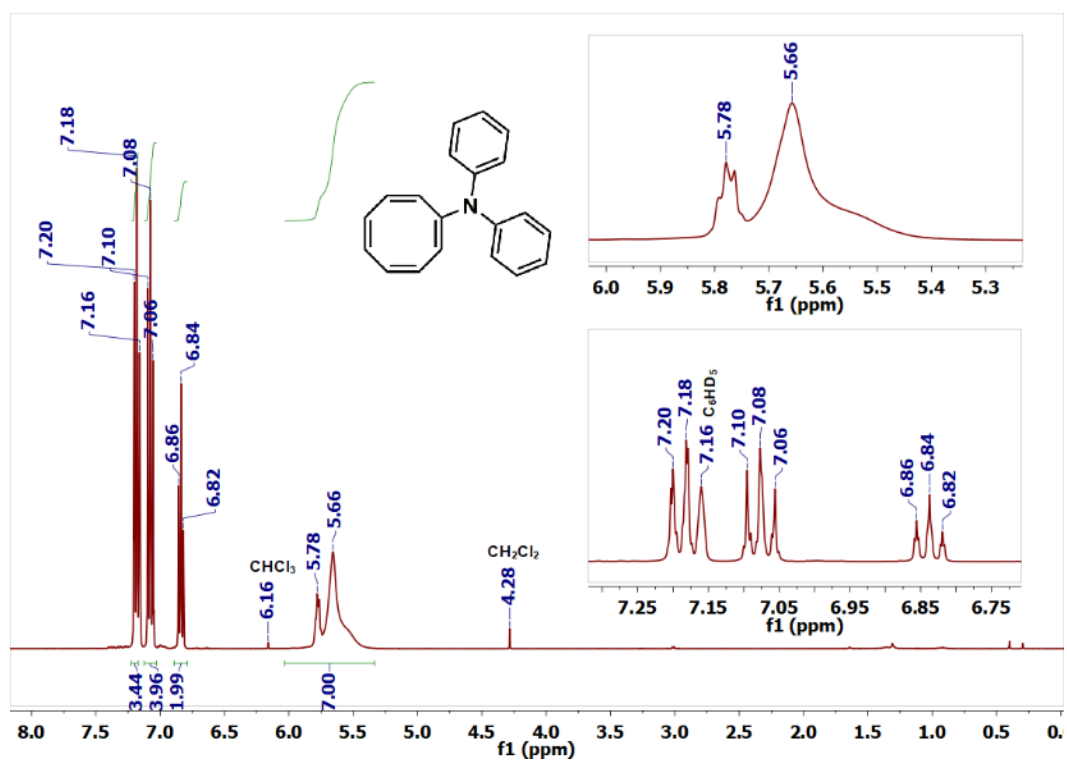


Figure 3.45. ^1H NMR spectrum (400 MHz) of COT-NPh₂ in C_6D_6 .

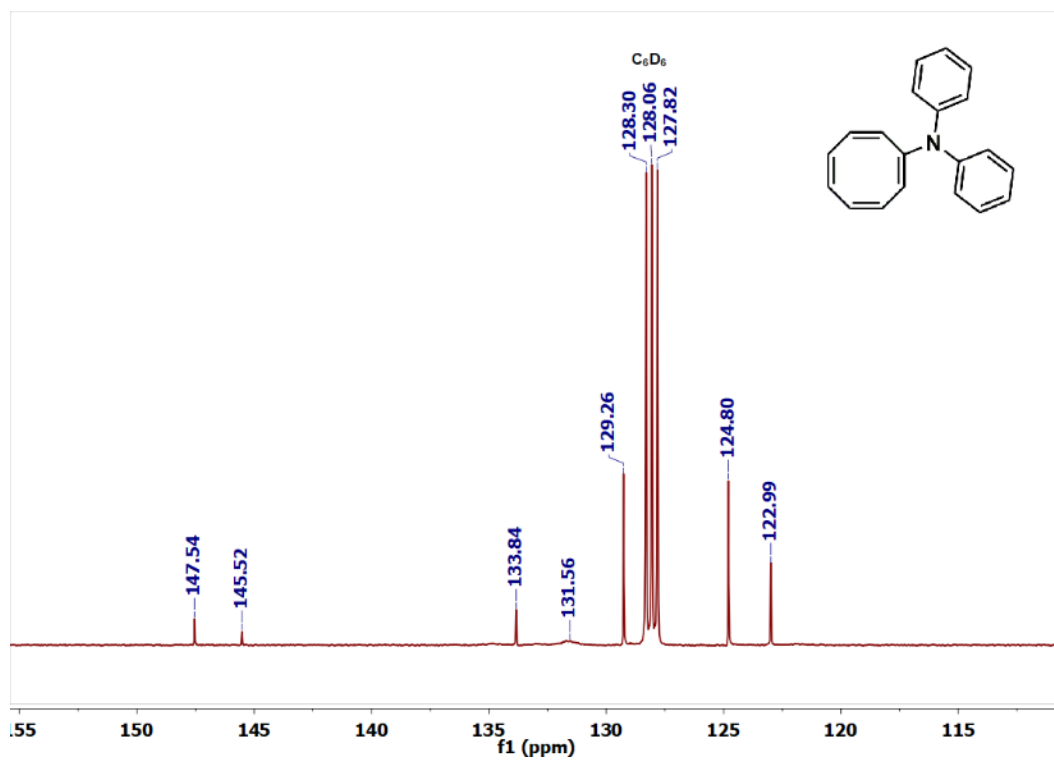


Figure 3.46. $^{13}\text{C}\{^1\text{H}\}$ NMR spectrum (101 MHz) of COT-NPh₂ in C₆D₆.

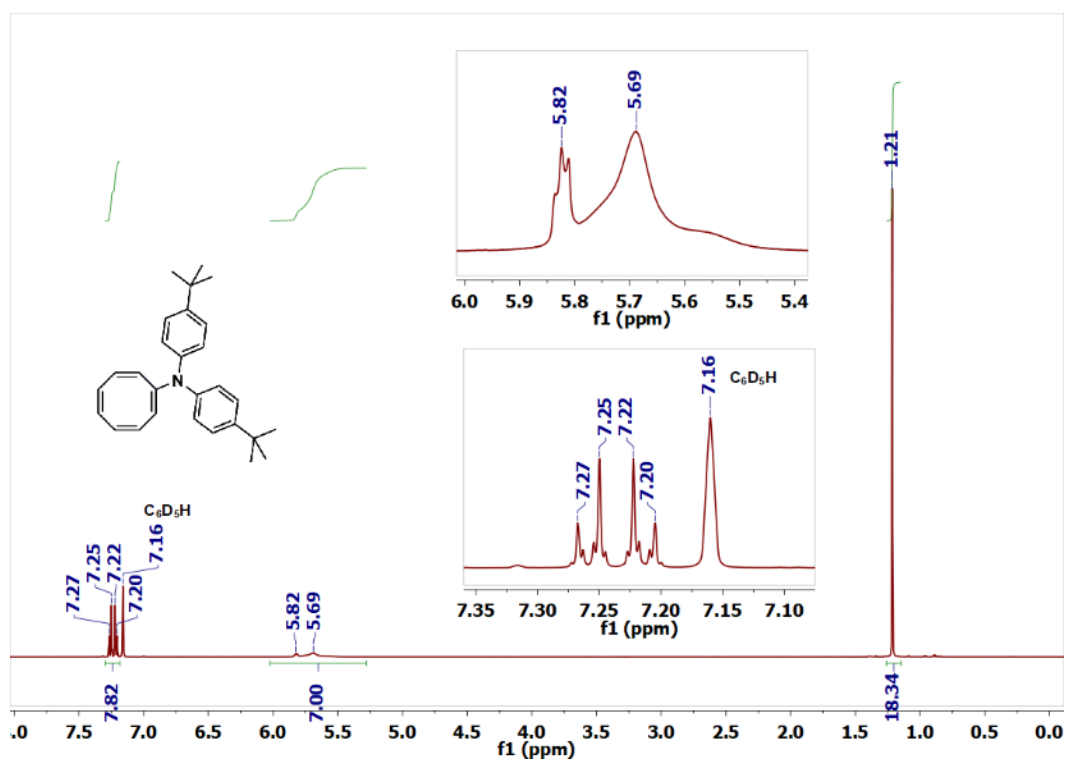


Figure 3.47. ^1H NMR spectrum (500 MHz) of $\text{COT-N}(\text{C}_6\text{H}_4^t\text{Bu})_2$ in C_6D_6 .

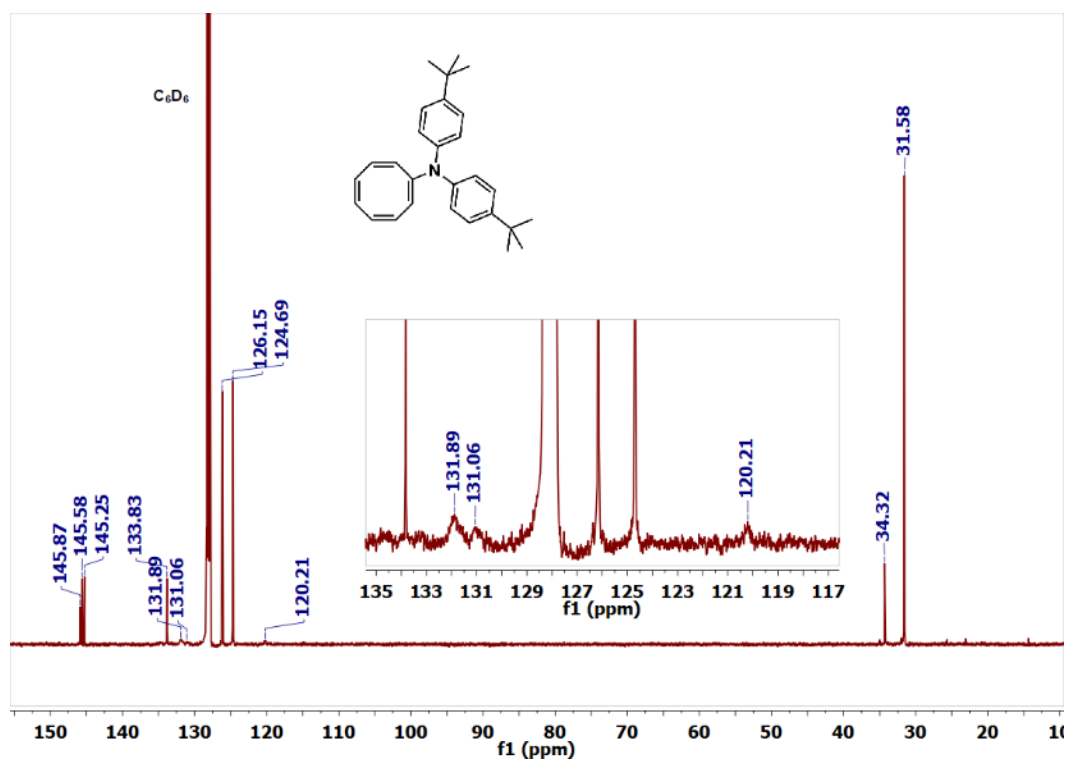


Figure 3.48. $^{13}\text{C}\{^1\text{H}\}$ NMR spectrum (126 MHz) of $\text{COT-N}(\text{C}_6\text{H}_4\text{tBu})_2$ in C_6D_6 .

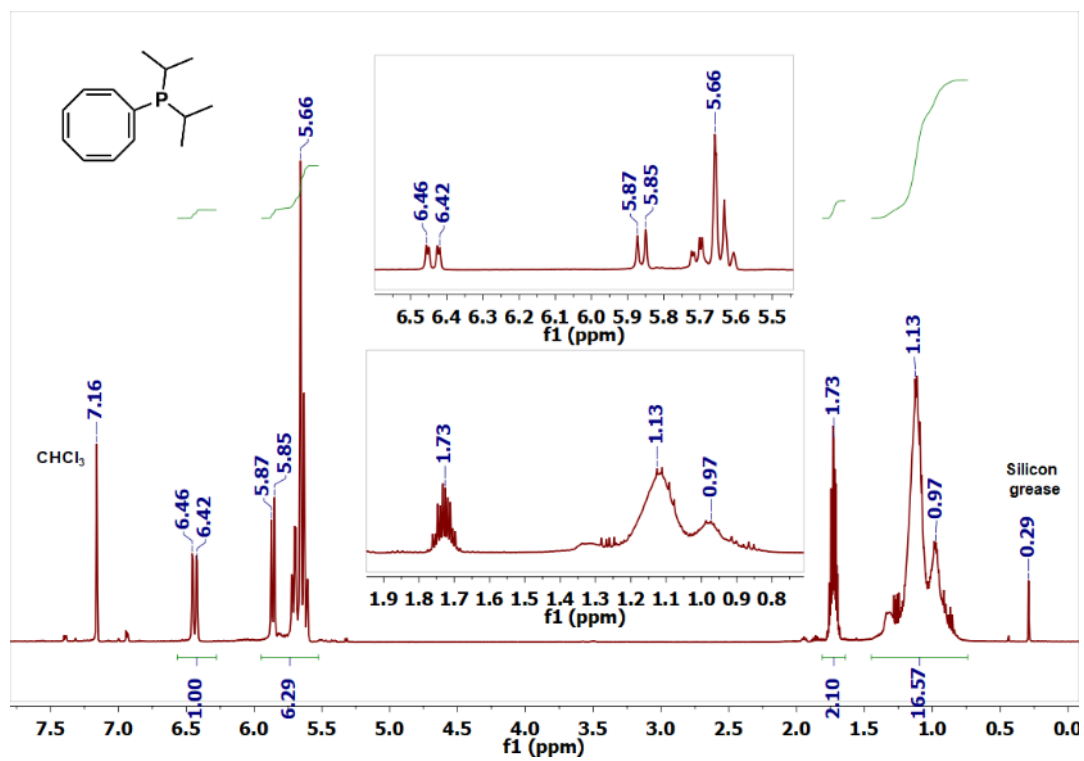


Figure 3.49. 1H NMR spectrum (500 MHz) of COT- P^iPr_2 in $CDCl_3$.

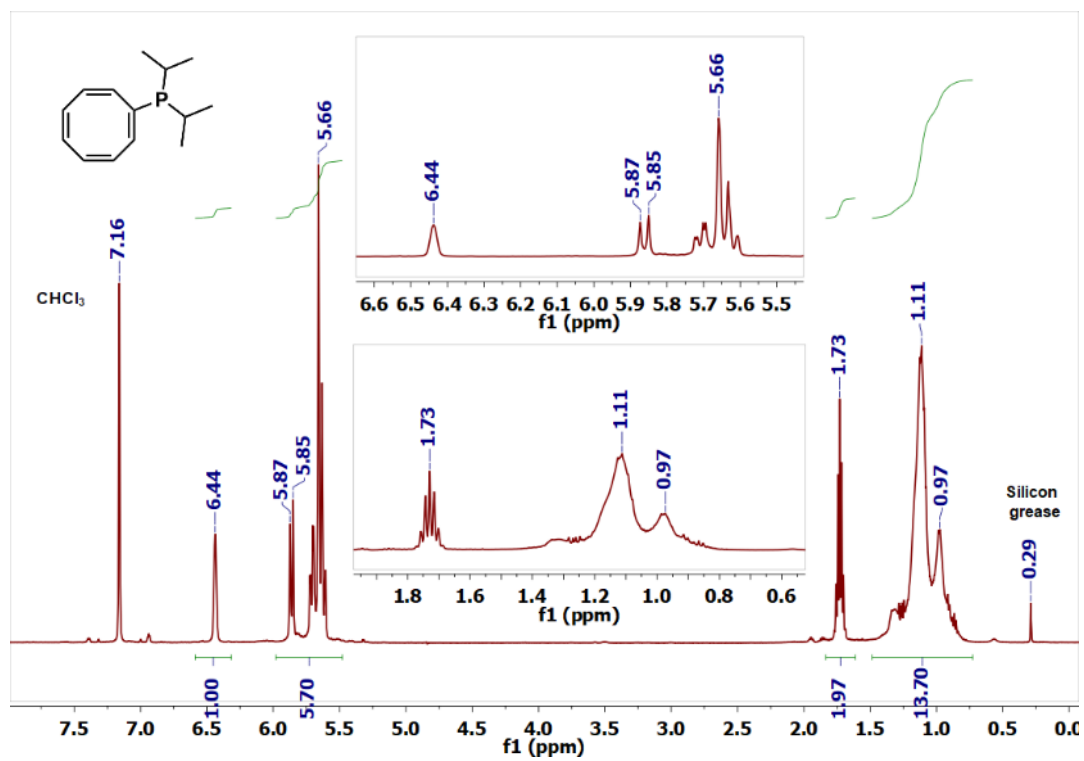


Figure 3.50. $^1\text{H}\{^{31}\text{P}\}$ NMR spectrum (500 MHz) of $\text{COT-P}^i\text{Pr}_2$ in CDCl_3 .

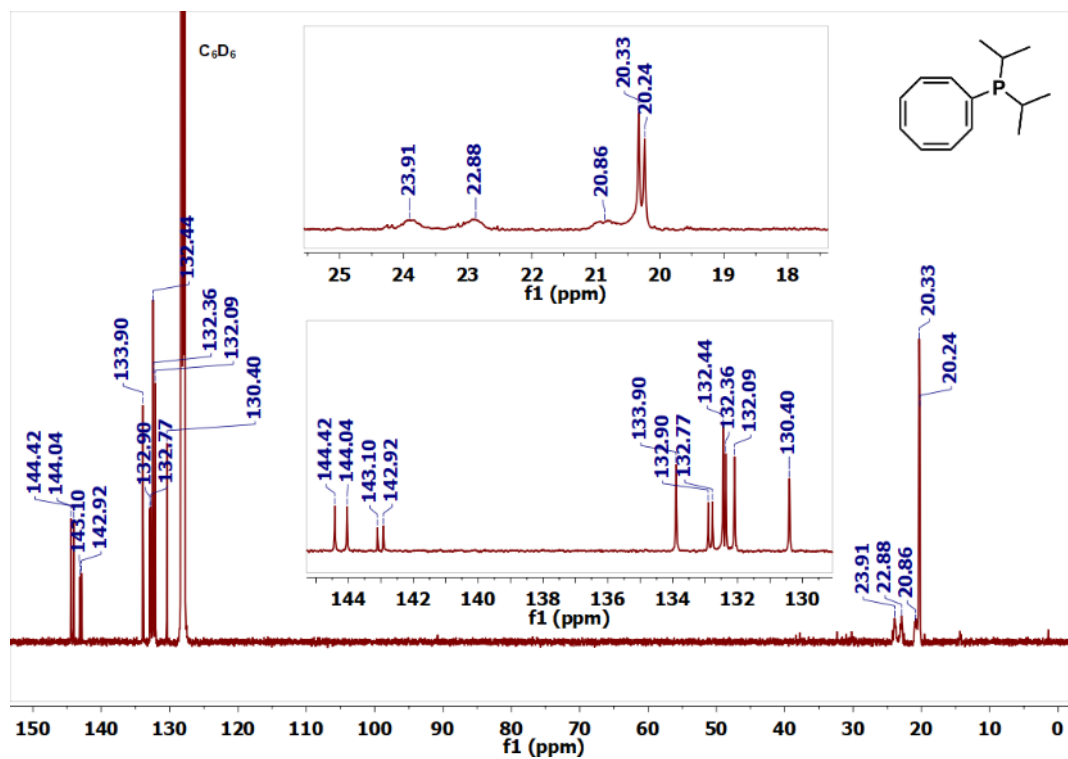


Figure 3.51. $^{13}\text{C}\{^1\text{H}\}$ NMR spectrum (126 MHz) of COT-PiPr₂ in CDCl₃.

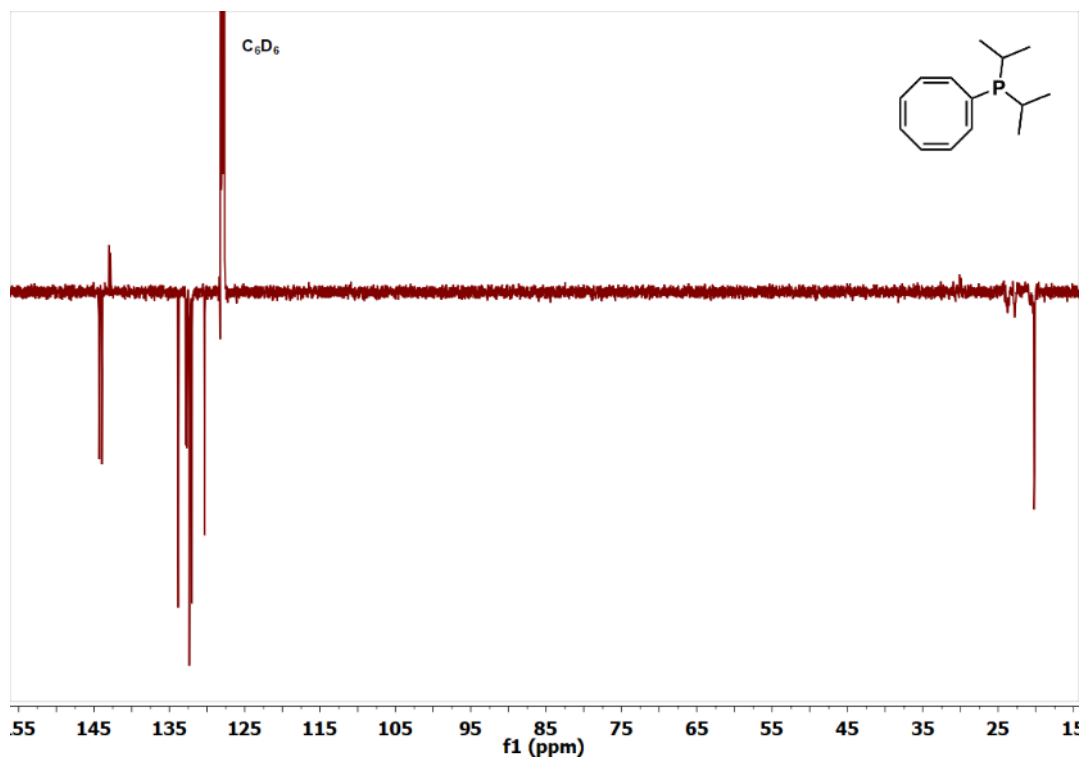


Figure 3.52. $^{13}\text{C}\{^1\text{H}\}$ DEPTq NMR spectrum (126 MHz) of COT- P^iPr_2 in CDCl_3 .

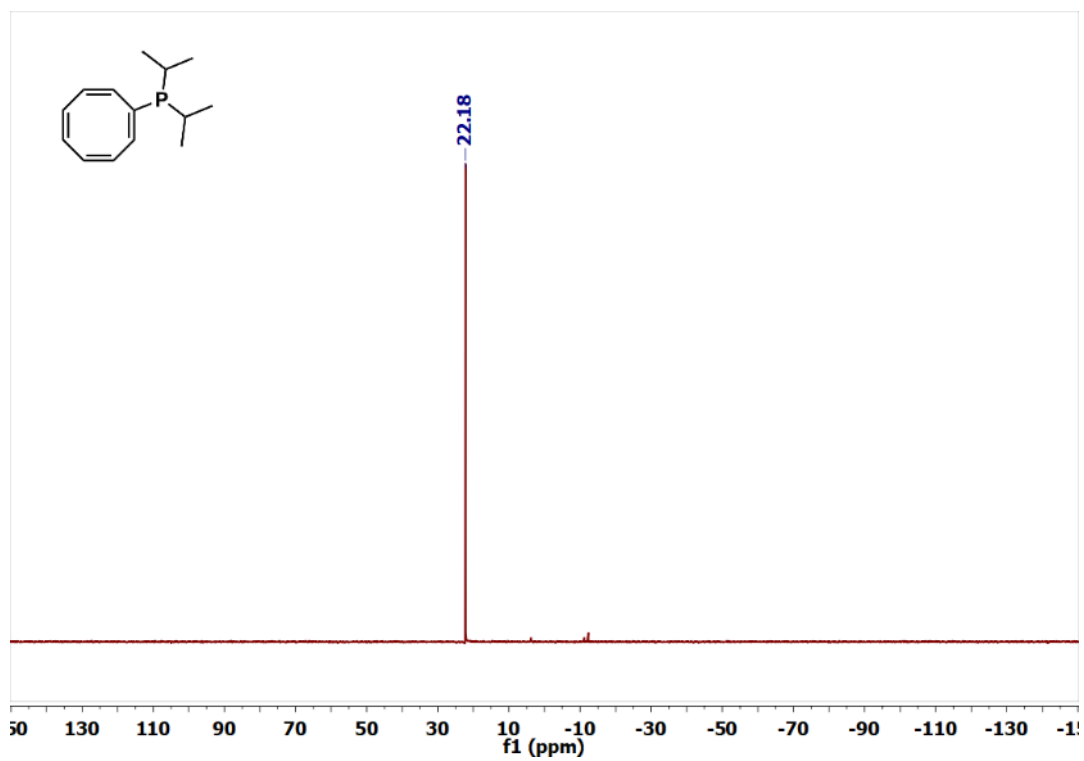


Figure 3.53. $^{31}\text{P}\{^1\text{H}\}$ NMR spectrum (202 MHz) of COT- P^iPr_2 in CDCl_3 .

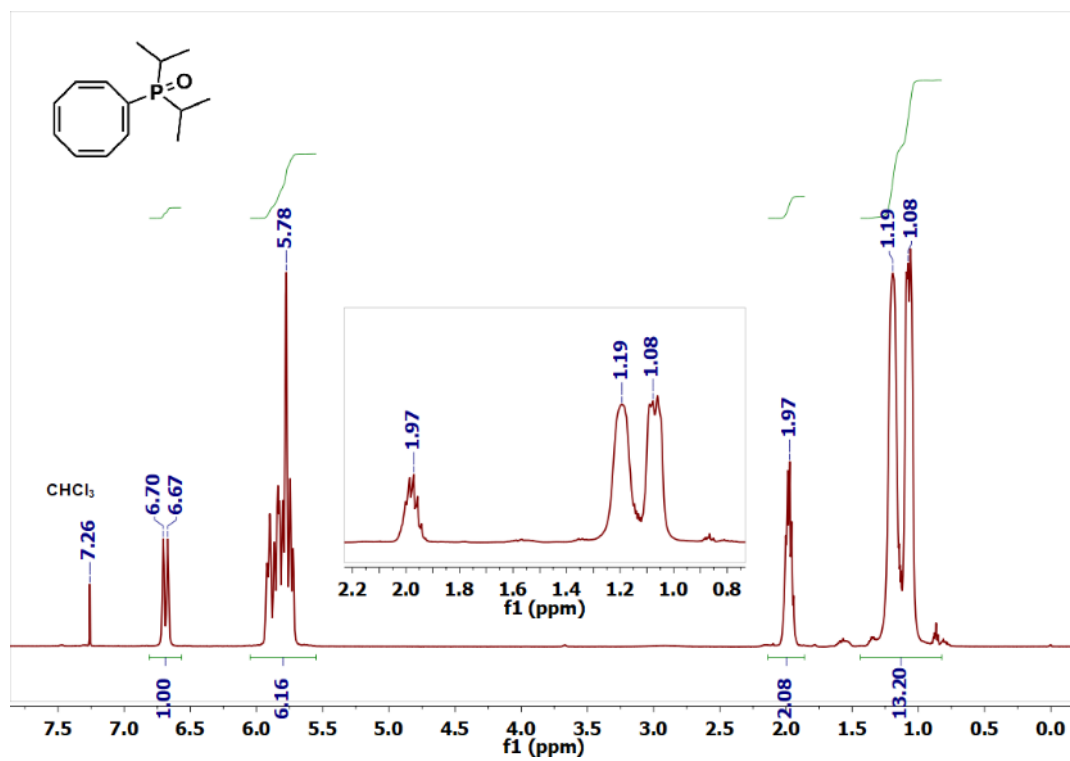


Figure 3.54. ^1H NMR spectrum (500 MHz) of COT-P(O)Pr_2 in CDCl_3 .

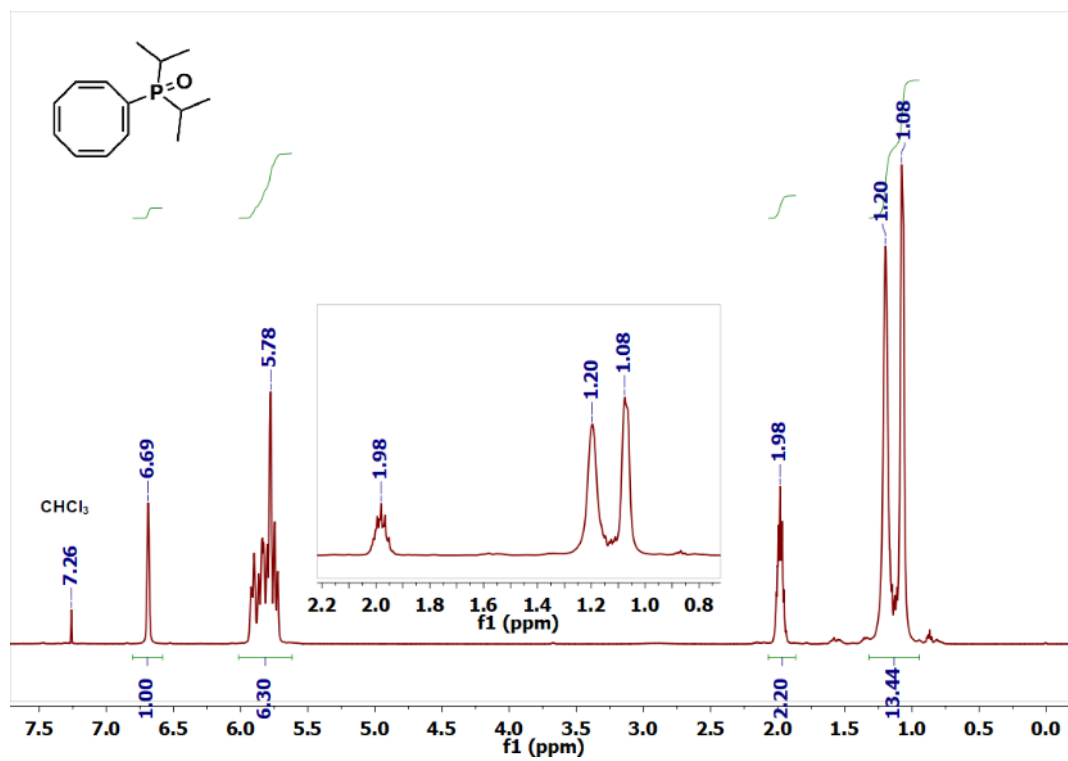


Figure 3.55. $^1\text{H}\{^{31}\text{P}\}$ NMR spectrum (500 MHz) of COT-P(O)Pr_2 in CDCl_3 .

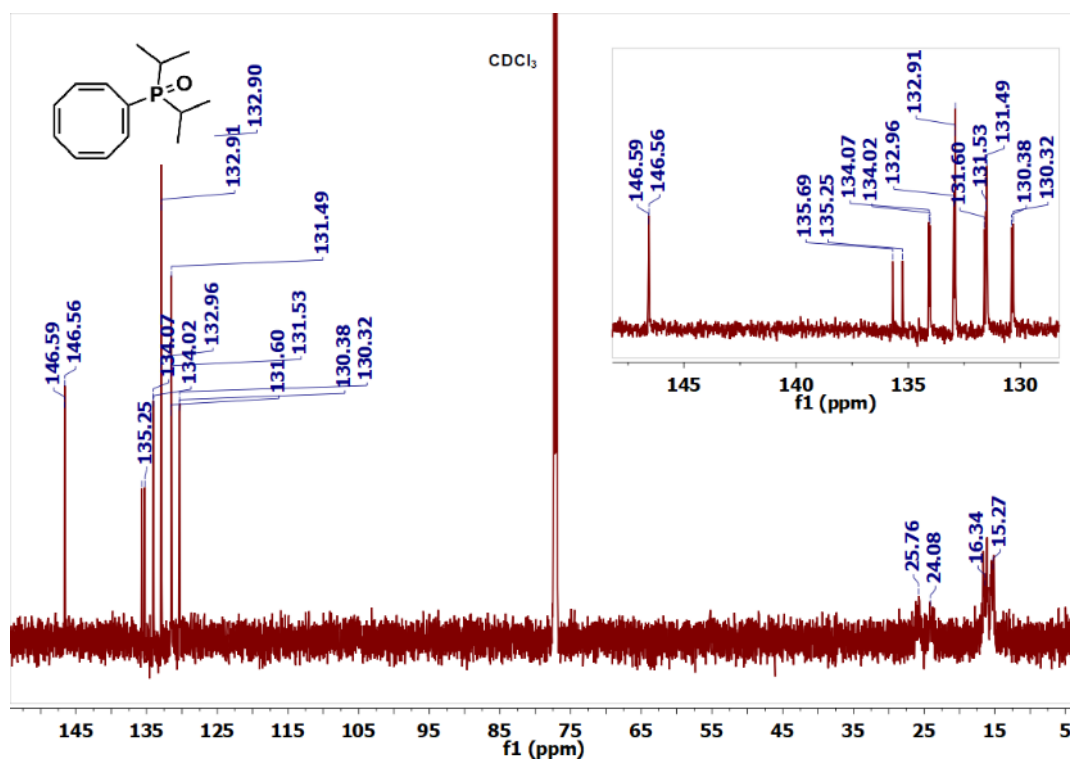


Figure 3.56. ¹³C{¹H} NMR spectrum (176 MHz) of COT-P(O)Pr₂ in CDCl₃.

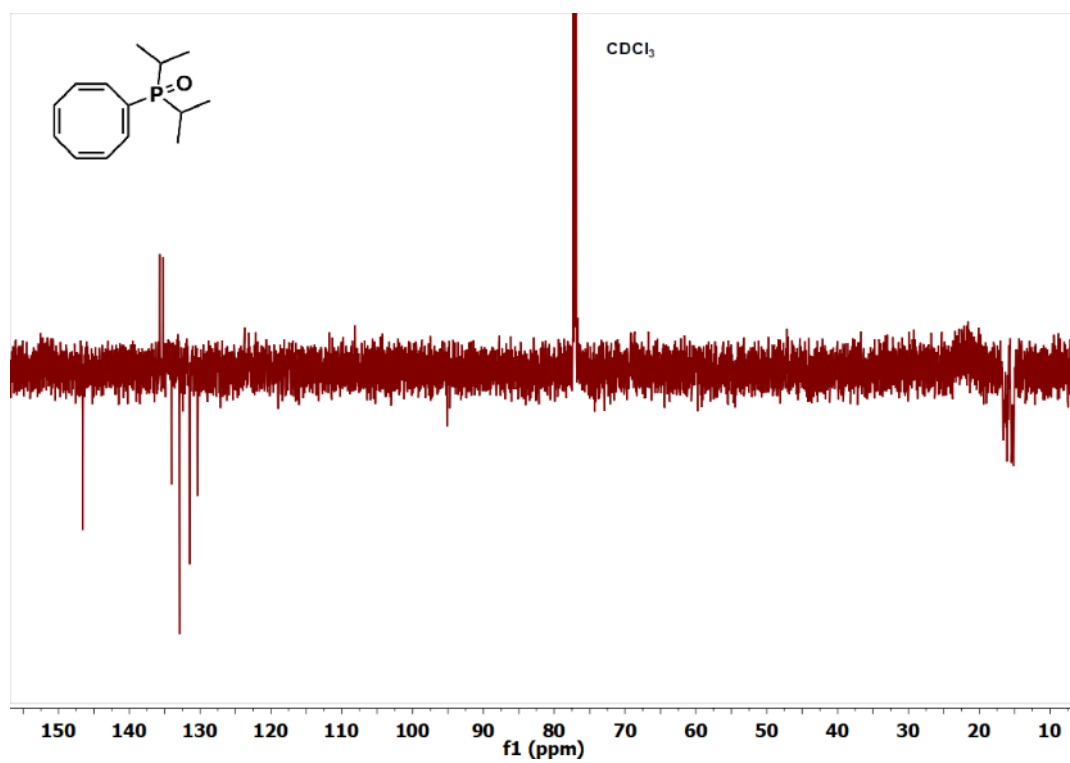


Figure 3.57. $^{13}\text{C}\{^1\text{H}\}$ DEPTq NMR spectrum (176 MHz) of COT-P(O)iPr_2 in CDCl_3 .

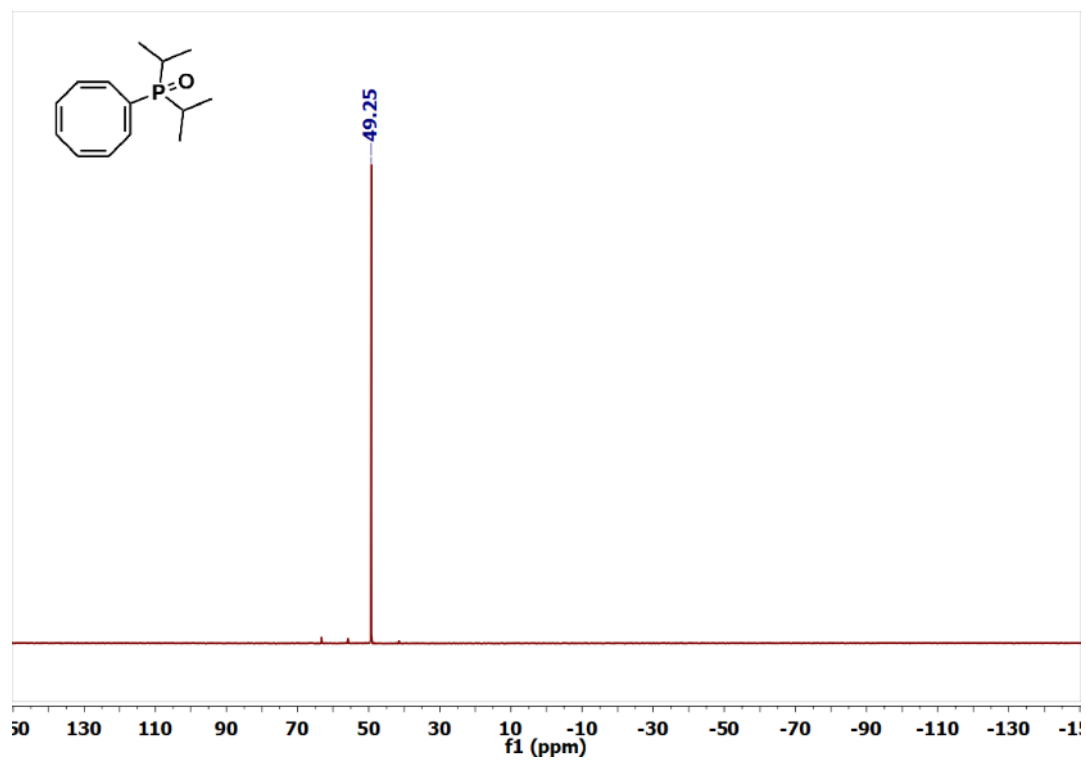


Figure 3.58. $^{31}\text{P}\{^1\text{H}\}$ NMR spectrum (202 MHz) of COT-P(O)Pr_2 in CDCl_3 .

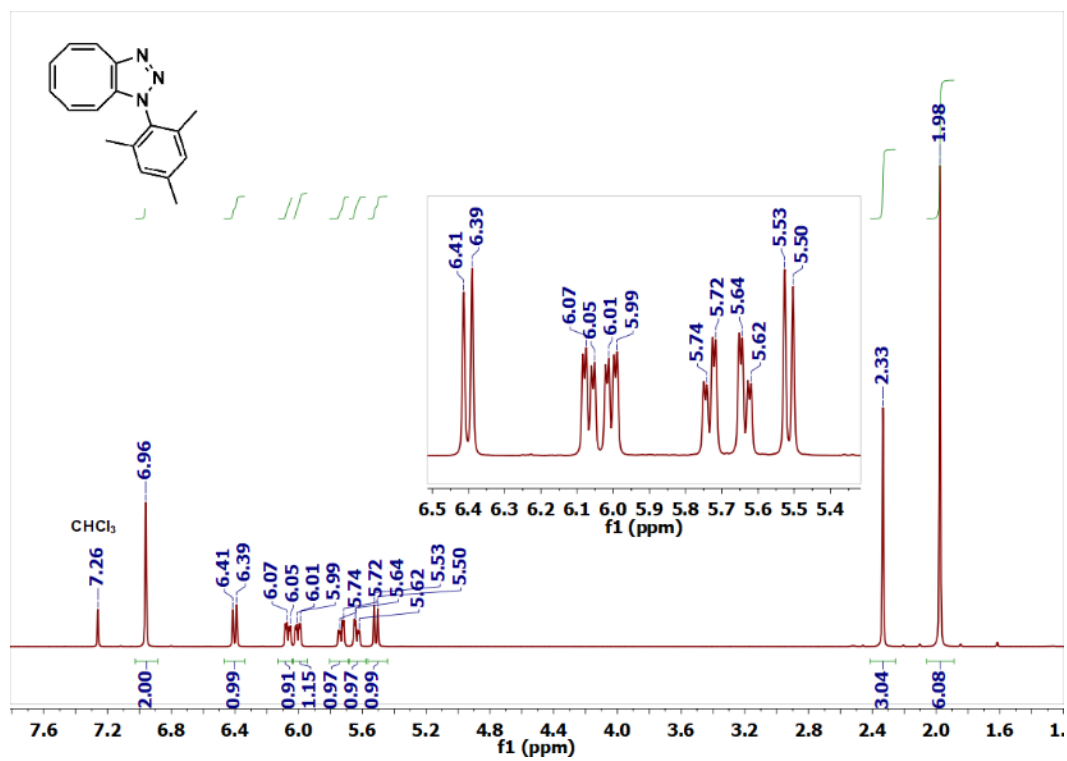


Figure 3.59. ¹H NMR spectrum (500 MHz) of COT-N₃-Mes in CDCl₃.

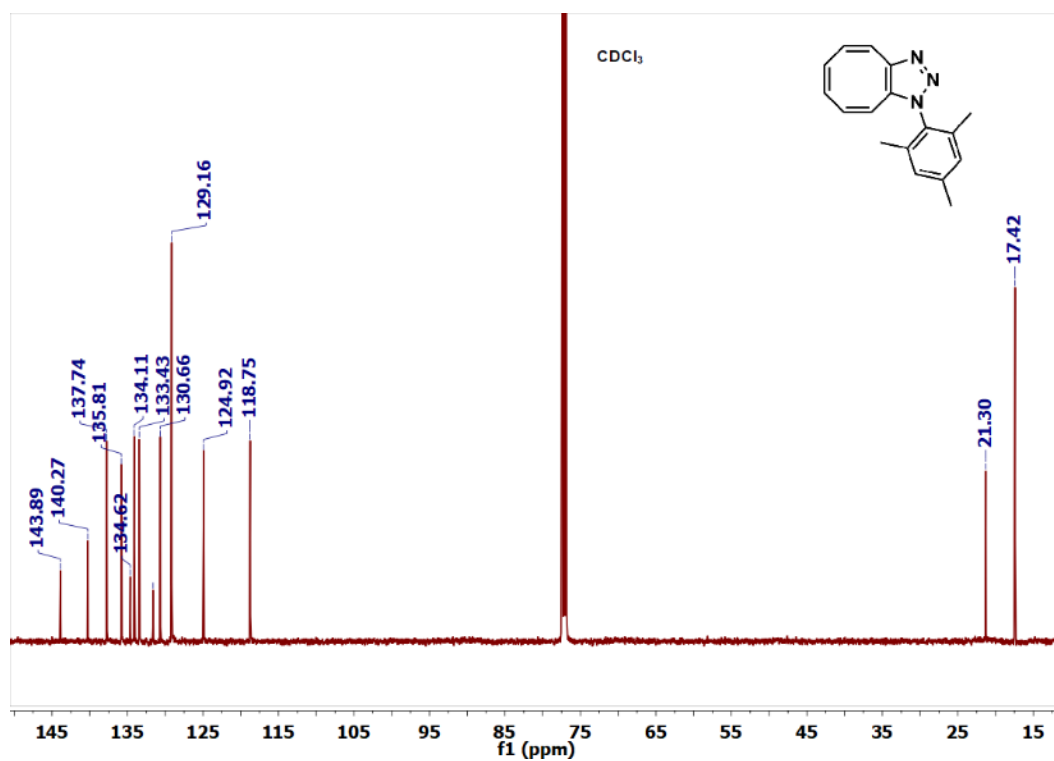


Figure 3.60. $^{13}\text{C}\{^1\text{H}\}$ NMR spectrum (126 MHz) of COT-N₃-Mes in CDCl₃.

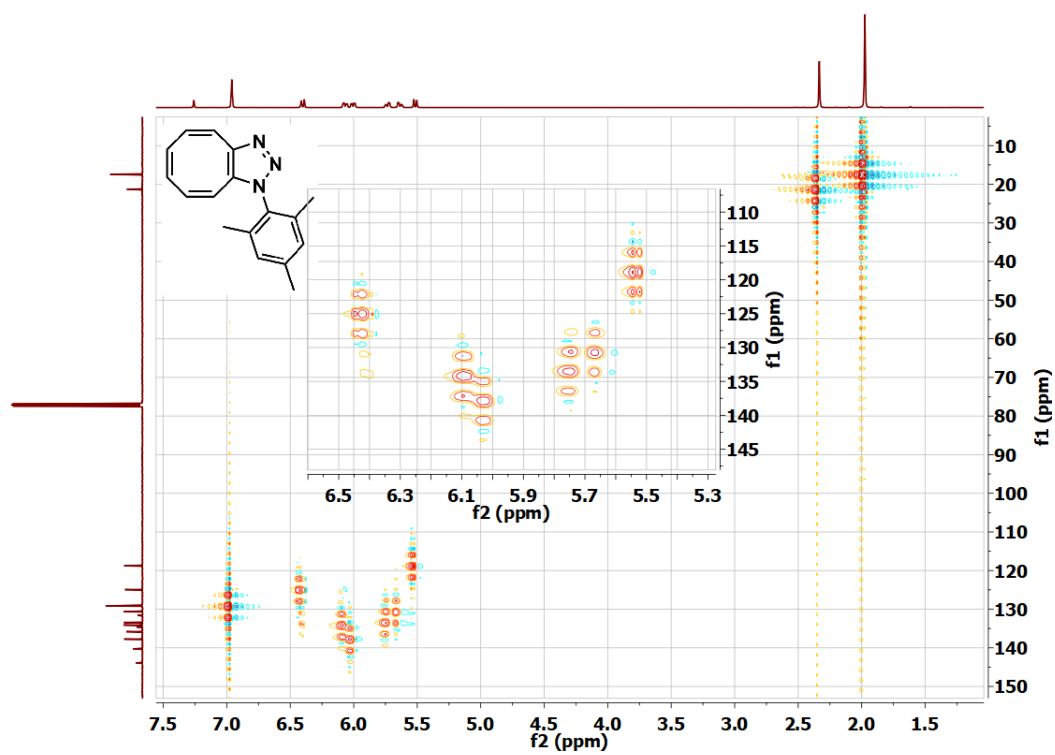


Figure 3.61. ^1H gHSQCAD NMR spectrum (500 MHz) of COT-N₃-Mes in CDCl₃.

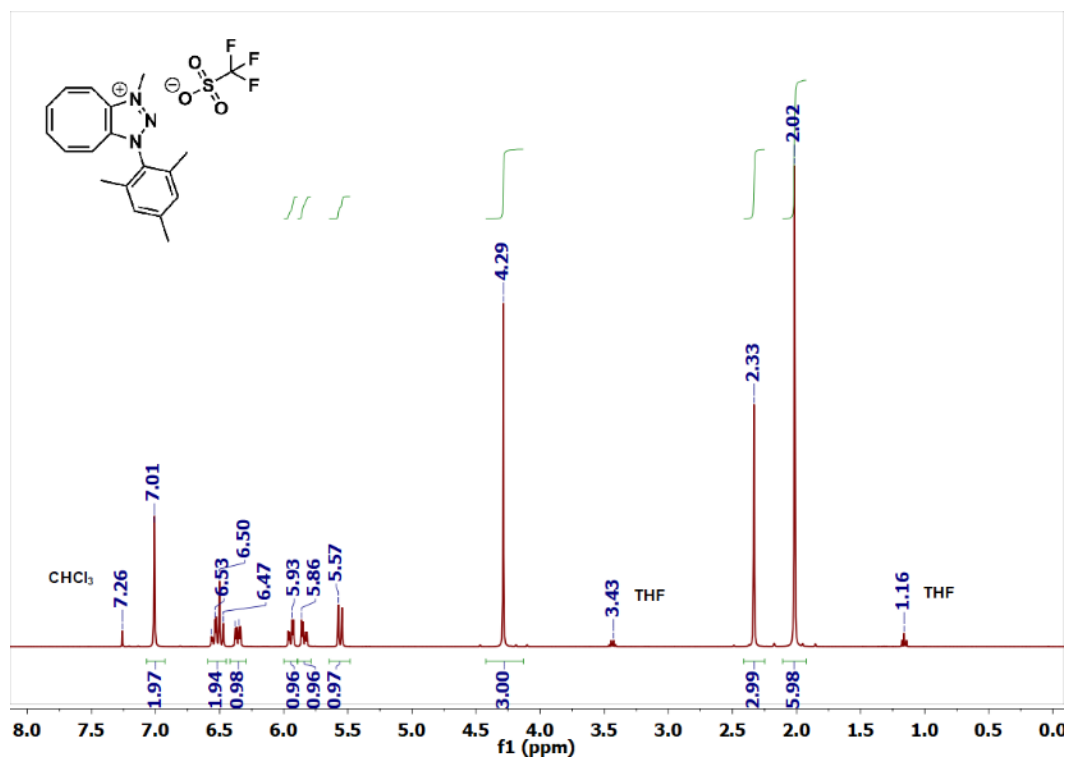


Figure 3.62. ¹H NMR spectrum (400 MHz) of [COT-N₃(Me)-Mes]⁺OTf⁻ in CDCl₃.

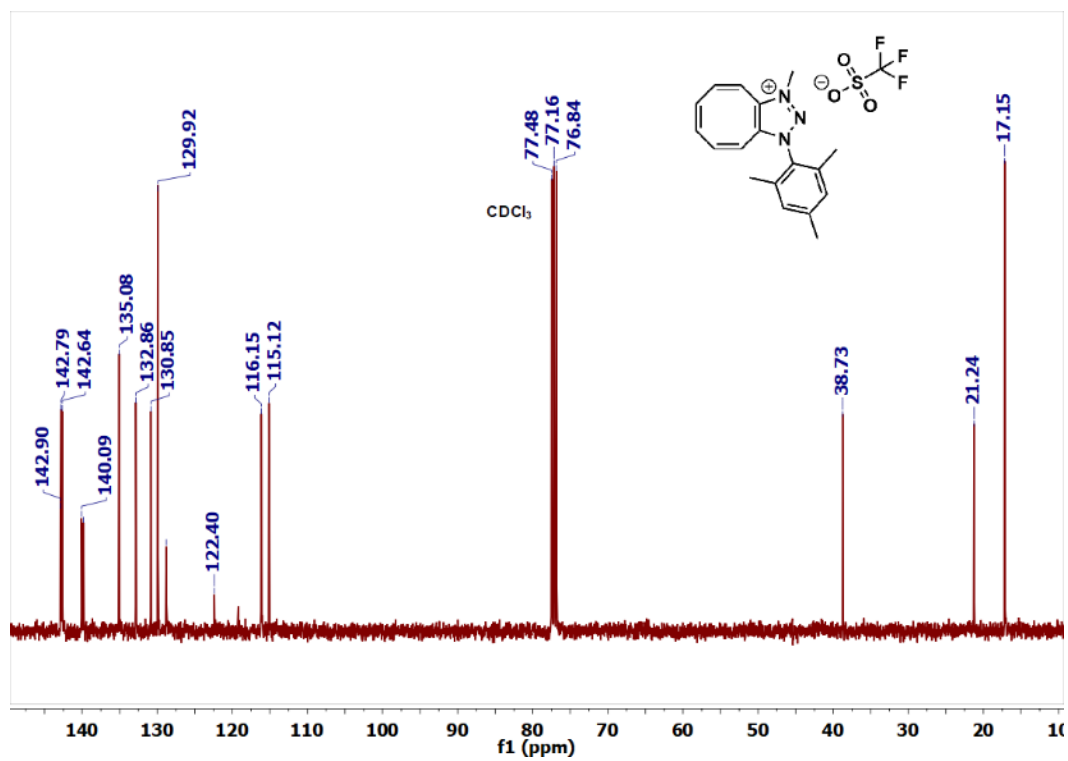


Figure 3.63. $^{13}\text{C}\{^1\text{H}\}$ NMR spectrum (101 MHz) of [COT- $\text{N}_3(\text{Me})$ -Mes] $^+\text{OTf}^-$ in CDCl_3 .

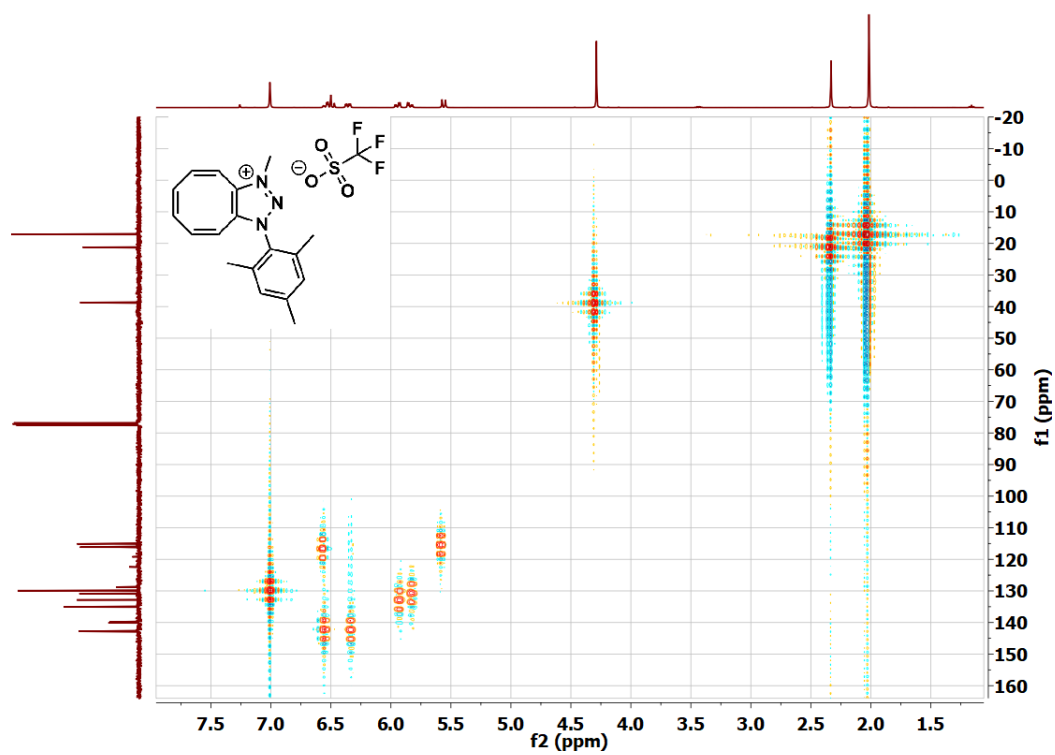


Figure 3.64. ¹H gHSQCAD NMR spectrum (500 MHz) of [COT-N₃(Me)-Mes]OTf in CDCl₃.

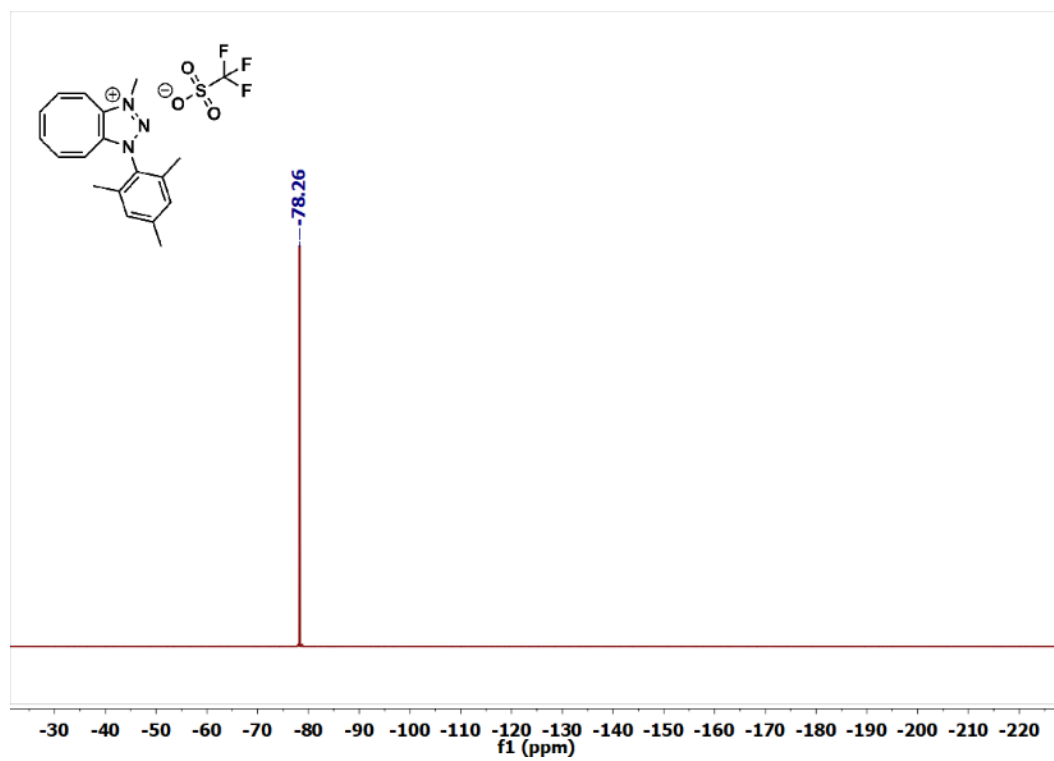


Figure 3.65. $^{19}\text{F}\{^1\text{H}\}$ NMR spectrum (500 MHz) of [COT- $\text{N}_3(\text{Me})$ -Mes]OTf in CDCl_3 .

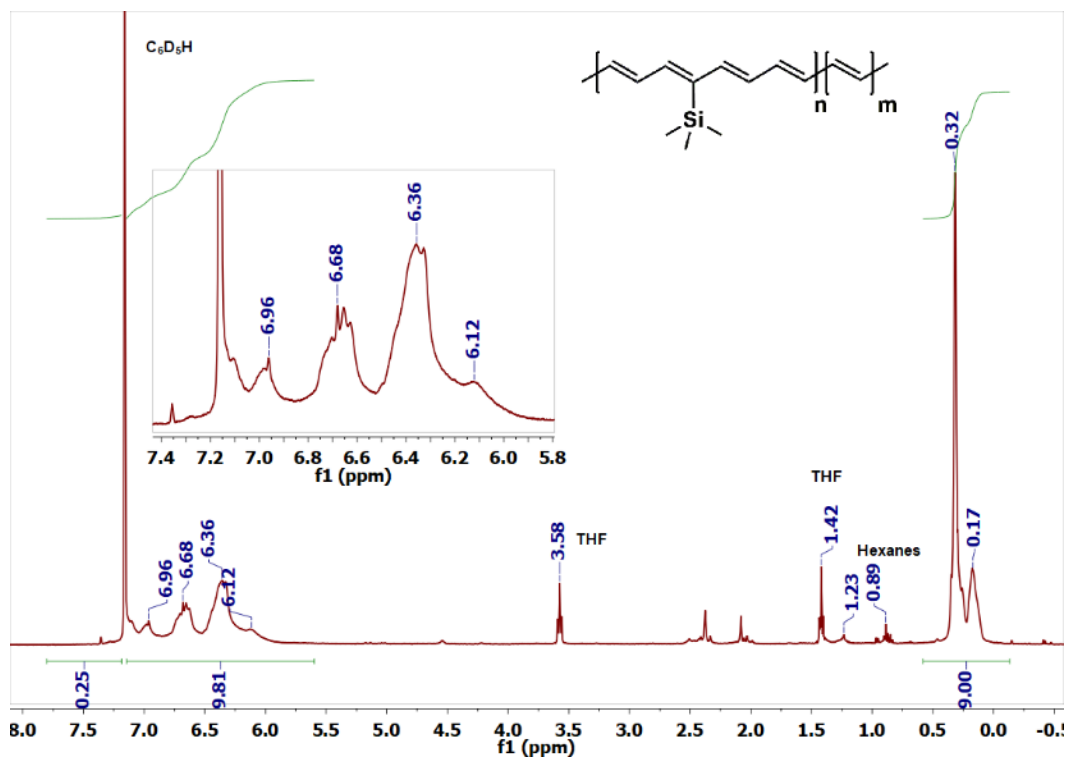


Figure 3.66. ^1H NMR spectrum (400 MHz) of pCOT-SiMe₃ in C_6D_6 .

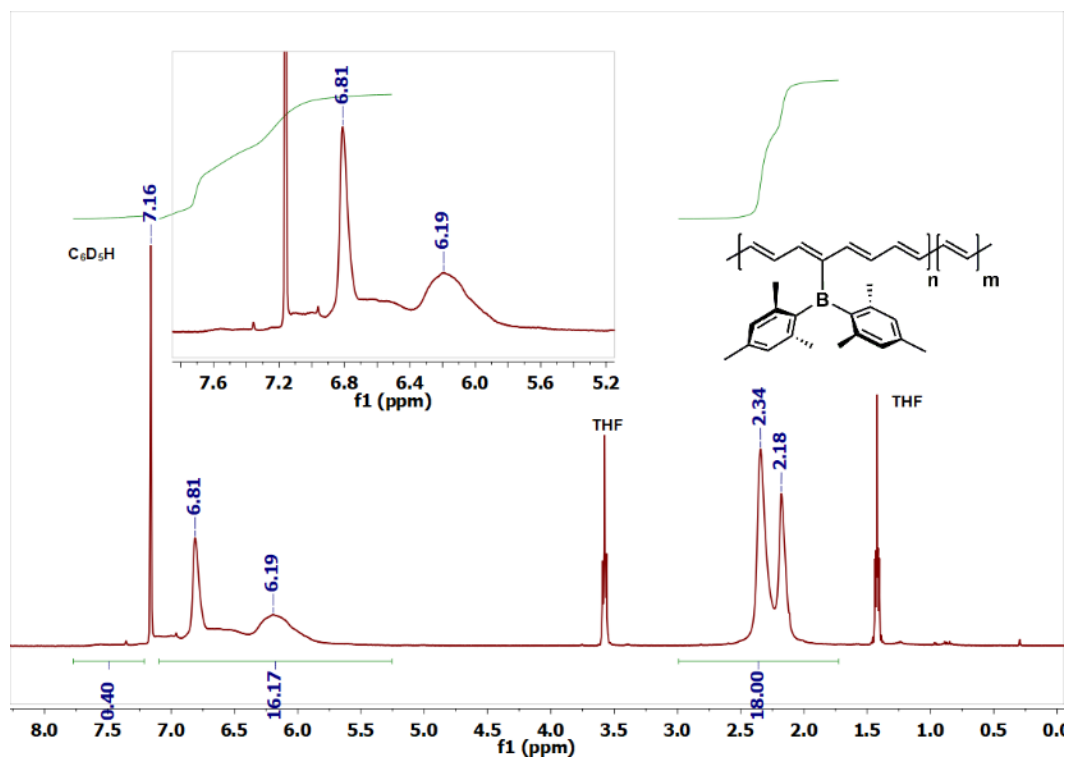


Figure 3.67. ^1H NMR spectrum (400 MHz) of pCOT-BMes₂ in C_6D_6 .

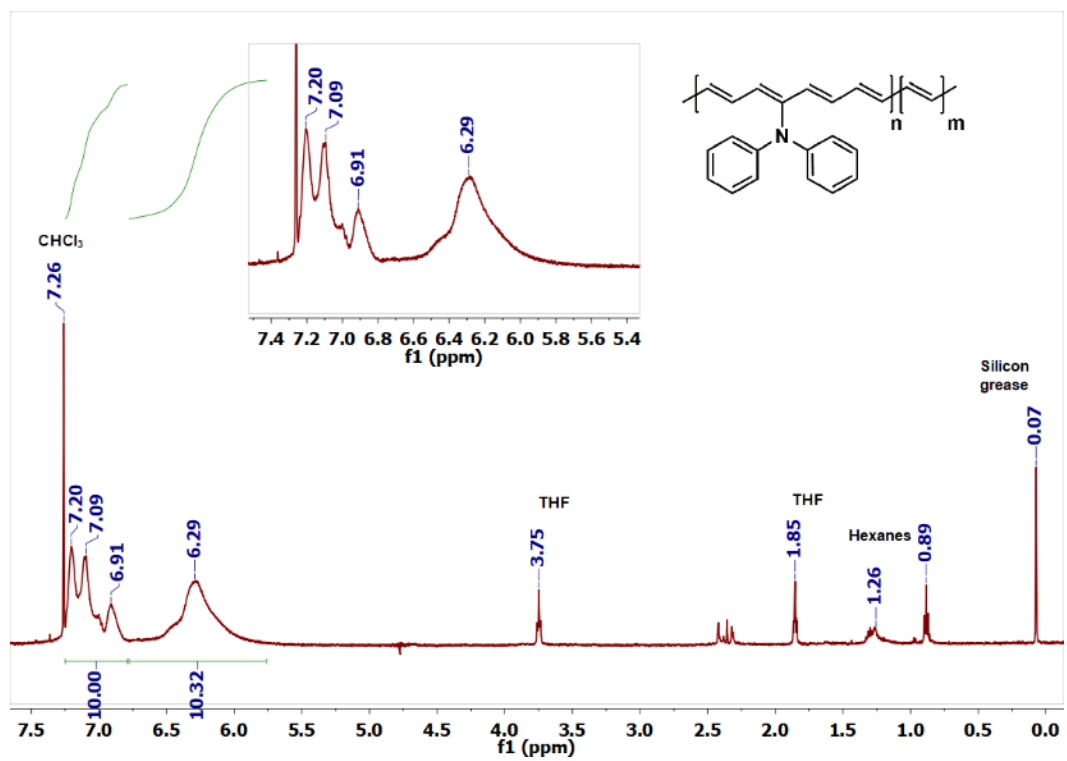


Figure 3.68. ^1H NMR spectrum (500 MHz) of pCOT-NPh₂ in CDCl_3 .

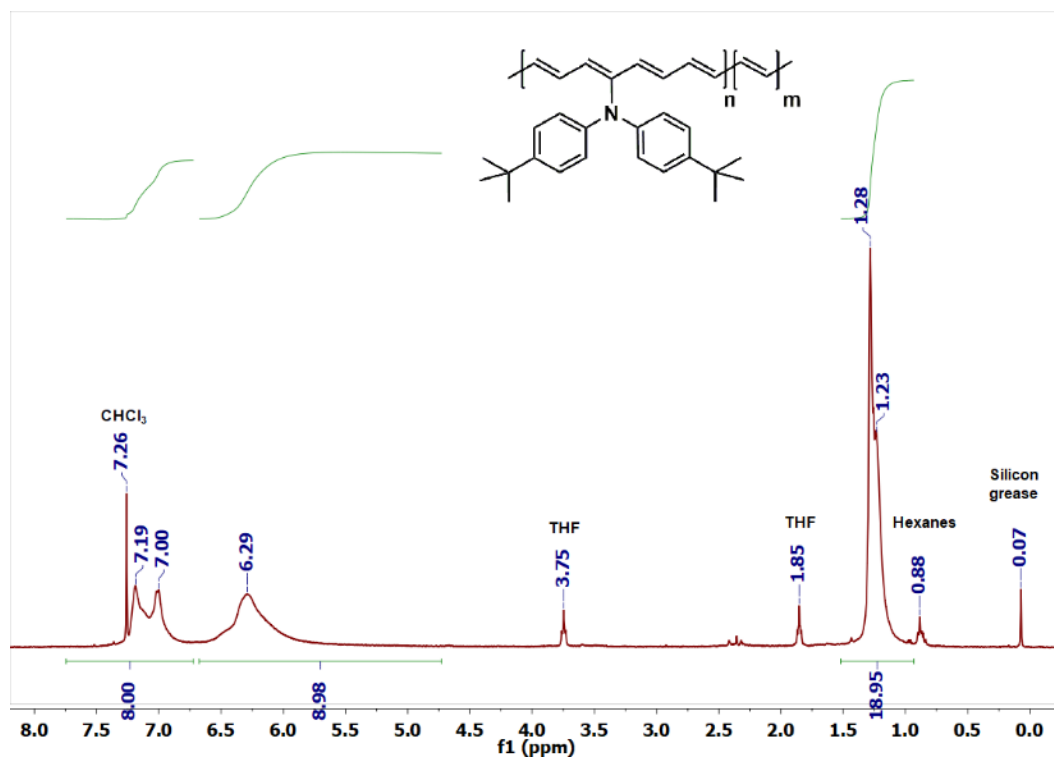


Figure 3.69. ¹H NMR spectrum (400 MHz) of pCOT-N(C₆H₄^tBu)₂ in CDCl₃.

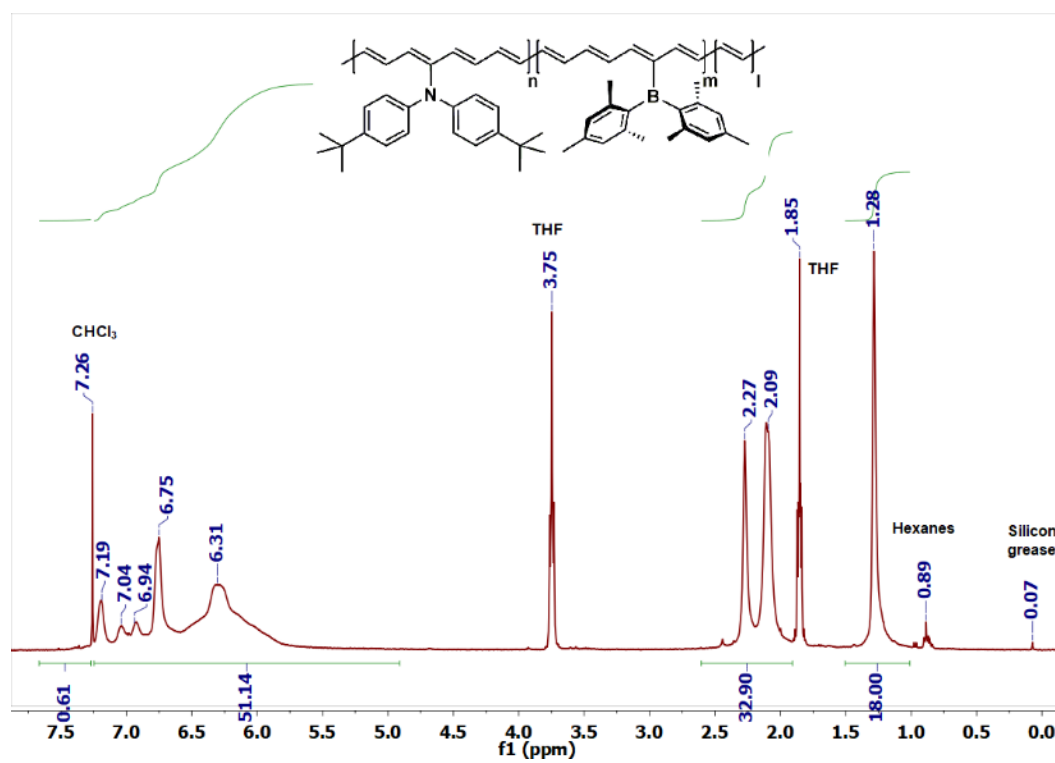


Figure 3.70. ¹H NMR spectrum (400 MHz) of p[COT-N(C₆H₄^tBu)₂-r-COT-BMes₂] in CDCl₃.

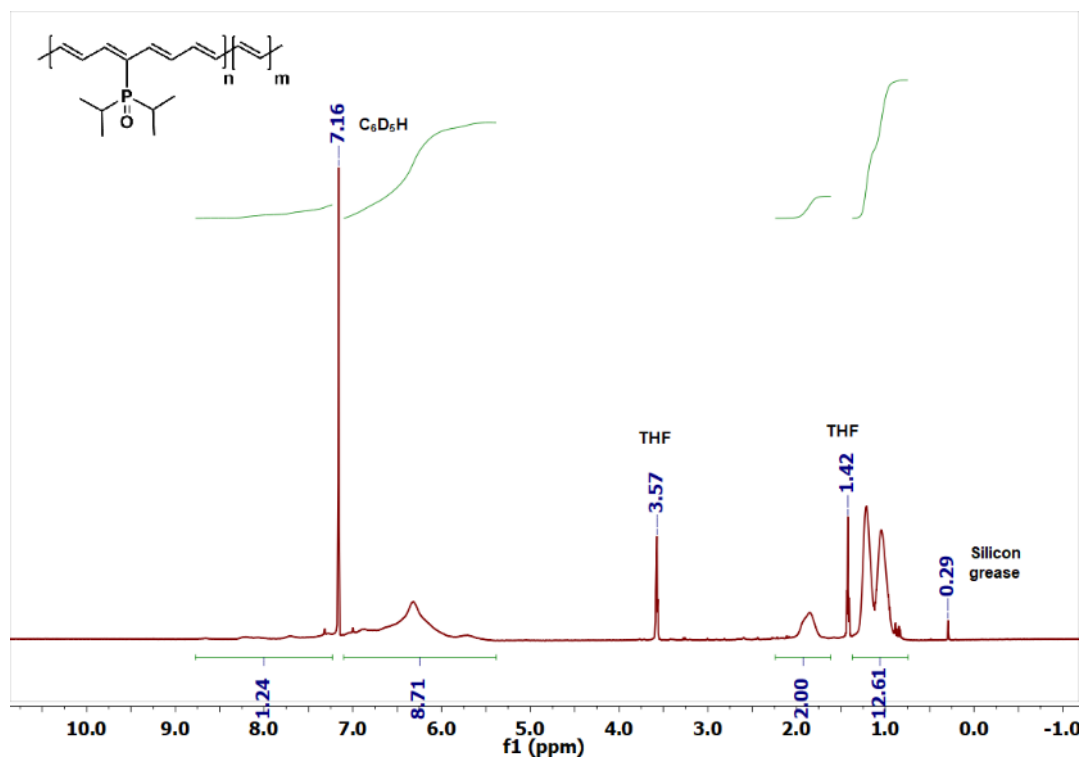


Figure 3.71. ^1H NMR spectrum (500 MHz) of pCOT-P(O)Pr_2 in C_6D_6 .

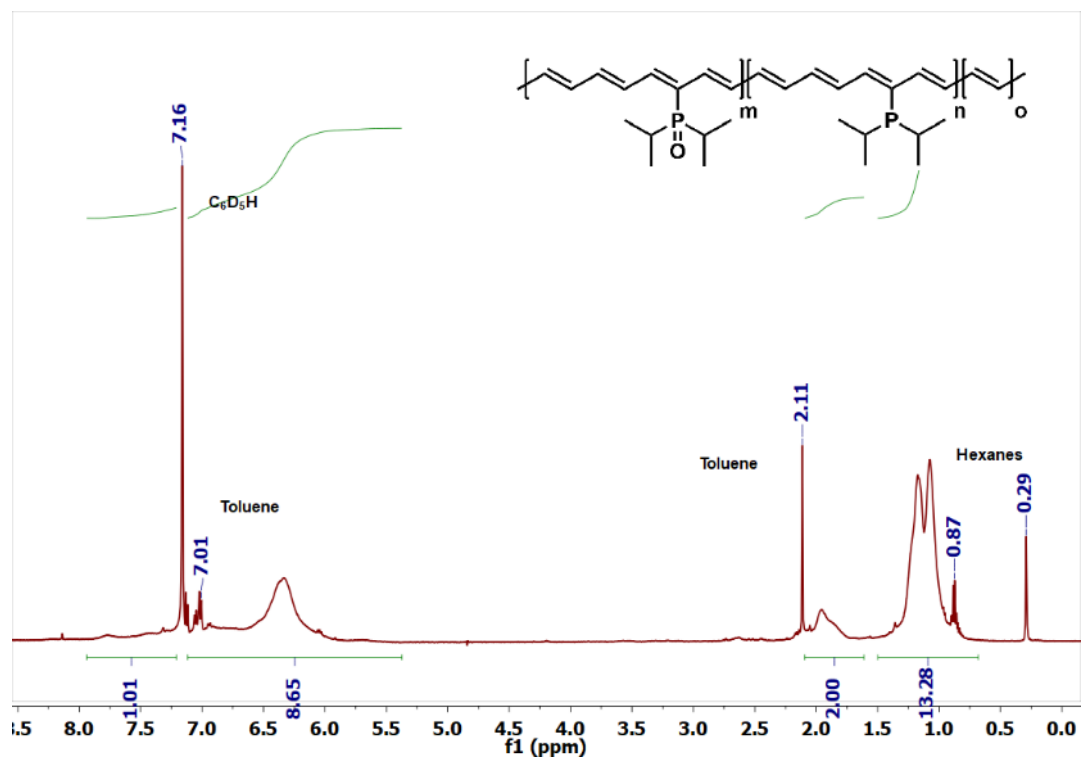


Figure 3.72. ^1H NMR spectrum (500 MHz) of $\text{pCOT-P}^i\text{Pr}_2$ in C_6D_6 .

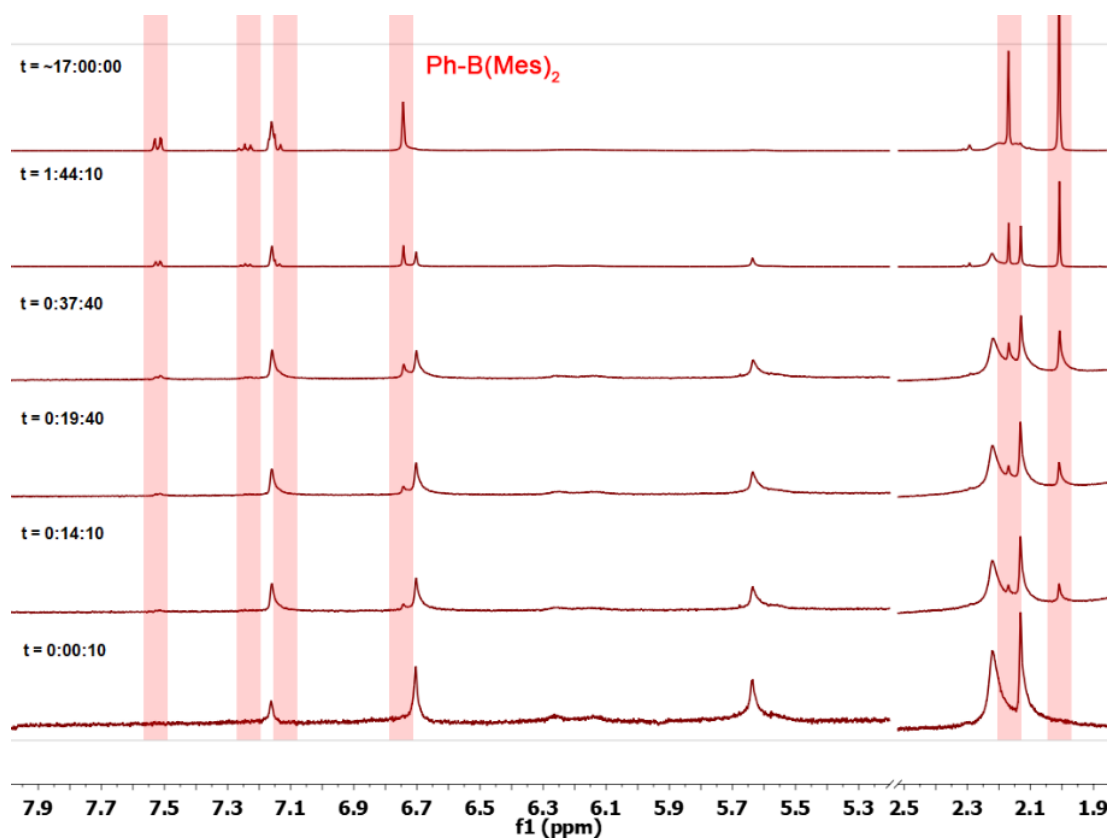


Figure 3.73. ^1H NMR monitoring (500 MHz) of the polymerization of COT-BMes_2 in a 1:1 THF: C_6D_6 mixture. The reaction progress can be tracked through the formation of the cycloextrusion side-product, PhBMes_2 (signals indicated with pink bars).

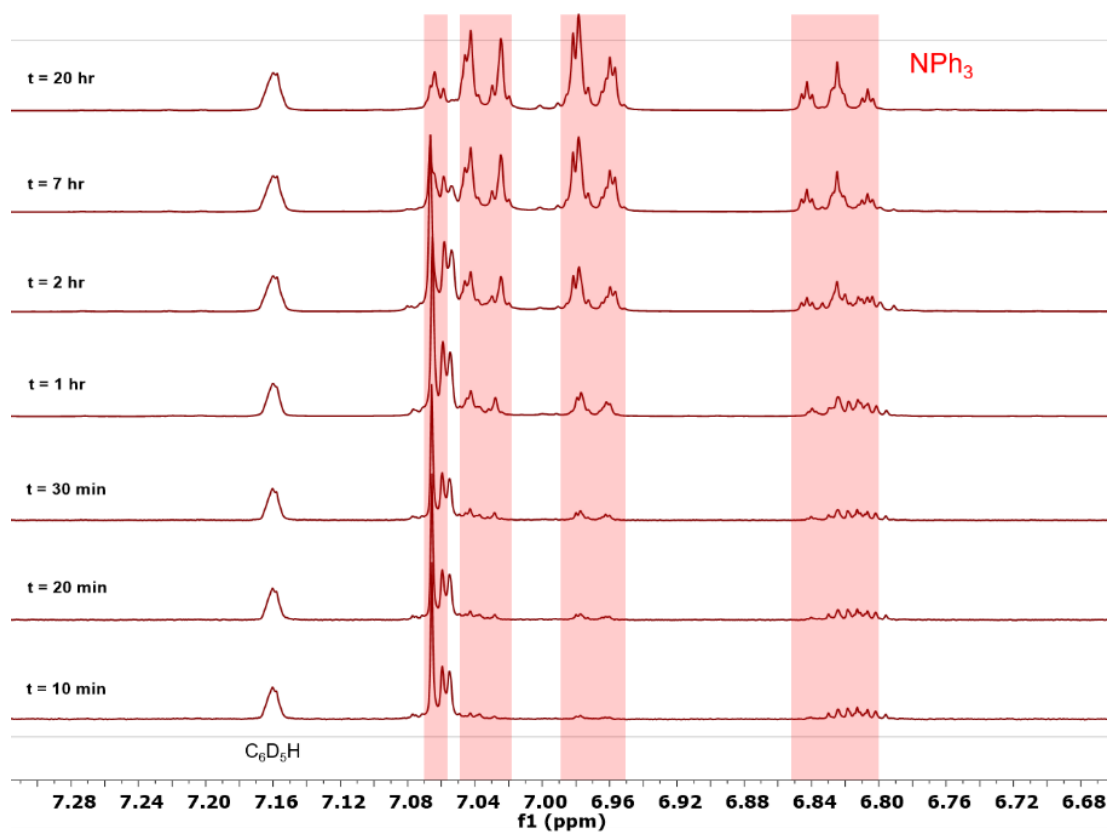


Figure 3.74. ^1H NMR monitoring (500 MHz) of the polymerization of **COT-NPh₂** in a 1:1 THF: C_6D_6 mixture. The reaction progress can be tracked through the formation of the cycloextrusion side-product, NPh_3 (signals indicated with pink bars).

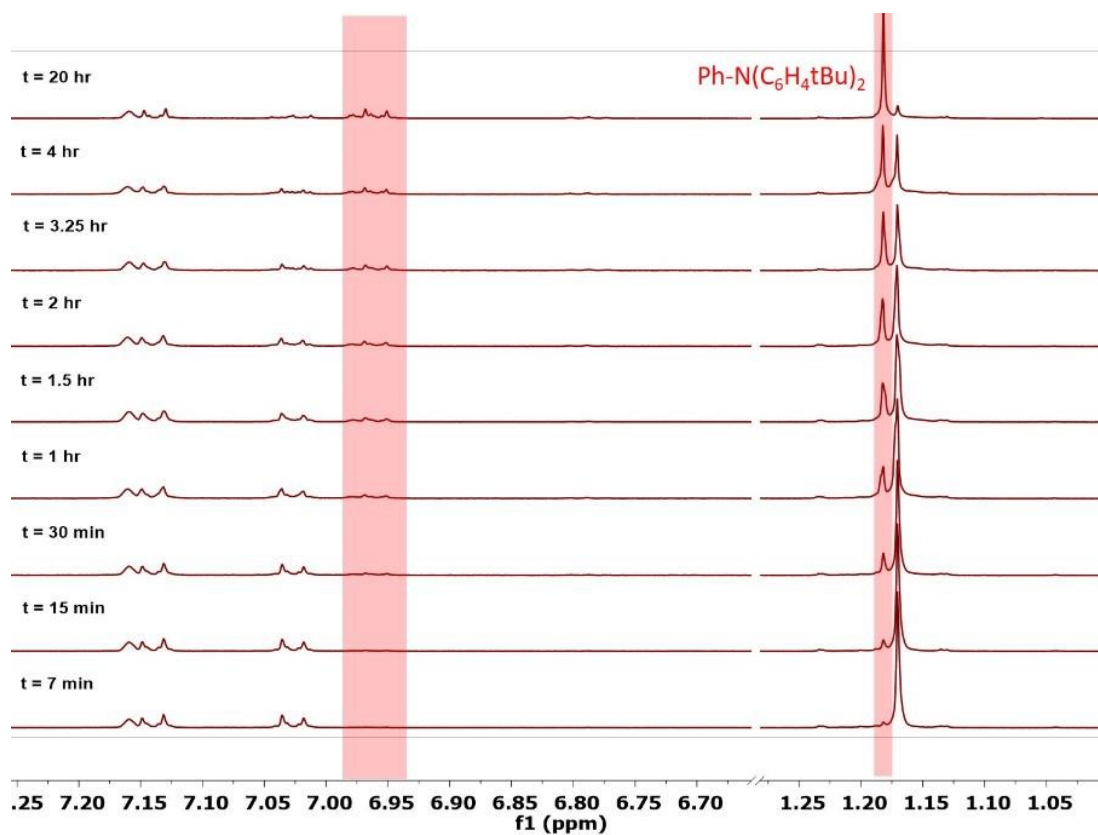


Figure 3.75. ^1H NMR monitoring (500 MHz) of the polymerization of $\text{COT-N}(\text{C}_6\text{H}_4^t\text{Bu})_2$ in a 1:1 THF: C_6D_6 mixture. The reaction progress can be tracked through the formation of the cycloextrusion side-product, $\text{Ph-N}(\text{C}_6\text{H}_4^t\text{Bu})_2$ (signals indicated with pink bars).

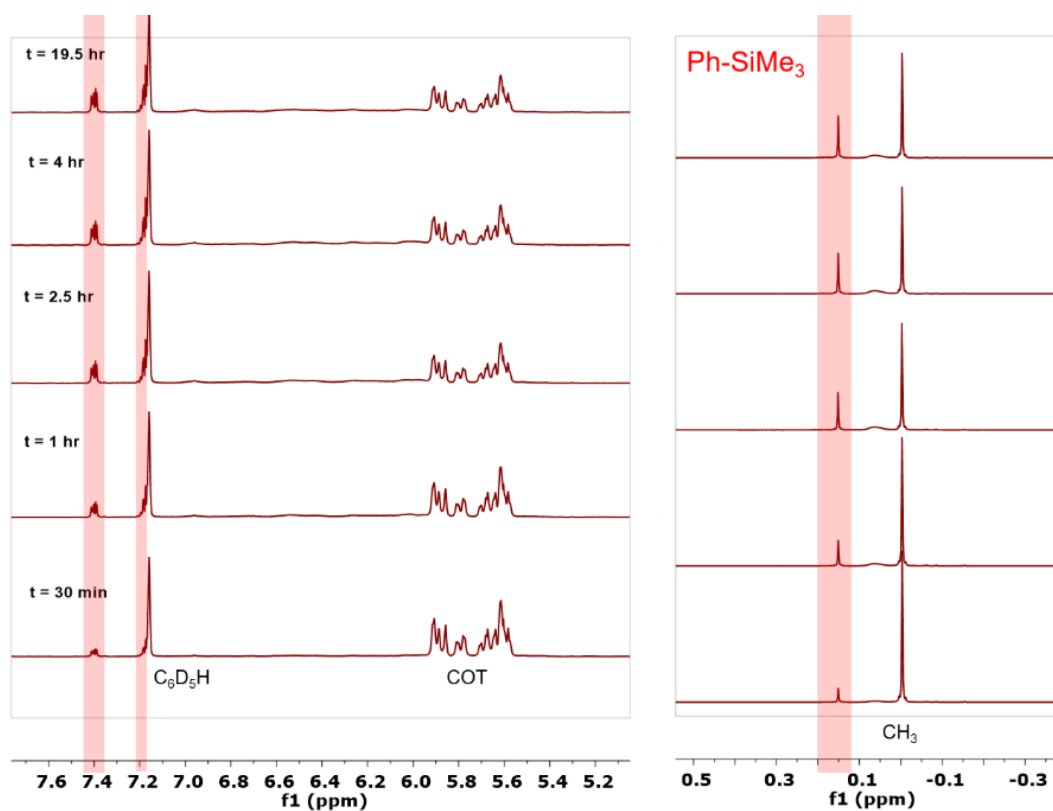


Figure 3.76. ¹H NMR monitoring (400 MHz) of the polymerization of COT-SiMe₃ in a 1:1 THF:C₆D₆ mixture. The alkyl and aryl regions are plotted at different intensities. The reaction progress can be tracked through the formation of the cycloextrusion side-product, PhSiMe₃ (signals indicated with pink bars).

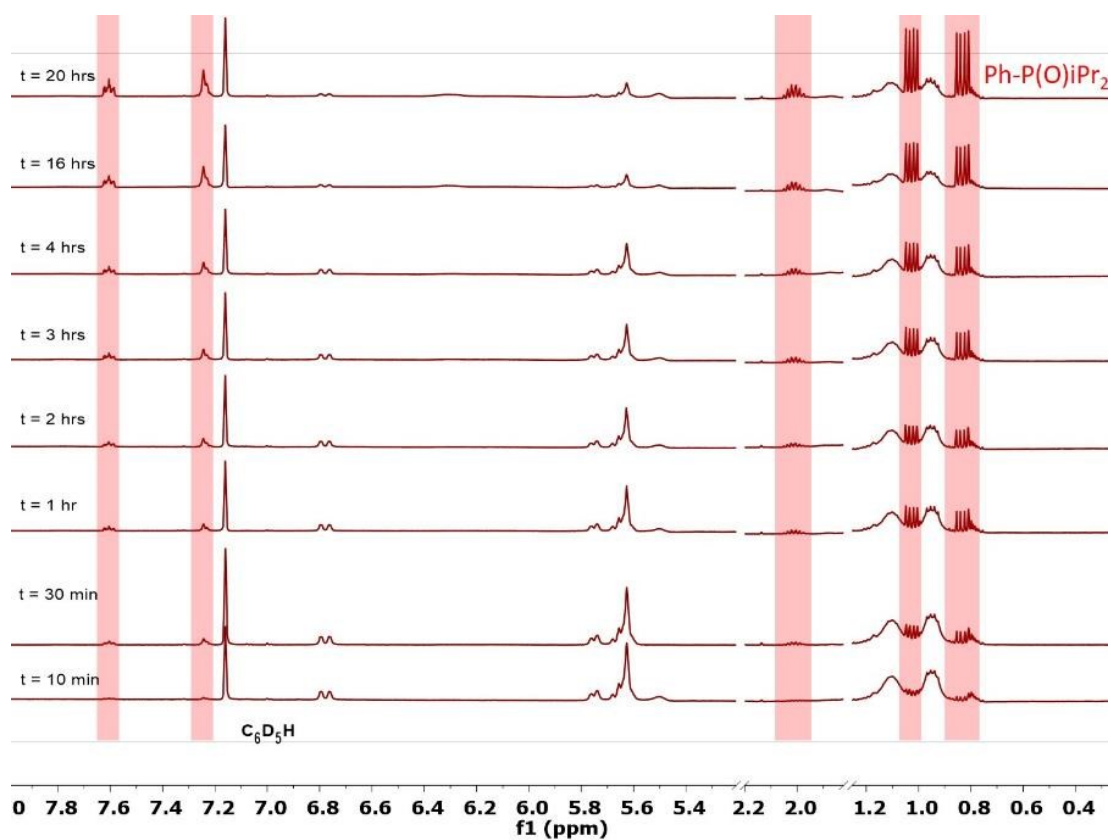


Figure 3.77. ^1H NMR monitoring (500 MHz) of the polymerization of COT-P(O)iPr_2 in a 1:1 THF: C_6D_6 mixture. The reaction progress can be tracked through the formation of the cycloextrusion side-product, PhP(O)iPr_2 .

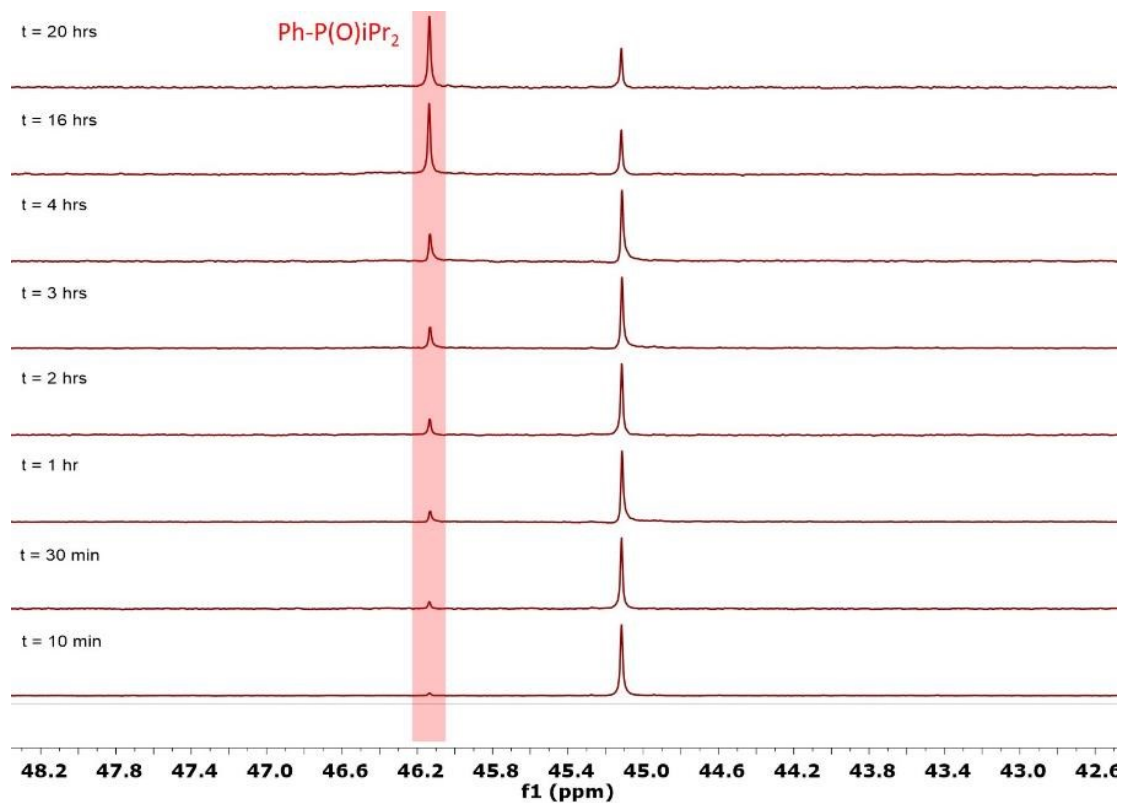


Figure 3.78. ^{31}P NMR monitoring (202 MHz) of the polymerization of COT-P(O)IPr_2 in a 1:1 THF: C_6D_6 mixture. The alkyl and aryl regions are plotted at different intensities. The reaction progress can be tracked through the formation of the cycloextrusion side-product, PhP(O)IPr_2 .

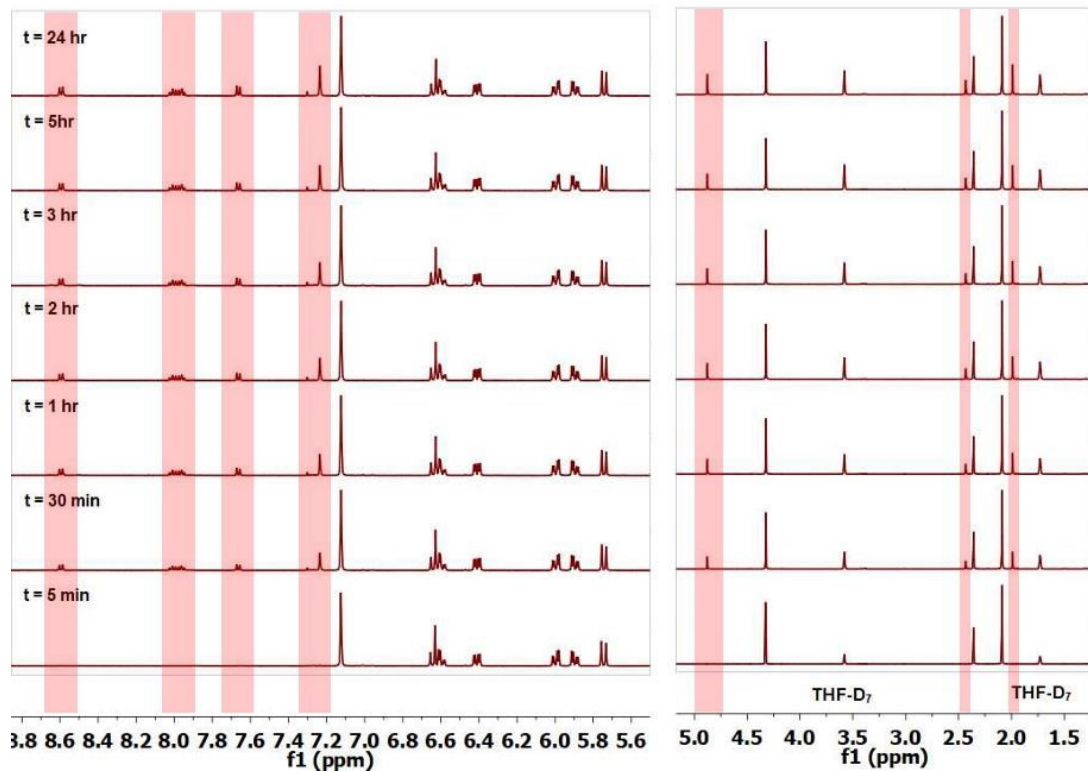


Figure 3.79. ^1H NMR monitoring (500 MHz) of the polymerization of $[\text{COT-N}_3(\text{Me})\text{-Mes}]\text{OTf}$ in THF-d_8 . The reaction progress can be tracked through the formation of the cycloextrusion side-product, $[\text{Ph-N}_3(\text{Me})\text{-Mes}]\text{OTf}$.

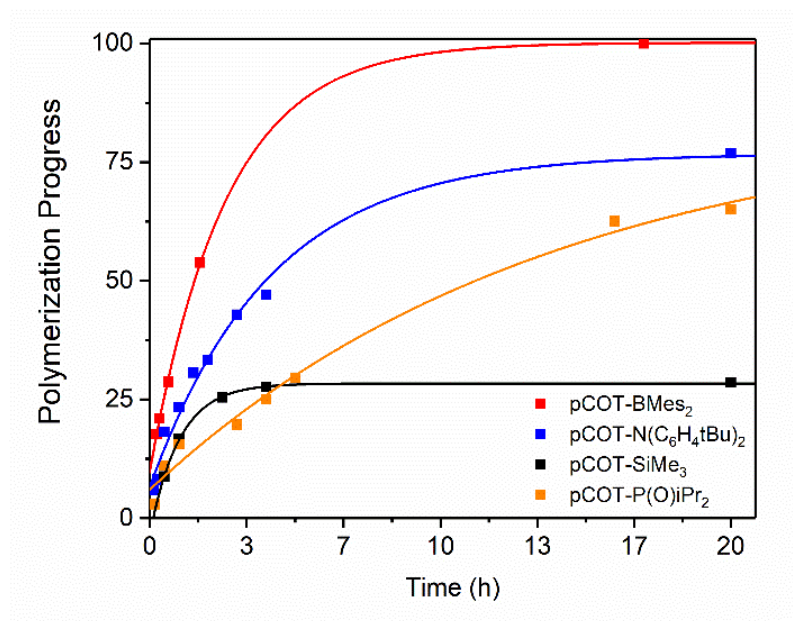


Figure 3.80. Conversion of monomers during polymerization as measured by NMR in a 1:1 THF:C₆D₆ mixture (0.080 M, 1 mol. % of 3rd gen. Grubbs catalyst). Lines are a result of exponential fitting of data points.

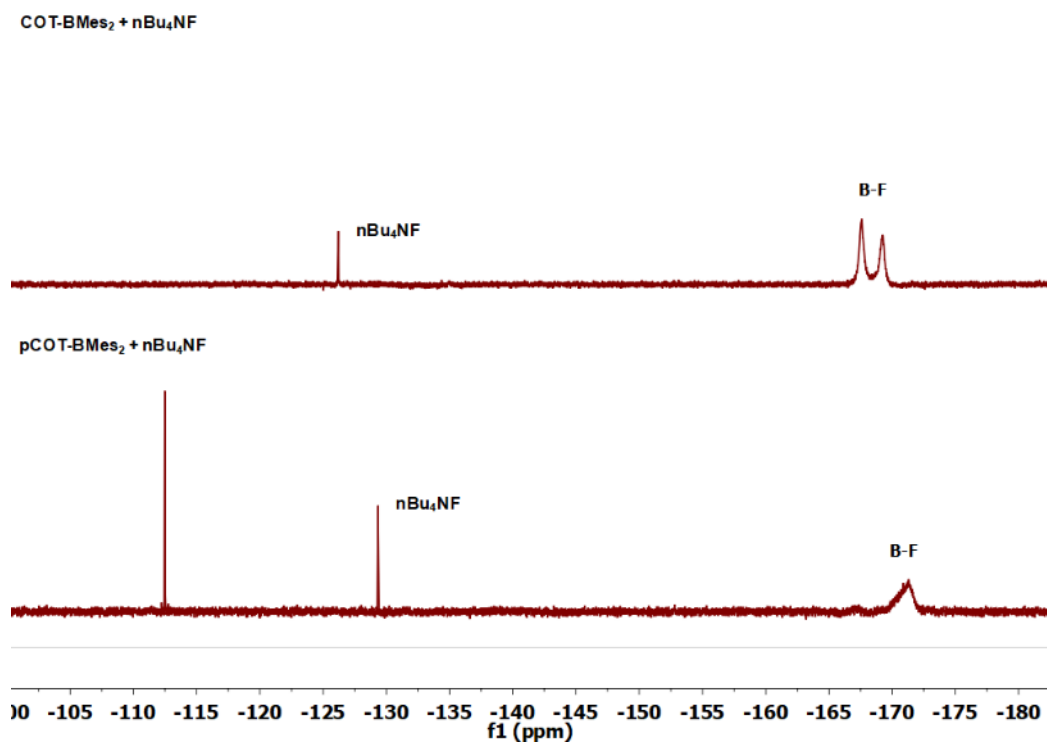


Figure 3.81. ^{19}F NMR spectrum (376 MHz) after fluoride binding to **COT-BMes₂** (C_6D_6 , top) and **pCOT-BMes₂** (THF + CDCl_3 , bottom).

3.4.5 Determination of Backbiting Percentage and Side Chain Density for Polyacetylenes

Here, we describe the calculation of the relative amount of cycloextrusion caused by backbiting during ring-opening metathesis polymerization of COT-based monomers. The calculations are based on the ^1H NMR spectrum of isolated polymers. In Equation 3.1 below, I_B is the ^1H NMR integration observed experimentally for the sp^2 region corresponding to the polymer backbone and I_S is the integration observed for a side chain signal that does not overlap with the backbone signals. Additionally, r is the number of monomer units that have reacted during polymerization and e is the number of molecules that eliminated from the polymer chain after cycloextrusion. H_B and H_S are the respective expected number of protons contributing for I_B and I_S immediately after the reaction of one monomer (i.e. before cycloextrusion); H_B^* and H_S^* are the number of protons that would be lost in the backbone and side chain NMR regions, respectively, for each cycloextruded side-product.

$$\frac{I_B}{I_S} = \frac{r \times H_B - e \times H_B^*}{r \times H_S - e \times H_S^*} \quad (3.1)$$

As an example, for the pCOT-BMes₂ ^1H NMR below in Figure 3.82, $I_B = 17$, $I_S = 18$, $H_B = 11$, $H_S = 18$, $H_B^* = 9$ and $H_S^* = 18$. Note that r is equal to the number of units incorporated in each polymer chain only if $e = 0$. Thus, it is expected that $I_B/I_S \geq H_B/H_S$ as each cycloextrusion reaction increases the relative integrated value

of the backbone region. Cycloextrusion reduces the side chain density in the polymer while leaving behind extra -CH=CH- units in the backbone. Equation 1 can be converted into the equation below (Equation 3.2), where %**CE** is the cycloextrusion percentage observed.

$$\%CE = e/r = \frac{H_B - H_S \times (I_B/I_S)}{H_B^* - H_S^* \times (I_B/I_S)} \quad (3.2)$$

From the resulting %**CE**, it is possible to calculate the average number of carbons (#**C**) between each side chain in the final polymer using Equation 3.3. Seeing that each monomer incorporated in the final polymer (**n**) contributes to 8 carbon atoms in the backbone per side chain that it carries and each cycloextrusion (**e**) effectively increases the relative number of carbons in the backbone by 2, the following relationship is true:

$$\#C = \frac{8n+2e}{n} \quad (3.3)$$

Because **n** = **r** - **e**, Equation 3 can be rewritten in terms of %**CE** (Equation 3.4).

$$\#C = 8 + \frac{2 \times \%CE}{1 - \%CE} \quad (3.4)$$

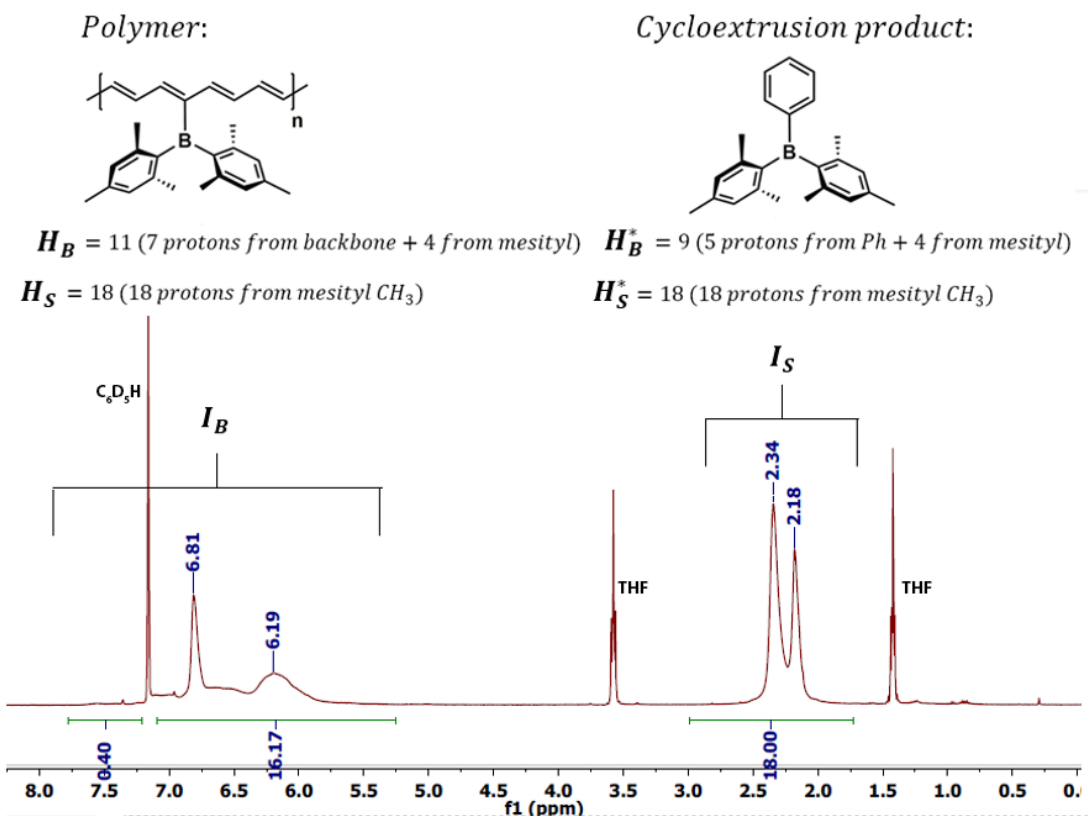


Figure 3.82. Example of the calculation of parameters used to obtain %CE and the average number of carbons between each side chain for polyacetylenes.

Note that this method can only be used if the polymer has at least one proton signal related to the side chain that does not overlap with the sp^2 backbone signals. This method is especially useful for cases where some side chain signals overlap with backbone signals (i.e. for **pCOT-BMes₂**), but only works for homopolymers. For copolymers, it is assumed that the rate of cycloextrusion is maintained for each type of

monomer and we calculate a weighted average final cycloextrusion percentage ($\%CE^{A+B}$) as:

$$\%CE^{A+B} = \%CE^A \times \frac{I_S^A}{I_S^A + I_S^B} + \%CE^B \times \frac{I_S^B}{I_S^A + I_S^B} \quad (3.5)$$

In Equation 5, $\%CE^A$ and $\%CE^B$ are the cycloextrusion percentage previously calculated for homopolymers of monomers A and B; I_S^A and I_S^B are the integration values of non-overlapping side chain signals in the 1H NMR of the pure AB copolymer related to the incorporation of monomers A and B, respectively. The A to B monomer incorporation ratio is given by I_S^A/I_S^B . The value of $\%CE^{A+B}$ can then be used with Equation 3.4 to calculate the average number of carbons between each side chain. Using Equations 3.2 and 3.4 for representative homopolymers and Equations 3.4 and 3.5 for copolymers, the data in Table 3.5 was obtained.

Table 3.5. Summary of calculated cycloextrusion percentage (%CE) and average number of carbon atoms in the backbone between each side chain (#C) compared to yield and number average molecular weight (M_n) of polymers.

	%CE	#C	Yield	M_n	R_h^a
pCOT-SiMe₃	60 %	11	7 %	9.8 kDa	--
pCOT-BMes₂	59 %	11	39 %	21.0 kDa	10 nm
pCOT-NPh₂	62 %	11	36 %	4.1 kDa	--
pCOT-N(C₆H₄^tBu)₂	43 %	10	13 %	7.8 kDa	--
p[COT-N(C₆H₄^tBu)₂-<i>r</i>-COT-BMes₂]	63 %	11	26 %	14.7 kDa	--
pCOT-P(O)ⁱPr₂	56 %	11	38 %	-- ^c	33 nm
pCOT-PⁱPr₂^b	57 %	10	12 % ^b	-- ^d	6 nm

^a – R_h = hydrodynamic radius

^b – From the reduction of **pCOT-P(O)ⁱPr₂**

^c – Based on R_h , M_n estimated to be 41 kDa (see Section 3.4.7)

^d – Based on R_h , M_n estimated to be 8 kDa (see Section 3.4.7)

3.4.6 GPC Data

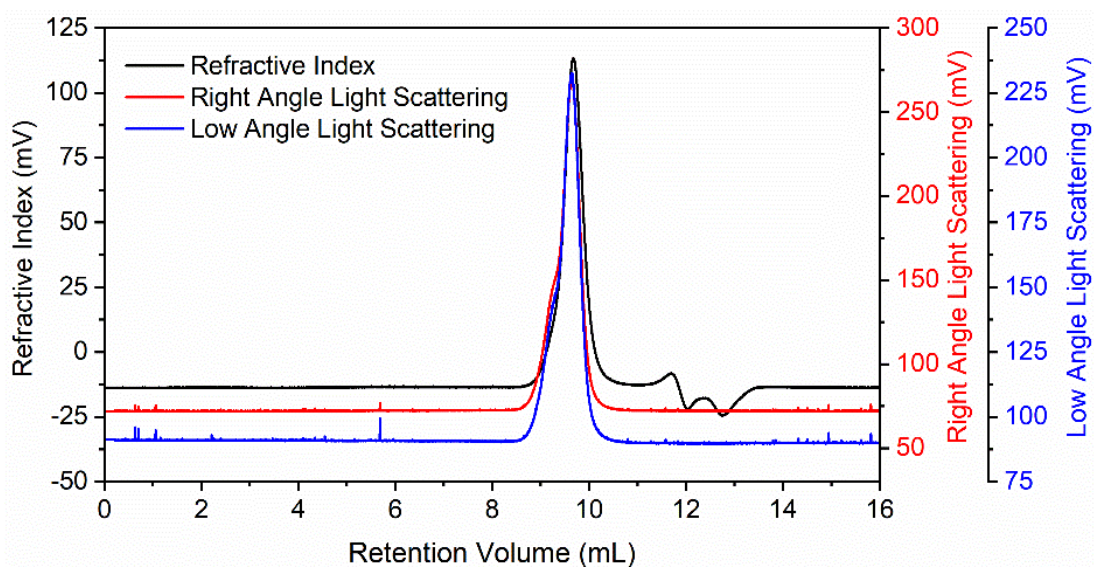


Figure 3.83. GPC elution profile for **pNBE-C₆H₄-BMes₂** in THF. The negative peaks in refractive index are artifacts of injection.

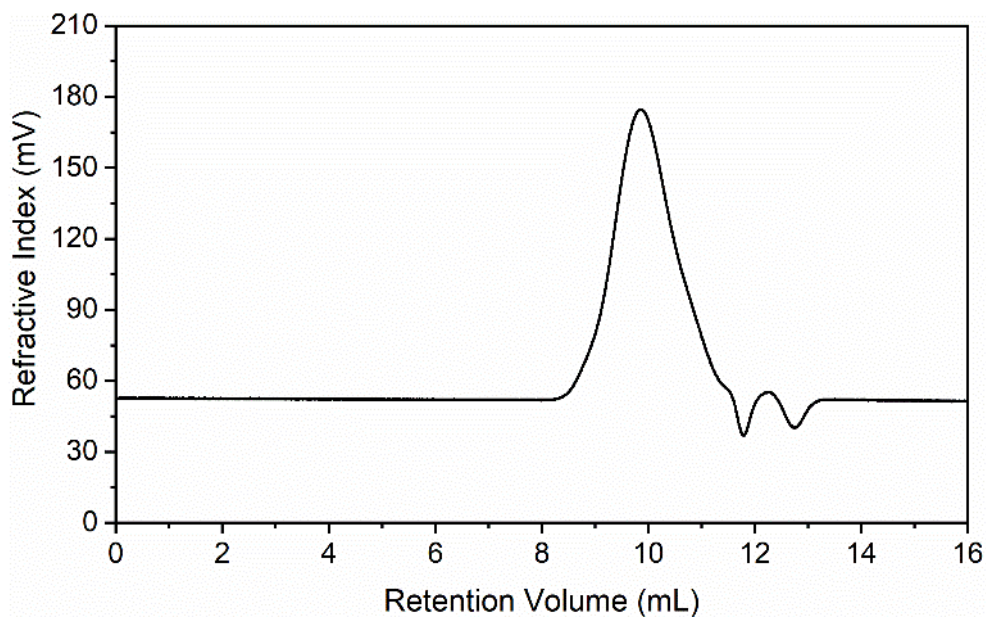


Figure 3.84. GPC elution profile for **pCOT-SiMe₃** in THF. The negative peaks are artifacts of injection.

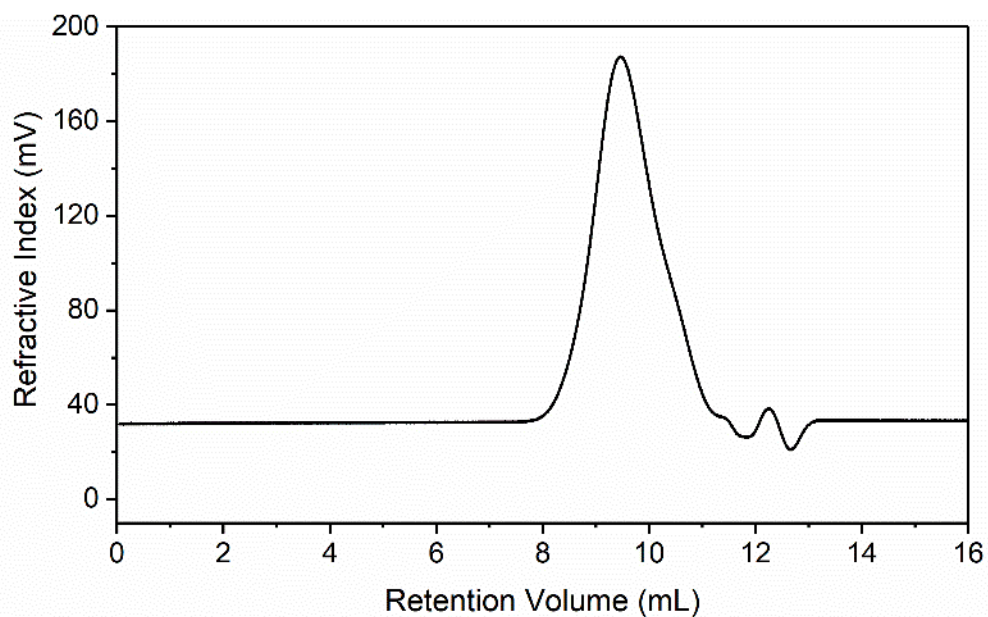


Figure 3.85. GPC elution profile for **pCOT-BMes₂** in THF. The negative peaks are artifacts of injection.

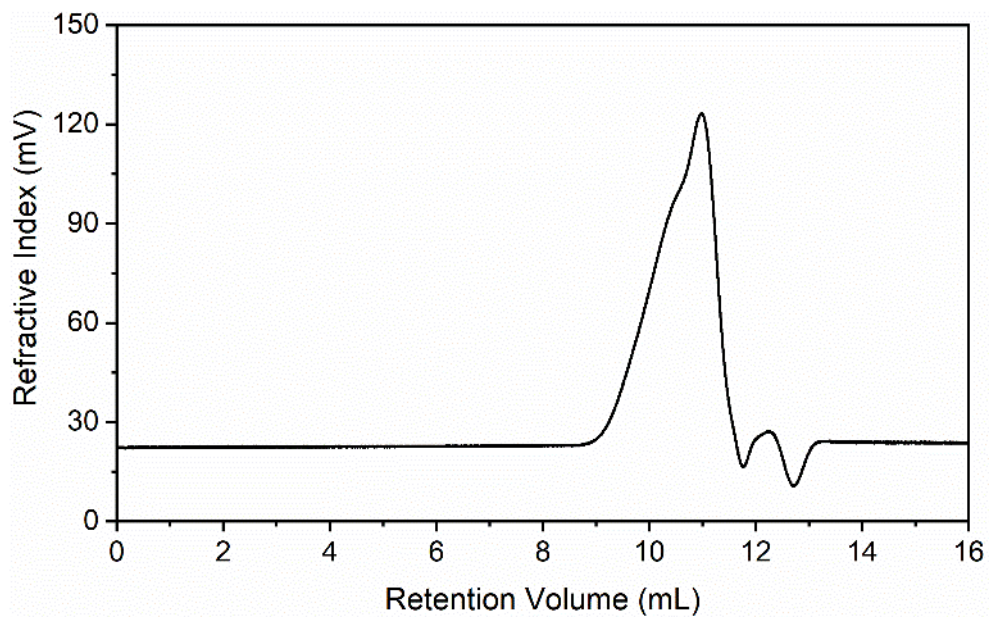


Figure 3.86. GPC elution profile for **pCOT-NPh₂** in THF. The negative peaks are artifacts of injection.

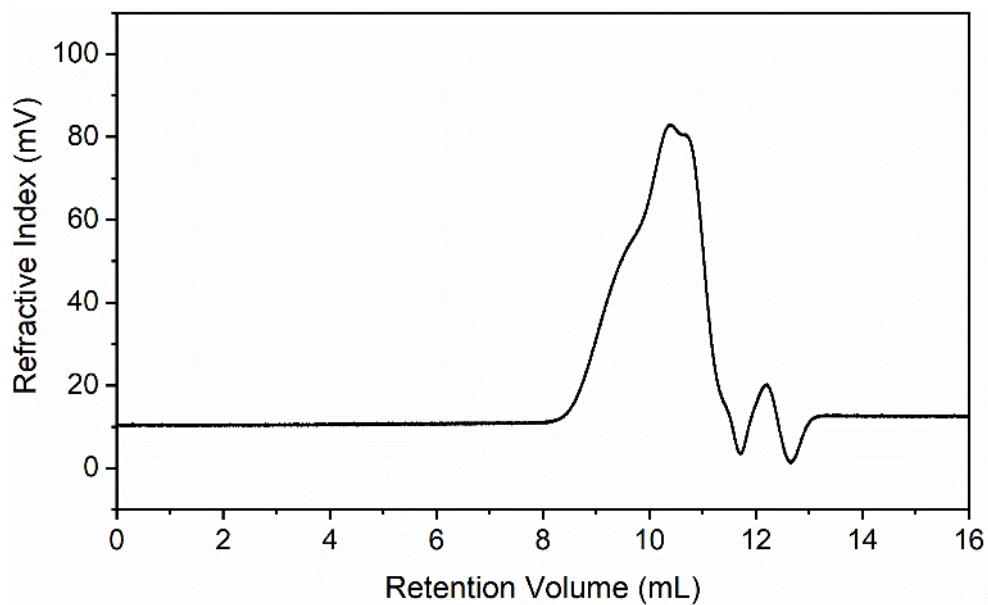


Figure 3.87. GPC elution profile for **pCOT-N(C₆H₄^tBu)₂** in THF. The negative peaks are artifacts of injection.

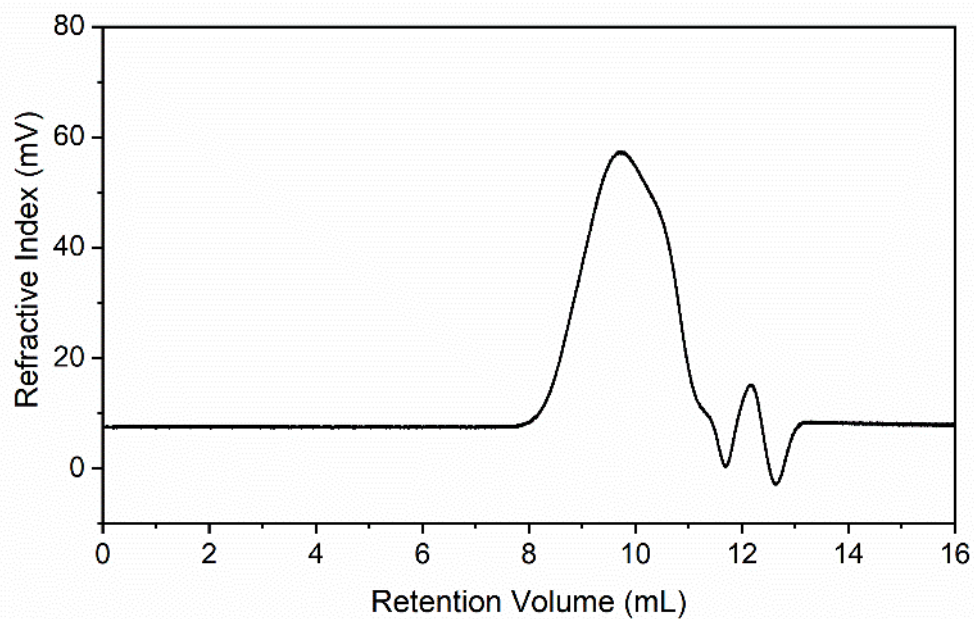


Figure 3.88. GPC elution profile for **p[COT-N(C₆H₄^tBu)₂-*r*-COT-BMes₂]** in THF. The negative peaks are artifacts of injection.

3.4.7 Calculation of Estimated M_n by Dynamic Light-Scattering (DLS)

DLS measurements were used as means to roughly estimate molecular weight when determination by GPC was not possible. To estimate M_n indirectly, **pCOT-BMes₂** (M_n of 21.0 kDa determined by GPC) was initially measured by DLS to determine its hydrodynamic radius ($R_h = 10$ nm). Assuming that the rigidity of the polymeric backbone and the behaviour of the polymers in solution did not change significantly, the following relationship was used to calculate molecular weights for **pCOT-P(O)ⁱPr₂** and **pCOT-PⁱPr₂** relative to the results of **pCOT-BMes₂**:

$$\frac{M_n^B \times R_h^X}{R_h^B} \times \frac{MW^X}{MW^B} \quad (3.6)$$

In Equation 3.6, M_n^B is the number average molecular weight of **pCOT-BMes₂** (21.0 kDa), R_h^B and R_h^X are the hydrodynamic radii of **pCOT-BMes₂** and of the polymer of interest (**pCOT-P(O)ⁱPr₂** or **pCOT-PⁱPr₂**), respectively, and MW^B and MW^X are the molecular weights of the average repeating units for **pCOT-BMes₂** (391.385 g/mol) and of the polymer of interest (**pCOT-P(O)ⁱPr₂** = 275.352 g/mol; **pCOT-PⁱPr₂** = 246.334 g/mol). Therefore, by knowing the ratio between hydrodynamic radii, the molecular weights are estimated. Equation 3.6 also assumes a linear relationship between molecular weight and hydrodynamic radius, as previously seen for polyacetylene copolymers.^{15b}

3.4.8 Thermal Gravimetric Analysis (TGA) Data

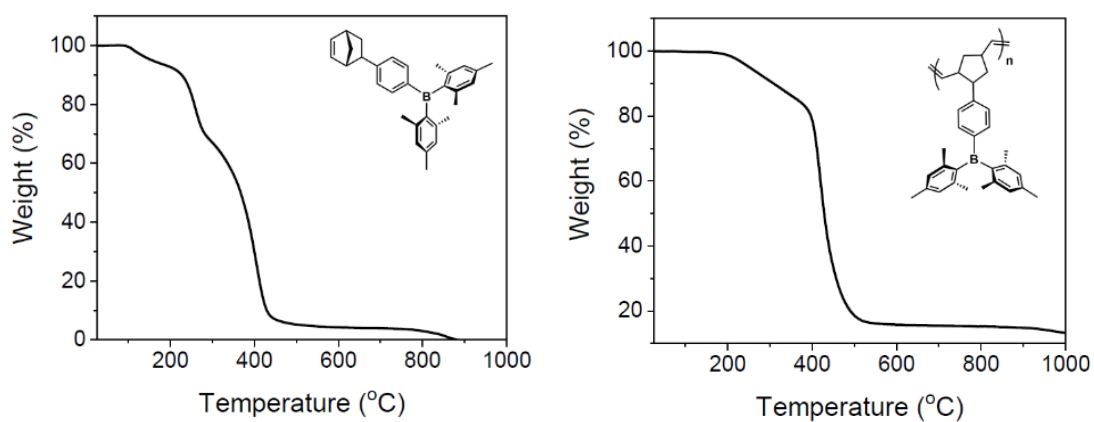


Figure 3.89. TGA of NBE-C₆H₄-BMes₂ (left) and pNBE-C₆H₄-BMes₂ (right) at 10 °C/min under N₂.

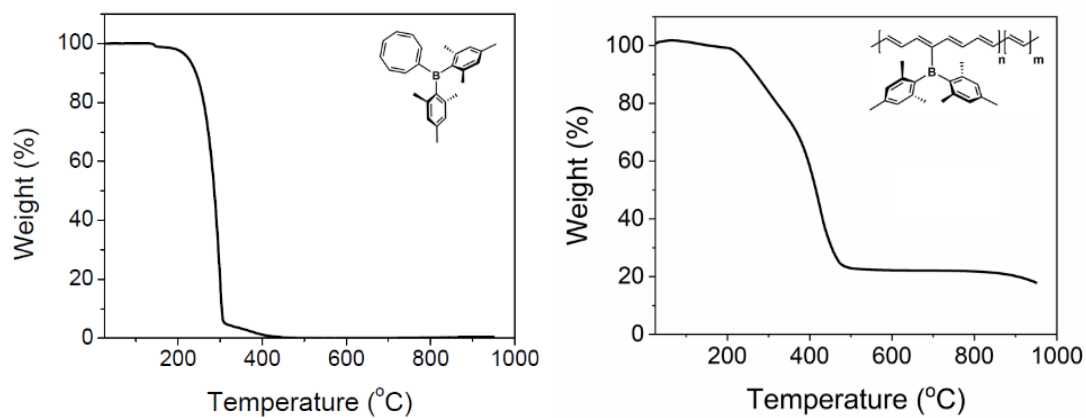


Figure 3.90. TGA of COT-BMes₂ (left) and pCOT-BMes₂ (right) at 10 °C/min under N₂.

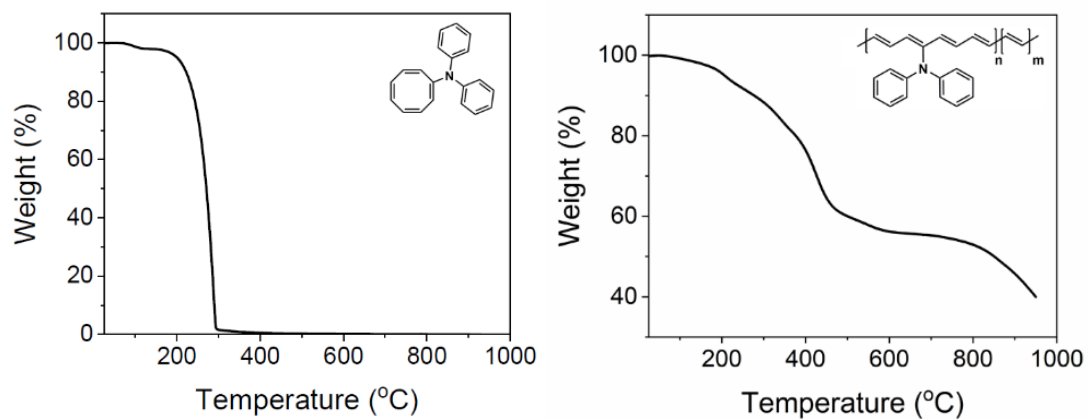


Figure 3.91. TGA of COT-NPh₂ (left) and pCOT-NPh₂ (right) at 10 °C/min under N₂.

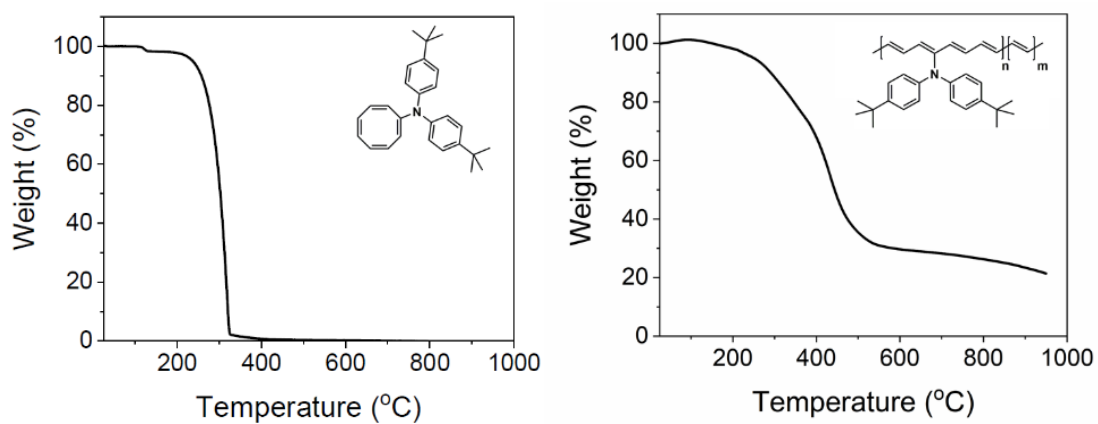


Figure 3.92. TGA of COT-N(C₆H₄^tBu)₂ (left) and pCOT-N(C₆H₄^tBu)₂ (right) at 10 °C/min under N₂.

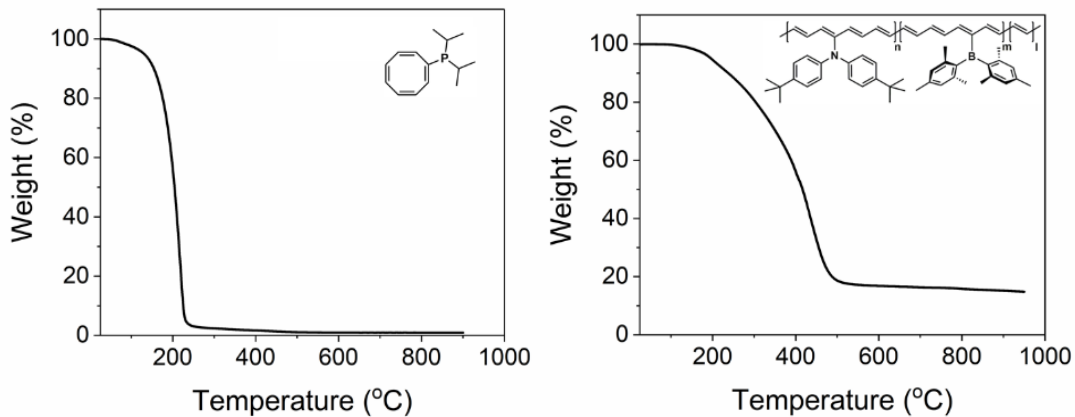


Figure 3.93. TGA of **COT-PⁱPr₂** (left) and **p[COT-N(C₆H₄^tBu)₂-*r*-COT-BMes₂]** (right) at 10 °C/min under N₂.

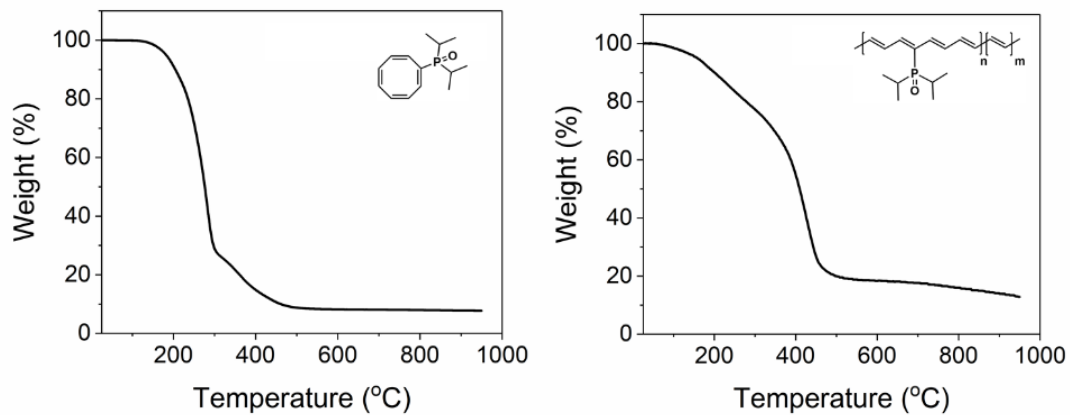


Figure 3.94. TGA of **COT-P(O)ⁱPr₂** (left) and **pCOT-P(O)ⁱPr₂** (right) at 10 °C/min under N₂.

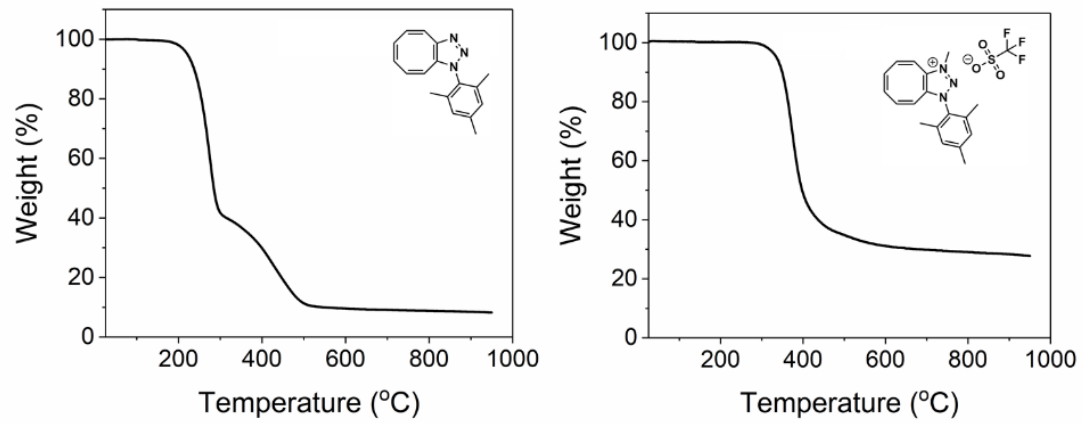


Figure 3.95. TGA of COT-N₃-Mes (left) and [COT-N₃(Me)-Mes]OTf (right) at 10 °C/min under N₂.

3.4.9 Additional UV-Vis Data

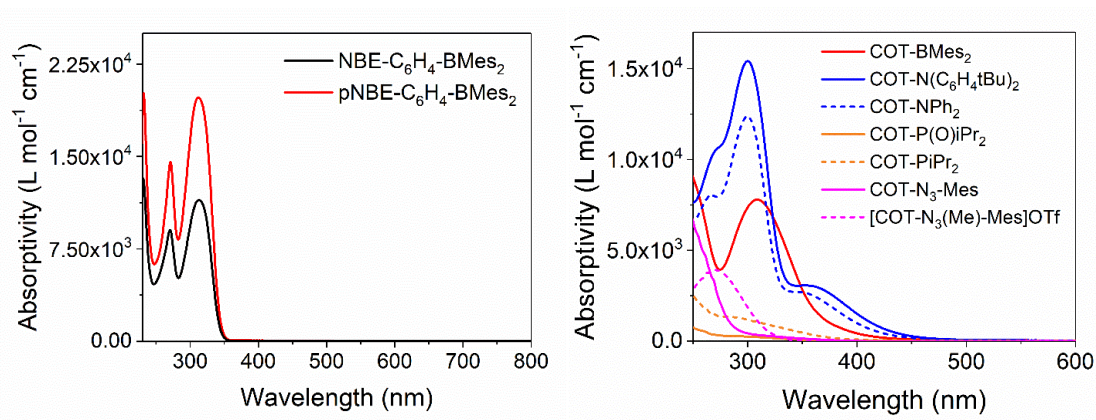


Figure 3.96. UV-Vis spectra of NBE-C₆H₄-BMes₂ and pNBE-C₆H₄-BMes₂ (left) and COT-based monomers (right) in THF.

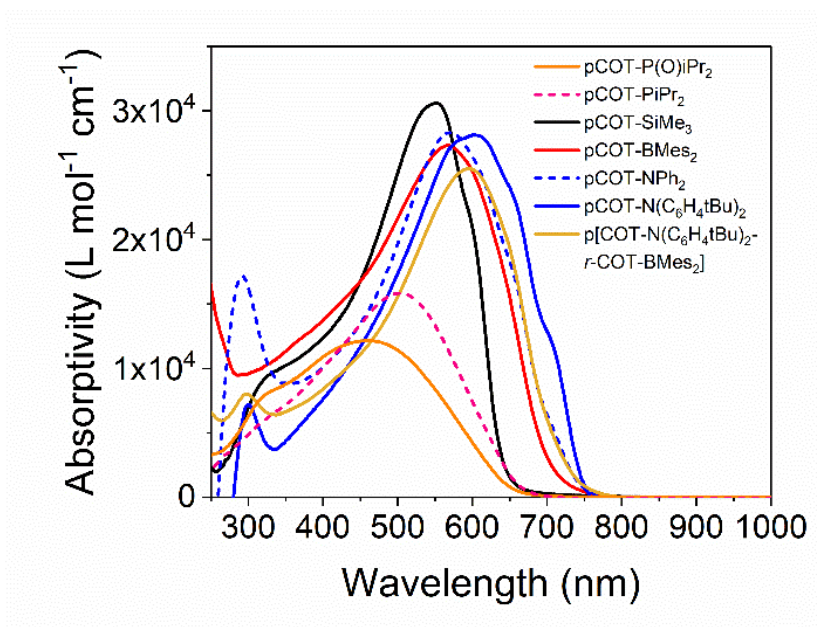


Figure 3.97. Molar absorptivity spectra (per repeat unit) of polymers in THF.

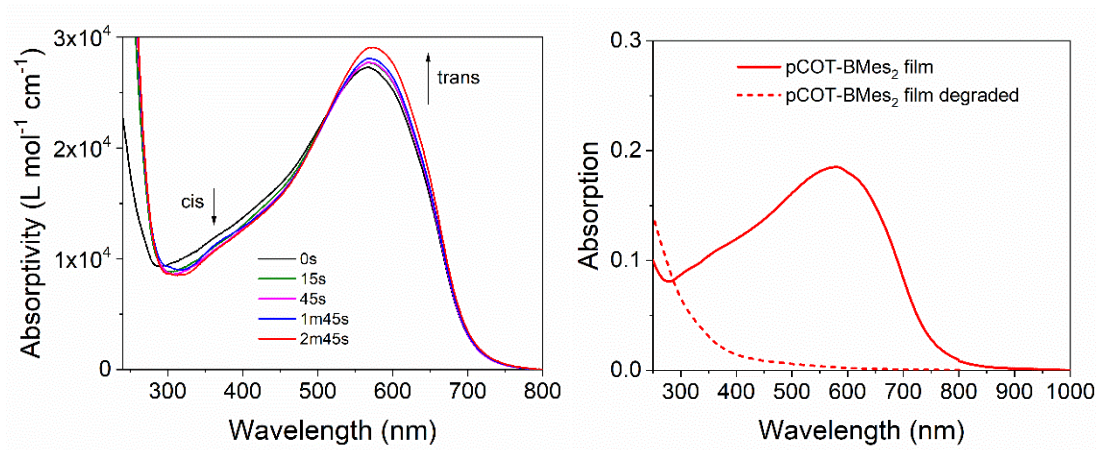


Figure 3.98. Isomerization of **pCOT-BMes₂** in THF at different total times of exposure to a mercury lamp (125 W high pressure, left) and absorption of a film of **pCOT-BMes₂** freshly drop-casted and degraded after 2 weeks of exposure to air and light (right). The small change in absorption profile for the isomerization indicates a high degree of *trans* sp² bonds in the as-synthesized polymer backbone.

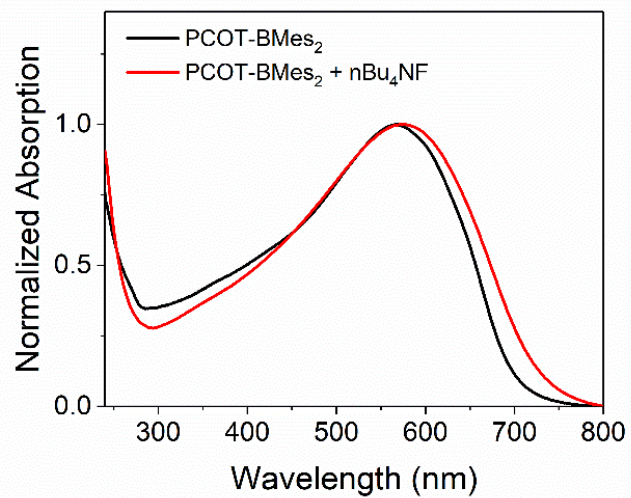


Figure 3.99. Normalized UV-Vis spectra of pCOT-BMes₂ before and after addition of 1 eq. of tetrabutylammonium fluoride ([ⁿBu₄N]F). Before addition: $\lambda_{\text{max}} = 568$ nm, $\lambda_{\text{onset}} = 703$ nm, $E_{\text{g}} = 1.76$ eV; after addition: $\lambda_{\text{max}} = 574$ nm, $\lambda_{\text{onset}} = 735$ nm, $E_{\text{g}} = 1.69$ eV.

3.4.10 Photoluminescence Data

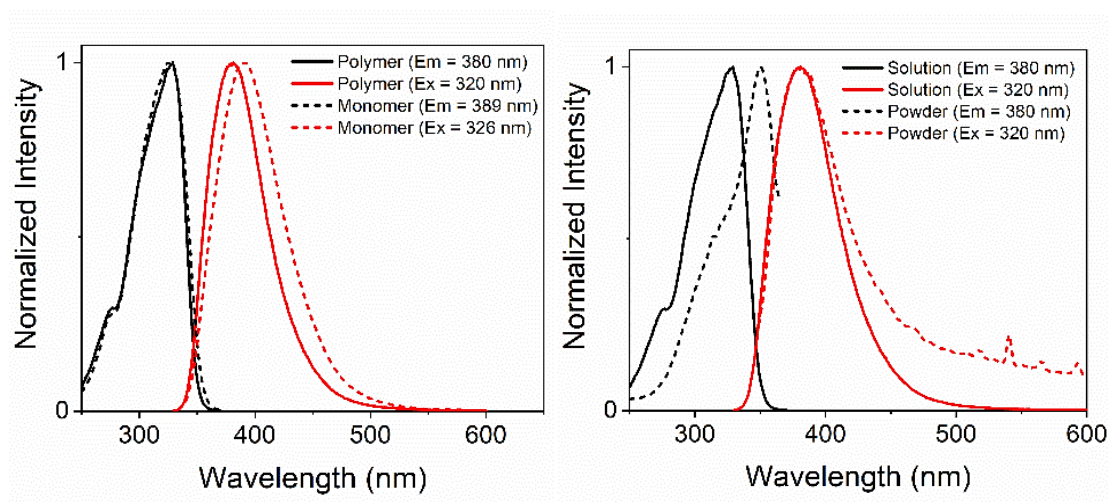


Figure 3.100. Emission and excitation spectra comparing the monomer **NBE-C₆H₄-BMes₂** and polymer **pNBE-C₆H₄-BMes₂** in THF solutions (left) and comparing the THF solution and powder of the polymer **pNBE-C₆H₄-BMes₂** (right). The numbers in parentheses represent the wavelength of emission used for the excitation spectra and wavelength of excitation for the emission spectra.

Table 3.6. Summary of luminescence data and absolute quantum yields for **NBE-C₆H₄-BMes₂** and **pNBE-C₆H₄-BMes₂**.

NBE-C₆H₄-BMes₂			
	Excitation λ_{ex}	Emission λ_{em}	Quantum yield (ϕ)
Solution (THF)	326 nm	392 nm	9.1 %
pNBE-C₆H₄-BMes₂			
	Excitation λ_{ex}	Emission λ_{em}	Quantum yield (ϕ)
Solution (THF)	329 nm	381 nm	8.2 %
Solid	350 nm	381 nm	3.6 %

3.4.11 Additional CV and NIR-SEC Data

Table 3.7. Peak potentials of the oxidation and reduction events of the monomers (scan rate = 100 mV/s). Potentials (V) are given vs. Fc^{+0} .

	$E_{p,c,1}$	$E_{p,c,2}$	$E_{p,c,3}$	$E_{p,a,1}$	$E_{p,a,2}$	$E_{p,a,3}$
COT-N(C₆H₄tBu)₂	-0.83	----	-2.45	-2.11	----	0.33
COT-BMes₂	----	-2.01	-2.20	-1.85	-1.38	----

Table 3.8. Peak potentials of the oxidation and reduction events of the polymers (scan rate = 100 mV/s). Potentials (V) are given vs. Fc^{+0} . ^aHalf wave potentials.

	$E_{p,a,1}$	$E_{p,a,2}$	$E_{1/2,c,1}^a$	$E_{1/2,c,2}^a$
pCOT-SiMe₃	0.15	0.66	-1.68	----
pCOT-BMes₂	0.17	0.57	-1.67	-2.58
pCOT-N(C₆H₄tBu)₂	0.10	0.46	-1.75	-2.36

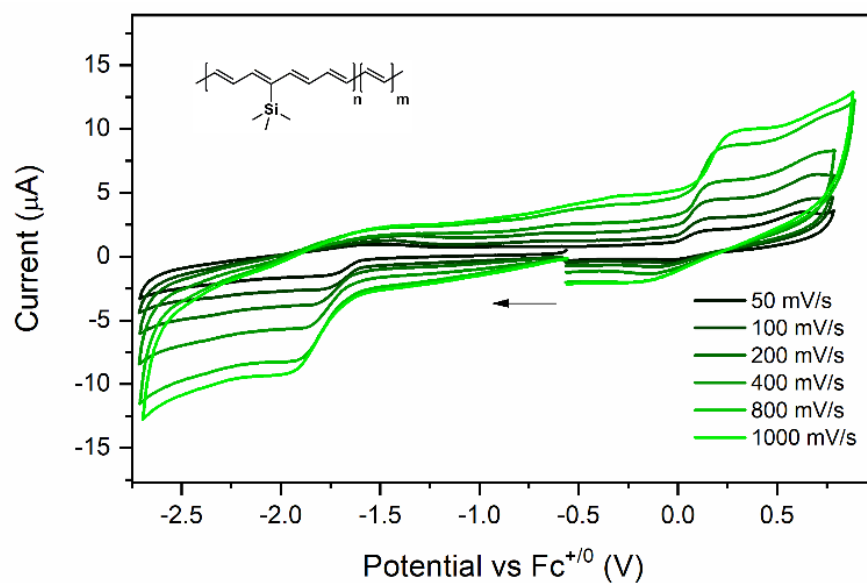


Figure 3.101. Scan rate dependent CV data of pCOT-SiMe₃ (0.5 mg/mL) in THF (0.10 M [ⁿBu₄N]BARF₄ electrolyte).

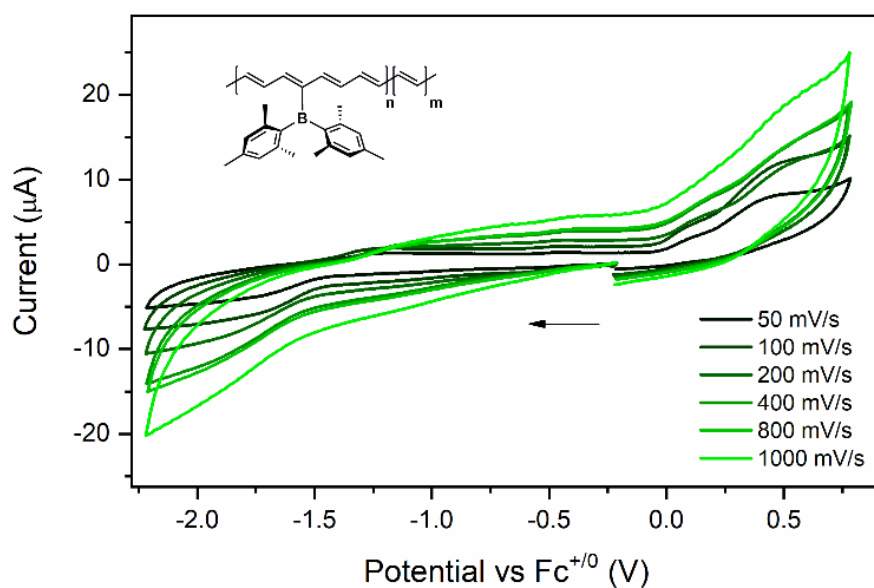


Figure 3.102. Scan rate dependent CV data of pCOT-BMes₂ (0.5 mg/mL) in THF (0.10 M [ⁿBu₄N]BARF₄ electrolyte).

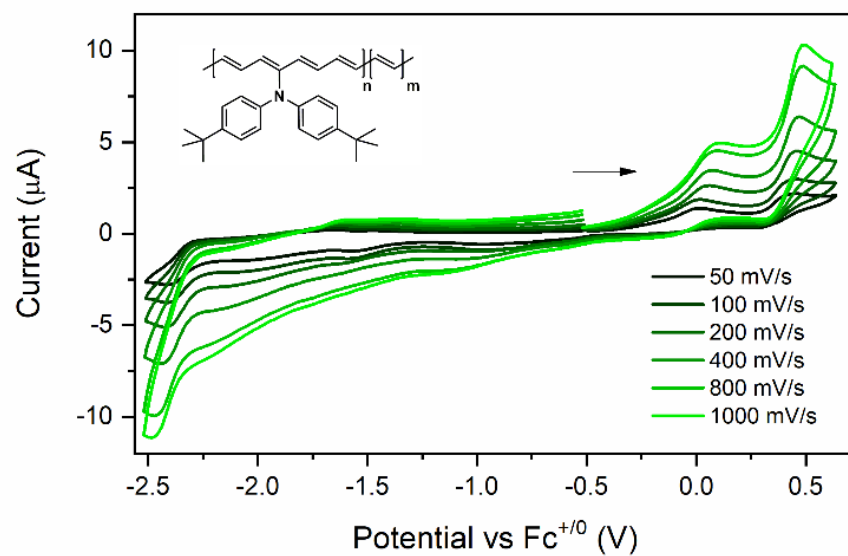


Figure 3.103. Scan rate dependent CV data of **pCOT-N(C₆H₄^tBu)₂** (0.5 mg/mL) in THF (0.10 M [ⁿBu₄N]BAr^F₄ electrolyte).

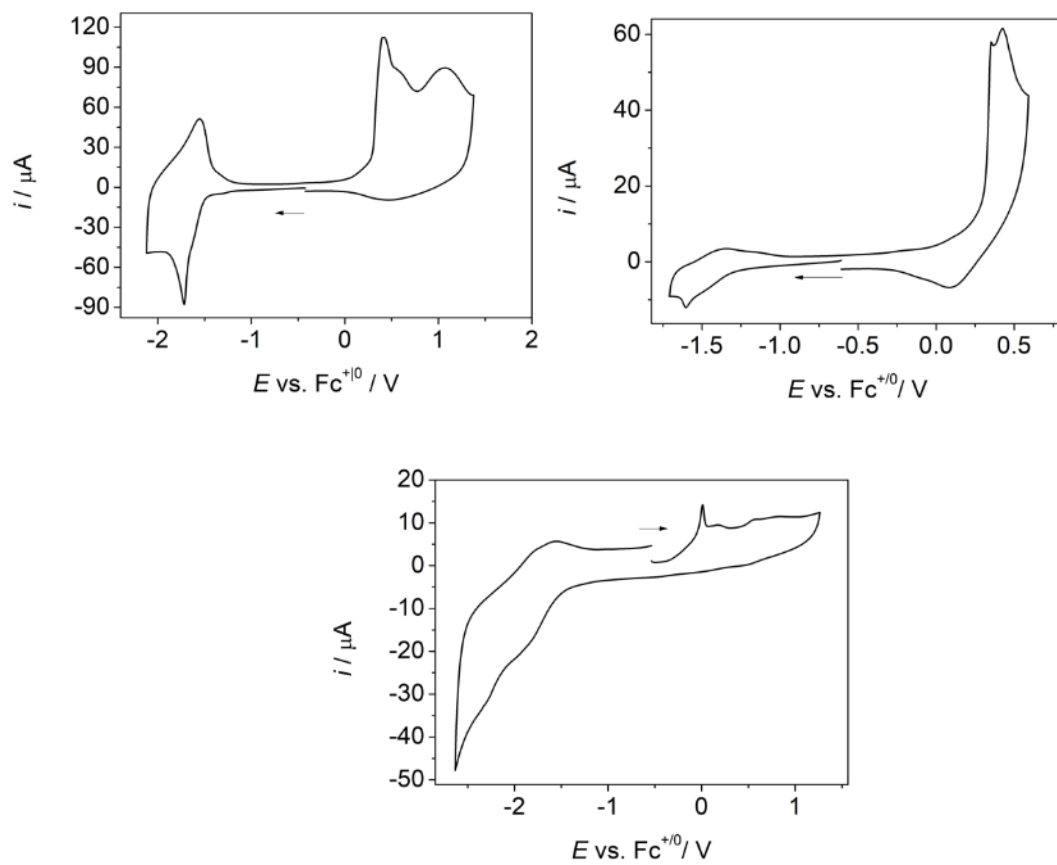


Figure 3.104. CV data of polymer films in MeCN (0.035 M [ⁿBu₄N]BAr^F₄ electrolyte, scan rate = 100 mV/s). Top left: **pCOT-SiMe₃**; top right: **pCOT-BMes₂**; bottom: **pCOT-N(C₆H₄^tBu)₂**.

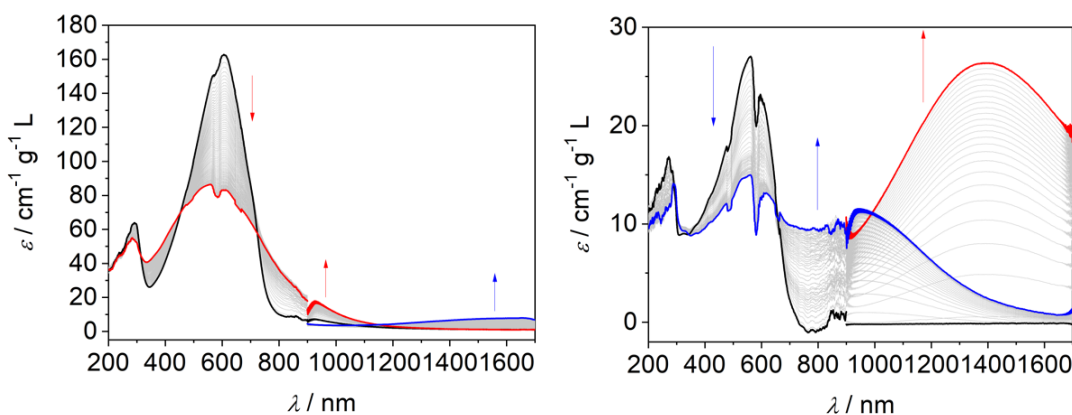


Figure 3.105. UV-Vis-NIR-SEC data of **pCOT-N(C₆H₄^tBu)₂** (left, 0.5 mg/mL) and **pCOT-BMes₂** (right, 0.5 mg/mL) in THF (0.10 M [ⁿBu₄N]BAR^F₄ electrolyte). Black: neutral polymer, blue: reduction (-1.5 V *vs.* Ag/AgNO₃), red: oxidation (0.25 V for **pCOT-N(C₆H₄^tBu)₂** and 0.5 V for **pCOT-BMes₂** *vs.* Ag/AgNO₃). Spectra were recorded every 12 seconds.

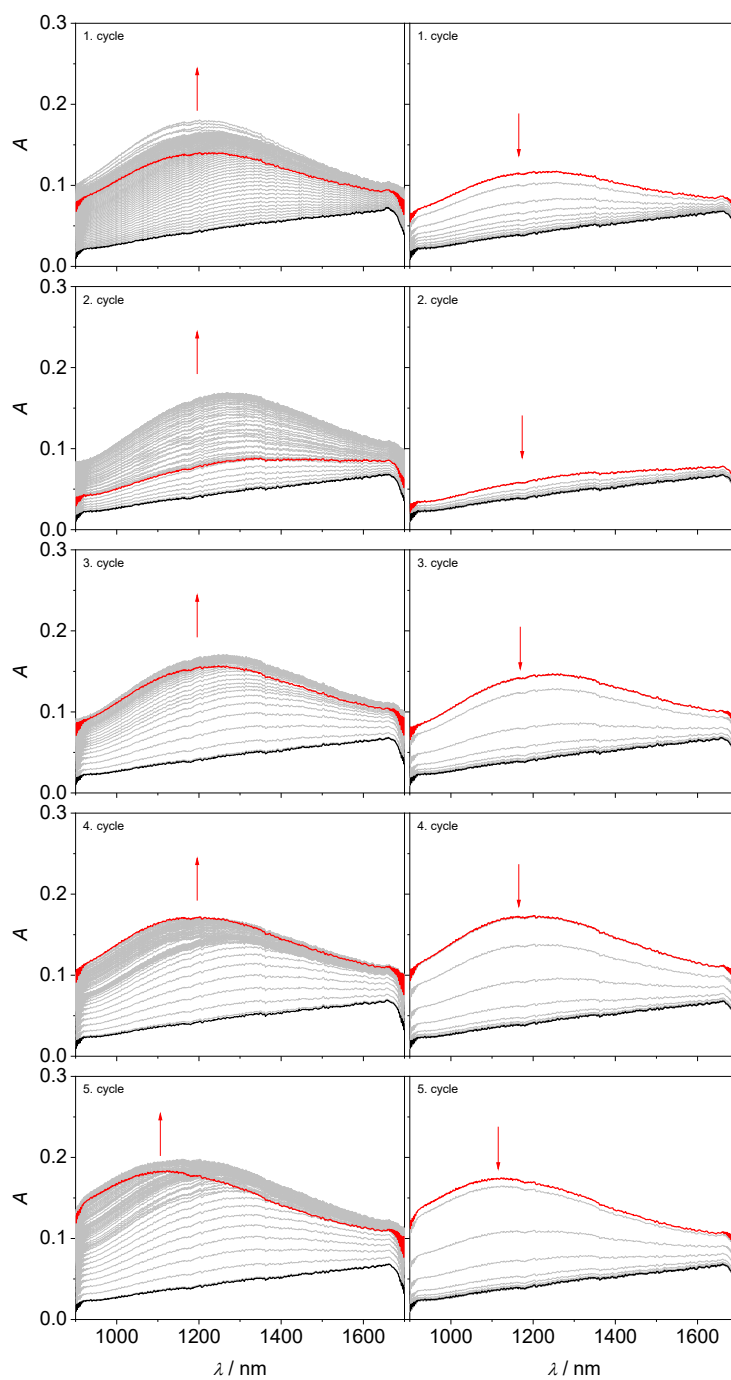


Figure 3.106. NIR-SEC data of **pCOT-SiMe₃** (0.5 mg/mL) in THF (0.10 M [ⁿBu₄N]BAr^F₄ electrolyte). Left: oxidation (1.4 V vs. Ag/AgNO₃), right: re-reduction (-1.0 V vs. Ag/AgNO₃). Spectra were recorded every 12 seconds.

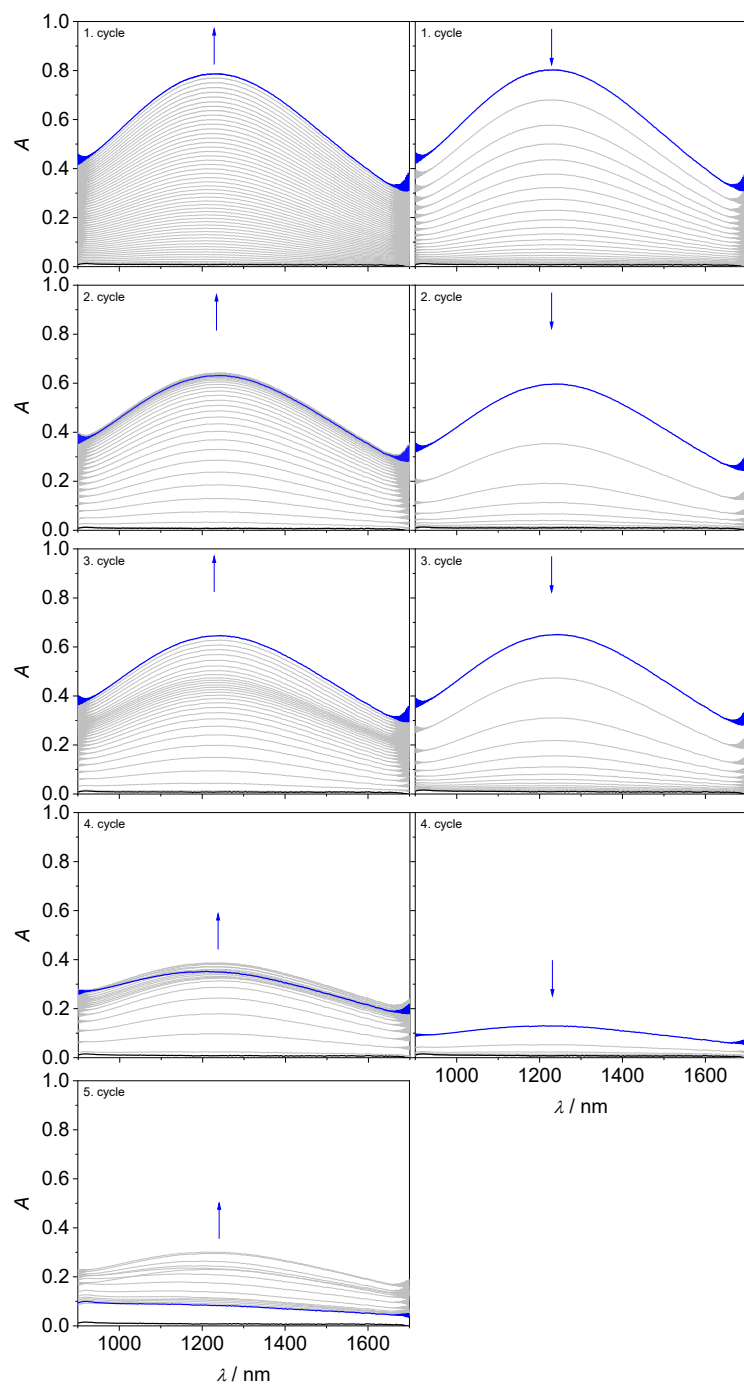


Figure 3.107. NIR-SEC data of **pCOT-SiMe₃** (0.5 mg/mL) in THF (0.10 M [ⁿBu₄N]BAR^F₄ electrolyte). Left: reduction (-2.5 V vs. Ag/AgNO₃), right: re-oxidation (0.5 V vs. Ag/AgNO₃). Spectra were recorded every 12 seconds.

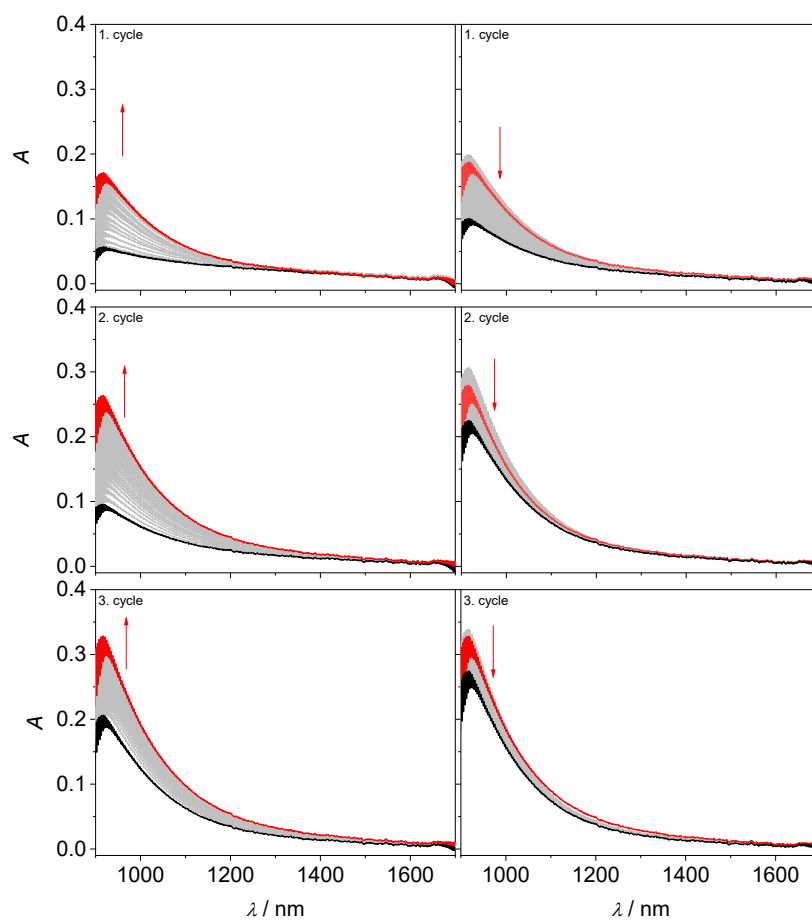


Figure 3.108. NIR-SEC data of **pCOT-N(C₆H₄^tBu)₂** (0.5 mg/mL) in THF (0.10 M [ⁿBu₄N]BAr^F₄ electrolyte). Left: oxidation (1.0 V vs. Ag/AgNO₃), right: re-reduction (-1.2 V vs. Ag/AgNO₃). Spectra were recorded every 12 seconds.

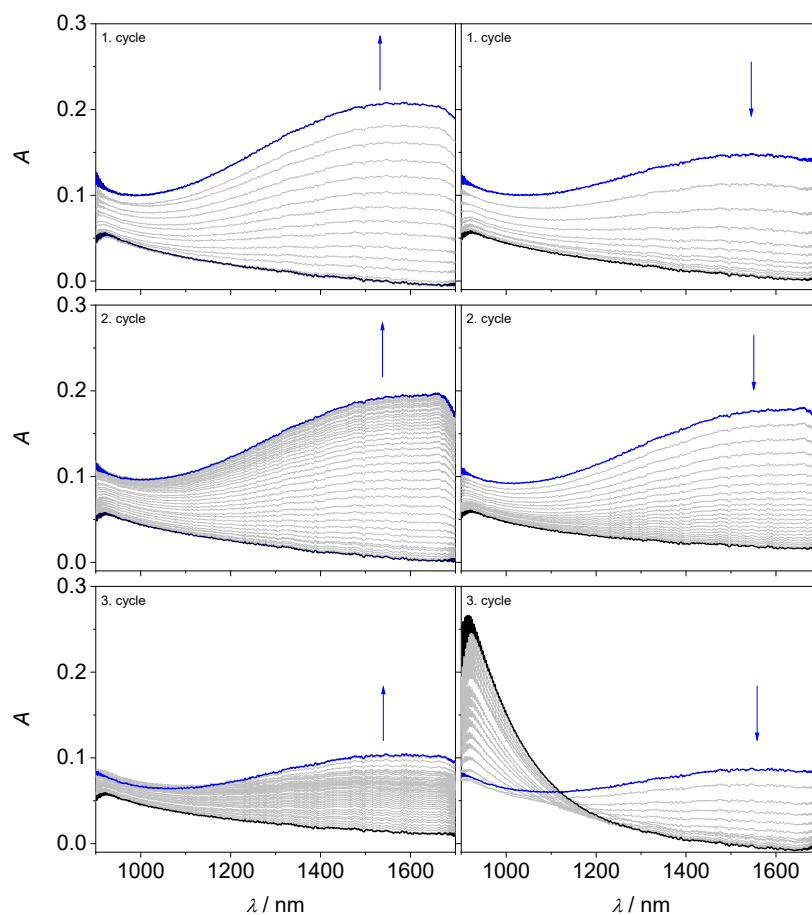


Figure 3.109. NIR-SEC of **pCOT-N(C₆H₄^tBu)₂** (0.5 mg/mL) in THF (0.10 M [ⁿBu₄N]BAr^F₄ electrolyte). Left: reduction (-2.0 V vs. Ag/AgNO₃), right: re-oxidation (-0.4 V vs. Ag/AgNO₃). The last cycle shows partial interconversion into the oxidized polymer as a potential of 1.0 V vs. Ag/AgNO₃ was applied. Spectra were recorded every 12 seconds.

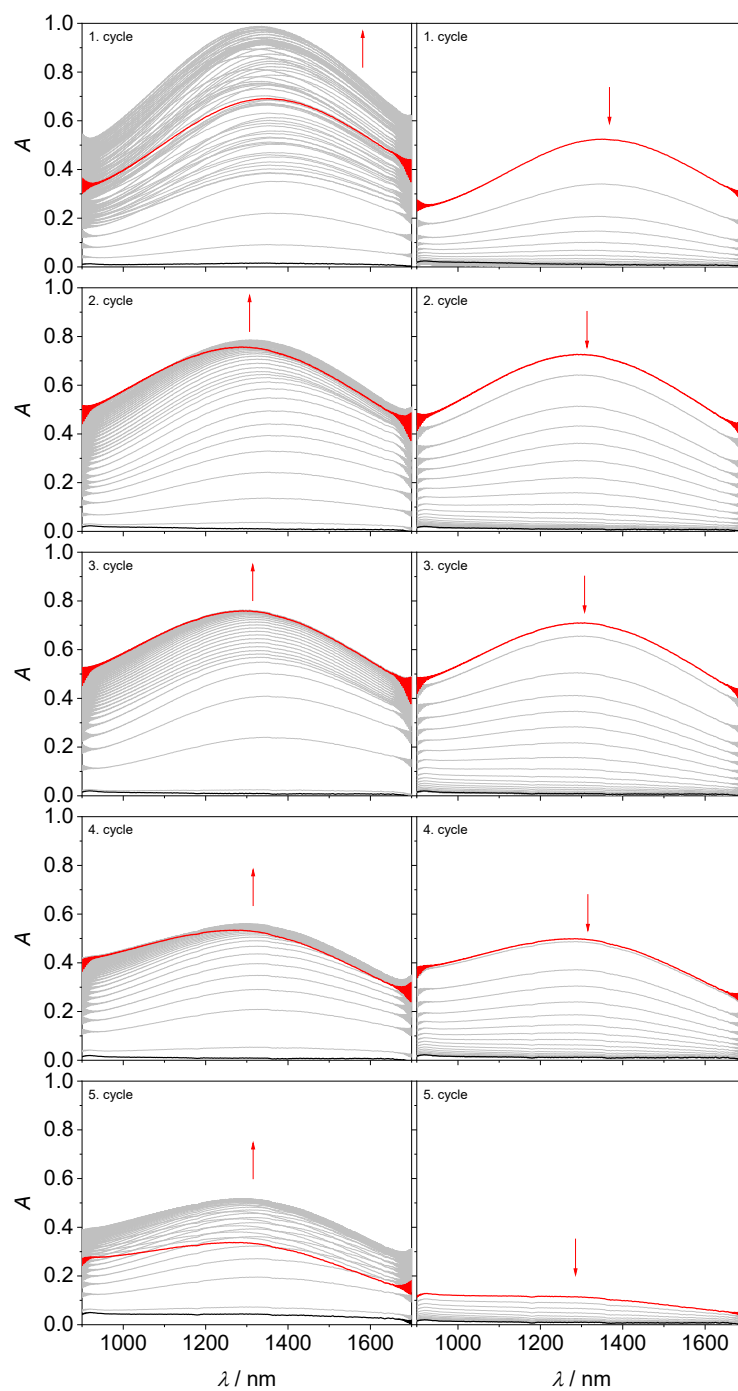


Figure 3.110. NIR-SEC data of **pCOT-BMes₂** (0.5 mg/mL) in THF (0.10 M [ⁿBu₄N]BAR^F₄ electrolyte). Left: oxidation (1.3 V vs. Ag/AgNO₃), right: re-reduction (-1.2 V vs. Ag/AgNO₃). Spectra were recorded every 12 seconds.

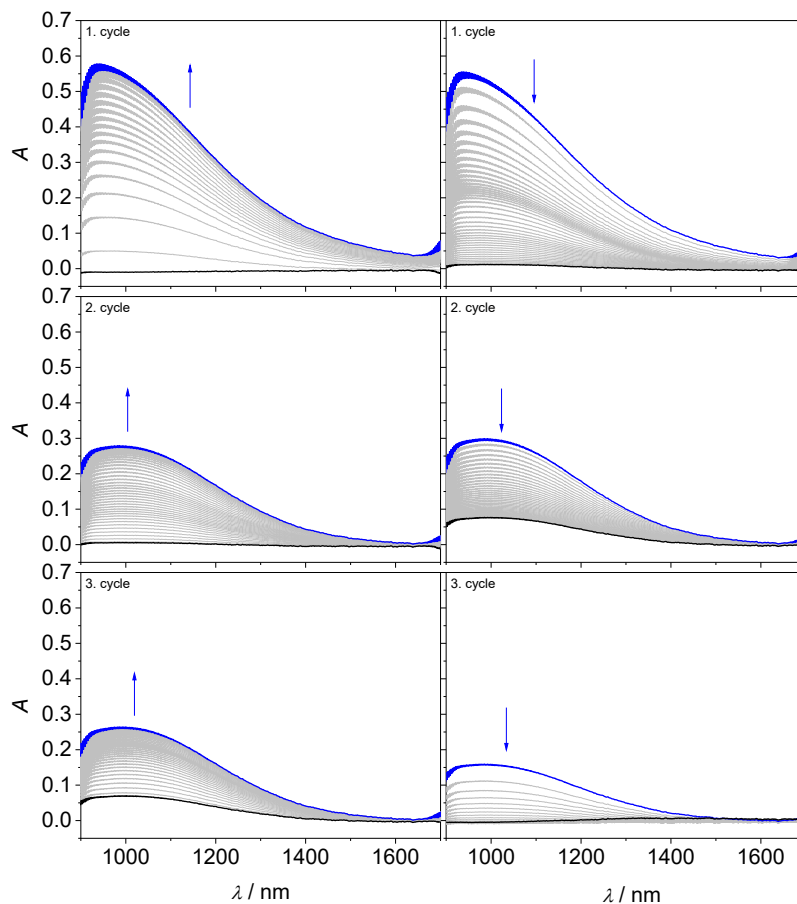


Figure 3.111. NIR-SEC data of **pCOT-BMes₂** (0.5 mg/mL) in THF (0.10 M [^tBu₄N]BAR^F₄ electrolyte). Left: reduction (-2.0 V vs. Ag/AgNO₃), right: re-oxidation (-0.1 V vs. Ag/AgNO₃). Spectra were recorded every 12 seconds.

3.4.12 Additional Optical Profilometry Data

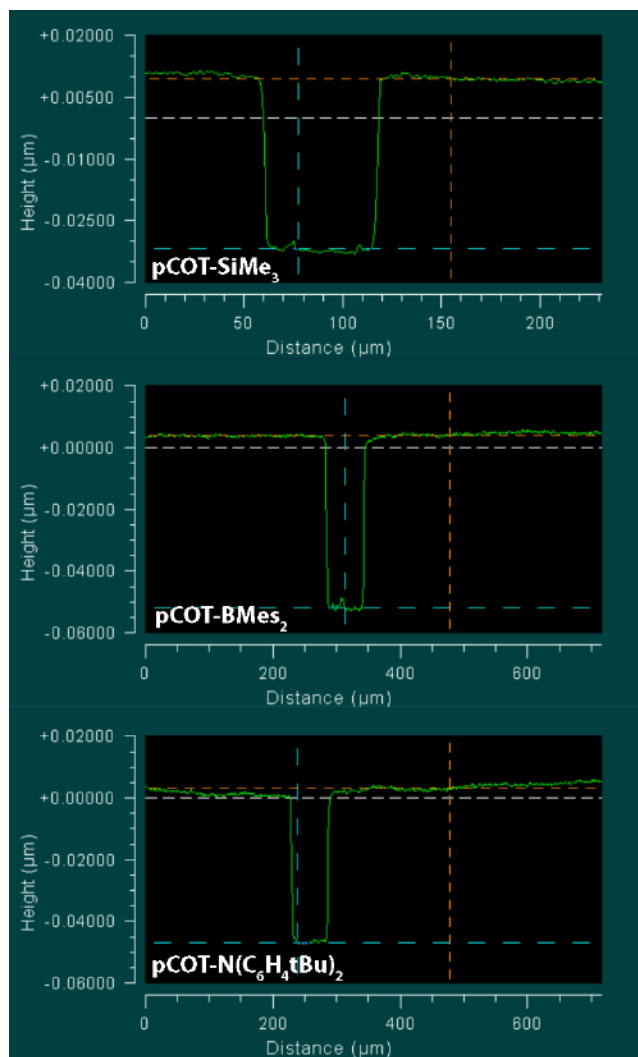


Figure 3.112. Representative height profiles of polymer films obtained by optical profilometry. Trenches were made with steel needles prior to Au-coating.

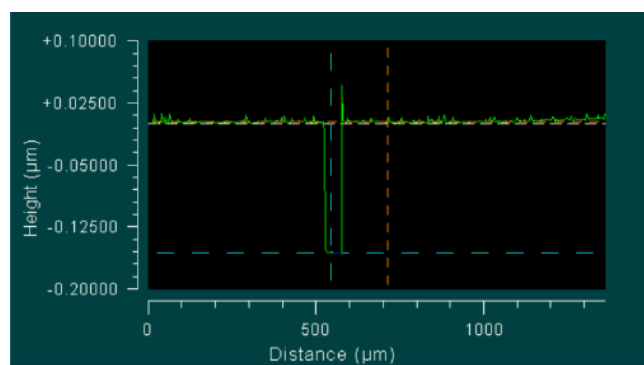
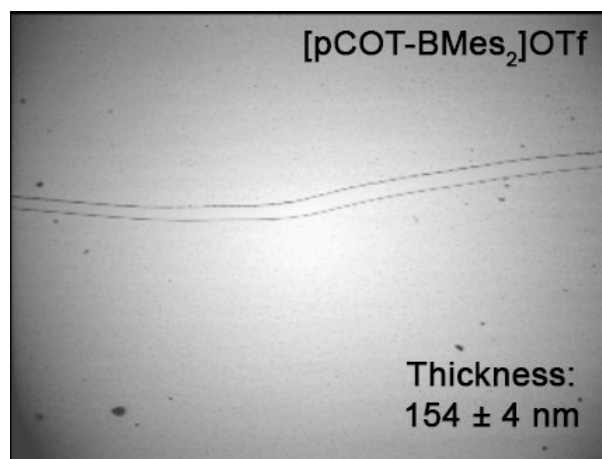


Figure 3.113. Optical microscope image of a spin-coated film of **pCOT-BMes₂** doped with [Fc]OTf (top) and representative height profile of the film obtained by optical profilometry (bottom). Trenches were made with steel needles prior to Au-coating.

3.5 DFT Computations and Methodology

Gas phase structure optimization was performed using density functional theory (DFT) with the B3LYP,^{48,49} CAM-B3LYP,⁵⁰ and wB97XD⁵¹ functionals and the cc-pVDZ⁵² and 6-31G(d)^{53,54} basis sets. Computations were performed with the Gaussian16 software package and frequency analysis confirmed all structures to be local minima on the potential energy surface.⁵⁵ Optimized chain fragments were modeled with 12 carbon atoms between each side chains to approximate the observed effect of cycloextrusion during ring-opening metathesis polymerization. Chain fragments with two side chains were computed for simplicity, thus a larger calculated HOMO/LUMO energy gap is expected when compared to the UV-Vis data of the actual polymers. For time-dependent DFT (TD-DFT) computations, the same functional/basis set combination was used for structure optimization and excited state calculations. For the oxidized and reduced polymers, TD-DFT was attempted using different functionals (B3LYP, CAM-B3LYP, wB97XD), but we were unable to reproduce the experimental spectra (Figures 3.121-3.123). The structures and orbitals are shown as visualized in Avogadro.⁵⁶

3.5.1 Additional DFT and TD-DFT Data

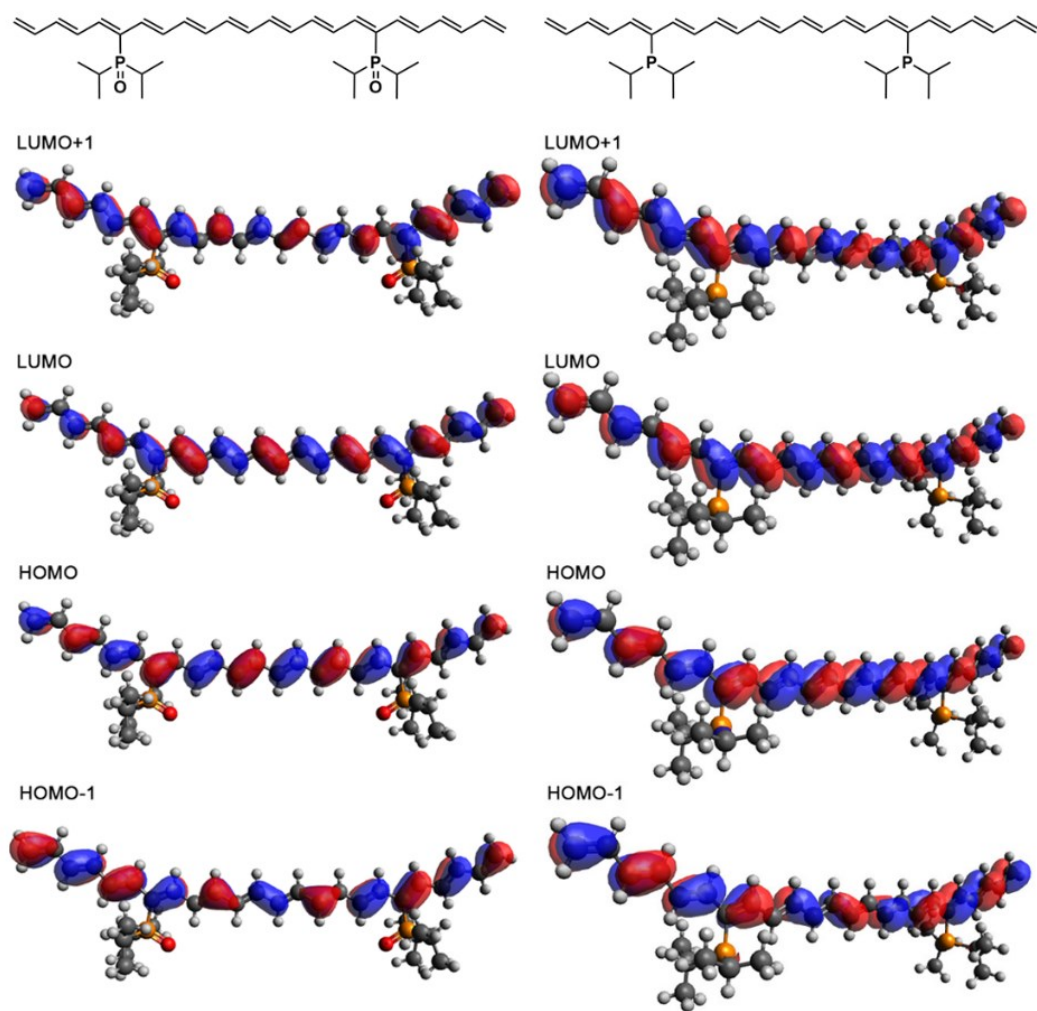


Figure 3.114. Frontier molecular orbitals for chain fragments of **pCOT-P(O)ⁱPr₂** (left) and **pCOT-PⁱPr₂** (right) computed at the B3LYP/cc-pVDZ level of theory.

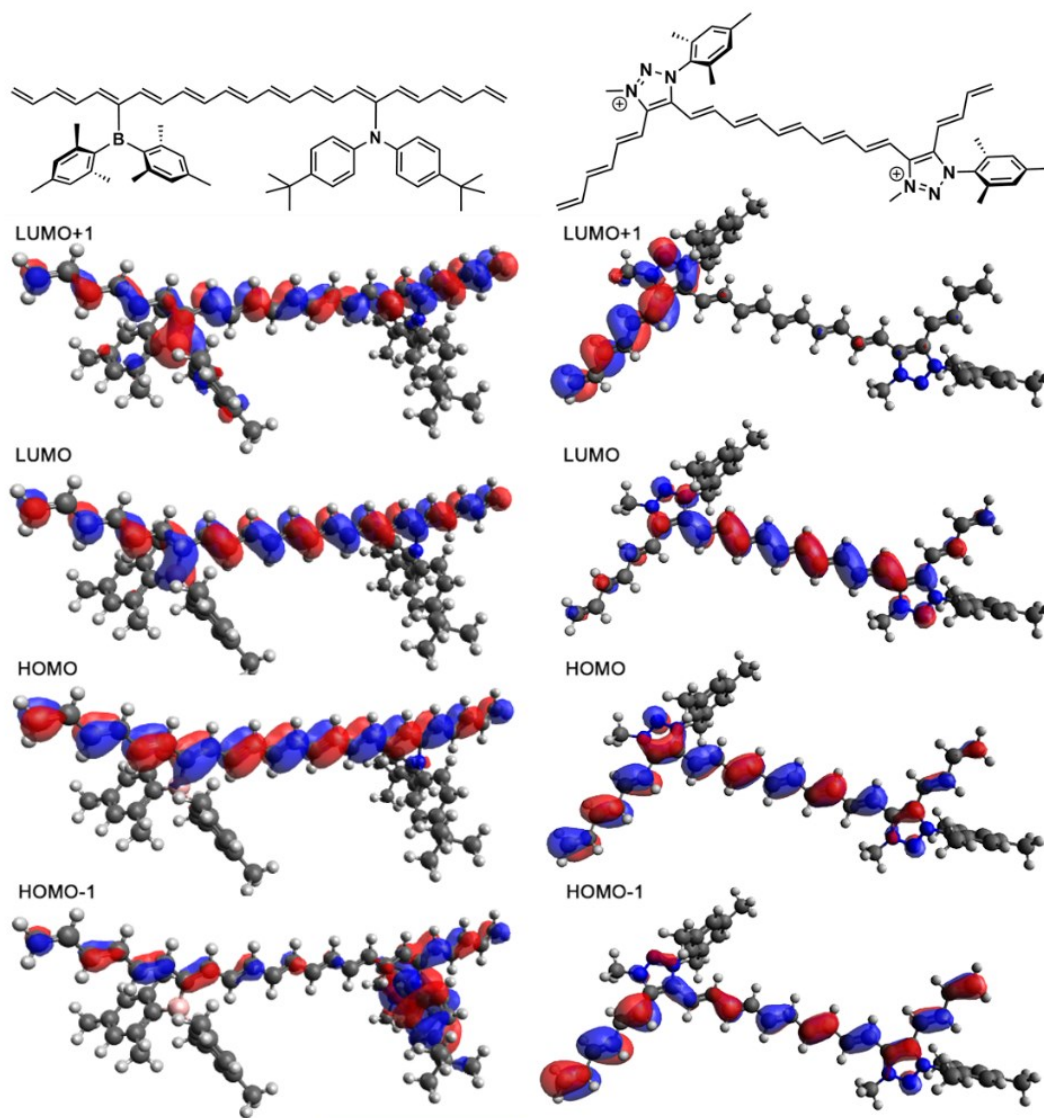


Figure 3.115. Frontier molecular orbitals for models of $p[\text{COT-N}(\text{C}_6\text{H}_4^t\text{Bu})_2-r\text{-COT-BMes}_2]$ (left) and $p[\text{COT-N}_3(\text{Me})\text{-Mes}]^+$ (right) computed at the B3LYP/cc-pVDZ level of theory.

Table 3.9. Computed frontier orbital energies (eV) for polymer models in the gas phase (B3LYP/cc-pVDZ level). Each polymer model contains two side chains separated by 12 carbons (except for parent polyacetylene, PA), reflecting the average separation of side chains due to backbiting followed by cycloextrusion.

	HOMO-1	HOMO	LUMO	LUMO+1	HOMO/LUMO gap (E_g)
PA	-5.425	-4.702	-2.694	-1.914	2.008
pCOT-SiMe ₃	-5.369	-4.658	-2.669	-1.903	1.989
pCOT-BMes ₂	-5.300	-4.597	-2.660	-2.075	1.937
pCOT-NPh ₂	-5.170	-4.683	-2.733	-1.969	1.950
pCOT-N(C ₆ H ₄ ^t Bu) ₂	-5.025	-4.624	-2.687	-1.923	1.937
p[COT-N(C ₆ H ₄ ^t Bu) ₂ - <i>r</i> -COT-BMes ₂]	-5.052	-4.651	-2.717	-1.943	1.934
pCOT-P(O) ⁱ Pr ₂	-5.494	-4.742	-2.778	-2.074	1.964
pCOT-P ⁱ Pr ₂	-5.391	-4.671	-2.697	-1.950	1.974
p[COT-N ₃ (Me)- Mes] ⁺	-9.766	-9.313	-7.003	-6.200	2.310

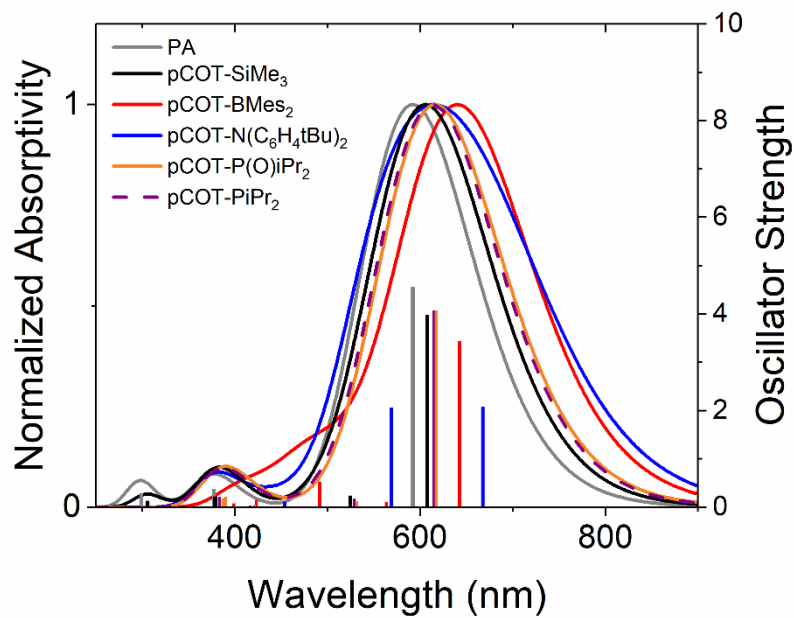


Figure 3.116. Computed UV-Vis spectra and corresponding oscillator strengths for all COT-based polymers with pendant side chains and one without (PA) for comparison.

Table 3.10. TD-DFT computed excited states for **pCOT-BMes₂** (B3LYP/cc-pVDZ level). Orbitals involved in the singlet state transitions are shown.

pCOT-BMes₂			
Excited State	Energy (eV)	Oscillator Strength	Main Orbitals Involved
T1	0.5988	0.0000	
T2	1.2488	0.0000	
T3	1.8231	0.0000	
S1	1.9302	3.4369	HOMO/LUMO
T4	2.1772	0.0000	
S2	2.1997	0.01121	HOMO/LUMO+1
T5	2.2072	0.0000	
S3	2.4495	0.0225	HOMO-1/LUMO
T6	2.4497	0.0000	
S4	2.5218	0.5221	HOMO/LUMO+2
T7	2.5683	0.0000	
T8	2.7636	0.0000	
T9	2.8160	0.0000	
T10	2.8953	0.0000	
S5	2.9301	0.1539	HOMO-1/LUMO+1
S6	2.9492	0.0374	HOMO-2/LUMO
S7	3.0139	0.0235	HOMO-3/LUMO
S8	3.0717	0.0080	HOMO-4/LUMO
S9	3.1095	0.0816	HOMO/LUMO+3
S10	3.2049	0.0451	HOMO-5/LUMO

Table 3.11. TD-DFT computed excited states for **pCOT-N(C₆H₄^tBu)₂** (B3LYP/cc-pVDZ level). Orbitals involved in the singlet state transitions are shown.

pCOT-N(C₆H₄^tBu)₂			
Excited State	Energy (eV)	Oscillator Strength	Main Orbitals Involved
T1	0.5997	0.0000	
T2	1.2522	0.0000	
T3	1.7807	0.0000	
S1	1.8571	2.0801	HOMO/LUMO
T4	1.9106	0.0000	
S2	1.9678	0.0283	HOMO-1/LUMO
T5	2.0613	0.0000	
S3	2.1796	2.0579	HOMO-2/LUMO
T6	2.3095	0.0000	
S4	2.3557	0.0011	HOMO/LUMO+1 HOMO-3/LUMO
T7	2.4970	0.0000	
T8	2.6996	0.0000	
S5	2.7311	0.1140	HOMO-1/LUMO+1
T9	2.8127	0.0000	
S6	2.8559	0.0195	HOMO-2/LUMO+1
T10	2.9742	0.0000	
S7	3.0358	0.0051	HOMO-4/LUMO HOMO/LUMO+2
S8	3.1834	0.0520	HOMO-3/LUMO HOMO/LUMO+1
S9	3.2668	0.2173	HOMO-3/LUMO+1
S10	3.5062	0.0053	HOMO-5/LUMO HOMO-1/LUMO+2

Table 3.12. TD-DFT computed excited states for **pCOT-P(O)ⁱPr₂** (B3LYP/cc-pVDZ level). Orbitals involved in the singlet state transitions are shown.

pCOT-P(O)ⁱPr₂			
Excited State	Energy (eV)	Oscillator Strength	Main Orbitals Involved
T1	0.6019	0.0000	
T2	1.2712	0.0000	
T3	1.8859	0.0000	
S1	2.0082	4.0757	HOMO/LUMO
T4	2.2591	0.0000	
S2	2.3315	0.1267	HOMO-1/LUMO
T5	2.4978	0.0000	
T6	2.8437	0.0000	
S3	2.9444	0.0486	HOMO-2/LUMO HOMO-1/LUMO
T7	2.9461	0.0000	
T8	3.0886	0.0000	
S4	3.1803	0.2086	HOMO-1/LUMO+1 HOMO-1/LUMO
S5	3.2034	0.1836	HOMO/LUMO+2
T9	3.3113	0.0000	
S6	3.3572	0.0014	HOMO-4/LUMO
T10	3.3739	0.0000	
S7	3.3900	0.0062	HOMO-3/LUMO
S8	3.4227	0.0002	HOMO-6/LUMO HOMO-5/LUMO
S9	3.4944	0.0106	HOMO-6/LUMO HOMO-5/LUMO
S10	3.7052	0.0216	HOMO-7/LUMO

Table 3.13. TD-DFT computed excited states for **pCOT-PⁱPr₂** (B3LYP/cc-pVDZ level). Orbitals involved in the singlet state transitions are shown.

pCOT-PⁱPr₂			
Excited State	Energy (eV)	Oscillator Strength	Main Orbitals Involved
T1	0.6006	0.0000	
T2	1.2706	0.0000	
T3	1.8966	0.0000	
S1	2.0165	4.0693	HOMO/LUMO
T4	2.2749	0.0000	
S2	2.3444	0.1762	HOMO-1/LUMO HOMO/LUMO+1
T5	2.4787	0.0000	
T6	2.6414	0.0000	
S3	2.6582	0.0270	HOMO-2/LUMO
T7	2.7459	0.0000	
S4	2.7759	0.0020	HOMO-3/LUMO
T8	2.8625	0.0000	
S5	2.9746	0.0353	HOMO-4/LUMO
T9	2.9831	0.0000	
T10	3.0974	0.0000	
S6	3.1793	0.1725	HOMO-1/LUMO+1 HOMO-4/LUMO
S7	3.2343	0.2172	HOMO/LUMO+2 HOMO-1/LUMO+1
S8	3.5246	0.0067	HOMO-2/LUMO+1
S9	3.5709	0.0013	HOMO-3/LUMO+1
S10	3.916	0.0092	HOMO-5/LUMO

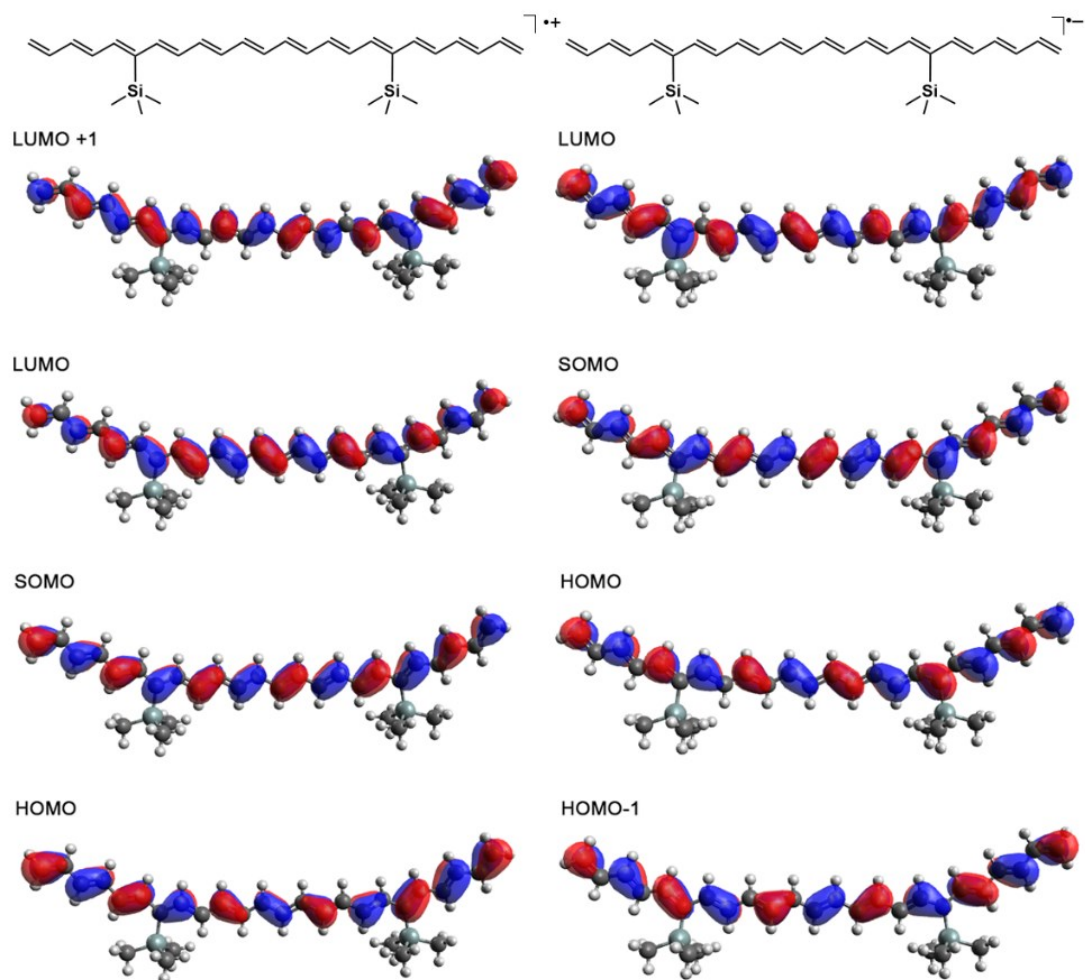


Figure 3.117. Frontier molecular orbitals for models of $p[\text{COT-SiMe}_3^+]$ (left) and $p[\text{COT-SiMe}_3^-]$ (right) computed at the B3LYP/cc-pVDZ level of theory.

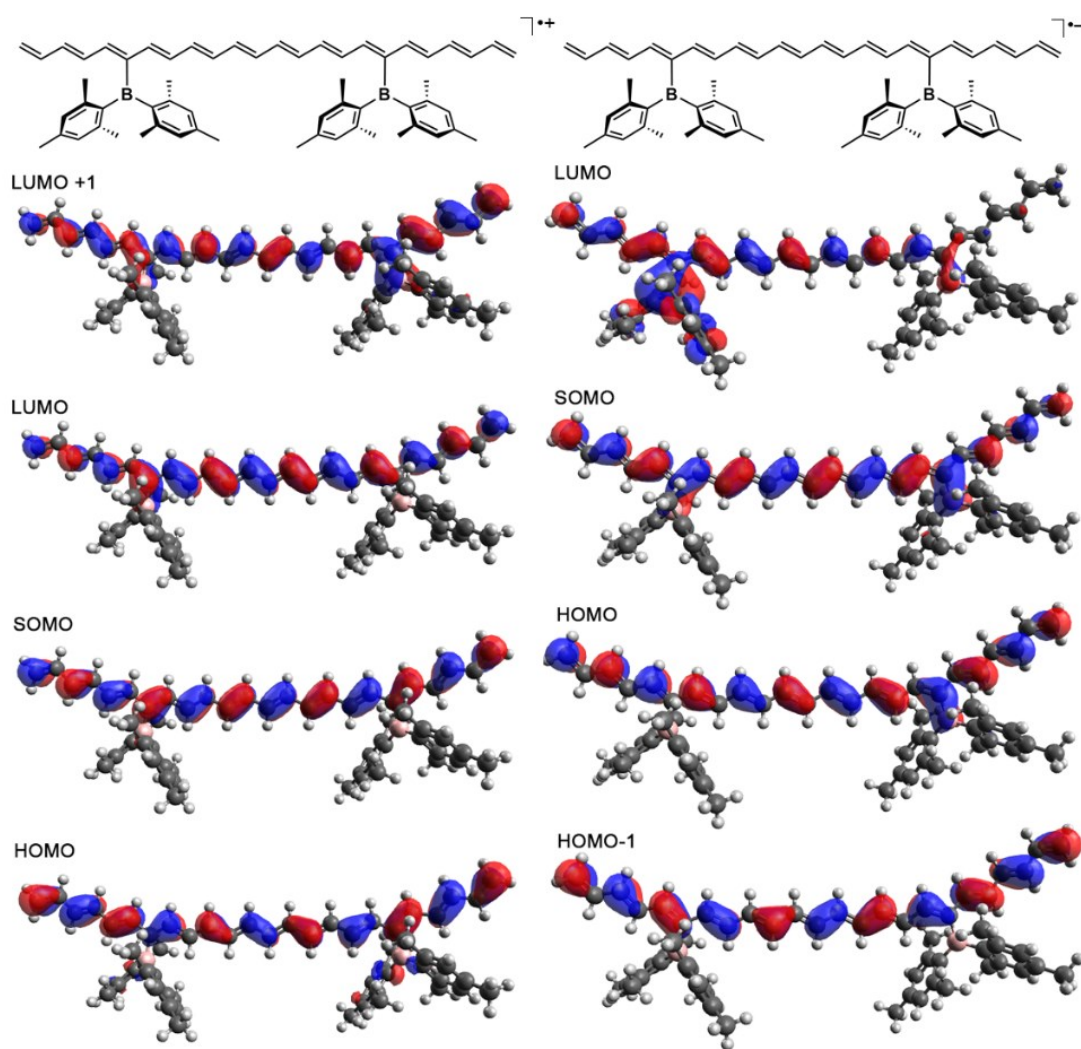


Figure 3.118. Frontier molecular orbitals for models of $p[\text{COT-BMes}_2^+]$ (left) and $p[\text{COT-BMes}_2^-]$ (right) computed at the B3LYP/cc-pVDZ level of theory.

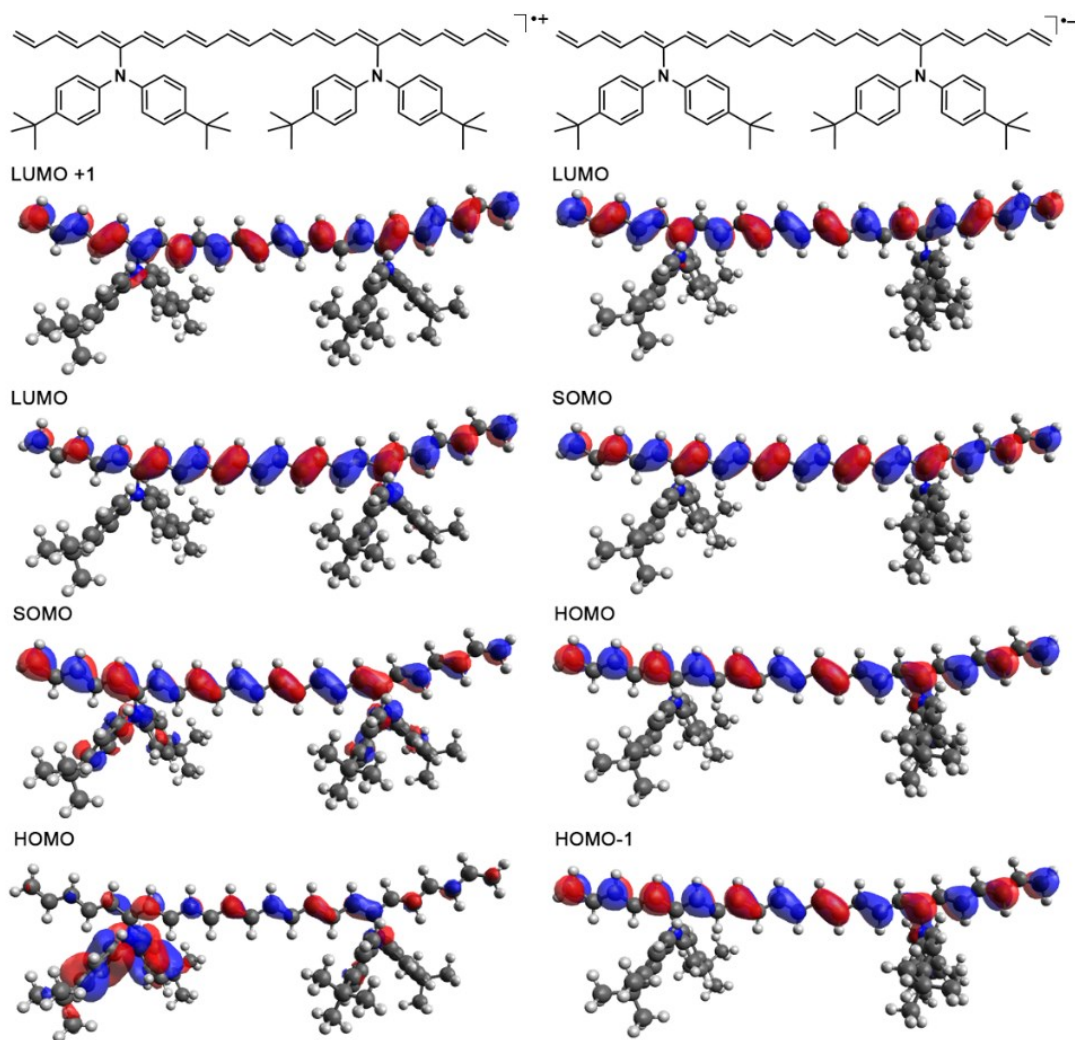


Figure 3.119. Frontier molecular orbitals for chain fragments of $p[\text{COT-N}(\text{C}_6\text{H}_4^t\text{Bu})_2^+]$ (left) and $p[\text{COT-N}(\text{C}_6\text{H}_4^t\text{Bu})_2^-]$ (right) computed at the B3LYP/cc-pVDZ of theory

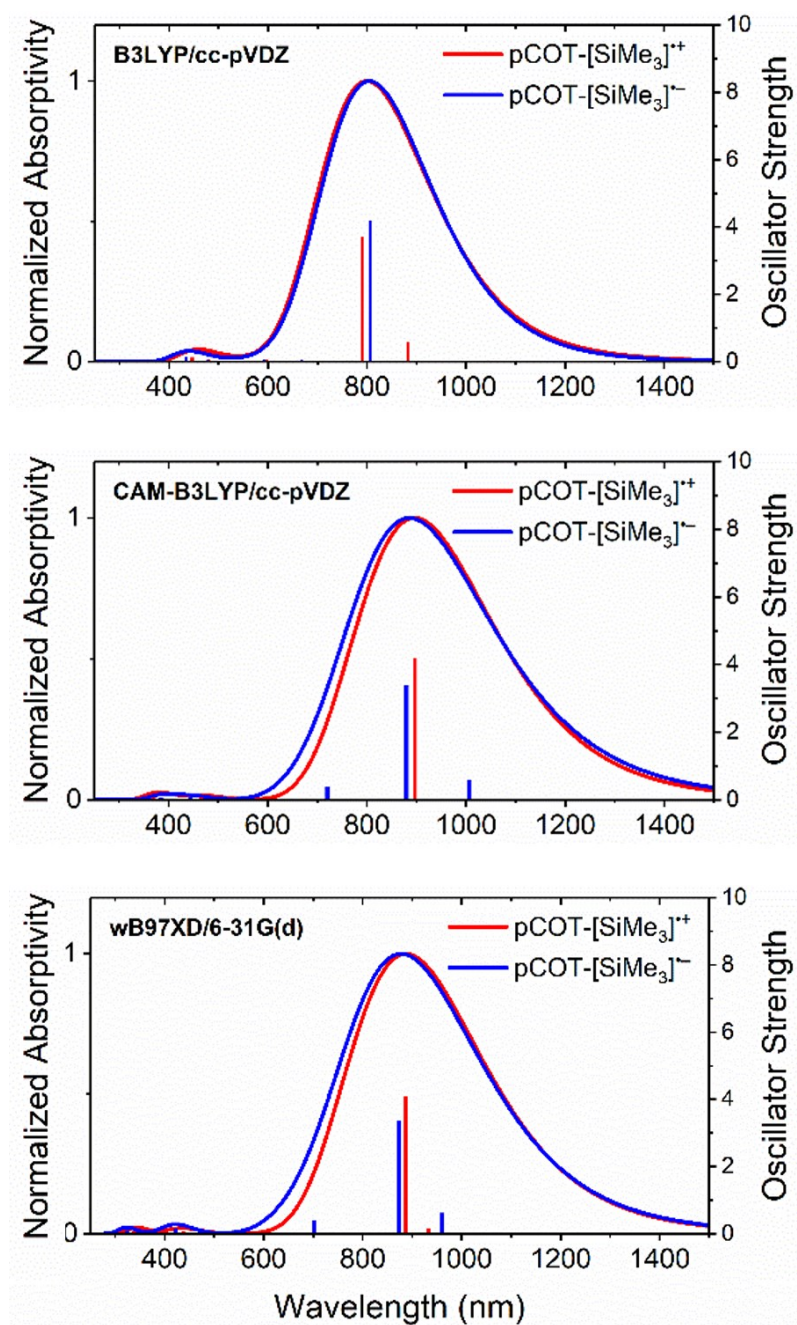


Figure 3.120. UV-Vis-NIR spectra computed for **p[COT-SiMe₃⁺]** and **p[COT-SiMe₃⁻]** by TD-DFT at different levels of theory.

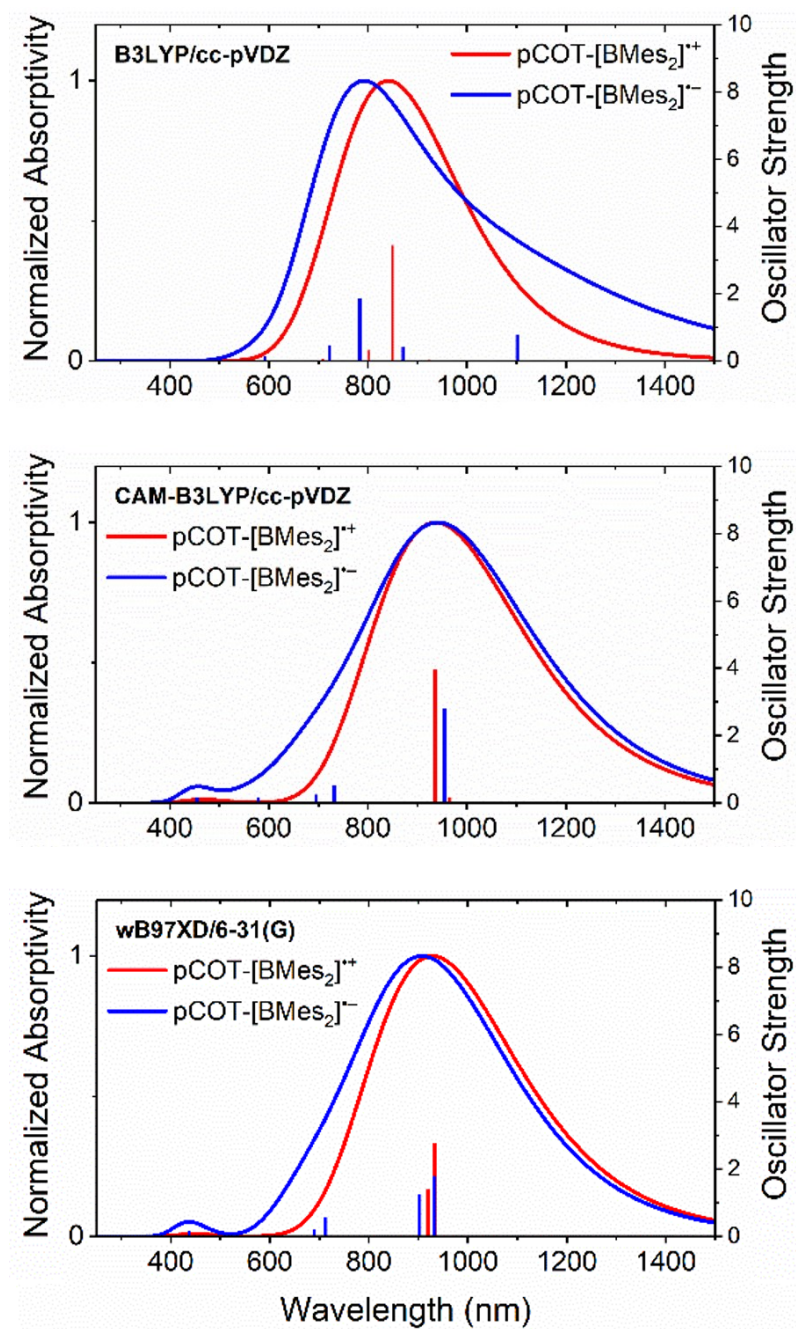


Figure 3.121. UV-Vis-NIR spectra computed for p[COT-BMe₂⁺] and p[COT-BMe₂⁻] by TD-DFT at different levels of theory.

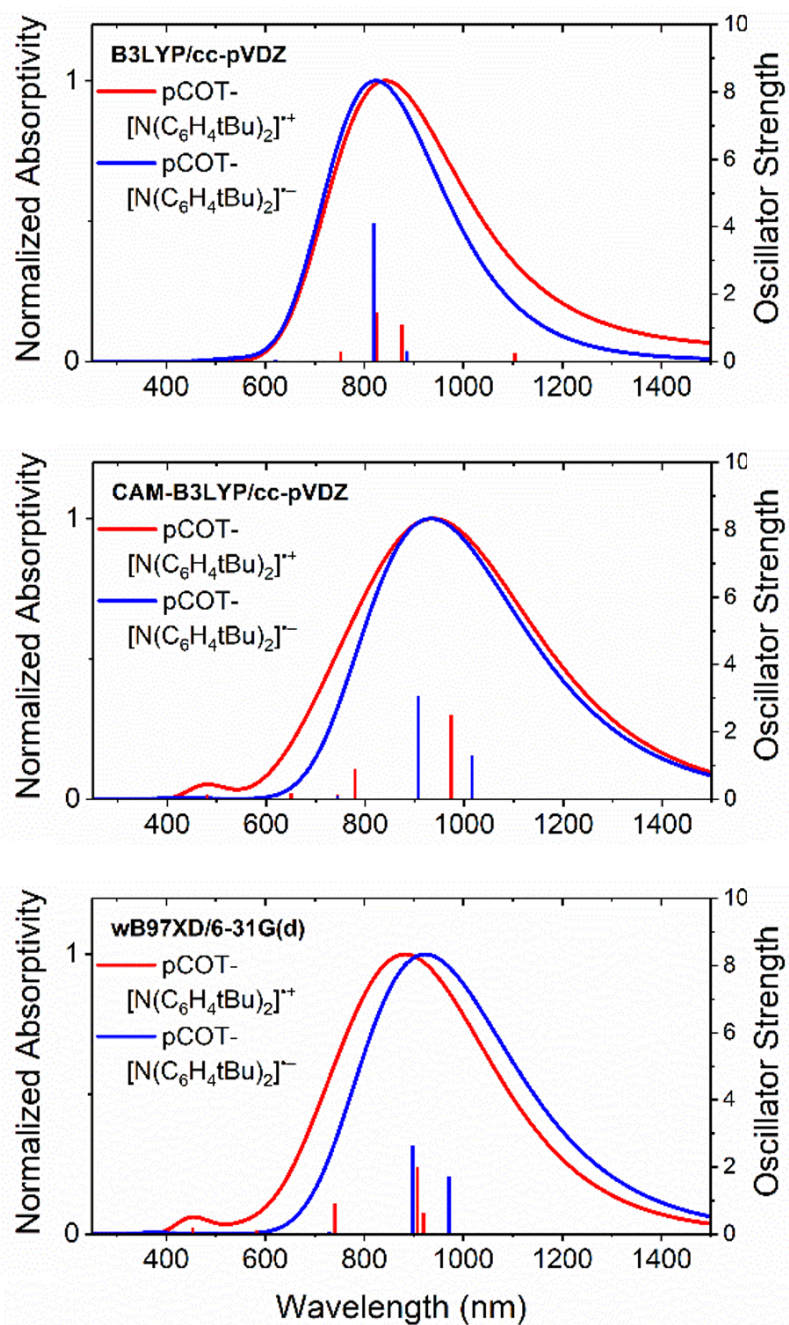


Figure 3.122. UV-Vis-NIR spectra computed for $\text{p[COT-N(C}_6\text{H}_4\text{tBu)}_2^+]$ and $\text{p[COT-N(C}_6\text{H}_4\text{tBu)}_2^-]$ by TD-DFT at different levels of theory.

3.6 References

1. A. G. MacDiarmid, *Angew. Chem. Int. Ed.*, **2001**, *40*, 2581–2590.
2. A. J. Heeger, *Angew. Chem. Int. Ed.*, **2001**, *40*, 2591–2611.
3. N. Suzuki, M. Ozaki, S. Etemad, A. J. Heeger and A. G. MacDiarmid, *Phys. Rev. Lett.*, **1980**, *45*, 1209–1213.
4. (a) B.-B. Cui, J.-H. Tang, J. Yao and Y.-W. Zhong, *Angew. Chem. Int. Ed.*, **2015**, *54*, 9192–9197; (b) M. Wałęsa-Chorab and W. G. Skene, *ACS Appl. Mater. Interfaces*, **2017**, *9*, 21524–21531; (c) Q. Hao, Z.-J. Li, B. Bai, X. Zhang, Y.-W. Zhong, L.-J. Wan and D. Wang, *Angew. Chem. Int. Ed.*, **2021**, *60*, 12498–12503
5. M. Casalino, G. Coppola, R. M. De La Rue and D. F. Logan, *Laser Photonics Rev.*, **2016**, *10*, 895–921.
6. (a) J. M. Pochan, D. F. Pochan, H. Rommelmann and H. W. Gibson, *Macromolecules*, **1981**, *14*, 110–114; (b) T. Masuda, B. Z. Tang, T. Higashimura and H. Yamaoka, *Macromolecules*, **1985**, *18*, 2369–2373.
7. E. J. Ginsburg, C. B. Gorman, S. R. Marder and R. H. Grubbs, *J. Am. Chem. Soc.*, **1989**, *111*, 7621–7622.
8. (a) A. A. Jahnke, B. Djukic, T. M. McCormick, E. Buchaca Domingo, C. Hellman, Y. Lee and D. S. Seferos, *J. Am. Chem. Soc.*, **2013**, *135*, 951–954; (b) G. He, L. Kang, W. Torres Delgado, O. Shynkaruk, M. J. Ferguson, R. McDonald and E. Rivard, *J. Am. Chem. Soc.*, **2013**, *135*, 5360–5363; (c) B. T. Luppi, R. McDonald, M. J. Ferguson, L. Sang and E. Rivard, *Chem. Commun.*,

- 2019**, *55*, 14218–14221; (d) H.-H. Liu, W.-W. Liang, Y.-Y. Lai, Y.-C. Su, H.-R. Yang, K.-Y. Cheng, S.-C. Huang and Y.-J. Cheng, *Chem. Sci.*, **2020**, *11*, 3836–3844; (e) S. M. Parke, M. P. Boone and E. Rivard, *Chem. Commun.*, **2016**, *52*, 9485–9505.
9. (a) S. R. Forrest, *Nature*, **2004**, *428*, 911–918; (b) L. Dou, Y. Liu, Z. Hong, G. Li and Y. Yang, *Chem. Rev.*, **2015**, *115*, 12633–12665; (c) L. Lu, T. Zheng, Q. Wu, A. M. Schneider, D. Zhao and L. Yu, *Chem. Rev.*, **2015**, *115*, 12666–12731.
10. Z. Miao, S. A. Gonsales, C. Ehm, F. Mentink-Vigier, C. R. Bowers, B. S. Sumerlin and A. S. Veige, *Nat. Chem.*, **2021**, DOI: 10.1038/s41557-021-00713-2.
11. B. R. Boswell, C. M. F. Mansson, J. M. Cox, Z. Jin, J. A. H. Romaniuk, K. P. Lindquist, L. Cegelski, Y. Xia, S. A. Lopez and N. Z. Burns, *Nat. Chem.*, **2021**, *13*, 41–46.
12. (a) J. W. Y. Lam and B. Z. Tang, *Acc. Chem. Res.*, **2005**, *38*, 745–754; (b) J. Z. Sun, A. Qin and B. Z. Tang, *Polym. Chem.*, **2013**, *4*, 211–223; (c) K. Akagi, *Chem. Rev.*, **2009**, *109*, 5354–5401; (d) K. Shimomura, T. Ikai, S. Kanoh, E. Yashima and K. Maeda, *Nat. Chem.*, **2014**, *6*, 429–434.
13. (a) F. L. Klavetter and R. H. Grubbs, *J. Am. Chem. Soc.*, **1988**, *110*, 7807–7813; (b) J. S. Moore, C. B. Gorman and R. H. Grubbs, *J. Am. Chem. Soc.*, **1991**, *113*, 1704–1712; (c) C. B. Gorman, E. J. Ginsburg and R. H. Grubbs, *J. Am. Chem. Soc.*, **1993**, *115*, 1397–1409; (d) O. A. Scherman and R. H. Grubbs, *Synth. Met.*,

- 2001**, *124*, 431–434; (e) B. L. Langsdorf, X. Zhou, D. H. Adler and M. C. Lonergan, *Macromolecules*, **1999**, *32*, 2796–2798; (f) M. C. Lonergan, C. H. Cheng, B. L. Langsdorf, and X. Zhou, *J. Am. Chem. Soc.*, **2002**, *124*, 690–701.
14. (a) M. J. Sailor, E. J. Ginsburg, C. B. Gorman, A. Kumar, R. H. Grubbs and N. S. Lewis, *Science*, **1990**, *249*, 1146–1149; (b) T. H. Jozefiak, E. J. Ginsburg, C. B. Gorman, R. H. Grubbs and N. S. Lewis, *J. Am. Chem. Soc.*, **1993**, *115*, 4705–4713.
15. (a) K.-Y. Yoon, I.-H. Lee, K. O. Kim, J. Jang, E. Lee and T.-L. Choi, *J. Am. Chem. Soc.*, **2012**, *134*, 14291–14294; (b) S. Shin, K.-Y. Yoon and T.-L. Choi, *Macromolecules*, **2015**, *48*, 1390–1397; (c) K.-Y. Yoon, S. Shin, Y.-J. Kim, I. Kim, E. Lee and T.-L. Choi, *Macromol. Rapid Commun.*, **2015**, *36*, 1069–1074.
16. A. Krebs and D. Byrd, *Liebigs Ann. Chem.*, **1967**, *707*, 66–74.
17. J. A. Love, J. P. Morgan, T. M. Trnka and R. H. Grubbs, *Angew. Chem., Int. Ed.*, **2002**, *41*, 4035–4037.
18. S. M. Parke, S. Tanaka, H. Yu, E. Hupf, M. J. Ferguson, Y. Zhou, K. Naka and E. Rivard, *Macromolecules*, **2019**, *52*, 7477–7488.
19. C. A. Harmon and A. J. Streitwieser, *J. Org. Chem.*, **1972**, *38*, 549–551.
20. (a) A. Krebs, *Angew. Chem., Int. Ed. Engl.*, **1965**, *4*, 953–954; (b) S. J. Peters, M. R. Turk, M. K. Kiesewetter and C. D. Stevenson, *J. Am. Chem. Soc.*, **2003**, *125*, 11264–11268.
21. A. S. Lankey and M. A. Ogliaruso, *J. Org. Chem.*, **1971**, *36*, 3339–3342.

22. (a) Y. Ren and F. Jäkle, *Dalton Trans.*, **2016**, *45*, 13996–14007; (b) F. Jäkle, *Chem. Rev.*, **2010**, *110*, 3985–4022; (c) M. Elbing and G. C. Bazan, *Angew. Chem. Int. Ed.*, **2008**, *47*, 834–838; (d) C. R. Wade, A. E. J. Broomsgrove, S. Aldridge and F. P. Gabbaï, *Chem. Rev.*, **2010**, *110*, 3958–3984; (e) S. M. Berger, M. Ferger and T. B. Marder, *Chem. -Eur. J.*, **2021**, *27*, 7043–7058.
23. M. Wang, F. Nudelman, R. R. Matthes and M. P. Shaver, *J. Am. Chem. Soc.*, **2017**, *139*, 14232–14236.
24. N. M. D. Brown, F. Davidson and J. W. Wilson, *J. Organomet. Chem.*, **1981**, *209*, 1–11.
25. R. I. Walter, *J. Am. Chem. Soc.*, **1955**, *77*, 5999–6002.
26. P. Bujak, I. Kulszewicz-Bajer, M. Zagorska, V. Maurel, I. Wielgus and A. Pron, *Chem. Soc. Rev.*, **2013**, *42*, 8895–8999.
27. (a) H. K. Mackenzie, B. W. Rawe, K. Samedov, H. T. G. Walsgrove, A. Uva, Z. Han and D. P. Gates, *J. Am. Chem. Soc.*, **2020**, *142*, 10319–10324; (b) T. Baumgartner, *Acc. Chem. Res.*, **2014**, *47*, 1613–1622; (c) L. A. Vanderark, T. J. Clark, E. Rivard, I. Manners, J. C. Slootweg and K. Lammertsma, *Chem. Commun.*, **2006**, 3332–3333; (d) H. Dorn, R. A. Singh, J. A. Massey, J. M. Nelson, C. A. Jaska, A. J. Lough and I. Manners, *J. Am. Chem. Soc.*, **2000**, *122*, 6669–6678.
28. M. Carnes, D. Buccella, J. Decatur, M. L. Steigerwald and C. Nuckolls, *Angew. Chem. Int. Ed.*, **2008**, *47*, 2982–2985.

29. (a) H. Jiang, P. Taraneekar, J. R. Reynolds and K. S. Schanze, *Angew. Chem. Int. Ed.*, **2009**, *48*, 4300–4316; (b) M. M. Obadia and E. Drockenmuller, *Chem. Commun.*, **2016**, *52*, 2433–2450.
30. (a) C. R. Wade, A. E. J. Broomsgrove, S. Aldridge and F. P. Gabbaï, *Chem. Rev.*, **2010**, *110*, 3958–3984; (b) J. Feng, L. Xiong, S. Wang, S. Li, Y. Li and G. Yang, *Adv. Funct. Mater.*, **2013**, *23*, 340–345.
31. (a) W. Kaim and A. Schulz, *Angew. Chem. Int. Ed. Engl.*, **1984**, *23*, 615–616; (b) J. Fiedler, S. Zališ, A. Klein, F. M. Hornung and W. Kaim, *Inorg. Chem.*, **1996**, *35*, 3039–3043; (c) W. Kaim, N. S. Hosmane, S. Záliš, J. A. Maguire and W. N. Lipscomb, *Angew. Chem. Int. Ed.*, **2009**, *48*, 5082–5091.
32. (a) Z. Wu, Y. Zhai, H. Kim, J. D. Azoulay and T. N. Ng, *Acc. Chem. Res.*, **2018**, *51*, 3144–3153; (b) Q. Li, Y. Guo, Y. Liu, *Chem. Mater.*, **2019**, *31*, 6359–6379.
33. (a) B. O. Pray, L. H. Sommer, G. M. Goldberg, G. T. Kerr, P. A. Di Giorgio and F. C. Whitmore, *J. Am. Chem. Soc.*, **1948**, *70*, 433–434; (b) R. I. Damja, C. Eaborn and W.-C. Sham, *J. Organomet. Chem.*, **1985**, *291*, 25–33; (c) G. A. Ayoko and C. Eaborn, *J. Chem. Soc. Perkin Trans. 2*, **1987**, 381–383.
34. Y. Aramaki, H. Omiya, M. Yamashita, K. Nakabayashi, S. Ohkoshi and K. Nozaki, *J. Am. Chem. Soc.*, **2012**, *134*, 19989–19992.
35. (a) E. T. Denisov, *Kinet. Catal.*, **2006**, *47*, 662–671; (b) E. Kumli, F. Montermini and P. Renaud, *Org. Lett.*, **2006**, *8*, 5861–5864.
36. A. M. Harned, H. S. He, P. H. Toy, D. L. Flynn and P. R. Hanson, *J. Am. Chem. Soc.*, **2005**, *127*, 52–53.

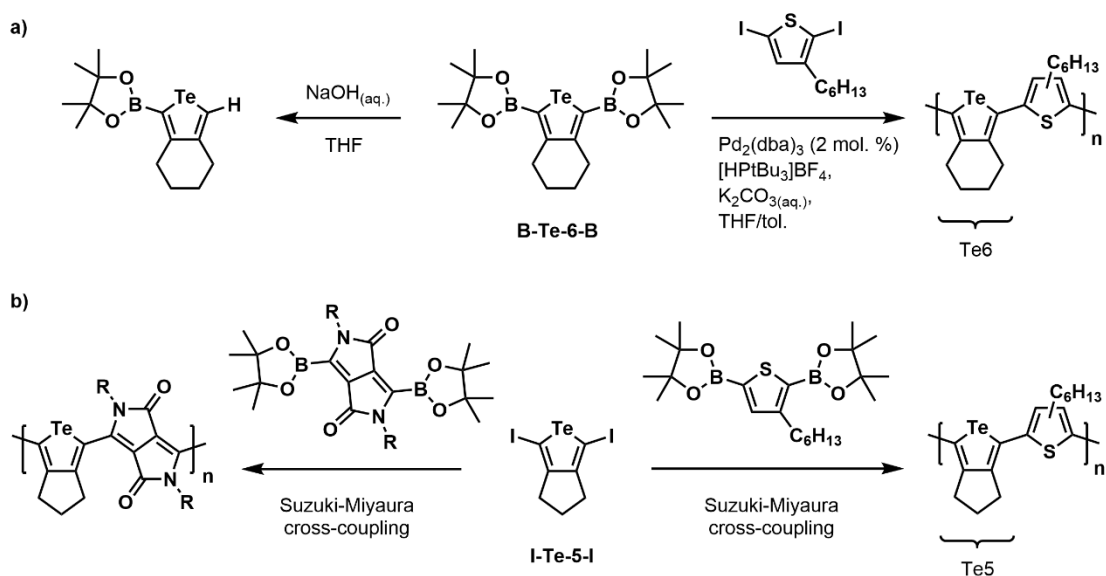
37. J. Gasteiger, G. E. Gream, R. Huisgen, W. E. Konz and U. Schnegg, *Chem. Ber.*, **1971**, *104*, 2412–2419.
38. M. A. Ogliaruso and A. S. Lankey, *J. Org. Chem.*, **1971**, *36*, 3339–3342.
39. M. Cooke, C. R. Russ and F. G. A. Stone, *J. Chem. Soc., Dalton Trans.*, **1975**, 256–259.
40. C. Li, S. K. Mellerup, X. Wang and S. Wang, *Organometallics*, **2018**, *37*, 3360–3367.
41. S. W. Kwok, J. R. Fotsing, R. J. Fraser, V. O. Rodionov and V. V. Fokin, *Org. Lett.*, **2010**, *12*, 4217–4219.
42. N. A. Yakelis and R. G. Bergman, *Organometallics*, **2005**, *24*, 14, 3579–3581.
43. T. Ono, M. Ohta and K. Sada, *ACS Macro Lett.*, **2012**, *1*, 1270–1273.
44. A. F. Burchat, J. M. Chong and N. Nielsen, *J. Organomet. Chem.*, **1997**, *542*, 281–283.
45. Ł. Kapuśniak, P. N. Plessow, D. Trzybiński, K. Woźniak, P. Hofmann and P. I. Jolly, *Organometallics*, **2021**, *40*, 693–701.
46. G. M. Sheldrick, *Acta Cryst. A*, **2015**, *71*, 3–8
47. P. T. Beurskens, G. Beurskens, R. de Gelder, J. M. M. Smits, S. Garcia-Granda and R. O. Gould, The DIRDIF-2008 program system, Crystallography Laboratory, Radboud University Nijmegen, The Netherlands.
48. A. D. Becke, *J. Chem. Phys.*, **1993**, *98*, 5648–5652.
49. C. Lee, W. Yang and R. G. Parr, *Phys. Rev. B*, **1988**, *37*, 785–789.
50. T. Yanai, D. P. Tew and N. C. Handy, *Chem. Phys. Lett.*, **2004**, *393*, 51–57.

51. J.-D. Chai and M. Head-Gordon, *Phys. Chem. Chem. Phys.*, **2008**, *10*, 6615–6620.
52. T. H. Dunning, Jr., *J. Chem. Phys.*, **1989**, *90*, 1007–1023.
53. A. Bennett, W. A. Shirley, M. A. Al-Laham, T. G. Tensfeldt, G. A. Petersson and J. Mantzaris, *J. Chem. Phys.*, **2002**, *89*, 2193–2218.
54. G. A. Petersson and M. A. Al-Laham, *J. Chem. Phys.*, **1991**, *94*, 6081–6090.
55. M. J. Frisch, G. W. Trucks, H. B. Schlegel, G. E. Scuseria, M. A. Robb, J. R. Cheeseman, G. Scalmani, V. Barone, G. A. Petersson, H. Nakatsuji, M. C. X. Li, A. Marenich, J. Bloino, B. G. Janesko, R. Gomperts, B. Mennucci, H. P. Hratchian, J. V. Ortiz, A. F. Izmaylov, J. L. Sonnenberg, D. Williams-Young, F. Ding, F. Lipparini, F. Egidi, J. Goings, B. Peng, A. Petrone, T. Henderson, D. Ranasinghe, V. G. Zakrzewski, J. Gao, N. Rega, G. Zheng, W. Liang, M. Hada, M. Ehara, K. Toyota, R. Fukuda, J. Hasegawa, M. Ishida, T. Nakajima, Y. Honda, O. Kitao, H. Nakai, T. Vreven, K. Throssell, J. A. J. Montgomery, J. E. Peralta, F. Ogliaro, M. Bearpark, J. J. Heyd, E. Brothers, K. N. Kudin, V. N. Staroverov, T. Keith, R. Kobayashi, J. Normand, K. Raghavachari, A. Rendell, J. C. Burant, S. S. Iyengar, J. Tomasi, M. Cossi, J. M. Millam, M. Klene, C. Adamo, R. Cammi, J. W. Ochterski, R. L. Martin, K. Morokuma, O. Farkas, J. B. Foresman and D. J. Fox, Gaussian 09, Revision A.02, *Gaussian, Inc., Wallingford CT*.
56. M. D. Hanwell, D. E. Curtis, D. C. Lonie, T. Vandermeersch, E. Zurek and G. R. Hutchison, *J. Cheminf.*, **2012**, *4*:17.

Chapter 4: Summary and Future Directions

4.1 Synthesis of New Polytellurophenes

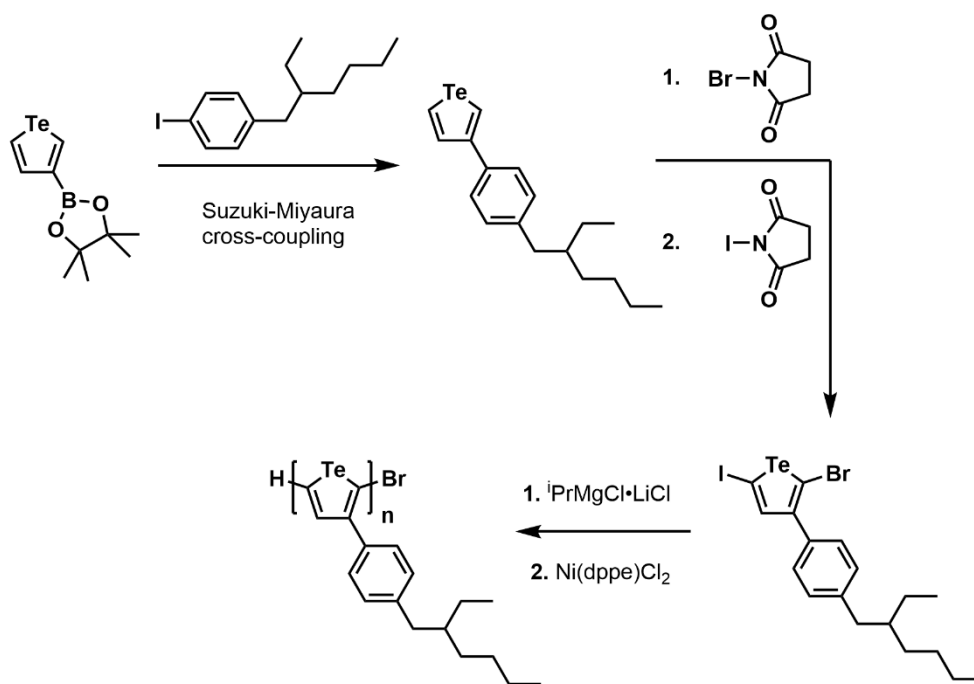
In Chapter 2, the synthesis and polymerization of new iodinated tellurophenes was reported. Oligomerization of **I-Te-5-I** and **I-Te-6-I** into **Oligo-Te5** ($E_g = 1.97$ eV) and **Oligo-Te6** ($E_g = 2.72$ eV) revealed a drastic change in optoelectronic properties depending on the choice of monomer, despite the small difference in the size of the fused cycloalkane side group (5- or 6-membered rings). The retention of a planar backbone for **Oligo-Te5** indicates that the Te5 unit (see Scheme 4.1) would be better suited for the formation of copolymers with extended π -conjugation, compared to the Te6 unit, which has been used in the past to form copolymers with relatively large E_g by reacting **B-Te-6-B** with halogenated co-monomers (*c.f.* Scheme 4.1a).¹ A possible coupling partner for **I-Te5-I** could be diborylated diketopyrrolopyrrole (Scheme 4.1b), as its electron-deficiency would lead to a “push-pull” effect with the electron-rich tellurophene and a possible lowering of the HOMO-LUMO energy gap (E_g).² Additionally, the presence of iodine atoms in **I-Te5-I** would allow for Suzuki-Miyaura coupling polymerization to transpire without substantial protodeboronation. The cleavage of C-BPin bonds in **B-Te-6-B** under Suzuki-Miyaura coupling conditions has been noted by the Rivard group in the past (Scheme 4.1a), which limited chain growth during copolymerization.³



Scheme 4.1. a) Use of the pinacolborane-functionalized tellurophene **B-Te-6-B** to form copolymers of large E_g values (right) and its protodeboronation under basic conditions (left); b) Possible uses of **I-Te-5-I** to form copolymers with planar backbones.

Additionally in Chapter 2, the synthesis of the first poly(3-aryltellurophene), **PolyTe-cumenyl** was reported. The required monomer was synthesized by a versatile Suzuki-Miyaura cross-coupling protocol, which should allow for a wide range of different side chains to be installed onto the final polytellurophene. The presence of the aryl (cumenyl) side chain was shown to further reduce E_g (to 1.3 eV vs. 1.4 eV for alkyl analogues)⁴ possibly through π - π stacking interactions in the solid state. However, despite the successful synthesis of **PolyTe-cumenyl**, MALDI-MS indicates the presence of chains terminated by H on both ends, which should not happen during controlled Grignard metathesis (GRIM) polymerization (also known as catalyst-

transfer polymerization, CTP).⁵ Reactivity studies showed a high propensity of the 3-aryltellurophene monomer, **I-Te-cumenyl-I**, of being activated/metallated at the position close to the aryl side chain when compared to alkylated tellurophenes.^{6a} This could reduce the yield of polymerization, since only monomers activated at the position away from the aryl side chain are polymerized under these conditions.⁵ Additionally, double-activation/metallation of **I-Te-cumenyl-I** was observed, which could explain the chain termination observed by MALDI-MS.



Scheme 4.2. Possible improved synthesis of an aryl-substituted polytellurophene.

Control over the polymerization of arylated tellurophenes could be improved in two ways (Scheme 4.2): first, an aryl side chain appended with a branched alkyl chain

in the *para* position could drastically improve solubility, while maintaining the desired polymer properties. It is important to note that the branching in this case should not impact polymerization, as observed for poly(3-alkyltellurophene)s,^{6a} since the branching point would be far away from the tellurophene units; second, an unsymmetrically halogenated tellurophene unit could be used to direct activation away from the side chain. This mixed bromo/iodo monomer could be synthesized by bromination with *N*-bromosuccinimide (NBS) followed by iodination with *N*-iodosuccinimide (NIS), and would further improve the rate of polymerization, as shown before for tellurophene monomers containing both iodine and bromine substitution.^{6b}

4.2 Soluble Polyacetylenes in Organic Electronics

Chapter 3 described the synthesis of polyacetylenes with side chains containing heteroatoms (B, N, P). As expected, these side chains not only provide solubility while maintaining extended π -conjugation, but also enabled tuning of optoelectronic properties through side group orbital interactions with the polymer backbone. The presence of heteroatoms also affected the NIR absorption band after doping films with I_2 , and in solution with $Na[COPh_2]$ or $[Fc]OTf$. Based on the interest in NIR-absorbing materials for photodetection,⁷ future research could involve the fabrication of such devices, especially using **pCOT-BMes₂** and **pCOT-SiMe₃**, which after doping show light absorption at around 1500 nm, a wavelength currently used in

telecommunications technology.^{7b} In fact, preliminary devices have been fabricated in collaboration with the McCreery group at the University of Alberta (Figure 4.1). However, the desired performances were not achieved so far due to challenges associated with air exposure and poor electrode contact deposition with the I₂-doped films.

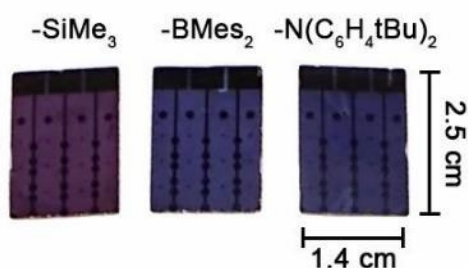


Figure 4.1. Photodetectors during fabrication with undoped films of functional polyacetylenes spin coated onto quartz substrates with contacts. Bottom contacts contained layers of, in order: Cr (3 nm), Au (30 nm) and carbon (10 nm); top contacts (not shown) contained, in order: carbon (10 nm) and Au (20 nm).

Additionally, oxidatively-doped polyacetylenes with $-NAr_2$ groups ($Ar = \text{aryl}$), such as **pCOT-N(C₆H₄^tBu)₂**, could also be explored in the context of spintronics.⁸ The nature of the polymerization method (ROMP) used to synthesize **pCOT-N(C₆H₄^tBu)₂** leads to side chains spaced always by an even number of carbons (8, 10, 12, *etc*), even when backbiting happens. Thus, radicals formed in the side chains (Ar_2N^+ , Figure 4.2) should not be able to recombine and should lead to a high-spin polymer, which could

show ferromagnetic properties. This concept has already been explored with densely-functionalized polyacetylenes containing $-NAr_2$ side groups (Figure 4.2, left),^{8a,b} similarly to **pCOT-N(C₆H₄^tBu)₂**. However, the previously reported polymers contain a high side chain density that leads to twisting of the olefinic backbone and limits ferromagnetic coupling between radicals in the same polymer chain, favoring through-space antiferromagnetic coupling. Conversely, the polymer **pCOT-N(C₆H₄^tBu)₂** would retain a planar backbone and likely be a better option for this application.

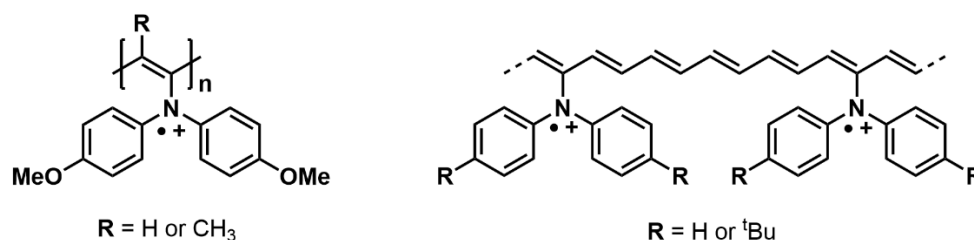
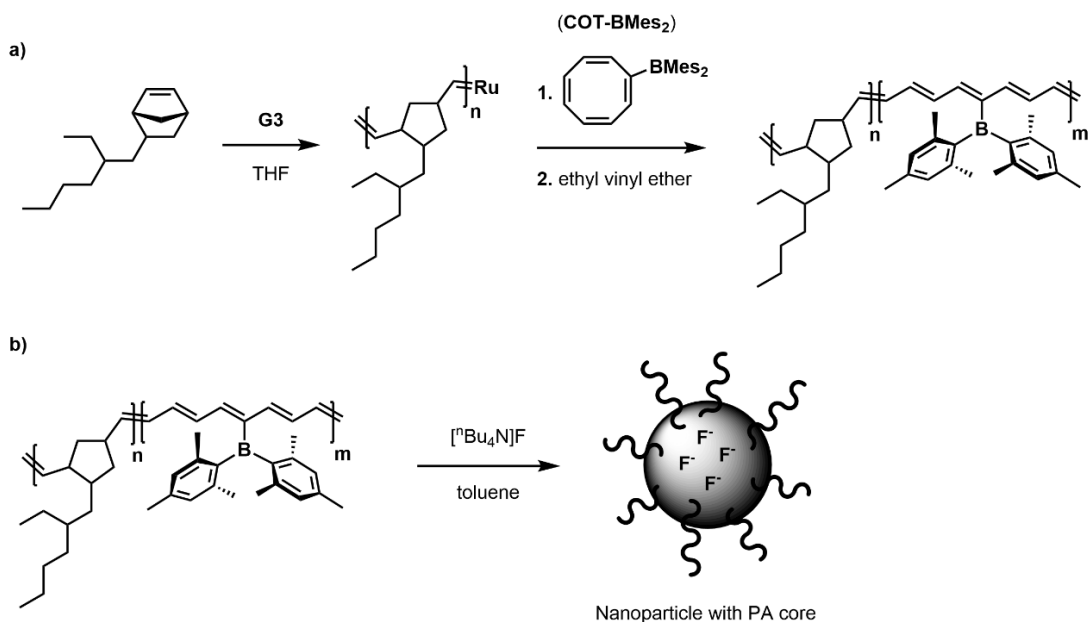


Figure 4.2. Nitrogen-appended polyacetylenes for spintronics. Left: polymers with high side chain density reported in the literature. Right: polyacetylenes synthesized through the ROMP of a substituted cyclooctatetraene.

4.3 Exploring Side Chain Functionality of Polyacetylenes

In Chapter 3, the reactivity of the polyacetylenes' side chains was briefly explored, but their functionality could be further explored in several different directions. For example, in Chapter 3, the available empty p-orbital on boron in **pCOT-BMes₂** was shown to bind fluoride through a reaction with $[^nBu_4N]F$. The resulting

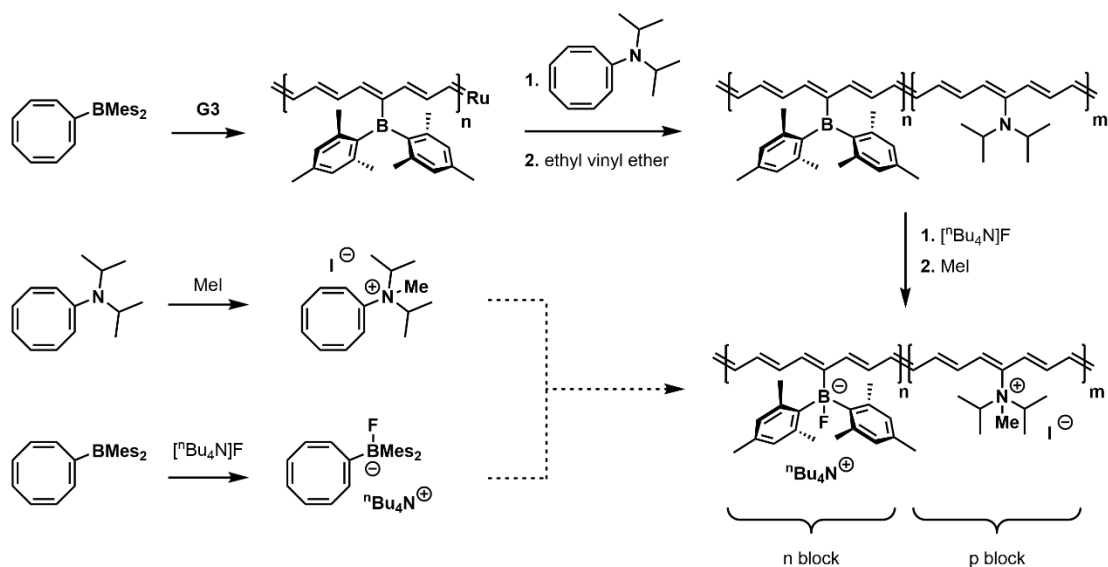
anionic polymer, **p[COT-BMes₂(F)]⁻**, retains a similar light absorption as **pCOT-BMes₂** (Figure 3.99, in Chapter 3), but shows different solubility (soluble in THF, but insoluble in toluene). This difference in solubility could be explored in block copolymers to form nanostructures, such as micelles, upon F⁻ binding (Scheme 4.3). By altering the initial ratio between each polymeric block, the supramolecular assembly could be tuned to yield formation of different PA-based nanostructures.⁹ Additionally, as seen for other polyacetylene block copolymers,^{9a} the norbornene shell could improve air stability of the polyacetylene core and would ensure high solubility, maintaining processability even after binding fluoride. Nanoparticles based on π -conjugated polymers have been explored in fields ranging from electronics to biomedical applications, including photothermal therapy based on NIR absorption (> 700 nm).¹⁰



Scheme 4.3. a) Possible synthesis of an insulating/semiconductor block copolymer with a -BMes_2 unit; b) Micelle formation upon F^- binding by the polyacetylene block.

Similarly, future research could aim at forming a block copolymer containing $\text{-BMes}_2(\text{F})^-$ and $\text{-NR}_2\text{Me}^+$ (where R = alkyl) groups (Scheme 4.4). Such a copolymer would mimic the structure of a device with a p-n junction,¹¹ where the anionic $\text{-BMes}_2(\text{F})^-$ would form the n-doped block and the cationic $\text{-NR}_2\text{Me}^+$ would form the p-doped block. There are already a few reported syntheses of alkylamine-substituted COTs,¹² but no reports of their polymerization. Due to the success in the polymerization of COT substituted with arylamines, polymerization of the alkyl analogues should proceed well, with the difference that the more available lone pair in the alkyl amines would allow for the facile formation of -NR_3^+ groups upon alkylation. Additionally, it could be interesting to study if the ionic monomers can be polymerized

to form ionic polymers without the need of post-polymerization reactions (Scheme 4.4, bottom), since post-polymerization modifications can suffer from incomplete conversion. Interestingly, preliminary calculations also indicate that for polyacetylene sections in between ionic $-\text{BMes}_2(\text{F})^-$ and $-\text{NR}_3^+$ groups, the π -system becomes completely delocalized, similarly to conductive polyacetylene, and all C–C bonds achieve the same length (Figure 4.3).



Scheme 4.4. Synthesis of ionic polyacetylene copolymers with B and N from the polymerization of neutral monomers followed by post-polymerization reactions (top) or directly from ionic monomers (bottom).

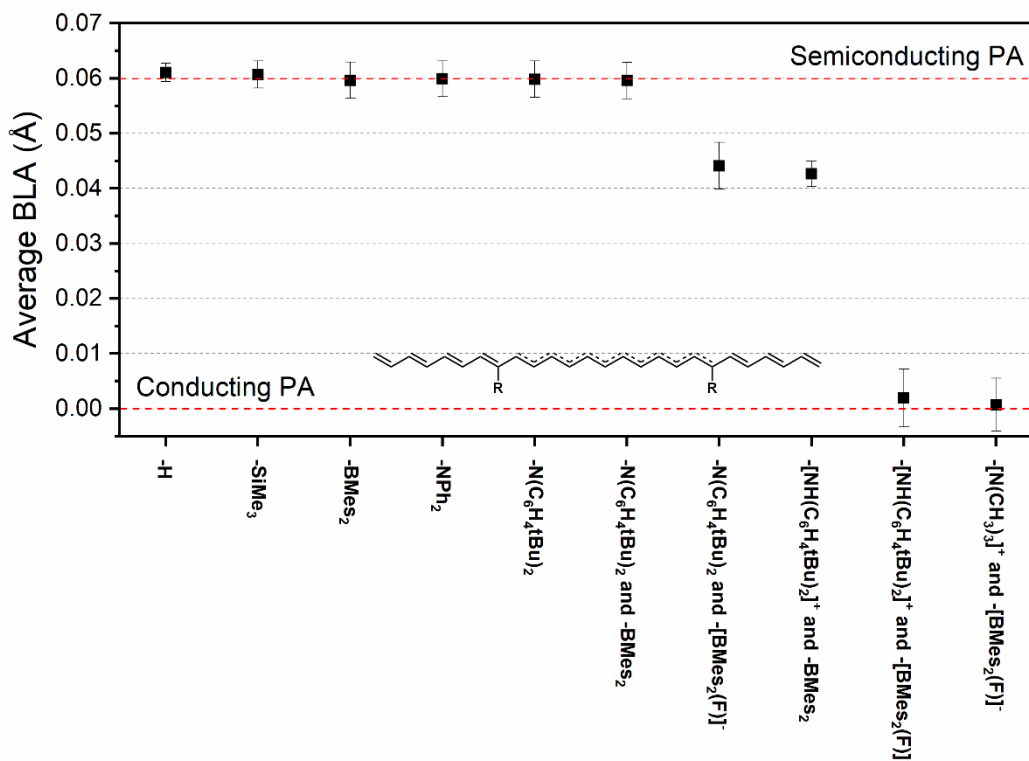
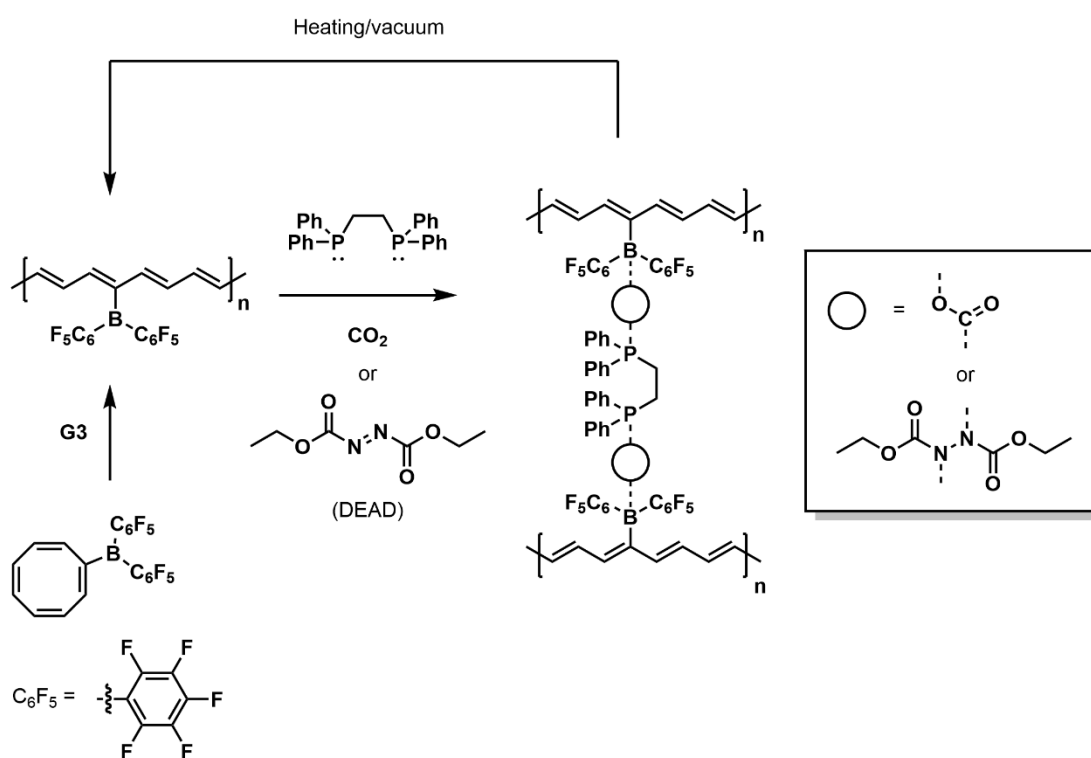


Figure 4.3. DFT computation of average bond length alternation (BLA, difference between the length of C–C and C=C bonds) in the polyacetylene fragment in between side chains. For a completely delocalized π -system, BLA = 0.

Finally, a B-containing polymer could be combined with phosphines to act as a frustrated Lewis pair (FLP) and promote the cooperative binding of CO₂ or of diethyl azodicarboxylate (DEAD).¹³ This reaction could lead to cross-linking and the formation of gels in the presence of a suitable diphosphine (Scheme 4.5). Due to the steric protection of the empty p-orbital on B imparted by the mesityl (Mes) groups, attempts of using **pCOT-BMe₂** for this purpose have failed so far. However, a

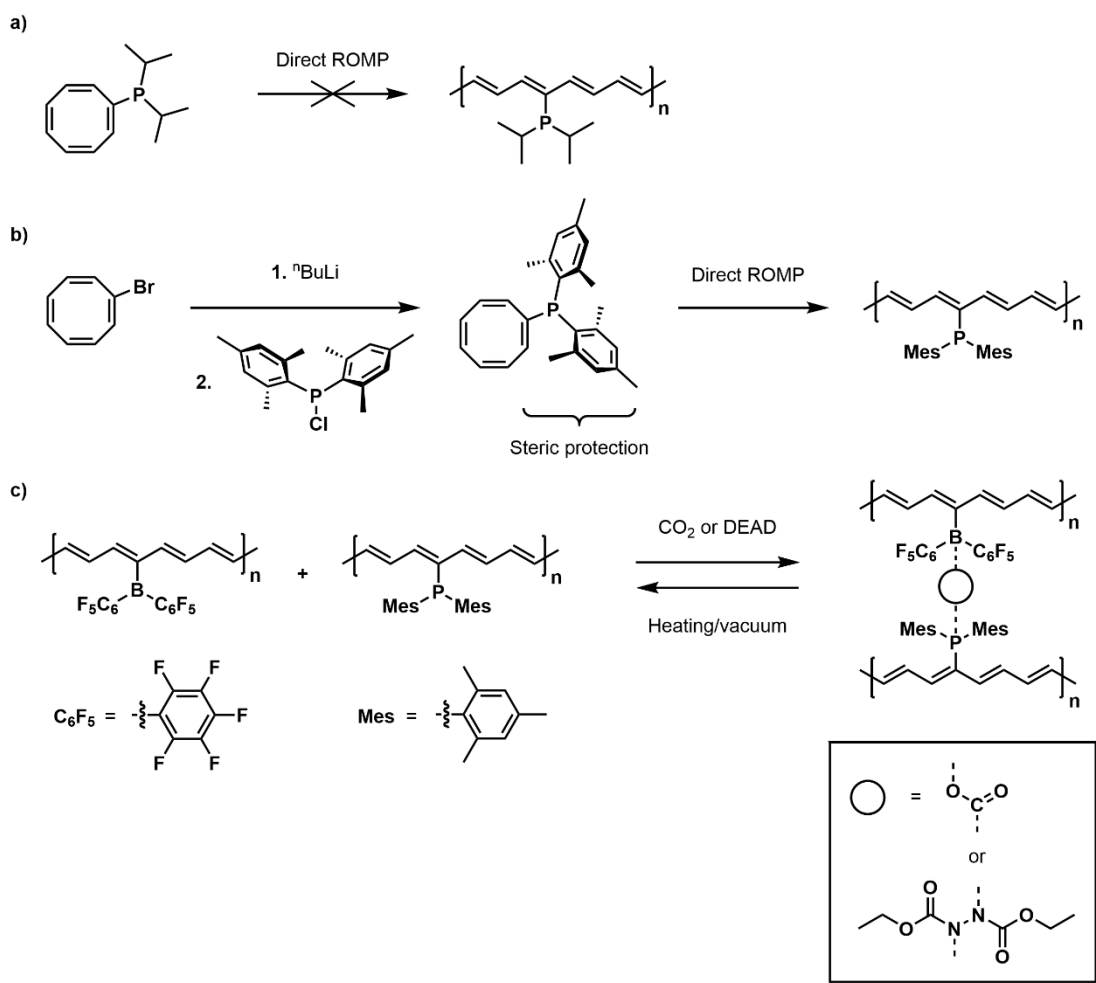
polymer with $-B(C_6F_5)_2$ groups (a classic type of Lewis acid used in FLPs)¹³ should be more electron-deficient and have an available empty p-orbital for the reaction with a diphosphine and CO_2 (or DEAD). Additionally, in the case of CO_2 , cross-linking could be reversed upon heating or application of vacuum to recover the soluble polymer, leading to a possible healable material.^{13a}



Scheme 4.5. Formation of a cross-linked polyacetylene *via* FLP interactions.

This FLP concept could also be extended to cross-link polymers containing B and P side groups, but a major challenge would be the synthesis of a phosphine-substituted polyacetylene. As described in Chapter 3, $COT-P^iPr_2$ cannot be directly

polymerized into **pCOT-PⁱPr₂** (Scheme 4.6a), likely due to the formation of strong P---Ru interactions with the catalyst. The polymer **pCOT-PⁱPr₂** could only be attained through reduction of its phosphine oxide analogue, **pCOT-P(O)ⁱPr₂**, and contained leftover -P(O)ⁱPr₂ groups. However, the use of bulky side groups on P, such as mesityl, could allow for the direct polymerization of the unoxidized COT-PR₂ monomer by minimizing coordination of the phosphine onto the Ru center in the catalyst (Scheme 4.6b). Additionally, molecules containing -PMes₂ and -B(C₆F₅)₂ units have been shown to form effective FLPs.^{13a} Thus, a similarly substituted set of polymers could later allow for the formation of a cross-linked network, as outlined in Scheme 4.6c.

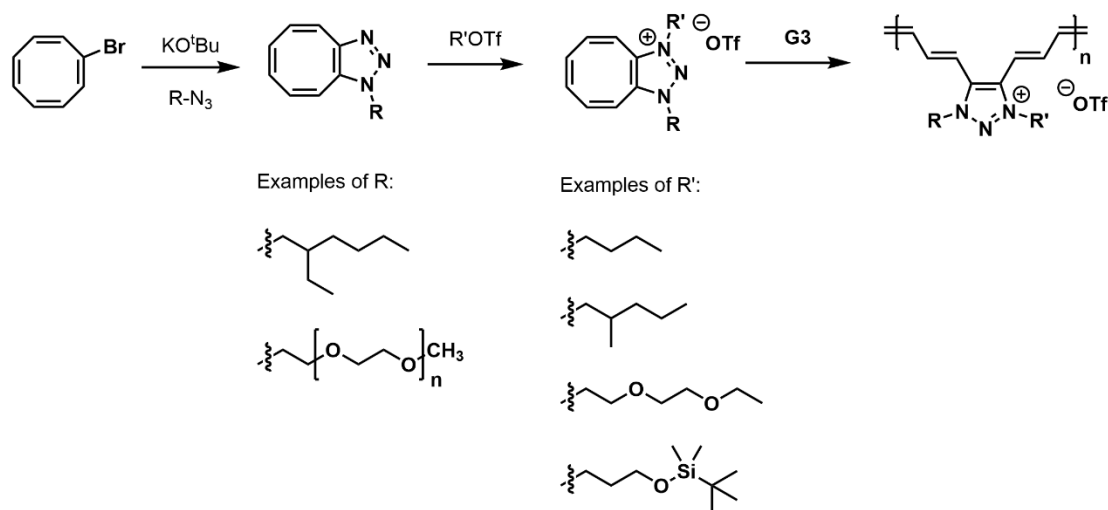


Scheme 4.6. a) Direct ROMP of **COT- P^iPr_2** , shown to not proceed in Chapter 3; b) Synthetic pathway to a **Mes₂P**-functionalized COT; c) Possible reversible cross-linking of polyacetylenes containing **-B(C₆F₅)₂** and **-P(Mes)₂** units *via* FLP interactions.

4.4 Synthesis of Soluble Triazolium Ring-Fused Polyacetylenes

Lastly, in Chapter 3 the polymerization of a triazolium ring-fused COT was also described, leading to a new class of polyacetylenes of possible interest for organic electronics and battery applications.¹⁴ Initial polymerization trials led to low yield of

insoluble polymers. However, based on the flexibility of the synthetic route developed, future research could involve preparing a monomer that would lead to increased polymer solubility by altering the substituents of the azides used (Scheme 4.7). Particularly, the use of oligoether substituents might lead to water-soluble polyacetylenes that retain a planar backbone and facilitate the fabrication of electronic devices, since layers of the water-soluble PA could be deposited on top or common water-insoluble materials.¹⁵ Additionally, the synthesis of soluble polymers would allow for further characterization and a better understanding of the polymerization of these fused COT monomers.



Scheme 4.7. Synthesis of new triazolium-fused polyacetylenes through the route developed in Chapter 3.

4.5 Concluding Remarks

Overall, the work described in this Thesis exemplifies how chemical design with the use of heteroatoms can lead to new processable polymers with interesting properties. As described in Chapter 1, the processability of polymers can facilitate device fabrication when compared to conventional inorganic semiconductors. Compared to most polymers used in modern organic electronics,¹⁶ the polymers described in this Thesis also have a simpler structure and require fewer synthetic steps, which could contribute to an eventual reduction in production costs and facilitate adoption in commercial devices.

However, challenges remain, as inorganic semiconductors can be produced in even fewer steps to afford very high purity, highly ordered materials that reliably give desired properties such as good conductivity and charge mobility. Conversely, the formation of ordered polymeric films can be much more challenging, since synthetic polymers can have different chain lengths (as indicated by the PDI) in addition to being able to bend, twist and form regions of different degrees of crystallinity. As show by the conductivity measurements of the soluble polyacetylenes in Section 3.2.6, different side chains can also influence the final properties of the films and might require optimization of film morphology to achieve the desired properties. Therefore, the field of π -conjugated polymers still offers room for future research until they are able to fully rival conventional inorganic semiconductors.

4.6 References

1. G. He, L. Kang, W. Torres Delgado, O. Shynkaruk, M. J. Ferguson, R. McDonald and E. Rivard, *J. Am. Chem. Soc.*, **2013**, *135*, 5360–5363.
2. C. Duan, F. Huang and Y. Cao, *J. Mater. Chem.*, **2012**, *22*, 10416–10434.
3. W. Torres Delgado, F. Shahin, M. J. Ferguson, R. McDonald, G. He and E. Rivard, *Organometallics*, **2016**, *35*, 2140–2148.
4. A. A. Jahnke, B. Djukic, T. M. McCormick, E. Buchaca Domingo, C. Hellmann, Y. Lee and D. S. Seferos, *J. Am. Chem. Soc.*, **2013**, *135*, 951–954.
5. (a) A. Kiriy, V. Senkovskyy and M. Sommer, *Macromol. Rapid Commun.*, **2011**, *32*, 1503–1517; (b) R. Tkachov, V. Senkovskyy, H. Komber and A. Kiriy, *Macromolecules*, **2011**, *44*, 2006–2015.
6. (a) S. Ye, M. Steube, E. I. Carrera and D. S. Seferos, *Macromolecules*, **2016**, *49*, 1704–1711; (b) S. Ye, S. M. Foster, A. A. Pollit, S. Cheng and D. S. Seferos, *Chem. Sci.*, **2019**, *10*, 2075–2080.
7. (a) Q. Li, Y. Guo and Yunqi Liu, *Chem. Mater.*, **2019**, *31*, 6359–6379; (b) M. Casalino, G. Coppola, R. M. De La Rue and D. F. Logan, *Laser Photonics Rev.*, **2016**, *10*, 895–921.
8. (a) H. Murata, D. Miyajima, R. Takada and H. Nishide, *Polym. J.*, **2005**, *37*, 818–825; (b) H. Murata, D. Miyajima and H. Nishide, *Macromolecules*, **2006**, *39*, 6331–6335; (c) P. Bujak, I. Kulszewicz-Bajer, M. Zagorska, V. Maurel, I. Wielgusa and A. Pron, *Chem. Soc. Rev.*, **2013**, *42*, 8895–8999.

9. (a) K.-Y. Yoon, I.-H. Lee, K. O. Kim, J. Jang, E. Lee and T.-L. Choi, *J. Am. Chem. Soc.*, **2012**, *134*, 14291–14294; (b) S. Shin, K.-Y. Yoon and T.-L. Choi, *Macromolecules*, **2015**, *48*, 1390–1397.
10. (a) L. Xiao, X. Chen, X. Yang, J. Sun and J. Geng, *ACS Appl. Polym. Mater.*, **2020**, *2*, 4273–4288; (b) L. R. MacFarlane, H. Shaikh, J. D. Garcia-Hernandez, M. Vespa, T. Fukui and I. Manners, *Nat. Rev. Mater.*, **2021**, *6*, 7–26
11. C. V. Hoven, H. Wang, M. Elbing, L. Garner, D. Winkelhaus and G. C. Bazan, *Nat. Mater.*, **2010**, *9*, 249–252.
12. C. A. Harmon and A. J. Streitwieser, *J. Org. Chem.*, **1972**, *38*, 549–551.
13. (a) D. W. Stephan and G. Erker, *Chem. Sci.*, **2014**, *5*, 2625–2641; (b) M. Wang, F. Nudelman, R. R. Matthes and M. P. Shaver, *J. Am. Chem. Soc.*, **2017**, *139*, 14232–14236.
14. (a) H. Jiang, P. Taranekar, J. R. Reynolds and K. S. Schanze, *Angew. Chem. Int. Ed.*, **2009**, *48*, 4300–4316; (b) M. M. Obadia and E. Drockenmuller, *Chem. Commun.*, **2016**, *52*, 2433–2450.
15. Y. Wen and J. Xu, *Polym. Sci. A Polym. Chem.*, **2017**, *55*, 1121–1150.
16. L. Dou, Y. Liu, Z. Hong, G. Li and Y. Yang, *Chem. Rev.*, **2015**, *115*, 12633–12665.

Complete Bibliography

Chapter 1:

1. S. C. Rasmussen, *ChemPlusChem*, **2020**, *85*, 1412–1429.
2. G. Li, W.-H. Chang and Y. Yang, *Nat. Rev. Mater.*, **2017**, *2*, 17043.
3. F. C. Krebs, *Sol. Energy Mater. Sol. Cells*, **2009**, *93*, 394–412.
4. R. R. Søndergaard, M. Hösel and F. C. Krebs, *J. Polym. Sci. Part B Polym. Phys.*, **2013**, *51*, 16–34.
5. K. Norrman, A. Ghanbari-Siahkali and N. B. Larsen, *Annu. Rep. Prog. Chem., Sect. C: Phys. Chem.*, **2005**, *101*, 174–201.
6. G. Li, R. Zhu and Y. Yang, *Nat. Photonics*, **2012**, *6*, 153–161.
7. N. Liang, W. Jiang, J. Hou and Z. Wang, *Mater. Chem. Front.*, **2017**, *1*, 1291–1303.
8. J. Hou, O. Inganäs, R. H. Friend and F. Gao, *Nat. Mater.*, **2018**, *17*, 119–128.
9. L. Zhu, M. Zhang, G. Zhou, T. Hao, J. Xu, J. Wang, C. Qiu, N. Prine, J. Ali, W. Feng, X. Gu, Z. Ma, Z. Tang, H. Zhu, L. Ying, Y. Zhang and F. Liu, *Adv. Energy Mater.*, **2020**, *10*, 1904234.
10. L. Meng, Y. Zhang, X. Wan, C. Li, X. Zhang, Y. Wang, X. Ke, Z. Xiao, L. Ding, R. Xia, H. L. Yip, Y. Cao and Y. Chen, *Science*, **2018**, *361*, 1094–1098.
11. Y. Zhu, Y. Zhang, B. Yao, Y. Wang, Z. Zhang, H. Zhan, B. Zhang, Z. Xie, Y. Wang and Y. Cheng, *Macromolecules*, **2016**, *49*, 4373–4377.
12. X. Zhao and X. Zhan, *Chem. Soc. Rev.*, **2011**, *40*, 3728–3743.

13. H. Sirringhaus, *Adv. Mater.*, **2014**, *26*, 1319–1335.
14. L. Dou, Y. Liu, Z. Hong, G. Li and Y. Yang, *Chem. Rev.*, **2015**, *115*, 12633–12665.
15. J. Qi, W. Qiao and Z. Y. Wang, *Chem. Rec.*, **2016**, *16*, 1531–1548.
16. M. Wang, P. Baek, A. Akbarinejad, D. Barker and J. Travas-Sejdic, *J. Mater. Chem. C*, **2019**, *7*, 5534–5552.
17. Z. Zhang, M. Liao, H. Lou, Y. Hu, X. Sun and H. Peng, *Adv. Mater.*, **2018**, *30*, 1704261.
18. D. T. McQuade, A. E. Pullen and T. M. Swager, *Chem. Rev.*, **2000**, *100*, 2537–2574.
19. T. H. Qazi, R. Rai and A. R. Boccaccini, *Biomaterials*, **2014**, *35*, 9068–9086.
20. T. Sen, S. Mishra and N. G. Shimpi, *RSC Adv.*, **2016**, *6*, 42196–42222.
21. H. N. M. E. Mahmud, A. K. O. Huq and R. B. Yahya, *RSC Adv.*, **2016**, *6*, 14778–14791.
22. R. Jain, N. Jadon and A. Pawaiya, *Trends Anal. Chem.*, **2017**, *97*, 363–373.
23. A. J. Heeger, *Angew. Chem. Int. Ed.*, **2001**, *40*, 2591–2611.
24. A. G. MacDiarmid, *Angew. Chem. Int. Ed.*, **2001**, *40*, 2581–2590.
25. H. Shirakawa, *Angew. Chem. Int. Ed.*, **2001**, *40*, 2574–2580.
26. H. Shirakawa and S. Ikeda, *Polym. J.*, **1971**, *2*, 231–244.
27. G. Perego, G. Lugli, U. Pedretti and M. Cesari, *Makromol. Chem.*, **1988**, *189*, 2657–2669.
28. C. Q. Wu, J. Miao, J.-Z. Yu and Y. Kawazoe, *Phys. Rev. B*, **1998**, *57*, 6–9.

29. K. Tanaka, K. Yoshizawa, K. Ohzeki and T. Yamabe, *Solid State Commun.*, **1983**, *45*, 391–393.
30. K. Tanaka, T. Koike, K. Yoshizawa, K. Ohzeki and T. Yamabe, *Solid State Commun.*, **1984**, *49*, 165–167.
31. G. Natta, F. Danusso and G. Moraglio, *Angew. Chem.*, **1957**, *69*, 686–687.
32. M. Hatano, S. Kambara and S. Okamoto, *J. Polym. Sci.*, **1961**, *51*, S26–S29.
33. S. Ikeda and A. Tamaki, *J. Polym. Sci. Part B*, **1966**, *4*, 605–607.
34. T. Ito, H. Shirakawa and S. Ikeda, *J. Polym. Sci. Polym. Chem. Ed.*, **1974**, *12*, 11–20.
35. H. Shirakawa, T. Ito and S. Ikeda, *Polym. J.*, **1973**, *4*, 460–462.
36. T. Ito, H. Shirakawa and S. Ikeda, *J. Polym. Sci. Polym. Chem. Ed.*, **1975**, *13*, 1943–1950.
37. H. Shirakawa, T. Ito and S. Ikeda, *Makromol. Chem.*, **1978**, *179*, 1565–1573.
38. R. Hoffmann, *Angew. Chem. Int. Ed. Engl.*, **1987**, *26*, 846–878.
39. P. G. Wilkinson and H. L. Johnston, *J. Chem. Phys.*, **1950**, *18*, 190–193.
40. N. Suzuki, M. Ozaki, S. Etemad, A. J. Heeger and A. G. MacDiarmid, *Phys. Rev. Lett.*, **1980**, *45*, 1209–1213.
41. R. E. Peierls, *Quantum Theory of Solids*, Oxford University Press, 1974, 108–112.
42. S. Roth and H. Bleier, *Adv. Phys.*, **1987**, *36*, 385–462.
43. C. S. Yannoni and T. C. Clarke, *Phys. Rev. Lett.*, **1983**, *51*, 1191–1193.
44. C. H. Choi, M. Kertesz and A. Karpfen, *J. Chem. Phys.*, **1997**, *107*, 6712–6721.

45. H. Shirakawa, E. J. Louis, A. G. MacDiarmid, C. K. Chiang and A. J. Heeger, *J. Chem. Soc., Chem. Commun.*, **1977**, 578–580.
46. C. K. Chiang, Y. W. Park, A. J. Heeger, H. Shirakawa, E. J. Louis and A. G. MacDiarmid, *J. Chem. Phys.*, **1978**, *69*, 5098–5104.
47. C. K. Chiang, M. A. Druy, S. C. Gau, A. J. Heeger, E. J. Louis, A. G. MacDiarmid, Y. W. Park and H. Shirakawa, *J. Am. Chem. Soc.*, **1978**, *100*, 1013–1015.
48. R. H. Baughman, N. S. Murthy and G. G. Miller, *J. Chem. Phys.*, **1983**, *79*, 515–520.
49. A. G. MacDiarmid and A. J. Heeger, *Synth. Met.*, **1979**, *1*, 101–118.
50. H. Shirakawa and S. Ikeda, *Synth. Met.*, **1979**, *1*, 175–184.
51. N. Basescu, Z. X. Liu, D. Moses, A. J. Heeger, H. Naarmann and N. Theophilou, *Nature*, **1987**, *327*, 403–405.
52. J. Tsukamoto, A. Takahashi and K. Kawasaki, *Jpn. J. Appl. Phys.*, **1990**, *29*, 125–130.
53. S. C. Rasmussen, *Mater. Today*, **2016**, *19*, 244–245.
54. S. Lefrant, L. S. Lichtmann and H. Temkin, *Solid State Commun.*, **1979**, *29*, 191–196.
55. G. Kaindl, G. Wortmann, S. Roth and K. Menke, *Solid State Commun.*, **1982**, *41*, 75–78.
56. B. François, N. Mermilliod and L. Zuppiroli, *Synth. Met.*, **1981**, *4*, 131–138.

57. J. C. W. Chien, F. E. Karasz and K. Shimamura, *Macromolecules*, **1982**, *15*, 1012–1017.
58. B. Francois, M. Bernard and J. J. Andre, *J. Chem. Phys.*, **1981**, *75*, 4142–4152.
59. C. D. Dimitrakopoulos and D. J. Mascaró, *IBM J. Res. Dev.*, **2001**, *45*, 11–27.
60. A. C. Jones and M. L. Hitchman, Overview of Chemical Vapour Deposition, in *Chemical Vapour Deposition: Precursors, Processes and Applications*, Royal Society of Chemistry, 2009.
61. P. Sundberg and M. Karppinen, *Beilstein J. Nanotechnol.*, **2014**, *5*, 1104–1136.
62. C. Müller, C. P. Radano, P. Smith and N. Stingelin-Stutzmann, *Polymer*, **2008**, *49*, 3973–3978.
63. Y. Zhao, X. Zhao, M. Roders, A. Gumyusenge, A. L. Ayzner and J. Mei, *Adv. Mater.*, **2017**, *29*, 1605056.
64. Y. Zhao, A. Gumyusenge, J. He, G. Qu, W. W. McNutt, Y. Long, H. Zhang, L. Huang, Y. Diao and J. Mei, *Adv. Funct. Mater.*, **2018**, *28*, 1705584.
65. J. M. Pochan, D. F. Pochan, H. Rommelmann and H. W. Gibson, *Macromolecules*, **1981**, *14*, 110–114.
66. D. J. Berets and D. S. Smith, *Trans. Faraday Soc.*, **1968**, *64*, 823–828.
67. T. Masuda, B. Z. Tang, T. Higashimura and H. Yamaoka, *Macromolecules*, **1985**, *18*, 2369–2373.
68. M. Aldissi, *Synth. Met.*, **1984**, *9*, 131–141.
69. R. Huq and G. C. Farrington, *J. Electrochem. Soc.*, **1984**, *131*, 819–823.

70. D. Yu, Y. Q. Yang, Z. Chen, Y. Tao and Y. F. Liu, *Opt. Commun.*, **2016**, *362*, 43–49.
71. J. Ahmad, K. Bazaka, L. J. Anderson, R. D. White and M. V. Jacob, *Renew. Sustain. Energy Rev.*, **2013**, *27*, 104–117.
72. J. W. Y. Lam and B. Z. Tang, *Acc. Chem. Res.*, **2005**, *38*, 745–754.
73. T. Masuda, *J. Polym. Sci. Part A Polym. Chem.*, **2007**, *45*, 165–180.
74. J. Z. Sun, A. Qin and B. Z. Tang, *Polym. Chem.*, **2013**, *4*, 211–223.
75. H. Murata, D. Miyajima, R. Tkada and H. Nishide, *Polym. J.*, **2005**, *37*, 818–825.
76. K. Akagi, *Chem. Rev.*, **2009**, *109*, 5354–5401.
77. H. Murata, D. Miyajima and H. Nishide, *Macromolecules*, **2006**, *39*, 6331–6335.
78. K. Shimomura, T. Ikai, S. Kanoh, E. Yashima and K. Maeda, *Nat. Chem.*, **2014**, *6*, 429–434.
79. S. Naumann, J. Unold, W. Frey and M. R. Buchmeiser, *Macromolecules*, **2011**, *44*, 8380–8387.
80. J. Kim, E.-H. Kang and T.-L. Choi, *ACS Macro Lett.*, **2012**, *1*, 1090–1093.
81. J.-A. Song and T.-L. Choi, *Macromolecules*, **2017**, *50*, 2724–2735.
82. K. Jung, K. Kim, J. C. Sung, T. S. Ahmed, S. H. Hong, R. H. Grubbs and T.-L. Choi, *Macromolecules*, **2018**, *51*, 4564–4571.
83. C. Kang, K. Jung, S. Ahn and T.-L. Choi, *J. Am. Chem. Soc.*, **2020**, *142*, 17140–17146.

84. G. I. Peterson, S. Yang and T.-L. Choi, *Acc. Chem. Res.*, **2019**, *52*, 994–1005.
85. Y. Korshak, V. Korshak, G. Kanischka and H. Höcker, *Makromol. Chem., Rapid Commun.*, **1985**, *6*, 685–692.
86. F. L. Klavetter and R. H. Grubbs, *J. Am. Chem. Soc.*, **1988**, *110*, 7807–7813.
87. K. H. Claus and C. Krüger, *Acta Cryst.*, **1988**, *44*, 1632–1634.
88. F. G. Klärner, *Angew. Chem. Int. Ed.*, **2001**, *40*, 3977–3981.
89. T. Nishinaga, T. Ohmae, K. Aita, M. Takase, M. Iyoda, T. Arai and Y. Kunugi, *Chem. Commun.*, **2013**, *49*, 5354–5356.
90. T. Hensel, D. Trpcevski, C. Lind, R. Grosjean, P. Hammershøj, C. B. Nielsen, T. Brock-Nannestad, B. E. Nielsen, M. Schau-Magnussen, B. Minaev, G. V. Baryshnikov and M. Pittelkow, *Chem.-Eur. J.*, **2013**, *19*, 17097–17102.
91. D. H. Lo and M. A. Whitehead, *J. Am. Chem. Soc.*, **1969**, *91*, 238–242.
92. A. R. Hlil, J. Balogh, S. Moncho, H. L. Su, R. Tuba, E. N. Brothers, M. Al-Hashimi and H. S. Bazzi, *J. Polym. Sci. Part A Polym. Chem.*, **2017**, *55*, 3137–3145.
93. P. v. R. Schleyer, J. E. Williams and K. R. Blanchard, *J. Am. Chem. Soc.*, **1970**, *92*, 2377–2386.
94. E. J. Ginsburg, C. B. Gorman, S. R. Marder and R. H. Grubbs, *J. Am. Chem. Soc.*, **1989**, *111*, 7621–7622.
95. T. Masuda and T. Higashimura, *Polyacetylenes with Substituents: Their Synthesis and Properties*, in *Advances in Polymer Science*, Vol. 81, Springer-Verlag Berlin GmbH, 2013, 122-165.

96. M. J. Sailor, E. J. Ginsburg, C. B. Gorman, A. Kumar, R. H. Grubbs and N. S. Lewis, *Science*, **1990**, *249*, 1146–1149.
97. C. B. Gorman, E. J. Ginsburg, S. R. Marder and R. H. Grubbs, *Angew. Chem. Adv. Mater.*, **1989**, *101*, 1603–1606.
98. C. B. Gorman, E. J. Ginsburg and R. H. Grubbs, *J. Am. Chem. Soc.*, **1993**, *115*, 1397–1409.
99. J. T. Miller, C. W. DeKock and M. A. Brault, *J. Org. Chem.*, **1979**, *44*, 3508–3510.
100. A. Y. Sokolov, D. B. Magers, J. I. Wu, W. D. Allen, P. v. R. Schleyer and H. F. Schaefer, *J. Chem. Theory Comput.*, **2013**, *9*, 4436–4443.
101. T. H. Jozefiak, E. J. Ginsburg, C. B. Gorman, R. H. Grubbs and N. S. Lewis, *J. Am. Chem. Soc.*, **1993**, *115*, 4705–4713.
102. J. S. Moore, C. B. Gorman and R. H. Grubbs, *J. Am. Chem. Soc.*, **1991**, *113*, 1704–1712.
103. M. J. Eis, J. E. Wrobel and B. Ganem, *J. Am. Chem. Soc.*, **1984**, *106*, 3693–3694.
104. T. M. Trnka and R. H. Grubbs, *Acc. Chem. Res.*, **2001**, *34*, 18–29.
105. F. Ciardelli, S. Lanzillo and O. Pieroni, *Macromolecules*, **1974**, *7*, 174–179.
106. B. L. Langsdorf, X. Zhou, D. H. Adler and M. C. Lonergan, *Macromolecules*, **1999**, *32*, 2796–2798.
107. B. L. Langsdorf, X. Zhou and M. C. Lonergan, *Macromolecules*, **2001**, *34*, 2450–2458.

108. M. C. Lonergan, C. H. Cheng, B. L. Langsdorf and X. Zhou, *J. Am. Chem. Soc.*, **2002**, *124*, 690–701.
109. A. C. Cope and D. F. Rugen, *J. Am. Chem. Soc.*, **1953**, *75*, 3215–3219.
110. L. A. Paquette and K. A. Henzel, *J. Am. Chem. Soc.*, **1975**, *97*, 4649–4658.
111. D. N. Bhattacharyya, C. L. Lee, J. Smid and M. Szwarc, *J. Phys. Chem.*, **1965**, *69*, 612–623.
112. C. W. Bielawski and R. H. Grubbs, *Prog. Polym. Sci.*, **2007**, *32*, 1–29.
113. O. A. Scherman, I. M. Rutenberg and R. H. Grubbs, *J. Am. Chem. Soc.*, **2003**, *125*, 8515–8522.
114. O. A. Scherman and R. H. Grubbs, *Synth. Met.*, **2001**, *124*, 431–434.
115. K.-Y. Yoon, I.-H. Lee, K. O. Kim, J. Jang, E. Lee and T.-L. Choi, *J. Am. Chem. Soc.*, **2012**, *134*, 14291–14294.
116. S. Shin, K.-Y. Yoon and T.-L. Choi, *Macromolecules*, **2015**, *48*, 1390–1397.
117. L. R. Gilliom and R. H. Grubbs, *J. Am. Chem. Soc.*, **1986**, *108*, 733–742.
118. K.-Y. Yoon, S. Shin, Y.-J. Kim, I. Kim, E. Lee and T.-L. Choi, *Macromol. Rapid Commun.*, **2015**, *36*, 1069–1074.
119. J. H. Edwards and W. J. Feast, *Polymer*, **1980**, *21*, 595–596.
120. K. Knoll and R. R. Schrock, *J. Am. Chem. Soc.*, **1989**, *111*, 7989–8004.
121. P. Dounis, W. J. Feast and G. Widawski, *J. Mol. Catal. A*, **1997**, *115*, 51–60.
122. J. H. Burroughes, C. A. Jones and R. H. Friend, *Nature*, **1988**, *335*, 137–141.
123. J. H. Burroughes, R. H. Friend and P. C. Allen, *J. Phys. D Appl. Phys.*, **1989**, *22*, 956–958.

124. T. M. Swager, D. A. Dougherty and R. H. Grubbs, *J. Am. Chem. Soc.*, **1988**, *110*, 2973–2974.
125. T. M. Swager and R. H. Grubbs, *Synth. Met.*, **1989**, *28*, D57–D62.
126. L. M. Leung and K. H. Tan, *Macromolecules*, **1993**, *26*, 4426–4436.
127. L. M. Leung and K. H. Tan, *Polymer*, **1994**, *35*, 1556–1560.
128. C. Wu, A. Niu, L. M. Leung and T. S. Lam, *J. Am. Chem. Soc.*, **1999**, *121*, 1954–1955.
129. J. I. Brauman and W. C. Archie Jr., *Tetrahedron*, **1971**, *27*, 1275–1280.
130. W. R. Dolbier Jr. and H. Koroniak, *J. Am. Chem. Soc.*, **1984**, *106*, 1871–1872.
131. S. F. Martin, M. S. Dappen, B. Dupre and C. J. Murphy, *J. Org. Chem.*, **1987**, *52*, 3708–3710.
132. M. Murakami, Y. Miyamoto and Y. Ito, *Angew. Chem. Int. Ed.*, **2001**, *40*, 189–190.
133. Q. Z. Yang, Z. Huang, T. J. Kucharski, D. Khvostichenko, J. Chen and R. Boulatov, *Nat. Nanotechnol.*, **2009**, *4*, 302–306.
134. M. T. Ong, J. Leiding, H. Tao, A. M. Virshup and T. J. Martínez, *J. Am. Chem. Soc.*, **2009**, *131*, 6377–6379.
135. Z. Chen, J. A. M. Mercer, X. Zhu, J. A. H. Romaniuk, R. Pfattner, L. Cegelski, T. J. Martinez, N. Z. Burns and Y. Xia, *Science*, **2017**, *357*, 475–479.
136. Z. Chen, X. Zhu, J. Yang, J. A. M. Mercer, N. Z. Burns, T. J. Martinez and Y. Xia, *Nat. Chem.*, **2020**, *12*, 302–309.
137. F. B. Schügerl and H. Kuzmany, *J. Chem. Phys.*, **1981**, *74*, 953–958.

138. J. K. Su, J. D. Feist, J. Yang, J. A. M. Mercer, J. A. H. Romaniuk, Z. Chen, L. Cegelski, N. Z. Burns and Y. Xia, *J. Am. Chem. Soc.*, **2018**, *140*, 12388–12391.
139. B. R. Boswell, C. M. F. Mansson, J. M. Cox, Z. Jin, J. A. H. Romaniuk, K. P. Lindquist, L. Cegelski, Y. Xia, S. A. Lopez and N. Z. Burns, *Nat. Chem.*, **2021**, *13*, 41–46.
140. T. Yamabe, K. Tanaka, H. Terema-E, K. Fukui, H. Shirakawa and S. Ikeda, *Synth. Met.*, **1979**, *1*, 321–327.
141. M. Springborg, *J. Am. Chem. Soc.*, **1999**, *121*, 11211–11216.
142. L. M. Abreu, T. L. Fonseca and M. A. Castro, *J. Chem. Phys.*, **2012**, *136*, 234311.
143. J. Seo, S. Y. Lee and C. W. Bielawski, *Macromolecules*, **2019**, *52*, 2923–2931.
144. E. E. van Tamelen and D. Carty, *J. Am. Chem. Soc.*, **1971**, *93*, 6102–6110.
145. J. Seo, S. Y. Lee and C. W. Bielawski, *Polym. Chem.*, **2019**, *10*, 6401–6412.
146. H. Nakako, Y. Mayahara, R. Nomura, M. Tabata and T. Masuda, *Macromolecules*, **2000**, *33*, 3978–3982.
147. G. Tourillon and F. Garnier, *J. Electrochem. Soc.*, **1983**, *130*, 2042–2044.
148. Y. Cao, P. Wang and R. Qian, *Makromol. Chem.*, **1985**, *186*, 1093–1100.
149. N. C. Billingham, P. D. Calvert, P. J. S. Foot and F. Mohammad, *Polym. Degrad. Stab.*, **1987**, *19*, 323–341.
150. F. Mohammad, P. D. Calvert and N. C. Billingham, *Bull. Mater. Sci.*, **1995**, *18*, 255–261.

151. C. E. Housecroft and A. G. Sharpe, *Inorganic Chemistry*, 4th Ed., Pearson, 2012, 546–590.
152. A. Bondi, *J. Phys. Chem.*, **1964**, 68, 441–451.
153. *CRC Handbook of Chemistry and Physics*, 97th Ed., CRC Press, 2017, 10–190.
154. W. C. Martin, *J. Res. Natl. Bur. Stand., Sect. A*, **1971**, 75A, 109–111.
155. E. Hückel, *Z. Phys.*, **1931**, 70, 204–286.
156. C. W. Bird, *Tetrahedron*, **1985**, 41, 1409–1414.
157. C. W. Bird, *Tetrahedron*, **1992**, 48, 335–340.
158. J. E. McDonough, A. Mendiratta, J. J. Curley, G. C. Fortman, S. Fantasia, C. C. Cummins, E. V Rybak-Akimova, S. P. Nolan and C. D. Hoff, *Inorg. Chem.*, **2008**, 47, 2133–2141.
159. U. Salzner, J. B. Lagowski, P. G. Pickup and R. A. Poirier, *Synth. Met.*, **1998**, 96, 177–189.
160. M. Heeney, W. Zhang, D. J. Crouch, M. L. Chabynyc, S. Gordeyev, R. Hamilton, S. J. Higgins, I. McCulloch, P. J. Skabara, D. Sparrowe and S. Tierney, *Chem. Commun.*, **2007**, 5061–5063.
161. A. A. Jahnke, B. Djukic, T. M. McCormick, E. Buchaca Domingo, C. Hellmann, Y. Lee and D. S. Seferos, *J. Am. Chem. Soc.*, **2013**, 135, 951–954.
162. G. He, L. Kang, W. Torres Delgado, O. Shynkaruk, M. J. Ferguson, R. McDonald and E. Rivard, *J. Am. Chem. Soc.*, **2013**, 135, 5360–5363.
163. B. T. Luppi, R. McDonald, M. J. Ferguson, L. Sang and E. Rivard, *Chem. Commun.*, **2019**, 55, 14218–14221.

164. A. Patra and M. Bendikov, *J. Mater. Chem.*, **2010**, *20*, 422–433.
165. S. Ye, L. Janasz, W. Zajaczkowski, J. G. Manion, A. Mondal, T. Marszalek, D. Andrienko, K. Müllen, W. Pisula and D. S. Seferos, *Macromol. Rapid Commun.*, **2018**, *40*, 1800596.
166. D. Venkateshvaran, M. Nikolka, A. Sadhanala, V. Lemaure, M. Zelazny, M. Kepa, M. Hurhangee, A. J. Kronemeijer, V. Pecunia, I. Nasrallah, I. Romanov, K. Broch, I. McCulloch, D. Emin, Y. Olivier, J. Cornil, D. Beljonne and H. Sirringhaus, *Nature*, **2014**, *515*, 384–388.
167. B. T. Luppi, D. Majak, M. Gupta, E. Rivard and K. Shankar, *J. Mater. Chem. A*, **2019**, *7*, 2445–2463.
168. M. Samiullah, D. Moghe, U. Scherf and S. Guha, *Phys. Rev. B*, **2010**, *82*, 205211.
169. K. T. Mahmudov, M. N. Kopylovich, M. F. C. Guedes da Silva and A. J. L. Pombeiro, *Dalton Trans.*, **2017**, *46*, 10121–10138.
170. D. J. Pascoe, K. B. Ling and S. L. Cockroft, *J. Am. Chem. Soc.*, **2017**, *139*, 15160–15167.
171. A. Bauzá and A. Frontera, *Angew. Chem. Int. Ed.*, **2015**, *54*, 7340–7343.
172. A. F. Cozzolino, P. J. W. Elder and I. Vargas-Baca, *Coord. Chem. Rev.*, **2011**, *255*, 1426–1438.
173. T. Chivers and R. S. Laitinen, *Chem. Soc. Rev.*, **2015**, *44*, 1725–1739.

174. G. He, W. Torres Delgado, D. J. Schatz, C. Merten, A. Mohammadpour, L. Mayr, M. J. Ferguson, R. McDonald, A. Brown, K. Shankar and E. Rivard, *Angew. Chem. Int. Ed.*, **2014**, *53*, 4587–4591.
175. E. Rivard, *Chem. Lett.*, **2015**, *44*, 730–736.
176. W. Torres Delgado, C. A. Braun, M. P. Boone, O. Shynkaruk, Y. Qi, R. McDonald, M. J. Ferguson, P. Data, S. K. C. Almeida, I. De Aguiar, G. L. C. De Souza, A. Brown, G. He and E. Rivard, *ACS Appl. Mater. Interfaces*, **2018**, *10*, 12124–12134.
177. C. A. Braun, E. Rivard, N. Martinek, Y. Zhou and M. J. Ferguson, *Dalton Trans.*, **2019**, *48*, 10210–10219.
178. C. A. Braun, M. J. Ferguson and E. Rivard, *Inorg. Chem.*, **2021**, *60*, 2672–2679.
179. B. A. Gregg, *MRS Bull.*, **2005**, *30*, 20–22.
180. D. R. Kozub, K. Vakhshouri, S. V. Kesava, C. Wang, A. Hexemer and E. D. Gomez, *Chem. Commun.*, **2012**, *48*, 5859–5861.
181. S. R. Yost, E. Hontz, S. Yeganeh and T. Van Voorhis, *J. Phys. Chem. C*, **2012**, *116*, 17369–17377.
182. A. Köhler and H. Bässler, *Mater. Sci. Eng. R Rep.*, **2009**, *66*, 71–109.
183. R. D. Pensack, Y. Song, T. M. McCormick, A. A. Jahnke, J. Hollinger, D. S. Seferos and G. D. Scholes, *J. Phys. Chem. B*, **2014**, *118*, 2589–2597.
184. J. G. Manion, S. Ye, A. H. Proppe, A. W. Laramée, G. R. McKeown, E. L. Kynaston, S. O. Kelley, E. H. Sargent and D. S. Seferos, *ACS Appl. Energy Mater.*, **2018**, *1*, 5033–5042.

185. F. Zheng, Y. Komatsuzaki, N. Shida, H. Nishiyama, S. Inagi and I. Tomita, *Macromol. Rapid Commun.*, **2019**, *40*, 1900171.
186. A. J. Musser, M. Al-Hashimi, M. Heeney and J. Clark, *J. Chem. Phys.*, **2019**, *151*, 044902.
187. K. Wen, L. Wu, X. Wu, Y. Lu, T. Duan, H. Ma, A. Peng, Q. Shi and H. Huang, *Angew. Chem. Int. Ed.*, **2020**, *59*, 12756–12761.
188. S. A. Gregory, A. K. Menon, S. Ye, D. S. Seferos, J. R. Reynolds and S. K. Yee, *Adv. Energy Mater.*, **2018**, *8*, 1802419.
189. J. R. Panchuk, A. W. Laramée, J. G. Manion, S. Ye and D. S. Seferos, *Synth. Met.*, **2019**, *253*, 57–61.
190. M. P. Gordon, S. A. Gregory, J. P. Wooding, S. Ye, G. M. Su, D. S. Seferos, M. D. Losego, J. J. Urban, S. K. Yee and A. K. Menon, *Appl. Phys. Lett.*, **2021**, *118*, 233301.
191. W. Mack, *Angew. Chem. Int. Ed. Engl.*, **1966**, *5*, 896.
192. D. P. Sweat and C. E. Stephens, *J. Organomet. Chem.*, **2008**, *693*, 2463–2464.
193. R. Sugimoto, K. Yoshino, S. Inoue and K. Tsukagoshi, *Jpn. J. Appl. Phys.*, **1985**, *24*, L425–L427.
194. S. Inoue, T. Jigami, H. Nozoe, T. Otsubo and F. Ogura, *Tetrahedron Lett.*, **1994**, *35*, 8009–8012.
195. T. Otsubo, S. Inoue, H. Nozoe, T. Jigami and F. Ogura, *Synth. Met.*, **1995**, *69*, 537–538.

196. A. Patra, Y. H. Wijsboom, G. Leitus and M. Bendikov, *Org. Lett.*, **2009**, *11*, 1487–1490.
197. S. C. Ng, H. Ding and H. S. O. Chan, *Chem. Lett.*, **1999**, *28*, 1325–1326.
198. M. Lapkowski, R. Motyka, J. Suwiński and P. Data, *Macromol. Chem. Phys.*, **2012**, *213*, 29–35.
199. H. Saito, S. Ukai, S. Iwatsuki, T. Itoh and M. Kubo, *Macromolecules*, **1995**, *28*, 8363–8367.
200. A. A. Jahnke, G. W. Howe and D. S. Seferos, *Angew. Chem. Int. Ed.*, **2010**, *49*, 10140–10144.
201. T. M. McCormick, A. A. Jahnke, A. J. Lough and D. S. Seferos, *J. Am. Chem. Soc.*, **2012**, *134*, 3542–3548.
202. E. I. Carrera and D. S. Seferos, *Dalton Trans.*, **2015**, *44*, 2092–2096.
203. E. I. Carrera, A. E. Lanterna, A. J. Lough, J. C. Scaiano and D. S. Seferos, *J. Am. Chem. Soc.*, **2016**, *138*, 2678–2689.
204. W.-H. Lee, S. K. Lee, W. S. Shin, S.-J. Moon and I.-N. Kang, *J. Polym. Sci., Part A Polym. Chem.*, **2013**, *51*, 2753–2758.
205. X. M. Jiang, R. Österbacka, O. Korovyanko, C. P. An, B. Horovitz, R. A. J. Janssen and Z. V. Vardeny, *Adv. Funct. Mater.*, **2002**, *12*, 587–597.
206. J. L. Dutton, G. J. Farrar, M. J. Sgro, T. L. Battista and P. J. Ragona, *Chem.-Eur. J.*, **2009**, *15*, 10263–10271.

207. D. M. González, K. N. Raftopoulos, G. He, C. M. Papadakis, A. Brown, E. Rivard and P. Müller-Buschbaum, *Macromol. Rapid Commun.*, **2017**, *38*, 1700065.
208. Y. S. Park, Q. Wu, C.-Y. Nam and R. B. Grubbs, *Angew. Chem. Int. Ed.*, **2014**, *53*, 10691–10695.
209. M. Planells, B. C. Schroeder and I. McCulloch, *Macromolecules*, **2014**, *47*, 5889–5894.
210. E. H. Jung, S. Bae, T. W. Yoo and W. H. Jo, *Polym. Chem.*, **2014**, *5*, 6545–6550.
211. R. S. Ashraf, I. Meager, M. Nikolka, M. Kirkus, M. Planells, B. C. Schroeder, S. Holliday, M. Hurhangee, C. B. Nielsen, H. Sirringhaus and I. McCulloch, *J. Am. Chem. Soc.*, **2015**, *137*, 1314–1321.
212. M. Kaur, D. H. Lee, D. S. Yang, H. A. Um, M. J. Cho, J. S. Kang and D. H. Choi, *Dyes Pigm.*, **2015**, *123*, 317–322.
213. L. Lv, X. Wang, X. Wang, L. Yang, T. Dong, Z. Yang and H. Huang, *ACS Appl. Mater. Interfaces*, **2016**, *8*, 34620–34629.
214. K. Zhang, L. Lv, X. Wang, Y. Mi, R. Chai, X. Liu, G. Shen, A. Peng and H. Huang, *ACS Appl. Mater. Interfaces*, **2018**, *10*, 1917–1924.
215. M. Al-Hashimi, Y. Han, J. Smith, H. S. Bazzi, S. Y. A. Alqaradawi, S. E. Watkins, T. D. Anthopoulos and M. Heeney, *Chem. Sci.*, **2016**, *7*, 1093–1099.
216. K. Wen, X. Xu, J. Chen, L. Lv, L. Wu, Y. Hu, X. Wu, G. Liu, A. Peng and H. Huang, *ACS Appl. Mater. Interfaces*, **2019**, *11*, 17884–17893.

217. B. M. Trost, *Science*, **1991**, *254*, 1471–1477.
218. R. D. McCullough, S. P. Williams, S. Tristram-Nagle, M. Jayaraman, P. C. Ewbank and L. Miller, *Synth. Met.*, **1995**, *69*, 279–282.
219. Z. Bao, A. Dodabalapur and A. J. Lovinger, *Appl. Phys. Lett.*, **1996**, *69*, 4108–4110.
220. H. Sirringhaus, P. J. Brown, R. H. Friend, M. M. Nielsen, K. Bechgaard, B. M. W. Langeveld-Voss, A. J. H. Spiering, R. A. J. Janssen, E. W. Meijer, P. Herwig and D. M. de Leeuw, *Phys. Rev. B*, **2000**, *62*, 685–688.
221. R. S. Loewe, P. C. Ewbank, J. Liu, L. Zhai and R. D. McCullough, *Macromolecules*, **2001**, *34*, 4324–4333.
222. R. Tkachov, V. Senkovskyy, H. Komber and A. Kiriy, *Macromolecules*, **2011**, *44*, 2006–2015.
223. A. Kiriy, V. Senkovskyy and M. Sommer, *Macromol. Rapid Commun.*, **2011**, *32*, 1503–1517.
224. Z. J. Bryan and A. J. McNeil, *Macromolecules*, **2013**, *46*, 8395–8405.
225. S. Ye, M. Steube, E. I. Carrera and D. S. Seferos, *Macromolecules*, **2016**, *49*, 1704–1711.
226. S. Ye, S. M. Foster, A. A. Pollit, S. Cheng and D. S. Seferos, *Chem. Sci.*, **2019**, *10*, 2075–2080.
227. R. L.-Y. Bao, R. Zhao and L. Shi, *Chem. Commun.*, **2015**, *51*, 6884–6900.
228. E. L. Lanni and A. J. McNeil, *J. Am. Chem. Soc.*, **2009**, *131*, 16573–16579.
229. E. L. Lanni and A. J. McNeil, *Macromolecules*, **2010**, *43*, 8039–8044.

230. A. K. Mahrok, E. I. Carrera, A. J. Tilley, S. Ye and D. S. Seferos, *Chem. Commun.*, **2015**, *51*, 5475–5478.
231. U. Belluco, R. Bertani, R. A. Michelin and M. Mozzon, *J. Organomet. Chem.*, **2000**, *600*, 37–55.
232. F. Guo, Y. G. Kim, J. R. Reynolds and K. S. Schanze, *Chem. Commun.*, **2006**, 1887–1889.
233. H. Nishiyama, F. Zheng, S. Inagi, H. Fueno, K. Tanaka and I. Tomita, *Polym. Chem.*, **2020**, *11*, 4693–4698.
234. T. Hamada, D. Suzuki, H. Urabe and F. Sato, *J. Am. Chem. Soc.*, **1999**, *121*, 7342–7344.
235. H. Nishiyama, T. Kino and I. Tomita, *Macromol. Rapid Commun.*, **2012**, *33*, 545–549.
236. S. Rühle, *Sol. Energy*, **2016**, *130*, 139–147.
237. S. Rafique, S. M. Abdullah, K. Sulaiman and M. Iwamoto, *Renew. Sustain. Energy Rev.*, **2018**, *84*, 43–53.
238. J. C. Bijleveld, A. P. Zoombelt, S. G. J. Mathijssen, M. M. Wienk, M. Turbiez, D. M. de Leeuw and R. A. J. Janssen, *J. Am. Chem. Soc.*, **2009**, *131*, 16616–16617.
239. M. B. Smith and J. Michl, *Chem. Rev.*, **2010**, *110*, 6891–6936.
240. M. J. Y. Tayebjee, S. N. Sanders, E. Kumarasamy, L. M. Campos, M. Y. Sfeir and D. R. McCamey, *Nat. Phys.*, **2017**, *13*, 182–189.

241. B. S. Basel, J. Zirzmeier, C. Hetzer, B. T. Phelan, M. D. Krzyaniak, S. R. Reddy, P. B. Coto, N. E. Horwitz, R. M. Young, F. J. White, F. Hampel, T. Clark, M. Thoss, R. R. Tykwinski, M. R. Wasielewski and D. M. Guldi, *Nat. Commun.*, **2017**, *8*, 1–8.
242. M. Kaur, D. S. Yang, J. Shin, T. W. Lee, K. Choi, M. J. Cho and D. H. Choi, *Chem. Commun.*, **2013**, *49*, 5495–5497.
243. I. Osaka and K. Takimiya, *Polymer*, **2015**, *59*, A1–A15.
244. A. A. Jahnke, L. Yu, N. Coombs, A. D. Scaccabarozzi, A. J. Tilley, P. M. Dicarmine, A. Amassian, N. Stingelin and D. S. Seferos, *J. Mater. Chem. C*, **2015**, *3*, 3767–3773.
245. J. Miao, F. Zhang, Y. Lin, W. Wang, M. Gao, L. Li, J. Zhang and X. Zhan, *Adv. Opt. Mater.*, **2016**, *4*, 1711–1717.
246. Y. Jin, J. Wang, B. Sun, J. C. Blakesley and N. C. Greenham, *Nano Lett.*, **2008**, *8*, 1649–1653.

Chapter 2:

1. E. I. Carrera and D. S. Seferos, *Macromolecules*, **2015**, *48*, 297–308.
2. (a) S. M. Parke, M. P. Boone and E. Rivard, *Chem. Commun.*, **2016**, *52*, 9485–9505, and references therein; (b) G. C. Hoover and D. S. Seferos, *Chem. Sci.*, **2019**, *10*, 9182–9188.
3. (a) A. A. Jahnke, B. Djukic, T. M. McCormick, E. Buchaca Domingo, C. Hellmann, Y. Lee and D. S. Seferos, *J. Am. Chem. Soc.*, **2013**, *135*, 951–954; (b) G. He, L. Kang, W. Torres Delgado, O. Shynkaruk, M. J. Ferguson, R.

- McDonald and E. Rivard, *J. Am. Chem. Soc.*, **2013**, *135*, 5360–5363; (c) L. Lv, X. Wang, X. Wang, L. Yang, T. Dong, Z. Yang and H. Huang, *ACS Appl. Mater. Interfaces*, **2016**, *8*, 34620–34629; (d) M. Al-Hashimi, Y. Han, J. Smith, H. S. Bazzi, S. Y. A. Alqaradawi, S. E. Watkins, T. D. Anthopoulos and M. Heeney, *Chem. Sci.*, **2016**, *7*, 1093–1099.
4. (a) S. Ye, L. Janasz, W. Zajaczkowski, J. G. Manion, A. Mondal, T. Marszalek, D. Andrienko, K. Mülllen, W. Pisula and D. S. Seferos, *Macromol. Rapid Commun.*, **2019**, *40*, 1800596; (b) W. Xing, P. Ye, J. Lu, X. Wu, Y. Chen, T. Zhu, A. Peng and H. Huang, *J. Power Sources*, **2018**, *401*, 13–19.
5. G. He, W. Torres Delgado, D. J. Schatz, C. Merten, A. Mohammadpour, L. Mayr, M. J. Ferguson, R. McDonald, A. Brown, K. Shankar and E. Rivard, *Angew. Chem., Int. Ed.*, **2014**, *53*, 4587–4591.
6. (a) G. He, B. D. Wiltshire, P. Choi, A. Savin, S. Sun, A. Mohammadpour, M. J. Ferguson, R. McDonald, S. Farsinezhad, A. Brown, K. Shankar and E. Rivard, *Chem. Commun.*, **2015**, *51*, 5444–5447; (b) W. Torres Delgado, C. A. Braun, M. P. Boone, O. Shynkaruk, Y. Qi, R. McDonald, M. J. Ferguson, P. Data, S. K. C. Almeida, I. de Aguiar, G. L. C. de Souza, A. Brown, G. He and E. Rivard, *ACS Appl. Mater. Interfaces*, **2018**, *10*, 12124–12134; (c) E. Hupf, Y. Tsuchiya, W. Moffat, L. Xu, M. Hirai, Y. Zhou, M. J. Ferguson, R. McDonald, T. Murai, G. He and E. Rivard, *Inorg. Chem.*, **2019**, *58*, 13323–13336.

7. R. D. Pensack, Y. Song, T. M. McCormick, A. A. Jahnke, J. Hollinger, D. S. Seferos and G. D. Scholes, *J. Phys. Chem. B*, **2014**, *118*, 2589–2597.
8. L. Yang, W. Gu, L. Lv, Y. Chen, Y. Yang, P. Ye, J. Wu, L. Hong, A. Peng and H. Huang, *Angew. Chem., Int. Ed.*, **2018**, *57*, 1096–1102.
9. B. T. Luppi, D. Majak, M. Gupta, E. Rivard and K. Shankar, *J. Mater. Chem. A*, **2019**, *7*, 2445–2463.
10. S. Ye, M. Steube, E. I. Carrera and D. S. Seferos, *Macromolecules*, **2016**, *49*, 1704–1711.
11. (a) W. Torres Delgado, F. Shahin, M. J. Ferguson, R. McDonald, G. He and E. Rivard, *Organometallics*, **2016**, *35*, 2140–2148; (b) C. A. Braun, N. Martinek, Y. Zhou, M. J. Ferguson and E. Rivard, *Dalton Trans.*, **2019**, *48*, 10210–10219.
12. For related studies, see: (a) B. Jiang and T. D. Tilley, *J. Am. Chem. Soc.*, **1999**, *121*, 9744–9745; (b) S. M. Parke, E. Hupf, G. K. Matharu, I. de Aguiar, L. Xu, H. Yu, M. P. Boone, G. L. C. de Souza, R. McDonald, M. J. Ferguson, G. He, A. Brown and E. Rivard, *Angew. Chem., Int. Ed.*, **2018**, *57*, 14841–14846; (c) S. Das and S. S. Zade, *Chem. Commun.*, **2010**, *46*, 1168–1170.
13. (a) K. Ohshimizu, A. Takahashi, Y. Rho, T. Higashihara, M. Ree and M. Ueda, *Macromolecules*, **2011**, *44*, 719–727; (b) For examples of monomeric (unpolymerized) 3-aryltellurophenes, see: V. Krishna Karapala, H.-P. Shih and C.-C. Han, *Org. Lett.*, **2018**, *20*, 1550–1554.

14. (a) I. Osaka and R. D. McCullough, *Acc. Chem. Res.*, **2008**, *41*, 1202–1214; (b) M. A. Baker, C.-H. Tsai and K. J. T. Noonan, *Chem. -Eur. J.*, **2018**, *50*, 13078–13088.
15. T. Yamamoto, A. Morita, Y. Miyazaki, T. Maruyama, H. Wakayama, Z. H. Zhou, Y. Nakamura, T. Kanbara, S. Sasaki and K. Kubota, *Macromolecules*, **1992**, *25*, 1214–1223.
16. C. Thiebes, G. K. Surya Prakash, N. A. Petasis and G. A. Olah, *Synlett*, **1998**, 141–142.
17. M. Kitano, T. Tanaka and A. Osuka, *Organometallics*, **2017**, *36*, 2559–2564.
18. Both **I-Te-5-I** and **I-Te-6-I** yield oligomers ($n \leq 4$) over time. This process takes months for **I-Te-6-I** but only days for **I-Te-5-I**. 2,5-Dibromoselenophenes are known to undergo the same process in the solid state: A. Patra, Y. H. Wijsboom, S. S. Zade, M. Li, Y. Sheynin, G. Leitius and M. Bendikov, *J. Am. Chem. Soc.*, **2008**, *130*, 6734–6736.
19. S. S. Zade and M. Bendikov, *Chem. -Eur. J.*, **2007**, *13*, 3688–3700.
20. For additional leading reviews on this topic, see: (a) K. Okamoto and C. K. Luscombe, *Polym. Chem.*, **2011**, *2*, 2424–2434; (b) J. P. Lutz, M. D. Hannigan and A. J. McNeil, *Coord. Chem. Rev.*, **2018**, *376*, 225–247.
21. (a) A. Patra, Y. H. Wijsboom, G. Leitius and M. Bendikov, *Org. Lett.*, **2009**, *11*, 1487–1490; (b) T. Johansson, W. Mammo, M. Svensson, M. R. Andersson and O. Inganäs, *J. Mater. Chem.*, **2003**, *13*, 1316–1323; (c) Y. Li, Y. Cao, J. Gao, D. Wang, G. Yu and A. J. Heeger, *Synth. Met.*, **1999**, *99*, 243–248.

22. S. Rühle, *Sol. Energy*, **2016**, *130*, 139–147.
23. D. Barnes-Seeman, M. Jain, L. Bell, S. Ferreira, S. Cohen, X.-H. Chen, J. Amin, B. Snodgrass and P. Hatsis, *ACS Med. Chem. Lett.*, **2013**, *4*, 514–516.
24. V. Gandon, D. Leca, T. Aechtner, K. P. C. Vollhardt, M. Malacria and C. Aubert, *Org. Lett.*, **2004**, *6*, 3405–3407.
25. J. Lozada, Z. Liu and D. M. Perrin, *J. Org. Chem.*, **2014**, *79*, 5365–5368.
26. J. L. Dutton, G. J. Farrar, M. J. Sgro, T. L. Battista and P. J. Ragogna, *Chem. - Eur. J.*, **2009**, *15*, 10263–10271.
27. T. R. Hoye, B. M. Eklov and M. Voloshin, *Org. Lett.*, **2004**, *6*, 2567–2570.
28. A. Krasovskiy and P. Knochel, *Synthesis*, **2006**, *5*, 890–891.
29. E. L. Tyson, M. S. Ament and T. P. Yoon, *J. Org. Chem.*, **2013**, *78*, 2046–2050.
30. J. K. Yano, T. T. Denton, M. A. Cerny, X. Zhang, E. F. Johnson and J. R. Cashman, *J. Med. Chem.*, **2006**, *49*, 6987–7001.
31. M. A. Truong, S. Fukuta, T. Koganezawa, Y. Shoji, M. Ueda and T. Higashihara, *J. Polym. Sci. Part A Polym. Chem.*, **2015**, *53*, 875–887.
32. G. M. Sheldrick, *Acta Cryst. A* **2015**, *71*, 3–8.
33. P. T. Beurskens, G. Beurskens, R. de Gelder, J. M. M. Smits, S. Garcia-Granda and R. O. Gould, The DIRDIF-2008 program system, Crystallography Laboratory, Radboud University Nijmegen, The Netherlands.
34. A. D. Becke, *J. Chem. Phys.*, **1993**, *98*, 5648–5652.
35. C. Lee, W. Yang and R. G. Parr, *Phys. Rev. B*, **1988**, *37*, 785–789.
36. A. Bennett, W. A. Shirley, M. A. Al-Laham, T. G. Tensfeldt, G. A. Petersson

- and J. Mantzaris, *J. Chem. Phys.*, **2002**, *89*, 2193–2218.
37. G. A. Petersson and M. A. Al-Laham, *J. Chem. Phys.*, **1991**, *94*, 6081–6090.
38. W. R. Wadt and P. J. Hay, *J. Chem. Phys.*, **1985**, *82*, 284–298.
39. M. J. Frisch, G. W. Trucks, H. B. Schlegel, G. E. Scuseria, M. A. Robb, J. R. Cheeseman, G. Scalmani, V. Barone, G. A. Petersson, H. Nakatsuji, M. C. X. Li, A. Marenich, J. Bloino, B. G. Janesko, R. Gomperts, B. Mennucci, H. P. Hratchian, J. V. Ortiz, A. F. Izmaylov, J. L. Sonnenberg, D. Williams-Young, F. Ding, F. Lipparini, F. Egidi, J. Goings, B. Peng, A. Petrone, T. Henderson, D. Ranasinghe, V. G. Zakrzewski, J. Gao, N. Rega, G. Zheng, W. Liang, M. Hada, M. Ehara, K. Toyota, R. Fukuda, J. Hasegawa, M. Ishida, T. Nakajima, Y. Honda, O. Kitao, H. Nakai, T. Vreven, K. Throssell, J. A. J. Montgomery, J. E. Peralta, F. Ogliaro, M. Bearpark, J. J. Heyd, E. Brothers, K. N. Kudin, V. N. Staroverov, T. Keith, R. Kobayashi, J. Normand, K. Raghavachari, A. Rendell, J. C. Burant, S. S. Iyengar, J. Tomasi, M. Cossi, J. M. Millam, M. Klene, C. Adamo, R. Cammi, J. W. Ochterski, R. L. Martin, K. Morokuma, O. Farkas, J. B. Foresman and D. J. Fox, Gaussian 09, Revision A.02, *Gaussian, Inc., Wallingford CT*.
40. M. J. Frisch, G. W. Trucks, H. B. Schlegel, G. E. Scuseria, M. A. Robb, J. R. Cheeseman, G. Scalmani, V. Barone, G. A. Petersson, H. Nakatsuji, X. Li, M. Caricato, A. V. Marenich, J. Bloino, B. G. Janesko, R. Gomperts, B. Mennucci, H. P. Hratchian, J. V. Ortiz, A. F. Izmaylov, J. L. Sonnenberg, D. Williams-Young, F. Ding, F. Lipparini, F. Egidi, J. Goings, B. Peng, A. Petrone, T.

Henderson, D. Ranasinghe, V. G. Zakrzewski, J. Gao, N. Rega, G. Zheng, W. Liang, M. Hada, M. Ehara, K. Toyota, R. Fukuda, J. Hasegawa, M. Ishida, T. Nakajima, Y. Honda, O. Kitao, H. Nakai, T. Vreven, K. Throssell, J. A. J. Montgomery, J. E. Peralta, F. Ogliaro, M. J. Bearpark, J. J. Heyd, E. N. Brothers, K. N. Kudin, V. N. Staroverov, T. A. Keith, R. Kobayashi, J. Normand, K. Raghavachari, A. P. Rendell, J. C. Burant, S. S. Iyengar, J. Tomasi, M. Cossi, J. M. Millam, M. Klene, C. Adamo, R. Cammi, J. W. Ochterski, R. L. Martin, K. Morokuma, O. Farkas, J. B. Foresman and D. J. Fox, Gaussian 16, Revision B.01, *Gaussian, Inc., Wallingford CT*.

41. M. D. Hanwell, D. E. Curtis, D. C. Lonie, T. Vandermeersch, E. Zurek and G. R. Hutchison, *J. Cheminf.*, **2012**, *4*, 17.

Chapter 3:

1. A. G. MacDiarmid, *Angew. Chem. Int. Ed.*, **2001**, *40*, 2581–2590.
2. A. J. Heeger, *Angew. Chem. Int. Ed.*, **2001**, *40*, 2591–2611.
3. N. Suzuki, M. Ozaki, S. Etemad, A. J. Heeger and A. G. MacDiarmid, *Phys. Rev. Lett.*, **1980**, *45*, 1209–1213.
4. (a) B.-B. Cui, J.-H. Tang, J. Yao and Y.-W. Zhong, *Angew. Chem. Int. Ed.*, **2015**, *54*, 9192–9197; (b) M. Wałęsa-Chorab and W. G. Skene, *ACS Appl. Mater. Interfaces*, **2017**, *9*, 21524–21531; (c) Q. Hao, Z.-J. Li, B. Bai, X. Zhang, Y.-W. Zhong, L.-J. Wan and D. Wang, *Angew. Chem. Int. Ed.*, **2021**, *60*, 12498–12503

5. M. Casalino, G. Coppola, R. M. De La Rue and D. F. Logan, *Laser Photonics Rev.*, **2016**, *10*, 895–921.
6. (a) J. M. Pochan, D. F. Pochan, H. Rommelmann and H. W. Gibson, *Macromolecules*, **1981**, *14*, 110–114; (b) T. Masuda, B. Z. Tang, T. Higashimura and H. Yamaoka, *Macromolecules*, **1985**, *18*, 2369–2373.
7. E. J. Ginsburg, C. B. Gorman, S. R. Marder and R. H. Grubbs, *J. Am. Chem. Soc.*, **1989**, *111*, 7621–7622.
8. (a) A. A. Jahnke, B. Djukic, T. M. McCormick, E. Buchaca Domingo, C. Hellman, Y. Lee and D. S. Seferos, *J. Am. Chem. Soc.*, **2013**, *135*, 951–954; (b) G. He, L. Kang, W. Torres Delgado, O. Shynkaruk, M. J. Ferguson, R. McDonald and E. Rivard, *J. Am. Chem. Soc.*, **2013**, *135*, 5360–5363; (c) B. T. Luppi, R. McDonald, M. J. Ferguson, L. Sang and E. Rivard, *Chem. Commun.*, **2019**, *55*, 14218–14221; (d) H.-H. Liu, W.-W. Liang, Y.-Y. Lai, Y.-C. Su, H.-R. Yang, K.-Y. Cheng, S.-C. Huang and Y.-J. Cheng, *Chem. Sci.*, **2020**, *11*, 3836–3844; (e) S. M. Parke, M. P. Boone and E. Rivard, *Chem. Commun.*, **2016**, *52*, 9485–9505.
9. (a) S. R. Forrest, *Nature*, **2004**, *428*, 911–918; (b) L. Dou, Y. Liu, Z. Hong, G. Li and Y. Yang, *Chem. Rev.*, **2015**, *115*, 12633–12665; (c) L. Lu, T. Zheng, Q. Wu, A. M. Schneider, D. Zhao and L. Yu, *Chem. Rev.*, **2015**, *115*, 12666–12731.

10. Z. Miao, S. A. Gonsales, C. Ehm, F. Mentink-Vigier, C. R. Bowers, B. S. Sumerlin and A. S. Veige, *Nat. Chem.*, **2021**, DOI: 10.1038/s41557-021-00713-2.
11. B. R. Boswell, C. M. F. Mansson, J. M. Cox, Z. Jin, J. A. H. Romaniuk, K. P. Lindquist, L. Cegelski, Y. Xia, S. A. Lopez and N. Z. Burns, *Nat. Chem.*, **2021**, *13*, 41–46.
12. (a) J. W. Y. Lam and B. Z. Tang, *Acc. Chem. Res.*, **2005**, *38*, 745–754; (b) J. Z. Sun, A. Qin and B. Z. Tang, *Polym. Chem.*, **2013**, *4*, 211–223; (c) K. Akagi, *Chem. Rev.*, **2009**, *109*, 5354–5401; (d) K. Shimomura, T. Ikai, S. Kanoh, E. Yashima and K. Maeda, *Nat. Chem.*, **2014**, *6*, 429–434.
13. (a) F. L. Klavetter and R. H. Grubbs, *J. Am. Chem. Soc.*, **1988**, *110*, 7807–7813; (b) J. S. Moore, C. B. Gorman and R. H. Grubbs, *J. Am. Chem. Soc.*, **1991**, *113*, 1704–1712; (c) C. B. Gorman, E. J. Ginsburg and R. H. Grubbs, *J. Am. Chem. Soc.*, **1993**, *115*, 1397–1409; (d) O. A. Scherman and R. H. Grubbs, *Synth. Met.*, **2001**, *124*, 431–434; (e) B. L. Langsdorf, X. Zhou, D. H. Adler and M. C. Lonergan, *Macromolecules*, **1999**, *32*, 2796–2798; (f) M. C. Lonergan, C. H. Cheng, B. L. Langsdorf, and X. Zhou, *J. Am. Chem. Soc.*, **2002**, *124*, 690–701.
14. (a) M. J. Sailor, E. J. Ginsburg, C. B. Gorman, A. Kumar, R. H. Grubbs and N. S. Lewis, *Science*, **1990**, *249*, 1146–1149; (b) T. H. Jozefiak, E. J. Ginsburg, C. B. Gorman, R. H. Grubbs and N. S. Lewis, *J. Am. Chem. Soc.*, **1993**, *115*, 4705–4713.

15. (a) K.-Y. Yoon, I.-H. Lee, K. O. Kim, J. Jang, E. Lee and T.-L. Choi, *J. Am. Chem. Soc.*, **2012**, *134*, 14291–14294; (b) S. Shin, K.-Y. Yoon and T.-L. Choi, *Macromolecules*, **2015**, *48*, 1390–1397; (c) K.-Y. Yoon, S. Shin, Y.-J. Kim, I. Kim, E. Lee and T.-L. Choi, *Macromol. Rapid Commun.*, **2015**, *36*, 1069–1074.
16. A. Krebs and D. Byrd, *Liebigs Ann. Chem.*, **1967**, *707*, 66–74.
17. J. A. Love, J. P. Morgan, T. M. Trnka and R. H. Grubbs, *Angew. Chem., Int. Ed.*, **2002**, *41*, 4035–4037.
18. S. M. Parke, S. Tanaka, H. Yu, E. Hupf, M. J. Ferguson, Y. Zhou, K. Naka and E. Rivard, *Macromolecules*, **2019**, *52*, 7477–7488.
19. C. A. Harmon and A. J. Streitwieser, *J. Org. Chem.*, **1972**, *38*, 549–551.
20. (a) A. Krebs, *Angew. Chem., Int. Ed. Engl.*, **1965**, *4*, 953–954; (b) S. J. Peters, M. R. Turk, M. K. Kiesewetter and C. D. Stevenson, *J. Am. Chem. Soc.*, **2003**, *125*, 11264–11268.
21. A. S. Lankey and M. A. Ogliaruso, *J. Org. Chem.*, **1971**, *36*, 3339–3342.
22. (a) Y. Ren and F. Jäkle, *Dalton Trans.*, **2016**, *45*, 13996–14007; (b) F. Jäkle, *Chem. Rev.*, **2010**, *110*, 3985–4022; (c) M. Elbing and G. C. Bazan, *Angew. Chem. Int. Ed.*, **2008**, *47*, 834–838; (d) C. R. Wade, A. E. J. Broomsgrove, S. Aldridge and F. P. Gabbaï, *Chem. Rev.*, **2010**, *110*, 3958–3984; (e) S. M. Berger, M. Fergner and T. B. Marder, *Chem. -Eur. J.*, **2021**, *27*, 7043–7058.
23. M. Wang, F. Nudelman, R. R. Matthes and M. P. Shaver, *J. Am. Chem. Soc.*, **2017**, *139*, 14232–14236.

24. N. M. D. Brown, F. Davidson and J. W. Wilson, *J. Organomet. Chem.*, **1981**, *209*, 1–11.
25. R. I. Walter, *J. Am. Chem. Soc.*, **1955**, *77*, 5999–6002.
26. P. Bujak, I. Kulszewicz-Bajer, M. Zagorska, V. Maurel, I. Wielgus and A. Pron, *Chem. Soc. Rev.*, **2013**, *42*, 8895–8999.
27. (a) H. K. Mackenzie, B. W. Rawe, K. Samedov, H. T. G. Walsgrove, A. Uva, Z. Han and D. P. Gates, *J. Am. Chem. Soc.*, **2020**, *142*, 10319–10324; (b) T. Baumgartner, *Acc. Chem. Res.*, **2014**, *47*, 1613–1622; (c) L. A. Vanderark, T. J. Clark, E. Rivard, I. Manners, J. C. Slootweg and K. Lammertsma, *Chem. Commun.*, **2006**, 3332–3333; (d) H. Dorn, R. A. Singh, J. A. Massey, J. M. Nelson, C. A. Jaska, A. J. Lough and I. Manners, *J. Am. Chem. Soc.*, **2000**, *122*, 6669–6678.
28. M. Carnes, D. Buccella, J. Decatur, M. L. Steigerwald and C. Nuckolls, *Angew. Chem. Int. Ed.*, **2008**, *47*, 2982–2985.
29. (a) H. Jiang, P. Taranekar, J. R. Reynolds and K. S. Schanze, *Angew. Chem. Int. Ed.*, **2009**, *48*, 4300–4316; (b) M. M. Obadia and E. Drockenmuller, *Chem. Commun.*, **2016**, *52*, 2433–2450.
30. (a) C. R. Wade, A. E. J. Broomsgrove, S. Aldridge and F. P. Gabbaï, *Chem. Rev.*, **2010**, *110*, 3958–3984; (b) J. Feng, L. Xiong, S. Wang, S. Li, Y. Li and G. Yang, *Adv. Funct. Mater.*, **2013**, *23*, 340–345.
31. (a) W. Kaim and A. Schulz, *Angew. Chem. Int. Ed. Engl.*, **1984**, *23*, 615–616; (b) J. Fiedler, S. Zališ, A. Klein, F. M. Hornung and W. Kaim, *Inorg. Chem.*,

- 1996, 35, 3039–3043; (c) W. Kaim, N. S. Hosmane, S. Záliš, J. A. Maguire and W. N. Lipscomb, *Angew. Chem. Int. Ed.*, **2009**, 48, 5082–5091.
32. (a) Z. Wu, Y. Zhai, H. Kim, J. D. Azoulay and T. N. Ng, *Acc. Chem. Res.*, **2018**, 51, 3144–3153; (b) Q. Li, Y. Guo, Y. Liu, *Chem. Mater.*, **2019**, 31, 6359–6379.
33. (a) B. O. Pray, L. H. Sommer, G. M. Goldberg, G. T. Kerr, P. A. Di Giorgio and F. C. Whitmore, *J. Am. Chem. Soc.*, **1948**, 70, 433–434; (b) R. I. Damja, C. Eaborn and W.-C. Sham, *J. Organomet. Chem.*, **1985**, 291, 25–33; (c) G. A. Ayoko and C. Eaborn, *J. Chem. Soc. Perkin Trans. 2*, **1987**, 381–383.
34. Y. Aramaki, H. Omiya, M. Yamashita, K. Nakabayashi, S. Ohkoshi and K. Nozaki, *J. Am. Chem. Soc.*, **2012**, 134, 19989–19992.
35. (a) E. T. Denisov, *Kinet. Catal.*, **2006**, 47, 662–671; (b) E. Kumli, F. Montermini and P. Renaud, *Org. Lett.*, **2006**, 8, 5861–5864.
36. A. M. Harned, H. S. He, P. H. Toy, D. L. Flynn and P. R. Hanson, *J. Am. Chem. Soc.*, **2005**, 127, 52–53.
37. J. Gasteiger, G. E. Gream, R. Huisgen, W. E. Konz and U. Schnegg, *Chem. Ber.*, **1971**, 104, 2412–2419.
38. M. A. Ogliaruso and A. S. Lankey, *J. Org. Chem.*, **1971**, 36, 3339–3342.
39. M. Cooke, C. R. Russ and F. G. A. Stone, *J. Chem. Soc., Dalton Trans.*, **1975**, 256–259.
40. C. Li, S. K. Mellerup, X. Wang and S. Wang, *Organometallics*, **2018**, 37, 3360–3367.

41. S. W. Kwok, J. R. Fotsing, R. J. Fraser, V. O. Rodionov and V. V. Fokin, *Org. Lett.*, **2010**, *12*, 4217–4219.
42. N. A. Yakelis and R. G. Bergman, *Organometallics*, **2005**, *24*, 14, 3579–3581.
43. T. Ono, M. Ohta and K. Sada, *ACS Macro Lett.*, **2012**, *1*, 1270–1273.
44. A. F. Burchat, J. M. Chong and N. Nielsen, *J. Organomet. Chem.*, **1997**, *542*, 281–283.
45. Ł. Kapuśniak, P. N. Plessow, D. Trzybiński, K. Woźniak, P. Hofmann and P. I. Jolly, *Organometallics*, **2021**, *40*, 693–701.
46. G. M. Sheldrick, *Acta Cryst. A*, **2015**, *71*, 3–8
47. P. T. Beurskens, G. Beurskens, R. de Gelder, J. M. M. Smits, S. Garcia-Granda and R. O. Gould, The DIRDIF-2008 program system, Crystallography Laboratory, Radboud University Nijmegen, The Netherlands.
48. A. D. Becke, *J. Chem. Phys.*, **1993**, *98*, 5648–5652.
49. C. Lee, W. Yang and R. G. Parr, *Phys. Rev. B*, **1988**, *37*, 785–789.
50. T. Yanai, D. P. Tew and N. C. Handy, *Chem. Phys. Lett.*, **2004**, *393*, 51–57.
51. J.-D. Chai and M. Head-Gordon, *Phys. Chem. Chem. Phys.*, **2008**, *10*, 6615–6620.
52. T. H. Dunning, Jr., *J. Chem. Phys.*, **1989**, *90*, 1007–1023.
53. A. Bennett, W. A. Shirley, M. A. Al-Laham, T. G. Tensfeldt, G. A. Petersson and J. Mantzaris, *J. Chem. Phys.*, **2002**, *89*, 2193–2218.
54. G. A. Petersson and M. A. Al-Laham, *J. Chem. Phys.*, **1991**, *94*, 6081–6090.

55. M. J. Frisch, G. W. Trucks, H. B. Schlegel, G. E. Scuseria, M. A. Robb, J. R. Cheeseman, G. Scalmani, V. Barone, G. A. Petersson, H. Nakatsuji, M. C. X. Li, A. Marenich, J. Bloino, B. G. Janesko, R. Gomperts, B. Mennucci, H. P. Hratchian, J. V. Ortiz, A. F. Izmaylov, J. L. Sonnenberg, D. Williams-Young, F. Ding, F. Lipparini, F. Egidi, J. Goings, B. Peng, A. Petrone, T. Henderson, D. Ranasinghe, V. G. Zakrzewski, J. Gao, N. Rega, G. Zheng, W. Liang, M. Hada, M. Ehara, K. Toyota, R. Fukuda, J. Hasegawa, M. Ishida, T. Nakajima, Y. Honda, O. Kitao, H. Nakai, T. Vreven, K. Throssell, J. A. J. Montgomery, J. E. Peralta, F. Ogliaro, M. Bearpark, J. J. Heyd, E. Brothers, K. N. Kudin, V. N. Staroverov, T. Keith, R. Kobayashi, J. Normand, K. Raghavachari, A. Rendell, J. C. Burant, S. S. Iyengar, J. Tomasi, M. Cossi, J. M. Millam, M. Klene, C. Adamo, R. Cammi, J. W. Ochterski, R. L. Martin, K. Morokuma, O. Farkas, J. B. Foresman and D. J. Fox, Gaussian 09, Revision A.02, *Gaussian, Inc., Wallingford CT*.
56. M. D. Hanwell, D. E. Curtis, D. C. Lonie, T. Vandermeersch, E. Zurek and G. R. Hutchison, *J. Cheminf.*, **2012**, 4:17.

Chapter 4:

1. G. He, L. Kang, W. Torres Delgado, O. Shynkaruk, M. J. Ferguson, R. McDonald and E. Rivard, *J. Am. Chem. Soc.*, **2013**, 135, 5360–5363.
2. C. Duan, F. Huang and Y. Cao, *J. Mater. Chem.*, **2012**, 22, 10416–10434.
3. W. Torres Delgado, F. Shahin, M. J. Ferguson, R. McDonald, G. He and E. Rivard, *Organometallics*, **2016**, 35, 2140–2148.

4. A. A. Jahnke, B. Djukic, T. M. McCormick, E. Buchaca Domingo, C. Hellmann, Y. Lee and D. S. Seferos, *J. Am. Chem. Soc.*, **2013**, *135*, 951–954.
5. (a) A. Kiriy, V. Senkovskyy and M. Sommer, *Macromol. Rapid Commun.*, **2011**, *32*, 1503–1517; (b) R. Tkachov, V. Senkovskyy, H. Komber and A. Kiriy, *Macromolecules*, **2011**, *44*, 2006–2015.
6. (a) S. Ye, M. Steube, E. I. Carrera and D. S. Seferos, *Macromolecules*, **2016**, *49*, 1704–1711; (b) S. Ye, S. M. Foster, A. A. Pollit, S. Cheng and D. S. Seferos, *Chem. Sci.*, **2019**, *10*, 2075–2080.
7. (a) Q. Li, Y. Guo and Yunqi Liu, *Chem. Mater.*, **2019**, *31*, 6359–6379; (b) M. Casalino, G. Coppola, R. M. De La Rue and D. F. Logan, *Laser Photonics Rev.*, **2016**, *10*, 895–921.
8. (a) H. Murata, D. Miyajima, R. Takada and H. Nishide, *Polym. J.*, **2005**, *37*, 818–825; (b) H. Murata, D. Miyajima and H. Nishide, *Macromolecules*, **2006**, *39*, 6331–6335; (c) P. Bujak, I. Kulszewicz-Bajer, M. Zagorska, V. Maurel, I. Wielgusa and A. Pron, *Chem. Soc. Rev.*, **2013**, *42*, 8895–8999.
9. (a) K.-Y. Yoon, I.-H. Lee, K. O. Kim, J. Jang, E. Lee and T.-L. Choi, *J. Am. Chem. Soc.*, **2012**, *134*, 14291–14294; (b) S. Shin, K.-Y. Yoon and T.-L. Choi, *Macromolecules*, **2015**, *48*, 1390–1397.
10. (a) L. Xiao, X. Chen, X. Yang, J. Sun and J. Geng, *ACS Appl. Polym. Mater.*, **2020**, *2*, 4273–4288; (b) L. R. MacFarlane, H. Shaikh, J. D. Garcia-Hernandez, M. Vespa, T. Fukui and I. Manners, *Nat. Rev. Mater.*, **2021**, *6*, 7–26

11. C. V. Hoven, H. Wang, M. Elbing, L. Garner, D. Winkelhaus and G. C. Bazan, *Nat. Mater.*, **2010**, *9*, 249–252.
12. C. A. Harmon and A. J. Streitwieser, *J. Org. Chem.*, **1972**, *38*, 549–551.
13. (a) D. W. Stephan and G. Erker, *Chem. Sci.*, **2014**, *5*, 2625–2641; (b) M. Wang, F. Nudelman, R. R. Matthes and M. P. Shaver, *J. Am. Chem. Soc.*, **2017**, *139*, 14232–14236.
14. (a) H. Jiang, P. Taranekekar, J. R. Reynolds and K. S. Schanze, *Angew. Chem. Int. Ed.*, **2009**, *48*, 4300–4316; (b) M. M. Obadia and E. Drockenmuller, *Chem. Commun.*, **2016**, *52*, 2433–2450.
15. Y. Wen and J. Xu, *Polym. Sci. A Polym. Chem.*, **2017**, *55*, 1121–1150.
16. L. Dou, Y. Liu, Z. Hong, G. Li and Y. Yang, *Chem. Rev.*, **2015**, *115*, 12633–12665.